

Geotechnologies and the Environment

Kory Konsoer
Michael Leitner
Quinn Lewis *Editors*

sUAS Applications in Geography

 Springer

Geotechnologies and the Environment

Volume 24

Series Editors

Jay D. Gatrell, Department of Geology & Geography, Eastern Illinois University,
Charleston, IL, USA

Ryan R. Jensen, Department of Geography, Brigham Young University, Provo, UT,
USA

The *Geotechnologies and the Environment* series is intended to provide specialists in the geotechnologies and academics who utilize these technologies, with an opportunity to share novel approaches, present interesting (sometimes counter-intuitive) case studies, and most importantly to situate GIS, remote sensing, GPS, the internet, new technologies, and methodological advances in a real world context. In doing so, the books in the series will be inherently applied and reflect the rich variety of research performed by geographers and allied professionals. Beyond the applied nature of many of the papers and individual contributions, the series interrogates the dynamic relationship between nature and society. For this reason, many contributors focus on human-environment interactions. The series are not limited to an interpretation of the environment as nature per se. Rather, the series “places” people and social forces in context and thus explore the many socio-spatial environments humans construct for themselves as they settle the landscape. Consequently, contributions will use geotechnologies to examine both urban and rural landscapes.

Kory Konsoer • Michael Leitner • Quinn Lewis
Editors

sUAS Applications in Geography

 Springer

Editors

Kory Konsoer
Department of Geography and
Anthropology
Coastal Studies Institute
Louisiana State University
Baton Rouge, LA, USA

Michael Leitner
Geography and Anthropology
Louisiana State University
Baton Rouge, LA, USA

Quinn Lewis
Geography and Environmental
Management
University of Waterloo
Waterloo, ON, Canada

ISSN 2365-0575 ISSN 2365-0583 (electronic)
Geotechnologies and the Environment
ISBN 978-3-031-01975-3 ISBN 978-3-031-01976-0 (eBook)
<https://doi.org/10.1007/978-3-031-01976-0>

© The Editor(s) (if applicable) and The Author(s), under exclusive license to Springer Nature Switzerland AG 2022

This work is subject to copyright. All rights are solely and exclusively licensed by the Publisher, whether the whole or part of the material is concerned, specifically the rights of translation, reprinting, reuse of illustrations, recitation, broadcasting, reproduction on microfilms or in any other physical way, and transmission or information storage and retrieval, electronic adaptation, computer software, or by similar or dissimilar methodology now known or hereafter developed.

The use of general descriptive names, registered names, trademarks, service marks, etc. in this publication does not imply, even in the absence of a specific statement, that such names are exempt from the relevant protective laws and regulations and therefore free for general use.

The publisher, the authors and the editors are safe to assume that the advice and information in this book are believed to be true and accurate at the date of publication. Neither the publisher nor the authors or the editors give a warranty, expressed or implied, with respect to the material contained herein or for any errors or omissions that may have been made. The publisher remains neutral with regard to jurisdictional claims in published maps and institutional affiliations.

This Springer imprint is published by the registered company Springer Nature Switzerland AG
The registered company address is: Gewerbestrasse 11, 6330 Cham, Switzerland

Contents

1	How sUAS Has Pushed Forward On-Demand Low Altitude Remote Sensing in Geography	1
	Quinn Lewis, Kory Konsoer, and Michael Leitner	
2	UAS Policies, Workflows, and Challenges in Hazard Environments	13
	Melissa A. Wagner and Robert K. Doe	
3	sUAS-Based Citizen Science Studies in Geography	41
	Erin L. Bunting, Ethan J. Theuerkauf, and Lucas Rabins	
4	Using sUAS to Map and Quantify Changes to Native American Archaeological Sites Along Coastal Louisiana Due to Climate Change and Erosion	71
	Kory Konsoer, David Watt, Mark Rees, Macy Linton, Tad Britt, and Sam Huey	
5	A Comparison of Different Software Packages in sUAS-Based Land Feature Reconstruction	95
	Yingkui Li and Nathan McKinney	
6	Assessing the Role of sUAS Mission Design in the Accuracy of Digital Surface Models Derived from Structure-from-Motion Photogrammetry	123
	Daniel S. Hostens, Toby Dogwiler, Joshua W. Hess, Robert T. Pavlowsky, Jacob Bendix, and Derek T. Martin	
7	Drones and Poles for Low-Elevation Oil and Gas Environmental Surface Inspections	157
	Chris W. Baynard, Robert D. Richardson, and Nicolas W. Baynard	

8 Application of UAS to Detect Infrequent and Local Large-Scale Surficial Displacements: Critical Examples from the Fields of Landslide and Erosion Research 203
M. J. Stumvoll, M. Konzett, E. M. Schmaltz, and T. Glade

9 Polar and Cryospheric Remote Sensing Using sUAS 235
Clare B. Gaffey, Anshuman Bhardwaj, Karen E. Frey,
and Lyndon Estes

10 Coastal Dune Eco-geomorphology: sUAS Applications and Opportunities 263
Alex Smith, Brianna Lunardi, Elizabeth George, Jacob Lehner,
and Chris Houser

11 Using Small Unoccupied Aircraft Systems (sUAS) for Characterizing Rivers and Streams in Forested Environments 301
David A. Reid, Marwan A. Hassan, Carina Helm, and Steve Bird

Index 327

Chapter 1

How sUAS Has Pushed Forward On-Demand Low Altitude Remote Sensing in Geography



Quinn Lewis, Kory Konsoer, and Michael Leitner

Abstract Geography has been fundamentally altered by the development, proliferation, and maturation of small unoccupied aerial systems (sUAS). sUAS range from ultra-small, low-cost systems that provide simple still imagery used for qualitative analysis to expensive, technologically advanced systems that provide data with high spatial, temporal, and spectral resolutions. This chapter introduces and provides a brief background on how the sUAS revolution has broadly affected Geography. Background topics discussed include how sUAS fit among allied technologies like satellite-based remote sensing; the power of sUAS to increase spatial, temporal, and spectral resolution of imagery and image-derived data; the pros and cons of sUAS methodology and tools; and legal and practical considerations for sUAS operation. Book chapter contributions are then examined, before the future outlook of sUAS in Geography and allied disciplines is discussed. This chapter emphasizes that sUAS have brought on an era of “personal” or “on-demand” remote sensing, which has been and will continue to be critical for scholarly and research activities in Geography.

Keywords sUAS · Geography · Multispectral · Spatial data · Structure from motion

Q. Lewis (✉)

Geography and Environmental Management, University of Waterloo, Waterloo, ON, Canada
e-mail: quinn.lewis@uwaterloo.ca

K. Konsoer

Department of Geography and Anthropology, Coastal Studies Institute, Louisiana State University, Baton Rouge, LA, USA

M. Leitner

Geography and Anthropology, Louisiana State University, Baton Rouge, LA, USA

1.1 Introduction

Geography is a broad and eclectic discipline, covering topics that include societies, cultures, economics, politics, ecosystems, climatology, and geomorphology. Despite the diversity in these subfields, the commonality among them is their inherent link to *spatial* data. Whether quantifying the distribution of grain size in small rivers (Reid et al., Chap. 11, this volume), assessing tourism activities for analysis of safety and security (Song and Ko 2017), and assessing the spatial extent of damage following a natural hazard (Wagner and Doe, Chap. 2, this volume), geographers use this lens of spatial analysis to conduct their research. Spatial data is central to any geographer's research, and thus the ways in which spatial data are obtained are a key methodological consideration within the discipline.

Traditionally, a trade-off has existed between spatial and temporal data resolution and areal coverage of data (Goodchild 2011). Geographers must balance the cost of obtaining data with the required amount of detail necessary to answer their research questions in terms of money, time, and human resource investment. Often the nature of questions that can be asked and answered depends on, or is limited by, the quality and quantity of spatial data that can reasonably be obtained (Lloyd 2014). A study of grain size distribution on a river point bar requires highly precise data at high resolution over a small area (Woodget et al. 2018), a study of crowd dynamics and individual movement requires nearly instantaneous data (Nagrare et al. 2021), and studies focusing on natural hazards might require a combination both high-resolution and large-scale data (Giordan et al. 2017). Improvements in technology can help offset this relationship between data coverage and data resolution, and geographers have often led this technological advancement with their close work on and with geospatial technology like global positioning systems (GPS), geographic information systems (GIS), and online spatial data capture and analysis (Goodchild 1991; Armstrong et al. 2019).

The development and maturation of small unoccupied aerial systems (sUAS) represent a considerable expansion to the geographer's toolkit. sUAS can bridge the gap between large coverage and low detail spatial observation techniques, like satellite imagery acquisition, with small coverage and high detail methods such as on-the-ground surveying and close-range photogrammetry (Anderson et al. 2019). sUAS can directly measure data such as spatial location through GPS or wind speed and altitude from on-board sensors. When coupled with a high-resolution camera, sUAS can obtain photographs that can be used for direct qualitative observation or measurement of geographical data through construction of orthorectified photographs. Secondary data can be constructed with these images, such as three-dimensional (3D) models computed with photogrammetric methods (Anderson et al. 2019) and land cover/land usage information from orthophotograph interpretation (Natesan et al. 2018). In addition, sUAS and sensor technology have improved, while costs have decreased such that sUAS can be equipped with light detection and ranging (lidar) and hyperspectral image capturing devices (Lewis et al. 2020). sUAS can also be rapidly employed or used in a variety of roles in a single

study, as they can be used to obtain spatial data on scales ranging from 10^0 to 10^3 square meters in a matter of minutes or be used to detect changes with high temporal resolution. Thus, the combination of low cost, flexibility, ease of use, and variety of equipped sensors characteristic of modern sUAS has helped to revolutionize the ways in which geographers obtain and analyze spatial data.

1.2 Background

Imagery is essential to many subdisciplines within Geography and is the basis for much innovation provided by sUAS. Aerial photographs have been used to better understand spatial relationships since the nineteenth century and is still commonly used as a relatively simple and low-cost way to analyze landscapes and obtain spatial data (Paine and Kiser 2012). Since the advent and development of orbital and geo-stationary satellites starting in the 1960s and continuing to the present day (including the 2021 launch of Landsat 9), geographers have also been able to obtain imagery over large regions in the visible spectrum and beyond. Thus, as technologies have improved, our improving ability to collect spatial data across various spatial and temporal scales has transformed the science of Geography. For example, the Landsat series of satellites provide remotely sensed data over large spatial extents, yielding uniform gridded data with spatial resolutions ranging from 1 to 30 m (Lulla 1983; Masek et al. 2020). These satellites acquire different bands of electromagnetic energy (multispectral), including visible light (blue, green, red), near-infrared (NIR), shortwave infrared (SWIR), thermal infrared (TIR), and panchromatic. However, satellites such as Landsat and other commonly used platforms in Geography have significant drawbacks. Satellites not in a geosynchronous orbit are limited in temporal resolution of the spatial data, which can be a major hindrance to studying many aspects of geographic research. In addition, some geographic processes and landforms of interest change on time scales between seconds to days or on spatial scales less than 1 square meter, meaning satellites are incapable of obtaining these data.

The spatial and temporal resolution of spatial data recorded with geodetic and surveying equipment is not as limited as satellite data. Global Navigation Satellite Systems (GNSS) have allowed researchers to directly collect spatial data in real-world coordinates (e.g., latitude/longitude), and with the introduction of real-time kinematic (RTK) and post-processed kinematic (PPK) solutions, these data can obtain centimetric level accuracy. Traditional surveying techniques such as those with a rod and level or laser surveying equipment can also achieve high spatial accuracy, but these methods require direct line of sight between the surveyor and the object and are thus time-consuming and challenging to use over large or diverse terrains or in rapidly changing conditions. Terrestrial laser scanning (TLS) more easily provides numerous data points quickly but also suffers from line-of-sight requirements and can be prohibitively expensive (Lemmens 2011). Although GNSS, traditional surveying, and TLS methods allow for highly accurate positional data, acquisition time and accessibility to areas of scientific interest often limit the ability

to collect positional data over large areas. As a result, surveys of large areas are often conducted using a sparse density of points or over multiple days or weeks during which time the conditions of interests may have changed. Lidar- and camera-equipped airplanes are also useful for obtaining high-resolution topographical information over relatively large areas, but acquiring this data can be expensive and unfit for certain situations, such as measurements of vertical landscape faces or when details on the order of cm in size are of interest (Carter et al. 2018).

One of the most important reasons why sUAS has been transformative in Geography is their ability to bridge the spatial gap between ground-based measurements and large-scale aerial photograph, satellite image, and lidar acquisition. The major advantage of sUAS is their flexibility: sUAS can fly at altitudes ranging from only a few meters to thousands of meters above the ground (within legal restrictions) and can carry a range of sensors. Some sUAS can carry relatively heavy sensors, like lidar systems complete with inertial measurement units (IMUs) that provide cm-level accuracy (Lewis et al. 2020), though technological advancement continues to decrease sensor size and allow for easier integration with light and low-cost systems. sUAS can be deployed quickly and can be operated manually for a flight of only a few minutes, which can be important for rapidly developing situations such as disaster relief and hazard management (Tanzi et al. 2016). Yet they can also follow detailed pre-planned flightpaths and with extra batteries and a field charging system can fly for hours a day for many days in a row. This is a considerable advantage over other methods that attempt to move beyond ground-based measurements, such as pole photography (Visser et al. 2019), which has a limited altitude and coverage area, and balloon-based photography (Boike and Yoshikawa 2003), which can be difficult to finely control. As opposed to the relatively low spatial and temporal resolution of satellite imagery, sUAS can essentially have an unlimited return period and can obtain images with spatial resolution limited only by the quality of the camera and the flight altitude.

There are significant disadvantages to using sUAS, however. These include legal limits and requirements such as permission required to fly in restricted zones, flight altitude restrictions, weight limits, flight time limits, the restriction to relatively light (< about 20 kg) payloads, poor weather or atmospheric conditions, and technological or piloting failures such as runaways and crashes. sUAS can operate in moderately windy conditions (up to about 10 m/s), but excessive wind, rain, high elevations, and shadows and sunlight glare can degrade the ability to fly the sUAS or the quality of imagery obtained. While most consumer-grade sUAS are equipped with gimbals, sUAS movement and rolling shutter effects of on-board cameras can also become an issue for some image-processing techniques (Lewis et al. 2018). sUAS technology is also still relatively young, so lack of technological support and rapid obsolescence of systems can be a problem. Regardless of these drawbacks, many subfields of Geography have benefitted immensely from the proliferation of sUAS (Green 2020).

sUAS are differentiated from “toy” sUAS and military/specialist UAS based on weight. Toy sUAS (less than 0.55 lbs. in the United States) do not require licensure to operate and rarely have sensors like cameras. Military-grade and specialist commercial UAS (greater than 55 lbs. in the United States) require considerable

operational skills and legal permits to operate (Stöcker et al. 2017). Both fixed-wing and propeller-driven (quad-, hexa-, or octo-copter) sUAS are commonly used for research in Geography; fixed-wing aircraft generally are capable of longer flights with heavier sensors than propeller-driven systems. Propeller-driven systems mimic the advantages of helicopters over airplanes, mainly in their ability to hover and take off/land in relatively close quarters, although continuing advancements in sUAS technology have recently seen the development of a fixed-wing aircraft with vertical take-off and landing (VTOL) capability (e.g., Wingtra; <https://wingtra.com/>). Both types of commonly used sUAS can be relatively simple to operate, requiring only a smartphone on the lower end of cost and on-board technology. On the higher end, these systems can integrate RTK or PPK GNSS solutions as well as IMU data to maintain high levels of positional accuracy – these systems are more complicated to set up and operate and may require a team of researchers to fly and operate sensors such as lidar or hyperspectral sensors.

Given the relatively low cost and simplicity of basic sUAS commonly used for research in Geography, it is not surprising that recreational use by citizens and by those employed in industry or government is common. Citizens use sUAS for work such as photography, real estate, and infrastructure monitoring (Lewis and Park 2018; Wood et al. 2021). The low cost of sUAS serves to equip these citizens with tools that can be used for scientific purposes, and thus sUAS have the potential to improve the quality and quantity of spatial data obtained from citizen science projects (Wood et al. 2021). Citizens can be directly involved with data acquisition, and imagery already obtained by citizens can be used to support geographical research (Lewis and Park 2018). Citizens equipped with sUAS can be especially helpful for observation of geographical phenomena that occur rapidly or in difficult-to-access locations, such as during natural hazards or political upheaval.

Both recreational and commercial/research operations of sUAS are subject to legal restrictions to certain operations, which often are a significant limitation for sUAS in Geography. Unless the sUAS is deemed a toy, in most countries licensing is required to operate the sUAS for research or commercial purposes (Stöcker et al. 2017). Beyond licensure, the specifics of which differ based on country of operation and sUAS registration, additional legal requirements such as maintaining clear sight of the system or flying below a height ceiling based on operational airspace must be followed. Permits are often available to remove or lessen some restrictions, but the permitting process varies by country, is subject to frequent change, and will require grounding of the system or limited operation until approved. Even when and where flight operation of sUAS is legal, care should be taken to limit disturbance to people or animals. When flying over or near a person's property, consent should be obtained, and notice should be given. In the case of a system crash, the operator is usually required to pay for any additional damage caused beyond the damage to their own system. Any fouling of the environment by crashes should be eliminated or limited, for example, by retrieving all plastic and electronic parts of the wreckage.

Finally, since sUAS are still relatively new and rapidly evolving, there has been some inconsistency in terminology used to describe them. The term “drone” is commonly used outside of academia but can imply military-style systems which

could be perceived negatively (PytlikZillig et al. 2018). Authors have called sUAS both systems and vehicles – we prefer the use of systems to indicate that operation of sUAS often encompasses more than just controlling the vehicle. Additionally, the terms “unmanned” and “unoccupied” have been used within the acronym, and different acronyms such as remotely piloted aircraft/aerial systems (RPAS) have been used. While “remotely piloted” agrees with the US-required “Remote Pilot Certification” for government or commercial use (FAA Part 107), here we advocate that the non-gendered term “unoccupied” should be preferred within the already widely accepted acronym sUAS. The inconsistent terminology appears to be a function of the diverse backgrounds of those who use these systems. While this diversity is a strength, a consistent name could help strengthen the ties among these diverse users. Thus, we use the term small unoccupied aerial systems (sUAS) throughout this book.

1.3 Chapter Contributions

One of the main purposes of this book is to highlight the various ways in which sUAS are used for research within a diverse discipline such as Geography. In addition to the chapters in this book presenting the most recent advancements in the science, they also discuss certain identified constraints, challenges, and workflows for conducting ethical, geographic research utilizing sUAS in the current state of the science. Methodological standards and procedures, as well as regulations and restrictions, are continually evolving as these technologies advance, and thus it is recommended that geographers are diligent about being aware of any changes to the operations of sUAS. The following paragraphs outline the organization of this book and provide an overview of the details included in each of the chapter contributions. Broadly, the chapters in this book have been organized into three groupings: (1) sUAS with human dimensions; (2) methods for improved acquisition and processing; and (3) topical methods within environmental and physical Geography.

As an introduction into the policies, workflows, and ethical concerns of sUAS, Chap. 2 focuses on applications to hazard environments. Locations recently impacted by natural disasters are highly sensitive areas, as many of the communities are still dealing with clean-up, repairs, relocation, and associated expenses. Collecting time-sensitive sUAS-based information to assess damage and key data necessary to evaluate the natural processes related to the disaster (e.g., tornado wind speed) requires coordination with emergency managers and law enforcement, as well as permissions from landowners. Obtaining these data also requires tact and ethical consideration prior to and during sUAS operation (Wagner and Doe, Chap. 2, this volume). As sUAS technologies improve and costs decrease, the ability of citizens to engage in the scientific process is rapidly expanding. While citizen science has been around for many years, the involvement of citizens in the science typically does not extend beyond the acquisition of the data. Chapter 3 explores

aspects of citizen science as it relates to sUAS, examining different case studies where citizen involvement varied. The authors found that when community members were engaged in collection, processing, and ownership of the results, public perceptions of the studies were improved and the community members were more confident in addressing and solving local challenges (Bunting et al., Chap. 3, this volume). sUAS also have great utility for human-cultural research that can allow for an interdisciplinary approach of qualitative and quantitative techniques. Chapter 4 presents a geoarchaeological example of using sUAS for rapid site reconnaissance, site assessment, and repeat monitoring of Native American archaeological sites within coastal Louisiana (Konsoer et al., Chap. 4, this volume). Through the examples given in the chapter, the authors discuss the challenges of conducting geoarchaeological research within coastal wetlands that are being rapidly modified due to land subsidence, sea level rise, coastal erosion, and direct anthropogenic alterations and how the use of sUAS can help overcome some of these challenges. This chapter also discusses the benefits of sUAS for training and educating undergraduate students in interdisciplinary science, as well as the benefits to engaging and collaborating with coastal communities and native tribes.

The continued advancements of sUAS with different payload integrations have resulted in increasingly larger datasets obtained with higher resolution, requiring software and methods for processing and visualizing those data to similarly expand and improve. Photogrammetric techniques such as structure from motion (SfM) allow for generation of three-dimensional point clouds, digital elevation models, and orthophoto mosaics. There are currently multiple options (open-source and commercial) available for such software packages. To evaluate the performance of these different softwares, the authors of Chap. 5 conduct a systematic investigation of five software packages using sUAS data acquired from three states within the United States across various land cover types (Li and McKinney, Chap. 5, this volume). Their findings revealed that when given identical input imagery, considerable differences were obtained in the final output products from the different software and that these results varied depending on land cover type. Another important consideration in achieving accurate sUAS-derived products is the selection of various flight plan parameters within the mission design. Chapter 6 evaluates the accuracy of digital surface models (DSM) derived from sUAS-SfM acquired from various mission designs using different image overlap, flight path orientation, and image obliqueness (Hostens et al., Chap. 6, this volume). Using a case study for the North Fork of the White River in south-central Missouri, USA, the authors demonstrate that relatively simple mission designs, with 80% image overlap and roughly 20-degree image obliqueness, resulted in more accurate DSM and considerably reduced post-processing time.

The third grouping of chapters starts with an example of how sUAS can be beneficial in the study and monitoring of oil and gas wells for environmental quality and compliance. Specifically, Chap. 7 presents examples of how sUAS, as well as pole aerial photography (PAP), can be used to create orthomosaics, 3D models of vegetation and elevation, and 360-degree low altitude video to aid in the inspection and evaluation of oil and gas wellpads on US Forest Service grasslands to determine

necessary remediation efforts (Baynard et al., Chap. 7, this volume). The authors show how these techniques can improve efficiency in site investigations and provide improved coordination and planning for regulators, thereby limiting environmental damage throughout the life cycle of oil and gas wells. Chapter 8 focuses on another aspect of environmental impacts related to slow-moving landslides and soil erosion from agricultural lands. The processes of slow mass wasting and soil erosion via rill formation are often difficult to measure directly over relatively large areas because the scales of change are often less than a few centimeters (Stumvoll et al., Chap. 8, this volume). In such cases, the use of sUAS-based lidar measurements can greatly improve the spatial and temporal resolution allowing for differencing of elevation models to quantify rates of erosion.

Perhaps one of the most impacted disciplines in Geography by the proliferation of sUAS for scientific research is the various subfields of geomorphology. While the reasons for the quick adoption of sUAS techniques in these fields are apparent, namely, high-resolution spatiotemporal data and relative ease of acquisition, the applications and boundaries for sUAS have been and will continue to be pushed forward. Chapters 9, 10 and 11 provide detailed discussions on the state of the art of sUAS research in polar and cryosphere environments (Gaffey et al., Chap. 9, this volume), coastal environments (Smith et al., Chap. 10, this volume), and riverine environments (Reid et al., Chap. 11, this volume) and present various advantages and disadvantages, as well as future directions for sUAS in the study of geomorphic systems. As pointed out in Chaps. 9 and 10, sUAS are now an invaluable tool for studying rapid changes to glaciers, permafrost, coastal dunes, and vegetation due to contemporary climate change. Chapter 11 reveals how sUAS provide opportunities to investigate smaller rivers within densely forested landscapes that were previously extremely difficult to study but offer tremendous insights into broader landscape processes and aquatic and riparian ecosystem functioning.

1.4 Future Outlook for sUAS in Geography

Predicting the future of technology is rarely an exercise recalled fondly by those making the forecast. However, the future of sUAS in Geography should be tied to recent technological developments and the continuation of current experiments, policies, and perspectives. Small-scale tests of state-of-the-art equipment and research might foretell the future of sUAS, and rigorous testing and improvement of these advancements might lead to widespread adoption within Geography and allied disciplines. Three avenues of future development we think will be important are (1) decreasing platform and sensor size, together with decreasing platform and sensor costs, to increase sUAS capability and flexibility; (2) automating communication between sUAS and operator and among numerous sUAS deployed simultaneously; and (3) extension of sUAS to include user-friendly and inexpensive land- and water-based platforms. All these technological avenues of expansion must

be carried out within the backdrop of changing societal, economic, and political values and policies.

One of the reasons why sUAS have become so important in Geography over the last decade is their small size and inexpensive price. sUAS that could be considered “pocket-sized” are already able to carry camera sensors that can capture in 4 K quality and with high frame rates (30+ frames per second (fps)) (Stanković et al. 2021). Although decreasing the size of these sUAS further might make them more vulnerable to adverse environmental conditions like high winds (Lewis et al. 2018), it seems reasonable to predict that similarly sized sUAS will continue to become more affordable. Smaller “microdrone” toy sUAS are common but are rarely associated with high-quality sensors, yet a sUAS like the DJI Mini 2 can obtain 4 K 30 fps imagery even though it is less than 250 grams and thus not subject to regulations that most sUAS must adhere to (Stanković et al. 2021). The future ability of these very small UAS to have high-resolution sensors would be a significant advancement in locations where it is difficult to operate the current generation of sUAS such as mines, buildings, or dense forests (Shahmoradi et al. 2020). Another way to increase the ability of sUAS is to bring down the size and cost of alternative or additional sensors such as lidar and multi- or hyperspectral cameras or to increase the cost-to-lifting power ratio of sUAS. Both developments would significantly increase the ability of geographers to obtain novel landscape data. Finally, improvements in battery capacity and recharging speed should continue.

A recent development in sUAS is the deployment of “drone swarms” that allow for simultaneous control of numerous sUAS (Chen et al. 2020). These deployments have become somewhat common for entertainment, such as for light shows during events and celebrations (Waibel et al. 2017). While pre-programming sUAS swarms is clearly already successful, current and future research is focused on using automated communication among sUAS and between operators to help in situations like disaster relief (Chen et al. 2020). It is encouraging to envision a sUAS swarm that can quickly and without cumbersome user input or operation search a large area and alert first responders to the locations and condition of people in need. In general, it is reasonable to predict that attempts to automate sUAS and sensor operation will follow a path similar to the rapid expansion of road vehicles that actively assist the driver and can even operate fully autonomously (Martínez-Díaz and Soriguera 2018). sUAS that can fly and obtain data with minimal input would be an important advantage for situations that are difficult to pre-program and can change quickly such as studies of severe weather such as tornadoes or floods, animal or human tracking, or landslides.

The sUAS revolution in Geography has mostly taken place in the air. However, unoccupied systems that traverse the land, water surface, or underwater (autonomous underwater vehicles, AUVs) have been developed and could prove a useful tool in Geography and allied disciplines (Wynn et al. 2014; Bimbraw 2015; Petillot et al. 2019). Remotely operated land systems could help obtain samples in difficult-to-access locations, for example, samples in unstable soil on the verge of mass movement. However, proliferation of unoccupied land-based systems might be

limited due to a relatively high cost compared to the relatively few situations where they are needed. Water surface systems and AUVs can easily obtain water samples, and sensors aboard these systems could allow for measurements that range from simple (e.g., temperature) to complex and data-rich (e.g., high-resolution bathymetry obtained with multibeam echo sounding) (Lucieer and Forrest 2016). However, when it comes to photographic imagery, on- and in-water unoccupied systems have a more limited use than sUAS because turbid waters and minimal light conditions yield smaller fields of view. In addition, these systems (with hydroacoustic sensors for bathymetric mapping) remain relatively costly and can be challenging to operate due to the possible need to be tethered to the operator or the potential to be affected by debris or hidden vegetation within the water (Wynn et al. 2014). While non-aerial systems may have a narrower application use than sUAS, geographers can no doubt use these cutting-edge technologies to improve understanding of the natural and human environment.

Finally, all predictions or expectations of how sUAS and similar technology might develop are inextricably bound to political, economic, and social changes – which are nearly impossible to predict. Policy governing the use of sUAS is subject to rapid change and is inconsistent among countries. A prediction such as the continued decrease in sUAS cost might be undermined by supply chain issues such as those caused by the ongoing COVID-19 global pandemic (Sarkis 2020). In contrast, the need to physically distance and other restrictions brought on by the pandemic could also invigorate certain sUAS-based advances such as sUAS-based package or food delivery (Kim et al. 2021). Ultimately, the future of any technology will be based on the current state of the art while also being controlled to a large extent by broad changes to society.

1.5 Conclusion

Small unoccupied aerial systems (sUAS) have provided geographers and those in allied disciplines a cutting-edge and highly flexible platform from which to explore new and exciting research. The ability to obtain imagery and imagery-derived data at a spatial and temporal resolution controlled by the needs of the researchers is unprecedented. While some technological, legal, and practical boundaries remain, the proliferation of sUAS into Geography has brought on the era of “personal” or “on-demand” low altitude remote sensing. The sUAS is now an essential part of the geographer’s toolkit and will continue to support research into topics, processes, and landscapes previously too complex or costly to characterize. A generation of undergraduate and graduate students has also been trained in the use of sUAS, so a formalized and rigorous approach to research with sUAS is both timely and necessary. This book highlights the various ways sUAS are used in the study of diverse subdisciplines within Geography.

References

- Anderson K, Westoby MJ, James MR (2019) Low-budget topographic surveying comes of age: structure from motion photogrammetry in geography and the geosciences. *Prog Phys Geogr Earth Environ* 43:163–173
- Armstrong MP, Wang S, Zhang Z (2019) The internet of things and fast data streams: prospects for geospatial data science in emerging information ecosystems. *Cartogr Geogr Inf Sci* 46(1):39–56
- Bimbraw K (2015, July) Autonomous cars: past, present and future a review of the developments in the last century, the present scenario and the expected future of autonomous vehicle technology. In: 2015 12th international conference on informatics in control, automation and robotics (ICINCO), vol 1. IEEE, pp 191–198
- Boike J, Yoshikawa K (2003) Mapping of periglacial geomorphology using kite/balloon aerial photography. *Permafrost Periglacial Process* 14(1):81–85
- Carter, Trevor G., et al. (2018) Innovative use of GIS and drone photogrammetry for cliff stability modelling. *Proceedings of the Institution of Civil Engineers-maritime engineering*. Vol. 171. No. 3. Thomas Telford Ltd
- Chen W, Liu J, Guo H, Kato N (2020) Toward robust and intelligent drone swarm: challenges and future directions. *IEEE Netw* 34(4):278–283
- Giordan D, Manconi A, Remondino F, Nex F (2017) Use of unmanned aerial vehicles in monitoring application and management of natural hazards. *Geomat Nat Haz Risk* 8:1–4
- Goodchild MF (1991) The technological setting of GIS. *J Environ Sci (China) English Ed* 45–54
- Goodchild MF (2011) Scale in GIS: an overview. *Geomorphology* 130(1–2):5–9
- Green DR (ed) (2020) *Unmanned aerial remote sensing: UAS for environmental applications*. CRC Press
- Kim JJ, Kim I, Hwang J (2021) A change of perceived innovativeness for contactless food delivery services using drones after the outbreak of COVID-19. *Int J Hosp Manag* 93:102758
- Lemmens M (2011) *Terrestrial laser scanning*. In: *Geo-information*. Springer, Dordrecht, pp 101–121
- Lewis QW, Park E (2018) Volunteered geographic videos in physical geography: data mining from YouTube. *Ann Am Assoc Geogr* 108(1):52–70
- Lewis QW, Lindroth EM, Rhoads BL (2018) Integrating unmanned aerial systems and LSPIV for rapid, cost-effective stream gauging. *J Hydrol* 560:230–246
- Lewis QW, Edmonds DA, Yanites BJ (2020) Integrated UAS and LiDAR reveals the importance of land cover and flood magnitude on the formation of incipient chute holes and chute cutoff development. *Earth Surf Process Landf* 45(6):1441–1455
- Lloyd CD (2014) *Exploring spatial scale in geography*. Wiley
- Lucieer VL, Forrest AL (2016) Emerging mapping techniques for autonomous underwater vehicles (AUVs). In: *Seafloor mapping along continental shelves*. Springer, Cham, pp 53–67
- Lulla K (1983) The Landsat satellites and selected aspects of physical geography. *Prog Phys Geogr* 7(1):1–45
- Martínez-Díaz M, Soriguera F (2018) Autonomous vehicles: theoretical and practical challenges. *Transport Res Proc* 33:275–282
- Masek JG, Wulder MA, Markham B, McCorkel J, Crawford CJ, Storey J, Jenstrom DT (2020) Landsat 9: empowering open science and applications through continuity. *Remote Sens Environ* 248:111968
- Nagrare SR et al (2021) Decentralized path planning approach for crowd surveillance using drones. In: 2021 international conference on unmanned aircraft systems (ICUAS). IEEE
- Natesan S, Armenakis C, Benari G, Lee R (2018) Use of UAV-borne spectrometer for land cover classification. *Drones* 2(2):16
- Paine DP, Kiser JD (2012) *Aerial photography and image interpretation*. Wiley
- Petillot YR, Antonelli G, Casalino G, Ferreira F (2019) Underwater robots: from remotely operated vehicles to intervention-autonomous underwater vehicles. *IEEE Robot Autom Mag* 26(2):94–101

- Pytlík Zillig LM et al (2018) A drone by any other name: purposes, end-user trustworthiness, and framing, but not terminology, affect public support for drones. *IEEE Technol Soc Mag* 37(1): 80–91
- Sarkis J (2020) Supply chain sustainability: learning from the COVID-19 pandemic. *Int J Oper Prod Manag* 41:63–73
- Shahmoradi J, Talebi E, Roghanchi P, Hassanalani M (2020) A comprehensive review of applications of drone technology in the mining industry. *Drones* 4(3):34
- Song BD, Ko YD (2017) Quantitative approaches for economic use of emerging technology in the tourism industry: unmanned aerial vehicle systems. *Asia Pac J Tour Res* 22:1–14
- Stanković M, Mirza MM, Karabiyik U (2021) UAV forensics: DJI mini 2 case study. *Drones* 5(2): 49
- Stöcker C, Bennett R, Nex F, Gerke M, Zevenbergen J (2017) Review of the current state of UAV regulations. *Remote Sens* 9(5):459
- Tanzi TJ, Chandra M, Isnard J, Camara D, Sébastien O, Harivelo F (2016, July) Towards “drone-borne” disaster management: future application scenarios. In: XXIII ISPRS congress, commission VIII (volume III-8), vol 3. Copernicus GmbH, pp 181–189
- Visser F, Woodget A, Skellern A, Forsey J, Warburton J, Johnson R (2019) An evaluation of a low-cost pole aerial photography (PAP) and structure from motion (SfM) approach for topographic surveying of small rivers. *Int J Remote Sens* 40(24):9321–9351
- Waibel M, Keays B, Augugliaro F (2017) Drone shows: creative potential and best practices. ETH Zurich
- Wood SA, Robinson PW, Costa DP, Beltran RS (2021) Accuracy and precision of citizen scientist animal counts from drone imagery. *PLoS One* 16(2):e0244040
- Woodget AS, Fyffe C, Carbonneau PE (2018) From manned to unmanned aircraft: adapting airborne particle size mapping methodologies to the characteristics of sUAS and SfM. *Earth Surf Process Landf* 43(4):857–870
- Wynn RB, Huvenne VA, Le Bas TP, Murton BJ, Connelly DP, Bett BJ et al (2014) Autonomous Underwater Vehicles (AUVs): their past, present and future contributions to the advancement of marine geoscience. *Mar Geol* 352:451–468

Chapter 2

UAS Policies, Workflows, and Challenges in Hazard Environments



Melissa A. Wagner and Robert K. Doe

Abstract Disaster areas are highly sensitive and stressful areas that require coordinating with emergency managers and law enforcement in order to successfully operate and collect UAS-based damage information. Coordinating UAS operations with government officials is key to (1) assisting these officials and other agencies with regard to their specific needs, (2) gaining access to these highly sensitive areas, and (3) staying up-to-date on airspace restrictions and other emergency operations. This chapter discusses navigating UAS policy and operations (workflows) for disaster monitoring and recovery and the challenges in the field based on years of experience. We discuss the logistics needed to successfully perform sUAS-based damage surveys in these highly sensitive areas. We present a robust workflow, which includes preflight planning, flight operations, and data processing and dissemination, for successful data collection in hazard environments. This workflow considers sUAS operations and data collection in urban and rural environments as well as the scale of operations. In rural environments, sUAS multispectral platforms are better suited to assess high-wind and hail damage to vegetation based on spectral response. Therefore, we include procedures for collecting and analyzing multispectral data in remote locations. We present solutions for data suitability, curation, formats, and distribution that are also cognizant of local, state, and federal agencies' needs. Disseminating this knowledge is vital to both the transferability of methodology and the replication of data collection in the ever-changing landscape of policy, legislation, and technology. We discuss the multiple challenges and limitations experienced in post hazard environments.

Keywords sUAS · UAV · UAS workflow · UAS operational management · Data collection · Natural hazards · UAS planning · Damage assessment

M. A. Wagner (✉)

Cooperative Institute for Mesoscale Meteorological Studies, University of Oklahoma, Norman, OK, USA

e-mail: mawagner@ou.edu

R. K. Doe

School of Environmental Sciences, University of Liverpool, Liverpool, UK

2.1 Introduction

The last decade has seen exponential growth in the usage and application of sUAS/ UAV/sUAV (small unpiloted aerial systems/unpiloted aerial vehicles/small unpiloted aerial vehicles) in (natural) hazard environments. For the context of this chapter, we adopt the term sUAS meaning not only the sUAV platform itself but the crew (e.g., pilot, visual observers (VO)) and connecting systems (e.g., flight mission software, ground control station). We reserve the use of UAS to discussions on policy and sensor-derived products even though the workflow presented here can be applied to both UAS and sUAS. The uptake of sUAS is reflected not only in the variety of technology available but the multitude of environments it can now be applied to, including hazard environments. The development of micro-sensors for monitoring, multi-band cameras, high pixel resolutions, as well as increased payload capabilities, has led to this growth. More importantly, technological advancement, increased vendor choice, and economies of scale have created relative affordability especially for those on restrictive budgets. The appeal for the applied geographer has therefore become greater, especially for those seeking to integrate such technology within fieldwork/research or student field methods classes.

There are additional benefits, and one of these is customization. While some equipment comes “plug and play” or “ready to go,” others are easily customizable to the specific needs of the user or even open to further experimental innovation. Lastly, the appeal to the applied geographer should be seen as ease of use. While we would not say adopting sUAS-based fieldwork should be taken lightly, and it does present a learning curve with some complexity, this is not too prohibitive to the novice. The intuitive nature of this progressive technology allows one to learn quickly, but standards, policy, and regulations discussed in this chapter should be adhered to in the first instance.

There is certainly no “one size fits all” approach to using sUAS in the field, but on the other hand, there is no end of possibilities for the applied geographer. There are clear benefits in taking on a sUAS-driven approach to fieldwork, research, or in situ experiments. The benefits include (1) gaining access to impassable or remote locations that otherwise would have been very difficult; (2) identifying hazards that would have been otherwise unobservable by ground or via the coarse resolution of satellite imagery; (3) being able to cover large surface areas at high spatial and temporal resolutions in a short time; (4) providing corroboration to ground-based site investigations; (5) acquiring data for digital outputs for measurements and modeling, for example, structure from motion (SfM); and (6) providing assistance for the management of hazard/emergency situations (Wagner et al. 2019).

There is much within the literature on the use of sUAS in monitoring and management of natural environmental hazards. Some of this is documented by Giordan et al. (2017), extending sUAS for search and rescue operations for missing people (Jurecka and Niedzielski 2016), and including multipurpose sUAS for mountain rescue operations (Silvagni et al. 2016). The use of sUAS has also been applied to 3D reconstruction of structures, in particular for infrastructure and

monuments after devastating earthquakes (Cabuk et al. 2007; Lambers et al. 2007; Sauerbier and Eisenbeiss 2010; Remondino et al. 2011). Lastly, in more recent years, there has been vital applications for sensing and assisting in wildfires (Akhoulfi et al. 2021), to name but a few valuable examples.

We write this chapter with a strong narrative, based on experience, multiple fieldwork campaigns, successes, and failures. As with all experimental science, we are always learning and developing, and this learning is enhanced as technology improves. We write this to share experience and knowledge in the hope that other geographers looking to start sUAS-based fieldwork in hazard environments for the first time find inspiration to embrace this technology. As early adopters of sUAS for multispectral tornado site investigations and customizing our own equipment for fieldwork, we had a steep learning curve. This learning curve was related to equipment selection, site logistics (see Fig. 2.1), devising new workflows, operational procedures, calibration techniques, as well as establishing the specific data needed for storage, analysis, and a holistic result-driven approach.

This chapter examines, among other things, policy considerations and, for those new to sUAS operations, development of workflows. A defined workflow is of critical importance not only for safety but optimum efficiency, transferability, and standards. Understanding how to develop your own workflow will undoubtedly lead to successful application. Working in hazard environments can be stressful and requires a degree of sensitivity in navigating these spaces. There will be many challenges. We hope this chapter addresses a few of them and that, after reading it, the reader will have confidence to tackle their own hazard research using UAS or sUAS.

2.2 Policy

A feasibility study is required to assess whether the location in which you *plan* to operate a UAS is viable based on the policy of operation for the country/region and also airspace regulations. Country, regional, and local policies are well-documented on the Internet, and some examples of these are included in the references. Airspace policy is governed by aviation authorities and air traffic control. In the USA, the Federal Aviation Administration (FAA) oversees national airspace regulations including those governing UAS operations. Recent changes in federal UAS policy require individuals who stand to gain any benefits from UAS operations (e.g., commercial use, research) to become certified remote pilots (FAA Part 107). Part 107 pilots can operate in class G airspace following FAA guidelines but will require additional waivers and/or training to operate in restricted airspace (Fig. 2.2) or outside FAA guidelines (e.g., UAS operations above 400 ft., nighttime flying).

While airspace can be checked using aeronautical navigational charts (e.g., Skyvector) and other online platforms (Federal Aviation Association (FAA) visualize it), airspace regulations may be best approached via app-based information. Apps like AirMap, Hover, B4UFLY (USA only), and Drone Assist (UK only) are a few

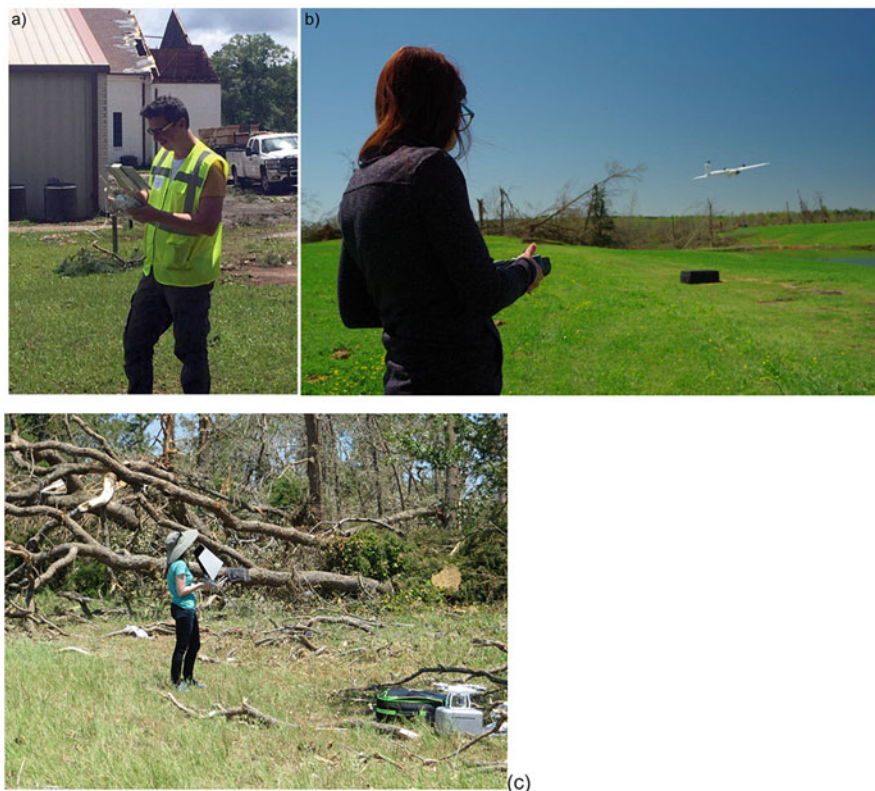


Fig. 2.1 Versatility of UAS technologies. (a) Robert Doe operating a high-resolution RGB UAS for damage modelling at Shiloh Baptist Church in Longview, Texas, 2017, after tornado impact. (b) Melissa Wagner operating at fixed-wing UAS equipped with visible and multispectral cameras for vegetation damage assessment following the 25 March 2021 Sawyerville, AL, tornado. (c) Melissa Wagner performing aerial videography reconnaissance to better delineate a tornado track and determine a flight planning strategy. (All images depict and are copyright the authors: © Wagner/Doe)

examples of the best way to identify airspace restrictions both in advance and on the day of deployment (see useful web resources). For example, in the USA, some apps (i.e., AirMap) may also include Low Altitude Authorization and Notification Capability (LAANC) authorizations, which automate the application and approval process for authorizations in controlled airspace. These apps can streamline the application process in LAANC-participating airports with rapid approvals when operating below ceiling height restrictions.

Special waivers may be required for real-time or near-real-time disaster response. Obtaining authorizations to operate in restricted airspace could take days or weeks in the case of non-LAANC-participating airports or other special use airspaces, especially following high-magnitude events. In the USA, UAS operators can apply for Special Government Interest (SGIs) waivers (previously known as an Emergency

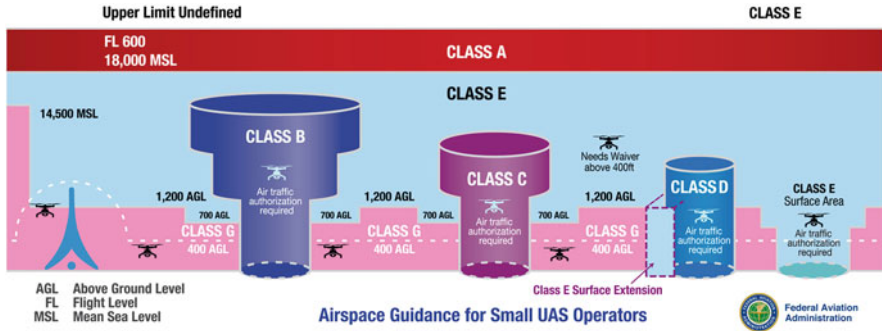


Fig. 2.2 Airspace guidance for small UAS operators. (Courtesy US Department of Transportation, Federal Aviation Administration. Airspace 101 – Rules of the Sky. Accessed 12 March 2021: https://www.faa.gov/UAS/recreational_fliers/where_can_i_fly/airspace_101/)

Certificate of Authorization (COA)) to quickly gain access in restricted airspace. SGIs are approved by the FAA System Operations Support Center (SOSC) usually within 1 hour or less from submission (FAA 2020). To qualify for this waiver, UAS operations must support emergency response operations or a similar effort that addresses exigent circumstances for public good. For example, SGI waivers can be used to collect critical damage information via UAS, which can be shared with local emergency managers to assist in their disaster response and recovery. These waivers also help researchers collect data shortly after an event better addressing the perishable nature of disaster imagery as people are quick to clean up (Womble et al. 2018).

In addition to airspace compliance, UAS operators must adhere to agency-specific policies. Most agencies have institutional mandates to ensure safe and efficient UAS operations that protect both the operator and public and establish a code of conduct. For example, the National Oceanic and Atmospheric Administration (NOAA) Uncrewed Systems (UxS) has their own set of procedures for obtaining approval to procure, operate, and maintain UAS (NOAA 2020). These procedures require additional steps to mitigate potential risks and ensure safe operations and apply to any UAS operations within or sponsored by NOAA. As with any agency, these guidelines establish code of conduct for UAS operations that protect both the operator and institution. Agencies may have additional requirements with regard to UAS operations in disaster environments given the sensitive nature of these areas. Therefore, UAS operators must adhere to their agency's policies and work with their institutions to understand disaster management protocol.

2.3 Equipment Considerations

Common sUAS platforms in disaster management include multi-rotor copters and fixed wings (Fig. 2.3), with the former used more commonly for quick assessments and small-scale mapping. Multi-rotor copters can be equipped with visible,



Fig. 2.3 UAS platform example of (a) quadcopter DJI Phantom 4 Pro and (b) fixed-wing Quantum Trinity F90+. (Images (a) © Wagner/Doe and (b) © James Murnan)

Table 2.1 List of sensors commonly used on UAS and applications in disaster management and research

Sensor	Sensor specification	Utility
Visible	RGB	True color imagery, videos
Multispectral	RGB, red edge, near-infrared	Vegetation mapping (detect vegetative stress/damage, monitor health)
Thermal	Infrared	Thermal mapping; search and rescue detect humans and animals
LiDAR	Pulsed LiDAR	3D mapping, structural assessments, plant structure

multispectral, or thermal cameras depending on the objective (see Table 2.1 and Fig. 2.3a). These platforms traditionally carry single payloads but may handle dual payloads.

Fixed-wing platforms are better suited to map large areas. These platforms can cover significantly larger areas due to the longer battery life (45–90 min vs. 20–30-min) and additional motors on board, leading to a more complete survey of the event. For example, the Quantum Trinity F90+ is a fixed-wing platform that can map up to 700 hectares at 120 m above ground level (AGL) during a single sortie (see Fig. 2.3b). Fixed-wing platforms with vertical take-off and landing (VTOL) capabilities can be especially advantageous in disaster-affected areas because they (1) are easier to operate than traditional fixed-wing sUAS platforms, (2) can be deployed with fewer limitations, and (3) do not require additional FAA waivers. Additionally, fixed-wing platforms are better equipped to handle dual payloads, permitting dual-data collections.

In addition to sUAS platforms, portable communication platforms are often needed to support sUAS operations in disaster-affected areas. Mapping disaster-affected areas requires an Internet connection to access aerial imagery used in mission planning. Wi-Fi signals needed for mission planning, however, can be weak or, depending on cellular service provider, non-existent. While Wi-Fi hotspots (e.g., Jetpacks) may be sufficient to provide stable Internet connection, signals can be especially problematic in remote locations or where existing communication

networks have been disrupted. Instead, portable communication platforms such as the Plumcase can provide satellite communication needed to connect equipment in areas of weak or limited signal as well as Internet connection for mission planning operations. These platforms can also facilitate the secure transfer of high-wind damage imagery in a timely manner (depending on bandwidth) to assist emergency managers with disaster response and recovery.

2.4 Workflow

2.4.1 Preflight Planning

Figure 2.4 shows a simple but robust workflow of stages necessary for effective operation and results. *Stage 1* begins with site identification, permissions, and legal compliance. The main points to consider with site identification are how safe it is to get on site and how safe it is to operate while on site. While some planning can be done before heading into the field using pre-event aerial imagery, site characteristics can change rapidly, so a visual assessment in situ is recommended. When establishing the site for take-off, landing, and flight operations, there should be enough clearance to safely navigate any potential obstacles directly in or surrounding the flight path. For example, it is highly recommended to factor in an additional horizontal distance in areas of tall vertical obstacles (e.g., forested areas, power lines) to account for wind gusts or changes in wind direction during take-off or landing. This is especially important with fixed wing with VTOL capabilities as these platforms require sufficient clearance to transition from vertical to horizontal flight and vice versa. In addition to visual assessments, you should also consult aeronautical navigational charts for any potential obstacles such as cellular towers or other communication antennas that could lie within or close to your flight path. Lastly, it is important to choose a site in which the remote pilot in command (PIC) and VOs can

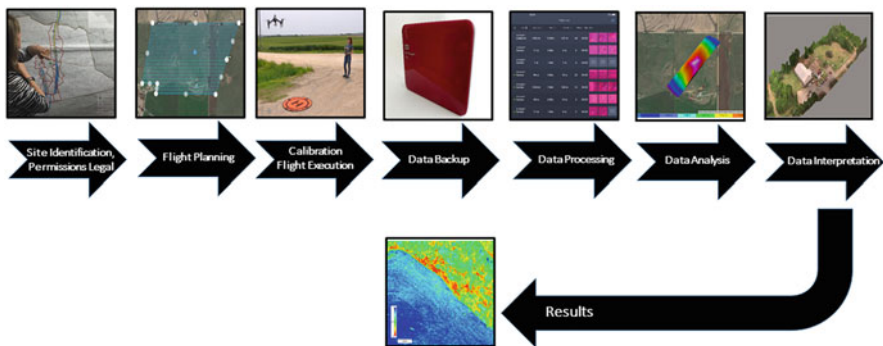


Fig. 2.4 Author defined UAS workflow beginning with site identification and permission (top left) and concluding with results (bottom middle). (Workflow and images: © Wagner/Doe)

always maintain visual line of sight (VLOS) with the sUAS platform, unless operating under a beyond visual line of sight (BVLOS) waiver, as well as a safe distance from existing emergency operations.

Working in collaboration with authorities is also a vital part of flight planning and operations. Local authorities (e.g., emergency managers, first responders, law enforcement) can provide guidance on the most effective site identification and placement strategy for your mission. More importantly, coordinating with emergency managers and other authorities can guide you toward a responsible data collection strategy while also identifying their needs. Emergency managers can provide access into sensitive or restricted areas as well as keep you up to date on airspace restrictions or other emergency management operations (Wagner et al. 2019). For example, airspace regulations can change rapidly as a result of search and rescue operations or aerial surveys that involve top government officials. Additionally, emergency managers are overloaded with incoming information while executing their operations (Wagner et al. 2019). Therefore, operating in hazard environments also requires a degree of sensitivity to safely navigating these stressful environments.

Other legal considerations include permission from landowners. If your site is on public land, you do not need permission. However, you will need permissions from property owners if taking-off or landing on their property. It is highly recommended to obtain permissions via written consent from the property owner as a means of documentation for you and the property owner. While you do not need permissions to fly over disaster-affected property, it is important to let property owners know of your objectives when feasible, given the high stress and emotional conditions associated with these sites. Informing those affected by the disaster can also establish trust especially in rural communities and ensure operations are not impeded (Wagner et al. 2019).

Working in hazard environments, safety must be of utmost consideration, and measures you take to mitigate risk are vital. It might be that you cannot position yourself to effectively perform flight missions needed. This could be from issues relating to VLOS to positional interference with the equipment or active emergency operations. Additionally, it may be that you cannot receive the permission of the landowner to operate from your selected site. The golden rule for this first stage of the workflow is to (1) make sure you have permissions, (2) coordinate with emergency managers, and (3) follow your safety checklist. Without these steps, you could be operating illegally.

2.4.2 Flight Planning and Operations

Stage 2 of the workflow looks at flight planning. It is recommended to use a formal *flight plan* to ensure all important checks are covered and therefore should be part of your standard flight checklist. An example of a *flight plan* can be seen in the useful web links section. Essentially, a *flight plan* is designed to perform the chosen runs



Fig. 2.5 Example of flight planning for the Quantum Trinity F90+ using QBBase 3D software. Green lines, referred to as legs, show the specified trajectory of the Trinity F90+. (Qbase © Quantum-Systems)

safely, with the aid of dedicated software and in accordance with VLOS monitoring in order to achieve the results needed for the area of interest. For example, there is much in the literature on workflow and best practices. Tmušić et al. (2020) present a detailed review of a data collection workflow for environmental studies. In this review, they examine two key challenges related to harmonizing and standardized guidance for data collection as well as establish protocols that are applicable across a broad range of environments and conditions.

Careful strategic decisions are needed to ensure the flight plan is achievable in the prevailing conditions. Figure 2.5 shows an example flight plan driven by operating software. Santamaria et al. (2008) present a concise explanation of such a plan as follows: “A flight plan specifies the path followed by the aircraft. Each flight plan is composed of a sequence of stages, such as take-off, departure procedure and others, which must come in correct order. Each flight plan stage is made up of a structured collection of legs. The leg concept is . . . used to specify the trajectory followed by the aircraft to reach a given waypoint from the preceding one. In the simplest case this trajectory will be a straight line. All flights require a single main flight plan, but additional emergency plans may be present. Emergency flight plans are partial plans, i.e. they lack some initial stages, whose purpose is to provide alternative courses when an emergency situation occurs.”

Indeed, the “emergency situation” plan is critical here, as, before any takeoff, it should be established what the procedure would be in an emergency situation and whether there are more than one viable alternative landing points should a mission have to be aborted quickly. These additional procedures are extremely important in

disaster-affected areas given potential air traffic in these environments. Some flight planning software such as QBase 3D integrates live air traffic with flight plans, which can help increase operational awareness.

Flight plans can also be tailored to specific data collection needs for disaster assessments. Mapping products and 3D models are frequently used to examine structural failure and vegetative damage. To achieve these 3D modeling capabilities, imagery should be collected using front and side overlaps of 70% or greater. While near-nadir camera angles may be sufficient for orthomosaics, it is highly recommended to set the camera angle to 70° for detailed 3D modeling assessments (Westoby et al. 2012; Carrivick et al. 2016). This oblique angle maximizes feature information collected by minimizing data loss normally obscured by shadows or with near-nadir angles (Milas 2017). There is much in the literature on flight planning and software-driven approaches. Links are included at the end of the chapter.

2.4.3 Calibration

Stage 3 of our workflow relates to calibration of the equipment and is an important part of equipment checks, maintenance, and data quality. Critical applications require the highest level of accuracy that is achievable; therefore it is important to regularly calibrate any sensor used for data collection (Yamamoto et al. 2015). Calibration of UAS equipment should follow the guidelines set by the manufacturer. Compass or magnetometer calibrations are an important part of equipment maintenance and function because they align the UAS platforms to magnetic north. These calibrations are usually conducted if it is the equipment's first flight, you have moved locations, or it has been a few weeks since your last flight. Equipment calibrations may also address operating errors observed during flight operations.

Depending on your camera, it may be necessary to calibrate these settings. Figure 2.6a shows the author flying a modified DJI Phantom 3 Advanced that records red and near infrared only (*full specifications top left of image*). For multispectral imagery, a reflectance calibration target should be used prior to, and following, each flight for radiometric corrections (see inset in lower right of Fig. 2.6a). Post-hazard such a technique is useful for identifying damage in rural areas as well as vegetation damage and health assessments. The goal of radiometric calibrations is to account for different illumination conditions with each flight by applying a correction factor based on a luminance value for each band (Tmušič et al. 2020). Ideally, multispectral imagery should be collected under uniform illumination conditions (i.e., full sun or overcast skies) (Tmušič et al. 2020). However, in post-disaster environments, it may be difficult to collect data under these conditions without also losing valuable information as clean-up occurs. Therefore, illumination conditions may vary for individual images due to environmental conditions (e.g., partly cloudy skies).



Fig. 2.6 Examples of equipment used in UAS damage surveys. **(a)** Custom multispectral camera used to survey tornado damage of the 30 April 2017 Canton, TX, tornado (inset top left camera specifications; inset bottom right camera calibration mat). Survey equipment **(b)** Trimble Geo7x and **(c)** Propeller AeroPoints used to collect ground control points. (Images depict the authors © Wagner/Doe)

While most software packages offer radiometric calibration as part of image processing, there is much literature on the techniques that can be applied depending on the camera and application. For example, Guo et al. (2019) detail radiometric calibration for multispectral cameras for different imaging conditions. Mamaghani and Salvaggio (2019) examine sensor calibration in using an end-user laboratory method for computing both the vignette correction and radiometric calibration

function that produce lower errors in radiance imagery. Nonetheless, it is important to understand how illumination conditions and corrections can affect data quality.

In addition to flight operations, ground control surveys should be conducted to ensure geospatial accuracy of data. Ground control points (GCP) obtained from ground surveys are used to georeference UAS imagery to remove positional distortions, resulting from errors in camera global positioning system (GPS) location (Johnson et al. 2014). GCP positional information can be collected using traditional survey equipment (see Fig. 2.6b) or via AeroPoints propeller mats (see Fig. 2.6c). Survey targets (GCP) should be distributed throughout the area of interest and at different elevations (Zimmerman 2020). Although UAS platforms equipped with post-processing kinematics (PPK) or real-time kinematics (RTK) have a higher degree of accuracy compared to standard sUAS platforms, it may still be necessary to obtain one or more GCP if precision mapping is required for your application.

A final word on equipment should be what we view as technological versatility. As with all technology, sUAS have a lifespan. As innovation develops, the user needs to embrace the fast-changing pace with an inquisitive and open mind as the benefits of new technologies can solve the limitations of its predecessors. For example, Fig. 2.1 shows the authors trying to solve two separate problems with two different technologies. In Fig. 2.1b, the author is collecting data for modelling and measuring structural tornado damage to a church at high resolution using a sUAS. In Fig. 2.1a, the author is using a fixed-wing sUAS to map large portions of the tornado track for research and assist in damage classification as measured by the Enhanced Fujita (EF) scale (see Doswell et al. 2009).

2.4.4 Data

Stages 4–7 of the workflow are dedicated to data. When using sUAS for research, the primary focus is on quality, consistent, data acquisition with a vision for optimal data processing (and thereby results). Therefore, data management is of critical importance. Without a data management plan, this will lead to problems as sUAS collect large volumes of data (big data). Depending on image resolution and research objective, volumes of data can range from tens of megabytes with aerial shots to tens of gigabytes with individual runs for photogrammetric analysis. In the case of multiple runs, the volume of data can increase substantially (e.g., hundreds of gigabytes) with hundreds to thousands of images collected in a single run. Video formats can also increase file size significantly. Collecting data in real time presents another consideration, especially how these data are stored with confidence “on the fly.” Working in a hazardous environment adds another layer of complexity as locational backups will be needed, sometimes fast, so a plan for this should be in place. Management of large complex datasets can be expensive and time-consuming. A data management plan is required in order to allow for sufficient backup (both on site and later to chosen location(s)), storage, processing, and ongoing sustainable access. Figure 2.7 is one example that shows the complex

of damage in a shorter time frame, which could facilitate better allocation and coordination of resources.

Regardless of your data management plan, it is vital your choice is sustainable. By this we mean that it should have continual, viable, and shareable access if costs are involved. If funds are lost, and data storage fees are not sustained, valuable data could be lost. Lastly, and most importantly, you should always consider data protection and privacy policy related to your location. Data collection via sUAS platforms has the potential to introduce significant privacy concerns, especially in areas impacted by storm-related structural damage where wind-strewn debris could contain personally identifiable information (PII). PII, as defined by the US Office and Management (OMB) policy number Memorandum 07–16, is any information that can be used to distinguish or trace an individual’s identity, such as name, Social Security number (SSN), biometric records, etc., alone or when combined with other personal or identifying information, which is linked or linkable to a specific individual, such as date and place of birth, mother’s maiden name, etc. PII can also reveal location information, raising concerns of geospatial privacy. Most government agencies prohibit the intentional collection of PII and require any accidental or “inadvertent” PII collected to be obscured or deleted. Policies, however, do vary given the complexities of PII and other sensitive information and according to agency regulations. Cifaldi (2018) looked at the key issues in detail, from the individual’s fundamental rights, privacy policy, and data protection legislation both in Europe and the USA. Before collecting any data, it is recommended you fully understand your location’s Privacy and Data Protection which can be found via your relevant governing agency’s website.

2.4.6 Data Processing

Stage 5 of the workflow relates to data processing. There are several software packages available for processing sUAS imagery, which vary according to cost, processing algorithms, and user options. All sUAS processing software utilize SfM to produce 2D modeling products (e.g., orthomosaics) and 3D modeling products (e.g., Digital Surface Models (DSMs), point clouds), which contain geographic coordinates and elevation information, from overlapping two-dimensional (2D) imagery (Westoby et al. 2012; Carrivick et al. 2016). This approach is a cost-effective alternative to Light Detection and Ranging (LiDAR) (Westoby et al. 2012; Johnson et al. 2014) and has been used in estimating fault line movement (Heredia et al. 2009; Johnson et al. 2014) as well as assessing typhoon (Ezequiel 2014; Chen et al. 2020) and tornado damage (Wagner et al. 2017; Womble et al. 2018).

Image corrections should be performed where applicable. Color corrections may be needed to balance brightness values if illumination conditions vary considerably. For multispectral imagery, orthomosaics should be calibrated using known albedo values from a reflectance panel to correct for radiometric conditions (Tmušić et al.

2020). Depending on the application, it may be necessary to convert digital numbers to reflectance values (0–1).

2.4.7 Data Analysis

Stage 6 of our workflow examines data analysis. There are a multitude of analyses that can be used in sUAS hazard assessments, and this versatility is one of the key benefits of such technologies. Visual assessments using stills, videos, or orthomosaics can be used to identify damage extent and variability. Figure 2.8 shows the extraordinary level of detail that can be achieved over a variety of different resolutions, providing different scales of information ranging from the tornado path through a forest (Fig. 2.8a) to a downed grove of trees (Fig. 2.8c,d). In particular, the

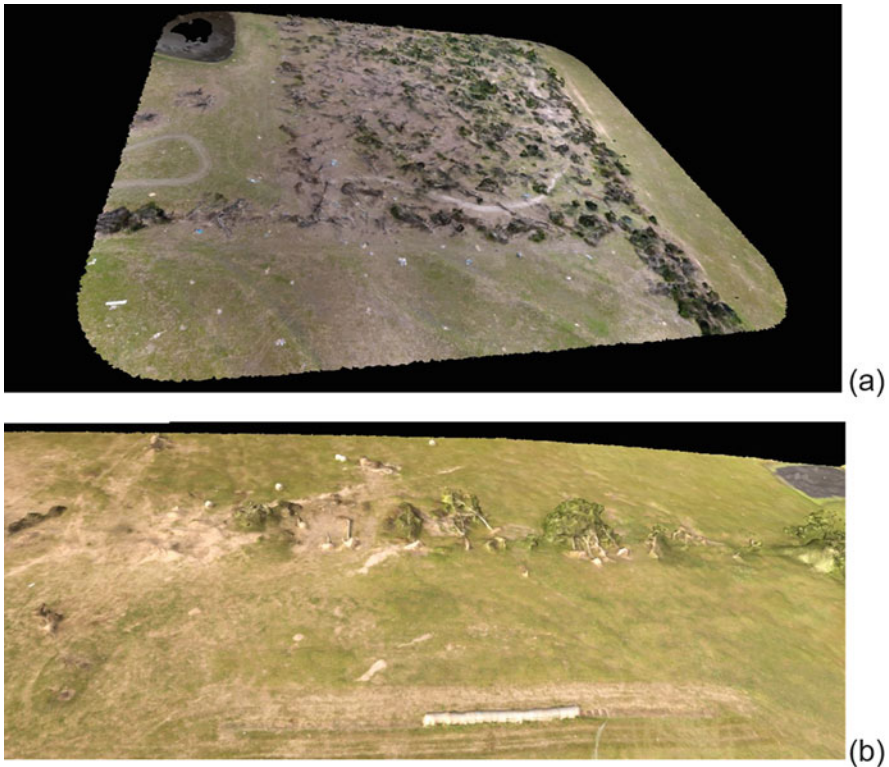


Fig. 2.8 This series of images depict the impact of the 29 April 2017 Canton, TX, tornado at different resolutions: (a) 1.48 inch-pixel (3.75 cm) collected at 260.15 ft. (79 m) AGL, (b) 0.74 inch-pixel (1.87 cm) collected at 149.70 ft. (49 m) AGL, (c) 0.98 inch-pixel (2.48 cm) collected at 129.24 ft. (39 m) AGL and (d) 0.48 inch-pixel (1.21 cm) collected at 87.06 ft. (26 m) AGL on a rural environment. [1 acre = 4046 m²] (Images © Wagner/Doe)



Fig. 2.8 (continued)

1.21 cm-pixel resolution shown in Fig. 2.8d highlights that even the smallest level of damage cannot only be identified but accurately measured post-event during desktop analysis.

To assess vegetation damage, multispectral analysis is commonly used due to the high spectral contrast of vegetation in the red edge and near-infrared (NIR) bands (Kingsfield and de Beurs 2017; Womble et al. 2018). While single-band analysis may provide some information on vegetation health, band ratios such as normalized difference vegetation index (NDVI), normalized difference red edge (NDRE), and enhanced vegetation index (EVI) can better depict damage to vegetation. These indices range from -1 to 1 with values close to 1 indicating dense, healthy vegetation; values close to 0 indicating bare soil or urban areas; and negative values indicating water (Carlson and Ripley 1997; Xue and Su 2017). Damaged or stressed vegetation will have lower index values (Yuan et al. 2002; Myint et al. 2008; Womble et al. 2018; Wagner et al. 2019). NDVI analysis, proven widely effective in disaster research, has been especially useful in detecting vegetation damage that would be otherwise undetected (Magsig et al. 2000; Yuan et al. 2002; Myint et al. 2008; Wagner et al. 2012, 2019). NDRE, however, may better reveal variations in vegetative health in part due to the red edge's sensitivity to measuring chlorophyll content (Gitelson et al. 1996).

Detailed 3D modeling assessments can be especially useful in examining structural damage and treefall patterns. In addition to 3D models, change detection can

quantify the magnitude of land cover change by differencing pre-event and post-event data (Singh 1989; Yuan et al. 2002; Myint et al. 2008; Womble et al. 2018). This method can be applied to UAS imagery where high-resolution pre-event is available as well as to point cloud data. Data must be resampled to match the coarsest spatial resolution and then properly aligned to ensure direct comparisons. The ability to quantify land cover change, however, is contingent on the resampled spatial resolution of the data.

2.4.8 Data Interpretation and Results

Stages 7 and 8 of our workflow look at the data interpretation leading to results. Much can be inferred from the data interpretation, whether these are measurable, converted, stitched, or modeled, to name a few examples. sUAS can be an invaluable tool, especially in storm damage assessments and improving our understanding of severe storm dynamics. Storm damage assessments utilizing sUAS platforms provide better access in remote or obstructed areas. These systems can be deployed almost immediately after a storm, allowing for capture of perishable data prior to extensive clean-up, and obtain very high-resolution (e.g., centimeter) data needed for a more complete damage assessment (e.g., assigning EF-scale ratings; distinguishing between tornadic and straight-line winds) (Womble et al. 2018; Wagner et al. 2019). In addition to visible imagery, UAS multispectral imagery can better detect vegetation damage because of the centimeter-scale spatial information and spectral response of vegetation in the red, red edge, and near-infrared (NIR) bands (Wagner et al. 2019). This section presents a few examples of the advantages of sUAS technologies in tornado damage surveys.

The very high spatial resolution of UAS (i.e., centimeter scale resolution) imagery may better resolve the type of land cover impacts compared to ground surveys and satellite-based damage assessments. For example, Fig. 2.9 shows a section of tornado damage path from the 30 Apr 2017 Canton, Texas, tornado captured by (a) Landsat Thematic Mapping imagery (30-m resolution), (b) satellite imagery courtesy of RapidEye (5-m resolution), (c) UAS imagery (1.2-cm spatial resolution), and (d) ground survey. The comparison between (a) and (b) clearly shows the benefits of the high-resolution satellite imagery and what appears to be denuded vegetation within the tornado track. However, in (c) we can see that sUAS detected this as distributed bales of hay. In fact, the top section of the track (b) was hay, and the bottom section below the water feature was a denuded track feature. Given the distance involved, this could only be established via the sUAS, as the ground survey (d) made this very hard to establish due to the perspective. Such detailed information can also help with the identification of damage indicators (DIs), which are used to rate tornado intensity based on the EF scale, as well as better understand the role of land cover in damage patterns (e.g., forested area, elevation changes) (Wagner et al. 2019).

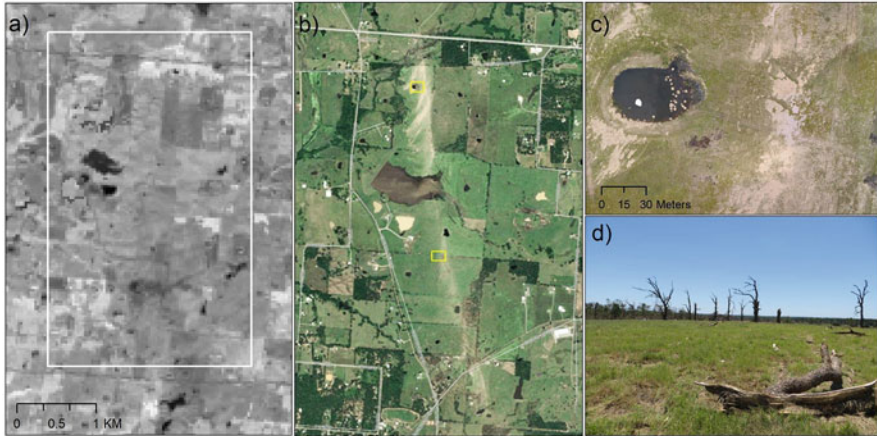


Fig. 2.9 Tornado damage information captured in (a) Landsat TM normalized difference vegetation index imagery (30-m resolution) (NASA/USGS), (b) RapidEye high-resolution imagery (5-m resolution) (Planet Lab), (c) UAS true color imagery (1.2-cm resolution) (Wagner/Doe), and (d) ground photo of the 30 Apr 2017 Canton, TX, tornado (Wagner/Doe). White box shown in (a) corresponds to the spatial extent of (b). Yellow boxes in (b) correspond to the spatial extent of (c) and (d)

The next example highlights how UAS multispectral imagery can better capture high-wind impacts to vegetation. Figure 2.10 shows a portion of the 28 May 2019 Tipton, KS, tornado in (a) UAS NDVI and (b) UAS visible imagery. In Fig. 2.10a, the dirt road (top of the image) and metal structure (bottom right) are displayed in red hues with NDVI values close to zero. Healthier vegetation is shown in green hues with NDVI values varying between 0.50 and 0.70. Damaged vegetation can be seen in yellow and orange hues with NDVI values less than 0.35. Debris and tree trunks from downed trees can be seen in the darker orange/red values with NDVI values close to 0. Interestingly, canopies of the downed trees still have high NDVI values and appear to blend into the healthier grass. Just south of the downed trees, there is noticeable vegetation damage with NDVI values close to 0.20 that is not easily discernible in the visible imagery (Fig. 2.10b). Multispectral imagery can also be used to calibrate high-wind impacts to vegetation from satellite imagery or radar-indicated damage (Skow and Cogil 2017).

3D modeling products, such as point clouds or digital surface models, can provide detailed information on high-wind impacts to structures and land cover. Figure 2.11 shows roof damage to the Shiloh Baptist Church and downed trees from the 11 May 2017, White Oak, TX, tornado. Damage to the front of the church can be seen where the steeple had been located (Fig. 2.11a). The DSM model, although it captures the steeple damage, really highlights the downed trees to the right of the church with the lower elevation values relative to nearby trees and the detailed spatial resolution (Fig. 2.11b). What appears to be damage near the back of the building (Fig. 2.11a) is actually an artifact from the SfM process due to insufficient data coverage associated with near-nadir angles. Therefore, it is important to collect additional data using

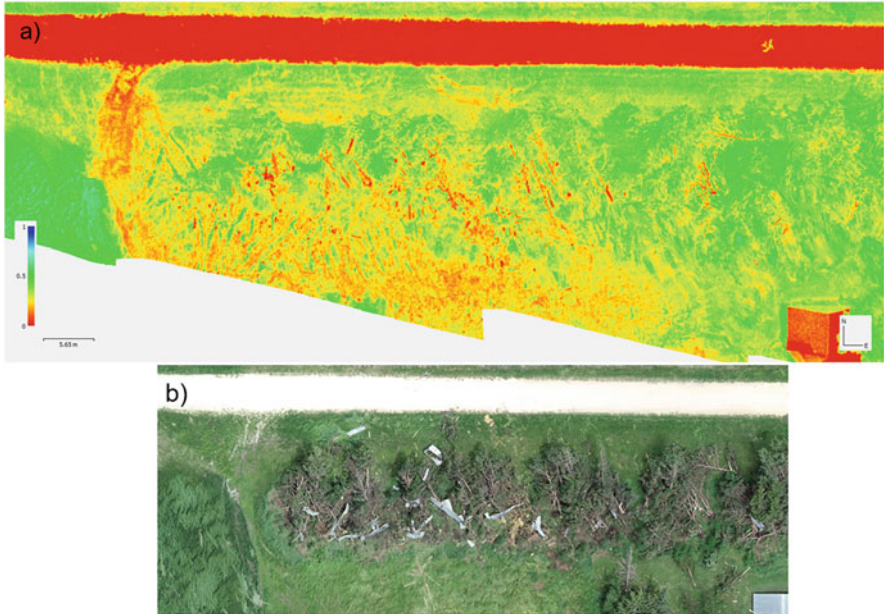


Fig. 2.10 (a) UAS normalized difference vegetation index (NDVI) (8-cm) and (b) UAS true color imagery (2-cm resolution) of a portion of the 28 May 2019 Tipton, KS, tornado. Green hues show healthier vegetation; yellow and orange hues show damaged vegetation; red hues correspond to bare soil and structures (metal building). (Images © Wagner/Doe)

oblique viewing angles to fill in potential data gaps. With sufficient data coverage and viewing angles, SfM products can provide detailed information needed to better understand the role of construction, structural variability, and land cover characteristics with high-wind impacts.

Change detection via point cloud differencing can highlight the amount of land cover change relative to wind interactions. This example uses USGS LiDAR data and resampled sUAS point cloud data obtained following the 01 May 2018 Tescott, KS, tornado. In Fig. 2.12, the geographic extent of a portion of the tornado track can be seen as a long thin linear feature crossing from the lower left to the upper right of the image. While overall land cover changes are relatively small (0.10 meters or less), there are some areas of maximum change ranging from 0.28 to 0.40 meters (see Fig. 2.12c). In fact, these areas of maximum erosion and scour coincide with areas of local maximum elevation (see Fig. 2.12a), pointing to enhanced scour with exposed features (check Wagner et al. 2021). Some of this land cover change, however, could be attributed to erosion based on geomorphic processes (e.g., wind patterns).

Ground surveys will always have a place in storm damage assessments and examining the role of construction variability. Complementing these surveys with sUAS technology will improve these efforts as this technology enables quick assessment of high-wind damage, better captures wind damage at the lower level of the EF scale and from non-tornadic events (e.g., straight-line winds and hail

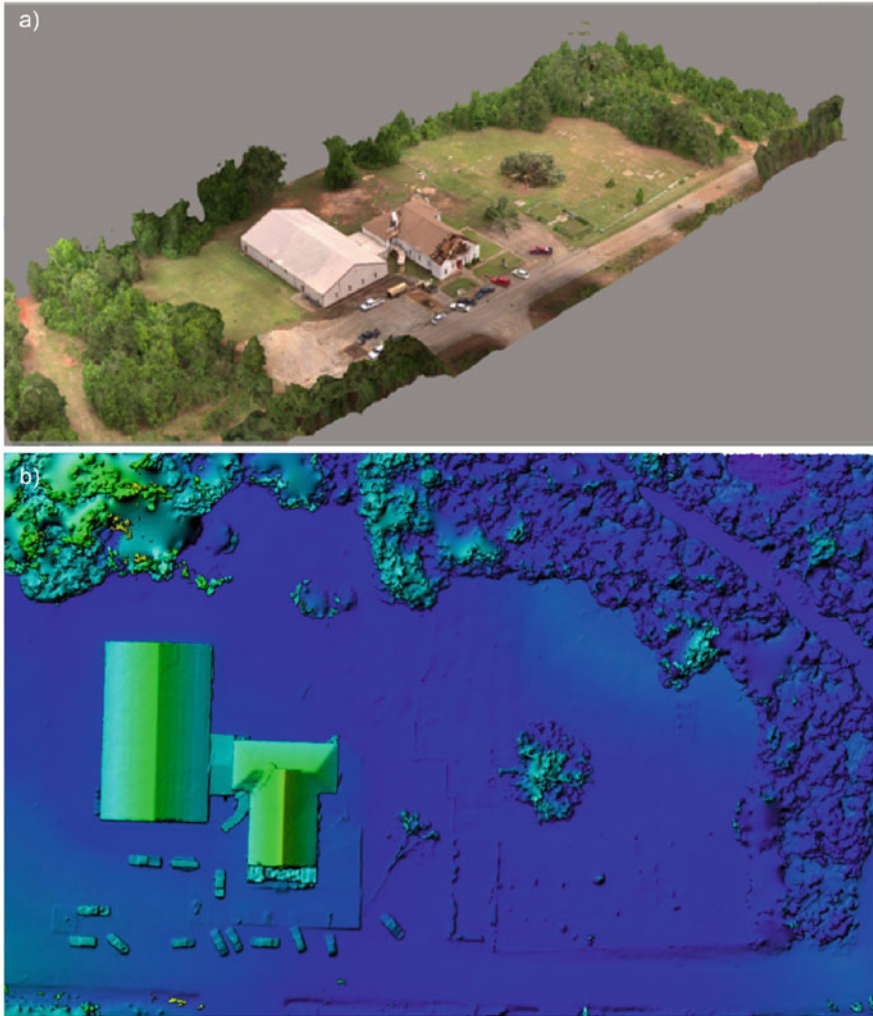


Fig. 2.11 (a) 3D model generated from Structure from Motion (SfM) and (b) digital surface model (DSM) of tornado damage from the 11 May 2017 White Oak, TX, tornado. The 3D model shows roof and tree damage to the right of Shiloh Baptist Church. DSM depicts fallen trees and roof damage based on detailed elevation information. (Images © Wagner/Doe)

damage), as well as serves as a more cost-effective and time-saving alternative to current rapid response surveys (Wagner et al. 2019). Additionally, it may provide a better understanding of high-wind damage at the macro-level that can improve our understanding of tornado climatology, especially in rural and agricultural areas, where damage indicators are limited (see Snyder and Bluestein 2014). This information can be disseminated to local, state, and federal agencies to aid in disaster response and recovery.

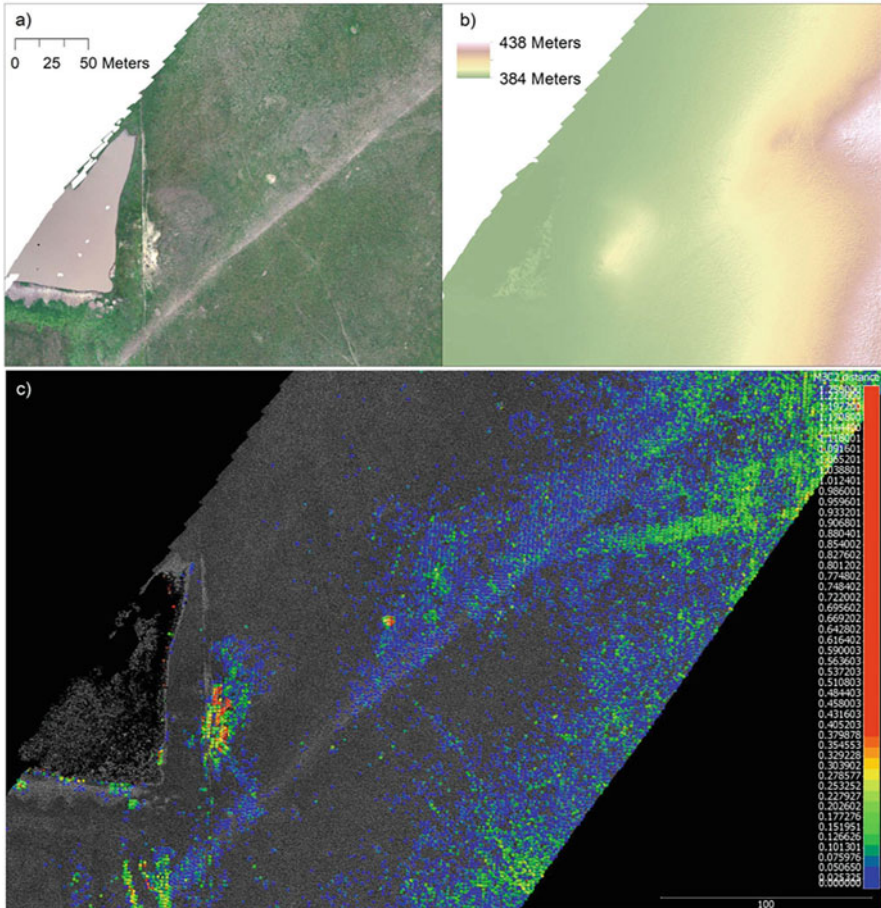


Fig. 2.12 UAS information of a portion of the 01 May 2018 Tescott KS tornado survey captured in (a) true color composite and (b) digital surface model. In (c), results from point cloud differencing using USGS LiDAR data and resampled unpiloted aerial system (UAS) point cloud data are shown. Small land cover changes are displayed in blue hues, while larger land cover changes are shown in red hues. (Images © Wagner/Doe)

2.5 Hazard Management, Sensing, and Verification

Post-event damage surveys utilizing sUAS technologies can help hazard management, sensing, and verification with overlapping benefits to multiple end-users (Fig. 2.13). In hazard management, sUAS technologies can improve disaster response and community awareness in part due to rapid deployments and access to obstructed areas or remote locations. Aerial coverage and detailed information provided by sUAS technologies can provide a more complete/accurate assessment of the societal and environmental costs associated with an event. In regard to hazard

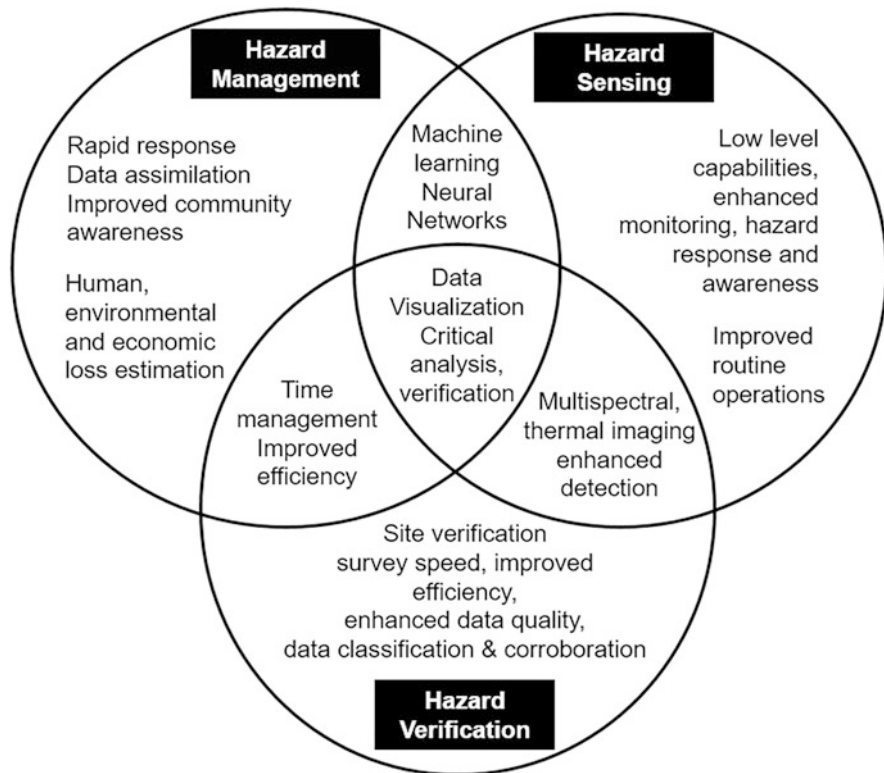


Fig. 2.13 Venn diagram from SCOUT (Severe Convective Post-Storm Observations utilizing Unpiloted Aerial Systems (UAS) based Technologies) (Wagner and Doe 2017) examining the relational elements of hazard management, sensing, and verification. (Image © Wagner/Doe)

sensing, UAS-based sensors (e.g., UAS multispectral camera) can also improve detection of low-magnitude events or events in remote locations that would otherwise go undetected (Wagner et al. 2019). This enhanced monitoring would lead to better documentation and, consequently, improve climatological records, increasing hazard awareness. Hazard verification via UAS technologies may also increase the efficiency of damage surveys by decreasing the time and resources needed to assess the event.

Improved efficiency, enhanced detection, and machine learning algorithms can help multiple agencies such as emergency managers, NOAA agencies, and researchers with their objectives. Accurate and timely information is critical to emergency manager operations and can better inform decision-making and planning with regard to disaster response and recovery planning. Government agencies such as NOAA National Weather Service need verification of warned events to improve training and decision-making criteria with future hazard events. Researchers, whether affiliated with academic or government institutions, could develop machine learning algorithms to improve damage detection and classification. UAS damage

information, when combined with other observational datasets, may help researchers better understand dynamics of these events. The critical overlap of benefits to end-users, here, is facilitated by visualizing and analyzing UAS damage data to better help delineate critical information more accurately.

2.6 Challenges

There will undoubtedly be challenges when using UAS in hazard environments, especially when practiced in what could also be stressful conditions post-event. Each location and hazard type will present its own set of challenges. These challenges range from those connected to the equipment itself, to environmental extremes, and to total awareness for the assistant(s)/VLOS. If we examine the environment itself, such challenges can range from hazardous damage to temperature and wind extremes, which affect UAS performance. It is well-documented that heat, cold, and wind speed affect battery life and performance. If wind speeds are too high, flight operations should be suspended until they can be performed safely. The operator also needs to be mindful of local nature, especially considering nesting birds and annoyance to livestock as an example.

Other challenges include the quality of data collection, site considerations and accessibility, and concurrent sUAS operations. To obtain the best image quality, one needs consistent daylight, avoiding varying illumination conditions (i.e., partly cloudy skies) and times of the day when shadows may protrude on features of interest (Tmuší' et al. 2020). This is not always possible, especially when multiple flight operations will need to be conducted within a limited time frame. Siting considerations could be constrained by permissions, terrain, or size of kit. Obtaining permissions for landing and take-off on private property can be quite the challenge considering landowners may not be present following the disaster. This can become frustrating especially when time is very limited. In the case of remote environments and varied terrain, accessibility may not be possible; therefore, traversing remote areas with a heavy kit also needs consideration. Lastly, you need to be cognizant of other concurrent sUAS operations. Following a disaster, the skies could be congested with other sUAS operations given damage severity and media coverage of the event. Therefore, you need to keep a keen eye to the sky to watch out for other sUAS operations.

2.7 Summary

This chapter has outlined both the usefulness and complexities in sUAS deployment in hazard environments. With exponential usage and multiple applications, the results obtained can be highly innovative, valuable, and quick. In the future, the application of equipment, workflows, and methodology will become even more

streamlined, but significant challenges will exist, for example, the ever-changing complex international policy and governance landscape.

We have shown that a robust workflow is essential before any operation. Whether you devise or modify your own workflow, a successful workflow is always based around safety. Working in hazard environments themselves can be unsafe, so your plan and formal procedures need extra-special attention. A robust workflow might require coordination and collaboration with multiple agencies and provide specific information either publicly or not publicly available. Therefore, we have shown a coordinated approach can be fruitful, especially for highly localized events.

The future is clear; the use of autonomous vehicles in hazard environmental assessments, rescue, or monitoring fieldwork will become the norm. The reason is the benefits outweigh time, costs, and spatial coverage in comparison to what a human can perform on the ground, in what are often harsh conditions. What such vehicles can do, on multiple levels, is bring new data insights, and with these insights comes the value needed to justify the learning curve, initial investment, and maintenance costs. There will always be challenges, firstly as each hazard environment is unique and then there is, with increased adoption, managing a crowded low-level airspace under a multiple operator environment. We hope the reader has found our concise journey to date useful, especially the applied geographer seeking sUAS fieldwork experience in hazard environments for the first time. We end the chapter as we started, reiterating the words; there is certainly no “one size fits all” approach to using sUAS in the field, but on the other hand, there is no end of possibilities for the applied geographer.

Acknowledgments The fieldwork presented between 2016 and 2019 was performed by the *Severe Convective Storm Observations Utilizing Unpiloted Aerial Systems-based Technologies* (SCOUT) team. Current funding for Melissa A. Wagner is provided through the NOAA/Office of Oceanic and Atmospheric Research under NOAA-University of Oklahoma Cooperative Agreement #NA11OAR4320072, US Department of Commerce. Robert K. Doe is an Honorary Research Fellow at the School of Environmental Sciences, University of Liverpool, and his research contribution was self-funded. The authors provide selected web resources as a helpful guide to those new to the field and do not have any conflict of interest with the particular resources mentioned.

References

- Akhloufi MA, Couturier A, Castro NA (2021) Unmanned aerial vehicles for wildland fires: sensing, perception, cooperation and assistance. *Drones* 5(1):15. <https://doi.org/10.3390/drones5010015>
- Cabuk A, Deveci A, Ergincan F (2007) Improving heritage documentation. *GIM Int* 21:1–2
- Carlson TN, Ripley DA (1997) On the relation between NDVI, fractional vegetation cover, and leaf area index. *Remote Sens Environ* 62(3):241–252
- Doswell CA III, Brooks HE, Dotzek N (2009) On the implementation of the enhanced Fujita scale in the USA. *Atmos Res* 93:554–563

- Ezequiel CAF, Cua M, Libatique NC, Tangonan GL, Alampay R, Labuguen RT, Favila CM, Honrado JLE, Canos V, Devaney C, Loreto AB (2014) UAS aerial imaging applications for post-disaster assessment, environmental management and infrastructure development. In: Unmanned Aircraft Systems (ICUAS), 2014 International Conference. IEEE, pp 274–283
- Giordan D, Manconi A, Remondino F, Nex F (2017) Use of unmanned aerial vehicles in monitoring application and management of natural hazards. *Geomat Nat Haz Risk* 8(1):1–4. <https://doi.org/10.1080/19475705.2017.1315619>
- Gitelson AA, Merzlyak MN, Lichtenthaler HK (1996) Detection of red edge position and chlorophyll content by reflectance measurements near 700 nm. *J Plant Physiol* 148(3–4):501–508. [https://doi.org/10.1016/S0176-1617\(96\)80285-9](https://doi.org/10.1016/S0176-1617(96)80285-9)
- Guo Y, Senthilnath J, Wu W, Zhang X, Zeng Z, Huang H (2019) Radiometric calibration for multispectral camera of different imaging conditions mounted on a UAV platform. *Sustainability* 11(4):978. <https://doi.org/10.3390/su11040978>
- Johnson K, Nissen E, Saripalli S, Arrowsmith JR, McGarey P, Scharer K, Blisniuk K (2014) Rapid mapping of ultrafine fault zone topography with structure from motion. *Geosphere* 10(5): 969–986
- Jurecka M, Niedzielski T (2016) A procedure for delineating a search region in the UAS-based SAR activities. *Geomat Nat Haz Risk*:17
- Kingfield DM, de Beurs KM (2017) Landsat identification of tornado damage by land cover and an evaluation of damage recovery in forests. *J Appl Meteor Climatol* 56:965–987. <https://doi.org/10.1175/JAMC-D-16-0228.1>
- Lambers K, Eisenbeiss H, Sauerbier M, Kupferschmidt D, Gaisecker T, Sotoodeh S, Hanusch T (2007) Combining photogrammetry and laser scanning for the recording and modelling of the late intermediate period site of Pinchango Alto, Palpa, Peru. *J Archaeol Sci* 34:1702–1712
- Mamaghani B, Salvaggio C (2019) Multispectral sensor calibration and characterization for sUAS remote sensing. *Sensors* 19(20):4453. <https://doi.org/10.3390/s19204453>
- Milas AS, Arend K, Mayer C, Simonson MA, Mackey S (2017) Different colours of shadows: classification of UAV images. *Int J Remote Sens* 38(8–10):3084–3100. <https://doi.org/10.1080/01431161.2016.1274449>
- Myint SW, Yuan M, Cerveny RS, Giri C (2008) Categorizing natural disaster damage assessment using satellite-based geospatial techniques. *Nat Hazard Earth Syst Sci* 8(4):707–719
- NOAA (2020) New NOAA program to support and expand agency's use of unmanned systems. Web site: <https://www.noaa.gov/media-release/new-noaa-program-to-support-and-expand-agency-s-use-of-unmanned-systems>. Accessed 30 Apr 2021
- Remondino F, Barazzetti L, Nex F, Scaioni M, Sarazzi D (2011) UAS photogrammetry for mapping and 3d modeling – current status and future perspectives. In: Eisenbeiss H, Kunz M, Ingensand H (eds) Proceedings of the ISPRS ICWG I/V UAS-g (Unmanned Aerial Vehicle in Geomatics) Conference. International Archives of the Photogrammetry, Remote Sensing and Spatial Information Sciences, Zurich, pp 25–31
- Santamaria E, Royo P, Barrado C, Pastor E, Lopez J, Prats X (2008) Mission aware flight planning for unmanned aerial systems. In: AIAA Guidance, Navigation and Control Conference and Exhibit. American Institute of Aeronautics and Astronautics, Honolulu, Hawaii. Aug 18–21, 2008
- Sauerbier M, Eisenbeiss H (2010) UASs for the documentation of archaeological excavations. In: Mills JP, Barber DM, Miller PE, Newton I (eds) Proceedings of part 5 commission V symposium. International Archives of Photogrammetry, Remote Sensing and Spatial Information Sciences, Newcastle upon Tyne, pp 526–531
- Silvagni M, Tonoli A, Zenerino E, Chiaberge M (2016) Multipurpose UAS for search and rescue operations in mountain avalanche events. *Geomat Nat Haz Risk* 16
- Singh A (1989) Review article digital change detection techniques using remotely-sensed data. *Int J Remote Sens* 10(6):989–1003

- Skow KD, Cogil C (2017) A high-resolution aerial survey and radar analysis of quasi-linear convective system surface vortex damage paths from 31 August 2014. *Weather Forecast* 32: 441–467. <https://doi.org/10.1175/WAF-D-16-0136.1>
- Tmušić G, Manfreda S, Aasen H, James MR, Gonçalves G, Ben-Dor E, Brook A, Polinova M, Arranz JJ, Mészáros J, Zhuang R, Johansen K, Malbeteau Y, de Lima IP, Davids C, Herban S, McCabe MF (2020) Current practices in UAS-based environmental monitoring. *Remote Sens (Basel)* 12(6):1001. <https://doi.org/10.3390/rs12061001>
- Wagner M, Doe RK (2017) Using Unmanned aerial vehicles (UASs) to modeling tornado impacts. AGU 2017 fall meeting abstracts. American Geophysical Union, San Francisco CA
- Wagner MA, Myint SW, Cervený RS (2012) Geospatial assessment of recovery rates following a tornado disaster. *Geosci Remote Sens IEEE Trans* 50(11):4313–4322
- Wagner M, Doe RK, Johnson A, Chen Z, Das J, Cervený RS (2019) Unpiloted aerial systems (UASs) application for tornado damage surveys: benefits and procedures. *Bull Amer Meteor Soc* 100(12):2401–2405
- Westoby MJ, Brasington J, Glasser NF, Hambrey MJ, Reynolds JM (2012) ‘Structure-from-motion’ photogrammetry: a low-cost, effective tool for geoscience applications. *Geomorphology* 179: 300–314
- Womble JA, Wood RL, Mohammadi ME (2018) Multi-scale remote sensing of tornado effects. *Front Built Environ* 4:1–21. <https://doi.org/10.3389/fbuil.2018.00066>
- Xue J, Su B (2017) Significant remote sensing vegetation indices: a review of developments and applications. *J Sensor* 201:–Article ID 1353691. <https://doi.org/10.1155/2017/1353691>
- Yamamoto H, Kouyama T, Obata K, Tsuchida S (2015) Assessment of HISUI radiometric performance using vicarious calibration and cross-calibration. *Proceedings of the 2015 IEEE International Geoscience and Remote Sensing Symposium (IGARSS)*, Milan., 26–31 July 2015, pp 2805–2808
- Zimmerman T, Jansen K, Miller J (2020) Analysis of UAS flight altitude and ground control point parameters on DEM accuracy along a complex, developed coastline. *Remote Sens (Basel)* 12(14):2305. <https://doi.org/10.3390/rs12142305>

Useful Web Resources¹

Policy

- Drones for Education (and model aircraft): If you are a teacher or a student looking to adopt drones into your curriculum/research: https://www.faa.gov/UAS/educational_users/
- European Aviation Safety Agency, Policy Statement Airworthiness Certification of Unmanned Aircraft Systems (UAS): https://www.easa.europa.eu/sites/default/files/dfu/E.Y013-01_%20UAS_%20Policy.pdf
- European Commission, EU policy on mobility and transport unmanned aircraft: https://ec.europa.eu/transport/modes/air/UAS_en

¹The following web resources present a small selection of useful links to aid the reader apply sUAV in a safe, informed, and practical way. Other resources do exist, and the links may update and change with time.

EU Regulations 2019/947 and 2019/945 set the framework for the safe operation of drones in European skies (EU and EASA Member States): <https://www.easa.europa.eu/domains/civil-drones-rpas>

Information and links to US Department of the Interior Bureau Aviation Policy Documents as well as links to FAA Policy for the use of Unmanned Aircraft Systems (UAS): <https://www.doi.gov/aviation/UAS/policy>

Regulations & Policies of the U.S. Department of Transportation, Federal Aviation Administration: https://www.faa.gov/regulations_policies/

UAS Policy Resources from the National Oceanic and Atmospheric Administration (NOAA): <https://UAS.noaa.gov/Policy>

Planning

A knowledge portal dedication to the actual operation of a UAS, see section 5.2 Flight planning: <https://www.stars-project.org/en/knowledgeportal/magazine/UAS-technology/flight-planning/>

Useful flight planning manual of UAS standard flight procedures prepared by the UAS program office of North Carolina Department of Transportation: https://connect.ncdot.gov/resources/Aviation%20Resources%20Documents/NCDOT_UAS_SOP.pdf

Airspace

Airmap: Visualize real-time airspace information, including official aeronautical data, regulations, dynamic restrictions, weather, and ground obstructions, on an easy-to-use digital map <https://www.airmap.com/>

B4UFLY (USA): Drone Safety & Airspace Awareness, check airspace and local advisories stay compliant and contribute to safer national airspace by making yourself aware of advisories and restrictions in the airspace and local advisories around you: https://www.faa.gov/UAS/recreational_fliers/where_can_i_fly/b4ufly/

Drone Assist (UK): safety app from NATS, the UK's main air traffic control provider presents users with an interactive map of airspace used by commercial air traffic so you can see areas to avoid or in which extreme caution should be exercised, as well as ground hazards that may pose safety, security or privacy risks <https://dronesafe.uk/safety-apps/>

Hover – Drone & UAS pilot app, features include: no-fly zone map, flight logs, weather data, flight readiness indicator, and industry news feed. <http://www.hoverapp.io/>

UAS Flight Planning powered by ArcGIS, you can use this application to check for No Fly Zones (US Only) and also to check for differences in elevation between your "Home Point" and your Area of Interest: <https://www.arcgis.com/apps/Viewer/index.html?appid=021e985e6e2d42a694db71ce4ba54312>

Data

Presentation detailing the Privacy and Data Protection Implications of the Civil Use of Drones from the Policy Department Citizen' Rights and Constitutional Affairs, European Parliament: <https://www.europarl.europa.eu/cmsdata/85184/Drones-%20formatted.pdf>

Unmanned Aerial Vehicles for Geographic Data Capture: A Review by Hanna Gustafsson and Lea Zuna. EXAMENSARBETE INOM TEKNIK, GRUNDNIVÅ. 15 HP STOCKHOLM, SVE-RIGE 2017: <https://www.diva-portal.org/smash/get/diva2:1116742/FULLTEXT01.pdf>

Workflow

FAA Aviation Handbooks and Manuals: a detailed resource of texts: https://www.faa.gov/regulations_policies/handbooks_manuals/aviation/

UAS Forecast: A useful tool to forecast wind/gust/cloud cover and with visibility and a predictor as to whether it is good condition to fly <https://www.UASforecast.com/>

Chapter 3

sUAS-Based Citizen Science Studies in Geography



Erin L. Bunting, Ethan J. Theuerkauf, and Lucas Rabins

Abstract Small unoccupied aerial systems (sUAS) are powerful tools for geographic research given their flexibility and rapidity in data collection. Combining sUAS platforms with citizen science creates an opportunity to combine data collection, education, and outreach. This approach is particularly valuable for mapping large areas, documenting changes across those areas, and integrating stakeholders in the research process to promote science-based decision-making. Although numerous examples exist where sUAS are incorporated into citizen science projects, this approach is still in its infancy. In this chapter, we will explore several case studies of crowdsourced implementation of sUAS data collection and analysis. We will use these case studies to explore best practices for incorporating sUAS into citizen science projects. Additionally, we will explore public perception of sUAS in the context of scientific research through a case study in Michigan, USA, and explore how participation in a sUAS-based citizen science project impacts those perceptions. Finally, we will explore how sUAS-based citizen science can empower communities to identify hazards and solve challenges.

Keywords UAS · Citizen science · Coastal monitoring

E. L. Bunting

Remote Sensing and GIS Research and Outreach Services, Michigan State University,
East Lansing, MI, USA

Department of Geography, Environment, and Spatial Sciences, Michigan State University,
East Lansing, MI, USA

E. J. Theuerkauf (✉) · L. Rabins

Department of Geography, Environment, and Spatial Sciences, Michigan State University,
East Lansing, MI, USA

e-mail: theuerk5@msu.edu

3.1 Introduction

We live in an ever-changing world that is shaped and altered by increased climate variability/change and human disturbance. With escalating loss of biodiversity (Butchart et al. 2010; Chapin et al. 2000; Dobson et al. 2006), land use change/landscape fragmentation, and socioenvironmental vulnerability, there is an urgent need for better landscape monitoring (Pocock et al. 2018). Through intensive monitoring of landscape processes, patterns, and trends, we can start to understand and assess impacts and environmental change, evaluate policy and management effectiveness, and develop models to better understand local- to global-scale vulnerability. One way to accelerate the pace and scale of monitoring is through the adoption and expansion of new technologies. One such technology, unoccupied aerial systems (UAS, aka drones), has been a catalyst for rapid changes in research, monitoring, and management of lands around the world. In 2016, there were approximately two million drones, but that number more than doubled by 2020 according to the Federal Aviation Administration (FAA; Garrett and Anderson 2018). This lightweight equipment is now collecting data on every continent on Earth.

Purely having the technology is not sufficient. Personnel and work hours are needed to utilize the technology including data collection, processing, analysis, and interpretation. Engaged citizens have long been a workforce in collecting spatiotemporal data and in monitoring landscapes through citizen science programs. As new technologies, such as UAS, come online and better platforms are created for managing citizen-collected data, the popularity of the citizen science approach is growing worldwide. However, a recent review of the literature conducted for this chapter (through 2019) found only a handful of studies that engaged citizen science in direct data collection using UAS.

UAS technology is being adopted across multiple fields and industries as these systems have great potential for assisting in landscape monitoring and management. Geographers, however, are particularly well-equipped to adopt, innovate, and expand the use of such systems given the long tradition of critical scholarship on the “view from above” (Garrett and Anderson 2018). With such a spatial perspective, as seen in the development and expansion of remote sensing and geographic information systems (GIS), applied research in the fields of physical and human geography has resulted in innovative methodologies and mapping with drones. However, as previously mentioned, to conduct such applied work, substantial human hours are needed, which can make operational usage of this technology for large-scale monitoring challenging. Within the geographic discipline, there are countless examples of participatory GIS in terms of both crowdsourcing and citizen scientist involvement.

This chapter assesses the small but rapidly growing body of literature on the use of drones in citizen science exploring the fields of study, regions, scales, and the way in which the citizen was utilized in the work. We focus particularly on the geographic discipline given the history of spatial sciences, geographic technologies, and

participatory GIS. In the closing portion of this chapter, we look to the future and assess how putting drones in the hands of citizens influences both its application and various fields of study.

3.1.1 Drones

UAS or drones are increasingly being utilized in a variety of sectors including recreation, business, military, and academia (Choi-Fitzpatrick 2016; Cummings et al. 2017b). Within academia drones are being applied in a range of disciplines including geography, geology, ecology, agriculture, atmospheric science, as well as urban and regional planning (Chahl 2015; Garrett and Anderson 2018; Wargo et al. 2014). One facet helping to drive the expanded use of drones is their ability to host a large and very expanding variety of sensors including cameras collecting information from the electromagnetic spectrum, meteorological sensors including temperature and pressure gauges, or more specialized sensors that can detect gasses or radioactive material (Boudergui et al. 2011; Collin et al. 2019; Cummings et al. 2017b; Jordan 2019; Li et al. 2017). This diversity of sensors has given researchers a new toolset for data collection. For example, in geology, drones have been used to survey volcanic gases during eruptions (Jordan 2019). In ecology, cameras collecting infrared and red edge imagery have been used to improve classification of reef ecosystems (Collin et al. 2019). In the atmospheric sciences, drones equipped with ozone-detecting sensors have aided in troposphere pollution assessment (Li et al. 2017).

The employment of various types of drones is dependent on the situation, field of study, and parameters to be collected. Due to increased usage in military, civil, and scientific research operations, significant efforts have been devoted to improving drone flight endurance and payload capacity. Understanding these two criteria is key when adopting such technology as they dictate the scale at which data can be collected and how agile a data collection effort is. Expanded usage and increased drone engineering have also resulted in various system configurations and sizes, though fixed-wing and multirotor (e.g., quadcopter, octocopter) are the present industry standard (Gupta et al. 2013; Fig. 3.1). With both drone types, there are capabilities to mount a camera or sensor in order to collect various types of high-resolution remotely sensed data. Such cameras and sensors, which range in size, weight, and price, can collect unique properties on the ground including thermal, LiDAR, hyperspectral, and multispectral, examples of each are seen in Fig. 3.2.

3.1.1.1 Satellite vs. UAS

Outside of drones, sources of aerial imagery have long relied on occupied aircraft and, most commonly, satellites. There are distinct differences between drone- and satellite-developed datasets requiring the user to understand the pros and cons of each. Satellite imagery varies in both spatial resolution (the ground footprint of a

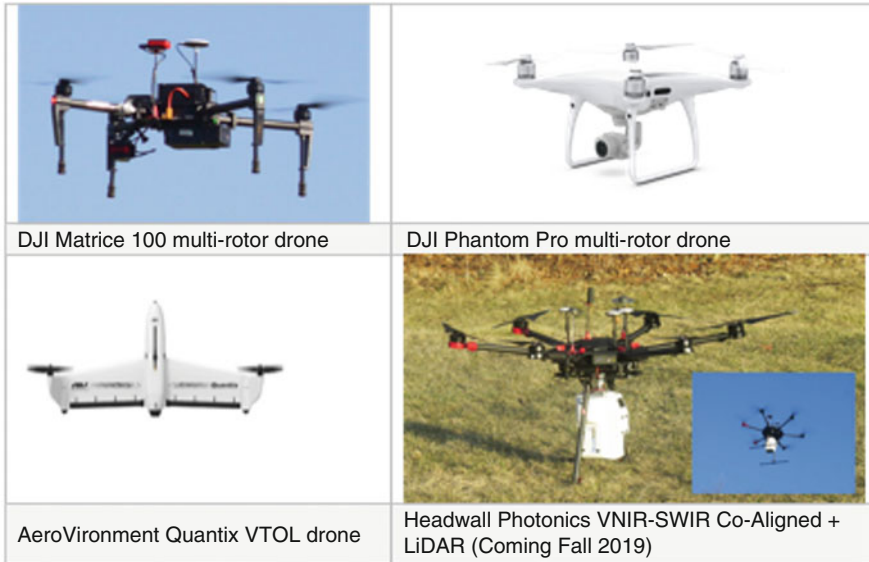


Fig. 3.1 Examples of fixed-wing and multirotor drones



Fig. 3.2 Examples of common sensors mounted to drones

single pixel observed by a sensor) and temporal resolution (the minimum time between successive image acquisitions of the same area). For instance, the MODIS (Moderate Resolution Imaging Spectroradiometer) satellite has a temporal resolution of 2 weeks and a spatial resolution of 250–500 m. Such data coverage and spatial resolution enable us to answer regional to landscape level questions of land cover, ecosystem health, and other similar questions. At a finer resolution than MODIS and potentially the most utilized satellite data, the USGS Landsat missions 1–9 have a multispectral resolution of 30 m (Landsat—Earth Observation Satellites 2020). This resolution, while ideal for land cover and vegetation mapping, is still too coarse for many applications such as crop disease detection or wildlife monitoring (Rey et al. 2017; Wiesner-Hanks et al. 2019). Additionally, the temporal resolution of a satellite limits the utility of its imagery for certain applications. More specifically, the temporal resolution, or time between acquisitions, is based on the

satellite orbit and not the event being monitored, meaning that the time of day and time between image collections might not be ideal for certain events. For example, in monitoring ecosystem health, a 2-week or monthly temporal resolution is sufficient, but with coastal monitoring of water level, the changes can occur on a finer scale. While satellite imagery is available for broad geographic areas, the highest-resolution satellites, such as WorldView-3, are only capable of ~0.3 m ground sampling distance (*WorldView-3 Data Sheet*, 05/14). Among these satellites the temporal resolution ranges from daily or less (WorldView-3) to weekly (Landsat), biweekly (MODIS), and monthly. This temporal frequency combined with the long life of these platforms and consistent global coverage dating back to the 1980s makes satellite remote sensing ideal for long-term time series analysis.

Beyond the spatial and temporal coverage, there are additional pros and cons to satellite image utilization. For instance, such imagery is not always usable for analysis as a satellite's ability to collect imagery is limited to the time the satellite is overhead and may be obscured by clouds on any given day (Ruwaimana et al. 2018). Ordering satellite imagery can also be expensive and may require substantial pre-processing to derive usable products. Currently, most moderate to coarse resolution remote sensing archives, from AVHRR (Advanced Very-High-Resolution Radiometer), MODIS, and Landsat, are freely available to the public through platforms developed by NASA and the USGS in addition to the Google Earth Engine platform. Finer-scale satellite imagery, such as WorldView, have variable costs ranging from \$14 to \$58 per square kilometer depending on the date and type of imagery requested (Satellite Imagery Pricing 2018). The costs associated with satellite imagery are further compounded when considering the time invested in pre-processing such datasets. Unlike drone imagery, satellite imagery often requires several critical corrections including atmospheric and topographic corrections to compensate for the satellite position and distance the reflected energy travels (Young et al. 2017). While there are essential pre-processing steps involved in drone image utilization, the steps for RGB and multispectral imagery are typically laid out in a straightforward manner when using off-the-shelf software.

Occupied aircraft photography presents a scale of data collection between satellite and drone imagery. Image collection with aircraft can provide a higher spatial resolution than satellite imagery but is labor-intensive and may be expensive depending on proximity to airports and the data products desired. Additionally, aerial photography is limited in temporal coverage as it requires occupied missions that cannot continuously or regularly be conducted over the same region. Therefore, aerial imagery typically does not have a consistent or standard temporal resolution, making monitoring of dynamic processes, such as coastal change, difficult.

3.1.1.2 Understanding Drone-Based Remote Sensing

Considering the limitations with traditional remote sensing methods, drone imagery can be a useful alternate source of imagery. Although drones provide an efficient means of generating high spatial and temporal resolution datasets, mission

requirements must be critically evaluated as there are costs, training requirements, and historical data limitations with drones. Unlike satellite and occupied aircraft imagery, drone imagery can be collected at extremely high resolution as they can fly just above the ground. It should be noted however that local laws may restrict drone flight operations in some cases. In the United States, there is a maximum drone flight height of 400 feet above the tallest object in proximity (https://www.faa.gov/uas/commercial_operators/). Drone temporal resolution can also be higher than satellite and occupied aircraft as there is rarely a limit to how often a drone can be flown over an area (Cummings et al. 2017b). Constraining this observation is the person hours needed to be in the field collecting such data. Unlike satellite imagery, drone flights require staff to be physically present during each flight which can pose a challenge for large-scale monitoring in remote areas. Additionally, while the volume of single images can be similar between drones and satellites, each drone flight consists of hundreds of substantially overlapping image captures that when developed into a time series represent a large volume of data that needs to be processed and analyzed. This contrasts to satellite imagery, which is more easily processed, due to well-established workflows. Given the long history of satellite remote sensing, there are well-established processing steps with proprietary and open-source software options including R packages, open-source software (Quantum Geographic Information System, QGIS), and industry standard software (Earth Resource Data Analysis System or ERDAS Imagine and Environment for Visualizing Imager or ENVI). Considering the novelty of and diversity of sensors used with drones (multispectral, Light Detection and Ranging or LiDAR, thermal, hyperspectral, etc.), workflows for pre-processing and analyzing such data are still being developed, especially for advanced sensors such as thermal and hyperspectral. Additionally, the software employed for such pre-processing (e.g., Pix4D and Agisoft Metashape) is substantially different than the aforementioned programs and, as of now, is rather expensive.

3.1.2 Citizen Science

Citizen science has existed for hundreds of years and is widely used today in many fields including astronomy, ecology, and archeology (Silvertown 2009). Broadly defined as the engagement of volunteers for collecting or analyzing data as part of a scientific inquiry, today citizen science has grown, in many instances, into a collaboration between the public and researchers in order to address real-world challenges (Silvertown 2009). This type of collaboration can be seen in the State of Washington where volunteers are responsible for periodically monitoring coastal habitats for invasive green crabs (Grason et al. 2018). Engaging citizen scientists in this way can prove mutually beneficial for both the researchers and the community at large. Typically, during these projects, researchers will train the citizen scientists who then collect data and provide it to the researchers. The research team then analyzes these data and reports their findings back to the citizen scientists and the community at large. Citizen science can take other forms as well including citizens working by

themselves without institutional support, for example, an amateur astronomer independently observing the cosmos in their backyard and reporting their findings online. Additionally, citizen science can include cases where the citizens unknowingly volunteer information to researchers not originally intended for a study. For example, researchers may scrape social media websites like Facebook and Twitter for posts that aid in their analysis. In ecology, Barve (2014) demonstrated the utility of this technique by utilizing geotagged posts to map occurrences of monarch butterflies and snowy owls over a broad geographic area.

The community-engaged format of data collection, monitoring, and analysis is now mainstream with millions of people contributing to an ever-growing array of citizen science projects (Callaghan et al. 2019). There are large advantages to such an approach including obtaining community support for research through engagement, potentially more spatially comprehensive data, and the ability to collect high-resolution field data when the research cannot be on site. However, there are also disadvantages or complications associated with citizen science including spatial and temporal bias in data collection and potential redundancies (Callaghan et al. 2019). Such citizen science programs are developing massive datasets that can be used to develop models and statistics to understand trends in ways not previously understood, but with such massive data comes data management and storage needs. Overall, from the local, state, and country to global scale, there are numerous interdisciplinary citizen science programs that represent data collection that is robust and community centric and stretches the limits of what a single researcher or team can accomplish. Citizen science represents an effective means to communicate and engage community members in research through focus groups, surveys, training events, and public presentations. As a result, research can transcend the academic and begin to impact and educate the community from which it originates.

3.1.3 Citizen Science and Drones

Currently, there are few publications involving direct interaction of citizen science and drones. As seen in the literature, there are three ways citizen science and drones can be used together.

1. *Using citizen science collected datasets.* In this case researchers could use existing citizen science datasets or scrape social media sites like Facebook and Twitter for data including photos, geotagged locations, and descriptions of events. In the latter, these data can be used to inform drone pilots where to focus efforts. For example, reports of disaster areas uploaded to social media can be aggregated and used to guide drone surveys in disaster relief situations as seen in Ramchurn et al. (2016).
2. *Having citizen scientists assist with on-the-ground data collection.* Through direct interaction with the drones, citizen scientists can collect data in various locations and settings to assist in research. This could mean citizen scientists

acting as drone pilots, field assistants, or visual observers to support drone missions. For example, the “Dronebird” group in Japan is a dispersed network of drone owners who voluntarily gather aerial imagery in disaster zones and release data to aid relief efforts (“Drone Bird Disaster Rescue Squad,” 2020). This can also mean citizens assisting with on-the-ground data collection without piloting drones. For example, community members could be deployed along with drone pilots to provide local knowledge to guide drone use as outlined in Larrain et al. (2020). Further, examples of citizen scientists aiding in ground data collection include collecting field samples, placing ground control points for drone image pre-processing, and GPS data collection for key landscape characteristics.

3. *Having citizen scientists assist in data processing.* Data processing, especially when using UAS data, can be complex and time-consuming typically involving numerous images that need to be mosaiced and then georeferenced using ground control data. Citizen scientists can play a significant role when the volumes of data produced by drone flights are too large for researchers to realistically process themselves. Data processing activities can include citizen scientists in multiple fashions including (1) helping to identify regions where UAS data collections should occur and where are the idea locations to place ground control points, (2) identifying objects of interest in imagery or video collected, (3) collecting field data including ground control points with high-resolution GPS units, and (4) assisting with post image capture data management and pre-processing.

While the opportunities for citizen science and drone usage are broad, there are several barriers that may inhibit more widespread adoption of such an approach. For citizens to be drone pilots, they must be trained in drone operation and, depending on local laws, must obtain a license to pilot drones. For example, in the United States, FAA (Federal Aviation Administration) regulations, persons looking to fly a drone for non-recreational purposes must become certified under Part 107 rules (https://www.faa.gov/news/fact_sheets/news_story.cfm?newsId=22615). Certification requires one to understand airspace, climatology and atmospheric science, emergency protocol, rules/guidelines, and other such critical information. Additionally, an exam must be taken, at a cost, to receive certification. This initial investment in certification may dissuade citizens from joining a citizen science program as a pilot. It should be noted though that the FAA certification does not actually teach one how to fly a drone. Instead, citizens need hands-on training in drone operation as well as preflight planning and post flight data quality assessment to effectively collect data. Certification and training of citizens are only one of the barriers to the development of citizen science drone programs. Not only are drones costly and prone to damage by amateur pilots; there are also a litany of potential hazards associated with drone use (Gettinger and Michel 2015) which may dissuade researchers from putting them in the hands of citizen scientists. Such hazards include regulatory compliance, adverse weather conditions, equipment failure (e.g., lost link to base station, bad batteries, engine failure, obstacle avoidance), and unfavorable public perception.

Once these challenges are overcome, coupling drones and citizen science has distinct advantages including the following:

1. Many drones used for scientific purposes are small and portable which are conducive to citizen science deployment. Indeed, many of the drones used by researchers are the same models used for recreation and are not prohibitively complex or expensive to operate.
2. Drone flights can produce large amounts of data, especially when flights are frequently repeated. Large groups of citizen scientists can be employed to collect and process these data as seen in Rey et al. (2017).
3. Hobby and personal drone usage have increased in recent years (Choi-Fitzpatrick 2016) leading to an increase in drone ownership and pilot skills in the general population that can be utilized for citizen science.

Applications of drone usage with citizen science are not only ripe with opportunity but a growing trend in scientific research. Utilizing drones as research tools is still relatively new, and as adoption continues, one would expect the citizen science engagement to expand. However, as of now the full range of these applications is unexplored. This chapter will illustrate the current use of citizen science and drones through a comprehensive review of the literature (through 09/2020).

3.1.4 Literature Review Methods

In this review, all academic journal publications including both *Citizen Science* and *Drone* terms were downloaded and synthesized using the Web of Science database (Fig. 3.3). Web of Science was selected over other databases (Google Scholar and EBSCO) due to its commonality of use and sophisticated filters. Variations on the drone term included in the search (UAV, UAS, unoccupied aerial vehicle, unoccupied aerial system, etc.) are largely synonymous and are used interchangeably in many applications. Citizen science terms on the other hand have more differentiation in their meaning, and choosing which variations to include will yield different search results. This review included the following citizen science terms or variations thereof: *Citizen science*, *Crowd sourcing*, *Community science*, *Amateur scientist*, *Public participation*, *Participatory monitoring*, *Participatory action research*, *Volunteer*, *Citizen involvement*, *Public involvement*. Our initial search yielded 94 records, of which we removed 18 that were either books, datasets, patents, or reports (Fig. 3.3). The remaining records included journal articles and peer-reviewed conference papers. The authors assessed each article to determine if it included both a citizen science element and drone element and should be included in the review. Articles in question were determined by consensus among the authors. Of these 75 publications, only 18 were used in our final analysis (Fig. 3.3; Table 3.1). A large portion of the removed articles fell into one of two categories: (1) non-English publications and (2) publications related to the medical field. In both cases sUAS (which in our case means small unoccupied aerial systems) are common abbreviations. For instance, *suas* is a possessive pronoun in the Portuguese language. Articles including citizen science terms (such as *volunteer*) in the publication, but not

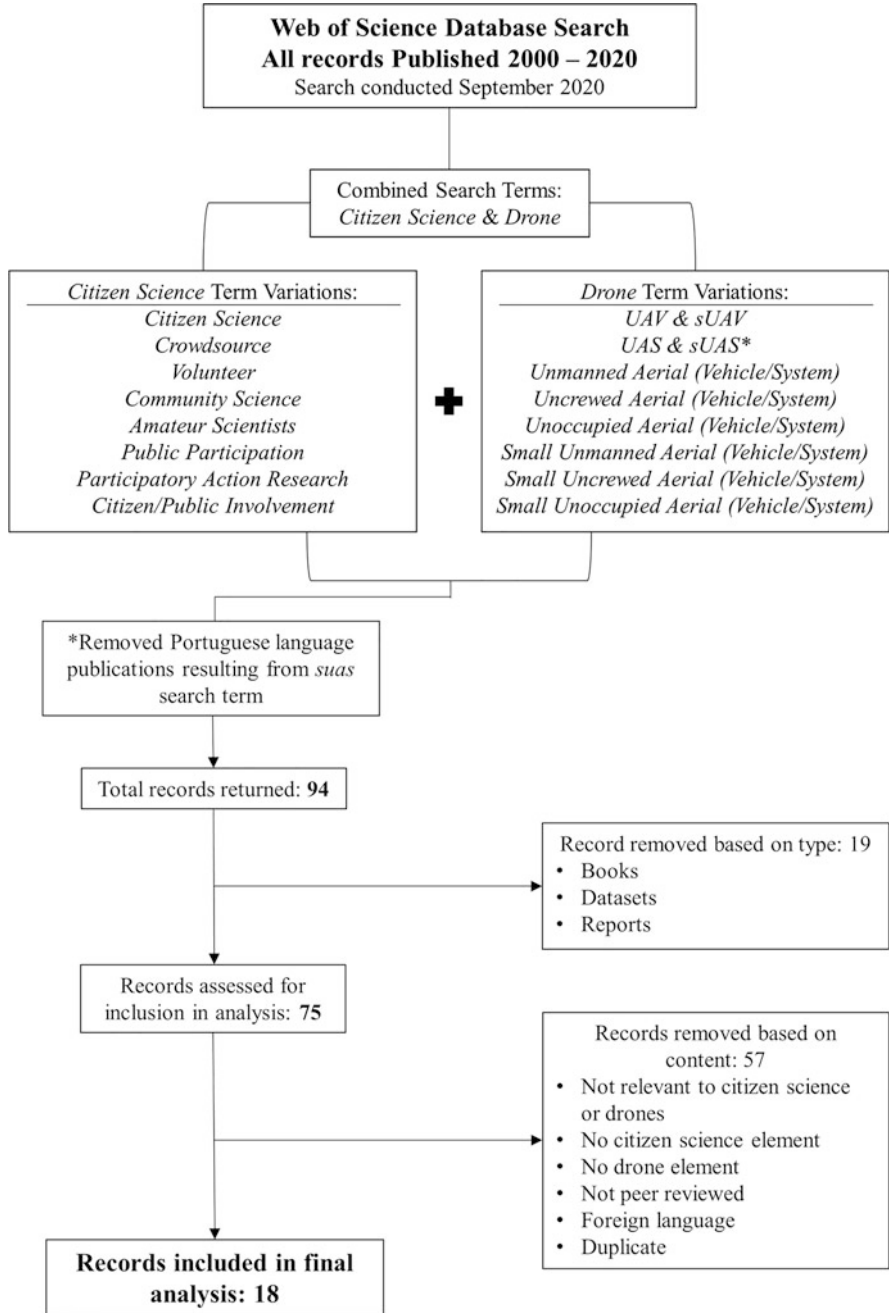


Fig. 3.3 Literature review methodological approach and decision-making process

Table 3.1 Final 18 publications included in the literature review highlighting the author, year published, title, journal, and scale of field site

Authors	Year published	Article title	Journal	Citizen science program scale
Alex et al.	2015	Crowdsourcing, for Search of Disaster Victims: A preliminary Study for Search and Rescue	Proceedings of the 20th International Conference on Engineering Design	NA (project done with existing data)
Attari et al.	2017	Nazr-CNN: Fine-Grained Classification of UAV Imagery for Damage Assessment	2017 IEEE International Conference on Data Science and Advanced Analytics	Country (Vanuatu)
Bowley et al.	2019	An Analysis of Altitude, Citizen Science and a Convolutional Neural Network Feedback Loop on Object Detection in Unmanned Aerial Systems	Journal of Computational Science	Region (Wapusk National Park, Manitoba Canada)
Cardil et al.	2017	Assessing Pine Processionary Moth Defoliation Using Unmanned Aerial Systems	Forests	Local (experimental plot)
Chirayath and Li	2019	Next-Generation Optical Sensing Technologies for Exploring Ocean Worlds—NASA FluidCam, MiDAR, and NeMO-Net	Frontiers in Marine Science	Local (American Samoa, Specific Sites not Country Wide)
Choi and Dyke	2020	CrowdLIM: Crowdsourcing to Enable Lifecycle Infrastructure Management	Computers in Industry	Local (Purdue University)
Cummings et al.	2017a, b	Developing a UAV-Based Monitoring Program with Indigenous Peoples	Journal of Unmanned Vehicle Systems	Local (village in Guyana)
Gülch et al.	2016	BEESMART – A Crowdsourcing Project with Smartphones	International Archives of the Photogrammetry, Remote Sensing and Spatial Information Sciences	Country (Germany)
Kaam and Reed	2019	Use of Visible Spectrum sUAS Photography for Land Cover Classification at Nest Sites of a Declining Bird Species (<i>Falco sparverius</i>)	Remote Sensing in Ecology and Conservation	Region (Massachusetts)

(continued)

Table 3.1 (continued)

Authors	Year published	Article title	Journal	Citizen science program scale
Larrain et al.	2020	Participatory Mapping and UAV Photogrammetry as Complementary Techniques for Landscape Archaeology Studies: An Example from North-Western Argentina	Archaeological Prospection	Local (Santa Mario, Argentina)
Lin et al.	2020	Quantifying Flood Water Levels Using Image-Based Volunteered Geographic Information	Remote Sensing in Ecology and Conservation	Local (Taipei City, Taiwan)
Ofii et al.	2016	Combining Human Computing and Machine Learning to Make Sense of Big (Aerial) Data for Disaster Response	Big Data	NA (project done with existing data)
Ramchurn et al.	2016	A Disaster Response System based on Human-Agent Collectives	Journal of Artificial Intelligence Research	Local (Port Au Prince, Haiti)
Rey et al.	2017	Detecting Animals in African Savanna with UAVs and the Crowds	Remote Sensing of Environment	Region (Kuzikus wildlife refuge)
Salisbury et al.	2015	Real-time Opinion Aggregation Methods for Crowd Robotics	Procedia Engineering	NA (method detailed, no location)
Salisbury et al.	2016	CrowdAR: A Live Video Annotation Tool for Rapid Mapping	Proceedings of the 14th international Conference on Autonomous Agents and Multiagent Systems	NA (method detailed, no location)
Scher et al.	2019	Drone-Based Photogrammetry for the Construction of High-Resolution Models of Individual Trees	Trees	Local (single trees)
Wiesner-Hanks et al.	2019	Millimeter-Level Plant Disease Detection from Aerial Photographs via Deep Learning and Crowdsourced Data	Frontiers in Plant Science	Local (individual fields)

incorporating any citizen science element in their study, were also excluded from the literature review.

To review publications, we completed an article evaluation survey in Qualtrics for each article (https://msu.co1.qualtrics.com/jfe/form/SV_3VhTBjplL8rnTsp). Survey questions, which had been vetted and tested prior to the study, included field of study, type of drone used, use of drone in study, role of citizen scientists, study environment, as well as benefits, drawbacks, and general notes about the article. Like the decision to include articles in the analysis, difficult survey responses were decided by group consensus.

3.2 Results and Discussion

3.2.1 Purpose of the Citizen Scientist

The articles analyzed highlight citizen science efforts, from around the world, that utilize drone technology in some capacity (Fig. 3.4; Table 3.2). We found such programs on every continent except Australia. These programs can be local in scale, for instance, Cardil et al. (2017) and Wiesner-Hanks et al. (2019) whose articles presented work at the individual field and plot level. Altogether, 9 of the 18 articles (50%) were local in scale including villages (Guyana), cities (Argentina, Taiwan, and Haiti), universities, and small islands. Regional scale programs, those at the state to province level, and those that occurred across national parks and wildlife refuges represent 2 of the 18 analyzed articles. At the country scale, 2 of the 18 articles had

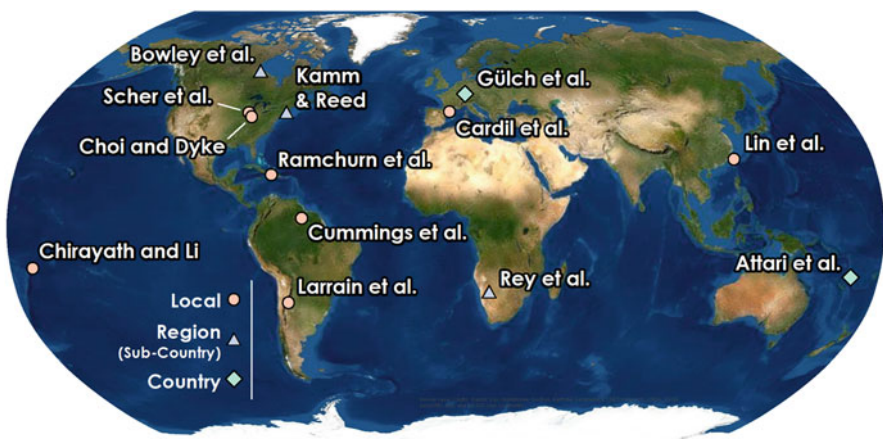


Fig. 3.4 Location of reviewed citizen science program field sites. Field sites indicate where data was collected during a study. Articles where researchers used preexisting datasets or authors did not specify field site locations are omitted. Scale indicates the geographic unit of the field site used for data collection. Specific locations can be found in Table 3.3

Table 3.2 Details of the 18 publications included in the literature review including a synopsis of the citizen science component and drone usage in the study

Authors	Use of Drone	Use of Citizen Science
Alex et al. (2015)	Drone used to stream live video of disaster areas	Citizens watch live drone footage and identifying disaster victims in real time
Attari et al. (2017)	Drone used to collect imagery of infrastructure.	Citizens identifying and categorizing infrastructure damage in drone imagery to be used as training dataset for image classification
Bowley et al. (2019)	Drone used to collect imagery of wildlife	Citizens identify wildlife from drone imagery to be used as training dataset for image classification
Cardil et al. (2017)	Drones used to collect imagery of and model forest habitats using photogrammetry	No citizen scientists included in study Noted potential for citizen scientists as drone pilots in future
Chirayath and Li (2019)	Drone used to host specialized sensors capable of imaging marine environments	Citizens used to generate training data to be used for image classification
Choi and Dyke (2020)	Drone used to model infrastructure using photogrammetry	Images uploaded on social media used to monitor infrastructure condition
Cummings et al. (2017a, b)	Drone used to collect imagery of cropland	Citizens used as drone pilot
Gülch et al. (2016)	Drone used to collect imagery of bee habitat	Citizens document bee habitat with mobile app
Kaam and Reed (2019)	Drone used to collect imagery of bird species habitat	Citizens scientists used to identify habitat types from drone imagery to be used in image classification Noted potential for citizens to be used as drone pilots in future
Larrain et al. (2020)	Drone used to survey and model archeological sites using photogrammetry	Citizens identify archeological sights to survey with drones
Lin et al. (2020)	Drones used to survey and model flood susceptible urban areas using photogrammetry	Images uploaded to social media are used to document water level during flood events
Oflı et al. (2016)	Drone used to collect imagery of wildlife (as a proxy for objects of interest in a disaster scenario)	Citizens identify wildlife from drone imagery to be used as training dataset for image classification
Ramchurn et al. (2016)	Drone used to investigate reports of disaster areas	Social media posts are used to identify potential disaster areas Citizens classify social media posts for more effective usage
Rey et al. (2017)	Drone used to collect imagery of wildlife	Citizens identify wildlife from drone imagery to be used as training dataset for image classification
Salisbury et al. (2015)	Wide range of potential uses	Crowd of citizens collectively piloting drone using input aggregation platform

(continued)

Table 3.2 (continued)

Authors	Use of Drone	Use of Citizen Science
Salisbury et al. (2016)	Drone used to stream live video of disaster areas	Citizens watch live drone footage and classify objects of interest in real time
Scher et al. (2019)	Drone used to model individual trees using photogrammetry	No citizen scientists included in study Noted potential for citizen scientist adoption of methods in future
Wiesner-Hanks et al. (2019)	Drone used to collect imagery of cropland	Citizens identify lesions on plants from drone imagery to be used as training dataset for image classification

projects that were developed across all of Germany and Vanuatu. None of the articles analyzed occurred at the global scale. It should be noted that five articles could not be directly tied to a specific scale. For instance, Offi et al. (2016) and Alex et al. (2015) utilized secondary or already existing data not pinpointed to a specific region (Table 3.3). Further, Salisbury et al. (2015, 2016) proposed or tested a methodology for citizen science with drones. Both articles did not test the methodology at a specific location.

While there is diversity in the application of drone-based citizen science, the utilization of citizen scientists can be divided into three main categories: (1) data collection, (2) data extraction, and (3) data mining.

3.2.1.1 Direct Citizen Scientists-Drone Interactions Through Data Collection

Of the publications assessed, only 4 of the 18 involved the citizen scientists with drone operation and data collection directly.

Two of these publications describe similar methods for disaster relief where citizen scientists watch live drone feeds and tag objects of interest such as victims in need of aid (Alex et al. 2015; Salisbury et al. 2016). In one of these publications, a crowd of observers outperformed both single observers and a computer identification algorithm in almost all cases (Alex et al. 2015). While citizen scientists may be uniquely suited to these disaster relief scenarios due to their ability to identify objects of interest in cluttered environments, there are drawbacks to citizen involvement. In particular, there may be ethical and legal concerns that must be considered, such as showing images of gore and death to citizen scientists (Alex et al. 2015). Another hurdle for using real-time citizen science in high-stakes scenarios, such as these, is the inconsistent response of volunteers to different disaster occurrences (Salisbury et al. 2016). Salisbury et al. (2016) address this concern by proposing the use of crowdsourcing marketplaces such as Amazon Mechanical Turk to supplement active observers when public participation is low. These crowdsourcing marketplaces allow customers to post tasks that cannot be easily automated, which are then fulfilled by online users of the platforms in exchange for small payments, typically

Table 3.3 Field of study and the study area land cover/use for the 18 publications included in the literature review

Authors	Article title	Field	Study area land cover/use
Alex et al. (2015)	Crowdsourcing for Search of Disaster Victims: A preliminary Study for Search and Rescue	Post Disaster Management	Mostly urban but other land covers too
Attari et al. (2017)	Nazr-CNN: Fine-Grained Classification of UAV Imagery for Damage Assessment	Post Disaster Management	Mostly urban but other land cover too
Bowley et al. (2019)	An Analysis of Altitude, Citizen Science and a Convolutional Neural Network Feedback Loop on Object Detection in Unmanned Aerial Systems	Ecology	Bogland/Peatland
Cardil et al. (2017)	Assessing Pine Processionary Moth Defoliation Using Unmanned Aerial Systems	Ecology	Forest
Chirayath and Li (2019)	Next-Generation Optical Sensing Technologies for Exploring Ocean Worlds—NASA FluidCam, MiDAR, and NeMO-Net	Ecology	Aquatic Systems
Choi and Dyke (2020)	CrowdLIM: Crowdsourcing to Enable Lifecycle Infrastructure Management	Infrastructure Management	Urban
Cummings et al. (2017a, b)	Developing a UAV-Based Monitoring Program with Indigenous Peoples	Agriculture	Cropland
Gülch et al. (2016)	BEESMART – A Crownsourcing Project with Smartphones	Ecology	Multiple land covers
Kaam and Reed (2019)	Use of Visible Spectrum sUAS Photography for Land Cover Classification at Nest Sites of a Declining Bird Species (<i>Falco sparverius</i>)	Ecology	Grassland
Larrain et al. (2020)	Participatory Mapping and UAV Photogrammetry as Complementary Techniques for Landscape Archaeology Studies: An Example from North-Western Argentina	Archeology	Scrubland
Lin et al. (2020)	Quantifying Flood Water Levels Using Image-Based Volunteered Geographic Information	Post Disaster Management	Urban
Ofli et al. (2016)	Combining Human Computing and Machine Learning to Make Sense of Big (Aerial) Data for Disaster Response	Post Disaster Management	Mostly urban but other land covers too
Ramchurn et al. (2016)	A Disaster Response System based on Human-Agent Collectives	Post Disaster Management	Urban
Rey et al. (2017)	Detecting Animals in African Savanna with UAVs and the Crowds	Ecology	Savanna
Salisbury et al. (2015)	Real-time Opinion Aggregation Methods for Crowd Robotics	Remote Sensing Method Development	Multiple land covers
Salisbury et al. (2016)	CrowdAR: A Live Video Annotation Tool for Rapid Mapping	Post Disaster Management	Mostly urban but other land covers too

(continued)

Table 3.3 (continued)

Authors	Article title	Field	Study area land cover/use
Scher et al. (2019)	Drone-Based Photogrammetry for the Construction of High-Resolution Models of Individual Trees	Ecology	Multiple land covers
Wiesner-Hanks et al. (2019)	Millimeter-Level Plant Disease Detection from Aerial Photographs via Deep Learning and Crowdsourced Data	Agriculture	Cropland

several cents per task (Ipeirotis 2010). While crowdsourcing platforms themselves are not citizen science, the methods they employ are analogous to those of citizen science and can indicate direct potential for citizen science expansion. In the other two articles with data collection, the citizen plays the role of the pilot, albeit in very different circumstances. One publication (Salisbury et al. 2015) investigates methods for allowing workers taken from crowdsourcing marketplaces (Amazon Mechanical Turk) to collectively pilot a drone through an online interface. This crowdsourced piloting allows professional drone operators to focus on the sensors while the drone is remotely controlled. This reduces strain on pilots who would traditionally have to monitor sensors while simultaneously piloting the drone. This method is applicable for any task where drone piloting cannot be automated, for example, infrastructure monitoring or drone-based parcel delivery (Salisbury et al. 2015). One major drawback of drone-centric citizen science noted in this article and other similar ones is the potential of nefarious actors among the crowd. People setting out to manipulate or sabotage data collections are nothing new. The problem of nefarious actors with the Amazon Mechanical Turk Platform was also observed in Wiesner-Hanks et al. (2019) when some workers seemed to identify lesions on plants seemingly at random within images. In this article the authors note that the cost for the Amazon Mechanical Turk workforce is quite low and annotation quality might increase if payment for these workers were to increase (Wiesner-Hanks et al. 2019). It is also possible that if these paid workers were to be replaced with volunteers, the occurrence of these malicious actors may decrease as participants are more invested in the success of the project.

The only other publication where citizen scientists are used as drone pilots and the only paper where citizens are directly trained to collect data is Cummings et al. (2017a). In this article researchers introduce drones to remote indigenous communities in Guyana to empower the community with improved methods of natural resource management. This program provided training for community members in all aspects of drone use from construction and maintenance to mission planning and data collection. While the initial introduction of the program in the communities involved help from the researchers, the long-term goal of this program was to allow these communities to conduct drone surveys independently. This project was largely successful with multiple lasting benefits to the community. For instance, when local community members conduct their own aerial survey, they are the first ones to have access to the data and can choose to share and use it how they please. This is not

possible when surveys are conducted by external entities. The aerial imagery generated by these flights also influenced the relationships of the communities with the surrounding flora and fauna by allowing them to observe previously unknown ecosystem functions. Most importantly the new perspective this drone imagery provides allows managers in these communities to track landscape changes and make more informed natural resource management decisions. This paper demonstrates that with an initial investment by programs like this, communities with no prior drone experience can establish beneficial drone programs. Considering the success in implementation and data collection with this program and the utility of drones in communities lacking the ability to collect aerial imagery, we see a great deal of potential to expand these types of projects to communities around the world.

To recap, of the 18 articles analyzed, only 4 (22%) involved citizen scientists in the data collection phase of the research. Only one article (5.5% of the sample) put the drone in the hands of the citizen scientists for the data collection efforts. Furthermore, 2 of the 18 (11%) solely utilized Amazon Mechanical Turks as their “crowd” instead of true volunteers.

3.2.1.2 Indirect Citizen Scientists Drone Interactions Through Data Extraction and Mining

In the remaining articles, 14 of 18, the citizen scientists have no interaction with the drone itself but were instead utilized in data extraction and mining activities (Fig. 3.5). In 7 of 18 articles, 39%, the citizen scientist extracts model training data from drone imagery for object identification algorithms (Attari et al. 2017; Bowley et al. 2019; Chirayath and Li 2019; Kamm and Reed 2019; Ofli et al. 2016;



Fig. 3.5 Examples of citizen science and drones. Using citizen science-collected datasets: image of hotspots of emergencies generated from emergency reports uploaded to the web after the Port-au-Prince 2010 Earthquake taken from Ramchurn et al. 2016 (left). Using citizen scientists to assist with on-the-ground data collection: image of community members participating in mapping activity, during which community members identified previously undocumented archeological ruins taken from Larrain et al. 2020 (center). Having citizen scientists assist in data processing: animals identified in drone imagery (surrounded by red identifying circles) by citizen scientists taken from Ofli et al. 2016 (right)

Rey et al. 2017; Wiesner-Hanks et al. 2019). Given the high resolution of drone imagery, species-level vegetation mapping is a common classification approach. Such classifications are completed using object identification algorithms. These algorithms, such as convoluted neural networks and other machine learning approaches, require large training datasets which can be developed by citizen scientists. Such training data development is vastly important to model and classification accuracy, but drones are capable of producing extremely large datasets, typically from multiple flights and/or time periods, requiring an enormous amount of labor to process and ultimately extract data from (Nature Conservation in Namibia – Drone Adventures 2014; Ofli et al. 2016). Multiple publications utilized volunteers in such a way for image-based training data development.

In 2 of 18 articles (11%) where citizen scientists had indirect interaction with the drone, the citizens acted as local experts and assisted in fieldwork in a variety of fashions including imagery verification and field-based training sample collection. In one study, citizens were tasked with collecting ground-based imagery of bee habitats through a mobile app on their cellphones. Drones were also used to collect similar imagery, but for more broad-scale classification as the imagery was not of high enough resolution to see individual flowers important to the study (Gülch et al. 2016). In this case, it is unlikely the citizen science was aware of the use of drones for the study. In the other study, an educational workshop led community members with their firsthand knowledge of the area to identify archeological sites previously unknown to researchers. These sites were then able to be rapidly mapped and documented by researchers using drones. In this case, the discovery of the new site was not planned and highlights the utility of local spatial knowledge gained by engaging community members directly. This study saw the benefit of increasing community engagement with the interpretation and enhancing management of the community's cultural heritage. Incorporating drones in this example also produced documentation of these archaeological sites that will stay in the community as educational resources for time to come (Larrain et al. 2020).

In 3 of 18 publications, where the citizen scientists had no direct interaction with the drone, the researchers employed data mining approaches to gather pictures and descriptions of events from social media to be used in tandem with drones (Choi and Dyke 2020; Lin et al. 2020; Ramchurn et al. 2016). In one example, social media reports of disasters were used to guide drone surveys in support of disaster relief (Ramchurn et al. 2016). In this example, citizen scientists were also used to further classify social media posts for more effective usage of the dataset. In the other publications, photos uploaded to social media were used to compare against baseline surveys conducted with drones to quantify flood hazards (Lin et al. 2020) and track infrastructure condition (Choi and Dyke 2020; Ramchurn et al. 2016).

Two publications in the review did not have any citizen science element but explicitly state that the methods developed could be used for citizen science in the future (Cardil et al. 2017; Scher et al. 2019). In Cardil et al. (2017), researchers outline the utility of drones to observe and quantify destructive insect defoliation in pine trees. The authors suggest similar methods could be adopted by drone-owning citizens to establish citizen science forest health monitoring programs. In Scher et al.

(2019), researchers demonstrate the ability of drones to be used for high-resolution modeling of individual trees. In this case, the authors state that all equipment and software used, as well as study methodology, are readily available to the public and can be adopted by citizen scientists. Additionally, Kamm and Reed (2019) describe the use of drones to classify bird species habitat. The authors note methods developed can be utilized by citizen scientists in the future. This article however also utilizes citizen scientists to create training datasets for land cover classification and thus is included as part of the *Indirect Citizen Scientists Drone Interactions* category of citizen science. The hypothetical role of the citizen scientists in both of these articles is that of the drone operator, should they be adopted for use with citizen scientists. This gives a small insight into the direction of future uses of citizen scientists and drones.

3.2.2 Study Field

Based on the literature review, citizen science and drones are used most often in the fields of ecology (seven articles, 38.8%) and post-disaster management (six articles, 33.3%). The majority of the publications in ecology fell into the data collection category (see Sect. 3.2.1.2). Many of these publications have similar methodologies and involve citizen scientists identifying objects of interest, training data, from drone imagery. This takes advantage of the capability of citizen scientists to quickly process large amounts of data. For instance, in the field of wildlife ecology, the volume of drone imagery needed to detect animals is quite large when animals are geographically dispersed. This volume of data combined with the miniscule proportion of an image that animals typically occupy leads to slow and resource intensive object identification ideal for citizen scientists (Bowley et al. 2019; Rey et al. 2017).

The disaster management articles involved both direct and indirect drone interactions. Processing a large amount of data is especially challenging in this field, when trying to distinguish and classify objects is time sensitive. Like ecology, several publications in post-disaster management utilize citizen science to generate training data for object identification algorithms. In fact, Ofli et al. (2016) utilize the same wildlife ecology drone image dataset as Rey et al. (2017) to evaluate its platform. Unlike the field of ecology, post-disaster management often necessitates rapid data processing of drone imagery, especially when imagery is being used to allocate aid and search for disaster victims. Two similar studies addressed this problem by having citizen scientists identify objects of interest within disaster areas in real time through a web application (Alex et al. 2015; Salisbury et al. 2016).

Other fields of study utilizing drones and citizen science include agriculture (two articles), infrastructure management (one article), and archeology (one article). As the use of drones and citizen science is still evolving, many of these articles are focused on developing methods for future work, rather than evaluating the success of methods employed in real-world scenarios. For instance, in Ofli et al. (2016), researchers developed a platform to incorporate citizen science and drones for

disaster response using existing drone imagery datasets. However, at the time of publication, the platform had not been deployed in actual disaster relief scenarios. Consequentially while these methods are typically developed for specific fields of study, their applicability beyond that field is often broad and will likely be adopted for work beyond their original scope.

While geographers embrace the spatial science, geographic technologies, and development of participatory GIS, they are not the leaders in linking citizen science with UAS technology. In fact, only 5 of the 18 articles analyzed as part of this review involved a researcher who identifies themselves as a geographer or is affiliated with a geography department. Instead, most researchers identified or were affiliated with computer science or engineering. Those articles that did involve geographers more heavily focused on participatory mapping efforts.

3.2.3 Study Area Land Cover/Use

Many publications took place entirely within a single land cover/use including cropland (Cummings et al. 2017a; Wiesner-Hanks et al. 2019), forest (Cardil et al. 2017), savanna (Rey et al. 2017), urban (Choi and Dyke 2020; Lin et al. 2020; Ramchurn et al. 2016), and aquatic (Chirayath and Li 2019). Other publications were applicable to multiple environments, for example, Scher et al. (2019) which developed a method to create high-resolution models of single trees using drones and is applicable to any environment where trees are found. Further, several articles did not take place in any specified environment and were instead focused on developing methods that could be used in multiple environments, for example, Salisbury et al. (2015) which took place entirely in virtual environments online or Alex et al. (2015) that used archival drone data to conduct its experiments. Overall, of the 18 articles, 13 (72.2%) were conducted in specific environments.

Urban environments were the most commonly observed among all publications (7 of 18). Of these publications three took place entirely within urban environments with two being in the field of post-disaster management (Lin et al. 2020; Ramchurn et al. 2016) and one being in the field of infrastructure management (Table 3.2). The four additional publications (Alex et al. 2015; Attari et al. 2017; Ofli et al. 2016; Salisbury et al. 2016) did not take place specifically within urban environments but were in the field of post-disaster management and thus highly applicable to urban areas. Citizen science and drones used for disaster management in urban environments are a logical crossroads for several reasons. Citizen science may be more realistic in urban environments in general due to the abundance of people residing in these areas. This is especially relevant when the form of citizen science includes utilizing social media posts to guide drone usage. For example, Ramchurn et al. (2016) researchers used crowdsourced data from social media to identify disaster hotspots and allocate drone reconnaissance resources more effectively. This sort of method may not be applicable to non-urban environments where the volume of social media posts available to guide resources is insufficient. Of all the examples we

see of citizen science and drones in urban environments, none has examples of citizens piloting the drones. This could be in part because of the regulations and safety concerns with citizens flying drones over persons or vehicles not involved in the flight which is more likely to happen in urban environments.

The remaining five articles (27.7%) highlighted citizen science research engagement that could take place in multiple environments. For example, Gülch et al. (2016) developed a method to monitor bee habitat through smartphones and drones. Such work is applicable anywhere bees are found, and while the extent of the article is limited, methods like these could be expanded globally.

3.2.4 *Drone Types*

The most common type of drones observed in citizen science drone programs was multirotor helicopter style drones with ten publications (Cardil et al. 2017; Chirayath and Li 2019; Choi and Dyke 2020; Cummings et al. 2017a; Kamm and Reed 2019; Larrain et al. 2020; Lin et al. 2020; Ramchurn et al. 2016; Salisbury et al. 2015; Scher et al. 2019). One of these ten publications, Ramchurn et al. (2016), did not specify the drone used, but was likely a helicopter style based on its described ability to hover. Of these ten publications, eight specified a quadrotor format, while Cummings et al. (2017a) specified a hexarotor format and Chirayath and Li (2019) an octorotor format. In studies where there was direct interaction between the citizen scientist and the drone (Sect. 3.2.1.1), helicopter-type drones were used exclusively. This could be in part because helicopter-style drones are much more agile, controllable, and responsive, which make them ideal for inexperienced pilots. For example, in Salisbury et al. (2015), drones are cooperatively controlled based on the collective input by multiple volunteers. In this case the ability to respond to rapidly changing flight control inputs is much more suited to helicopter-style drones. Additionally, these types of drones can be lower in cost; therefore, putting the drone in the citizen's hands is not as risky. While helicopters, particularly quadcopters, were most common in citizen science engagement, it should be noted that fixed-wing and other classes of drones have been expanding their target audience to include the general public.

Only three publications used fixed-wing drones (Bowley et al. 2019; Gülch et al. 2016; Rey et al. 2017). All of the instances of fixed-wing drone use were in cases where citizen scientists were being used to assist in data processing, for example, identifying objects of interest in previously collected drone images. In these cases, the citizen has no interaction with the drone, and the type of drone used is irrelevant to the citizen scientist. Using fixed-wing drones in this case would decrease the ability of the drone to respond to rapidly changing crowd input in real time. Additionally in cases where citizens are assisting with image and video processing in real time, for example, in Alex et al. (2015) and Salisbury et al. (2016), the ability to slow down and hover may be helpful for the image and video acquisition and is

not possible with fixed-wing drones (Adams and Friedland 2011; Ollero and Merino 2004).

Three publications (Attari et al. 2017; Salisbury et al. 2016; Wiesner-Hanks et al. 2019) did not specify the type of drone although based on its use we can infer drone type. In both publications (Attari et al. 2017; Salisbury et al. 2015), the drone is used to assess damage from disasters. These missions would be best suited for a multirotor drone due to increased control and maneuverability that would allow the pilots to divert course and hover in order to easily investigate and identify objects. In Wiesner-Hanks et al. (2019), the drone is used to collect images of crops. Given the size and simple dimensions of many crop fields, fixed-wing drones may be the most effective as they can cover large areas with minimal maneuvering, although helicopter-style drones can be applicable in this case as well.

The remaining two publications did not use drones but used previously collected drone imagery and video to develop methods to be used with drones in the future. Alex et al. (2015) used footage from the VIRAT (Video Image Retrieval and Analysis Tool) aerial footage database and did not specify the type of drone used to collect the imagery. Ofli et al. (2016) used the image dataset collected by Rey et al. (2017) which was collected through a fixed-wing drone.

3.2.5 *Purpose of Drone*

In 16 of 18 publications reviewed, drones were equipped with mounted sensors for collecting natural color (RGB) imagery or video. In eight of these publications, these RGB imagery and video were used to identify objects of interest such as animals or disaster victims by citizen scientists (Alex et al. 2015; Attari et al. 2017; Bowley et al. 2019; Kamm and Reed 2019; Ofli et al. 2016; Rey et al. 2017; Salisbury et al. 2016; Wiesner-Hanks et al. 2019). The use of RGB in these cases, as opposed to multispectral data, is appropriate for citizen scientists who might not be trained in interpreting imagery from outside the natural color spectrum. In five publications RGB imagery was used to build 3D models and orthomosaics using photogrammetry software (Cardil et al. 2017; Choi and Dyke 2020; Larrain et al. 2020; Lin et al. 2020; Scher et al. 2019). In the remaining three articles using RGB imagery, the imagery was interpreted by researchers (Gülch et al. 2016; Ramchurn et al. 2016) or by community members (Cummings et al. 2017a). This narrow use of sensors in citizen science studies is notable given the wide range of sensors capable of being mounted on drones. The absence of citizen science programs engaging multispectral, LiDAR, thermal, and non-image base sensors (e.g., temperature probes) can be the result of sensor cost, training to understand the sensor mechanics, and/or the fact that drone technology is expanding and citizen science has not caught up. The fact that natural color cameras/sensors are the most used is not surprising as there are drones that, for a reasonable price, come equipped with this. Conversely, the use of specialized sensors involves increased complexity including new preflight planning steps and flight considerations. As previously discussed, most articles with active

drone-based citizen scientist participation look to incorporate them to accelerate tedious object identification tasks or assist with rapid image collection and processing. These sorts of tasks cannot be easily automated and often require human assistance to complete. Such tasks are typically more easily completed with the use of natural color imagery; this is not necessarily the case with multispectral data as the general public is not familiar with visualizing and interpreting trends from the electromagnetic spectrum.

Of all publications reviewed, there were two not strictly utilizing drones to collect RGB imagery. Chirayath and Li (2019) outline the use of two specialized sensors for aquatic remote sensing: FluidCam which can obtain refraction-free imagery of aquatic systems and MiDAR which uses active remote sensing to observe aquatic systems in light-limited environments. Salisbury et al. (2015) do not use any drones in its study but instead simulate drones in a virtual environment to test methods of citizen scientists collectively piloting the drone. Should this method be put into practice in the field, the drones used would be equipped with live video to relay back to citizen scientists controlling the drone; however additional sensors for environmental monitoring could be utilized on the drone as well.

3.2.6 Future Drone Use

Of the relatively few publications utilizing citizen science and drones, there are even fewer utilizing the citizen scientists as the drone pilot. Given the success and community benefits of direct involvement of citizens in drone operation (e.g., Cummings et al. 2017a) as well as the high potential for expansion of this approach (e.g., Cardil et al. 2017; Scher et al. 2019), there will likely be an increase in future projects utilizing citizens as the drone operator.

In addition to the citizen benefits, this form of citizen science has tangible benefits to the researchers. For example, having a network of geographically dispersed citizens capable of operating drones without the assistance of researchers allows for rapid and contemporaneous data collection across multiple areas in response to events. An example of such a network is the “Dronebird” Disaster Drone Rescue Team in Japan. This network of drone owners rapidly deploys to collect drone imagery of disaster areas and uploads maps of their findings online for the public and first responders to use (“Drone Bird Disaster Rescue Squad,” 2020). Additionally, in Australia the Victorian CoastalMonitoring Program (VCMP) has embraced the use of citizen-operated drone data collection (Pucino et al. 2021). This work was published after the literature review was conducted for this chapter; however, this program represents a key advancement in citizen science and coastal change science. VCMP developed a citizen science program centered around mapping coastal areas with consumer-grade drones in order to support adaptation planning by providing communities with information on coastal hazards and potential future impacts to coastal landscapes. This is a community-focused project aimed at empowering the residents to actively monitor and predict beach movement in response to changing

environmental conditions and management interventions. This program uses consumer drone technology (i.e., Phantom 4 Pro quadcopter drone) and cloud data processing to engage citizen scientists in the collection, processing, and analysis of sand movement along Victoria's beaches (Pucino et al. 2021).

A similar program has been developed independently in the United States by the authors of this chapter. The program, Interdisciplinary Citizen-based CoastalREmote Sensing for Adaptative Management program (IC-CREAM), is led by Michigan State University (MSU) and aims to empower small communities along the Great Lakes of North America to collect their own coastal change data and infuse these datasets into proactive coastal management. The IC-CREAM citizen scientists are trained to become FAA Part 107 pilots and collect shoreline imagery in their community seasonally as well as in response to storm events or management actions. While this program, which is funded by the National Science Foundation, just began in January 2020, initial results from one of the participating communities indicate that highly accurate data can be generated from citizen-based drone monitoring, similar to the findings of VCMP. Additionally, these data can be used to document patterns of erosion and accretion associated with fluctuating lake levels and storms as well as provide important information on coastal hazards to decision-makers. For example, data gathered in Marquette, Michigan, from June 2020 through November 2020 documented the geomorphic impacts (e.g., erosion, accretion) on a sandy beach from a large coastal storm with significant wave heights in excess of 4 m (Fig. 3.6). These data not only provided the research team with a high-quality pre- and post-storm dataset that can be used to gain insight into coastal geomorphic processes but will also be used by the City of Marquette to develop a management plan.

3.3 Conclusion

As drones become more cost-efficient and commonplace, the potential for citizen science and drones will inevitably increase. Currently the majority of publications utilizing drones and citizen science have little to no interaction between the citizen scientists and the drone. Instead, the citizens are generally used as either the data processor for drone imagery or to unknowingly generate data through social media that will be used in conjunction with drones. The few examples of citizen science interaction with drones we do see generally consist of citizens viewing live drone footage via web application and either tagging the imagery or collectively piloting the drone through aggregated crowd inputs. We found only one example of citizen scientists being responsible for all aspects of the drone operation. This direct interaction provided several benefits to the community unseen in other studies. For example, allowing communities to collect and own their own data increases engagement of community members with their surroundings as well as empowering communities with state-of-the-art data for improved decision-making.

Given the benefits to both researchers and the local community when the drone is in the hands of the citizen scientists, the lack of studies utilizing this intersection of

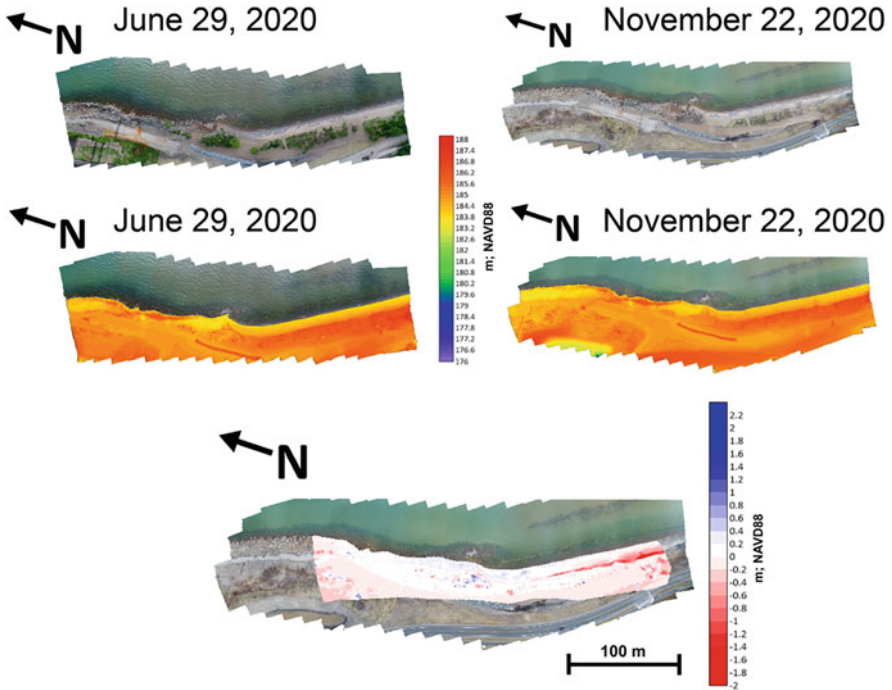


Fig. 3.6 Rapid coastal erosion documented with drones in Marquette Michigan. Top: mosaiced imagery of coastline generated from drone flights on June 29, 2020, and November 22, 2020. Center: digital elevation models for the coastlines across both dates. Bottom: difference in elevation observed between the drone flights indicating substantial change (erosion) over the period

drones and citizen science is surprising. This method is applicable in virtually all environments where drones can safely be flown, and with a near limitless need for geospatial data and imagery in communities, we see this use of citizen science to be ripe for development in the coming years. Monitoring for coastal change, landslides, floods, agriculture, traffic, and other fields of study and practice where remotely sensed imagery is used will be greatly enhanced by the spatial and temporal coverage afforded by citizen scientists equipped with drones. Of course, these benefits are not realized without great care to ensure flights are conducted safely and legally; thus training must be a principal focus of future projects that enlist citizen scientists to fly drones. The success of citizen-based drone monitoring projects such as VCMP and IC-CREAM proves that citizens can be trained to successfully operate drones for specific research and management applications.

3.3.1 sUAS-Based Citizen Science Studies in Geography

Improvements and expansion of UAVs and associated sensors and hardware are transforming the geographic discipline. From biogeography to geomorphology,

economic geography, cultural geography, and climatology, we can see countless examples of newly developed datasets, maps, and methodologies. However, in the merger of citizen science and UAVs, there are very few programs with origins in the geographic discipline. This lack of geography-centric UAV citizen science programs could be due to several factors including the following:

1. The collaborative nature of the discipline. Geography is highly collaborative by nature, and we can see the trends of collaboration and methodological sharing in the articles associated with this literature review. Thus, while a program is not led by a traditional geographer or based in a geography department, the ideals of participatory mapping, GIS, remote sensing, and spatial science are still associated.
2. Department identity is not self-identity. In this review we looked at the author department affiliation to highlight the presence of geography in UAS-based citizen science. However, given the interdisciplinarity of geographic training, it is highly likely for geographers to be associated with differing named departments such as environmental studies and computer sciences.

UASs offer new ways of seeing, sensing, and sharing powerful landscape data. As this technology continues to grow, so will its use within citizen science programs. Geography, which in many ways is at junction of data science, ecology, and social science, is posed to not only embrace but greatly expand the utility of UAS-based citizen science. From the authors' personal experience, given our development of the IC-CREAM program, such expansion includes (1) the fusion of historical aerial imagery with drone-based data to develop robust time series imagery, (2) development of time series statistics in order to analyze landscape change in a statistically robust manner, and (3) the coordination of batch data processing given large data volumes.

Drones have a clear role in the spatial sciences by bridging the temporal gap between satellite imagery or through high-resolution output. The future of UAS usage, even beyond citizen science, will incorporate drone swarms, new sensors (e.g., full waveform LiDAR), and large payload or long flight time drones all of which have data outputs strongly grounded in remote sensing science. Therefore, given the spatial perspective, data science, and remote sensing premise, there will long be a critical role for geographers not only in the use of UAS but in its application within citizen science.

References

- Adams SM, Friedland CJ. (2011, September) A survey of unmanned aerial vehicle (UAV) usage for imagery collection in disaster research and management. In: 9th international workshop on remote sensing for disaster response, vol. 8, pp. 1–8
- Alex B, Charlie B, Matthew J-R, Max Yi R, Gonzalez R, Panos P (2015) Crowdsourcing for search of disaster victims: a preliminary study for search system design. In: Proceedings of the 20th international conference on engineering design (ICED15), p 12
- Attari N, Ofli F, Awad M, Lucas J, Chawla S (2017) Nazr-CNN: fine-grained classification of UAV imagery for damage assessment. In: 2017 IEEE international conference on data science and advanced analytics (DSAA), pp 50–59. <https://doi.org/10.1109/DSAA.2017.72>

- Barve V (2014) Discovering and developing primary biodiversity data from social networking sites: a novel approach. *Eco Inform* 24:194–199
- Boudergui K, Carrel F, Domenech T, Guénard N, Poli J, Ravet A, Schoepff V, Woo R (2011) Development of a drone equipped with optimized sensors for nuclear and radiological risk characterization. In: 2011 2nd international conference on advancements in nuclear instrumentation, measurement methods and their applications, pp 1–9. <https://doi.org/10.1109/ANIMMA.2011.6172936>
- Bowley C, Mattingly M, Barnas A, Ellis-Felege S, Desell T (2019) An analysis of altitude, citizen science and a convolutional neural network feedback loop on object detection in unmanned aerial systems. *J Comput Sci* 34:102–116. <https://doi.org/10.1016/j.jocs.2019.04.010>
- Butchart SH, Walpole M, Collen B, Van Strien A, Scharlemann JP, Almond RE, Baillie JE, Bomhard B, Brown C, Bruno J (2010) Global biodiversity: indicators of recent declines. *Science* 328(5982):1164–1168
- Callaghan CT, Rowley JLL, Cornwell WK, Poore AGB, Major RE (2019) Improving big citizen science data: moving beyond haphazard sampling. *PLoS Biol* 17(6):e3000357. <https://doi.org/10.1371/journal.pbio.3000357>
- Cardil A, Vepakomma U, Brotons L (2017) Assessing pine Processionary moth defoliation using unmanned aerial systems. *Forests* 8(10):402. <https://doi.org/10.3390/f8100402>
- Chahl J (2015) Unmanned aerial systems (UAS) research opportunities. *Aerospace* 2(2):189–202. <https://doi.org/10.3390/aerospace2020189>
- Chapin FS, Zavaleta ES, Eviner VT, Naylor RL, Vitousek PM, Reynolds HL, Hooper DU, Lavorel S, Sala OE, Hobbie SE (2000) Consequences of changing biodiversity. *Nature* 405(6783):234–242
- Chirayath V, Li A (2019) Next-generation optical sensing Technologies for Exploring Ocean Worlds—NASA FluidCam, MiDAR, and NeMO-Net. *Front Mar Sci* 6:521. <https://doi.org/10.3389/fmars.2019.00521>
- Choi J, Dyke SJ (2020) CrowdLIM: crowdsourcing to enable lifecycle infrastructure management. *Comput Ind* 115:103185. <https://doi.org/10.1016/j.compind.2019.103185>
- Choi-Fitzpatrick A (2016) Up in the air: a global estimate of non-violent drone use 2009–2015. University of San Diego. <https://doi.org/10.22371/08.2016.001>
- Collin A, Dubois S, James D, Houet T (2019) Improving intertidal reef mapping using UAV surface, red edge, and near-infrared data. *Drones* 3:12
- Cummings AR, Cummings GR, Hamer E, Moses P, Norman Z, Captain V, Bento R, Butler K (2017a) Developing a UAV-based monitoring program with indigenous peoples. *J Unmanned Veh Syst*:juvs-2016-0022. <https://doi.org/10.1139/juvs-2016-0022>
- Cummings AR, McKee A, Kulkarni K, Markandey N (2017b) The rise of UAVs. *Photogramm Eng Remote Sens* 83(4):317–325. <https://doi.org/10.14358/PERS.83.4.317>
- Dobson A, Lodge D, Alder J, Cumming GS, Keymer J, McGlade J, Mooney H, Rusak JA, Sala O, Wolters V (2006) Habitat loss, trophic collapse, and the decline of ecosystem services. *Ecology* 87(8):1915–1924
- Drone Bird Disaster Rescue Squad (2020, 25) Pix4D Blog. /blog/drone-disaster-rescue
- Garrett B, Anderson K (2018) Drone methodologies: taking flight in human and physical geography. *Trans Inst Br Geogr* 43(3):341–359. <https://doi.org/10.1111/tran.12232>
- Gettinger D, Michel A (2015) Drone sightings and close encounters: an analysis. Center for the Study of the Drone Bard College
- Grason E, McDonald S, Adams J, Litle K, Apple J, Pleus A (2018) Citizen science program detects range expansion of the globally invasive European green crab in Washington State (USA). *Manag Biol Invasions* 9(1):39–47. <https://doi.org/10.3391/mbi.2018.9.1.04>
- Gülch E, Uddin S, Willi B (2016) Beesmart – a crowdsourcing project with smartphones. In: ISPRS – international archives of the photogrammetry, remote sensing and spatial information sciences, XLI-B3, pp 863–870. <https://doi.org/10.5194/isprsarchives-XLI-B3-863-2016>
- Gupta S, Ghonge M, Jawandhiya P (2013) Review of unmanned aircraft system (UAS). *Int J Adv Res Comput Eng Technol* 9. <https://doi.org/10.2139/ssm.3451039>

- Ipeirotis PG (2010) Analyzing the Amazon mechanical Turk marketplace. *XRDS Crossroads ACM Mag Stud* 17(2):16–21. <https://doi.org/10.1145/1869086.1869094>
- Jordan BR (2019) Collecting field data in volcanic landscapes using small UAS (sUAS)/drones. *J Volcanol Geotherm Res* 3:11
- Kamm M, Reed JM (2019) Use of visible spectrum sUAS photography for land cover classification at nest sites of a declining bird species (*Falco sparverius*). *Remote Sens Ecol Conserv* 5(3): 259–271. <https://doi.org/10.1002/rse2.104>
- Landsat—Earth Observation Satellites (Fact Sheet No. 3081; Fact Sheet) (2020) USGS
- Larrain AÁ, Greco C, Tarragó M (2020) Participatory mapping and UAV photogrammetry as complementary techniques for landscape archaeology studies: an example from North-Western Argentina. *Archaeol Prospect:arp*.1794. <https://doi.org/10.1002/arp.1794>
- Li X-B, Wang D-S, Lu Q-C, Peng Z-R, Lu S-J, Li B, Li C (2017) Three-dimensional investigation of ozone pollution in the lower troposphere using an unmanned aerial vehicle platform. *Environ Pollut* 224:107–116. <https://doi.org/10.1016/j.envpol.2017.01.064>
- Lin Y-T, Yang M-D, Han J-Y, Su Y-F, Jang J-H (2020) Quantifying flood water levels using image-based volunteered geographic information. *Remote Sens* 12(4):706. <https://doi.org/10.3390/rs12040706>
- Nature conservation in Namibia – Drone Adventures (2014, April 8) <https://droneadventures.org/index.php/2014/08/04/nature-conservation-namibia/>
- Offi F, Meier P, Imran M, Castillo C, Tuia D, Rey N, Briant J, Millet P, Reinhard F, Parkan M, Joost S (2016) Combining human computing and machine learning to make sense of big (aerial) data for disaster response. *Big Data* 4(1):47–59. <https://doi.org/10.1089/big.2014.0064>
- Ollero A, Merino L (2004) Control and perception techniques for aerial robotics. *Annu Rev Control* 28:167–178
- Pocock MJO, Chandler M, Bonney R, Thornhill I, Albin A, August T, Bachman S, Brown PMJ, Cunha DGF, Grez A, Jackson C, Peters M, Rabarijaon NR, Roy HE, Zaviezo T, Danielsen F (2018) Chapter 6: A vision for global biodiversity monitoring with citizen science. In: Bohan DA, Dumbrell AJ, Woodward G, Jackson M (eds) *Advances in ecological research*, vol 59. Academic, pp 169–223. <https://doi.org/10.1016/bs.aecr.2018.06.003>
- Pucino N, Kennedy DM, Carvalho RC, Allan B, Ierodiaconou D (2021) Citizen science for monitoring seasonal-scale beach erosion and behaviour with aerial drones. *Sci Rep* 11(1): 3935. <https://doi.org/10.1038/s41598-021-83477-6>
- Ramchurn SD, Huynh TD, Wu F, Ikuno Y, Flann J, Moreau L, Fischer JE, Jiang W, Rodden T, Simpson E, Reece S, Roberts S, Jennings NR (2016) A disaster response system based on human-agent collectives. *J Artif Intell Res* 57:661–708. <https://doi.org/10.1613/jair.5098>
- Rey N, Volpi M, Joost S, Tuia D (2017) Detecting animals in African savanna with UAVs and the crowds. *Remote Sens Environ* 200:341–351. <https://doi.org/10.1016/j.rse.2017.08.026>
- Ruwaimana M, Satyanarayana B, Otero V, Muslim AM, Syafiq AM, Ibrahim S, Raymaekers D, Koedam N, Dahdouh-Guebas F (2018) The advantages of using drones over space-borne imagery in the mapping of mangrove forests. *PLoS One* 13(7):e0200288. <https://doi.org/10.1371/journal.pone.0200288>
- Salisbury E, Stein S, Ramchurn SD (2015, May) Real-time opinion aggregation methods for crowd robotics. In: *Proceedings of the 2015 international conference on autonomous agents and multiagent systems*, pp. 841–849
- Salisbury E, Stein S, Ramchurn S (2016) CrowdAR: a live video annotation tool for rapid mapping. *Proc Eng* 159:89–93. <https://doi.org/10.1016/j.proeng.2016.08.069>
- Satellite Imagery Pricing (2018) Land info worldwide mapping. http://www.landinfo.com/LAND_INFO_Satellite_Imagery_Pricing.pdf
- Scher LC, Griffoul E, Cannon CH (2019) Drone-based photogrammetry for the construction of high-resolution models of individual trees. *Trees Struct Func*
- Silvertown J (2009) A new dawn for citizen science. *Trends Ecol Evol* 24(9):467–471. <https://doi.org/10.1016/j.tree.2009.03.017>

- Wargo CA, Church GC, Glaneueski J, Strout M (2014) Unmanned aircraft systems (UAS) research and future analysis. In: 2014 IEEE Aerospace conference, pp 1–16
- Wiesner-Hanks T, Wu H, Stewart E, DeChant C, Kaczmar N, Lipson H, Gore MA, Nelson RJ (2019) Millimeter-level plant disease detection from aerial photographs via deep learning and crowdsourced data. *Front Plant Sci* 10:1550. <https://doi.org/10.3389/fpls.2019.01550>
- WorldView-3 Data Sheet. (05/14). DigitalGlobe
- Young NE, Anderson RS, Chignell SM, Vorster AG, Lawrence R, Evangelista PH (2017) A survival guide to Landsat preprocessing. *Ecology* 98(4):920–932. <https://doi.org/10.1002/ecy.1730>

Chapter 4

Using sUAS to Map and Quantify Changes to Native American Archaeological Sites Along Coastal Louisiana Due to Climate Change and Erosion



Kory Konsoer, David Watt, Mark Rees, Macy Linton, Tad Britt, and Sam Huey

Abstract The risks and challenges to archaeology and cultural resource management planning in wetland landscapes are not unique to the north-central Gulf Coast. Similar challenges are being experienced in deltaic and estuarine landscapes across the globe, where erosion and relative sea level rise demand rapid and effective responses to catastrophic and widespread impacts on living populations and cultural resources. Sites at risk from the dire consequences of anthropogenic climate change are being adversely affected at a faster rate than can be satisfactorily mitigated by traditional data recovery. Implementing actionable and cost-effective strategies of investigations and survey methodology utilizing small unoccupied aerial systems (sUAS) technology will be critical in balancing research potential and the multifaceted value of cultural resources. The research presented in this chapter highlights the use of sUAS in ongoing efforts to monitor, study, mitigate, and preserve a record of Native American archaeological sites in the coastal wetlands of Louisiana. Discussions include the benefits and challenges of operating sUAS in alluvial landscapes and how these technologies can be implemented in interdisciplinary research and used as educational/training tools and for public outreach and engagement.

K. Konsoer (✉)

Department of Geography and Anthropology, Coastal Studies Institute, Louisiana State University, Baton Rouge, LA, USA

e-mail: kkonsoer@lsu.edu

D. Watt · T. Britt

National Center for Preservation Technology and Training, National Park Service, Natchitoches, LA, USA

M. Rees · S. Huey

Louisiana Public Archaeology Lab, University of Louisiana – Lafayette, Lafayette, LA, USA

M. Linton

Louisiana State University, Baton Rouge, LA, USA

Keywords sUAS · Physical Geography · Geoarchaeology · Native American archaeology · Coastal erosion · Sea level rise · Earthen mound · Shell midden

4.1 Introduction

Louisiana’s coastal lands are being lost at an alarming rate due to a combination of sea level rise, land subsidence, and coastal erosion (González and Törnqvist 2006; Penland and Ramsey 1990). This land loss is further exacerbated by human-induced climate change and anthropogenic alterations to the Mississippi riverine landscape, including numerous dams within the upper portions of the watershed (Kemp et al. 2016), levees along the Mississippi River and its delta distributary channels (Kessel 1989, 2003), and navigation canals cut throughout the Mississippi deltaic plain (Fearnly et al. 2009). Since the 1930s, Louisiana has lost roughly 4900 square kilometers and is predicted to lose over 10,000 square kilometers in the next 50 years (Barras et al. 2008). While the rates of land loss for Louisiana’s coastal zone (CZ) have varied through time (Couvillion et al. 2010), current rates are estimated at over 42 square kilometers per year, driven by climate change, relative sea level rise, and erosion (Figs. 4.1 and 4.2). These rates, commonly stated as one

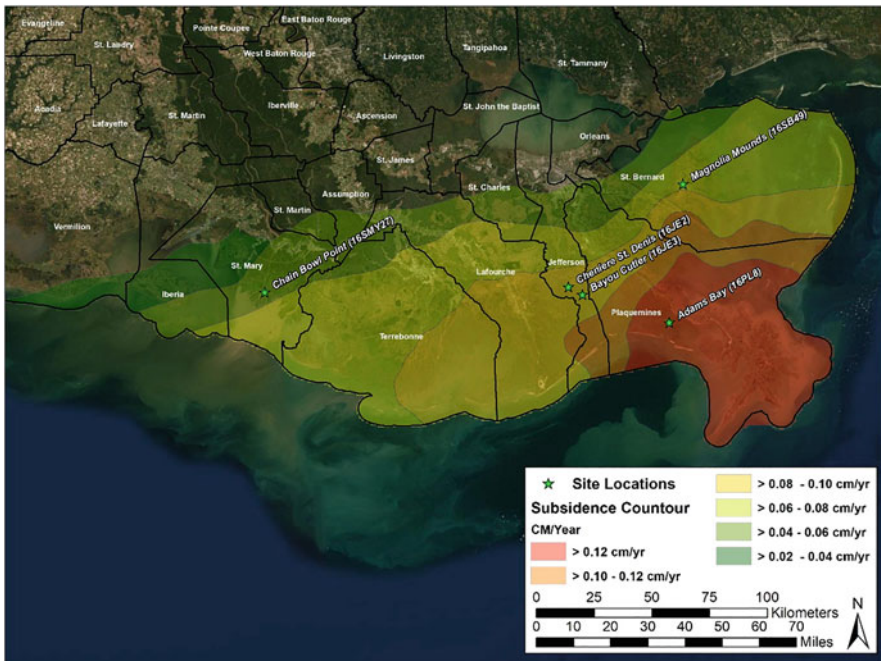


Fig. 4.1 Projected rates of land subsidence for southeastern Louisiana and the Mississippi River Delta. Green stars indicate approximate locations of Native American archaeological sites presented herein

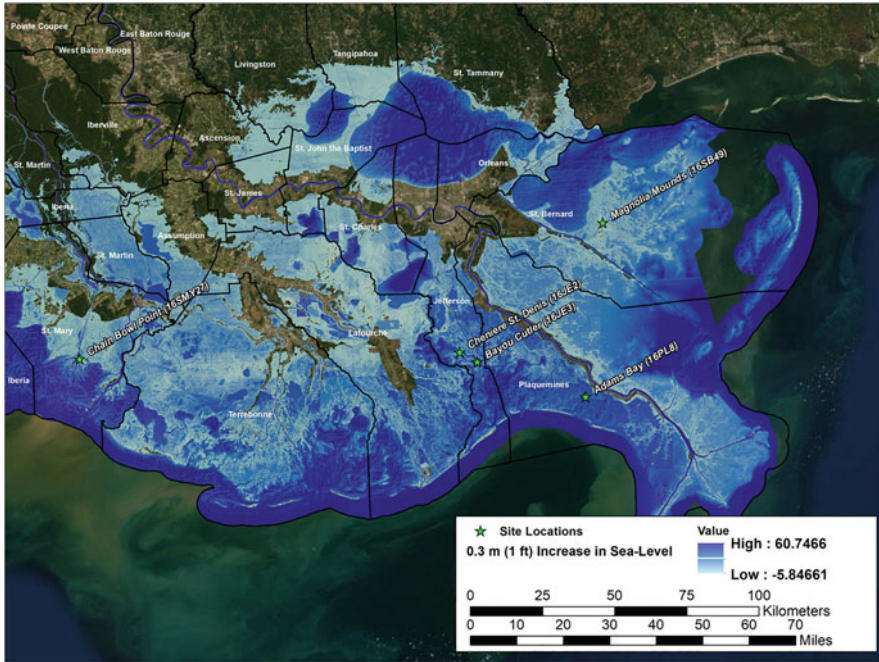


Fig. 4.2 Projected increase in sea level of 30 cm (~1 ft) for southeastern Louisiana by 2050. Green stars indicate approximate locations of Native American archaeological sites presented herein

football field per hour, are faster than anywhere else in the USA (Anderson et al. 2017).

Contained within Louisiana's deltaic plain are thousands of Native American archaeological sites, culturally and historically significant landscapes, and traditional cultural properties (TCPs) representing millennia of human habitation in this dynamic coastal zone (Britt et al. 2020). Although various restoration and mitigation efforts have been planned and applied to reduce the rates of coastal land loss, led primarily by the Coastal Protection and Restoration Authority (CPRA), these irreplaceable sites are being rapidly destroyed, inundated, and/or rapidly buried. Once these sites are lost, the cultural and ecological history contained within them is similarly lost. As such, there is an urgency to map, monitor, and study these unique, culturally significant places to preserve and mitigate the loss of scientific information and ongoing obliteration of cultural heritage. Utilizing an interdisciplinary approach that combines methods from physical geography, geomorphology, climatology, and archaeology can provide a means for studying these important sites through rapid reconnaissance and new remote sensing technologies during the current time-sensitive, perilous conditions of coastal land loss in Louisiana.

Archaeological investigations in coastal Louisiana began intermittently during the early twentieth century, but the cumulative effects of human actions on cultural resources were not recognized until mid-century (Collins 1927; Howe et al. 1935;

Kniffen 1936). McIntire (1954, 1958) performed the first large-scale coastal survey of Louisiana, demonstrating the need for regional data to address connections between landforms, settlement patterns, site distributions, and chronology. Drawing on Fisk's (1944) geological study of the lower Mississippi River and earlier archaeological studies (Kniffen 1936, 1938; Phillips et al. 1951), McIntire's culture chronology and classification of sites were correlated with deltaic progression, subsidence, and site submergence. Studies by Gagliano (1963, 1967) and Saucier (1963, 1974, 1981) further examined the connections between geomorphology and chronology in the Mississippi River Delta (MRD) and helped lay the groundwork for culture-historical syntheses, geoarchaeology, and understanding of human adaptations in the MRD and CZ (see also Gagliano 1984; Gagliano and van Beek 1970; Gagliano et al. 1981).

Archaeological research substantially increased in the 1970s following the passage of legislation for the management of historic properties and the human environment (e.g., Davis et al. 1978; Gagliano et al. 1975, 1976, 1977, 1978, 1979, 1982; Gibson 1978; Neuman 1970, 1973, 1974, 1975a, b, 1977a; Wiseman et al. 1979). Five decades later, the anthropogenic causes of coastal erosion, climate change, and sea level rise are widely recognized, along with the immediate and long-term impacts on cultural resources (Anderson 2017; Britt et al. 2020; Dawson et al. 2020; Hale 2017; Jones 2014). Despite growing recognition of this unmitigated disaster (Watt et al. 2020), a majority of the sites within the MRD and CZ have not been scientifically investigated. Many of the sites recorded decades ago are rarely revisited, and the challenges remain unaddressed. Attempts to revisit coastal sites are often unsuccessful, revealing deeply subsided landforms, deteriorating marsh, or open water at the locations of formerly terrestrial sites (Cloy and Ostahowski 2015). Unknown numbers of sites along Louisiana's coast have already been lost, and hundreds more are vulnerable and at imminent risk (Britt et al. 2020).

One of the challenges limiting recurring site monitoring and intensive scientific investigation of Native American archaeological sites within coastal Louisiana is the dynamic aspect of the deltaic landscape. Sites that were previously miles away from the shoreline and accessible by land are now surrounded by shallow coastal waters and sinking into the Gulf of Mexico. Sites along shorelines and on barrier islands are inundated, eroded, and redeposited by wave action and storm surges intensified by climate change. Anthropogenic processes are augmenting and accelerating long-term and cyclic changes in sea level, subsidence, and deltaic progression that occurred throughout the Holocene (Gagliano 1984: 11–24).

These conditions make site access increasingly difficult, requiring shallow-draft watercraft for sites connected to open bays and channels, while other interior, inundated wetland sites may be accessible only by amphibious vehicle or on foot. Reaching inaccessible coastal sites for pedestrian survey is consequently very time-consuming and costly. Neuman (1977b) demonstrated the use of the helicopter and aerial photography for visiting and documenting sites on Louisiana's coast, at the

time finding it to be more expedient and as cost effective as a survey by watercraft. High-altitude aerial photography has also been used to identify visually prominent sites with shell midden and earthen mounds, based in part on shoreline exposures of midden and discernible differences in vegetation from the surrounding marsh (Neuman and Byrd 1981). These techniques are less effective, however, for densely wooded landforms and swamps (Neuman and Byrd 1981: 107). Nor does aerial photography yield imagery of sufficiently high resolution to discern smaller or less visible, subsided sites or allow for close-up and frequent monitoring of changing site conditions due to deteriorating landforms and relative sea level rise. Neuman and Byrd (1981: 108) further suggested: “lower altitude imagery will be very useful in actual surface mapping of the sites, particularly mound sites where the spatial configuration has cultural significance.” Such technology, however, was mostly nonexistent 40 years ago.

The advent of small unoccupied aerial systems (sUAS) presents an opportunity for substantial improvements in acquiring high-resolution imagery and data for Native American archaeological sites and assessing geomorphic change within inaccessible coastal wetlands. sUAS provide both a cost- and time-efficient method for capturing photographs, video, and other multispectral imagery depending on the sensors included in the payload. Using post-processing photogrammetric methods, such as structure-from-motion (SfM), high-resolution three-dimensional point clouds, and digital elevation models (DEMs), is easily produced. Additionally, as long as visual contact with the sUAS is maintained (per FAA Part 107 regulations), surveys can be conducted on sites that are unreachable by watercraft or foot. Utilizing sUAS in geoarchaeological research thus allows for rapid site reconnaissance and revisits for continued monitoring of at-risk Native American archaeological sites, historically significant places, and TCPs.

This chapter aims to highlight the recent use of sUAS in the ongoing efforts to monitor, study, and, where possible, mitigate and preserve a record of Native American archaeological sites within Louisiana’s coastal wetlands. These efforts, known as the Mississippi River Delta Archaeological Mitigation (MRDAM), are being conducted by a consortium of universities and federal and state agencies, in partnership with Native American tribes and coastal communities. This consortium consists of an interdisciplinary team of scientists from disciplines including archaeology, geomorphology, physical geography, climatology, civil engineering, and geology. In this chapter, we will focus on selected sites that are being damaged by coastal dynamics and anthropogenic processes, such as erosion, subsidence, rapid burial, and redeposition. We discuss the benefits and challenges of operating sUAS in coastal wetlands and compare sUAS application in coastal environments to inland archaeological sites through examples from the literature. Lastly, we discuss how the use of these technologies can be used to train and educate undergraduate students in interdisciplinary research while also raising awareness among the general public.

4.2 Study Area and Methods

The MRD and CZ encompass 20 parishes across south Louisiana (Figs. 4.1 and 4.2). During fieldwork conducted in late summer and early fall of 2019, rapid reconnaissance and site assessments were performed at 27 different sites throughout the CZ, and 15 of those sites included sUAS surveys. Field sites were accessed either via a small boat rented from the Louisiana Universities Marine Consortium (LUMCON) in Cocodrie, LA, or by a truck when accessible. sUAS surveys were conducted using a DJI Phantom 4 quadcopter. GPS track flight plans were prepared in the lab before fieldwork for all sites using DJIFlightPlanner software and integrated into the fieldwork using Litchi UAS App. The GPS flight plans were prepared based on an estimated area of interest surrounding the coordinates (latitude and longitude) for each site, using a forward overlap of 70% and side overlap of 60%, an altitude of 22 m or 30 m, and camera time-lapse rate of 2 Hz. Depending on site location, weather conditions, and accessibility determined upon arrival to each site, sUAS surveys were performed using either a pre-designed flight plan or manual operation. When site conditions allowed, ground control targets were placed within the survey region and were surveyed using a Trimble R8s RTK-GPS with a local-based station providing subcentimetric accuracy.

The sUAS surveys resulted in high-resolution video and photographs for each site. For most sites, over 200 individual photographs were acquired. These photographs were post-processed in the Louisiana State University (LSU) Geomorphology Lab using Agisoft Metashape, a program that semi-automatically performs a structure-from-motion (SfM) technique to produce high-resolution three-dimensional point clouds, DEMs, and orthorectified mosaics (orthomosaics). The RTK-GPS ground control points (GCPs) were integrated into the SfM processing, and the resulting orthomosaics had a positional error on average of 2–6 centimeters. Processing time for each site ranged between 30 min to 12 h depending on the aerial extent of the site and the number of photos.

For each site, aerial photographs ranging in date from the 1950s to 2019 were acquired from the LSU Cartographic Information Center housed within the Department of Geography and Anthropology. These printed aerial photographs were made digital using a high-resolution large-scale scanner and were georeferenced using ArcMap and vectorized maps of shorelines. Cultural site extents were digitized and used to estimate rates of land erosion and subsidence. For this chapter, we focus the results on five sites that are undergoing different processes of site obliteration. The five sites are (1) Adams Bay (16PL8), located in Plaquemines Parish; (2) Magnolia Mounds (16SB49), located in Saint Bernard Parish; (3) and (4) Cheniere St. Denis (16JE2) and Bayou Cutler (16JE3), located in Jefferson Parish; and (5) Chain Bowl Point (16SMY27), located in Saint Mary Parish (Figs. 4.1 and 4.2). The geographic coordinates are not being released to protect these sites from unauthorized visits and looting.

4.3 Results

4.3.1 Adams Bay (16PL8) – Coastal Erosion, Land Subsidence, and Storm Surges

Adams Bay was once a multi-mound complex (Hale 2017; Mehta et al. 2020), first documented in 1936 with three mounds exhibiting topographically diverse vegetation around a plaza (Kniffen 1936). The earthen mounds, or at least Mound 1, appears to have been constructed during the latter part of the Barataria phase (1200–1550 CE) of Plaquemine culture, with evidence for earlier Cole Creek influence and subsequent interactions with Bayou Petre phase Mississippian culture to the east (Hale 2017: 92; Mehta et al. 2020: 27). As recently as 1977, the three mounds still existed; however, only one mound (Mound 1) remains today. The US Geological Survey topographic maps from 1892 show that the Adams Bay earthen mounds were over 350 meters from the nearest shoreline (Fig. 4.3). Throughout the twentieth century, coastal erosion resulted in the progressive loss of the wetlands surrounding the mounds. The sUAS survey conducted in 2019 revealed nearly half of the eastern portion of Mound 1 has been destroyed and the land around the mound

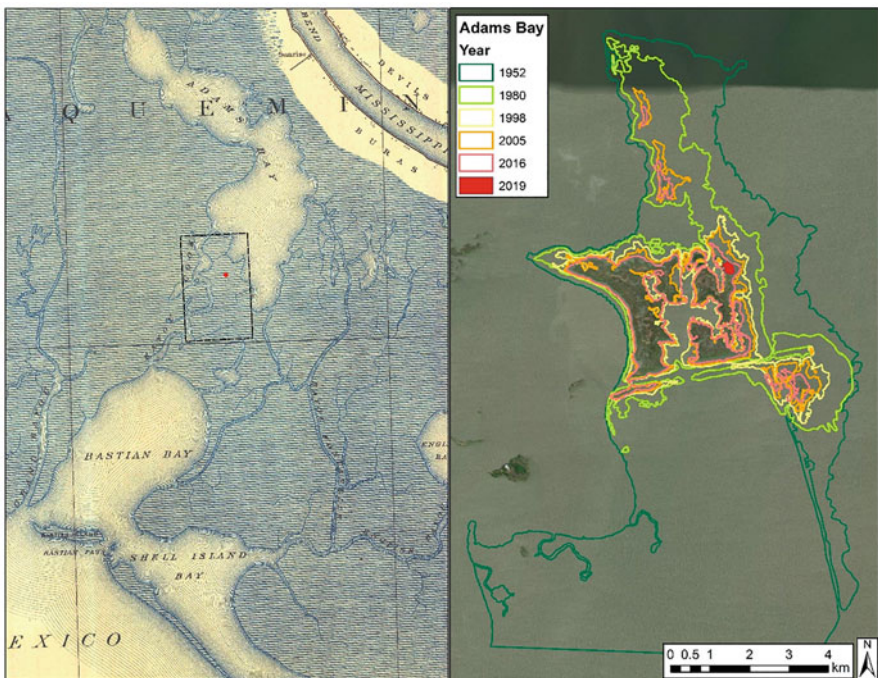


Fig. 4.3 (Left) USGS topographic maps from 1892 showing the location of Adams Bay (red dot) surrounded by coastal wetlands. (right) Progression of land erosion at Adams Bay derived from aerial photographs and sUAS 2019 survey. Extent of 3b shown in 3a by black box



Fig. 4.4 Oblique sUAS photograph showing the last remaining mound (tall trees by the boat) of Adams Bay. The white arrow shows the approximate original extent of the mound shown by the presence of the trees eroded in the water

has been reduced to an approximately 35-m-wide area of rapidly deteriorating marsh (Fig. 4.4). The sUAS photos show a clear distinction between vegetation, with the higher elevation mound being covered in trees, while the surrounding lower elevations are covered in wetland grass. The photos also reveal evidence of rapid site destruction, with the presence of trees in the water (white arrow in Fig. 4.4) that were originally on the mound delineating the approximate extent of the original constructed mound. On the southern side of the mound, coastal wetlands have been eroded over 2.5 km since 1892, with nearly 5 km² of land loss occurring since 1952 (Fig. 4.3). This substantial loss of land has increased the fetch length and made the Adams Bay site particularly susceptible to wave erosion. The most recent site destruction came from storm surges that removed vegetation and trees, further accelerating erosion (Mehta et al. 2020: 25).

4.3.2 Magnolia Mounds (16SB49) – Land Subsidence and Sea Level Rise

Magnolia Mounds represents a multi-mound complex located within the coastal wetlands on the southeastern extremity of Lake Borgne (Gagliano et al. 1982; McIntire 1958: 65–66). This complex is by far the largest in southeastern Louisiana, consisting of 12 or more earthen mounds. The earthworks are located on the western

natural levee of the La Loutre-Mississippi River course, laid out roughly in the shape of an oval following the levee landform. The central portion of the site may have served as a communal plaza that is now lower than the surrounding levee sediments and inundated. The site is believed to have been initially occupied during the late Marksville period (200–400 CE) and reoccupied during the late Coles Creek (1000–1200 CE) and Mississippi (1200–1400 CE) periods (Gagliano et al. 1982: 22), when the natural levee was situated along the still flowing La Loutre-Mississippi channel. The site was affected by land subsidence as the active channel was replaced by the slow-moving Bayou la Loutre, gradually creating the familiar backswamp landscape and marshlands found there today.

Unlike Adam's Bay, Magnolia Mounds has more than 15 km of patchy wetlands separating the site from the Gulf of Mexico. These wetlands help to buffer storm surge and wave action, limiting the amount of direct erosion to the earthen mounds. Instead, this site is being lost due to land subsidence and inundation from sea level rise (relative sea level rise). Aerial photographs from 1952 show only a small portion of open water (~10,000 m²) within the immediate region of the archaeological site (Fig. 4.5). Aerial photographs from subsequent decades reveal an increasing amount of water area with most of the central portion of the complex being inundated by 2019 (Fig. 4.5). The rates of site loss due to relative sea level rise have varied since the 1950s, with lower rates measured at ~192 m²/year during the 1980s and 1990s and current rates increasing to ~770 m²/year estimated from the 2019 sUAS survey (Fig. 4.6 and Table 4.1). As relative sea level rise continues at this site, access to high-resolution sUAS surveys will be even more important as the mounds continue to subside and become submerged.

4.3.3 Cheniere St. Denis (16JE2) and Bayou Cutler (16JE3) – Anthropogenic Damage, Shoreline Erosion, and Storm Surge

Cheniere St. Denis and Bayou Cutler are located approximately 1.8 km apart along the northeast bank of Bayou St. Denis. The Bayou Cutler site is now bisected by Bayou Cutler, an artificial shipping channel that connects Lafitte, LA, to Barataria Bay (Fig. 4.7). Cheniere St. Denis consists of two shell and earth mounds, shell midden, and a surface scatter of unmodified faunal remains, lithic materials, and high densities of indigenous ceramics, both on the surface and within the mounds and shell midden, dating from the Coles Creek (700–1200 CE) period and potentially the Baytown (400–700 CE) period (Cropley et al. 2020: 64–65). Bayou Cutler is an extensive shell midden previously described as a mound complex and the basis of Kniffin's (1936: 415–416) Bayou Cutler Complex. The shell midden consists primarily of *Rangia* and oyster shells with faunal and human remains, lithics, and high densities of indigenous ceramics both within the shell midden matrix and as wave-worn deposits along the shoreline. The cultural materials date from the

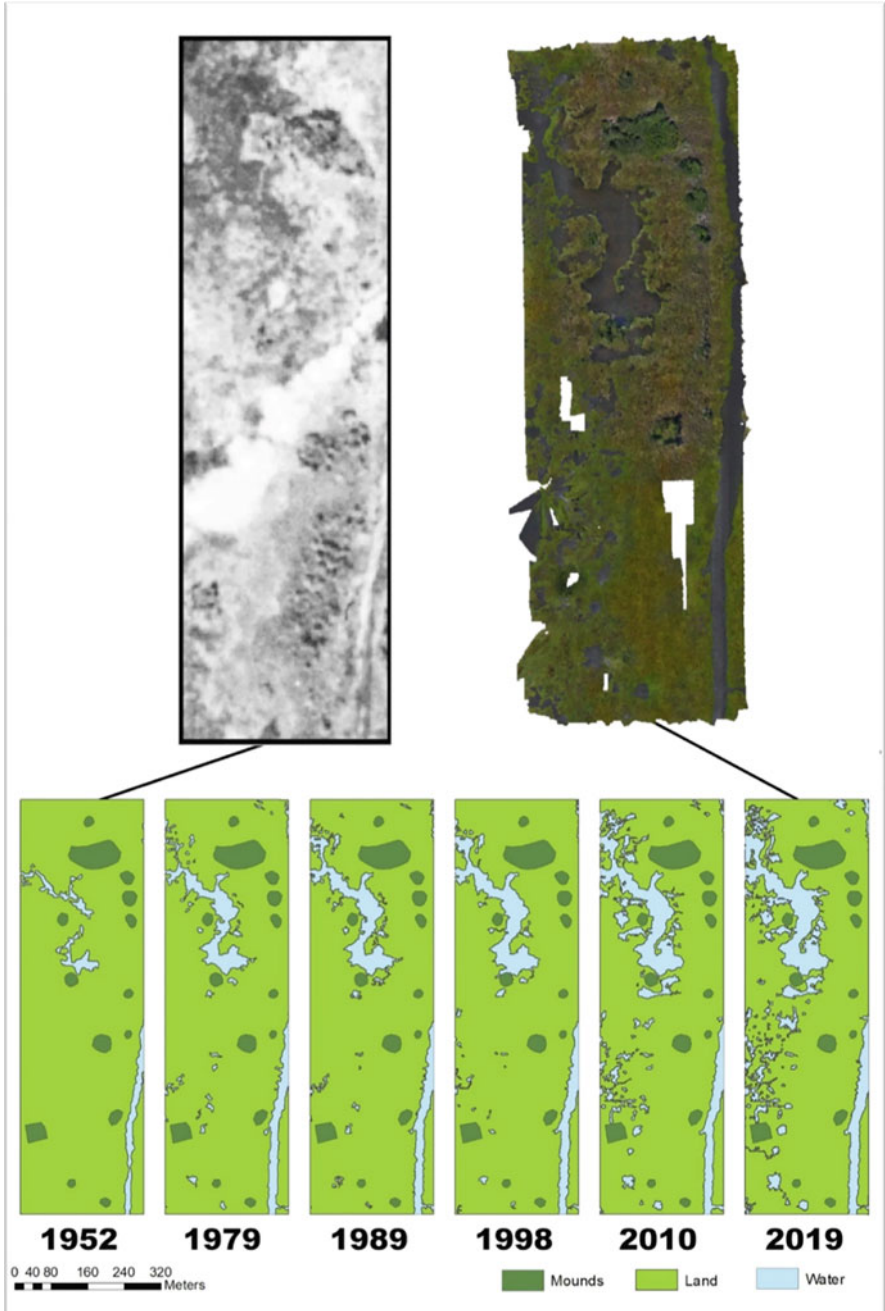


Fig. 4.5 Aerial photographs of Magnolia Mounds from 1952 aerial photograph (top left) and sUAS orthomosaic (top right). (Bottom) Progression of inundation at Magnolia Mounds. Site boundaries encompass the area shown that includes mounds and plaza

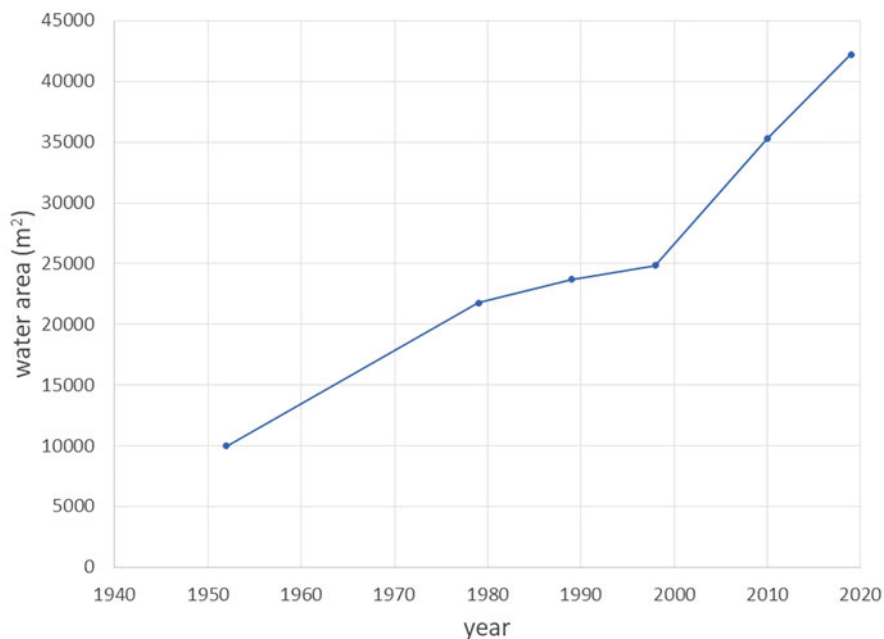


Fig. 4.6 The increasing extent of water area at Magnolia Mounds

Table 4.1 Land area, water area, and % change of site inundated at Magnolia Mounds

	Land area (m ²)	Water area (m ²)	% change
1952	234,242	10,003	4
1979	222,478	21,767	9
1989	220,541	23,704	10
1998	219,405	24,840	10
2010	208,958	35,287	14
2019	202,040	42,205	17

Marksville period (1–400 CE) through the Mississippi period (1200–1700 CE) (Cropley et al. 2020: 65–66).

While nearly all archaeological sites within coastal Louisiana have experienced some degree of damage due to anthropogenic alterations of the landscape, these two sites exhibit direct and extensive damage due to canal dredging and heavy shipping traffic. Construction of the Barataria Waterway destroyed a central portion of the Bayou Cutler site and left the remainder of the site more susceptible to erosion. It also facilitated and increased traffic to the sites. As boats and vessels pass near these sites, the wakes produce repeated wave action and erosion, causing channel widening and shoreline retreat. Both sites are consequently also more susceptible to erosion from storm surges. A major portion of the Bayou Cutler site is now redeposited and submerged. Future impacts to these sites might include accelerated erosion and site burial from the proposed Mid-Barataria Sediment Diversion, as part



Fig. 4.7 (Left) Oblique sUAS photograph showing Bayou Cutler archaeological site. The site includes the land in the foreground and the island in the background. (Right) Oblique sUAS photograph (location given by white arrow in the photo on the left), showing extensive shell midden along the shoreline



Fig. 4.8 (Left) Oblique sUAS photograph of Cheniere St. Denis earthen mound (trees along the shoreline by boat). (Right) sUAS photograph acquired during GPS flight path survey showing differences between shell midden along the coast and damaged wetland vegetation in the central portion of the photo. Location of photo given by white arrow in the photo on the left

of ongoing coastal protection and restoration efforts (G.E.C. 2021). The photographs from the sUAS surveys prove highly useful at distinguishing between shell midden and damaged wetland vegetation (Fig. 4.8), allowing for accurate mapping of extensive shell midden along ~2 km of shoreline from Cheniere St. Denis on the west to Bayou Cutler on the east.

4.3.4 Chain Bowl Point (16SMY27) – Rapid Deposition and Burial

Chain Bowl Point is located in one of the few places in Louisiana's CZ that are experiencing deposition and the creation of new subaerial lands, the Wax Lake Delta. This river-dominated delta began forming in 1942 when the US Army Corps of Engineers dredged the Wax Lake Outlet from the Atchafalaya River to alleviate flooding in Morgan City, LA (Roberts et al. 2003). Since the first emergence of subaerial land in 1973, Wax Lake Delta has developed over 100 km² of new deltaic land (Roberts et al. 1997, 1998).

Chain Bowl Point consists of shell midden first identified by researchers in 1952 on the shore of Atchafalaya Bay west of Belle Isle. At this time, the site was visible as an exposed shell midden with wave-washed pottery sherds along the shoreline (Smith et al. 2006: 36). By 2005, the site could not be relocated or mapped, as there was no evidence of midden or cultural materials on the surface. Although investigators attributed this to subsidence or erosion (Smith et al. 2006: 45), the Wax Lake Delta has transformed the landscape where the site is located. With the artificial Wax Lake Outlet carrying 38.4 Mt./year of sediment to the delta (Kim et al. 2009), Chain Bowl Point is now located over 80 meters inland from the current shoreline (Fig. 4.9). The 2019 sUAS survey clearly shows the paleoshoreline and approximate location of the archaeological site, despite the accretion of land. Detailed inspection of sUAS photographs and additional video from this site, however, did not reveal evidence of the shell midden, suggesting the site might be completely buried (Fig. 4.10).

4.4 Discussion

As demonstrated by the five selected examples, sUAS surveys along with site assessments show that there are at least six interrelated processes in which archaeological sites within coastal Louisiana are being damaged, destroyed, and lost: (1) coastal and shoreline erosion; (2) storm surges; (3) land subsidence; (4) sea level rise; (5) sediment deposition and burial; and (6) direct human alteration of landscapes and waterways. For most sites in the MRD and CZ, these mechanisms are interrelated and not mutually exclusive, although site destruction can be often attributed to one or more dominant forces. For example, Adam's Bay has been losing land surrounding the mound site at an alarmingly rapid rate predominantly due to shoreline erosion and storm surge (Fig. 4.3). In contrast, Magnolia Mounds is located within the interior of marshland southeast of Lake Borgne and is thus mostly sheltered from erosion by wave action, yet is being adversely impacted by land subsidence and sea level rise (Fig. 4.5). In fact, most of the sites in the marshes of St. Bernard Parish are being adversely affected by subsidence, with relatively less damage from shoreline erosion.

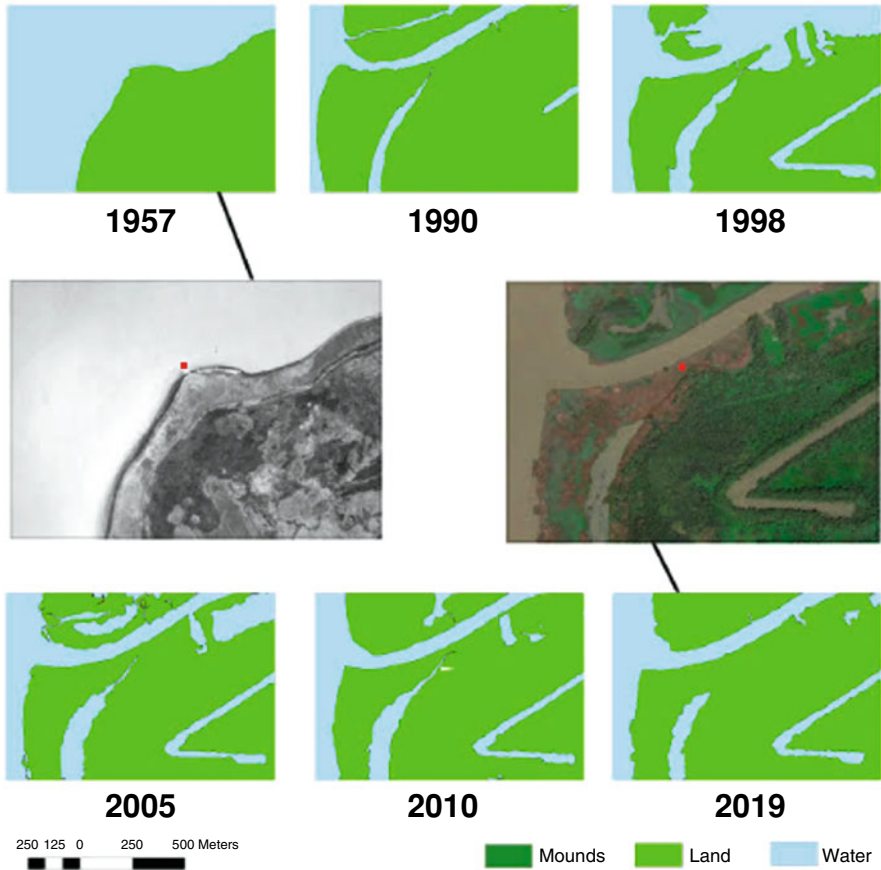


Fig. 4.9 Aerial photograph from 1957 showing the location of Chain Bowl Point along the shoreline and progressive deposition of sediment within Wax Lake Delta until the 2019 sUAS survey

Sites that exhibit the greatest damages from direct human intervention are primarily located adjacent to levees, roads, and channelized waterways. The two examples shown above, Cheniere St. Denis and Bayou Cutler, are being damaged in part due to boat traffic producing wakes that contribute to the erosion of the shoreline and channel widening (Figs. 4.7 and 4.8). Throughout the MRD, countless shipping channels and pipeline canals cut across the wetlands and through Native American archaeological sites (Jones 2014; McLain 2014). These artificial waterways not only bring unwanted wave damage due to boats but also provide pathways for storm surges, the Mississippi River Gulf Outlet and the Hurricane Katrina storm surge of 2005 being the most notorious example (Freudenburg et al. 2009: 91–98). Oil and gas extraction has also been associated with increased land subsidence, further contributing to relative sea level rise (Morton et al. 2006). Additionally, oil and gas platforms within the Gulf of Mexico and the MRD are prone to leaks and spills



Fig. 4.10 Oblique photograph from sUAS showing the location of Chain Bowl Point archaeological site (white arrow) and recent rapid deposition within the Wax Lake Delta

that adversely affect the archaeological record and shoreline vegetation that protects sites from erosion (Rees et al. 2018). The myriad forces of site destruction in Louisiana's MRD and CZ are interrelated and increasingly anthropogenic.

Archaeological sites within the Wax Lake Delta (Chain Bowl Point) and the neighboring Atchafalaya Delta are primarily affected by the rapid deposition of sediment. As high sediment loads from the Atchafalaya River reach these outlets, the deltas exhibit active progradation, covering older land surfaces and building new land. These sites are at risk of complete burial, and in the case of Chain Bowl Point, sUAS surveys suggest complete burial has already occurred. Observations from continued monitoring of sites around the Wax Lake and Atchafalaya deltas can inform an understanding of the adverse effects of planned sediment diversions from the Mississippi River into Barataria Bay and Breton Sound (Cropley et al. 2020). Endangered sites within the areas of potential effect of those and other planned coastal restoration efforts should be regularly and frequently monitored through the use of sUAS.

The use of sUAS to conduct surveys of archaeological sites within the coastal wetlands of Louisiana proved highly successful. The surveys assisted in rapid site reconnaissance while in the field, aiding in site location and identification. Many of the sites visited during the Fall 2019 field campaign had not been visited in decades, and the coordinates for their locations were often hundreds of meters away from the

actual location. While this may not seem a challenge for inland landscapes, traversing inundated marshy wetlands by foot can be extremely difficult and dangerous. Access to sites is complicated by the terrain in terms of access and site visibility and is often cost prohibitive. Furthermore, many of the sites located in subsiding wetlands are hundreds of meters from the closest waterway, and sUAS can provide a quick aerial perspective for locating sites in topographically limited environments.

Another advantage of sUAS for archaeological sites in coastal wetlands is detailed repeat mapping and rapid monitoring of sites. sUAS surveys provide high-resolution photographs and video that can be used to readily distinguish between exposed shell midden and damaged wetland vegetation. Photographs of the sites can also be used to distinguish between subtle elevation changes based on differences in vegetation type, where earthen mounds typically exhibit small trees and shrubs while the surrounding lands contain wetland grasses. The orthomosaics produced from the SfM processing then allow for easy site delineation over relatively large areas, and repeat surveys can be used to monitor changes and damage to the site through time. Rapid site monitoring is critical after major storms and hurricanes to assess the potential damages from storm surges, often involving hundreds of sites. sUAS can provide this capability more efficiently and cost effectively than a conventional survey by watercraft or helicopter and with greater resolution than high-altitude aerial photography.

Despite the many advantages of sUAS for coastal geoarchaeological surveying, there are a few challenges. One of the main challenges is related to the positional accuracy of the sUAS and the resulting post-processed products, such as three-dimensional point clouds, DEMs, and orthomosaics. In coastal lands covered in wetland grass, it can be difficult to place ground control targets throughout the survey area. These challenges arise from difficulties traversing the entire survey area, as well as putting control targets on the actual ground surface. Wetland grass can be quite dense and tall, and control targets large enough to be visible in the photographs often cannot be placed on the ground without damaging the vegetation. This becomes even more challenging when the site is surrounded by shallow water and control targets represent the water surface rather than the ground. In some cases, it may be possible to conduct the sUAS survey without the use of ground control targets and rely directly on the onboard GPS. However, this depends on the sUAS model, whether real-time kinematic (RTK)-GPS is available for the survey area, and the accuracy required for the survey based on the spatial scale of the site.

The challenges associated with dense ground vegetation, shallow waters surrounding survey sites, and potential limitations with ground control points and onboard GPS make accurate elevation models difficult for coastal archaeological sites. While sUAS surveys can be very useful for mapping and monitoring the areal extent and changes to sites, direct estimates of subsidence can be problematic. However, for sites that exhibit earthen mounds without dense tree cover, three-dimensional point clouds and DEMs can be easily obtained from SfM, as shown by an example of the LSU Campus Mounds (Fig. 4.11). Mapping coastal wetland sites with total stations and hand-held GPS can be difficult, time-consuming, and often hazardous, especially in marshlands frequently overgrown with dense stands of

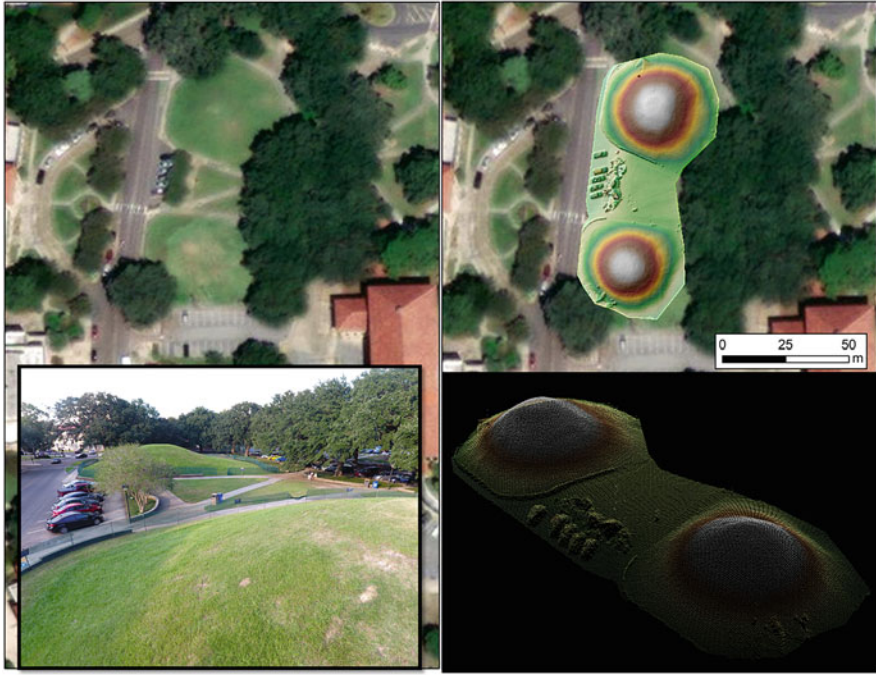


Fig. 4.11 (Top left) Satellite image of the LSU Campus Mounds. (top right) Satellite image with a sUAS-derived DEM showing elevations of the mounds. (bottom right) Oblique view of the sUAS-derived three-dimensional point cloud (looking north). (Bottom left) Ground photograph (looking north) showing LSU Campus Mounds

roseau cane. Similar limitations apply in mapping sites inundated by shallow water. A possible alternative for accurate elevation mapping would be to utilize sUAS-LiDAR, which might allow for the mapping of surface features underneath dense vegetation as well as subsided and partly inundated sites. Targeted utilization of sUAS-LiDAR for at-risk sites with earthen mounds or shell midden would mitigate the need for traditional mapping techniques.

Another promising application of sUAS for coastal archaeological surveys is the use of multispectral imagery. Multispectral sensors on sUAS capture specific wavelength ranges of the electromagnetic spectrum, typically four to five bands including blue, green, red, near-infrared, and thermal. These bands can be combined in different ways to produce false-color images that can provide more insight into landscape characteristics than true-color images (i.e., blue, green, red). The normalized difference vegetation index (NDVI) has long been used to differentiate between types of vegetation and healthy and unhealthy vegetation from Landsat-derived imagery (e.g., Tucker 1979; Townshend et al. 1984). With multispectral sensors included in sUAS payloads, it is now possible to map and monitor variations in vegetation at a much higher resolution than the 30-m satellite imagery, and it is now becoming commonplace to apply these principles to investigate coastal vegetation

dynamics (Chabot et al. 2018; Yang et al. 2019). sUAS-derived multispectral imagery has also recently been applied in archaeological studies to enhance the detection of features of interest (Agudo et al. 2018; Hill et al. 2020; Abate et al. 2021). The use of these approaches for archaeological sites within coastal wetlands would immensely improve site identification and mapping. It would allow for continued, periodic monitoring to determine subtle changes in vegetation as sites actively erode, subside, and become inundated.

In addition to the promising new scientific insights offered by sUAS in studying geoarchaeology is the relative ease and excitement that these technological advances offer for education among undergraduate students. The sUAS utilized in the examples above (DJI Phantom 4) could be considered quite basic compared to the current state-of-the-art sUAS systems that incorporate RTK-GPS, LiDAR, or other multispectral sensors. However, even relatively inexpensive sUAS with standard cameras can be invaluable for interdisciplinary education and getting undergraduate students engaged in scientific research. Learning how to pre-design surveys and flight paths and operate the sUAS in the field, post-processing the data after returning to the lab, and potentially presenting the results at conferences are skillsets that can make undergraduate students highly desirable upon graduation and encourage them to seek advanced degrees. These research opportunities can be offered to students underrepresented in the STEM fields, including Native Americans culturally affiliated with the sites discussed here, thereby helping to promote diversity and equity, as well as indigenous partnerships and collaboration.

Lastly, sUAS can be a powerful instrument for fostering working relationships with local communities, Native American tribes, and the general public, raising awareness about socially relevant issues such as climate change, coastal land loss, and anthropogenic alterations to landscapes. In coastal Louisiana, local communities are well aware of the immediate consequences of land loss. They might not be fully aware, however, of the current conditions of many Native American archaeological sites. Aerial images and videos acquired from low-altitude sUAS can be highly effective visual and communication tools to bring attention to sites that are being rapidly destroyed and lost due to coastal erosion, storm surges, subsidence, sea level rise, sediment deposition, and human alterations of landscapes and waterways. While the widespread impacts of coastal land loss and climate change are evident within the changing landscape of south Louisiana, the endangered cultural heritage of the MRD and CZ is often inaccessible and remains largely unseen. The utilization of sUAS in archaeological survey and site monitoring reveals spatial, spectral, and structural features often obscured by terrain and time and very clearly shows both the long-term and immediate impacts to these at-risk sites.

4.5 Conclusions

Louisiana's coastal lands are rapidly being lost due to land subsidence, sea level rise, coastal erosion, and storm surge, processes that have intensified due to climate change and direct anthropogenic alterations to the landscape. Within Louisiana's

dynamic coastal landscape, Native American archaeological sites, TCPs, and other historically significant sites are currently in the process of being obliterated, with thousands more at serious risk of being lost in the coming decades. This chapter presents examples of site destruction for five sites throughout the Mississippi River deltaic plain and how sUAS were utilized to conduct rapid reconnaissance, site assessments, and high-resolution mapping and monitoring. While sUAS surveys provide detailed data that can be used to evaluate and quantify rates of geomorphic change at these sites, the high-resolution photographs and video also allow for easy identification and discernment of shell midden and differences in vegetation associated with archaeological sites. In coastal wetland landscapes, access to sites is increasingly difficult due to subsidence and sea level rise. These wetlands are characterized by difficult exploration conditions, which often require complicated and costly excavation techniques due to the impact of groundwater, tidal, or brackish water inflow and/or unstable margins of archaeological excavations. Consequently, sufficient archaeological knowledge and understanding of wetlands and coastal zones are often patchy in availability, and surveys as well as excavations remain challenging. sUAS can provide a low-altitude perspective of terrestrial sites on now partially submerged and inundated landforms, helping to relocate sites that in many instances have not been visited for decades. sUAS facilitate site mapping and the identification of previously unidentified cultural features. High-resolution 3D information on the spatial layout of Native American archaeological sites can reveal with a high degree of accuracy the vertical and horizontal dimensions of large cultural features such as mounds, plazas, and midden, as well as changes to those features and surrounding landforms. Rapid and frequent monitoring of endangered sites, especially after major storm surges, is becoming more urgent for cultural resource management (CRM) planning with continued sea level rise, subsidence, and coastal erosion. sUAS provide an efficient and highly effective means of collecting accurate datasets for site monitoring.

The low cost of many entry-level sUAS and their relative ease of operation are also highly conducive for training and educating undergraduate students in interdisciplinary research. sUAS imagery and datasets can be a powerful communication tool for public outreach and immersing audiences in coastal science adaptations through compelling visual media. Incorporating sUAS into interdisciplinary investigations focused on the changing coastal landscape and impacts to Native American archaeological sites can also help foster working relationships and collaborations with local communities and Native American tribes, engaging coastal communities in scientific research while promoting advocacy and equity in CRM.

The risks and challenges to archaeology and CRM planning in wetland landscapes are not unique to the north-central Gulf Coast. Similar challenges are being experienced in deltaic and estuarine landscapes across the globe, where erosion and relative sea level rise demand rapid and effective responses to catastrophic and widespread impacts on living populations and cultural resources (Anderson et al. 2017; Watt et al. 2020). Sites at risk from the dire consequences of anthropogenic climate change are being adversely affected at a faster rate than can be satisfactorily mitigated by traditional CRM data recovery. Implementing actionable and cost-

effective strategies of investigations and survey methodology utilizing sUAS technology will be critical in balancing research potential and the multifaceted value of cultural resources.

References

- Adate N, Frisetti A, Marazzi F, Masini N, Lasaponara R (2021) Multitemporal-multispectral UAS surveys for archaeological research: the case study of san Vincenzo al Voltumo. *Remote Sens (Basel)* 13:2719
- Agudo PU, Pajas JA, Perez-Cabello F, Redon JV, Lebron BE (2018) The potential of drones and sensors to enhance detection of archaeological cropmarks: a comparative study between multi-spectral and thermal imagery. *Drones* 2:29
- Anderson DG, Bissett TG, Yerka SJ, Wells JJ, Kansa EC, Kansa SW, Myers KN, DeMuth RC, White DA (2017) Sea-level rise and archaeological site destruction: an example from the southeastern United States using DINAA (digital index of north American archaeology). *PLoS One* 12(11):1–25
- Barras JA, Bernier JC, Morton RA (2008) Land area change in coastal Louisiana – a multidecadal perspective (from 1956 to 2006). U.S. Geological Survey Scientific Investigations. <https://doi.org/10.3133/sim3019>
- Britt T, Watt DJ, Rees MA, Konsoer K, Huey SM (2020) A perfect storm: an archaeological management crisis in the Mississippi River Delta. *Parks Stewardship Forum* 36(1):70–76
- Chabot D, Dillon C, Shemrock A, Weissflog N, Sager E (2018) An object-based image analysis workflow for monitoring shallow-water aquatic vegetation in multispectral drone imagery. *Int J Geo-Inform* 7:294
- Cloy CB, Ostahowski BE (2015) Archaeological investigations in support of the MC252 (Deep-water horizon) oil spill response in the state of Louisiana. 4 vols. Gulf Coast incident management team. HDR environmental, operations and construction, Inc, New Orleans
- Collins HB (1927) Archaeological work in Louisiana and Mississippi: explorations and field-work of the Smithsonian Institution in 1926. *Smithson Misc Collect* 78(7):200–207
- Couvillion BA, Carras JA, Steyer GD, Sleavin W, Fischer M, Beck H, Trahan N, Griffin B, Heckman D (2010) Land area change in coastal Louisiana from 1932 to 2010. US Geological Survey Scientific Investigations, Map no. 3164
- Cropley P, Boyko WCJ, Heller N, Meaden E, Smith SB, Bowen R (2020) Cultural resources investigations of the mid-Barataria sediment diversion (MBSD) construction impacts APE and the MBSD operations impacts APE in Plaquemines and Jefferson parishes, Louisiana. Prepared by R. Christopher Goodwin and associates, Inc., for Royal Engineers and consultants, LLC, New Orleans, Louisiana
- Davis DD, Giardino MJ, Hartley JD (1978) Cultural resources survey, New Orleans to Venice hurricane protection levee, reach a, Plaquemines parish, Louisiana. U.S. Army Corps of Engineers, New Orleans District. Department of Anthropology, Tulane University, New Orleans
- Dawson T, Hambly J, Kelley A, Lees W, Miller S (2020) Coastal heritage, global climate change, public engagement, and citizen science. *PNAS* 117(15):8280–8286. <https://doi.org/10.1073/pnas.1912246117>
- Fearnley S, Peneland S, Britsch LD (2009) Mapping the geomorphology and processes of coastal land loss in the Pontchartrain Basin: 1932 to 1990 and 1990 to 2001. *J Coast Res* 10054:48–58
- Fisk HN (1944) Geological investigations of the Alluvial Valley of the lower Mississippi River. Mississippi River Commission, Vicksburg
- Freundenburg WR, Gramling R, Laska S, Erikson KT (2009) Catastrophe in the making: the engineering of Katrina and the disasters of tomorrow. Island Press, Washington, DC

- G.E.C. (2021) Environmental Impact Statement for the Proposed Mid-Barataria Sediment Diversion Project, Plaquemines Parish, Louisiana. Prepared by G.E.C., Inc., Baton Rouge, for the U.S. Army Corps of Engineers, New Orleans District
- Gagliano SM (1963) A survey of preceramic occupations in portions of South Louisiana and South Mississippi. *Florida Anthropol* 16(4):105–132
- Gagliano SM (1967) Occupation sequence at Avery Island. Coastal studies series no. 22. Louisiana State University Press, Baton Rouge
- Gagliano SM (1984) Geoaerchaeology of the northern gulf shore. In: Davis DD (ed) *Perspectives on Gulf Coast prehistory*. University Press of Florida, Gainesville, pp 1–40
- Gagliano SM, van Beek JL (1970) Geologic and geomorphic aspects of deltaic processes, Mississippi Delta system. In: hydrologic and geologic studies of coastal Louisiana, vol 1. Louisiana State University, Baton Rouge, Coastal Studies Institute
- Gagliano SM, Weinstein RA, Burden EK (1975) Archaeological investigations along the Gulf Intracoastal waterway: coastal Louisiana area. U.S. Army Corps of Engineers, New Orleans District. Coastal environments, Inc, Baton Rouge
- Gagliano SM, Weinstein RA, Burden EK (1976) Archaeological survey of the port Fourchon area, Lafourche parish, Louisiana. Greater Lafourche port commission, Galliano, LA. Coastal Environments, Inc., Baton Rouge
- Gagliano SM, Smith WG, Burden E, Weinstein R, Emmer R, Brooks K, Hair L, King P (1977) Cultural resources evaluation of the northern Gulf of Mexico continental shelf, offshore Louisiana. 3 vols. U.S. Department of the Interior, National Park Service Office of archaeology and historic preservation. Contract no. 08550-MU5-40. Coastal Environments, Inc, Baton Rouge
- Gagliano SM, Weinstein RA, Burden EK (1978) Preliminary study of the cultural resources of the St. Bernard parish wetlands, Louisiana: an approach to management. Coastal Environments, Inc., Baton Rouge
- Gagliano SM, Weinstein RA, Burden EK, Glander WP, Brooks KL (1979) Cultural resources survey of the Barataria, Segnette, and Rigaud waterways, Jefferson parish, Louisiana. 2 vols. U.S. Army Corps of Engineers, New Orleans District. Coastal environments, Inc, Baton Rouge
- Gagliano SM, Meyer-Arendt KJ, Wicker KM (1981) Land loss in the Mississippi River deltaic plain. *Trans Gulf Coast Assoc Geol Soc* 31:295–300
- Gagliano SM, Pearson CE, Weinstein RA, Wiseman DE, McClendon CM (1982) Sedimentary studies of prehistoric archaeological sites. Criteria for the identification of submerged archaeological sites of the northern Gulf of Mexico continental shelf. Preservation Planning Series. Coastal Environments, Inc., Baton Rouge
- Gibson JL (1978) Archaeological survey of the lower Atchafalaya region, south Central Louisiana. Report no. 5, Center for Archaeological Studies, University of Southwestern Louisiana, Lafayette
- González JL, Törnqvist TE (2006) Coastal Louisiana in crisis: subsidence or sea level rise? *Eos Trans Am Geophys Union* 87(45):493–498
- Hale RA (2017) Archaeological investigations at the Adams Bay site (16PL8), Plaquemines Parish, Louisiana: Assessing Natural and Anthropogenic Effects to a Louisiana Coastal Archaeological Site. M.A. Thesis. St. Cloud State University. Culminating Projects in Cultural Resource Management. 15. https://repository.stcloudstate.edu/crm_etds/15
- Hill AC, Laugier EJ, Casana J (2020) Archaeological remote sensing using multi-temporal, drone-acquired thermal and near infrared (NIR) imagery: a case study at the Enfield Shaker Village, New Hampshire. *Remote Sens (Basel)* 12:690
- Howe HV, Russell RJ, McGuirt JH (1935) Submergence of Indian mounds. In reports on the geology of Cameron and Vermilion parishes. *Geol Bull* 6(1):64–68
- Jones D (2014) Slip Slidin' away: the Toncrey site (16PL7). *Louisiana Archaeol* 38(2011):51–81. Louisiana Office of Cultural Development, Division of Archaeology. Cultural Resources Map. Accessed 27 June 2021, at <https://www.crt.state.la.us/archaeology/>

- Kemp GP, Day JW, Rogers JD, Giosan L, Peyronnin N (2016) Enhancing mud supply from the lower Missouri River to the Mississippi River Delta USA: dam bypassing and coastal restoration. *Estuar Coast Shelf Sci* 183:304–313
- Kesel RH (1989) The role of the Mississippi River in wetland loss in southeastern Louisiana, USA. *Environ Geol Water Sci* 13(3):83–193
- Kesel RH (2003) Human modifications to the sediment regime of the lower Mississippi River flood plain. *Geomorphology* 56:325–334
- Kim W, Mohrig D, Twilley R, Paola C, Parker G (2009) Is it feasible to build new land in the Mississippi River Delta? *Eos Trans Am Geophys Union* 143(6):03117003
- Kniffen FB (1936) A preliminary report on the Indian mounds and middens of Plaquemines and St. Bernard parishes. In *lower Mississippi River Delta: reports on the geology of Plaquemines and St. Bernard parishes*. *Geol Bull* 8:407–422
- Kniffen FB (1938) The Indian mounds of Iberville parish: reports on the geology of Iberville and Ascension parishes. *Geol Bull* 13:189–207
- McIntire WG (1954) Correlation of prehistoric settlement and Delta development. Coastal research institute technical report 5. Louisiana State University, Baton Rouge
- McIntire WG (1958) Prehistoric Indian settlements of the changing Mississippi River Delta. Coastal studies series no. 1. Louisiana State University Press, Baton Rouge
- McLain RB (2014) Investigations at the Toncrey site (16PL7): analysis of a late prehistoric site in extreme southeastern Louisiana. *Louisiana Archaeol* 38(2011):82–137
- Mehta J, Ostahowski B, Marks T (2020) The disappearing environments and native ecosystems of coastal Louisiana. *The Society for American Archaeology Archaeological Record* 20(5):23–28
- Morton RA, Bernier JC, Barras JA (2006) Evidence of regional subsidence and associated interior wetland loss induced by hydrocarbon production, Gulf Coast region, USA. *Environ Geol* 50: 261–274. <https://doi.org/10.1007/s00254-006-0207-3>
- Neuman RW (1970) Archaeological survey of the Lake Pontchartrain hurricane project area, Southeast Louisiana. Louisiana State University, Baton Rouge
- Neuman RW (1973) Archaeological survey of the bayou Lafourche and Lafourche-jump waterway, Louisiana. Louisiana State University, Baton Rouge
- Neuman RW (1974) Archaeological survey of the Houma Navigational Canal and bayous LaCarpe, Terrebonne, petit Caillou, and grand Caillou, Terrebonne parish. Louisiana State University, Baton Rouge
- Neuman RW (1975a) Archaeological survey of the bayou Baratavia - bayou Perot projects, Jefferson parish, Louisiana. Louisiana State University, Baton Rouge
- Neuman RW (1975b) Archaeological salvage excavations at the bayou jasmine site, Saint John the Baptist parish, Louisiana, 1975. Louisiana State University, Baton Rouge
- Neuman RW (1977a) An archaeological assessment of coastal Louisiana. *Mélanges* 11(1):1–43
- Neuman RW (1977b) Archaeological techniques in the Louisiana coastal region. *Louisiana Archaeol* 3(1976):1–21
- Neuman R, Byrd KM (1981) Aerial imagery in locating and managing archaeological resources along the Louisiana coast. *Louisiana Archaeol* 7:101–108
- Penland S, Ramsey KE (1990) Relative sea-level rise in Louisiana and the Gulf of Mexico: 1908–1988. *J Coast Res* 6(2):323–342
- Phillips P, Ford JA, Griffin JB (1951) Archaeological survey of the lower Mississippi Alluvial Valley, 1940–1947. In: *Papers of the Peabody Museum of Archaeology and Ethnology*, vol 25. Harvard University, Cambridge, MA
- Rees MA, Huey SM, Sorset S (2018) Assessment of the effects of an oil spill on coastal archaeological sites in Louisiana. US Dept. of the Interior, Bureau of Ocean Energy Management, Gulf of Mexico OCS Region, New Orleans (LA)
- Roberts H (1998) Delta switching: early response to the Atchafalaya River diversion. *J Coast Res* 14(3):882–899

- Roberts H, Walker N, Cunningham R, Kemp G, Majersky S (1997) Evolution of sedimentary architecture and surface morphology: Atchafalaya and wax Lake deltas, Louisiana (1973–1994). *Gulf Coast Assoc Geol Soc Trans* 47:477–484
- Roberts H, Coleman J, Bentley S, Walker N (2003) An embryonic major delta lobe: a new generation of delta studies in the Atchafalaya-wax Lake delta system. *Gulf Coast Assoc Geol Soc Trans* 53:690–703
- Saucier RT (1963) Recent geomorphic history of the Pontchartrain Basin, Louisiana. Coastal studies series no. 9. Louisiana State University Press, Baton Rouge
- Saucier RT (1974) Quaternary geology of the lower Mississippi Valley. *Arkansas Archeological Survey Research Series* 6, pp 1–26
- Saucier RT (1981) Current thinking on riverine processes and geologic history as related to human settlement in the southeast. *Geosci Man* 22:7–18
- Smith RL, Apollonio H, Lintott KB (2006) Archaeological investigations for the proposed bayou Sale swamp three dimensional seismic survey, St. Mary parish, Louisiana. Prepared by earth search, Inc., for seismic exchange, Inc, New Orleans, Louisiana
- Townshend JRG, Justice CO, Holben BN, Tucker CJ (1984) Monitoring and mapping global vegetation cover using data from meteorological satellites. In: *Proc. ESA/EARSeL Symp. Integrated. Approaches remote Sens. ESA SP-124, Guildford*, p 75
- Tucker CJ (1979) Red and photographic infrared linear combinations for monitoring vegetation. *Remote Sens Environ* 8(2):127–150
- Watt DJ, Rees MA, Britt T, Konsoer K, Huey SM (2020) Mitigating engineered disaster on Louisiana’s Gulf Coast. *The Society for American Archaeology Archaeological Record* 20(5): 16–21
- Wiseman DE, Weinstein RA, McClosky KG (1979) Cultural resources survey of the Mississippi River—gulf outlet, Orleans and St. Bernard parishes, Louisiana. U.S. Army Corps of Engineers, New Orleans District. Coastal Environments, Inc, Baton Rouge
- Yang B, Hawthorne TL, Torres H, Feinmann M (2019) Using object-oriented classification for coastal management in the east central coast of Florida: a quantitative comparison between UAV, satellite, and aerial data. *Drones* 3(3):60

Chapter 5

A Comparison of Different Software Packages in sUAS-Based Land Feature Reconstruction



Yingkui Li and Nathan McKinney

Abstract The integration of small, unmanned aircraft systems (sUAS) and structure from motion (SfM) provides a simple, cost-effective, and unique opportunity to map detailed land features in a much finer (up to cm-level) resolution. Software packages are available to process sUAS-collected photos into three-dimensional (3D) point clouds, digital surface models, and orthomosaics. However, the differences between the products generated by various software packages are seldom addressed. In this chapter, we compared the 3D point cloud reconstruction of various natural and man-made land features, including trees/forest, grassland, roads, parking lots, and buildings, using five software packages: Pix4DMapper, Pix4D Cloud, Metashape (previously Photoscan), GlobalMapper, and OpenDroneMap. We demonstrated this work based on the sUAS-collected data from three sites in Missouri, Tennessee, and Florida.

Keywords Structure from motion · Unmanned aircraft systems · Point cloud · Land features

5.1 Introduction

The advances of a variety of technologies have revolutionized the fields of geographical and environmental sciences by the production of high-resolution topographic and land surface datasets (Fonstad et al. 2013; Tarolli 2014; Smith et al. 2016). In particular, the developments of light detecting and ranging (LiDAR) and structure from motion (SfM) have allowed the generation of up to millimeter and centimeter resolution digital surface models (DSMs) to quantify earth surface processes (e.g., Eltner et al. 2015; Lu et al. 2019; Li et al. 2020) and obtain detailed three-dimensional (3D) information for terrain and vegetation analysis (e.g., Tian et al. 2021; Li et al. 2019). Integrated with small, unmanned aircraft systems (sUAS),

Y. Li (✉) · N. McKinney
Department of Geography, University of Tennessee, Knoxville, TN, USA
e-mail: yli32@utk.edu; mckinney@utk.edu

LiDAR and SfM are extremely promising to map detailed land features up to centimeter resolutions for relatively larger areas (Javernick et al. 2014; Cook 2017).

SfM is an image-based technology with relatively low cost. Different from traditional stereo-photogrammetry that requires specific and expensive cameras and aircrafts to obtain precise camera position and orientation for the three-dimensional (3D) reconstruction of both natural and man-made land features, SfM is an advance in computer vision that significantly simplified image-based feature identification and surface reconstruction (Fonstad et al. 2013; Smith et al. 2016; Nouwakpo et al. 2016). It only requires highly overlapped images taken with commonly used cameras, smartphones, and tablets (Fonstad et al. 2013; Smith et al. 2016); thus, the cost of the survey can be reduced significantly. More importantly, despite the low cost, studies have demonstrated that the SfM-based surface reconstructions can reach the accuracy of mm to cm levels in comparison to the surface reconstructed using LiDAR and traditional stereo-photogrammetry (Eltner et al. 2015, 2016; Nouwakpo et al. 2016; Kaiser et al. 2018). In recent years, the integration of SfM with low-cost sUAS has become popular in conducting large-scale surface reconstructions in geographic and environmental related projects (Javernick et al. 2014; Ouédraogo et al. 2014; Eltner et al. 2016).

With the popularity of SfM and sUAS, software packages and web services are available to process sUAS-collected photos into 3D point clouds, DSMs, and orthomosaics. However, most studies have only used one specific software package available to the authors for the 3D reconstruction, and the differences between the products generated by different software packages are seldom addressed (Eltner and Schneider 2015). Given the fact that different SfM software packages may use different algorithms and/or parameters in the reconstruction and that users typically treat the SfM reconstruction as a black box, lacking specific knowledge in the SfM algorithms and/or parameters, it is of critical importance to examine the similarities and differences of various software packages in reconstructing land features. In this chapter, we explore the products generated by a set of commonly used SfM software packages and compare the point clouds of various natural and man-made land features, including trees/forest, grassland, roads, parking lots, and buildings, at three sites from Missouri, Tennessee, and Florida.

5.2 Study Sites

We choose three sites to examine the similarities and differences of various software packages in reconstructing natural and man-made land features (Fig. 5.1). The first site (A) is a suburban neighborhood in St. Peters, a western suburb of St. Louis, Missouri, including typical land features of residential houses, roads, schools, grassland, and some forest. The second site (B) is an undeveloped hilltop area in Knoxville, Tennessee. The land features include roads, grassland, and forest. The



Fig. 5.1 The three study sites in St. Peters, Missouri (a); Knoxville, Tennessee (b); and Santa Rosa Island, Florida (c). The orthomosaics for each site in this figure were processed by Pix4DMapper

third site (C) is located on Santa Rosa Island near the western end of the Florida panhandle, representing typical coastal landforms with wetland (salt marsh), shallow water, and both vegetated and unvegetated sand dunes. We present a detailed analysis of the SfM reconstruction for different land features for site A, while sites B and C are only used for a general comparison of the reconstructed point clouds, DSMs, and orthomosaics, as well as processing times.

5.3 Methods

5.3.1 Drone Photo Collection

To compare the impacts of different software packages on the reconstructed point clouds, DSMs, and orthomosaics, we used the same set of images collected by a Parrot ANAFI drone (<https://www.parrot.com/us/drones/anafi>) using the integrated 21-megapixel camera. Photos used for the SfM reconstruction can be collected in manual or automatic flight modes. We preferred to conduct this task automatically because the built-in mission plans use a set of parameters to control the photo

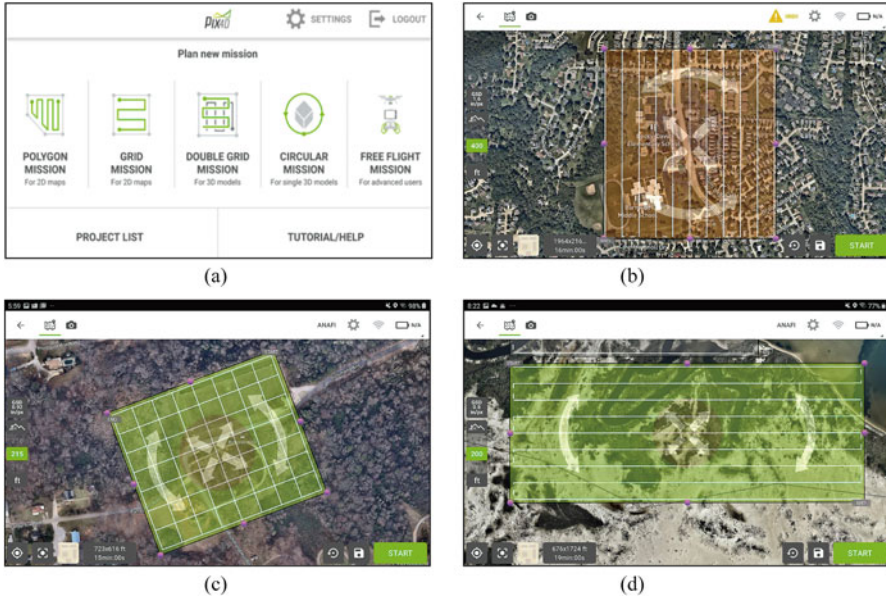


Fig. 5.2 (a) A screenshot of the Pix4DCapture app, showing five different flight patterns that can be used for photo collection; (b) the grid mission in site A; (c) the double grid mission in site B. (d) the grid mission in site C

Table 5.1 sUAS flight information for the three sites

Studysite	Flight altitude (m)	Estimated GSD (m)	Area coverage (acre)	Flight pattern	Camera angle (°)	Photo count
A	121	0.04	147.0	Grid	90	220
B	65	0.02	19.1	Double grid	70	254
C	61	0.02	40.3	Grid	90	349

quality, overlap percentage, flight speeds, and other related parameters. We used Pix4D Capture to design and control the flight mission (Fig. 5.2a). Two of our flights (sites A and C) use a “Grid” mission pattern, while the third (site B) is a “Double Grid Mission” that can capture more vertical details for 3D model reconstruction (Fig. 5.2b–d) (<https://support.pix4d.com/hc/en-us/articles/209960726-Types-of-mission-Which-type-of-mission-to-choose>). Table 5.1 lists detailed information for the flights, including altitude, estimated ground sampling distance (GSD) based on the flight height and camera resolution, area coverage, flight pattern, flight time, camera angle, and number of photos collected for the three sites. The same overlap values of 80% in front and 70% at the sides are used for all three flights.

5.3.2 *Surface Reconstruction Using Different Software Packages*

We tested four desktop software packages, including Pix4DMapper, Agisoft Metashape, GlobalMapper, and OpenDroneMap, and one cloud service, Pix4DCloud, for elevation reconstruction. All these software packages can produce georeferenced point clouds, DSMs, and orthomosaics of the surveyed areas.

Pix4DMapper is a popular commercial photogrammetry software for professional drone mapping developed by Pix4D S.A. in Switzerland (<https://www.pix4d.com/product/pix4dmapper-photogrammetry-software>). It provides a user-friendly interface and processing templates for 3D reconstruction and mapping. We used Pix4DMapper version 4.6.4 and the “3D Maps” processing template as the default settings. In addition to the desktop software, we also tested the software-as-a-service version Pix4DCloud, which uses an Amazon Web Services Linux platform to process images through a streamlined browser interface.

GlobalMapper is a geographic information system software package developed by Blue Marble Geographics, USA (<https://www.bluemarblegeo.com/products/global-mapper.php>). Its optional LiDAR Module includes the Pixels to Points tool to generate georeferenced 3D point clouds, DSMs, and orthomosaics based on the SfM technology.

OpenDroneMap (ODM) is an open-source software for drone image processing to generate georeferenced point clouds, DSMs, and orthomosaics (<https://www.opendronemap.org/odm/>). It has been developed as a command line toolkit since 2014. It also provides a user-friendly web front end (WebODM) to allow for easy access of the data processing through a browser. We used a Docker image of WebODM version 1.8.0 based on the ODM version 2.4.3 engine for the data processing (OpenDroneMap 2020).

Agisoft Metashape is a widely used SfM software package developed by Agisoft LLC (<https://www.agisoft.com/>) and was known in previous versions as Agisoft Photoscan. The Metashape standard edition uses SfM to create point clouds and digital models for applications, such as visual effects, game design, and archaeological reconstructions, while the professional edition can also produce georeferenced DSMs and orthomosaics. The version used in this study is Metashape Professional v1.7.2.

The processes of these software packages follow a similar workflow to generate point clouds, DSMs, and orthomosaics (Fig. 5.3). The first step is to identify corresponding locations (keypoints) on the images and match these keypoints among the images using feature and gradient detection. These matched keypoints will be used to calculate relative camera positions, orientations, and spatial relationships between the image locations. This step also conducts the sparse bundle adjustment and triangulations to locate the identified keypoints in 3D space, generating a sparse point cloud (Strecha et al. 2003; Agisoft LLC 2021). For sUAS-collected photos, this sparse point cloud can be georeferenced based on the GPS locations embedded in the image metadata.



Fig. 5.3 An example of the three major steps in Pix4DMapper for generating point cloud, DSM, and orthomosaic. The description of each step is detailed in the text. All software packages use the similar workflow to generate these products

The second step is to increase the spatial density of 3D points using a multi view stereo (MVS) method, creating a series of depth maps that are combined into a high-resolution spatial reconstruction. This densification step produces a dense point cloud (Strecha et al. 2003; Hiep et al. 2010).

The final step derives various georeferenced products from the dense point cloud and the images. An orthomosaic is created as a rectified 2D projection of the images. A DSM is created as a common product for geospatial analysis. The resolution of these products can be controlled in the software parameters with the maximum approximately equal to the GSD of the input images. Other products that may be created in this step include a digital terrain model (DTM), vectorized contour lines, and maps of normalized difference vegetation index (NDVI) or reflectance surfaces depending on the input images (Pix4D SA 2017; Blue Marble Geographics n.d.).

Many parameters can be adjusted in these software packages. Some of these parameters can be complicated and require extensive knowledge of the SfM algorithm. Because regular users usually treat the SfM reconstruction as a black box, lacking the knowledge in the customization of specific parameters, we used the default settings of each software for the data processing. Each software uses slightly different default settings. Based on the documentations, the default parameters for each package are set for balancing reconstruction details and the processing time/resources required. Different software packages use varied down-sampling of images to reduce processing time because reduction of image size leads to an exponential decrease in processing time but may have much less influence on the resulting quality and point cloud density (Pix4D SA 2017; Blue Marble Geographics n.d.). Table 5.2 summarizes the default image sizes of different software packages in each of the three major steps.

Each of the software packages was installed on a separate computer with an identical hardware configuration and a fresh install of Windows 10 Pro. The configuration includes an Intel Core i7-9700 3.0GHz 8-core processor, 32 GB

Table 5.2 The default image sizes and resolutions of different software packages in generating point clouds, DSMs, and orthomosaics

	Step 1 (Camera calibration)	Step 2 (Cloud densification)	Step 3 Orthomosaicresolution	Step 3 DSMresolution
Pix4DMapper	Full resolution	½ of input	1 × GSD	1 × GSD
Pix4DCloud	Full resolution	½ of input	1 × GSD	1 × GSD
GlobalMapper	½ of input	½ of input	1 × point spacing	5 × point spacing
ODM	2048 pixels	2048 pixels	5 cm or 10 × GSD ^a	5 cm or 30 × GSD ^a
Metashape	Full resolution	¼ of input	1 × GSD	4 × GSD

^aODM allows the user to set a desired resolution and adjusts the output if a minimum GSD is not met. The different resolutions for orthomosaic and DSM were only for our processed data and may not be the same for other applications

RAM, 500 GB NVMe m.2 SSD drive, and Intel 630 integrated graphics. This configuration meets the minimum suggested system resources recommended for each package and represents a widely attainable system for the average user (OpenDroneMap2020; Agisoft LLC 2021; Blue Marble Geographics n.d.; Pix4D SA 2017).

5.3.3 Point Cloud Registration

We proceeded to register the point clouds generated by different software packages in site A using an open-source software, CloudCompare (<https://danielgm.net/cc/>). Due to the lack of geographic referencing points, we used the Align tool to manually pick up a set of control points that represent fixed objects in the area, such as the corners of buildings and the one-way or turning signs on roads and within the parking lots, to register the point clouds. We treated the point cloud generated using Pix4DMapper as the reference, and all other point clouds were adjusted to this point cloud. We tried out different control points and removed the points with the high errors to make sure that the registration can reach the lowest root mean square error (RMSE) value that we can achieve. We did not use the ICP (iterative closest point) algorithm (Besl and McKay 1992) for the point cloud registration because of its poor performance on the point clouds with different point spacings. Figure 5.4 shows the control points on the two point clouds in site A generated by Pix4DMapper and Pix4DCloud, respectively, and the final RMSE value of the registration. Note that most identified control points are distributed on the center of the region. The registration errors may increase toward the margins.

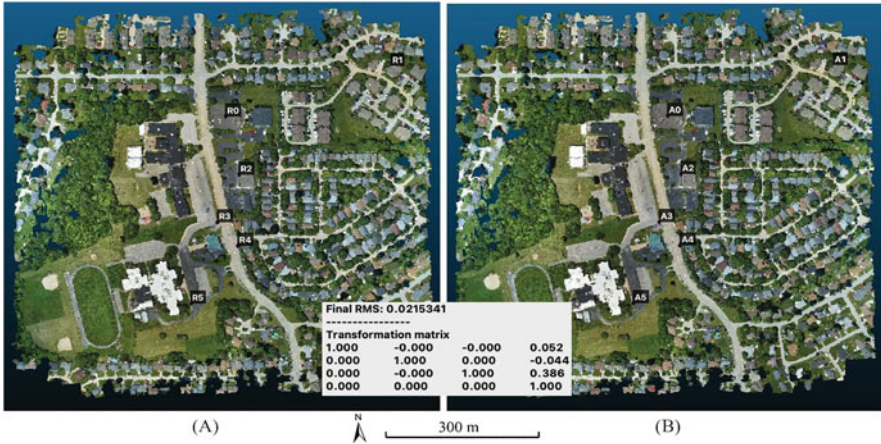


Fig. 5.4 An example of point cloud registration in CloudCompare for site A. (a) A screenshot of the reference point cloud generated using Pix4DMapper, showing six referenced control points (R0 to R5). (b) A screenshot of the aligned point cloud generated by Pix4DCloud, showing six aligned control points (A0 to A5). The middle screenshot shows the final RMSE value of the registration (about 2.15 cm) and the transformation matrix that applied to the aligned point cloud for the registration

5.3.4 Point Cloud Comparison and Quality Assessment

After point cloud registration, we first used the Rasterize tool in CloudCompare to convert the referenced and registered point clouds to a set of rasters representing the statistics of point clouds in a 2 m by 2 m window. We chose this window size to minimize the potential impact of the registration error (a few cm to 20 cm) on the point cloud statistics. The statistics include the maximum (Z-Max), minimum (Z-Min), mean (Z-Mean), and standard deviation (Z-STD) of the point elevations, as well as the point count.

We then opened the orthomosaic generated using Pix4DMapper (corresponding to the reference point cloud) in ArcGIS 10.7 and manually digitized five natural and man-made land features, including trees/forest, grassland, roads, parking lots, and buildings (the roofs of apartments, single-family houses, hospital, and schools) in this area (Fig. 5.5). During the digitization, we focused on the areas that only represent one type of the features and avoided the potential overlaps, such as trees over the top of the houses. We also tried to distribute the digitized features across the whole area to reduce the bias that may be introduced by a specified area.

We used the Create Fishnet tool in ArcGIS 10.7 to generate a fishnet polygon layer of 2-m by 2-m, corresponding to the raster cell size that we used to rasterize the point cloud. We only extracted the fishnet polygons completely within the digitized land features and assigned the feature code to each fishnet polygon. We then extracted the point cloud statistics generated using CloudCompare to the center

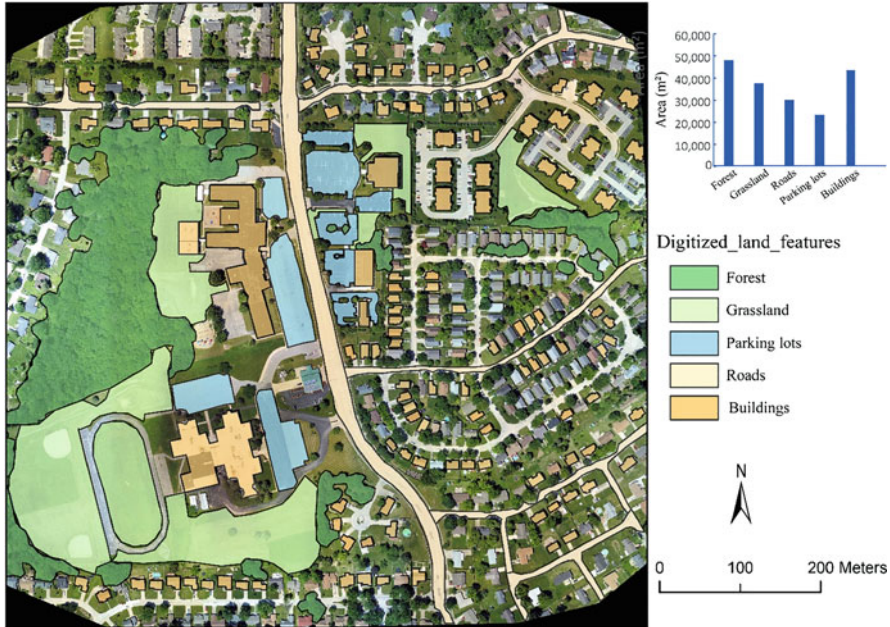


Fig. 5.5 Digitized land covers and man-made features for site A

point of each fishnet polygon and used these statistics to evaluate the performance of different software packages on these land features.

We calculated the difference between Z-Mean of each fishnet polygon generated by the five software packages and summarized the mean and standard deviation of the Z-Mean difference for each feature. We then conducted Pearson’s correlation to examine the relationships between the Z-Mean values generated using different software packages.

We also compared the SfM-reconstructed land features with the 1-m LiDAR DEM of this area. This DEM was generated using airborne LiDAR data obtained in February 2017 and available from the USGS TNM download site (<https://apps.nationalmap.gov/downloader/#/>). Due to the uncertainty of the internal drone GPS in the latitude and longitude measurement (about 3–5 m), we used the identifiable features, such as street and building corners, to register the SfM-reconstructed DSMs and the 1-m LiDAR DEM. We only conducted the linear regression of the DEM elevations with the Z-Min values of the fishnet polygons from the roads and parking lots (representing the bare earth) because the LiDAR DEM data represents the bare earth topography.

5.4 Results

5.4.1 General Comparison of Products from Three Sites

Each of the five software packages was able to successfully produce the point cloud, DSM, and orthomosaic for all three sites using default settings without human intervention beyond loading the images and triggering the processing pipeline. Despite being given identical images, the results from the packages showed considerable variations in attributes, such as point density and resolution (Table 5.3). In every site, the open-source ODM produced much smaller point clouds than the other packages, with a resultant point count of 20–60%, likely due to more aggressive image resampling settings. Pix4DMapper and Pix4DCloud generate similar, but not identical, point clouds. It appears that the Pix4DCloud generates a point count about 1% larger than Pix4DMapper although the difference in the overall point spacing is negligible. The relative point density between the Pix4D, Metashape, and particularly the GlobalMapper clouds appears to be highly influenced by different image parameters associated with each flight. In site A, which uses the lowest GSD images, the GlobalMapper cloud is nearly equal to Metashape for most points generated and has the smallest point spacing. This contrasts heavily with sites B and C in which GlobalMapper produces only about half as many points as the densest clouds produced by other commercial software and with a point spacing closer to the open-source ODM. The point densities produced by the Pix4D products and Metashape also suggest some site-influenced variations in performance. While the point counts for these two packages were approximately equal for site B, Metashape

Table 5.3 A summary of the point clouds, DSMs, and orthomosaics generated by different software packages for the three study sites

Site	Software	Point count	Point spacing (m)	DSMresolution (m)	Orthomosaicresolution (m)
A	Pix4DMapper	23,905,991	0.164	0.042	0.042
	Pix4DCloud	24,029,477	0.164	0.042	0.042
	GlobalMapper	30,873,374	0.131	0.560	0.112
	ODM	7,359,467	0.293	0.383	0.087
	Metashape	30,896,673	0.149	0.165	0.041
B	Pix4DMapper	23,417,668	0.055	0.021	0.021
	Pix4DCloud	23,572,890	0.055	0.021	0.021
	GlobalMapper	10,110,044	0.107	0.315	0.063
	ODM	4,968,526	0.109	0.110	0.050
	Metashape	23,810,138	0.069	0.073	0.018
C	Pix4DMapper	43,724,230	0.065	0.019	0.019
	Pix4DCloud	44,242,349	0.065	0.019	0.019
	GlobalMapper	21,440,633	0.086	0.366	0.073
	ODM	12,845,882	0.112	0.199	0.050
	Metashape	40,169,436	0.063	0.068	0.017

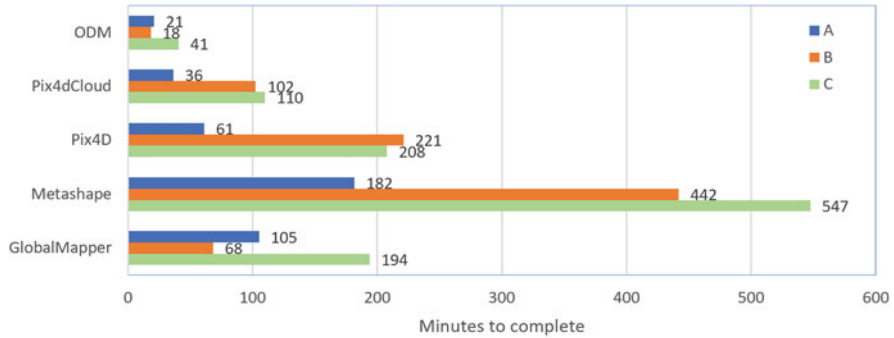


Fig. 5.6 The processing time (in minutes) for the three sites using the five software packages

produced about 28% more points for site A, and in site C the Pix4D count was about 10% higher.

The time required to perform camera calibration, point cloud densification, and surface generation (Fig. 5.6) appears influenced by but not fully dependent on the output resolutions. For every set of images, ODM finished much quicker than any other package, taking only between 18 and 41 minutes to complete under the default settings. Metashape consistently required a much longer time (182–547 minutes), despite not always creating higher-resolution products. The Pix4DCloud performed faster than Pix4DMapper on our test machines, likely due to greater memory and processor allocations on the cloud (69GB and Xeon 8124 M 18-core, respectively). Processing time for the cloud service only includes the time in the generated report and not any queueing period between uploading the images and the start of processing since this may be highly dependent on uncontrollable demand factors. The logs indicate that any queue delay may have added only about 5–15 minutes to the overall time.

5.4.2 Detailed Point Cloud Comparison of Land Features in Site A

5.4.2.1 Point Cloud Registration

Depending on the quality and spacing of the point clouds, the RMSE value of the registration among each point cloud and the reference point cloud of Pix4DMapper ranges from ~0.02 m to ~0.20 m in site A. The RMSE value between the point clouds of Pix4DMapper and Pix4DCloud is 0.022 m, much smaller than the average spacing of these two point clouds (~0.15 m). The RMSE value between the point clouds of Pix4DMapper and GlobalMapper is 0.076 m, about half of the average spacing of these two point clouds (0.131–0.152 m). The RMSE value between the point clouds of Pix4DMapper and Metashape is 0.189 m, slightly larger than the

average spacing of these two point clouds (0.138–0.152 m). The RMSE value between the point clouds of Pix4DMapper and ODM is 0.203 m, larger than the average spacing of the point cloud of Pix4DMapper (0.152 m), but smaller than the average spacing of the ODM point cloud (0.267 m). Note that these RMSE values are only calculated from the control points that are mainly distributed on the center part. The registration errors may be higher toward margins.

The registration errors may cause some disparities between point clouds. We therefore compared the point cloud statistics based on the much larger 2 by 2 m fishnet polygons to limit the impact of the registration errors because the size of the fishnet polygon is at least one magnitude larger than the registration errors. The following sections summarize detailed comparisons of each land feature for the point clouds generated using different software packages.

5.4.2.2 Point Cloud Comparison of Land Features

Trees/Forest

Figure 5.7 shows descriptive statistics for the 2 × 2 m fishnet polygons of trees / forest sampled from point clouds of each software package. All point clouds have significant percentages of NoData fishnet polygons (zero point within the 2 × 2 m window). The Metashape point cloud has the lowest percentage of NoData fishnet polygons (5.67%), followed by GlobalMapper (10.29%), ODM (11.22%), Pix4DMapper (14.61%), and Pix4D Cloud (15.14%). The ODM point cloud has the lowest point count (density), while the Metashape point cloud has the highest point density. The two point clouds generated by Pix4D (Mapper and Cloud) have almost identical point density, and the GlobalMapper point cloud has slightly lower

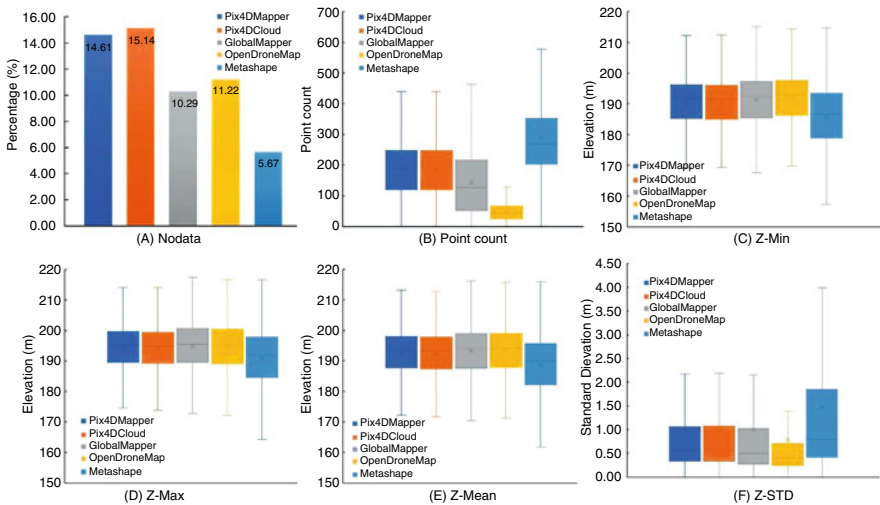


Fig. 5.7 The point cloud statistics of trees/forest based on the 2 × 2 m fishnet

Table 5.4 The absolute Z-Mean differences (in meters) and Pearson's correlations of 2×2 m trees/forest fishnets between point clouds generated using different software packages

	Pix4DMapper	Pix4DCloud	GlobalMapper	ODM
Pix4DCloud	0.599 ± 1.866 (0.966)			
GlobalMapper	1.721 ± 2.800 (0.922)	1.790 ± 2.932 (0.919)		
ODM	1.744 ± 2.898 (0.915)	1.779 ± 3.001 (0.912)	1.174 ± 2.097 (0.963)	
Metashape	4.780 ± 4.375 (0.860)	4.851 ± 4.430 (0.852)	4.207 ± 3.465 (0.926)	3.839 ± 3.578 (0.914)

point density than the Pix4D ones. For the point elevation statistics, the Pix4Dpoint clouds have almost identical Z-Min, Z-Max, Z-Mean, and Z-STD values. The elevation statistics of the GlobalMapper and ODM point clouds are similar (slightly higher) to the Pix4D ones, except for the Z-STD value of the ODM point cloud, probably affected by the low point density. In contrast, the elevation statistics of the Metashape point cloud are different from the other point clouds. Specifically, the Z-Min, Z-Max, and Z-Mean values are apparently lower, while the Z-STD value is apparently higher than the other point clouds.

As listed in Table 5.4, the absolute difference between Z-Mean values of the Pix4DMapper and Pix4DCloud point clouds is around 0.6 m, while their differences with the Global Mapper and ODM point clouds are 1.7–1.8 m. The absolute Z-Mean difference between the GlobalMapper and ODM point clouds is about 1.2 m. In contrast, the absolute Z-Mean differences between these point clouds and the Metashape point cloud are much larger, ranging from 3.8 to 4.9 m. The Pearson's correlations between different point clouds are all >0.85 , but the correlation coefficients are higher between Pix4D, GlobalMapper, and ODM point clouds and slightly lower between these point clouds and the Metashape point cloud (Table 5.4).

Figure 5.8 illustrates an example of the tree reconstruction by different software packages. The Metashape and ODM clouds each have a large hole (NoData) in the tree crown area when viewed from above. The Pix4D and GlobalMapper clouds have smaller coverage gaps in the overhead view of the tree crown. The side view of these clouds also shows very different reconstructions in the point vertical distribution. GlobalMapper generates points almost exclusively along the top of the tree, while the Pix4D and Metashape have a more complete vertical distribution with points from the sides and middle of the tree. ODM only reconstructs the tree trunk area, and the tree crown area has been completely missed.

Grassland

The NoData fishnet polygons are negligible for the point clouds of grassland areas. Only the point clouds of Pix4DCloud and ODM have 0.01% of NoData polygons (Fig. 5.9a). The ODM point cloud has the lowest point density, while the GlobalMapper point cloud has the highest and highly varied point density. The point densities of the two Pix4Dpoint clouds are almost identical. The point density

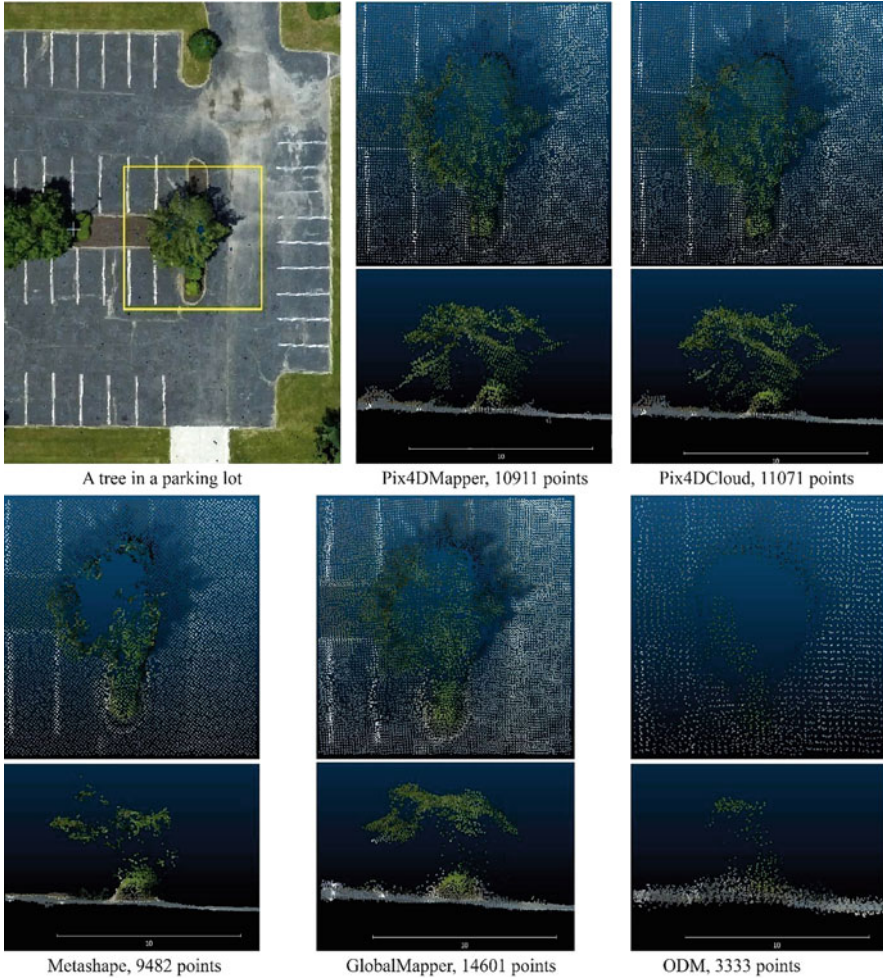


Fig. 5.8 The comparison of point clouds generated using different software packages for a tree in a parking lot. The yellow box in the upper left panel represents the extent of the subset point cloud. The top panel for each point cloud subset is the top view, and the bottom one is the front view

of the Metashape point cloud is similar to the Pix4D ones, but highly clustered (Fig. 5.9b). The Pix4D point clouds have almost identical elevation statistics. The elevation statistics of the GlobalMapper and ODM point clouds are similar (slightly lower) to the Pix4D ones, except for the Z-STD of the ODM point cloud with higher and highly varied values. In contrast, the elevation statistics of the Metashape point cloud are different with much lower Z-Min, Z-Max, and Z-Mean values, but similar Z-STD values (Fig. 5.9c–f).

The absolute Z-Mean difference of the Pix4DMapper and Pix4DCloud point clouds is around 0.11 m, while their differences with the Global Mapper and

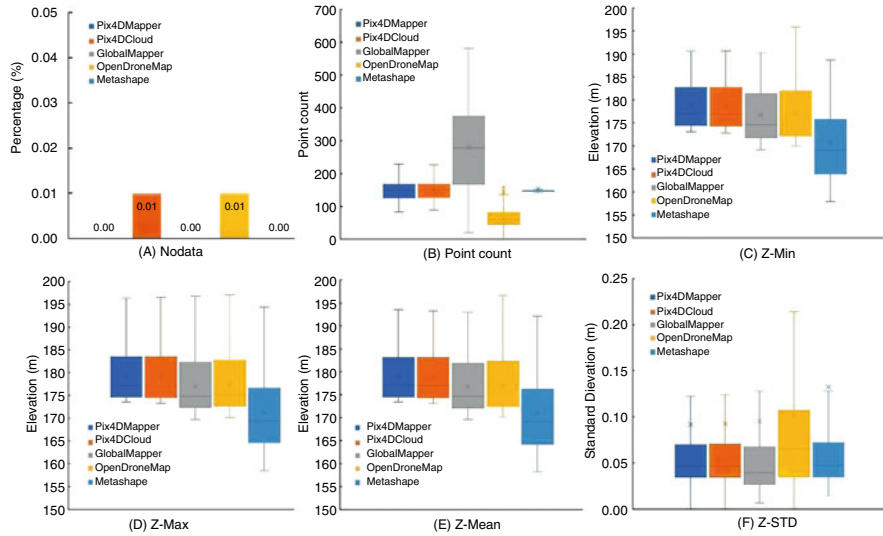


Fig. 5.9 The point cloud statistics of grassland based on the 2×2 m fishnet

Table 5.5 The absolute Z-Mean differences (in meters) and Pearson’s correlations of 2×2 m grassland fishnets between point clouds generated using different software packages

	Pix4DMapper	Pix4DCloud	GlobalMapper	ODM
Pix4DCloud	0.112 ± 0.090 (1.000)			
GlobalMapper	2.139 ± 1.173 (0.992)	2.030 ± 1.107 (0.992)		
ODM	1.761 ± 0.990 (0.994)	1.652 ± 0.918 (0.995)	0.480 ± 0.369 (0.997)	
Metashape	7.991 ± 4.296 (0.921)	7.882 ± 4.232 (0.924)	5.865 ± 3.173 (0.961)	6.270 ± 3.401 (0.948)

ODM point clouds are from 1.65 to 2.14 m (Table 5.5). The absolute Z-Mean difference between the GlobalMapper and ODM point clouds is only about 0.48 m. In contrast, the absolute Z-Mean differences between these point clouds and the Metashape point cloud are much higher, ranging from 5.87 to 7.99 m (Table 5.5). The Pearson’s correlations between different point clouds are all >0.92 , but the correlation coefficients are higher between Pix4D, GlobalMapper, and ODM point clouds (>0.99) and slightly lower between these point clouds and the Metashape point cloud (0.92–0.96, Table 5.5).

Roads

The point clouds of roads have a small percentage of NoData fishnet polygons (Fig. 5.10a). The point clouds produced by Pix4DMapper and Pix4DCloud have about 1.4% NoData fishnet polygons. The GlobalMapper and ODM point clouds have about 4.4% and 4.7% NoData fishnet polygons, respectively. The Metashape

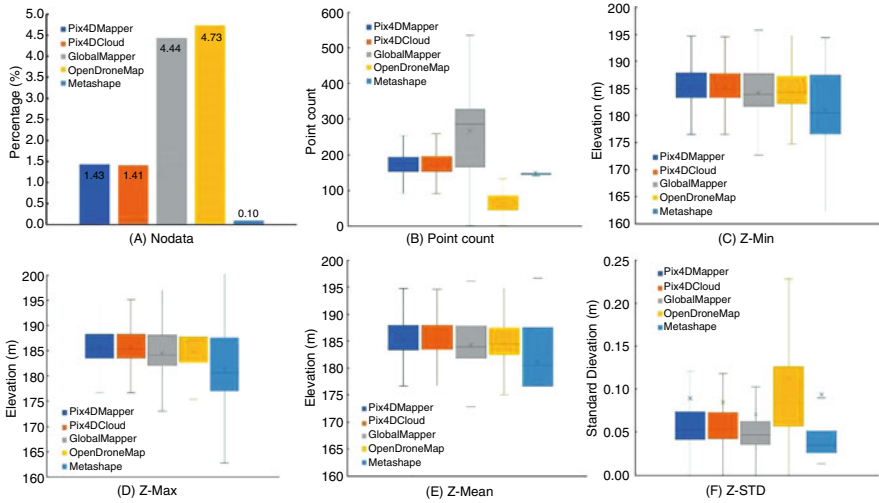


Fig. 5.10 The point cloud statistics of roads based on the 2×2 m fishnet

Table 5.6 The absolute Z-Mean differences (in meters) and Pearson’s correlations of 2×2 m road fishnets between point clouds generated using different software packages

	Pix4DMapper	Pix4DCloud	GlobalMapper	ODM
Pix4DCloud	0.047 ± 0.149 (0.999)			
GlobalMapper	1.135 ± 1.079 (0.986)	1.144 ± 1.071 (0.986)		
ODM	0.803 ± 0.749 (0.989)	0.797 ± 0.742 (0.989)	0.697 ± 0.442 (0.993)	
Metashape	4.286 ± 4.157 (0.881)	4.278 ± 4.155 (0.882)	3.204 ± 2.962 (0.945)	3.542 ± 3.523 (0.916)

point cloud has the lowest percentage of NoData fishnet polygons (0.1%). The ODM point cloud has the lowest point density, while the GlobalMapper point cloud has the highest but highly varied point density. The point densities of the two Pix4Dpoint clouds are almost identical. The point density of the Metashape point cloud is slightly lower than the Pix4D ones, but highly clustered (Fig. 5.10b). The Pix4D point clouds have almost identical elevation statistics. The elevation statistics of the GlobalMapper and ODM point clouds are similar (slightly lower) to the Pix4D ones, except for the Z-STD of the ODM point cloud with higher and highly varied values. In contrast, the elevation statistics of the Metashape point cloud are different with much lower Z-Min, Z-Max, and Z-Mean values, but similar Z-STD values (Fig. 5.10c-f).

The absolute Z-Mean difference of the Pix4DMapper and Pix4DCloud point clouds is around 0.05 m, while their differences with the Global Mapper and ODM point clouds are around 1.14 and 0.80 m, respectively (Table 5.6). The

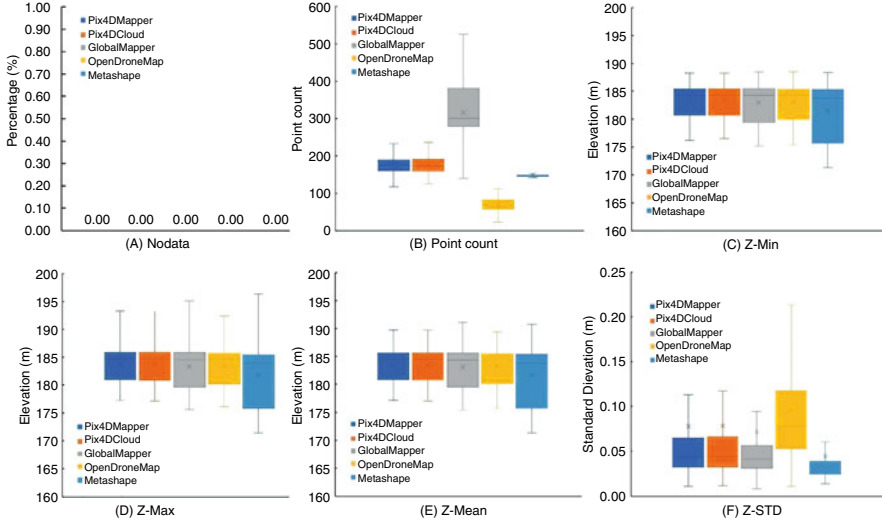


Fig. 5.11 The point cloud statistics of parking lots based on the 2 × 2 m fishnet

absolute Z-Mean difference between the GlobalMapper and ODM point clouds is about 0.70 m. In contrast, the absolute Z-Mean differences between these point clouds and the Metashape point cloud are much higher, ranging from 3.20 to 4.29 m (Table 5.6). The Pearson’s correlations between different point clouds are all >0.88, but the correlations are higher between Pix4D, GlobalMapper, and ODM point clouds (>0.98) and slightly lower between these point clouds and the Metashape point cloud (0.88–0.95, Table 5.6).

Parking Lots

As expected, most statistical plots for parking lots (Fig. 5.11) are similar to the plots of roads (Fig. 5.10) because both features represent hard and relatively flat ground surfaces. The only difference is that no fishnet polygons for parking lots are empty NoData polygons (Fig. 5.11a). The point clouds produced by Pix4DMapper and Pix4DCloud are almost identical for all statistics. GlobalMapper produced the highest point density, while ODM generated the lowest point density (Fig. 5.11b). The elevation statistics of GlobalMapper and ODM point clouds are similar (slightly lower) to the Pix4D ones, except the Z-STD of the ODM point cloud with much higher and highly varied values. The Metashape point cloud has relatively lower values for all elevation related statistics (Fig. 5.11c–f).

Table 5.7 shows very small absolute Z-Mean difference between the Pix4DMapper and Pix4DCloud point clouds (0.03 m), similar to the registration error of these two point clouds. The differences between the Pix4D point clouds and the GlobalMapper and ODM point clouds are around 0.50–0.51 and 0.33–0.35 m, respectively (Table 5.8). The absolute Z-Mean difference between the GlobalMapper and ODM point clouds is about 0.32 m. The absolute Z-Mean

Table 5.7 The absolute Z-Mean differences (in meters) and Pearson’s correlations of 2×2 m parking lots fishnets between point clouds generated using different software packages

	Pix4DMapper	Pix4DCloud	GlobalMapper	ODM
Pix4DCloud	0.027 ± 0.056 (1.000)			
GlobalMapper	0.510 ± 0.576 (0.998)	0.504 ± 0.555 (0.998)		
ODM	0.346 ± 0.324 (0.998)	0.330 ± 0.310 (0.998)	0.319 ± 0.230 (0.998)	
Metashape	1.924 ± 2.189 (0.977)	1.916 ± 2.173 (0.977)	1.491 ± 1.578 (0.988)	1.731 ± 1.802 (0.981)

Table 5.8 The absolute Z-Mean differences (in meters) and Pearson’s correlations of 2×2 m buildings fishnets between point clouds generated using different software packages

	Pix4DMapper	Pix4DCloud	GlobalMapper	ODM
Pix4DCloud	0.064 ± 0.099 (1.000)			
GlobalMapper	0.925 ± 0.766 (0.988)	0.915 ± 0.758 (0.988)		
ODM	0.684 ± 0.614 (0.988)	0.667 ± 0.604 (0.989)	0.556 ± 0.497 (0.993)	
Metashape	3.792 ± 4.025 (0.880)	3.791 ± 4.013 (0.881)	3.218 ± 3.151 (0.934)	3.464 ± 3.555 (0.909)

differences between these point clouds and the Metashape point cloud are from 1.49 to 1.92 m (Table 5.7). All Pearson’s correlations between different point clouds are >0.97 with slightly higher correlations between Pix4D, GlobalMapper, and ODM point clouds (0.998, Table 5.7).

Figure 5.12 shows the colored point clouds as rendered in CloudCompare for a section of parking lot with painted traffic arrows. The points in this section are 2516 for GlobalMapper, 1049–1066 for Pix4DMapper and Pix4DCloud, 899 for Metashape, and 547 for ODM, respectively. The appearance of the arrows varies greatly between the clouds. Both Pix4D clouds and GlobalMapper clouds show shapes that are instantly recognizable as arrows. GlobalMapper generated about 2.5 times more points than the Pix4D ones, but the arrow edges are not as sharp as the Pix4D ones. Metashape produced about 15% fewer points than the Pix4D ones, but the arrow edges appear substantially less sharp. It is hard to identify these arrows from the ODM cloud due to the low point density. It seems that Pix4D point clouds preserve the sharpness of the edges well and retain the most contrast between the asphalt and paint color even with relatively less points than GlobalMapper.

Buildings

The point clouds of buildings (including condos, single family houses, schools, and hospitals) have negligible NoData fishnet polygons, ranging from 0.02 to 0.25% (Fig. 5.13a). The point cloud produced by Pix4DCloud has the smallest percentage (0.02%) of NoData fishnet polygons, whereas the ODM point cloud has the highest

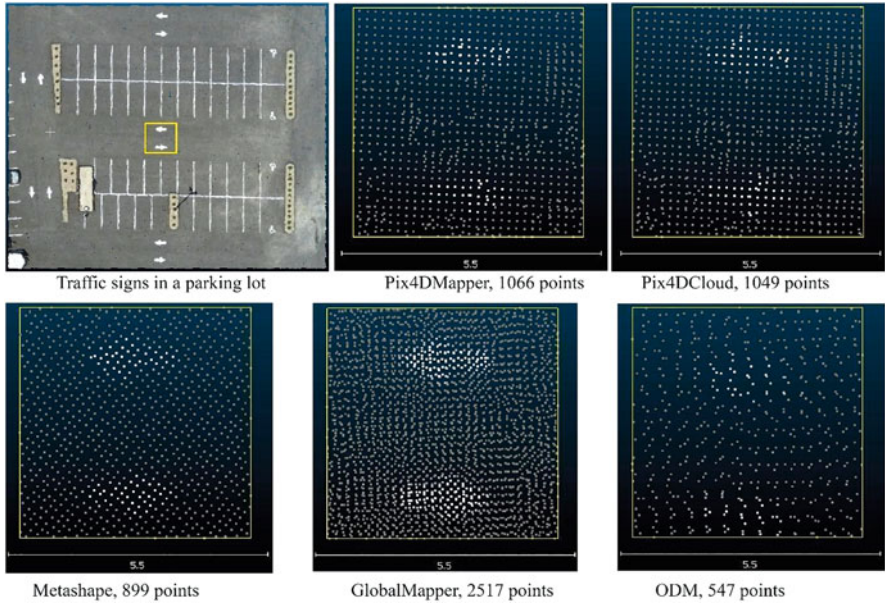


Fig. 5.12 The comparison of point clouds generated using different software packages for the traffic signs in a parking lot. The yellow box in the upper left panel represents the extent of the subset point cloud. All point cloud subsets are the top (nadir) view

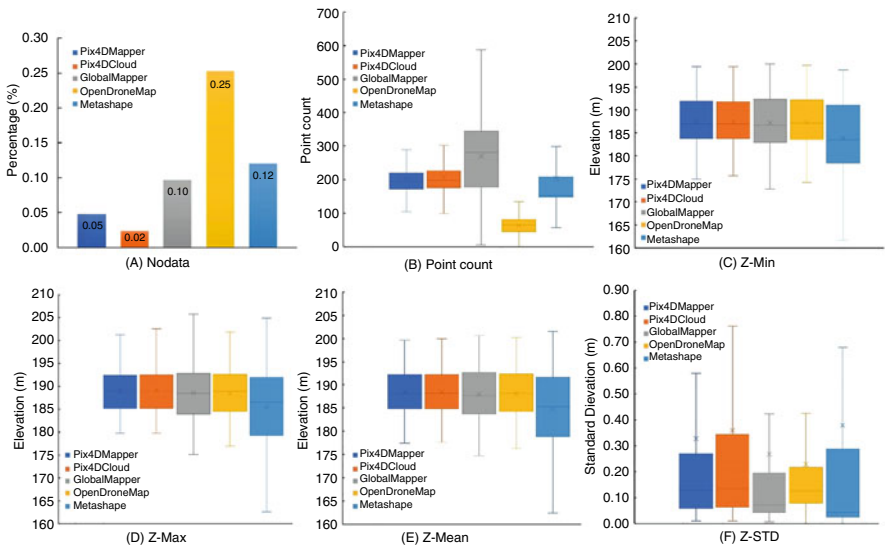


Fig. 5.13 The point cloud statistics of buildings based on the 2×2 m fishnet

percentage (0.25%). The ODM point cloud has the lowest point density, while the GlobalMapper point cloud has the highest but highly varied point density. The point densities of the two Pix4D point clouds are similar. The point density of the Metashape point cloud is slightly lower than the Pix4D ones (Fig. 5.13b). The Pix4D point clouds have almost identical elevation statistics. The elevation statistics of the GlobalMapper and ODM point clouds are similar to the Pix4D ones. The elevation statistics of the Metashape point cloud are lower than the other point clouds (Fig. 5.13c–f).

The absolute Z-Mean difference of the Pix4DMapper and Pix4DCloud point clouds is around 0.06 m, while their differences with the GlobalMapper and ODM point clouds are 0.92–0.93 and 0.67–0.68 m, respectively (Table 5.8). The absolute Z-Mean difference between the GlobalMapper and ODM point clouds is about 0.56 m. In contrast, the absolute Z-Mean differences between these point clouds and the Metashape point cloud are much higher, ranging from 3.22 to 3.79 m (Table 5.8). All Pearson's correlations between different point clouds are >0.88 with slightly higher correlations between Pix4D, GlobalMapper, and ODM point clouds (>0.98 , Table 5.8).

Figure 5.14 shows an example of the point cloud reconstructions for a single-family house. Each software package is able to create a general 3D pitched roof shape with few substantial gaps in data. Even the relatively low-density cloud generated by ODM can capture the general shape of the roof. This example also demonstrates that although GlobalMapper generates the most points, the side view of the cloud shows that more points do not visually lead to a more accurate representation of the house. Both Pix4D and Metashape were better in creating the sharp angles and straight lines than the overly smoothed shape in the GlobalMapper cloud. The Pix4D products appear to be best suited to reconstructing the angles and lines of the roof shape, but the fewer points on the side walls leave a less complete structure than Metashape, which created smoother angles but greater wall coverage.

5.4.3 Comparison with the 1-m LiDAR DEM

Figure 5.15 illustrates the linear regression results between the Z-Min values of the fishnet polygons from the parking lots and roads and their corresponding elevations extracted from the 1-m LiDAR DEM. All linear regressions were adjusted to a fixed slope of 1. Although all elevations interpreted by the SfM technology are 6.70–9.65 m higher than the 1-m LiDAR DEM, the R^2 values of the linear regressions are high (>0.78). The vertical offsets are likely caused by the uncertainty of the internal drone GPS measurement, as well as the potential inclusion of non-ground points within the SfM-reconstructed parking lots and roads. The regression coefficients suggested that the elevations of the Pix4D generated point clouds have the highest consistency ($R^2 = 0.998$) with the 1-m LiDAR DEM after removing the vertical offset. The regression coefficients between the point clouds generated from

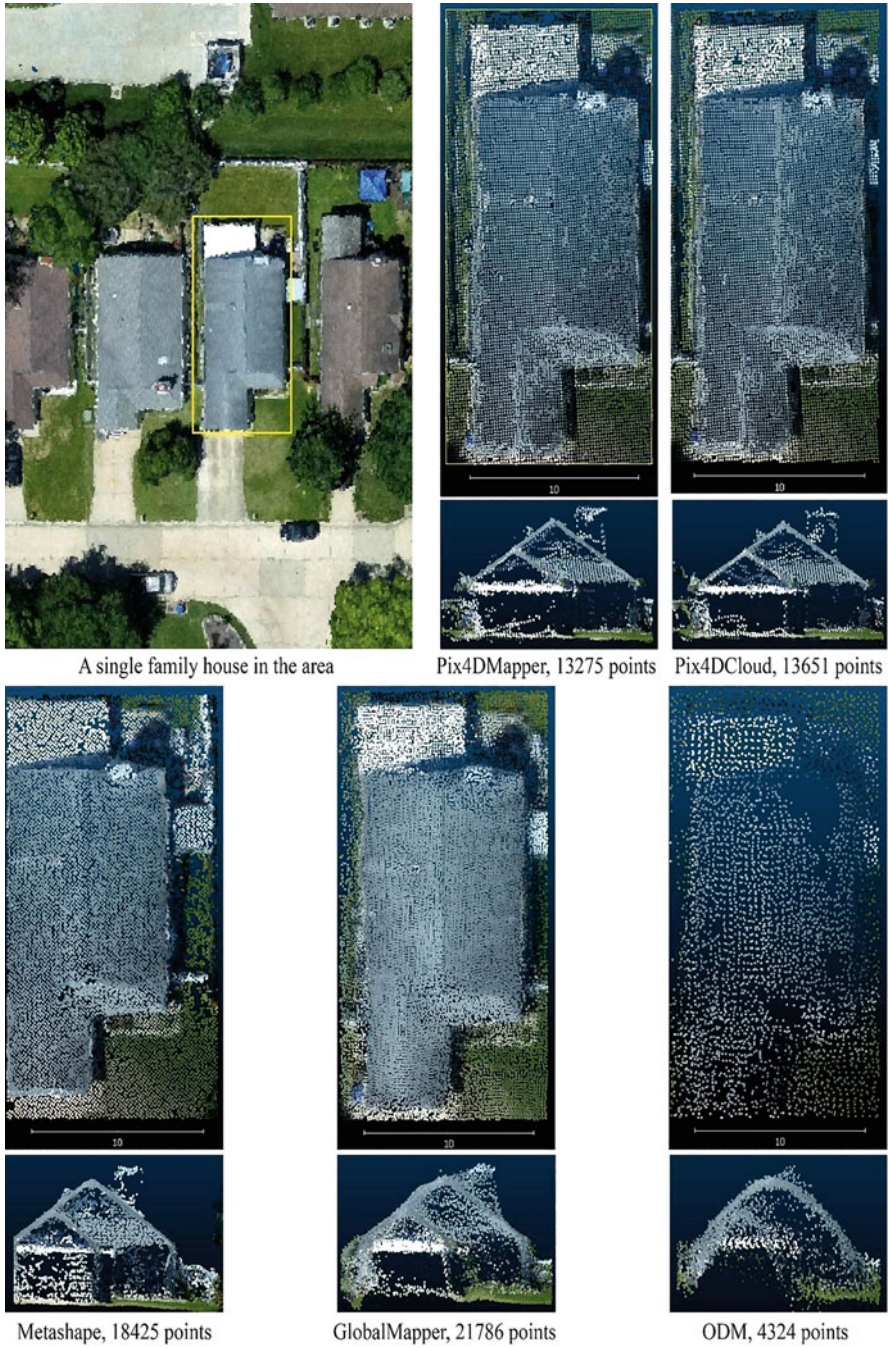


Fig. 5.14 The comparison of point clouds generated using different software packages for a single-family house. The yellow box in the upper left panel represents the extent of the subset point cloud. The top panel for each point cloud subset is the top view, and the bottom one is the front view

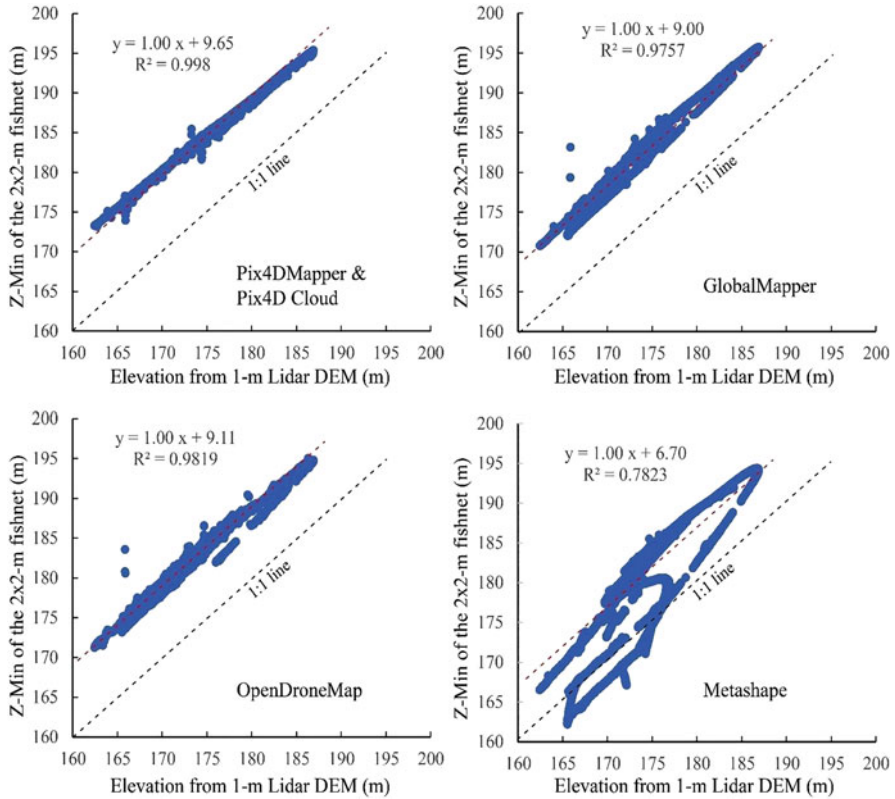


Fig. 5.15 The comparison of ground elevation (Z-Min in the 2×2 m fishnet) of each point cloud and 1-m LiDAR DEM

GlobalMapper and ODM and the 1-m LiDAR DEM are similar (R^2 of 0.976 and 0.982) with similar offsets of 9.00 and 9.11 m, respectively. The worst regression comes from the point cloud generated using Metashape (R^2 of 0.782, offset of 6.70 m). We also tested Z-Mean, showing similar results.

5.5 Discussion

5.5.1 Uncertainties Caused by Point Cloud Registration

This study compared the differences in the point clouds generated using Pix4DMapper, Pix4DCloud, GlobalMapper, ODM, and Metashape. The differences between the point clouds are likely caused by the varied SfM algorithms and default

parameter settings of these software packages. However, some differences may also be resulted from the registration errors between the point clouds. As we mentioned earlier, we used the point cloud generated using Pix4DMapper as the reference and the best registration that we can achieve range from 0.02 m to 0.20 m (RMSE values) for different point clouds. The registration is affected by the density and quality of each point cloud, as well as the control points that we chose for the registration. To mitigate the impact of registration error, we used the 2 m by 2 m fishnet polygons (10 times larger than the largest RMSE value) as the unit to compare the difference between point clouds.

The smallest registration error of 0.02 m comes from the point clouds generated using the Pix4DMapper and Pix4DCloud. It is understandable because these two point clouds were generated using the same software package (algorithm), just with different versions or computational settings. If assuming these two point clouds are basically the same on the “hard” surface areas, including roads, parking lots, and buildings, the differences between these two point clouds on these areas can be treated as the errors mainly caused by the misalignment (shift and rotation) of the point clouds during the registration. Our results indicate that the differences between these two point clouds in the 2 m by 2 m fishnet polygons are from 0.03 to 0.06 m on these areas (Tables 5.5–5.8), indicating that the impact of registration errors is likely within three times of the RMSE values. If this is the case, we can estimate that the differences caused by the registration error are likely within 0.23 m for the GlobalMapper point cloud (RMSE = 0.076 m), 0.80 m for the ODM point cloud (RMSE = 0.267 m), and 0.57 m for the Metashape point cloud (RMSE = 0.189 m). Based on these estimates, it is interesting that the ODM point cloud is close to the Pix4D point clouds on “hard” surfaces (0.3–0.8 m differences between the two point clouds, Tables 5.6, 5.7 and 5.8) although the point density of the ODM point cloud is much lower. The GlobalMapper point cloud is slightly different from the Pix4D point clouds (0.5–1.1 m differences, Tables 5.5–5.8), while the difference between the Metashape point cloud and Pix4D point clouds (1.5–4.3 m differences, Tables 5.5–5.8), as well as the point clouds produced by GlobalMapper and ODM, is significant.

5.5.2 Difference in Land Feature Reconstruction

Our comparison indicates that the point cloud differences in “hard” surfaces are smaller than that in vegetations (trees and grassland), except for the Metashape point cloud. This is probably because the “hard” features have relatively regular surfaces (flat or straight sloped) and the SfM can easily identify and match the keypoints during the reconstruction. Among these “hard” surfaces, parking lots have the smallest difference and zero NoData fishnet polygons. This is likely caused by the relatively low reflective surface (asphalt), plenty of markers (parking lot lines and traffic signs), and wide coverage. The low reflective surface and markers increase the

contrast of the photos and help identify and match the keypoints, while the wide coverage minimizes the impact of the registration errors in the point cloud comparison. Other “hard” surfaces, including roads and buildings, have relatively larger differences than the parking lots. One potential reason is because the digitized individual buildings or roads have relative smaller or narrow coverage, so that they are more vulnerable to the impact of registration errors. In addition, some of these surfaces may be highly reflective, such as some sections of roads, and lack identifiable markers for the SfM reconstruction to identify key matching points, leading to the appearance of NoData fishnet polygons.

Compared to the hard surfaces, the differences in the point clouds of trees/forest and grassland are much larger. The SfM reconstruction of an irregular, complex shape, such as trees, is challenging because it is difficult to identify key matching points from the leaves and from leaf movement due to the wind. For example, the percentages of NoData fishnet polygons are much higher in trees/forest, likely caused by the keypoint matching and leaf movement issues. The percentages of NoData fishnet polygons in grassland are negligible because grass is short and close to the ground and the impact of leaf movement or matching issues is minor.

5.5.3 Do More Points Represent a Better Reconstruction for a Land Feature?

The point densities reconstructed using Pix4DMapper, Pix4DCloud, GlobalMapper, ODM, and Metashape are different for our digitized land features. As expected, the ODM point cloud produced the lowest density because the default setting of ODM uses a reduced resolution (2048 pixels) of the images for the SfM reconstruction, and the point clouds reconstructed using Pix4DMapper and Pix4DCloud have similar point density for different land features. For the point clouds generated using GlobalMapper and Metashape, it is interesting that GlobalMapper consistently produces higher point densities for “hard” surface features and grassland than the Pix4D point clouds and lower point densities for trees/forest. This may also explain why GlobalMapper produced such a higher overall density of points in site A compared to the sites with fewer man-made features (Table 5.3). In contrast, the Metashape produces higher point density for trees/forest, but lower densities for other land features than the Pix4D point clouds.

Would this mean that high point density represents a better reconstruction for the land feature? As illustrated in Figs. 5.8, 5.12, and 5.14 earlier, more points do not necessarily represent a better reconstruction of land features. It seems that Pix4D-produced point clouds tend to have a better preservation of the edges, angles, and shapes, as well as the contrast between colors, while GlobalMapper tends to produce a smooth surface and Metashape may have an advantage in reconstructing parts of vertical man-made features.

5.5.4 *Ground Truth Calibration*

The comparison of the SfM-reconstructed ground elevation and 1-m LiDAR DEM (Fig. 5.15) suggests a large difference exists between Metashape-reconstructed ground surfaces and the surfaces reconstructed by other software packages. After removing the vertical shift, it seems that the Pix4D point clouds have the best reconstruction of the ground elevations in our study area. GlobalMapper and ODM produce good correlations. In contrast, the ground elevations reconstructed by Metashape are not fully consistent with the 1-m LiDAR DEM. Note that our observations are only from this specific site; more work is needed to examine if it is the case for other types of landscapes.

The differences between these software packages in reconstructing ground elevations do stress the need to include ground truth calibration, such as the use of ground targets with differential GPS measurements and the comparison with the airborne LiDAR or terrestrial LiDAR measurements, in work related to the SfM reconstruction. It is important to verify the quality of the point clouds generated using different software packages and select the best product for further analysis.

5.6 Conclusions

In this study, we investigated the impacts of various SfM software packages, including Pix4DMapper, Pix4DCloud, GlobalMapper, ODM, and Metashape, on land feature reconstruction based on the comparison of point clouds generated using the software default parameters. Our results indicate that when given identical image sets, these software packages produce markedly different point clouds and that these variations may be amplified by certain types of land features. The differences on “hard” surfaces, such as parking lots, roads, and buildings, are smaller than vegetated surfaces, especially trees/forest, except for the Metashape point cloud. High point density does not necessarily signal better quality reconstruction. It seems that Pix4D-produced point clouds have a better preservation of the edges, angles, and shapes, as well as the contrast between colors, while GlobalMapper tends to smooth the surface and Metashape may have an advantage in reconstructing parts of vertical man-made features. The large differences between Metashape point cloud and other point clouds cannot be simply explained by registration errors. The comparison between the ground elevations derived from point clouds with the 1-m LiDAR DEM also indicates a relatively poor ground reconstruction by Metashape and relatively consistent reconstructions by other software packages. Although open-source ODM produced the lowest density point cloud, it is broadly consistent with the point clouds generated using other commercial software, except Metashape. We acknowledge that our observations are only from one specific suburban neighborhood and more work is needed to examine if the findings from this site are consistent on other types of landscapes. Nonetheless, the potential inconsistency between the

SfM-derived ground elevations and the LiDAR DEM stresses the need of ground truth calibration and vegetation filtering in SfM-related feature reconstruction. This study provides useful insights into the use of sUAS and SfM to reconstruct natural and man-made land features.

Several limitations exist in this study. First, it is essential to improve the registration between point clouds. In our study, after trying different techniques, we used simple point picking to register the point clouds. Future work may use additional ground targets or advanced methods, for example, the ICP method, to improve the registration. Second, we only investigated five land features that are typical in the suburban areas. More work is needed to explore the land features in other environments. Finally, this work only investigated the default parameters of the software packages. It is also worthwhile to examine the impacts of different parameters of these packages, including methods requiring additional intervention, such as georeferenced ground control points and manually identified keypoints, as well as other available processing options, on the quality of land feature reconstruction.

Acknowledgments This research was supported by an EPA Small Urban Grant (UW-00D45316) and two teaching innovation grants in supporting the use of UAS in teaching and training at the University of Tennessee. We thank Meghan Russell, Kristina Cairns, and Ming Shen for the support in data processing. We would like to thank two anonymous reviewers for their constructive comments and suggestions to improve the chapter.

References

- Agisoft LLC (2021) Agisoft Metashape User Manual Professional Edition, Version 1.7. https://www.agisoft.com/pdf/metashape-pro_1_7_en.pdf
- Besl PJ, McKay ND (1992) A method for registration of 3-D shapes. *IEEE Trans Pattern Anal Mach Intell* 14(2):239–256. <https://doi.org/10.1109/34.121791>
- Blue Marble Geographics (n.d.) Pixels to points tool documentation. Accessed 27 Mar 2021. https://www.bluemarblegeo.com/knowledgebase/global-mapper-21/Image_to_Point_Cloud.htm
- Carr S, Douglas B, Crosby C (2013) *Terrestrial laser scanning (TLS) field camp manual*. Boulder, CO
- Cavalli M, Tarolli P, Marchi L, Fontana GD (2008) The effectiveness of airborne LiDAR data in the recognition of channel-bed morphology. *Catena* 73(3):249–260. <https://doi.org/10.1016/j.catena.2007.11.001>
- Cook KL (2017) An evaluation of the effectiveness of low-cost UAVs and structure from motion for geomorphic change detection. *Geomorphology* 278(February):195–208. <https://doi.org/10.1016/j.geomorph.2016.11.009>
- Eltner A, Schneider D (2015) Analysis of different methods for 3D reconstruction of natural surfaces from parallel-axes UAV images. *Photogramm Rec* 30(151):279–299. <https://doi.org/10.1111/phor.12115>
- Eltner A, Baumgart P, Maas HG, Faust D (2015) Multi-temporal UAV data for automatic measurement of rill and interrill erosion on loess soil. *Earth Surf Process Landf* 40(6):741–755. <https://doi.org/10.1002/esp.3673>
- Eltner A, Kaiser A, Castillo C, Rock G, Neugirg F, Abellán A (2016) Image-based surface reconstruction in geomorphometry – merits, limits and developments. *Earth Surf Dyn* 4(2): 359–389. <https://doi.org/10.5194/esurf-4-359-2016>

- Fonstad MA, Dietrich JT, Courville BC, Jensen JL, Carbonneau PE (2013) Topographic structure from motion: a new development in photogrammetric measurement. *Earth Surf Process Landf* 38(4):421–430. <https://doi.org/10.1002/esp.3366>
- Heritage G, Hetherington D (2007) Towards a protocol for laser scanning in fluvial geomorphology. *Earth Surf Process Landf* 32(1):66–74. <https://doi.org/10.1002/esp.1375>
- Hiep VH, Keriven R, Labatut P, Pons JP (2010) Towards high-resolution large-scale multi-view stereo. *Institute of Electrical and Electronics Engineers (IEEE)*, pp 1430–1437. <https://doi.org/10.1109/cvpr.2009.5206617>
- Hohenthal J, Alho P, Hyypää J, Hyypää H (2011) Laser scanning applications in fluvial studies. *Prog Phys Geogr: Earth Environ* 35(6):782–809. <https://doi.org/10.1177/0309133311414605>
- Javernick L, Brasington J, Caruso B (2014) Modeling the topography of shallow braided Rivers using structure-from-motion photogrammetry. *Geomorphology* 213(May):166–182. <https://doi.org/10.1016/j.geomorph.2014.01.006>
- Kaiser A, Erhardt A, Eltner A (2018) Addressing uncertainties in interpreting soil surface changes by multitemporal high-resolution topography data across scales. *Land Degrad Dev* 29(8): 2264–2277. <https://doi.org/10.1002/ldr.2967>
- Li H, Gao J, Hu Q, Li Y, Tian J, Liao C, Ma W, Xu Y (2019) Assessing revegetation effectiveness on an extremely degraded grassland, southern Qinghai-Tibetan plateau, using terrestrial LiDAR and field data. *Agric Ecosyst Environ* 282(October):13–22. <https://doi.org/10.1016/j.agee.2019.05.013>
- Li Y, McNelis JJ, Washington-Allen RA (2020) Quantifying short-term erosion and deposition in an active gully using terrestrial laser scanning: a case study from West Tennessee, USA. *Front Earth Sci* 8(October). <https://doi.org/10.3389/feart.2020.587999>
- Lu X, Li Y, Washington-Allen RA, Li Y (2019) Structural and sedimentological connectivity on a Rilled hillslope. *Sci Total Environ* 655(March):1479–1494. <https://doi.org/10.1016/j.scitotenv.2018.11.137>
- Nouwakpo SK, Weltz MA, McGwire K (2016) Assessing the performance of structure-from-motion photogrammetry and terrestrial LiDAR for reconstructing soil surface microtopography of naturally vegetated plots. *Earth Surf Process Landf* 41(3):308–322. <https://doi.org/10.1002/esp.3787>
- OpenDroneMap (2020) OpenDroneMap 2.4.7 Documentation. 2020. <https://docs.opendronemap.org/>
- Ouédraogo MM, Degré A, Debouche C, Lisein J (2014) The evaluation of unmanned aerial system-based photogrammetry and terrestrial laser scanning to generate DEMs of agricultural watersheds. *Geomorphology* 214(June):339–355. <https://doi.org/10.1016/j.geomorph.2014.02.016>
- Perroy RL, Bookhagen B, Asner GP, Chadwick OA (2010) Comparison of gully erosion estimates using airborne and ground-based LiDAR on Santa Cruz Island, California. *Geomorphology* 118(3–4):288–300. <https://doi.org/10.1016/j.geomorph.2010.01.009>
- Pix4D SA (2017) Offline Getting Started and Manual (Pdf) – Support. 2017. <https://support.pix4d.com/hc/en-us/articles/204272989-Offline-Getting-Started-and-Manual-pdf>
- Smith MW, Carrivick JL, Quincey DJ (2016) Structure from motion photogrammetry in physical geography. *Prog Phys Geogr: Earth Environ* 40(2):247–275. <https://doi.org/10.1177/0309133315615805>
- Strecha C, Tuytelaars T, Gool LV (2003) Dense matching of multiple wide-baseline views. In: *Proceedings of the IEEE International Conference on Computer Vision*, vol 2. Institute of Electrical and Electronics Engineers Inc, pp 1194–1201. <https://doi.org/10.1109/icc.2003.1238627>
- Tarolli P (2014) High-resolution topography for understanding earth surface processes: opportunities and challenges. *Geomorphology* Elsevier. <https://doi.org/10.1016/j.geomorph.2014.03.008>
- Tian J, Li H, Li Y, Liao C, Ma W, Xu Y (2021) Feasibility of terrestrial laser scanning for quantification of vegetation structure parameters of restored Sandy land in the southern Qinghai-Tibetan plateau. *Land Degrad Dev* 32(4):1667–1679. <https://doi.org/10.1002/ldr.3784>

Chapter 6

Assessing the Role of sUAS Mission Design in the Accuracy of Digital Surface Models Derived from Structure-from-Motion Photogrammetry



Daniel S. Hostens, Toby Dogwiler, Joshua W. Hess, Robert T. Pavlowsky, Jacob Bendix, and Derek T. Martin

Abstract The mission design used to acquire imagery with small unmanned aerial systems (sUAS) incorporates decisions that determine the quality and accuracy of derived products. This study assesses the influence of sUAS mission design strategies on the accuracy of the resulting digital surface models and orthophotography in order to determine an optimal approach to image acquisition. Imagery was collected in the spring of 2018 during leaf-off conditions at six field sites along the North Fork of the White River in south-central Missouri. The aerial imagery was collected using a DJI Phantom Pro 4 sUAS. Four different mission designs were tested at each of the sites. Each of these designs yielded a set of base mission imagery. Each of these base mission datasets was processed individually and in various combinations using the structure-from-motion photogrammetry (SfM) software Agisoft Metashape to produce digital surface models (DSMs). Fifty-four resulting DSMs derived from those datasets were assessed based on their ability to accurately interpolate the planimetric and vertical coordinates of GNSS-surveyed check points (CPs). Simpler base mission designs with 80% image overlap yielded equal or better DSM accuracy than more complex mission designs. Additionally, slightly oblique imagery (20 ° above

D. S. Hostens · T. Dogwiler (✉)

Department of Geography, Geology, and Planning, Missouri State University, Springfield, MO, USA

e-mail: Shay93@live.missouristate.edu; tdogwiler@missouristate.edu

J. W. Hess · R. T. Pavlowsky

Ozarks Environmental Water Resources Institute, Department of Geography, Geology, and Planning, Missouri State University, Springfield, MO, USA

e-mail: Joshua16@live.missouristate.edu; BobPavlowsky@MissouriState.edu

J. Bendix

Department of Geography and the Environment, Syracuse University, Syracuse, NY, USA

e-mail: jbendix@maxwell.syr.edu

D. T. Martin

Department of Geography and Planning, Appalachian State University, Boone, NC, USA

e-mail: martindj1@apstate.edu

nadir) provided a small additional advantage in terms of accuracy. The simpler base mission datasets also provided advantages during SfM processing. With fewer images, the time required during both field work and data processing was reduced significantly.

Keywords sUAS · Digital surface models · Structure from motion · sUAS mission design · Photogrammetry

6.1 Introduction

One of the advantages of small unmanned aerial systems (sUAS) is the ability to acquire on-demand imagery quickly and inexpensively. Such imagery can be processed with structure-from-motion photogrammetry (SfM) to create digital surface models (DSMs) and orthorectified imagery. These *just in time* products can facilitate change detection over time and rapid assessments in the wake of extreme events and sudden natural hazards. Using sUAS platforms for SfM photogrammetry has become standard practice in a wide range of geomorphic applications (Wheaton et al. 2010; James and Robson 2012; James and Varley 2012; Fonstad et al. 2013; Bemis et al. 2014; Javernick et al. 2014; Woodget et al. 2015; Eltner et al. 2016). The growth in usage of sUAS-based SfM photogrammetry can be attributed to the affordability of sUAS hardware and SfM software, the development of mission planning software that optimizes field-based data acquisition, and the ability for SfM methods to generate 3D spatial data with comparable accuracies and densities to that of modern terrestrial laser scanners (Carrivick et al. 2016). SfM photogrammetry also benefits from the ability to be used at a wide range of scales. Studies have applied this method to cm-scale rock hand sample analysis (James and Robson 2012) up to multiple kilometers for fluvial studies (Dietrich 2016) and active lava dome analysis (James and Varley 2012).

sUAS mission planning and autonomous flight software facilitates the design of repeatable acquisition missions with precise control over flight pattern, camera angle, and image overlap. The primary objective of this study is to ascertain which mission designs optimize the quality and accuracy of the resulting three-dimensional SfM products. Because of the ease of image acquisition with sUAS and a lack of scientific literature exploring best practices in mission design, our experience indicates that many sUAS projects err on the side of obtaining excessive quantities of images to ensure a suitable final product, such as an SfM-derived DSM or orthoimage. The over-collection of images results in inefficiencies in both the field and SfM processing phases of sUAS-based studies. Furthermore, excessive imagery does not equate to more accurate SfM products and, in some cases, can reduce the quality of the products. The extra imagery also increases the burden of storing and archiving sUAS imagery and datasets. As such, important questions remain about optimal mission design strategies involving the variables described above in relation to the quality and accuracy of the final SfM products. Relatively little investigation has focused on these questions, especially in the rugged terrain of moderate relief

and densely forested landscape as is typically found in the Ozarks physiogeographic region of southern Missouri and northern Arkansas in the midcontinental USA.

Achieving an accurate result from a sUAS-based SfM photogrammetric survey is dependent upon a wide range of variables. Some of these, such as image overlap, flight path orientation, camera angle, flying height, and ground control point (GCP) quantity and placement, are under the control of the sUAS user. Other factors such as the terrain, vegetation, and, in some cases, weather conditions are inherent characteristics of the study area. There have been a variety of publications reviewing the methods of using sUAS to collect imagery for SfM (e.g., Fonstad et al. 2013; Gonçalves and Henriques 2015), but many questions about how best to optimize the variables listed above remain unresolved. This study uses sUAS-acquired imagery from the North Fork of the White River within the Mark Twain National Forest in south-central Missouri to explore how various sUAS mission designs, and their associated choices regarding these variables, influence the quality and accuracy of the derived SfM products.

6.1.1 Mission Planning and Autonomous Flight Control

The variables over which the sUAS user can control over are generally set within mission planning software and executed by an autopilot system (most sUAS mission planning and autopilot software are integrated). These software packages are generally run on a tablet computing device that is connected to the sUAS, usually via the remote controller. The ability to precisely control image overlap, flight path, camera angle, and flying height via mission design software was a critical step in the evolution of sUAS as scientific instruments. Employing mission design software to program sUAS data acquisition makes the process reproducible to a level not possible via manual flight of the sUAS.

Flight and mission planning normally occurs prior to field work. Careful planning of aircraft trajectory, such as waypoints, flight pattern, speed, and altitude along with real-time mission management, is important for achieving successful and repeatable missions (Colomina and Molina 2014). Autonomous flights are designed and controlled through a ground control station. The GNSS/INS on the sUAS is used to guide image acquisition at specified waypoints along the flight path (Remondino et al. 2011). The flight plan designed dictates the specific amount of longitudinal and transversal overlap of images acquired during the flight (Remondino et al. 2011), which is ideally optimized based on the requirements for the desired SfM products.

An important aspect of planning an ideal mission design is understanding the effect of those design decisions on the accuracy of the final SfM products as well as the repercussions those decisions have on the required time investment to gather and process the data. The importance of the variables typically defined within mission planning software is well documented in the literature (e.g., Mancini et al. 2013; Rossi et al. 2017; Sanz-Ablanedo et al. 2020). Altitude has the most significant effect on the quality of imagery and SfM products, but others such as imagery overlap and

camera angle also affect the accuracy of the resulting products (Rock et al. 2011). Efficient mission designs will yield SfM products, such as DEMs and orthophotos, with high accuracy without any unnecessary time invested in the collection of excess imagery and ground control as well as during data processing stages.

6.1.1.1 Altitude

The required ground sample distance (GSD) will be a determining factor in choosing a flight altitude. Higher altitudes result in higher GSDs and lower-resolution SfM products. The GSD refers to the distance between pixel centers as measured on the ground. As such, the GSD of sUAS-acquired imagery is a function of imaging sensor resolution (e.g., as measured in megapixels), camera focal length, and flight altitude. The same imaging sensor will yield lower resolution imagery when it is flown at a higher altitude above the ground level. As the area of a field site increases, it is often necessary to decrease the resolution of the acquired imagery and derived products in order to keep acquisition and processing times feasible. Choosing an appropriate resolution for a sUAS-based SfM project often involves a cost and benefit analysis that optimizes the balance between planned project GSD, field site size, and the objectives of the study. As such, larger study areas are often surveyed at lower GSDs with a linear degradation of precision and a similar effect on the root mean square error (RMSE) (Carrivick et al. 2016; James and Robson 2012; Sanz-Ablanedo et al. 2018; Micheletti et al. 2015b).

One benefit of SfM photogrammetry is that it is capable of being used at a wide range of scales. Accuracy for a survey is limited by the scale of the study area (Carrivick et al. 2016) and distance between the camera and the surface (Eltner et al. 2016; Küng et al. 2011). Eltner et al. (2016) found that the absolute error values of SfM photogrammetry are generally low at close ranges and the relative error becomes larger at greater distances. The altitude necessary for a survey will be dependent upon the goal of the survey and the camera used. Using a camera image sensor with a higher resolution provides the ability to obtain the same GSD from higher altitudes, thus reducing the number of images necessary to cover a study area. In the application of sUAS for rangeland assessment, Rango et al. (2009) required a GSD finer than 25 cm for proper estimates of rangeland indicators. Higher-altitude flights require fewer photos to obtain sufficient overlapping imagery. Understanding the limitations of the camera sensor being used and finding a balance between the required altitude for the survey and the necessary GSD for project objectives will promote a more efficient flight plan and mission design. Localities with sUAS flight ceilings, such as the 122 m (400 ft) sUAS flight ceiling imposed by the Federal Aviation Administration in the USA, when combined with the sensor resolutions of typical sUAS cameras, may make unnecessarily high GSDs unavoidable.

Obtaining imagery from various altitudes can be important for 3D scene reconstruction. Larger-scale imagery can be used to cover the entire scene, while the addition of closer imagery can be used to obtain the GSD or detail required (Eltner et al. 2016). Multi-scale imagery is also advantageous in that it provides a wider

range of image directions that aid in the accurate solution of camera models (Eltner et al. 2016). Flight altitude also affects the ability to detect and accurately mark GCPs in the imagery (although this can be countered, in part, with larger GCPs). Study areas with high relief will also cause the GSD to vary across the resulting imagery if flight elevation is constant during the mission. Increasingly, mission planning and flight control software incorporates DEMs in the flight plan and provide the option of maintaining a single GSD by maintaining a constant above-ground altitude during imaging acquisition.

6.1.1.2 Image Overlap

Higher degrees of overlap increase the amount of matching key points available to generate DEMs. Additional overlap in the imagery producing a higher number of images across the study area can provide additional camera perspectives that will help to decrease DEM error (James and Robson 2012). Higher overlap may also increase photo alignment for imagery of homogenous terrains (e.g., forests, grasslands, etc.) during SfM processing. However, the higher the overlap, the greater the number of photos that must be acquired. Micheletti et al. (2015a) found that additional photos and greater image overlap do not linearly increase the accuracy of the results. The additional photos and overlap may increase the density of the resulting sparse point cloud; however, this does not guarantee an increase in the quality of the final derived products, such as orthoimagery and DSMs (Carrivick et al. 2016; Fonstad et al. 2013; James and Robson 2012; Micheletti et al. 2015b; Westoby et al. 2012). Indeed, the additional imagery may only lead to unnecessary additional processing time without noticeable benefits. An optimal amount of overlap will yield accurate results without acquiring needless additional imagery and increasing processing time.

6.1.1.3 Camera Angle

The angle of the camera during imagery acquisition affects the accuracy of the DEM produced. SfM techniques require features to be recognizable in at least three images (ideally more) for effective feature tracking and surface reconstruction (Carrivick et al. 2016). Various camera angles and points of view across the study area improve the image network geometry (Carrivick et al. 2016). Convergent imagery refers to image acquisition with the focal point of consecutive photographs to tend toward or approach intersecting points on the surface of a study area. This is opposed to parallel imagery where each individual photograph has an independent focal point on the surface of the study area. A strong image network geometry will increase the quality and accuracy of the results; however, the use of GCPs is still necessary to reduce radial errors and other distortions and achieve the highest accuracy (Sanz-Ablanedo et al. 2018).

Complex terrain with steep or sub-vertical surfaces can be difficult to reconstruct, but Rossi et al. (2017) and Helm et al. (2020) have demonstrated that the use of oblique imagery can increase the consistency of the reconstructed surfaces. When the imagery consists of all near-parallel viewing directions and camera self-calibration is used, radial distortion can occur in the DEM (James and Robson 2014). Artificial “doming” of the landscape occurs in derived SfM products due to inaccuracies in modeling radial camera lens distortion when using parallel viewing imagery (James and Robson 2012, 2014). James and Robson (2014) identify solutions to doming, such as the inclusion of oblique angle imagery and the use of GCPs. Other investigators have found that the use of oblique convergent imagery can help to minimize systematic error in SfM-based DEMs (Wackrow and Chandler 2008, 2011).

6.1.1.4 Course Angle

Mission planning and autonomous flight control software also provides the opportunity to vary the orientation of the flight path or course angle. Course angle is often determined based on in-field conditions, especially wind direction. However, multirotor sUAS with gimballed cameras are generally able to adapt, within reason, to wind conditions during flight and still maintain a constant orientation of the camera toward the ground. Most sUAS imagery acquisition flight plans employ a “lawn mower” pattern of back-and-forth flight paths that systematically traverse the study area. Some mission planning packages include mission design templates with multiple course angles, usually at a 90-degree angle. Little investigation has explored the effect of multiple course angles and camera orientations on the quality, accuracy, and precision of SfM products.

6.1.2 Other sUAS Mission Parameters Affecting Accuracy

Some variables related to sUAS image acquisition missions are not controlled through mission planning and flight control software. An example is GCP and check point (CP) placement. Other variables are outside of the user’s control, such as the relief of the study area, the surface texture of the study area, lighting conditions, and wind speed and direction. Some of the latter may be partially accounted for by the decisions made during the mission planning process. For example, the course angle of the flight path may be changed in accordance with wind direction, or higher image overlap may be planned for areas with difficult to align imagery such as forests, large homogenous fields, or other landcovers that make it difficult for key points to be identified by the SfM software.

6.1.2.1 Ground Control

Lower SfM product accuracies have been found by studies where no GCPs or an individual GCP was used as compared with missions where sufficient ground control was established (Mian et al. 2015, 2016). In addition to GCPs, the use of CPs, which are ground control that are not used to process and georeference the SfM products, provides a more robust approach to assessing the accuracy of SfM-derived DSMs and orthoimagery. CPs are not used in the SfM processing procedure. They are reserved for the error analysis phase as points of known x , y , and z coordinates that can be compared to the interpolated values of those points in the derived DSMs and orthophotos. Using the known CPs, rather than comparing the known and interpolated coordinates of GCPs, provides a better estimation of point cloud accuracy. Geometric camera model optimization through the bundle adjustment attempts to obtain a best fit of the GCP data used. This creates a bias where the used GCPs have a higher accuracy than may be present in the rest of the DSM resulting in a false estimation of the accuracy of the dataset (Sanz-Ablanedo et al. 2018).

Both GCPs and CPs are deployed throughout the study area and located using a GNSS survey. Deploying sufficient GCPs and CPs is a time-consuming process, and while more GCPs do aid in higher accuracies, the return on investment diminishes as the optimal amount of GCPs is surpassed (Carrivick et al. 2016; Sanz-Ablanedo et al. 2018). Optimizing the number of GCPs and CPs used in a project is critical to efficiency in both the field and data processing. The time required in the field for GCP and CP deployment, surveying, and retrieval varies non-linearly with the size of the study area, the ruggedness of the topography, the density of the understory and canopy vegetation, property access issues, and other logistical considerations. Greater quantities of GCPs and CPs, especially in combination with greater quantities of photos (either due to imagery overlap or high GSDs), also compound the time requirements for marking the targets on the photos during SfM processing. Sanz-Ablanedo et al. (2018) demonstrated that in large projects greater than 3 GCP per 100 photos achieved a high level of accuracy. Other studies have looked at GCP needs in terms of study site size (Agüera-Vega et al. 2017). Additionally, most guidance suggests that GCPs should be evenly distributed across the entire field site. Gaps in GCP coverage, localized concentrations of GCPs, and peripheral focused distribution strategies may produce unfavorable accuracies (Sanz-Ablanedo et al. 2018). It is worth noting that as sUAS with onboard real-time kinetic and post-processed kinetic GNSS become more broadly used, the number of GCPs required for projects may be significantly reduced (Štroner et al. 2020).

6.1.2.2 Surface Texture

Feature matching in scale-invariant feature transform (SIFT) requires texture and contrast sufficient to distinguish individual features and allow for suitable image key points to be identified (Lowe 1999). Areas with low texture and contrast are

problematic as fewer image features will be identified by the SIFT algorithm (Carrivick et al. 2016; Eltner et al. 2016). Vegetation also causes problems for feature detection due to the differences in appearance from various viewing angles. Trees especially complicate the image matching as their appearance changes with the viewing angle, even light winds create motion that confounds feature identification, and they block the view of the ground surface around them hindering the ability for understory ground features to be identified. Large vegetation can also create shadows, and the presence of shadows tends to locally reduce accuracy within models (Wackrow and Chandler 2008, 2011). The presence of shadows can be reduced by acquiring imagery during overcast or diffuse light conditions. Acquiring higher image overlap in datasets can also improve the alignment of images that are largely composed of dense canopy during SfM processing.

6.1.3 Objectives

Data collection of sUAS imagery occurred in six North Fork sub-watersheds ranging in size from 1 to 16 ha with dense tree canopy, and stream channels are often confined within steep valley walls (Fig. 6.1 and Table 6.1). Based on the rugged, densely forested terrain of the study area, the specific objective reported on here was to determine the sUAS image acquisition mission design that optimized both time and effort in the field and during SfM processing and the accuracy of the SfM-derived DSMs.

6.1.4 Study Area

Six tributary stream reaches of the North Fork of the White River watershed (i.e., the North Fork) located in the Mark Twain National Forest were investigated (Fig. 6.1 and Table 6.1). The chosen study sites were representative of the range of channel types, sizes, floodplain characteristics, and flood impacts within the portion of the North Fork watershed that was investigated. This portion of the North Fork watershed spans ~3600 km² in the counties of Douglas, Howell, and Ozark in the south-central most portion of Missouri, USA (Miller and Wilkerson 2001). The region is underlain by Ordovician and Mississippian age sandstone and carbonate bedrock. Karst terrain is extensive within the study area with numerous caves, springs, losing streams, and sinkholes. The area is characterized by steep, rugged topography with up to 165 m of total relief. The North Fork lies within the Oak Woodlands land type association of the Ozark Highlands ecological section, which is typified by dense stands of oak-hickory and oak-pine forest (Raeker et al. 2011). Approximately two-thirds of the watershed, and most of the area encompassed by the study sites, is densely forested (Miller and Wilkerson 2001).

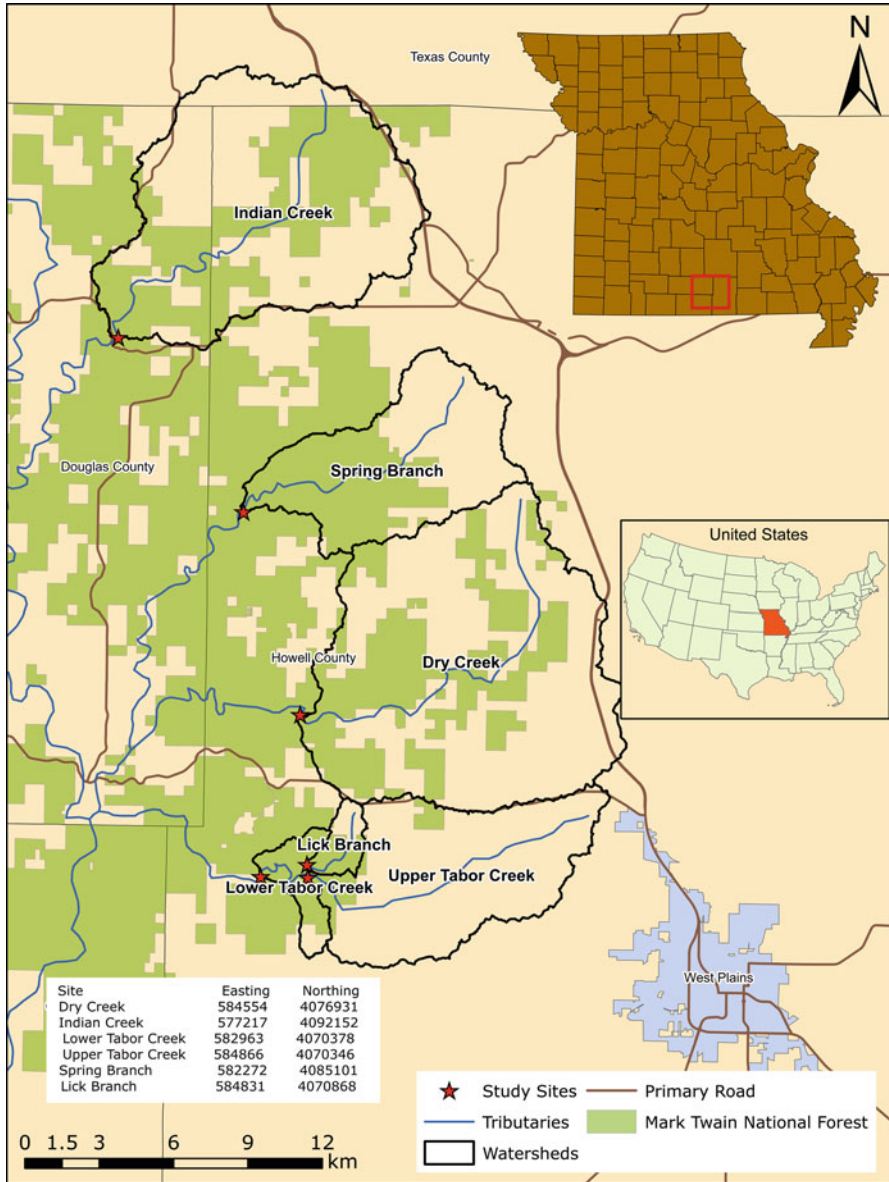


Fig. 6.1 Study sites in the North Fork of the White River watershed in south-central Missouri. (After Hess 2019)

According to the National Weather Service reports, on April 28 and April 30, 2017, a major storm system over the midwestern USA yielded widespread precipitation amounts totaling 10–20 cm and local areas of 25–30 cm. More than 20 streams in the region experienced record peak discharges. As described in

Table 6.1 Area surveyed and the quantity of ground control points and check points deployed for image acquisition

	Field Site Size (Hectares)	GCPs Used	CPs Used
Spring Creek	5.3	6	5
Indian Creek	5.7	6	5
Lower Tabor	16.2	10	10
Upper Tabor	4.8	6	6
Lick Branch	1.0	5	3
Dry Creek	2.6	6	3

Heimann et al. (2018), 14 of these streams were in southern Missouri, including the North Fork of the White River (Fig. 6.1). The study area experienced some of the highest reported rainfalls associated with this event with precipitation totals in the North Fork watershed ranging from 20 to 30 cm. The USGS gage (gage number 07057500) at Tecumseh, Missouri, recorded a peak discharge of 5350 m³/s and a stage of approximately 13 m. The flood was estimated to have an annual exceedance probability of <0.02 (i.e., greater than 1 in 500-year recurrence interval) (Heimann et al. 2018). This extreme event caused extensive riparian corridor damage, deposits of woody debris, and extensive modification of channel and floodplain landforms along the North Fork and its tributaries.

The broader post-flood investigation of this extreme event, of which this study was one part, had multiple objectives related to understanding the short-term effects of a large flood on channel morphology and riparian forests in a typical Ozark Plateau stream. This included assessments of channel morphology and floodplain landforms, channel substrate, surveys of large woody debris, and a biogeographic survey of tree damage. The steep, rugged, and heavily forested terrain of the study area in combination with the spatially extensive effects of the flooding made it impossible to quantify the flood effects solely through on-the-ground field work. To complete the assessment efficiently and rapidly, we employed sUAS to collect aerial imagery to create SfM-derived DSMs and orthoimagery that could serve as base maps for field mapping, GIS-based analysis, and quantification of areal and volumetric characteristics of channel and floodplain landforms (e.g., Bendix et al. 2018; Hess 2019; Fig. 6.2) and woody debris deposits (Martin et al. 2020).

The densely forested and steep topography of our stream channel study sites posed interesting questions and challenges regarding how best to acquire sUAS imagery that would ensure the highest accuracy SfM products with the least effort necessary during both field work and subsequent SfM processing. The combination of a topographically complex and densely forested landscape posed significant challenges for SfM techniques because of difficulties in image alignment, key point identification, and tie point matching in the homogeneously forested terrains. These site characteristics in combination with the short timeframe available for field work demanded that we design our sUAS image acquisition missions to ensure adequate imagery was obtained to allow for quality DSMs and orthoimages to be derived through SfM. Questions about how best to design sUAS missions to acquire

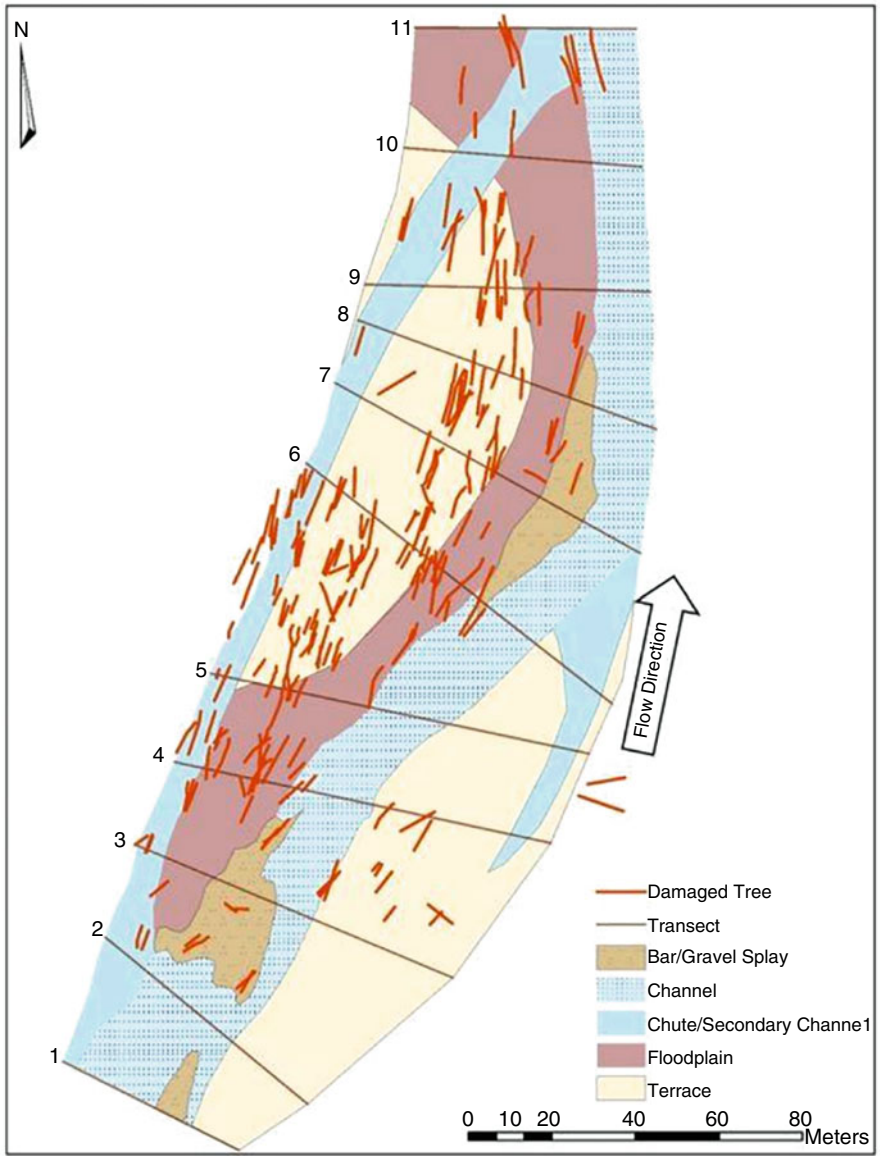


Fig. 6.2 A map of channel and floodplain features for the Dry Creek site with the location of damaged trees. This map was drafted using field-based observations as well as observations and measurements from an orthophoto and DSM. The sUAS imagery facilitated a more efficient use of field time by allowing some aspects of the survey, including quantitative measurements to occur in the office. (From Hess 2019)

imagery datasets adequate for our purposes were not clearly outlined in the literature. The relative ease and low cost of sUAS-based image acquisition have often been a motivation to “over collect” imagery during field campaigns under the premise of ensuring that the SfM processing workflow is not hindered by insufficient image overlap. However, acquiring unnecessary imagery exacts costs in both the time and effort required in the field and in the SfM processing workflow.

6.2 Methods

6.2.1 Mission Design for Image Acquisition

DJI Phantom 4 Pro sUAS were used to collect imagery for SfM processing using Agisoft Metashape. The integrated camera on the Phantom 4 Pro has an effective sensor resolution of 20 megapixels. The camera utilizes a global shutter which captures the entire scene within the photo simultaneously. Global shutters are preferred for sUAS SfM applications because they are not prone to the image distortions inherent in rolling shutters, which introduce errors into the photogrammetric process (Carrivick et al. 2016). DJI Ground Station Pro was the mission planning and autonomous flight control software used for image acquisition (Fig. 6.3). The Phantom 4 sUAS can reliably fly 20 min on one battery with an acceptable portion of remaining flight time (5–7 min) reserved for a margin of safety. Larger field sites may require multiple flights to complete an individual mission. Individual flights of the Phantom 4 usually last 20–25 min, and multiple flights may be required for each mission.

Four separate image acquisition missions, each with a separate flight plan, were flown at each study site. We refer to these four missions as the base missions. Each base mission was designed as a standalone flight plan designed to acquire all the imagery necessary to produce DSMs and orthoimages of the site from SfM methods. Each base mission was created in advance and sent to the sUAS before take-off to allow for automated flight. At one of the sites, manual take-offs and landings were performed through narrow openings in the tree canopy, but all other aspects of the flights were completed by the autopilot system.

Each base mission was flown at an altitude of approximately 108 m (355 ft) above ground level (AGL). This altitude in combination with the Phantom 4 Pro camera yields an estimated GSD of about ~ 3.0 cm/pix. However, due to the topography of the field sites, the true AGL altitude varied across each field site, and it was estimated that the actual GSDs ranged by as much as ± 0.25 cm/pix. Flight paths included longitudinal and transversal image overlap of 80%. Two of the base missions collected orthogonal imagery using a camera angle of 90^0 (pointed straight down). The other two base missions used a camera pitch angle of 70^0 (i.e., 20^0 above nadir) to acquire oblique imagery. Both the orthogonal and the oblique mission pairs included one mission with a north-to-south course angle and one with an east-to-

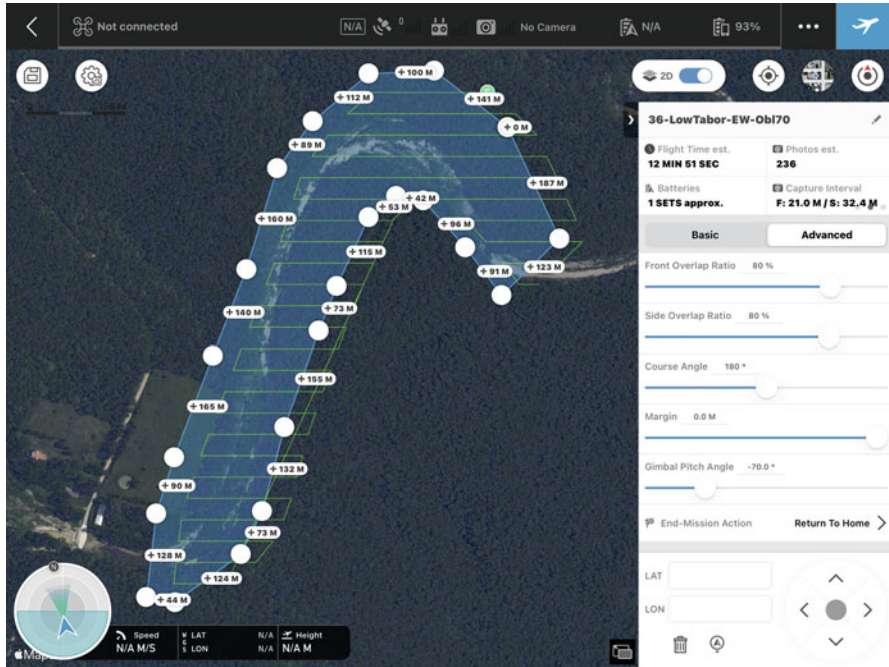


Fig. 6.3 A screenshot from the DJI Ground Station Pro software of the flight plan for the Lower Tabor site. The blue area of interest (AOI) is the desired coverage of the imagery to be collected during the flight. The green line is the calculated flight path determined by the software necessary to acquire the imagery. Note that the flight path is slightly offset from the AOI to compensate for the oblique angle of image acquisition. Longitudinal (front) and transversal (side) overlap as well as camera angle are set with the parameters in the white box on the right

west course angle. The missions were flown in “lawnmower” patterns, and the general design of the four unique base missions is depicted in Fig. 6.4.

In case additional flooding occurred prior to the opportunity to acquire leaf-off imagery of the field sites, an initial round of leaf-on imagery was flown in September 2017. However, no significant channel altering flows occurred between the April 2017 floods and the March 2018 acquisition of leaf-off imagery. As such, all of our analyses were performed on the March 2018 imagery.

The four base missions were flown at each of the six field sites over the course of 3 days in March 2018. The details of the flights performed to complete each mission are listed in Table 6.2. Due to constraints in completing the field work, flights were conducted throughout each field day. Thus, ambient lighting conditions varied from site to site and mission to mission. Some image datasets captured in the morning or late afternoon included significant shadowing contrasting with brightly lit areas. Nonetheless, individual missions at each site were flown consecutively in a relatively short period of time (Table 6.2) under uniform lighting conditions. All four base missions were completed at each site over a period ranging from approximately 30 min to 2.5 h, depending on the size of the site.

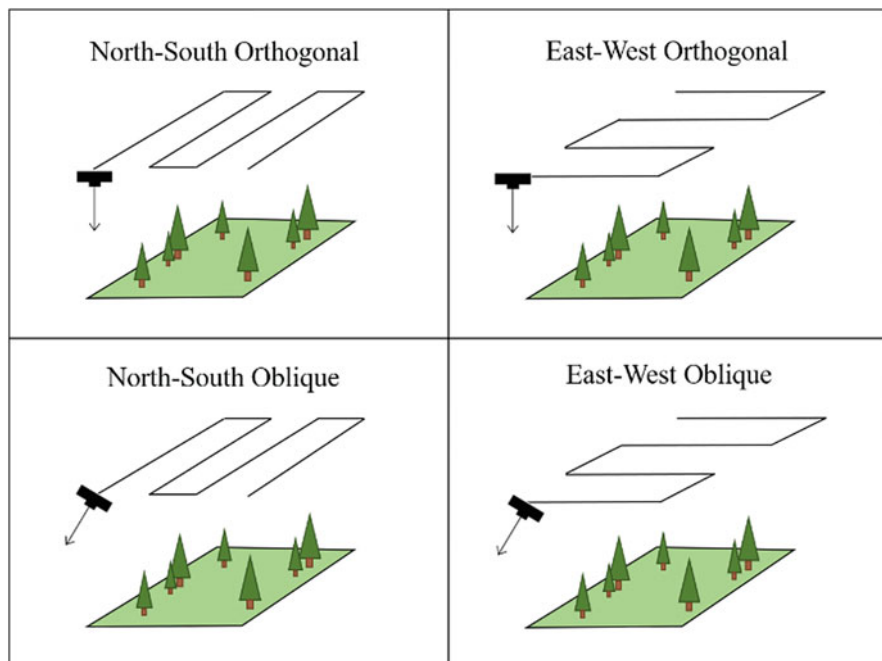


Fig. 6.4 Base mission designs used for sUAS imagery acquisition

The imagery collected during each of the four base missions for each site was processed separately to derive associated DSMs and orthoimages. Additionally, five combined imagery datasets were created by combining the imagery from the four base missions, as indicated in Fig. 6.5. As a result, for each of the six field sites, a total of nine different datasets were separately processed to derive DSMs and orthoimages (i.e., 54 total DSMs and an equal number of orthoimages).

6.2.2 Ground Control

Slow-moving vehicle triangles (bright orange with a reflective red outline) were used for both GCPs and CPs during image acquisition. Each ground control was randomly designated as a GCP or a CP. GCPs were used during SfM processing to georeference the derived point clouds and other products such as DSMs and orthophotos. CPs were only for error analysis of the resulting DSMs. Due to the extent and density of the tree canopy at the sites, there were a limited number of locations suitable for placing GCPs and CPs. The number and spatial distribution of control points were to some extent limited by these factors. At each of the six field

Table 6.2 Base mission flight time information for each of the six field sites

Field site	Base mission flight	Flight number	Start time	End time	Date
Upper Tabor	EW Ortho	1	10:04	10:13	3/2/2018
	NS Ortho	1	10:14	10:26	3/2/2018
	EW Oblique	1	10:39	10:46	3/2/2018
	NS Oblique	1 of 2	10:47	10:54	3/2/2018
		2 of 2	10:56	11:06	3/2/2018
Lick Branch	EW Ortho	1	11:32	11:38	3/2/2018
	NS Ortho	1	11:40	11:48	3/2/2018
	EW Oblique	1	11:48	11:54	3/2/2018
	NS Oblique	1	11:55	12:04	3/2/2018
Dry Creek	EW Ortho	1	14:26	14:32	3/2/2018
	NS Ortho	1	14:33	14:38	3/2/2018
	EW Oblique	1 of 2	14:39	14:47	3/2/2018
		2 of 2	14:49	14:52	3/2/2018
	NS Oblique	1	14:53	15:02	3/2/2018
Spring Creek	EW Ortho	1	16:37	16:47	3/2/2018
	NS Ortho	1	16:48	17:00	3/2/2018
	EW Oblique	1	17:01	17:10	3/2/2018
	NS Oblique	1	17:11	17:21	3/2/2018
Lower Tabor	EW Ortho	1 of 2	9:33	9:52	3/3/2018
		2 of 2	9:54	10:04	3/3/2018
	NS Ortho	1	10:09	10:29	3/3/2018
	EW Oblique	1 of 2	10:30	10:49	3/3/2018
		2 of 2	10:53	10:57	3/3/2018
	NS Oblique	1 of 2	10:58	11:12	3/3/2018
		2 of 2	11:16	11:22	3/3/2018
Indian Creek	NS Ortho	1	13:00	13:09	3/4/2018
	NS Oblique	1 of 2	13:10	13:18	3/4/2018
		2 of 2	13:21	13:32	3/4/2018
	EW Ortho	1	12:55	13:05	3/4/2018
	EW Oblique	1 of 2	13:06	13:16	3/4/2018
		2 of 2	13:33	13:41	3/4/2018

sites, GCPs were placed in suitable locations that would be visible from the aerial imagery. The areal size of the field sites and the number of GCPs and CPs deployed varied for each site (Table 6.1). Each GCP and CP was surveyed using a pair of GNSS receivers (Geneq SXblue Platinum base and a Gintec G10 rover) in a real-time kinetic configuration to collect sub-decimeter positional data. Each surveyed position was the result of averaging 60–180 s of 1 Hz positional data. The duration of the averaging was varied to compensate for GNSS errors induced by limited horizon, tree cover, and extended GNSS correction age due to topography.

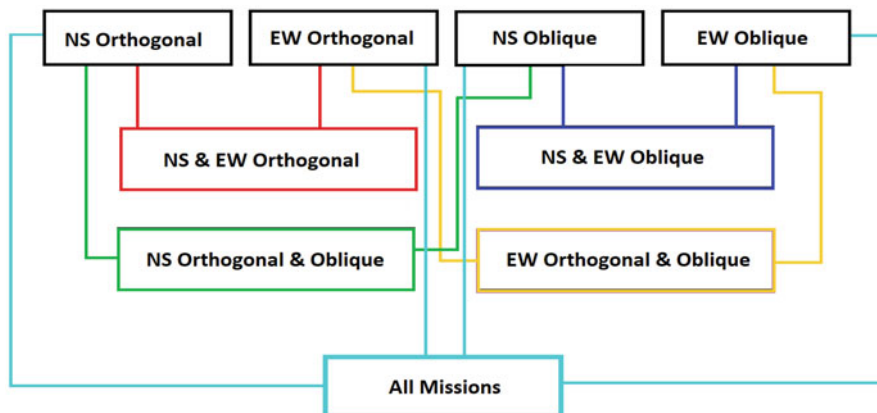


Fig. 6.5 The four base missions flown at each site are represented by the black boxes (top row). Five additional “combined imagery” datasets were also created from the indicated combinations of the four base missions

6.2.3 Structure-from-Motion Photogrammetry Processing

6.2.3.1 Imagery Alignment

The acquired imagery was processed in Agisoft Metashape version 1.4 (including builds 5076 through 7354, which was previously named Agisoft Photoscan at the time these data were processed) following the workflow in Noble and Matthews (2017) with some slight modifications as described in Hostens (2019). The gradual selection portion of the workflow, which identifies and removes erroneous points from the sparse point cloud, was automated in Metashape using a Python script documented in Hostens (2019). Image alignment was completed with an accuracy setting of “highest” with key point limit of 60,000 and tie point limit of 0, which allows the software to use any number of matched key points as tie points. After alignment a least squares bundle adjustment, which is referred to as “camera optimization” in Metashape, was run to refine the tie point positions and the estimates of camera position and orientation (Moore et al. 2009; Chien et al. 2015). As specified in Noble and Matthews (2017), the parameters f , c_x , c_y , $k1$, $k2$, $k3$, $p1$, and $p2$ are used for this bundle adjustment (Table 6.3).

6.2.3.2 Ground Control

After image alignment, the GNSS data for the ground control were loaded into Metashape. All GCPs and CPs were located, marked, and labeled accordingly on all images. The Metashape marker data for the GCPs and CPs were exported and added to all imagery sets being processed to ensure all the base and combined imagery datasets were processed with consistent marker data. CPs at each site were used to

Table 6.3 The definition of the least squares bundle adjustment parameters used in the Agisoft Metashape camera optimization procedure

Camera alignment parameter definitions	
f	Camera focal length (x, y)
cx, cy	Center of camera sensor of principal point (x, y)
k values	Distortions from center of the lens (radial distortions)
p values	Lens misalignments (tangential distortions)
b values	Values that compensate for non-square pixels

Table 6.4 RMSE and MAE values for the residual errors found from the comparison between each imagery set and the best-case imagery set in this study, the NS Oblique. All values are in meters

	RMSE	MAE
NS Ortho	0.065	0.028
EW Ortho	0.108	0.076
NS Oblique	–	–
EW Oblique	0.069	0.034
Ortho Missions	0.092	0.064
Oblique Missions	0.052	0.020
NS Missions	0.237	0.189
EW Missions	0.085	0.053
All Missions	0.216	0.177

compare the accuracy between each imagery set. Though CPs were identified with markers in Metashape, they were not used to georeference the data or generate the SfM products. The advantage of marking the CPs in Metashape, but not including them in the georeferencing of the SfM products, is that the software will report an estimated projected 3D coordinate position and error for each CP. As such, the CP is a known three-dimensional point in space (based on the field-surveyed GNSS position) that does not influence the bundle adjustment solution and can be used to assess product accuracy (Carrivick et al. 2016; Dietrich 2016; Eltner et al. 2016; Javernick et al. 2014; Sanz-Ablanedo et al. 2018). The accuracy information reported by Metashape are used to calculate RMSE (Eq. 6.1) and mean absolute error (MAE, Eq. 6.2) values. The GCPs are used in the subsequent processing steps in the bundle adjustment and to georeference the SfM products.

$$\text{RMSE} = \sqrt{\frac{\sum_{i=1}^n (e_i)^2}{n}} \quad (6.1)$$

$$\text{MAE} = \frac{\sum_{i=1}^n |e_i|}{n} \quad (6.2)$$

The error values for the CPs reported by Metashape were used to obtain the RMSE and MAE for each of the imagery sets (Table 6.4). When calculating the overall RMSE and MAE values, a total of 32 CPs from all the field sites were used

(Table 6.1). Most studies involving assessment of SfM products utilize RMSE to report error (Carrivick et al. 2016). While RMSE does represent the error magnitude within a dataset, it has some limitations. The RMSE characterizes the magnitude of errors with higher priority due to the nature of finding the squared difference of errors in the calculation. The MAE is used as a compliment to the RMSE because it displays a more consistent average error within the data (Willmott and Matsuura 2005). Some GCPs and CPs were located near trees along stream banks, and the GNSS-surveyed accuracy of their positions was influenced by factors such as the presence of shadows and obscuration by vegetation and topographic barriers. Additionally, the same factors limited the number of photos in which these GCPs and CPs could be effectively marked in Metashape. Across the six field sites, we had to eliminate three ground control targets (two at Dry Creek and one at Lick Branch) that yielded high error values inconsistent with the rest of the GCPs and CPs. The error values within these points were very high and suggested that the surveyed point location was most in the tree canopy rather than on the ground.

6.2.3.3 Gradual Selection

A Python script (documented in Hostens 2019) was written to automate the sparse point cloud error reduction via the Gradual Selection tool in Metashape. Gradual selection is a point filtering and reduction process that removes points in the sparse cloud. The procedure is usually performed iteratively such that points up to an error threshold are removed from the point cloud and then a bundle adjustment is run on the remaining points. The gradual selection process can be a time-intensive task to accomplish manually, especially for large sparse point clouds. Automation of the gradual selection process with the script enabled this task to be efficiently accomplished on all 54 of the base missions and combined imagery datasets processed as part of this study. In addition to saving user time, the script ensures the error-reduction thresholds are applied consistently during gradual selection and reduces the chances of user error during a monotonous series of steps.

Gradual selection involves three primary types of error reduction performed in the following order: (1) reconstruction uncertainty, which removes points with poor geometry; (2) projection accuracy, which removes points with pixel matching errors; and (3) reprojection error, which removes points with pixel residual errors. The gradual selection process was the main area where we deviated from the workflow in Noble and Matthews (2017). Whereas their workflow specifies adding the ground control between the projection accuracy and reprojection error steps, we added the ground control prior to gradual selection. Marking the ground control prior to gradual selection has no adverse effect on the ultimate SfM products but enables the gradual selection procedure to be automated in a single script.

6.2.3.4 Dense Cloud and Data Products

After gradual selection, a three-dimensional dense point cloud is generated from the points remaining in the sparse cloud. Depth map creation and subsequent dense point cloud generation are a very computationally intensive process. The quantity of acquired imagery is a function of mission design (i.e., photo overlap and flight altitude). To assess the effect of image quantity on SfM processing times, the data were processed one at a time on a single workstation to allow an equitable comparison of the required processing times. The computer hardware used for processing SfM data is a limiting factor on the quality of the end products and the time required to generate them. Inadequate hardware resources can dramatically slow down the data processing. The workstation we used exceeded the minimum system requirements for Metashape, and our data processing tasks did not exceed the capacity of the RAM, graphics cards, or processors. Thus, our results provide an accurate relative comparison of the effect of image quantity on the time required to process the SfM data. A report was generated for each imagery dataset that recorded the processing details including sparse point cloud size, dense point cloud size, point density, and the associated processing times.

Mission planning parameters, such as the GSD, the resolution of the photos, and the longitudinal and transversal image overlap, also influence the computational requirements, quality, and accuracy of the SfM products. Wisely choosing the specifications for these aspects of the mission design will ensure excess effort is not expended during field work or the SfM processing workflow. In addition to removing noisy and inaccurate data, gradual selection thins the sparse cloud, which ultimately reduces the computational requirements of generating the dense point cloud and presents the opportunity to output higher-quality and more accurate results for an equivalent investment of processing time.

Metashape allows specification of a quality setting when building a dense cloud. The quality setting determines the detail and accuracy of the geometry of the dense cloud as a trade-off with the time and computational power required to produce the end result. We used a “High” setting that results in the downscaling of the resolution of the original images by a factor of 4. This setting yields a significant savings in processing time and hardware requirements while still yielding excellent quality results. We also used an “Aggressive” setting for depth filtering, which is the recommended setting for aerial imagery processing and does a good job of filtering out outlier data at the expense of retaining small details in the dense cloud.

After generation of the dense cloud, a derivative DSM can be generated. Because our data products were being produced for broader objectives related to mapping and analyzing the effects of the April 2017 flooding on our field sites, we did not want to perform vegetation removal on our DSMs as would be necessary to yield DEMs. We exported our DSMs at their native maximum resolution as determined by the Metashape processing algorithm. Our source imagery and the GNSS survey of our ground control were georeferenced to World Geodetic System 1984 (EPSG:4326). We maintained this projection throughout the processing workflow and in the

derived products. The mosaicked orthoimages were orthorectified using the DSMs and also exported at their maximum native resolutions.

6.3 Results

6.3.1 Mission Design and SfM Product Accuracy

Based on our analysis of the four base missions and the five combined imagery datasets we processed at our field site, the RMSE and MAE results are shown in Fig. 6.6. Tables 6.5 and 6.6 display the RMSE and MAE results in order of

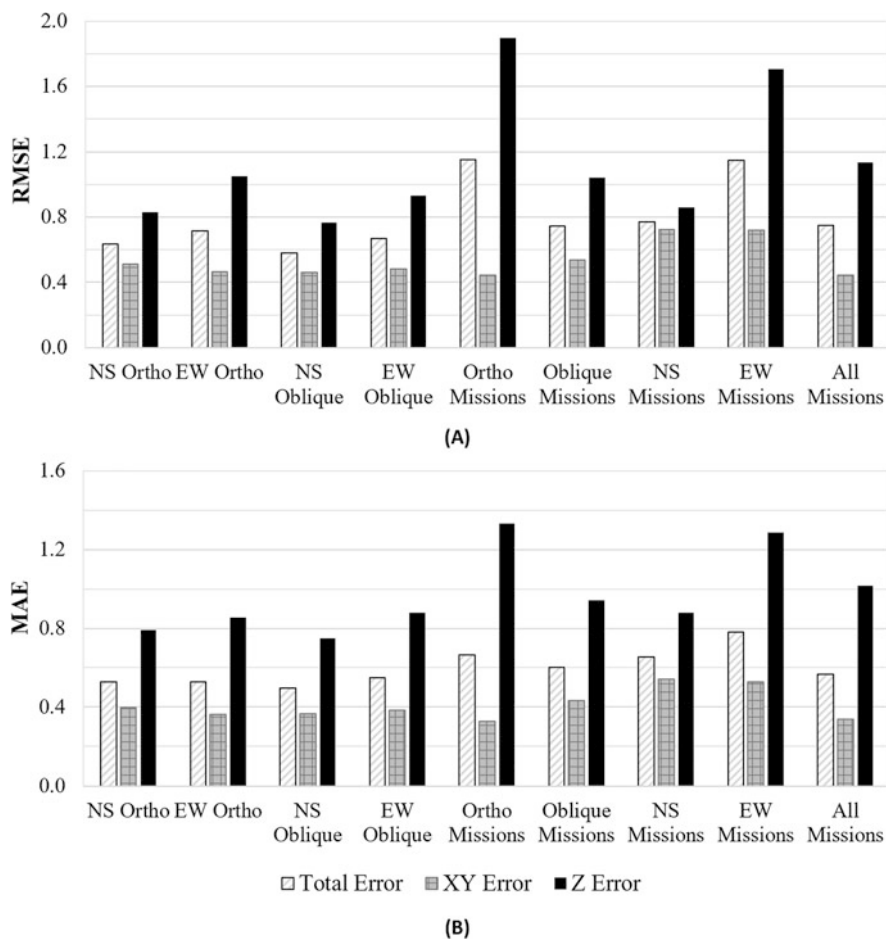


Fig. 6.6 (a) Overall RMSE values of CPs from all sites for each imagery set. (b) Overall MAE values of CPs from all sites for each imagery set. All values are in meters

Table 6.5 RMSE values, sorted by ascending total error, for all imagery sets. All values are in meters

Imagery dataset	RMSE				
	Total error	XY error	X error	Y error	Z error
NS Oblique	0.581	0.462	0.466	0.458	0.766
NS Ortho	0.637	0.514	0.499	0.528	0.830
EW Oblique	0.667	0.482	0.479	0.485	0.933
EW Ortho	0.717	0.467	0.477	0.457	1.052
Oblique Missions	0.744	0.537	0.505	0.568	1.041
All Missions	0.749	0.444	0.405	0.480	1.136
NS Missions	0.770	0.722	0.787	0.650	0.857
EW Missions	1.146	0.719	0.555	0.851	1.705
Ortho Missions	1.153	0.445	0.394	0.491	1.896

Table 6.6 MAE values, sorted by ascending total error, for all imagery sets. All values are in meters

Imagery dataset	MAE				
	Total error	XY error	X error	Y error	Z error
NS oblique	0.495	0.367	0.393	0.342	0.750
EW Ortho	0.528	0.364	0.401	0.327	0.856
NS Ortho	0.530	0.398	0.405	0.392	0.792
EW oblique	0.549	0.384	0.418	0.351	0.880
All Missions	0.565	0.340	0.337	0.342	1.017
Oblique Missions	0.602	0.432	0.445	0.419	0.943
NS Missions	0.653	0.540	0.597	0.484	0.878
Ortho Missions	0.663	0.329	0.301	0.356	1.332
EW Missions	0.780	0.528	0.439	0.617	1.285

ascending magnitude of error. The imagery dataset with the lowest overall total RMSE and total MAE values when considering the error values of all CPs for the six sites was the *NS Oblique* imagery dataset. The *All Missions* and *Ortho Missions* imagery datasets had slightly lower planimetric RMSE and MAE values than the *NS Oblique* imagery dataset. The *EW Ortho* imagery dataset had slightly higher planimetric RMSE values than the *NS Oblique* design but a lower MAE planimetric value. The *NS Oblique* imagery dataset had the lowest Z RMSE and MAE values of all imagery sets by a good margin. The closest in Z accuracy in both cases was the *NS Ortho* imagery dataset.

Combining base missions to create combined imagery datasets or using all imagery as is the case for the *All Missions* imagery dataset did not improve the overall total RMSE or MAE values in relation to the individual base missions. Base mission imagery datasets consistently performed better than, or similar to, the combined imagery datasets. Among the combined imagery datasets, the *Oblique Missions* appears to handle Z errors better than the *Ortho Missions*; however, this relationship does not hold true for the base mission datasets. The *NS Oblique* had the

lowest Z RMSE and MAE values compared to all other imagery sets. The *EW Oblique* had the second highest RMSE Z error value and the highest MAE Z error value among the base mission imagery sets but was comparable to and better than most RMSE and MAE results for combined imagery sets. Mixed camera angle imagery sets such as the *EW Missions* and the *NS Missions* imagery sets did not consistently produce improved planimetric or Z accuracy.

A cross-sectional profile from the Spring Creek site was used to compare the results of each base mission and combined imagery dataset. It is important to note that a field survey across the site was not performed during the fieldwork. Rather, a profile was extracted from the *NS Oblique* image dataset, which had the lowest overall error values. The *NS Oblique* profile was used as the baseline for comparison between the other eight image datasets. Figure 6.7 shows the location of the profile line. The location was chosen to display a cross-sectional profile of the creek while avoiding trees and vegetation. Complex tree canopies can result in difficult to compare profiles because each imagery dataset may reflect the location of a single branch or leaf. Figure 6.8a compares the profile lines created for each imagery set,

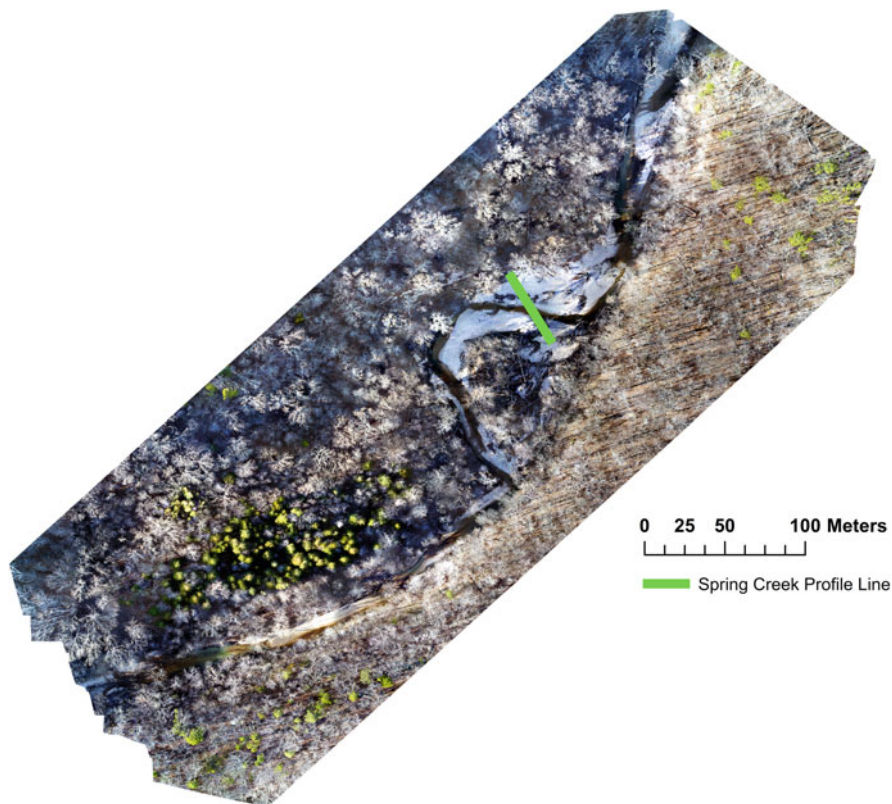


Fig. 6.7 Orthophoto of the Spring Creek site showing the location of the profile line (green line) used for profile elevation extraction for each imagery set

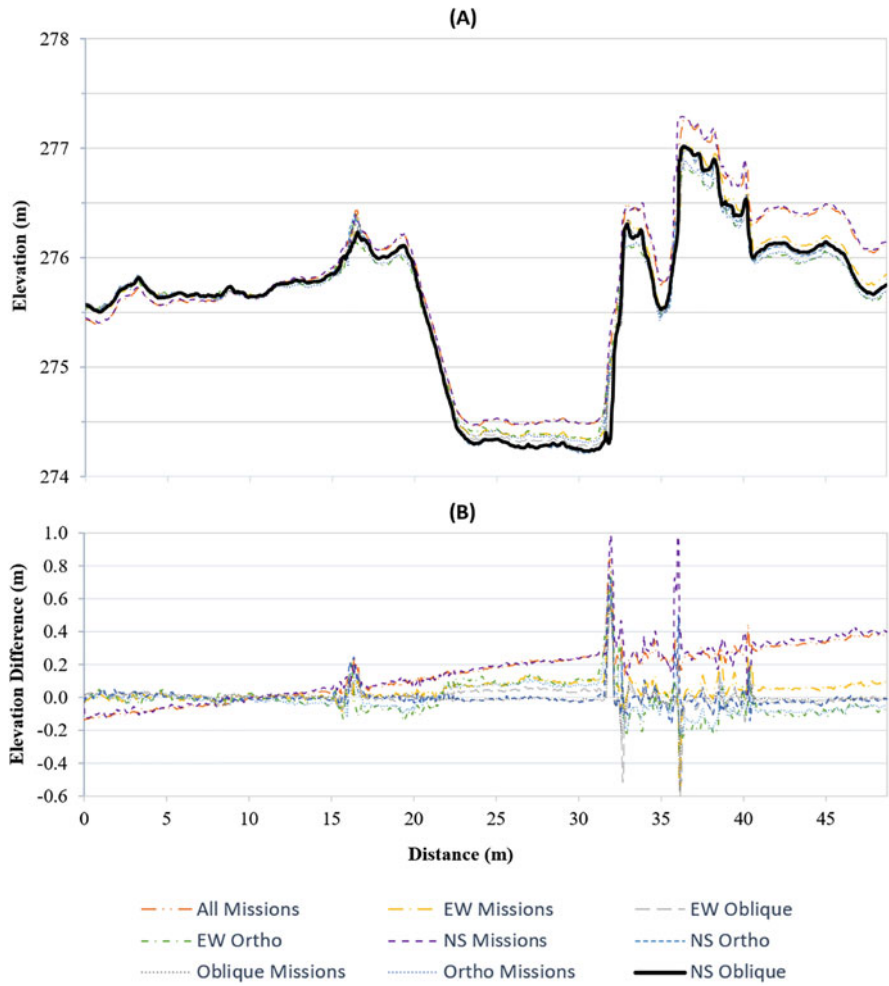


Fig. 6.8 (a) Comparison of profiles extracted from the DSMs of the various imagery datasets. (b) Residual difference between the NS Oblique DSM profile and the profiles of each of the other imagery datasets

and Fig. 6.8b displays the residual difference relative to the *NS Oblique* imagery set. The *NS Oblique* is shown as the thick bright green line in the profile line comparison. Table 6.7 shows the RMSE and MAE values for the residuals of each imagery set.

Mission design determines the number of images acquired for a study site. Figures 6.9 and 6.10 display the RMSE and MAE values of the CPs in relation to the number of base missions included in the imagery datasets we included in our analysis. Although there are slight increases in the error values as the number of photos per imagery dataset increases, there is no significant correlation. This suggests that additional imagery does not improve the accuracy of the SfM products as

Table 6.7 RMSE and MAE values for the residual errors found from the comparison between each imagery set and the best-case imagery set in this study, the NS Oblique. All values are in meters

Imagery dataset	RMSE	MAE
NS Ortho	0.065	0.028
EW Ortho	0.108	0.076
NS Oblique	–	–
EW Oblique	0.069	0.034
Ortho Missions	0.092	0.064
Oblique Missions	0.052	0.020
NS Missions	0.237	0.189
EW Missions	0.085	0.053
All Missions	0.216	0.177

different mission designs are combined. Additional imagery significantly affects the computational overhead associated with SfM processing. As shown in Fig. 6.11, combining imagery from multiple base mission datasets to create the combined imagery datasets had a non-linear effect on the required processing time. The non-linear trend demonstrates that additional photos can greatly increase the necessary processing time relative to processing the base mission imagery sets.

Greater numbers of photos had no effect on the dense point cloud density (Fig. 6.12). What appears to have a greater affect is the camera angle in the imagery set. Orthogonal camera angles led to larger dense point cloud densities than oblique camera angles (Table 6.8 and Fig. 6.13). The dense point cloud density for combined imagery sets with both oblique and orthogonal camera angles was typically between the range in densities of the oblique only and orthogonal only combined imagery sets.

6.4 Discussion

Accuracies reported in various studies of sUAS surveys suggest a relationship where accuracy decreases as GSD increases (Harwin and Lucieer 2012; Vallet et al. 2012; Vericat et al. 2016). As such, it follows that there are inherent variations in accuracy with increasing GSDs (as a function of height and image sensor resolution). Eltner et al. (2016) found that the absolute error values of SfM photogrammetry are generally low at close ranges and the relative error becomes larger at greater distances. Our flight altitude of 108 m yields a GSD of ~ 3.0 cm. The varying relief of the field sites, the presence of shadows during image acquisition, and errors inherent in the GNSS surveys used for ground control positioning, all introduce errors into the results. However, our study design should cause these errors to be approximately equal for each of the four base mission imagery datasets and the derivative combined imagery datasets. Differences in RMSE or MAE errors between the various imagery datasets we analyzed across our six field sites should primarily reflect the effects of the mission design on accuracy of the SfM products.

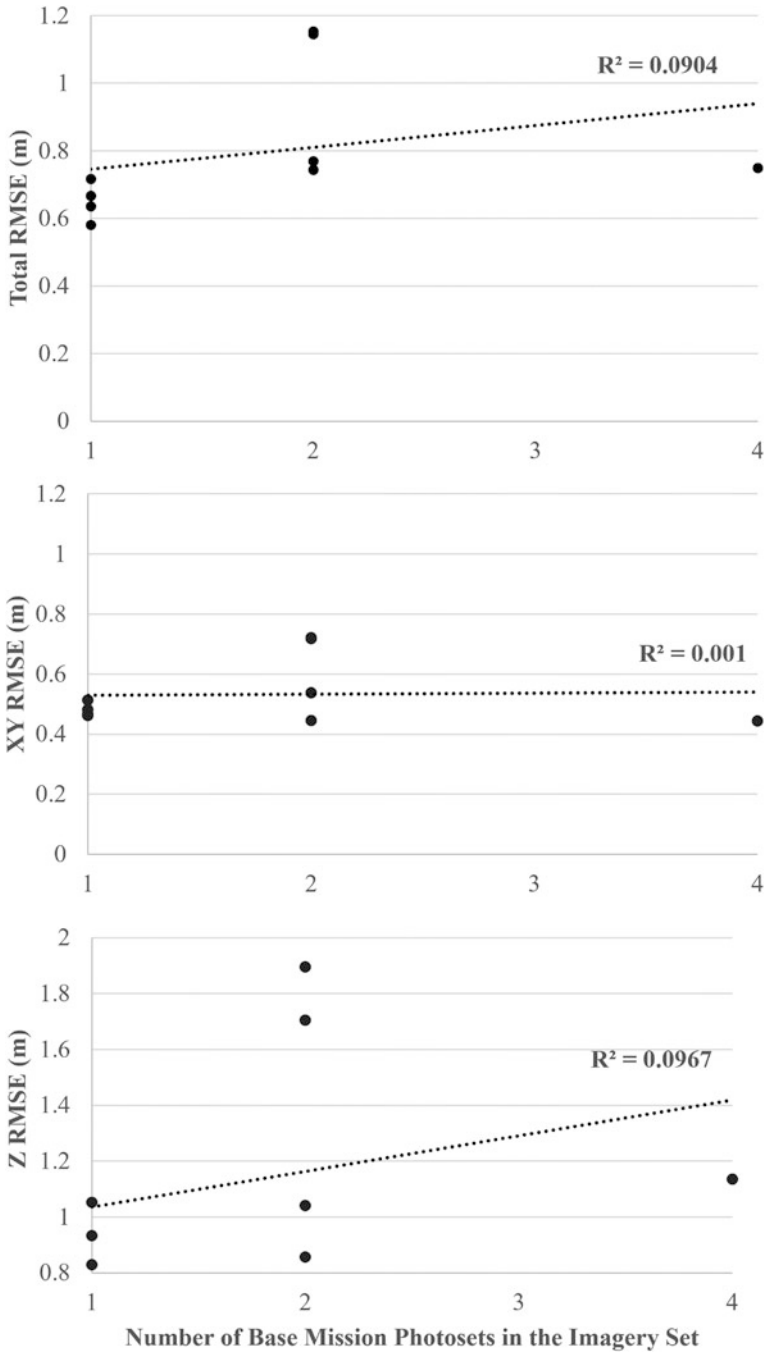


Fig. 6.9 RMSE three-dimensional (top), XY (middle), and Z (bottom) values of all CPs for each imagery set separated by number of base missions combined into the imagery set

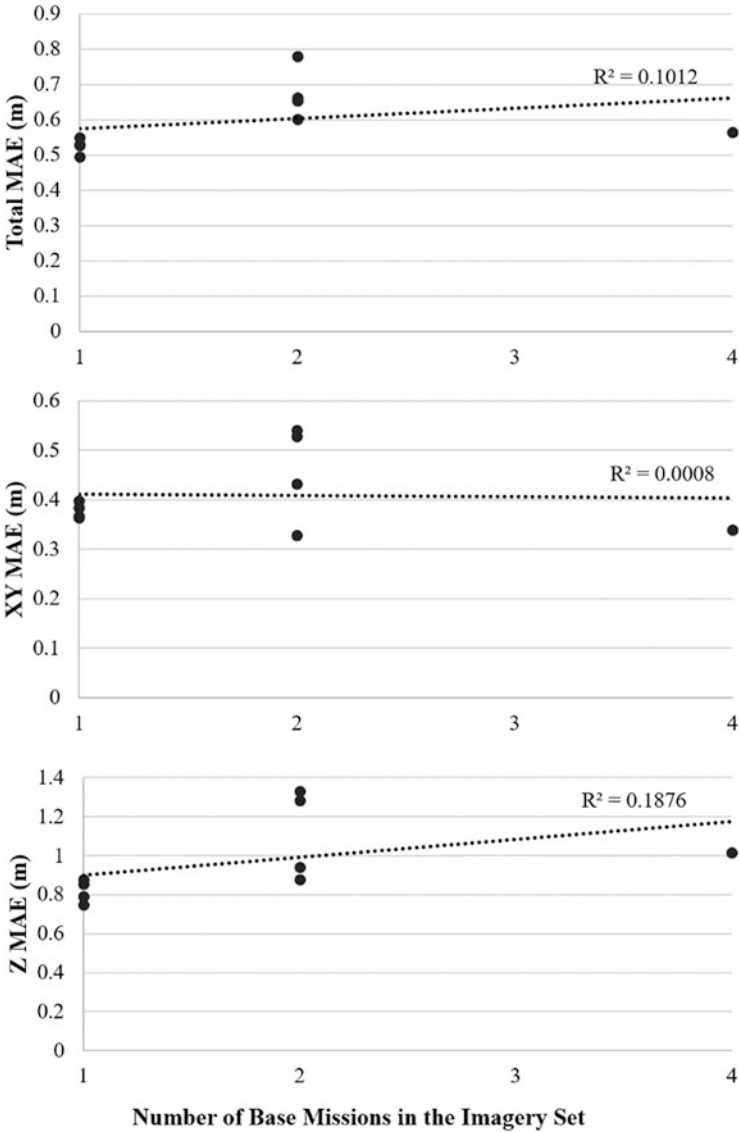


Fig. 6.10 MAE three-dimensional (top), XY (middle), and Z (bottom) values of all CPs for each imagery set separated by number of base missions combined into the imagery set

Our base mission designs utilized an 80% longitudinal and transversal image overlap. We did not systematically test how variations in longitudinal and transversal image overlap affect the accuracy of the SfM products. However, our experience in the steep, vegetated terrain of our field sites indicates that less than 80% overlap results in a significant number of images not being aligned due to fewer key point

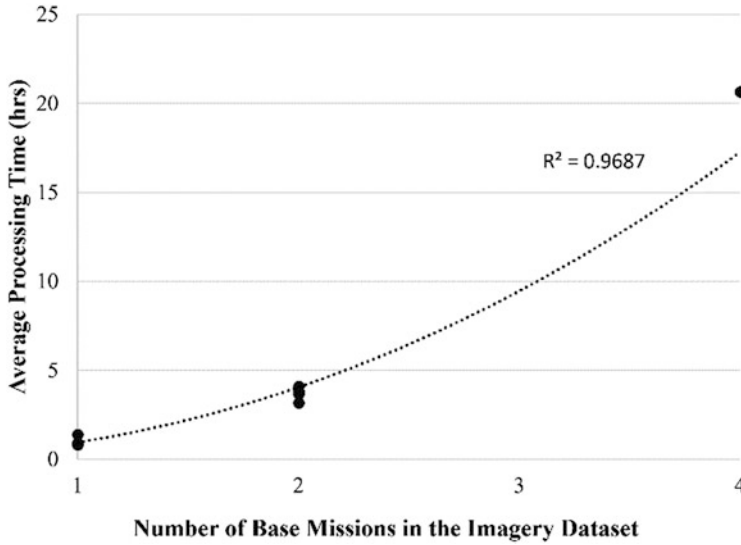


Fig. 6.11 Comparison of the average processing time required to create dense point clouds for each imagery set separated by the number of base missions used in the imagery set

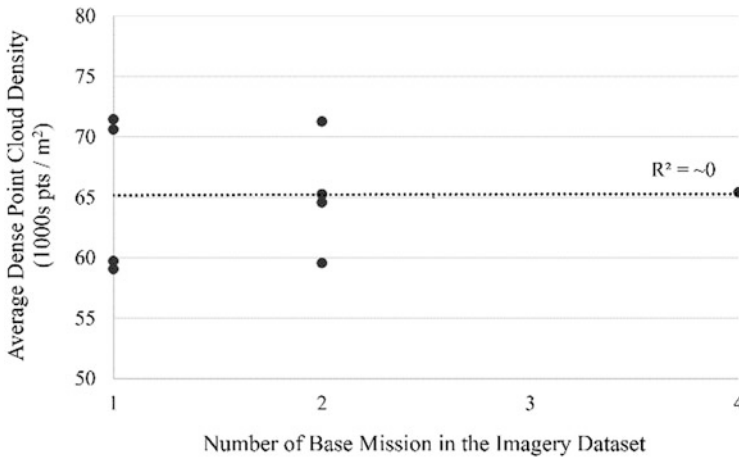


Fig. 6.12 Average dense point cloud density for each imagery dataset in relation to the number of included base mission photosets. Dense point cloud density is in thousands of points/m²

matches during SfM processing. The poor image alignment leaves the datasets as unworkable or only partially covering the field site due to the resulting “holes” in the resulting SfM products. Our combined imagery datasets functionally increase the effective imagery overlap beyond 80%. However, as discussed below, the combined imagery datasets yield lower RMSE and MAE accuracies and require greater time in the field to acquire and significant increases in the time required to process the data.

Table 6.8 Average dense point cloud density (in points/ m^2) and required processing time (in hours) obtained from an average of the results for the six study sites

Imagery dataset	Average dense point cloud	
	Density	Processing time
NS Ortho	71,433	0.90
EW Ortho	70,595	0.91
NS Oblique	59,058	0.85
EW Oblique	59,712	1.41
Ortho Missions	71,261	4.13
Oblique Missions	59,553	3.21
NS Missions	65,247	3.68
EW Missions	64,574	3.86
All Missions	65,412	20.68

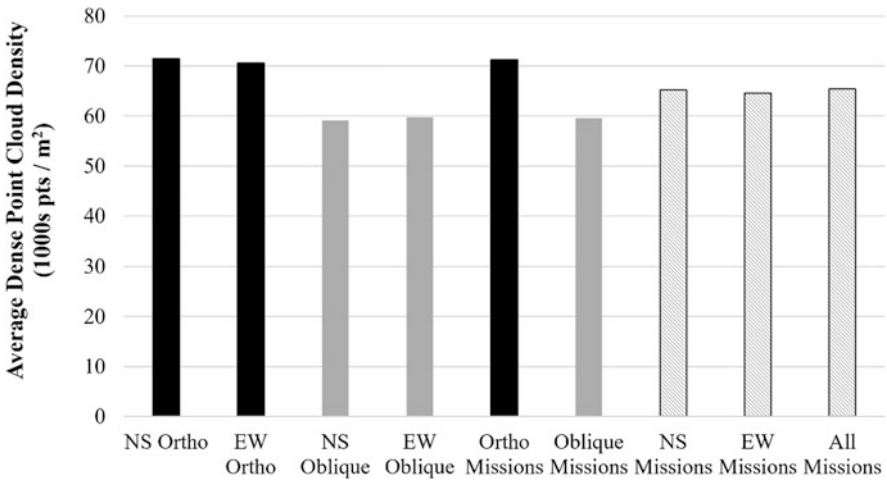


Fig. 6.13 The average dense point cloud density is consistently higher for missions with orthogonal imagery (solid black bars). Oblique camera angles yield slightly lower point densities (solid gray bars) while imagery datasets with both orthogonal and oblique imagery (bars with diagonal pattern) have intermediate densities

Thus, our base mission designs each represent a minimum image dataset adequate for SfM in the terrain of the study sites.

The imagery dataset that yielded the highest overall CP accuracy and shortest relative processing times was the *NS Oblique* imagery set. The base mission imagery datasets yielded accuracy levels similar to, or better than, the combined imagery sets. The dense point cloud processing times were also significantly shorter for base mission imagery sets, with differences ranging from 3.5x to 20x longer for the combined imagery datasets (Fig. 6.11). These results confirm the suggestions by other authors that excess images provide little benefit in terms SfM product accuracy (Fonstad et al. 2013; James and Robson 2012; Micheletti et al. 2015a, b; Westoby et al. 2012). It is worth noting that after we completed our analysis, subsequent versions of Metashape have increased the algorithmic efficiency of the alignment

and dense cloud generation processes. These updates improve the absolute processing times of datasets, but it is unclear how they would affect the relative differences in processing times reported above.

Complex terrains with heavy tree canopy, the presence of shadows, and poor visual texture pose challenges for SfM photogrammetry. Additional image overlap obtained through combinations of base imagery datasets provides additional camera perspectives and key points that could improve the products and accuracy of the SfM photogrammetric processing. However, our results do not support this hypothesis. Indeed, we find that the additional imagery resulted in higher average errors in the DSMs. One possible reason for this result may be that the additional imagery introduced conflicting estimates of camera orientations that led to greater uncertainties in key point locations. During bundle adjustment these uncertainties result in higher tie point residuals that cause improper parameter adjustments that contribute to surface error (James et al. 2017).

Gradual selection procedures should help to reduce instances of high tie point residual error, but our results suggest that some of the additional uncertainty passes through the filtering process and ultimately is propagated into the derived DSM. The systematic error associated with the *All Missions* and *NS Missions* imagery sets in the profile lines comparison is a potential example of this (Fig. 6.8). The base mission imagery datasets did not individually display significant systematic error in the profile, yet, when that imagery was combined in the *NS Missions* and *All Missions* imagery datasets, they did. Most of the higher relative RMSE and MAE total error values in the combined imagery sets seem to be due to higher Z error relative to the base mission imagery datasets (Fig. 6.6). The systematic error resulted in elevation inaccuracies, while the planimetric accuracy was generally less affected.

Another potential reason for the higher error values in the combined imagery datasets could be due to small differences between the base mission imagery datasets particularly in ambient light, shadows, and similar factors. For example, slight changes in the position of shadows between missions could lead to uncertainties in the estimation of key points, which would translate into errors in tie point matching and reconstruction of camera orientation. Though the base mission flights were flown in back-to-back sequence over relatively short time periods for each field site (Table 6.2), there are certainly some differences. However, this is not an effect unique to our methodology. Any sUAS imagery acquisition campaign, regardless of mission design, occurs over a period of time in which ambient conditions are likely to change between the start and finish of the flights. To the extent that this explains a portion of the additional error in the combined imagery datasets, it is an inherent constraint posed by any campaign that attempts to acquire more than the minimum requirement of imagery. A future opportunity exists to tease apart the effect of inter- and intra-mission ambient changes across the field site by using multiple sUAS to simultaneously acquire imagery for a site using varying mission designs.

Our comparison of the profiles extracted from the various mission DSMs is inherently constrained by the lack of a ground-surveyed profile to use as an objective reference. However, our analysis nonetheless demonstrates the relative magnitude and distribution of variation between the various mission profiles. The profiles

display a similar shape that captures the overall trend in elevation across the profile line (Fig. 6.8a). However, there are differences in the magnitude of the elevation changes across the profile. Variations in the residual values of all imagery datasets are apparent in Fig. 6.8 at profile distances greater than 32 m where the profile line intersected woody debris alongside the channel. A smaller variation is seen in the stream bed where approximately 15 cm of shallow water was present. The greatest residuals are in the *NS Missions* and *All Missions* imagery datasets (Fig. 6.8b). The residuals for these datasets have a positive slope indicating a systematic divergence in elevation with distance across the profile. This may be evidence of the doming effect in those datasets (James and Robson 2012, 2014).

The *NS Oblique* base mission image dataset yielded the least RMSE and MAE error of the various mission designs. However, especially among the base mission designs, there were only small and probably insignificant differences in most of the error ranges (Fig. 6.6). Unsurprisingly, camera orientation (east-west vs. north-south) seemed to have a minimal effect on the accuracy of the base imagery sets. When comparing the orthogonal and oblique imagery datasets, the oblique imagery consistently yielded less error than the similar orthogonal mission design (Fig. 6.6). The *All Missions* imagery set yielded total RMSE and MAE errors similar to the *Oblique Missions* imagery set; however, the *All Missions* data acquisition required significantly longer field and processing times. These results suggest that the base missions were the most efficient in terms of yielding higher accuracy DSMs with the minimum time required in the field and for SfM processing. Furthermore, oblique imagery may provide slight benefits over orthogonal imagery, especially with respect to elevation errors.

There appears to be no significant difference in dense point cloud density or processing time based on flight path orientation (Fig. 6.13 and Table 6.8). In comparison, camera angle may have a small effect. The oblique imagery datasets produced dense point clouds with the lowest point densities (Table 6.8). However, the greater quantity of images in the combined imagery datasets had no effect on the dense point cloud density but resulted in a non-linear increase in the required processing times. In summary, there is no correlation between point cloud density and the accuracy of the final DSMs. As such, the base mission designs are optimal in terms of the time and effort required in comparison to the accuracy of the final DSM.

Extreme events, such as the flooding we studied in the Ozarks, are occurring with increasing regularity (Mallakpour and Villarini 2015). Imagery datasets such as ours may be of value to future studies that investigate the long-term impacts of the April 2017 floods or as a point of comparison for evaluating the effects of future floods. Toward this end, another consequence of our results speaks to the issue of archiving sUAS imagery for future studies. Although the question of how to archive and share sUAS imagery for future investigations is beyond the scope of this work, our results suggest that the resources necessary for archival can be more efficiently used by not over-collecting and archiving unnecessary imagery that does not improve the accuracy of the SfM products.

6.5 Summary

Our investigation was part of a broader project tasked with the rapid post-flood assessment of the North Fork of the White River after major flooding in April 2017. Our specific role in this investigation was to provide high-resolution DSMs and orthoimagery that provided basemaps for analysis of the flood impacts on the riparian corridor and the accumulation, distribution, and size of woody debris within the floodplain. The terrain in which our field sites are located is typical of the Ozark Plateau and more generally representative of the steep, hilly, forested landscapes in many temperate mid-latitude regions. When planning our imagery acquisition, we faced uncertainty about the most efficient mission designs for obtaining the necessary data to produce accurate DSMs and orthoimages via SfM photogrammetry. Our conclusions suggest that relatively simple mission designs utilizing “lawnmower-type” flight paths to collect slightly oblique imagery with approximately 80% longitudinal and transverse overlap yield maximum accuracy in the SfM products while reducing field acquisition time and processing requirements. In contrast, mission designs that capture imagery using multiple flight path orientations or camera angles yield larger datasets that require greater field and processing efforts but yield no benefit in terms of DSM and orthoimagery accuracy.

Future research exploring this topic could pursue several possible questions. This investigation focused on “lawnmower-pattern” mission designs, which remain the most commonly employed approach in sUAS image acquisition (Sanz-Ablanedo et al. 2020). Sanz-Ablanedo et al. (2020) found that point-of-interest mission designs, where the camera remains obliquely oriented toward the center of the study area, yielded significantly reduced doming errors in comparison to other flight patterns. However, their study was based on imagery of a flat parking lot, and it is unclear how effective such an approach would be on a linear corridor, such as a stream channel, or in areas with dense canopy and steep topographic relief. Additionally, our investigation did not explore the effects of image overlap or various camera angles. However, oblique imagery is known to reduce doming errors and produce more accurate three-dimensional SfM products (as documented in our results and elsewhere such as Rossi et al. 2017, and Sanz-Ablanedo et al. 2020). Reducing image overlap, which may be feasible in terrains with less dense canopy, would result in fewer images per dataset and reduce processing demands. Understanding how different camera angles or image overlap affects the accuracy of SfM products would allow these mission parameters to be optimized for accuracy and minimum processing requirements.

Acknowledgments This research was supported by the National Science Foundation under Grant No. 1748816. The authors would also like to express appreciation to the US National Forest Service for facilitating access to the field sites and to a number of MSU students for assistance with the field work.

References

- Agüera-Vega F, Carvajal-Ramírez F, Martínez-Carricondo P (2017) Assessment of photogrammetric mapping accuracy based on variation ground control points number using unmanned aerial vehicle. *Measurement* 98:221–227
- Bemis SP, Micklethwaite S, Turner D, James MR, Akciz S, Thiele ST, Bangash HA (2014) Ground-based and UAV-based photogrammetry: a multi-scale, high-resolution mapping tool for structural geology and paleoseismology. *J Struct Geol* 69:163–178
- Bendix J, Pavlowsky RT, Martin DJ, Dogwiler TJ (2018) Impact of an extreme flood on riparian forests in the Missouri Ozarks: American Association of Geographers Annual Meeting, New Orleans, LA
- Carrivick J, Smith M, Quincey D (2016) *Structure from motion in the geosciences: analytical methods in earth and environmental science series*. Blackwell, Wiley, 208 p
- Chien H-J, Geng H, Klette R (2015) Bundle adjustment with implicit structure modeling using a direct linear transform. In: Azzopardi G, Petkov N (eds) *Computer analysis of images and patterns, Lecture notes in computer science*. Springer International Publishing, Cham, pp 411–422
- Colomina I, Molina P (2014) Unmanned aerial systems for photogrammetry and remote sensing: a review. *ISPRS J Photogramm Remote Sens* 92:79–97
- Dietrich J (2016) Riverscape mapping with helicopter-based structure-from-motion photogrammetry. *Geomorphology* 252:144–157
- Eltner A, Kaiser A, Castillo C, Rock G, Neugirg F, Abellán A (2016) Image-based surface reconstruction in geomorphometry—merits, limits and developments. *Earth Surf Dyn* 4(2): 359–389
- Fonstad MA, Dietrich JT, Courville BC, Jensen JL, Carbonneau PE (2013) Topographic structure from motion: a new development in photogrammetric measurement. *Earth Surf Process Landf* 38(4):421–430
- Gonçalves JA, Henriques R (2015) UAV photogrammetry for topographic monitoring of coastal areas. *ISPRS J Photogramm Remote Sens* 104:101–111
- Harwin S, Lucieer A (2012) Assessing the accuracy of georeferenced point clouds produced via multi-view stereopsis from unmanned aerial vehicle (UAV) imagery. *Remote Sens* 4(6): 1573–1599
- Heimann DC, Holmes Jr RR, Harris TE (2018) Flooding in the southern Midwestern United States, April–may 2017: Open-File Report 2018–1004, 46 p
- Helm C, Hassan MA, Reid D (2020) Characterization of morphological units in a small, forested stream using close-range remotely piloted aircraft imagery. *Earth Surf Dyn* 8:913–929
- Hess JW (2019) Stream Channel morphology and riparian Forest response to a 500-year flood in the Missouri Ozarks. Missouri State University, 89 p
- Hostens DS (2019) Determining the effect of Mission design and point cloud filtering on the quality and accuracy of SfM photogrammetric products derived from sUAS imagery [M.S. thesis]. Missouri State University, 108 p
- James MR, Robson S (2012) Straightforward reconstruction of 3D surfaces and topography with a camera: accuracy and geoscience application. *J Geophys Res Earth* 117(F3):F03017
- James MR, Robson S (2014) Mitigating systematic error in topographic models derived from UAV and ground-based image networks. *Earth Surf Process Landf* 39(10):1413–1420
- James MR, Varley N (2012) Identification of structural controls in an active lava dome with high resolution DEMs: Volcán de Colima, Mexico. *Geophys Res Lett* 39(22):L22303
- James MR, Robson S, d’Oleire-Oltmanns S, Niethammer U (2017) Optimising UAV topographic surveys processed with structure-from-motion: ground control quality, quantity and bundle adjustment. *Geomorphology* 280:51–66
- Javernick L, Brasington J, Caruso B (2014) Modeling the topography of shallow braided rivers using structure-from-motion photogrammetry. *Geomorphology* 213:166–182

- Küing O, Strecha C, Beyeler A, Zufferey JC, Floreano D, Fua P, Gervais F (2011) The accuracy of automatic photogrammetric techniques on ultra-light UAV imagery. In: UAV-g 2011-unmanned aerial vehicle in geomatics (No. EPFL-CONF-168806)
- Lowe DG (1999) Object recognition from local scale-invariant features. In: Computer vision, 1999. The proceedings of the seventh IEEE international conference on, vol 2, pp 1150–1157
- Mallakpour I, Villarini G (2015) The changing nature of flooding across the Central United States. *Nat Clim Chang* 5:250–254
- Mancini F, Dubbini M, Gattelli M, Stecchi F, Fabbri S, Gabbianelli G (2013) Using unmanned aerial vehicles (UAV) for high-resolution reconstruction of topography: the structure from motion approach on coastal environments. *Remote Sens* 5:6880–6898
- Martin DJ, Pavlowsky RT, Bournival L, Bendix J, Dogwiler T (2020) Impacts of a large flood (~1,000 yr) on in-channel wood loads in the North Fork River Basin, Ozark Mountains, Missouri. Annual meeting of the American Association of Geographers, Seattle, Washington (Virtual)
- Mian O, Lutes J, Lipa G, Hutton JJ, Gavelle E, Borghini S (2015) Direct georeferencing on small unmanned aerial platforms for improved reliability and accuracy of mapping without the need for ground control points. *Int Arch Photogramm Remote Sens Spat Inf Sci* 40(1):397
- Mian O, Lutes J, Lipa G, Hutton JJ, Gavelle E, Borghini S (2016) Accuracy assessment of direct georeferencing for photogrammetric applications on small unmanned aerial platforms. *Int Arch Photogramm Remote Sens Spat Inf Sci* 40:77 p
- Micheletti N, Chandler JH, Lane SN (2015a) Section 2.2.2. Structure from motion (SfM) photogrammetry. In: Cook SJ, Clarke LE, Nield JM (eds) *Geomorphological techniques*, Online edn. British Society for Geomorphology, London, pp 1–12
- Micheletti N, Chandler JH, Lane SN (2015b) Investigating the geomorphological potential of freely available and accessible structure-from-motion photogrammetry using a smartphone. *Earth Surf Process Landf* 40(4):473–486
- Miller SM, Wilkerson Jr TF (2001) North Fork River watershed inventory and assessment. Missouri Department of Conservation, 216 p
- Moore Z, Wright D, Schinstock DE, Lewis C (2009) Comparison of bundle adjustment formulations. In: American Society for Photogrammetry and remote sensing annual conference, March 9–13, 2009, vol 2. The American Society for Photogrammetry and Remote Sensing, Baltimore, MD, pp 567–575
- Noble T, Matthews N (2017) Unmanned aircraft systems data post-processing structure-from-motion photogrammetry: section 1–digital single-lens reflex (DSLR) imagery. USGS National UAS Project Office, 21 p
- Raeker G, Moser WK, Butler BJ, Fleming J, Gormanson DD, Hansen MH, Kurtz CM, Miles PD, Morris M, Treiman TB (2011) Missouri's forests 2008, Northern Research Station Resource Bulletin NRS-54. U.S. Department of Agriculture, Forest Service, 55 p
- Rango A, Laliberte A, Herrick JE, Winters C, Havstad K, Steele C, Browning D (2009) Unmanned aerial vehicle-based remote sensing for rangeland assessment, monitoring, and management. *J Appl Remote Sens* 3(1):033542
- Remondino F, Barazzetti L, Nex F, Scaioni M, Sarazzi D (2011) UAV photogrammetry for mapping and 3d modeling—current status and future perspectives. *Int Arch Photogramm Remote Sens Spat Inf Sci* 38(1):C22
- Rock G, Ries JB, Udelhoven T (2011) Sensitivity analysis of UAV-photogrammetry for creating digital elevation models (DEM). In: Proceedings of conference on unmanned aerial vehicle in geomatics
- Rossi P, Mancini F, Dubbini M, Mazzone F, Capra A (2017) Combining nadir and oblique UAV imagery to reconstruct quarry topography: methodology and feasibility analysis. *Euro J Remote Sens* 50:211–221
- Sanz-Ablanedo E, Chandler J, Rodríguez-Pérez J, Ordóñez C (2018) Accuracy of unmanned aerial vehicle (UAV) and SfM photogrammetry survey as a function of the number and location of ground control points used. *Remote Sens* 10(10):1606

- Sanz-Ablanedo E, Chandler JH, Ballesteros-Pérez P, Rodríguez-Pérez JR (2020) Reducing systematic dome errors in digital elevation models through better UAV flight design. *Earth Surf Process Landf* 45(9):2134–2147
- Štroner M, Urban R, Reindl T, Seidl J, Brouček J (2020) Evaluation of the Georeferencing accuracy of a photogrammetric model using a Quadcopter with onboard GNSS RTK. *Sensors* 20:2318
- Vallet J, Panissod F, Strecha C, Tracol M (2012) Photogrammetric performance of an ultra light weight swinglet “UAV”. *Int Arch Photogramm Remote Sens Spat Inf Sci XXXVIII-1/C22:253–258*. <https://doi.org/10.5194/isprsarchives-XXXVIII-1-C22-253-2011>
- Vericat D, Muñoz-Narciso E, Béjar M, Ramos-Madrona E (2016) Case study: multitemporal reach-scale topographic models in a wandering river-uncertainties and opportunities. In: Carrivick JL, Smith MW, Quincey DJ (eds) *Structure from motion in the geosciences. New analytical methods in the earth environmental science*. Wiley-Blackwell, p 208
- Wackrow R, Chandler JH (2008) A convergent image configuration for DEM extraction that minimises the systematic effects caused by an inaccurate lens model. *Photogramm Rec* 23(121):6–18
- Wackrow R, Chandler JH (2011) Minimising systematic error surfaces in digital elevation models using oblique convergent imagery. *Photogramm Rec* 26(133):16–31
- Westoby MJ, Brasington J, Glasser NF, Hambrey MJ, Reynolds JM (2012) ‘Structure-from-motion’ photogrammetry: a low-cost, effective tool for geoscience applications. *Geomorphology* 179:300–314
- Wheaton JM, Brasington J, Darby SE, Sear DA (2010) Accounting for uncertainty in DEMs from repeat topographic surveys: improved sediment budgets. *Earth Surf Process Landf J Br Geomorphol Res Group* 35(2):136–156
- Willmott C, Matsuura K (2005) Advantages of the mean absolute error (MAE) over the root mean square error (RMSE) in assessing average model performance. *Clim Res* 30:79–82
- Woodget AS, Carbonneau PE, Visser F, Maddock IP (2015) Quantifying submerged fluvial topography using hyperspatial resolution UAS imagery and structure from motion photogrammetry. *Earth Surf Process Landf* 40(1):47–64

Chapter 7

Drones and Poles for Low-Elevation Oil and Gas Environmental Surface Inspections



Chris W. Baynard, Robert D. Richardson, and Nicolas W. Baynard

Abstract This chapter highlights how small unoccupied aerial vehicles (sUAVs), or drones, and pole aerial photography (PAP) can provide actionable information for regulators and stakeholders on the state or condition of oil and gas wellpads on US federal grasslands. We believe that imagery-derived datasets such as orthomosaics, vegetation, elevation, and 3D models, as well as 360° drone video and very low-elevation pole aerial video, can help regulators such as the US Forest Service (USFS), as well as industry, identify major surface compliance issues from their office computers and therefore enhance the quantity and quality of site visits. Furthermore, we anticipated that these datasets would prove most useful when determining if remediation efforts met compliance targets during the 5-year reclamation phase, where abandoned wellpads are returned to a natural state. Findings suggest that 70% of the annual inspection can be conducted utilizing these datasets. For reclamation sites, they had broad applications. Though vegetation cover conditions could be detected, it was difficult to distinguish the grass seed mix, weeds, and invasive plants, as well as the condition of fences from visual analysis. Overall, access to and interpretation of these data can speed up inspections, increase efficiency, greatly enhance field visits, and target locations that indeed require additional field reviews and appropriate responses. We conclude that while these methods can improve current Forest Service field inspections, perhaps operators benefit more, since they can more readily adopt the latest aerial surveillance methods to monitor surface effects as they occur. This allows them to address areas of concern

C. W. Baynard (✉)

Department of Economics and Geography, University of North Florida, Jacksonville, FL, USA
e-mail: cbaynard@unf.edu

R. D. Richardson

College of Computing, Engineering and Construction, University of North Florida,
Jacksonville, FL, USA
e-mail: robert.richardson@unf.edu

N. W. Baynard

College of Liberal Arts and Sciences, Florida State College at Jacksonville,
Jacksonville, FL, USA
e-mail: S3547632@students.fscj.edu

prior to and after inspections, thus better coordinating planning and actions with the USFS regulators throughout the life cycle of the well. Hence, operators can save time and money and reduce legal exposure while enhancing communication with regulators.

Keywords Oil and gas · Energy · Grasslands · Forest service · Drones · Pole aerial photography · US West · North Dakota

7.1 Introduction

Surface effects associated with oil and gas production on western federal grasslands are monitored by the USDA Forest Service (FS) and include two main types of reviews, annual active well compliance inspections and 5-year final reclamation site inspections. The annual inspection list consists of about 40 items that focus on the condition of infrastructure features located on the wellpad, such as signs, tanks, fences, stairs, and cattle guards. It also includes environmental features such as erosion, access road conditions, weeds, vegetation, and catch basins (USDA Forest Service Dakota Prairie Grasslands 2019a). The 5-year reclamation forms contain five categories: erosion stability, revegetation and plant vigor, fence condition, reclamation status/time frames, and follow-up actions (USDA Forest Service Dakota Prairie 2019b). See [Appendix](#).

A wellpad is a large, often rectangular cleared area of land, though the shape varies, that contains the O&G infrastructure features needed to extract hydrocarbons, such as the wells, pumps, and storage tanks (see examples in [Fig. 7.8](#)). Out west, in the Little Missouri National Grasslands of western North Dakota, the FS allows oil and gas drilling and production and is the regulator overseeing surface inspections. A major challenge is that a small number of personnel oversee large tracts of land and are required to visit each active wellpad at least once a year. On the other hand, since final reclamation sites take 5 years, annual inspections are not necessary.

To alleviate the pressure placed on staff who may have missed something during the inspection phase and to enhance procedures, we propose an aerial imagery acquisition process that utilizes small unoccupied aerial vehicles (sUAVs)¹, or drones, to capture imagery and video. In this case sUAVs refer to lightweight multirotor drones that can hover, take off, and land vertically and can be handled by one person (Botlink 2021).

We couple drone imagery acquisition with pole aerial video, adding a higher-than-eye-level perspective to enhance the data gathered via sUAVs. While the resulting imagery products cannot fully substitute for an onsite field inspection, we wanted to know if they would provide sufficient spatial information to detect most items on the inspection sheet. If so, this might speed up the number of inspections per visit and season, benefitting personal through reduced long drive times in remote

¹Throughout this chapter we use sUAV to represent small unoccupied aerial vehicles.

areas and decreased potential exposure to environmental hazards. The increased efficiency would allow FS inspectors to spend more time on locations with the most problems. We also anticipated that these methods would prove most useful when determining if remediation efforts met compliance targets during the reclamation phase, where abandoned wellpads are returned to a natural state.

Findings suggest these datasets allow regulators to identify up to 70% of items on the annual inspection form. For reclamation sites, the data had broad applications. Overall vegetation cover conditions could be detected; however, the datasets made it difficult to distinguish the grass seed mix, weeds, and invasive plants, as well as the condition of fences. This finer-grained approach is possible, with additional analysis, since the needed imagery is acquired during field visits. Identifying different types of vegetation from imagery goes beyond the visual analysis methods proposed here, but it is certainly possible through remote sensing techniques such as imagery classification, the use of vegetation indices, and machine learning.

We conclude that this data acquisition approach enhances FS service field inspections by creating robust time-series spatial datasets that can be reviewed as needed by various regulators to follow the life cycle of the wellpads. Furthermore, operators may benefit the most, since they can keep up with surface effects more quickly through regular data acquisition and therefore better coordinate their planning and actions with regulators. Additionally, by addressing areas of concern prior to and after inspections, industry can save time and money and, just as importantly, reduce legal exposure.

7.1.1 sUAVs for Oil and Gas Inspections

The use of drones and aerial imagery for oil and gas inspections has been growing over the last 10 years, whereby large energy companies are using them to improve data collection, investigate hazardous locations, enhance security, and conduct early warning detection (Al Amir and Al Marar 2018; Cho et al. 2015). A central mission is safety, given the large legal exposure and negative press coverage that industry faces when catastrophes lead to human injuries and death, environmental pollution, and damage.

The Deepwater Horizon accident that occurred in the Gulf of Mexico in 2010 was a catalyst for adopting sUAVs, and they were implemented soon after the accident. Prior to this large-scale spill, the use of sUAVs was not commonplace, but following this disaster they were increasingly “deployed to gain advanced intelligence on the behavior of the plume” (Nelson and Grubestic 2018). This included a blossoming citizen scientist movement to help stop the flow of oil, estimate the amount of the spill, and protect coastal resources (Lubchenco et al. 2012). In fact, this approach represents a transition from lay mapping to a broader and more inclusive data gathering system that helps detect environmental alterations (McCormick 2012).

Other applications of sUAVs include offshore platform inspections and live flare-stack examinations (both on- and off-shore) (Kridsada et al. 2016; Marinho et al. 2012). Moving from sUAVs, which are light and only require one operator, to large UAVs that require a team, Uninhabited Aerial Vehicle Synthetic Aperture Radar (UAVSAR) has been used on auto-piloted NASA airplanes (such as Gulfstream III) to study such oil spill effects on wetland and coastal environments in the Gulf of Mexico (JPL 2014). This equipment was actually “designed to be operable on an uninhabited aerial vehicle” (Liu et al. 2011). Researchers such as Dabbiru et al. (2015) applied fusion techniques on UAVSAR data and hyperspectral imagery from the Airborne Visible/Infrared Imaging Spectrometer (AVIRIS) to classify coastal vegetation affected by oil spills. Meanwhile, Liu et al. (2011) used these data to test effective approaches for detecting oil spills related to this accident.

While oil and gas pipelines create a vast network on- and offshore (throughout the world), onshore the USA has 4.2 million kilometers of pipelines, many above ground (US DOT PHMSA 2018). Naturally, these require inspections and traditionally involve “regular patrols via foot, vehicle and air, using small fixed-wing aircraft and helicopters” (Hausmann et al. 2005). Given the vast array of global pipeline networks, spills occur due to negligence, age, lack of maintenance, natural hazards, accidents, and sabotage, which can lead to broad environmental damages, health problems and death, large economic losses, and even disruptions to international energy markets (Gómez and Green 2017; Lustenberger et al. 2019). Kheraj (2020) argues that onshore pipeline spills are endemic because these systems were mainly built for economic efficiency, not environmental protection. Therefore, detecting leaks as soon as possible is paramount, and the ability to customize larger UAVs with distinct sensors and fly as often as needed has demonstrated their value in pipeline inspections and in many areas. After all, UAVs excel in “their ability to cover large areas at a fixed altitude and speed under a wide range of wind and weather conditions” (Casana et al. 2014).

The advent of prosumer sUAVs combined with photogrammetry software designed to process this imagery has led to increased applications for site inspections in various contexts and settings. This now includes using remote inspection workflows to record site conditions for prioritizing response teams during a disaster and chronicling the entire construction process to render digital site replicas (DroneDeploy 2021a). Therefore O&G field inspections using in situ remote sensing techniques are timelier than ever.

In this chapter, we are interested in the application of sUAVs and pole aerial video for onshore surface inspections of wellpads located on federal grasslands in the US West. They are simple to deploy, are cost-effective, and produce actionable data. A key objective is to provide data for a visual analysis approach, since it mirrors the visual surface inspection conducted by FS personnel. This tactic also keeps it accessible to a wide range of stakeholders and citizen scientists interested in land management who may not possess advanced geospatial training.

7.1.2 Surface Effects of Onshore Oil and Gas Production Activities

Oil and gas exploration and production activities can create extensive and permanent surface changes related to land clearing and operations. This includes the removal of soil and vegetation to construct wellpads, the often-rectangular flat area where extraction operations take place, as well as the building of roads and infrastructure features (Marcellus Shale Coalition 2012; Resolve 2021; Weidner 2017; Colorado Oil and Gas Conservation Commission n.d.; Baynard et al. 2017); see Fig. 7.8 for examples. These activities contribute to landscape fragmentation (Londe et al. 2019), soil loss and degradation (Minnick and Alward 2015), and increased soil toxicity and alterations to the landscape hydrology (Di Stéfano et al. 2020).

Noise from road and pipeline construction as well as drilling operations can lead to changes in wildlife behavior, such as avoidance of sites and nearby roads; shifting of habitat use to less suitable areas (Green et al. 2017; Thompson et al. 2015; Londe et al. 2019), especially during migration (Jakes et al. 2020); reduction in nesting success of some bird species (Bernath-Plaisted and Koper 2016); lower types diversity; oil pollution; and the introduction of invasive species (Olive 2018; Nasen et al. 2011). Therefore, monitoring these actions closely is important for early detection of potential ecological problems and for appropriate responses.

7.1.3 Wellpads

In this study, wellpads are the unit of analysis. Depending on the type of resource (oil or gas), the age and size of the wellpad, and terrain characteristics, one can find some or all of these features: pump(s), compressor, storage tanks for oil and produced water,² pipelines, flares and flare pits, natural gas tanks, and waste pits (see Fig. 7.1).

When wellpads are first built, a larger area of land is cleared to accommodate heavy equipment that can navigate the area and provide room for storing supplies. Once the wellpad is established, the size is reduced to allow production operations to continue, and the unused part of the wellpad can revegetate (USDA Forest Service 2021a; CSUR n.d.). Finally, once a well is abandoned or retired on federal grasslands, it is supposed to be returned to 70% of the original way it appeared in the landscape (USDA Forest Service Dakota Prairie Grasslands 2019b). This usually occurs within 5–7 years of seeding and “achieving a minimum of three consecutive growing season(s) without disturbance and/or damage” (USDA Forest Service Dakota Prairie Grasslands 2019b). The US Forest Service (FS) conducts surface inspections and approves the decommissioning of these sites.

²Produced water refers to the water, often brine, that comes out of the ground when oil is extracted. This must be separated from the oil and stored either in storage pits constructed onsite or in storage containers until the contents are trucked away to a treatment facility.

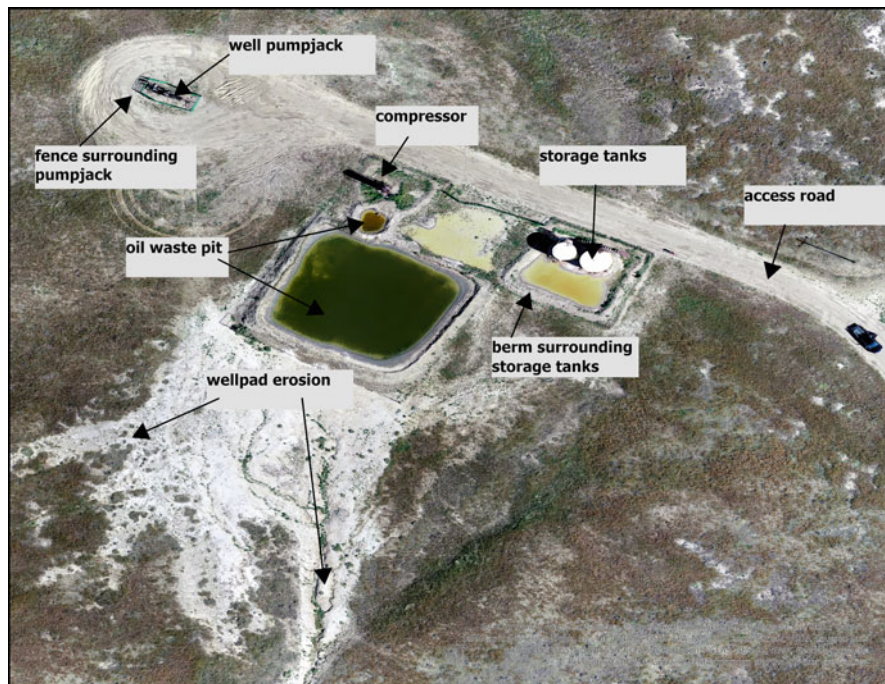


Fig. 7.1 Example of a grassland oil wellpad with associated infrastructure features

Personnel must travel to each active wellpad at least once per year and conduct an environmental surface inspection which includes checking 40 items on a form, taking notes, and capturing still digital photographs. The form includes inspection items, area of operations, facilities equipment, flare pits, oil waste pits, waste (trash), and roads (see [Appendix](#)). Meanwhile, abandoned and plugged wells which are being reclaimed require fewer inspections, given the time frame it takes for these sites to recuperate.

Inspection items on the 5-year reclamation phase list include:

- Access route condition and percent vegetation cover.
- Pad area condition and percent vegetation cover.
- Bare spots.
- Plant vigor.
- Representative seed mixture.
- Noxious weeds, invasive plants.
- Reserve pit condition.
- Closed gate.
- Fence condition and signs of cattle within fenced areas.

Identifying all these items is time-consuming, especially in large remote areas such as North Dakota. This exposes personnel to long drives as well as potential

hazards such as the presence of hydrogen sulfide gas (H_2S), a toxic and potentially fatal gas that is considered the primary chemical hazard of O&G production (Doujaiji and Al-Tawfiq 2010; Seaman 2017).

To supplement these field inspections, we propose the use of sUAVs for two main reasons. First, sUAVs provide updated imagery, showing the *current* situation on the ground. This contrasts with outdated imagery provided in image services like Google Earth, ESRI's ArcGIS Pro Imagery base map, and Bing Maps. While more current (and free) satellite imagery and air photos are accessible, the spatial resolution (the size of the pixel in reference to the ground) is often too coarse for this type of inspection. Examples include Landsat (with 30 m resolution) and Sentinel data (with up to 10 m resolution). The NAIP program (National Agricultural Imagery Program—part of the USDA) acquires aerial imagery (via planes) during the agricultural seasons in the continental US every 3 years (USDA 2021). Even though recent imagery has a high resolution of 60 cm in our North Dakota study area, the most current imagery dates to 2018 (USDA 2019a) and therefore is not up-to-date.

The second reason for acquiring imagery is that very high spatial resolution can be achieved by a field-quality sUAV, such as the DJI Phantom 4 Pro V2 that we utilized. The camera sensor has a 1-inch complementary metal oxide semiconductor (CMOS) capturing 20-megapixel images (DJI 2021), which, depending on the altitude flown, produced as high as 1 cm spatial resolution orthoimagery (see Fig. 7.2).

7.2 Methods

7.2.1 Study Area and Site Selection

The study area includes 14 oil and gas wellpad locations in North Dakota's Little Missouri National Grasslands (LMNG) visited during August 2019 (see Fig. 7.3). Located in western North Dakota, these are the largest grasslands in the USA and are managed by the Forest Service (FS) as part of the Dakota Prairie Grasslands (USDA Forest Service 2021b). The terrain is rugged and studded by high buttes, or badlands, which are soft sedimentary formations that easily erode (National Park Service 2020; USDA Forest Service 2021b). This mixed grass prairie contains short and long grasses and consists of a mosaic of federal, state, and private land ownership (USDA Forest Service 2021c). Land and resource management activities here support recreation, wildlife habitat, grazing, and mineral development (USDA Forest Service 2021c).

The subsurface in this region forms part of the Williston Basin, a large structural and sedimentary basin containing rich oil and gas deposits covering several thousand square kilometers in the states of South Dakota, North Dakota, and Montana and the Canadian Provinces of Saskatchewan and Manitoba (North Dakota Geological Survey 1997). Much of the oil in this basin is located in North Dakota, which not



Fig. 7.2 Comparing the spatial resolution of NAIP imagery (60 cm) in the top half of the image to our sUAV imagery (1 cm) on Site 01

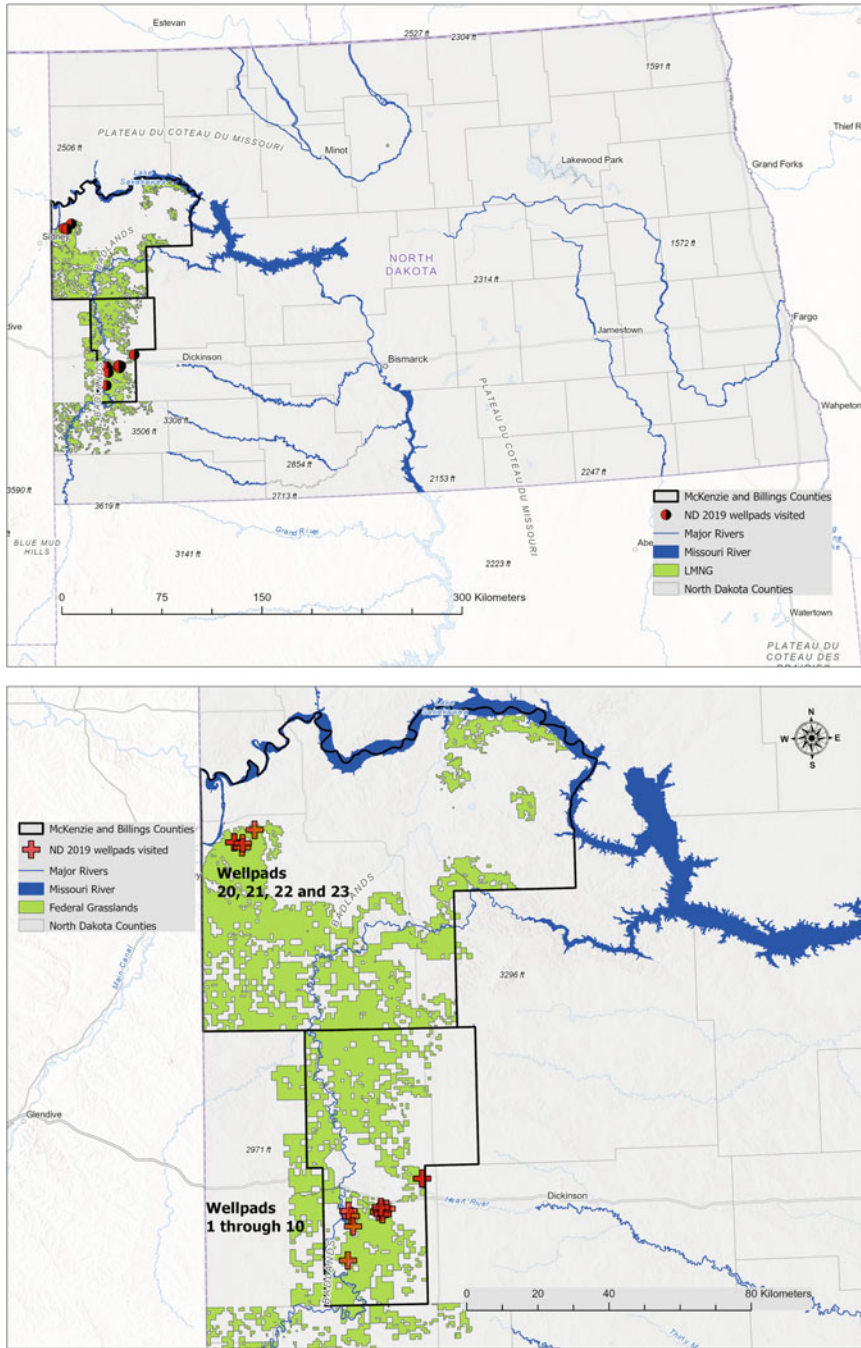


Fig. 7.3 The North Dakota study area, with the Little Missouri National Grasslands (LMNG) and wellpads visited, top. Close-up view of McKenzie and Billings Counties and the location of the wellpads and their number, at bottom

only has the second largest crude oil reserves but also ranks as the second top producer in the USA (after Texas) (EIA 2020). On the other hand, North Dakota is a small producer of natural gas, and most of it is associated with oil (EIA 2020). Even so, “natural gas production exceeds the state’s takeaway pipeline capacity, resulting in much of the gas being flared, or burned at the wellhead” (EIA 2020). In our study area, 13 out of 14 wellpads contained oil wells.

Site selection began with spatial data of oil well locations downloaded from the North Dakota’s Department of Mineral Resource’s Oil and Gas Division GIS Map Server (NDDMR 2019). Additional spatial datasets included national forests and federal grasslands extracted from US Department of Agriculture (USDA) Forest Service (FS) Geodata Clearinghouse (USDA 2019b). We utilized ArcGIS Desktop 9.4 software to map, extract, and analyze spatial datasets of oil and gas fields, well locations, and forest/grassland locations.³

Previous fieldwork efforts in Wyoming and Colorado federal grasslands helped us determine which places we would visit, which were then narrowed with help from FS personnel in North Dakota and the US Geological Survey (USGS) personnel in Wyoming and North Dakota. With their aid, we were able to identify wellpads that did not contain hydrogen sulfide wells (H_2S), as we clearly wanted to avoid this toxic and deadly gas.⁴ Additionally, we looked for well density, as that would offer multiple locations to choose from once we were in the field. Previous experience had shown us that just because the well data indicated a well was present, even when the imagery confirmed it, this was not always the case once arriving in the field. Wells get shut down or abandoned, fences get put up, and imagery is often outdated.

We focused on wells located on federal grasslands so that we would be visiting public lands and not trespass on private property. We still needed permission from the Dakota Prairie Grasslands FS and applied to conduct fieldwork in these locations. They were very helpful, and their main concern was determining if we were going to collect plant or soil samples. After clarifying that we were only gathering images and taking notes, and providing information regarding our previous oil and gas research in the US West, we received permission. Because we were examining surface features, we did not need to get permission from the Bureau of Land Management (BLM), who focus on subsurface land changes. Nevertheless, they also provided help and suggestions.

While we had a general idea of the wellpads we wanted to visit, we waited until we were out in the field to collect data at specific wellpads. There, we could determine if sites were indeed accessible. Sometimes there was a locked gate preventing entrance, workers might be onsite in which case we would visit another location, or we believed that H_2S might be present and therefore sought other wellpads (or flew the sUAV from a distance). Due to the density of oil wells in the area, we were able to find sufficient locations to visit and gather imagery. We chose a

³Subsequent analysis was conducted with ESRI’s ArcGIS Pro 2.7.1.

⁴We did wear H_2S meters while conducting fieldwork to alert us of potential gas as part of our safety protocol.

combination of wellpads that contained producing and abandoned wells in McKenzie and Billings counties to test our methods on two types of inspections, active and reclaimed.

7.2.2 *Flight Preparation*

Equipment used included a DJI Phantom 4 Pro V 2 quadcopter and GoPro 7 Hero Black action cameras with 3D printed GoPro bases mounted on extendable 3.7-m telescopic poles (DocaPole).

Prior to visiting the field, we used DroneDeploy's online software to draw out flight path plans for various wellpads and downloaded the underlying basemap to an iPad, which formed part of the flight controller. The flight path directs the sUAV's trip and looks like a grass cutting pattern, whereby it flies straight in one direction, turns around, and closely parallels the path it just flew (see Fig. 7.4). Due to the remoteness of these locations, we realized there would be no Wi-Fi or even cellular coverage when the iPad was connected to the sUAV controller. This meant the base map would appear as blank, without an image, if the imagery was not downloaded ahead of time. On occasions where we had to fly another location for which we did not have a base map, we drew out a flight path based on a best guess of our current location and the wellpad before us.

In the field, we followed FAA protocols and ran through the sUAV inspection checklist to ensure the drone was safe to fly and had a fully charged battery and the SD storage card (with sufficient storage) installed. Then, we connected either an iPad or an iPhone to the sUAV controller and tested the connection with the DJI software (DJI is the drone manufacturer). If the flight software called for a compass calibration, this was done next. Here, the visual observer (VO) stands about 5 m away from

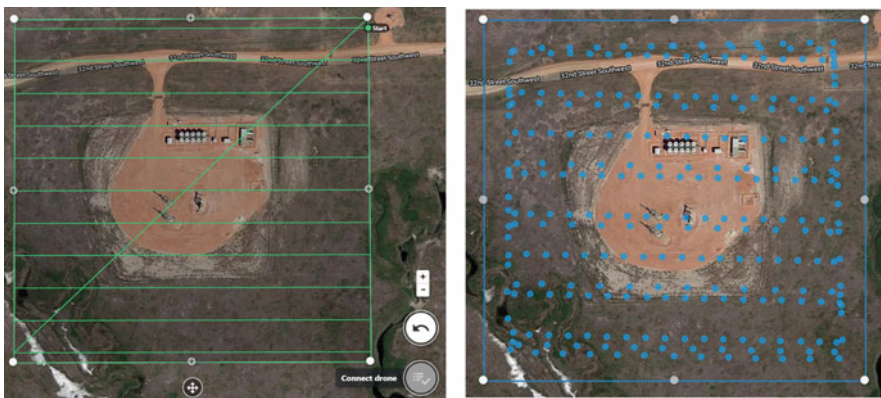


Fig. 7.4 Flight path plan for Site 03 on the left and the actual flight path image locations captured on the right and represented by blue dots

the pilot (or PIC, pilot in command) and holds the drone in front of him/her with arms stretched out and rotors pointing skyward. Next, the VO rotates his/her body counterclockwise, completing a couple of circles with the sUAV held in front. The horizontal calibration is followed by the vertical calibration. This time the process is repeated, with the VO holding the sUAV with the rotors facing the horizon and the camera looking at the ground.

Once the calibration was finished, we then placed the device on a flat surface (usually an access road—we were often alone in these remote locations), and the DJI software would run through a checklist. Once complete, we would open the DroneDeploy software and use the pre-planned flight path. If we needed to make changes, such as extending a leg of the flight or changing the altitude due a tall antenna on or near the wellpad, we would do so and then start the flight. Each flight path contained overlap segments at the perimeter to ensure proper coverage of each wellpad, an important step for constructing orthomosaics later.

Most trips occurred at about 61-m elevation, and depending on the size of the flight path, the sUAV would require one battery or two, and the camera would capture an image at nadir about every second (see blue dots in Fig. 7.4). In addition to relying on the VO, the controller showed the pilot where the drone was flying along the path. For the few sites where H₂S was a potential concern, we flew from a greater distance than normal, and given the open grasslands, we were able to maintain a line of sight. We also wore H₂S monitors on our hips.

Our field transportation vehicle was a full-sized four-wheel drive pickup truck, which proved handy for carrying and moving about our gear and equipment as needed and getting through some tough terrain. There we had drone batteries charging on a converter running from the truck battery.

We purposely did not use ground control points during field data collection. During previous field research, we found that they were not necessary for our objectives since we were not aiming for survey-level accuracy. The quality of the GPS sensor on our sUAV combined with DroneDeploy's ability to process the imagery produced quite satisfactory georeferenced results. Plus, our DroneDeploy license did not include ground control point verification.

On half of the wellpads visited (seven), once the flight path was completed, we would choose a center point in the wellpad and direct the drone to automatically cover a 360° oblique flight around it, this time recording video. This video supplemented the perspective available from a nadir orthomosaic and allows the user to later freeze, rewind, and fast-forward as needed (see Fig. 7.5).

After each flight we checked the sUAV, replaced the storage card, and then uploaded the files to our laptop to ensure a data backup. Given that most sites were not near each other, we used the drive time to the next location to accomplish this. Back at headquarters in the evening, we would upload the imagery to cloud storage for redundancy. We then sorted through the images of each particular flight and removed those that were too close to the takeoff and landing site or out of focus, though the latter was usually not an issue. Given the sunny daylight conditions and lack of trees (that might be moving in the wind), almost all the images were useful and included for cloud processing on DroneDeploy.



Fig. 7.5 A still shot from the 360° video captured with the sUAV, Site 23. Notice the oblique, rather than nadir (top down) perspective

7.2.3 Imagery Processing and Data Products

The wellpads studied ranged in size from 0.31 to 3.34 hectares or from less than half a FIFA soccer pitch to 4.7 soccer pitches (FIFA 2015/2016). This in turn affected the amount of time spent at one location gathering imagery, the number of batteries needed to run the sUAV, and therefore overall the number of wellpads we could visit during a given fieldwork day. The acquired images were processed with DroneDeploy photogrammetry software into four products: orthomosaics, vegetation health, elevation, and 3D models. Since our DJI Phantom 4 Pro V2 sUAV only had an RGB camera (that collects light in the red, green, and blue wavelengths), DroneDeploy applies a Visual Atmospheric Resistance Index (VARI) to create a vegetation health model (DroneDeploy 2021a, b, c). This index uses the visible spectral range bands (red, green, and blue) to estimate vegetation health and produce maps of greenness (Polinova et al. 2019).

Elevation datasets indicated in which direction a wellpad drains plus the surrounding topographic features. Meanwhile the 3D model allowed us to move about the landscape and get an idea of the relationship of infrastructure features to the wellpad and surrounding landscape.

A 360-degree video drone flight around the wellpad captured at an oblique angle provided a different perspective that could be paused and reviewed as needed. This sideways angle, as opposed to top down, provided a more cinematographic viewpoint that lent a 3D perspective to the scene. This permitted the viewer to see and detect landscape features from the surrounding terrain beyond the wellpad such as the location of a nearby creek that may be subject to runoff from the wellpad or a truck

driving by on the dirt access road, kicking up dust onto the grasslands on either side of the road.

For the pole aerial video, we utilized a GoPro 7 Black camera which is GPS enabled and attached it to the end of an extendable pole raised to about 4.5 m. The researcher then recorded video while walking the perimeter of the wellpad. Additional video was then captured by walking inside the wellpad (when possible), recording the installation and infrastructure features. The user could pause and focus on particular items of interest and had the flexibility of tilting the pole to get a close-up view, examine the top of a structure, or stretch over a fence, such as those surrounding an oil pit. Additionally, the video recorded sound, providing an auditory track of noise disturbance created by compressors, well pumps, and flares (that may cause avoidance behavior in wildlife). These sounds were not captured by the sUAV.

Together, these three datasets provide a robust record of the surface conditions of a given wellpad. We believed that knowing that these datasets will provide valuable information that can be later examined at the office, FS inspectors could potentially spend less time on each wellpad during field inspections while directing their attention to items that indeed require in-person assessment. This would also allow them to spend more time on wellpads that are clearly not in compliance, potentially saving time and money.

We also expected that these data would be especially useful in determining compliance for closed-down and abandoned sites. Here, operators as well as regulators would benefit from having as much spatial data as possible as the 5-year final reclamation site inspection approaches. The imagery information provided can help highlight compliance or problem areas that can (quickly) be addressed, thus allowing the abandonment process to be completed and the site returned to a natural state as determined by regulators.

7.2.4 Inspection Forms

The two main inspection forms the FS uses in the study area include the active well compliance inspection and 5-year final reclamation site inspection (USDA Forest Service Dakota Prairie Grasslands 2019a, b.) Different versions and variations of the annual well compliance form exist, but they tend to focus on the same 40 items (see [Appendix](#)), which can be grouped into seven classes:

- Inspection items
- Area of operations
- Facilities equipment
- Flare pits
- Oil waste pits
- Waste
- Roads

The fifteen inspection codes include the following:

O = OK	G = gone/missing	M = maintenance/repair	S = spills/leaks/drips
C = clean (up/out)	H = health and/or safety	N = noncompliance	U = unauthorized
D = dikes (ditches) inadequate	I = inadequate/not to specifications	P = paint or T = touch-up	W = waste (s) removal
E = excessive equipment	J = junk/junky	R = reclamation needs	

7.3 Findings

Our own analysis yielded the following results. For active wellpads, key compliance items that required detection due to environmental and safety risks include the following:

- Clear road access to site.
- Clean area of operations.
- Intact cattle guards and fences to keep people, cattle, and wildlife away from moving parts and toxic areas, such as oil waste pits and flare pits.
- Marked and legible operator and safety signs and windsock.
- Cages around the pumps and machinery.
- Spills at the wellhead, around the storage tanks and pipelines (when present).
- Berms around storage tanks and other equipment where spills need to be contained.
- Functioning flare pit ignitor.
- Tank battery condition.
- Drainage and erosion.

We found that all these items could be detected and inspected with one or more of the datasets. Regarding the flare, if it was not burning, we could not determine the condition of the ignitor.

For reclaimed wellpads, the key inspection items include the following:

- All facilities removed.
- Access route condition and percent vegetation cover.
- Pad area condition and percent vegetation cover.
- Bare spots.
- Plant vigor.
- Representative seed mixture.
- Noxious weeds, invasive plants.
- Reserve pit condition.
- Closed gate.
- Fence condition and signs of cattle within fenced areas.

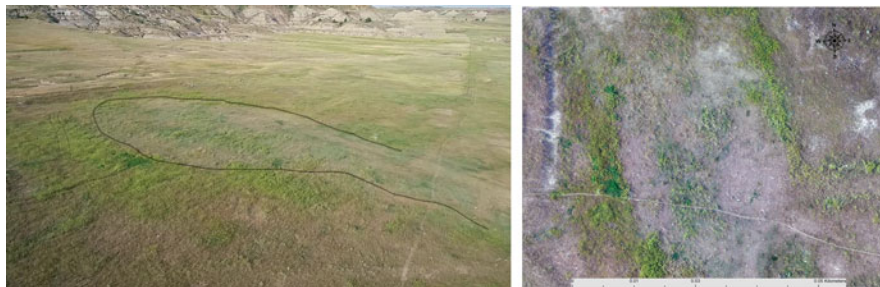


Fig. 7.6 Still shot taken from the 360° aerial video (left) for Site 05. The black outline marks the potential site of the abandoned wellpad. The image at right shows cleared ground from the orthomosaic

Inspections on these sites proved harder. Some of these wellpads were apparently abandoned and reclaimed more than 17 years ago, thus making it hard to inspect anything. However, Nasen et al. (2011) note that these effects can last more than 50 years after well site construction. To confirm, we compared the orthoimagery generated from our data collection to 2003 NAIP images and did not detect much of a difference for Sites 07 and 08, for example. Sites 05 and 09 were very hard to find, if at all. The 360° aerial video suggests a slight clearing in site 05, which can be seen in the ortho, but it is not certain (see Fig. 7.6).

Site 06 appeared to be recuperating well with seeded vegetation growing within its fenced area. Meanwhile the access road and wellpad on Site 04 had been scraped clean, awaiting seeding.

7.3.1 *Orthomosaics*

The entire still imagery dataset begins with the individual sUAV images captured and then processed into an orthomosaic, whereby geometric distortions, camera perspectives, distances, and elevation are corrected to form one large georeferenced image. When imagery is first captured, “it has perspective geometry that results in distortions that are unique to each image” (ESRI 2021). These distortions, or errors, are caused by the curvature of the Earth, instrumentation, and terrain displacement (ESRI 2021). Luckily, modern photogrammetry software used to process sUAV imagery, like the program DroneDeploy that we used, corrects these distortions to produce its imagery products.

These large mosaics provide the landscape-level imagery that allows visual inspection of the wellpads and surrounding area. Furthermore, the photogrammetry software also generates additional datasets such as elevation, vegetation, and 3D models. This information can be used to detect and measure the direct disturbance footprint of most wellpads, evidenced by the cleared dirt area comprising the sites. However, the indirect footprint can also be gleaned at times. For example, Nasen



Fig. 7.7 Minor fluid spill located behind the well pump on Site 01 in the shaded area at the bottom of the image

et al. (2011) found that indirect effects on grasslands wellpads extend 20–25 m beyond the direct disturbance footprint. This measure, therefore, can indicate how well the operator is managing the site, since ostensibly the disturbance should be kept to the wellpad itself and the surrounding area should contain planted grass or natural vegetation.

In general, it was possible to determine if oil spills were present on the wellpads. We did not find any, though at times ground discoloration at the wellhead or near compressor was discernible. They did not appear as a major oil spill but perhaps were fluid leaks from the compressor (see Fig. 7.7). Stairs and some infrastructure, such as the pump jack, were at times distorted in the orthomosaic.

Fences, often made of barbed wire, were hard to detect from the orthoimages due to the nadir view. Sometimes when the sun was shining on a particular section, the fence line could be made out. Wellpad identification signs and the windsock were impossible to see, much less read, particularly because of the camera nadir perspective. Figure 7.8 provides the general location as well as thumbnail images of the orthomosaics for all the study area sites.

7.3.2 *Elevation*

The elevation datasets proved particularly useful in three areas (see Fig. 7.9). One is to show which way the wellpad was draining, so that if erosion was present, it could

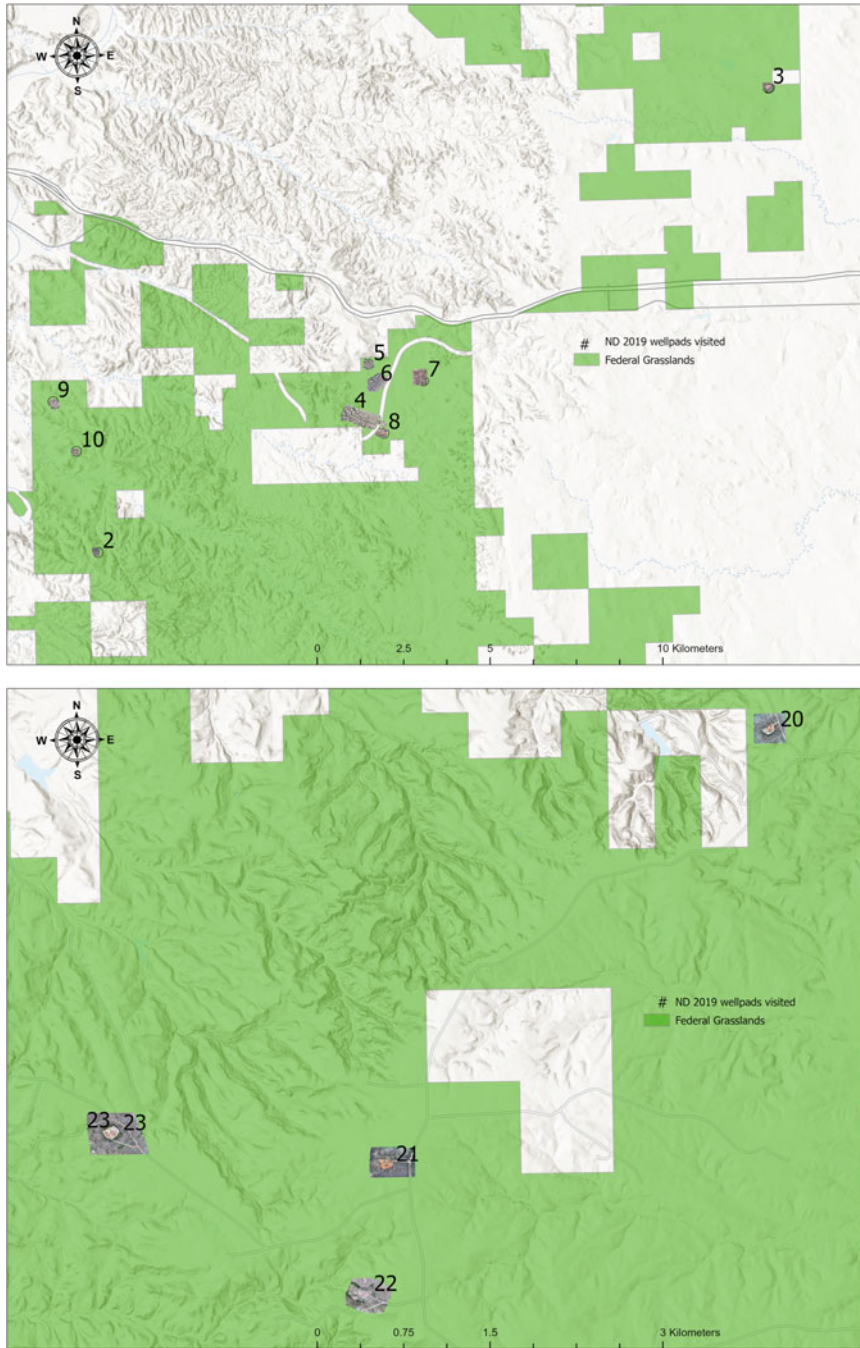


Fig. 7.8 Site location of wellpads studied, 1 through 10, top image, and 20–23 in the middle image. Bottom images (inside the table) show individual orthomosaic representations of the 14 wellpads. For overall reference of the sites, see the bottom of Fig. 7.3

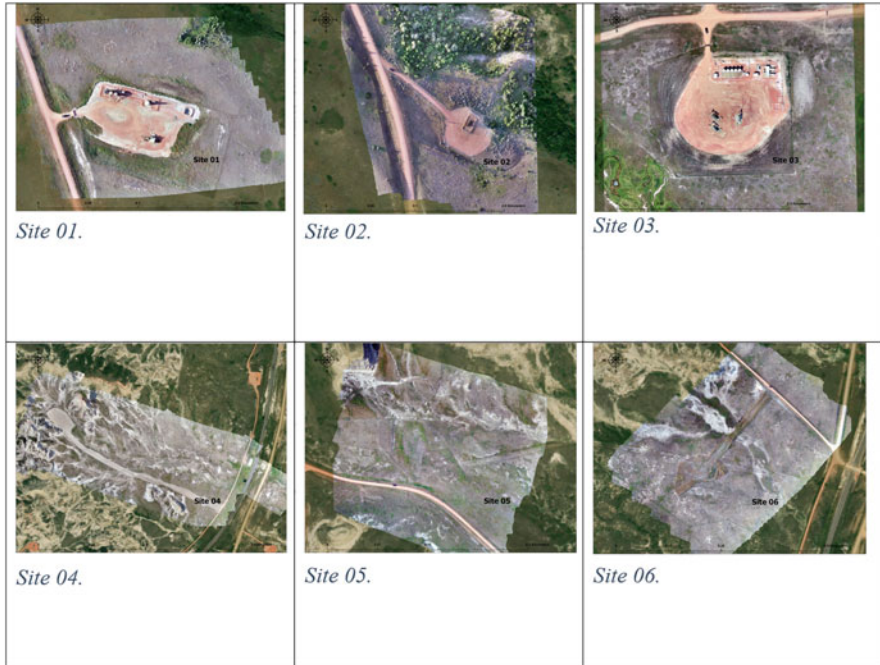


Fig. 7.8 (continued)

be traced to waterbodies if they were located nearby. These datasets also highlighted the berms surrounding tank farms, where large storage tanks are located. These raised earthen mounds are supposed to contain spills from the tanks. While some berms were hard to see in the orthomosaics, they stood out in the elevation models. Third is the flare pits, with their lower elevation also popped out (see Fig. 7.10).

Finally, draping an elevation dataset over the ortho is also helpful when the wellpad is not clearly apparent, such as Site 22, where potential spills would flow down to the nearby water bodies (see Fig. 7.11).

7.3.3 *Vegetation Health*

The camera onboard the sUAV we utilized collects RGB data (red, green, and blue bands), similar to most digital cameras. Therefore, the DroneDeploy photogrammetry software could not calculate the more common normalized difference vegetation index, or NDVI, which is widely used in vegetation studies when the near-infrared (NIR) band is present. Instead, the VARI was employed (DroneDeploy 2021a, b, c), which uses all three bands (Mehrotra and Srinivasan 2019) “to emphasize vegetation in the visible portion of the spectrum, while mitigating illumination differences and atmospheric effects” (Viswambharan 2018). Researchers such as Zhang et al. (2019) observe that the success of the VARI Index for detecting the percentage of green



Fig. 7.8 (continued)

ground cover justifies the more affordable use of RGB cameras over hyperspectral ones.

$$VARI = \frac{(G - R)}{(G + R - B)}$$

7.3.4 Formula 1 Visible Atmospherically Resistant Index

Because the wellpads are often flat cleared areas devoid of vegetation, they naturally show up as dark red or areas with no grass (see Fig. 7.12). That is expected.

However, this information becomes more interesting when examining the borders of the wellpad to potentially determine if too much land has been cleared or if operations are affecting the nearby natural vegetation. If so, then these hotspot areas can be addressed.

Site 03 provides an example whereby the cleared vegetation appears relegated to the wellpad itself, while grasses and plants are growing within the fence boundaries. Sites 20 and 21 show a similar pattern, while Site 23 shows established vegetation inside the fence perimeter.

On the abandoned wellpads that are restored or being restored, the pattern of missing or light vegetation sometimes matches the shape of the former wellpad. This suggests that the reclamation effort is still ongoing or that the seeding of required grasses has not been successful. More information is needed, however, since a dry season when the imagery was captured could affect plant phenology. Recent studies examining the relationships between climate change and NDVI suggest that past climate patterns mark the NDVI and therefore time-lag effects need to be considered (Zhe and Zhang 2021).

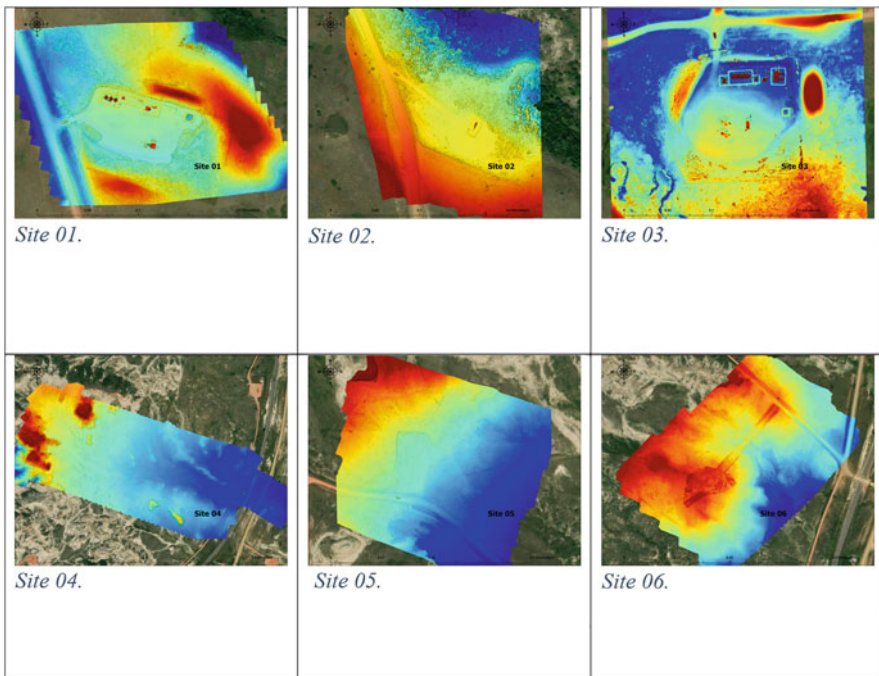


Fig. 7.9 Elevation models for the study area wellpads. Low areas appear in blue and higher elevations are in red. The elevation graph above represents ND Site 01 and shows how values on the left are low and move higher toward the right

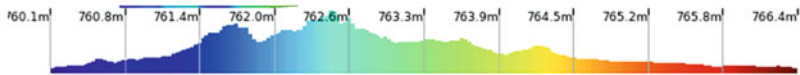
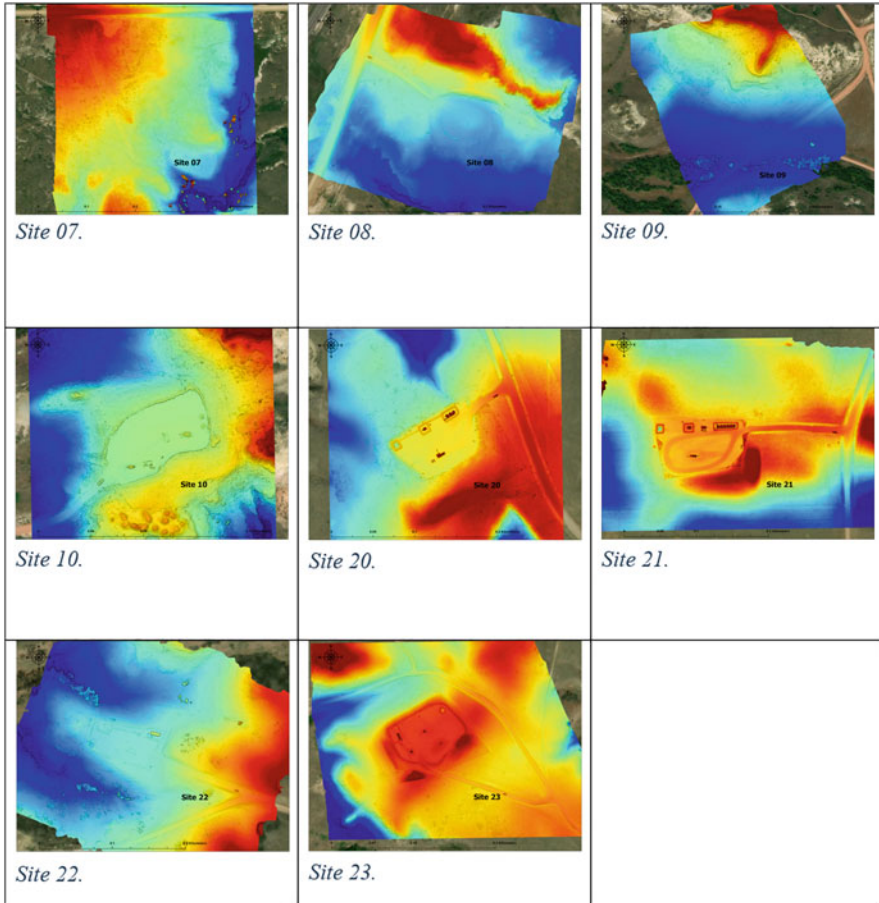


Fig. 7.9 (continued)

7.3.5 3D Models

The 3D models generated with the DroneDeploy photogrammetry software provide a novel perspective for visualizing the wellpads and getting an idea of how the infrastructure features relate to the wellpad (see Fig. 7.13). They also provide a topographic/elevation perspective that highlights drainage patterns, as well as nearby features, such as buttes (see Fig. 7.14).

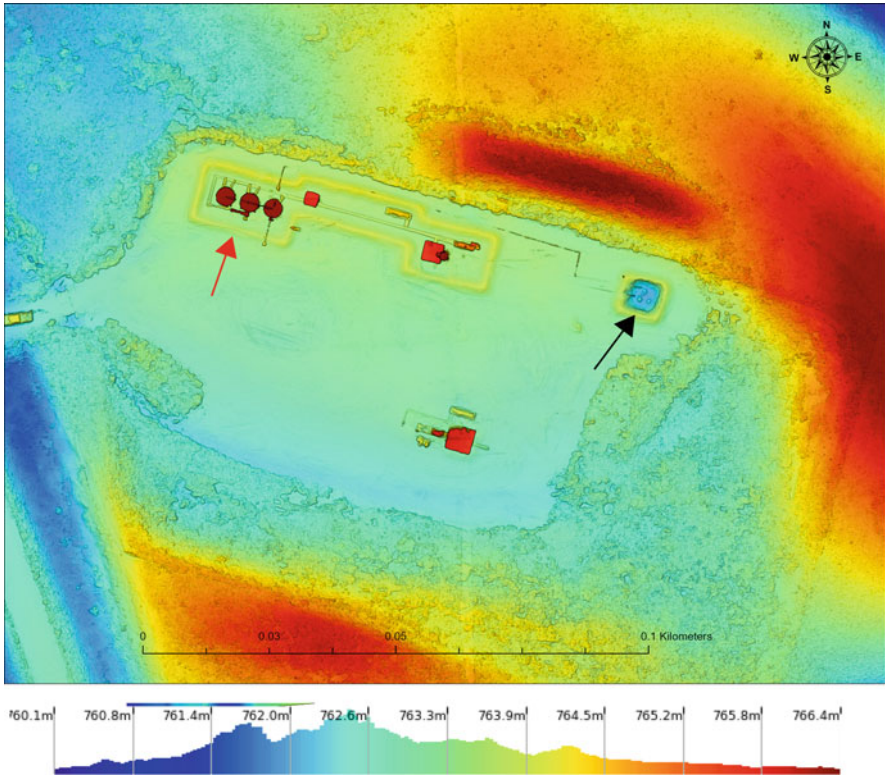


Fig. 7.10 In this elevation model, notice the red arrow pointing to the yellow outline berm surrounding the tank farm and connecting lines and the black arrow pointing to the flare pit in Site 01

7.3.6 360° Aerial sUAV Video

The 360° aerial video had the great advantage of not suffering from distortions that sometimes occur when the orthomosaic is created (see Fig. 7.15). Its oblique view provides needed context to the study area (see Fig. 7.16) and allows the inspector to more easily see elevation differences and distinguish different types of plants. While it is still difficult to identify specific plant species, a global assessment can be made regarding vegetation coverage surrounding the wellpad.

Another feature only distinguishable in the video is the windssock. This cloth wind indicator is flown to announce the potential presence of H₂S or other harmful gases, and so can warn inspectors which way to approach/avoid the wellpad. The identification sign announcing the operator and providing warnings is only detectable in the video. However, the resolution is insufficient to read it clearly.

The crisper detail of the video shows the size and shape of the pump jacks in Site 02, for example, whereas in the ortho, they can only be made out because of the

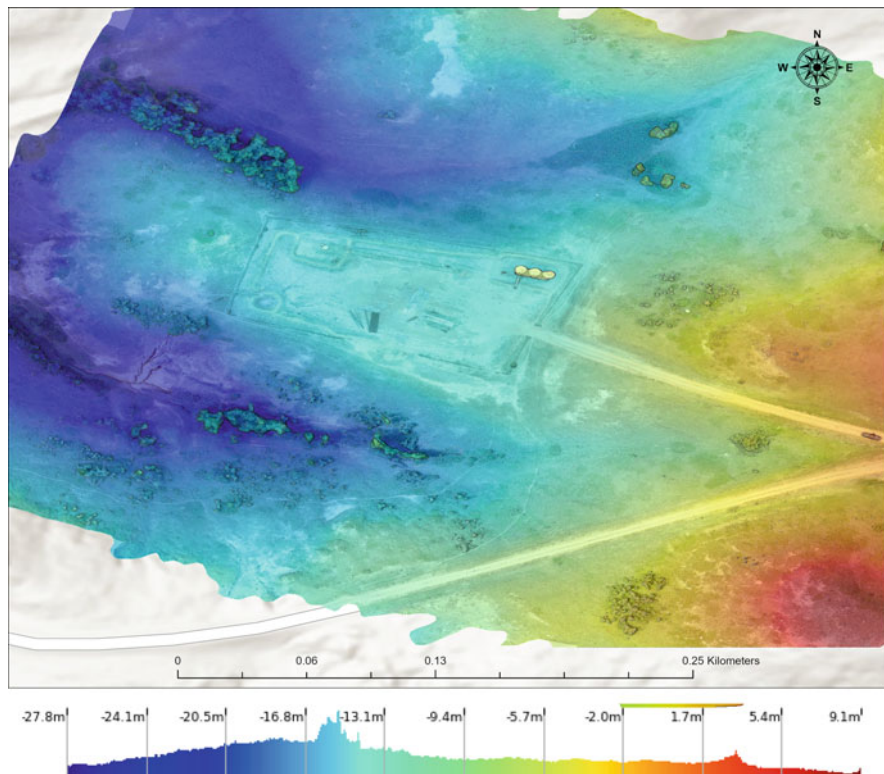


Fig. 7.11 Draping the elevation model over the ortho provides a more informed perspective (Site 22). If spills were to occur on the wellpad, they would flow to the lower, dark blue areas, where water bodies are located, potentially contaminating them. Elevation values range from low, in blue, to high values in dark red

shadow they cast. Furthermore, the flare is clearly burning on the right side of the video but cannot be seen at all in the ortho (see Fig. 7.17).

7.3.7 Pole Aerial Video

Pole aerial photography provides a solid complement or even alternative to flying an sUAV for several reasons. First, researchers have more control over where the camera enters and what it records because it accompanies them as they walk the study area. The height of the camera is easily adjusted, and because it is tethered to a pole, it can be directed over fences and places not quite accessible, such as the surface above an oil pit or under stairs. Second, the low elevation ensures good resolution so that features on the wellpad, or study area, remain in focus and

distinguishable. Third, using a camera with GPS and an intervalometer allows acquired images to be processed the same way as sUAV imagery, creating orthomosaics, elevation, vegetation, and 3D models. We have had success with this approach in monitoring coastal areas, the establishment of new roads into forested landscapes, and recording infrastructure features in northeast Florida. (Kite and balloon aerial photography provides additional approaches. We actually utilized kite aerial photography in a few wellpad locations, but do not report those findings here).

Compared to an sUAV, like the DJI Phantom 4 Pro V2 that we used, the pole camera has its limitations. It is more time-consuming to walk a wellpad or study area in the same manner as the grass cutting path of an sUAV, especially if there are features one must walk around or avoid. Also, the megapixel resolution on the cameras we used was 12, compared to 20 on the sUAV. However, no FAA approval or special permission is needed to handhold a camera, albeit 4 m above your head. You can also quickly stop and check your recordings to ensure all is working and adjust right away.

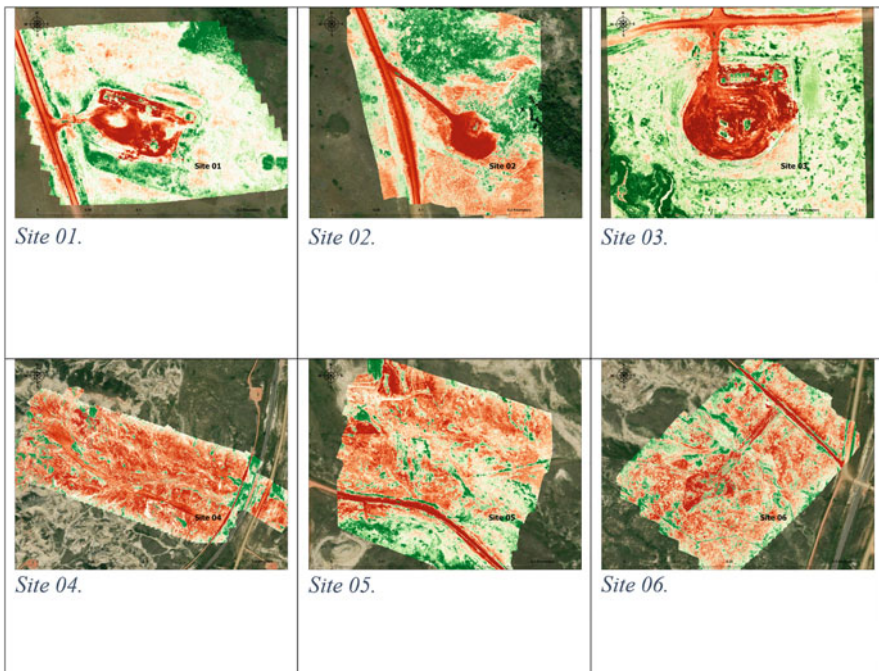


Fig. 7.12 Vegetation health perspectives, using the VARI index, for the study area wellpads. Red indicates cleared areas devoid of vegetation or lightly vegetated, while green represents vegetation. The last graphic shows the plant health graph for Site 22. Note how the values in dark red, on the left, represent cleared landscape or lack of vegetation, while on the right, green values stand for healthy/vigorous vegetation

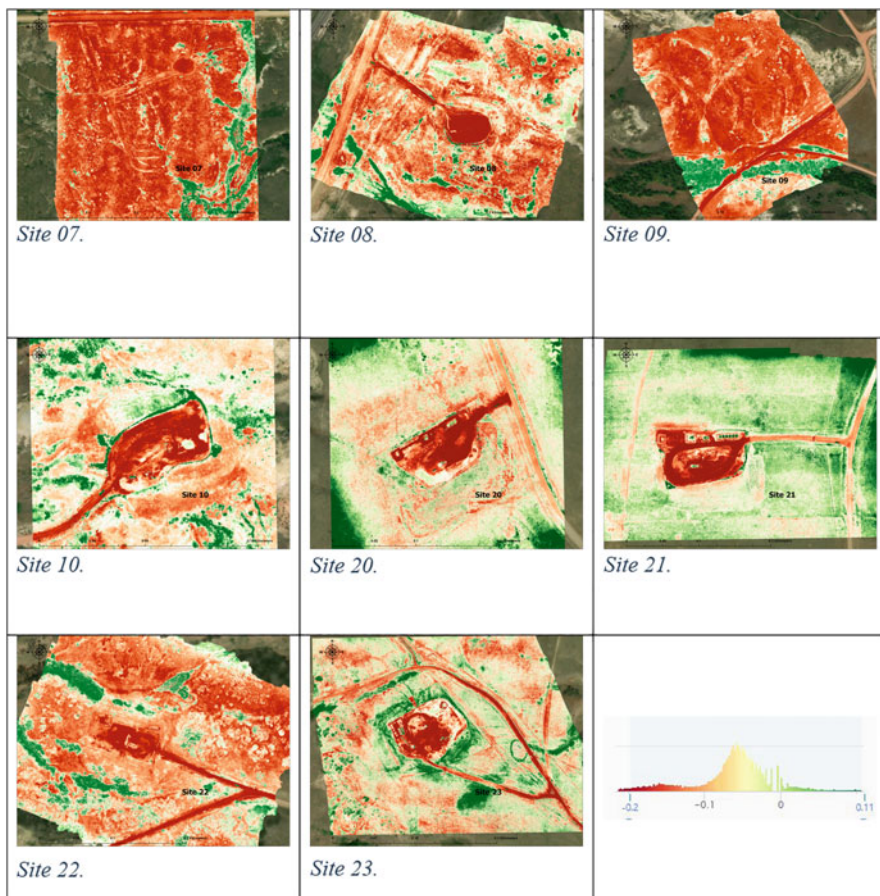


Fig. 7.12 (continued)

During the fieldwork phase, we chose to use the video feature and capture pole aerial video at a few locations, rather than still images. Since the sUAV was already capturing stills, we engaged the video to provide an on-the-ground perspective that greatly enriched our datasets, rather than provide redundancy. Plus, we could extract still images from the video when needed, and it recorded sound (see Figs. 7.8 and 7.19).

We acquired pole aerial video at four sites. In two locations we had access to the wellpad and could walk onto it. In the other two, we could only record from the perimeter. Like the 360° sUAV video, the pole video provided very good detail, which is not surprising given we were standing on the wellpad with the camera lifted about 4.5 m from the ground. The GoPro camera excelled due to its solid image stabilizer. Furthermore, because of its GPS features, the camera recorded the GPS track that we walked on the wellpad (see Fig. 7.18). This information can later be

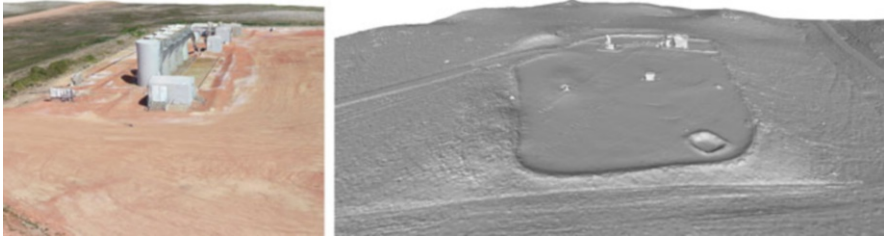


Fig. 7.13 Storage tanks appear more vividly in the 3D model of Site 03 at the left. Another 3D view of Site 23 underscores how the wellpad has been carved into the grasslands (at right). Note how the flare pit is easily distinguishable in the lower right of this image

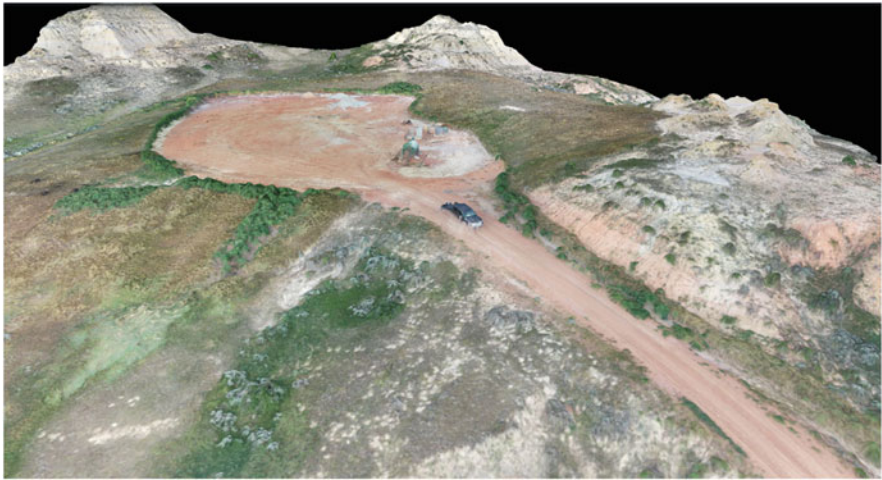


Fig. 7.14 3D model of Site 10. Note how the wellpad is atop a ridge, and potential spills would flow down to nearby water bodies. Unlike the orthomosaics, the topography of the buttes is evident. Our truck is visible near the entrance to the wellpad



Fig. 7.15 A still shot from the 360° sUAV aerial video (left) shows crisp details of Site 01 storage tanks. The windsock is visible just behind the third tank furthest away from the stairs where the cleared land meets the grass. The ladder conditions and pipe structures are clear, vegetation inside the fence is detectable, and even the corner fence structure can be made out. Meanwhile the same tanks shown in the ortho on the right display some distortion, which is more evident on the pipe network in front of the tanks and along the stairs to the right, which appear to have gaps



Fig. 7.16 A still shot of the 360° sUAV video captured as the drone was about to land provides a richer perspective than can be attained from the orthomosaic with its nadir view (Site 01)



Fig. 7.17 Image on the left shows a still captured from the 360° video at Site 03, where the pump jacks can be clearly made out, and the flare (at the very right) can be seen burning. The image on the right is from the orthomosaic, where the pump jack shadows can be seen, but the flare cannot



Fig. 7.18 GPS tracks recorded while capturing pole aerial video on Site 01, left, and Site 22, right



Fig. 7.19 Still photo of the pole aerial video hovering over the flare pit at Site 01 (at left) and the pump jack (on the right). Note: while this may seem like a still photograph that FS inspectors could take, it's actually a video, providing various perspectives, and it also captures sound

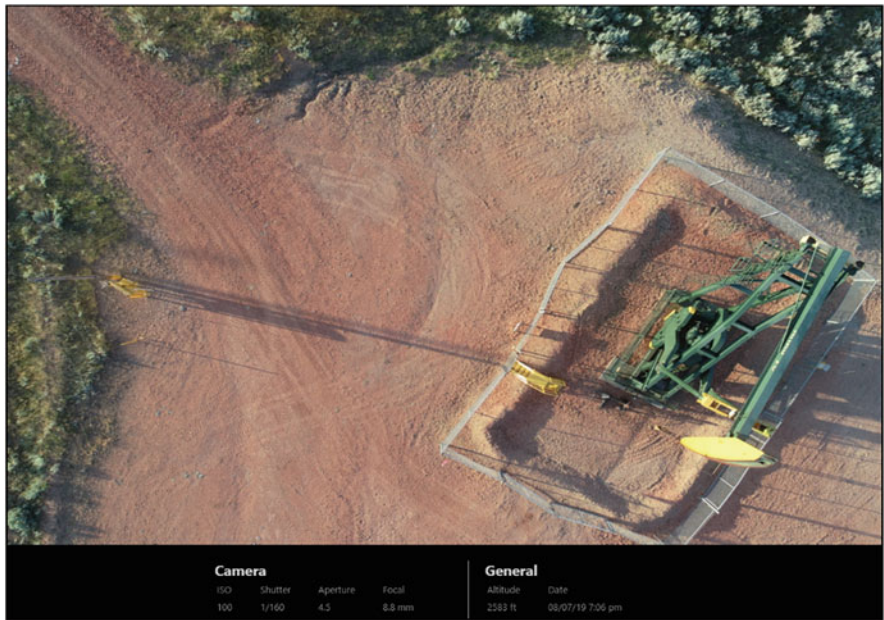


Fig. 7.20 The original single sUAV image of the pump jack and surrounding cage in Site 02 allows for inspectors to determine overall condition

used to determine if a given part of the wellpad was insufficiently examined. Conversely, a clustering of points could indicate where a problem was identified.

With pole aerial video, signs identifying the well site and the condition of all the infrastructure features are now clear. If a building needs paint or the roof needs attention, it is plainly detected. The condition of the fence can also be noticed, and the sound of the jack pumps, compressor, and flare (if present) is recorded. Plus, the flare pit condition is visible from several angles (see Fig. 7.20).

7.3.8 *Forest Service Expert Inspections*

More important than our findings were responses from the FS, who must visit and inspect all active wellpads at least once per year to confirm the condition of about 40 items on their compliance inspection form. Reclamation visits can occur annually but are not required.

For this chapter, the FS were kind enough to conduct a mock field inspection using our spatial datasets and concluded that about 70% of the items on their list could be identified/addressed (Dekker 2021). The items they could not easily detect were cattle guards needing to be cleaned out, the adequacy of well signs and warning signs, fence condition, the functionality of flare pit ignitors, and the presence of noxious weeds on and around the wellpad (Dekker 2021).

Though we only had pole aerial video for four wellpad locations, we found that this video provided a lot of this information. For example, well and warning signs and fence conditions could be read or detected. We hypothesize that had pole aerial video been available for more wellpad sites, this FS assessment might have changed to an even higher value.

Though a trained expert would be needed to determine the condition of flare pit ignitors, the presence of noxious weeds could eventually also be identified in sUAV and PAP imagery. Recent research utilizing sUAVs for examining abandoned wellpads suggests this method is quite robust. By gathering aerial images during the sUAV flights, species identification can occur later, “rather than relying on one team’s plant identification skill level” (McKim 2020). The resulting spatial record could be examined at various times by different experts, reducing observer bias (Curran et al. 2020). Furthermore, a standard two-person inspection team takes an average of 99 min to inspect a site, whereas a sUAV pilot can accomplish the same work in 20 min (McKim 2020). This strongly supports our imagery data gathering approach. Consequently, while federal agencies such as the FS may not yet be in the position to adopt sUAVs, they can introduce pole aerial video, which consists of an extendable pole and a GoPro camera, quite easily. Capturing video from above and being able to extend the camera to places they cannot readily reach will greatly increase the data showing the conditions of the wellpad and will also capture sound.

The FS mock inspection did find that the 360° sUAV video and the pole aerial video proved the most useful to gather inspection information (Dekker 2021). We concur the two types of videos provide very beneficial and focused material. Not only could the footage be stopped and rewound, still images can be captured, and again, they contribute to a spatial data record that can be reviewed as needed by various agencies or stakeholders.

Regarding the reclamation sites, the FS found that the aerial imagery (orthomosaics) was beneficial for determining overall vegetation cover and providing an informative landscape-level view of the sites (Dekker 2021). We propose that derived elevation and vegetation datasets can also be used to supplement the

inspection, as well as the combination of datasets, such as draping elevation files over the orthomosaics (see Fig. 7.11). These steps would require FS inspectors to have access and training to GIS software, such as ESRI's ArcGIS Pro.

In short, the resulting aerial intelligence provides insights for resolving issues, integrating data, and managing resources for onshore wellpad surface inspections. This suggests that annual inspections could be completed more quickly perhaps if an sUAV, pole, or both types of imagery are acquired during the site visit for closer review back at the office. This means more wellpads could be inspected during a given day, increasing efficiency and perhaps reducing the number of long-distance drives to remote regions. Plus, if H₂S is present, using an sUAV with imagery capture and 360° video could reduce exposure of FS staff to these harmful gases.

7.4 Conclusion and Discussion

This chapter highlighted how sUAVs and pole aerial photography (PAP) can be utilized to provide actionable information on the state or condition of oil and gas wellpads on US Federal grasslands. The rationale is that drone imagery and the associated products, i.e., orthomosaics, vegetation health, elevation, and 3D models, combined with 360° drone video captured at an oblique angle around the wellpad, pole aerial video taken at the wellpad surface, and individual sUAV images, provide valuable inspection data. These can be examined over and over as needed by regulators, their teams, and other stakeholders to create a detailed geospatial record that tracks temporal changes. Currently, visual field inspections are carried out by two to three FS personnel, where items are checked, notes are added on a compliance sheet, and standard digital camera photographs are captured (see [Appendix](#)).

While annual field inspections by trained experts are currently the way the FS complies with its mandate to visit every active well once per year, we believe this snapshot-in-time approach renders temporal comparisons difficult because still photographs from the field may not line up with surface features or improper lighting conditions may affect the identification of attributes captured. This is particularly true if only one or two photos are taken of a given item during an inspection. Meanwhile the redundancy of images captured by an sUAV greatly enhances the chances that adequate images are recorded, since overlapping images are needed for stitching together the orthomosaic (ESRI 2021) of the entire wellpad.

Overall, the spatial data record provided by the sUAV is robust and allows the re-examination of every part of the wellpad, thus overcoming limitations inherent to particular datasets. For example, distorted views of features such as stairs, pump jacks, and cages visible in the orthomosaics can be clearly observed and inspected in the *original* individual images captured during the drone flight. While the FS inspectors did not have access to these files, but instead the orthomosaic, distinct

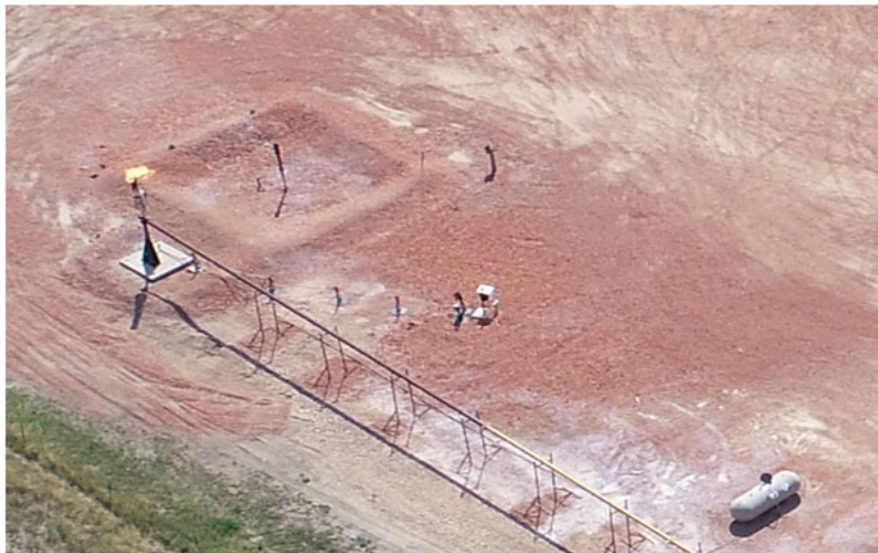


Fig. 7.21 The flare is clearly working in this individual original image captured by the sUAV on Site 03. It was not detected in the ortho

still photos provide high-resolution perspectives that can answer various inspection questions, perhaps reducing the need to watch some of the videos and increasing the FS confidence in being able to examine datasets in the office to complete surface inspections.

For example, Fig. 7.20 shows the intact pump jack and surrounding cage, which is hard to detect in the orthoimage. In Fig. 7.21, the flare burns bright.

Therefore, individual sUAV flight images, 360° aerial sUAV video, pole video, or the individual still images extracted from both videos provide perspectives from different angles and distinct levels of detail that greatly aid the identification and condition of many of the surface features on the FS service inspection sheet.

Regarding 5-year reclamation inspections, more work is needed. The FS personnel that carried out a mock inspection using the datasets we collected concluded that they could not determine the type of vegetation present nor the seed mix planted. However, with appropriate ground truth data and image processing, this too could be accomplished at the office computer. In fact, new research in Wyoming oil and gas fields highlights the benefits of collecting sUAV data over traditional field inspections. This includes the time and money saved, the rich spatial datasets produced, and the ability for experts and stakeholders to review and interpret these data as needed (McKim 2020; Curran et al. 2019; University of Wyoming 2020).

Furthermore, remote sensing techniques such as supervised image classification combined with expert field knowledge and vegetation indices can be effectively used to identify the different types and amounts of vegetation present on and around a wellpad. Sampling points taken during field inspections using a GPS receiver and/or a GPS-enabled camera enhance this approach. Here, researchers standing in the middle of an area covered with weeds record the GPS coordinates to create ground reference points (while imagery is being acquired). They repeat this for healthy grass, invasive species, and other areas of interest. Later, when the imagery is analyzed with appropriate software, training samples can be created in locations on the imagery that represent weeds, grass, and invasive species identified in the field with the GPS coordinates to classify the imagery pixels in a process known as supervised classification. And even in cases where a plant cannot be identified at the moment, this information can be used at a later time once the species is known (Dukowitz 2018). This is especially important, note Minnick and Alward (2015), so that specific plant species suited to that ecosystem can be replanted on recovering wellpads during restoration phases.

In one of the few examples of researchers studying oil and gas wellpad restoration with sUAVs, Minnick et al. (2018) found that sUAV-acquired imagery of soil and vegetation could be analyzed to accurately estimate ground cover. Using the Optimized Soil-Adjusted Vegetation Index (OSAVI), they found that ground cover estimates were strongly related to the slow traditional field sampling methods, but unlike the traditional approach, the imagery findings could be extrapolated to larger areas.

Interestingly, state regulators, such as the Colorado Oil and Gas Conservation Commission (COGCC), are now using sUAVs to follow all stages of oil and gas development. According to Gomez (DroneDeploy 2020a), COGCC transitioned from an organization that facilitated oil and gas production in the state to one that oversees environmental protection. To that end, they are using drones to provide the necessary spatial data for field inspections, environmental protection, and reclamation (Webb 2019). In fact, they are now using them during the entire life cycle of a wellpad, from construction to well capping (DroneDeploy 2020b). These five steps include the following:

1. Permitting, getting a first look, and gathering baseline data.
2. Assessing best management practices such as examining water drainage, noise, and proximity to urban areas.
3. Regular inspections, where they identify issues such as stained soil next to a compressor, or if the wellpad size has been reduced from the initial construction to the production phase.
4. Enforcement and environmental compliance. Here, a problem area is identified and marked with orange squares on the imagery. Later, they examine newer data and determine if the problem area shrunk or was addressed.

5. Reclamation and the orphaned well program. Abandoned wells are numerous and often unrecorded. Imagery is also used to monitor contractors during construction and verify if the work was completed.

Industry wise, the use of drones and other aerial platforms provides two critical functions related to oil and gas (O&G) wellpad operations: asset management and monitoring and environmental safety and compliance (Airborne drones 2019). Oil and gas producers increasingly recognize the use of drones as a cost-effective and flexible way to conduct surface inspections, improve the quality of examinations, enhance worker safety, reduce costs related to field inspections, and minimize shutdowns (Digital Aerolus 2021). Currently at least seven major oil and gas companies are using drones to monitor their operations. These include BP (British Petroleum), the first company in the USA to get a license for operating commercial drones; Chevron which is utilizing augmented reality (AR) with the drone imagery feeds during field inspections; ConocoPhillips inspects oil tankers and offshore platforms with drones; Equinor is developing drone technologies to maneuver areas that inspectors find hard to reach; ExxonMobil is using drones to mainly address offshore platforms and petrochemical complexes; Gazprom is testing them for monitoring assets in very cold conditions; and Royal Dutch Shell applies them to flare stack inspections (Murray 2020).

The COGCC operations are similar to the approach we propose for the Forest Service, who regulates surface activities on O&G wellpads located on in the Little Missouri National Grasslands located in western North Dakota. The FS personnel we worked with were amenable to allowing us to visit these locations and conduct our data gathering. They were also interested in seeing how these datasets might help them manage their surface inspections and even conducted mock inspections to gauge their usefulness.

Moving forward, having access to additional data products such as vegetation health and elevation models provides a broader perspective to detect patterns that might not be evident during a single visit. For example, pad erosion, whereby part of the wellpad is continuously (though perhaps slowly) eroding toward a nearby waterbody and potentially adversely affecting it or nearby habitats, can be more easily tracked over time. Another consideration is that field inspections require regulators to drive long distances in remote regions to carry out these surveys and sometimes exposes them to hazards, such as H₂S. The chances of automobile accidents also increase, and more vehicle maintenance is required. Being able to reduce the number of trips by increasing the number of inspections per visit is advantageous.

Given the major benefits of acquiring and using aerial imagery to monitor and inspect oil and gas wellpads on federal grasslands in western North Dakota, we propose that FS personnel add the sUAV flights and pole aerial video to their inspection visits. As noted, this has the potential to reduce the amount of time spent on each wellpad. At minimum, one inspector could focus on the 30% of the

items that are hard to detect in the imagery, while the other inspector acquires the imagery for later use on the remaining items. Even if the FS does not provide a budget and training for sUAV flights, personnel can indeed use an action camera such as a GoPro mounted to a pole and record valuable and useful video (and sound).

Considering that FS personnel may not be tasked with these methods in the future, then we suggest operators take on this responsibility by either providing these services in-house or contracting them out and then providing the FS with pertinent datasets. Beginning with phase 1, operators can create a spatial record starting with the baseline stage, which is the time before land was cleared or when they took over from another operator. Then, they can monitor all phases of construction and identify problem areas prior to the FS inspection. And if the FS finds problems, the operator can address them and send the (dated) imagery to confirm the issues have been fixed, thus potentially saving the FS an additional trip. This approach would also save the operator money in terms of fines, shutdowns, and legal exposure.

During the reclamation phase, operators can clearly follow these stages toward meeting final compliance. Here, the imagery acquisition could be semi-annually or annually, and with the right ground-based vegetation training samples and expertise, they could potentially detect the type and amount of seeded grass mixture, as well as differentiate noxious weeds and invasive species from the computer.

New developments in photogrammetry software now allow sUAV-generated maps to tile directly into geographic information systems (GIS) software such as ESRI's ArcGIS, eliminating various manual steps and streamlining the entire process (DroneDeploy 2021c). This indeed could be a game changer for managing oil and gas site inspections.

The pole aerial video greatly aids the inspection process. As mentioned, not only is the video sharp, showing infrastructure features without distortions, it captures sound and can be stopped for still images and rewind/forwarded as needed. However, this method does require researchers or inspectors to actively walk onto the wellpad when accessible, potentially exposing them to harm such as to H₂S gas, flares, or excessive noise.

Emran et al. (2017) propose using UAVs equipped with (methane) gas detectors to inspect and map landfills and natural gas infrastructures as a safer and more viable alternative to vehicle or in-person visits. We have considered a similar approach to detecting H₂S gas on wellpads; however, because this gas is heavy, it sinks. Therefore, the sUAV would have to fly quite low, potentially too low, and its rotors might disrupt and spread the column of gas if present. More research is required in this area.

Another approach to replace the pole system could be targeted sUAV flights with the use of goggles, in what is known as first person video or FPV flight. Usually these sUAVs are quite small and light (can fit in your hand), and aficionados race them in obstacle courses—not on wellpads. In this case, the experienced pilot could fly in and out of all types of structures while recording the video feed. Issues of

image quality, given the small onboard cameras and signal loss, could be an issue, but recent models are now strong enough to carry a payload, such as a GoPro camera (IFlight 2021). It still is risky, due to the potential of striking a feature on the wellpad, but experienced pilots can maneuver these small sUAVs very well.

The pole video has several advantages. One, it records track locations, allowing the user to later look for patterns. This could include identifying areas that were not examined sufficiently, or detecting a cluster, whereby a potential problem was identified. It's important to note that the video is of high quality. Second, the user has solid control of the pole camera and can angle it inside spaces, like a compressor building, without having to go inside, or place above an oil pit or flare pit while keeping a safe distance. Third, the video can be stopped and re-watched as needed, and still images can be extracted. Finally, sounds are also captured in the video, providing up-to-date conditions of noises on the wellpad, such as compressors and flares.

Other promising new methods include the use of rovers with 360° cameras and gas sensors that could be controlled and directed from a safe distance. This ground-site capture approach is now being used in commercial construction projects, and with advancements in photogrammetry software analysis, images can be compared over time and side by side, to follow all phases of the construction project (DroneDeploy 2020b). As imagery surveillance technology improves and both (smaller) operators and regulators become more aware of the benefits, the inspection process will likely begin relying on these methods.

One easy way to get started is to adopt sUAVs and/or pole aerial photography methods to enhance current oil and gas field surface inspections.

Acknowledgments Research support was provided by the National Science Foundation (NSF) CRDF 2017 Bio/Chem/Geo Research Competition (2017–2018). Award Number: FSCX-18-63878-0.

Equipment funding was also provided by the Coggin College of Business.

Thank you to Misty Hays, Jason Dekker, and Macario J. Herrera from the USDA Forest Service, Dakota Prairie Grasslands for providing information, guidance, and permission to conduct research on the Little Missouri National Grasslands (a beautiful location).

The US Geological Survey (USGS) and the Bureau of Land Management (BLM) in Wyoming and North Dakota were also helpful in providing data, explaining the workings of wellpads, and helping us avoid wells known to contain H₂S gas.

We are grateful to Albina Mikhaylova and Angela Gibson from the University of North Florida's Office of Sponsored Research for their help during the grant writing and awards phase.

Naji Younes, from George Washington University, provided feedback and suggestions during the manuscript writing phase.

Our thanks also go out to Eric Baker, Noah DeDeo, Adam Doering, Jackson Subbarao, Anastasia Utley, and Allison Worthington, students in Intermediate GIS 4048 Fall 2020 class for providing feedback on the use of these imagery products for wellpad inspections.

We also thank the anonymous reviewers who provided thoughtful and beneficial comments and suggestions to improve this chapter.

Finally, we thank Kory M. Konsoer and Michael Leitner, from Louisiana State University and Quinn Lewis from the University of Waterloo, for organizing and editing this book, sUAS Applications in Geography.

Appendix: Active Well Compliance Inspection Form (3 Pages) and 5-Year Final Reclamation Site Inspection Form (3 Pages)

COMPLIANCE INSPECTION

USDA Forest Service				Dakota Prairie Grasslands			F18-2800-2019v1			
Operator:				Well #	Road #		Ownership Status			
Legal		QQ	Sec	Twlp	Rng	API #	H2S Hazard			
CTB Off-Site						Tanks	Shacks			
CTB Name						Treaters	PumpUnit			
NNC Codes		E = Excessive Equipment		J = Junk/Junky		R = Reclamation Needs		Z = Noxious Weeds		
O = OK		G = Gone/Missing		M = Mtnc./Repair		S = Spills/Leaks/Drips				
C = Clean (up/out)		H = Health and/or Safety		N = Non-Compliance		U = Un-Authorized		Appearance		
D = Dikes Inadequate		I = Inadequate/Not to Spec		P = Paint or T = Touch-up		W = Waste(s) Removal		1 = Good 3 = Fair 5 = Poor		
Inspection Item				Year or Current Date:		7/16/2019	2018	2017	2016	2015
Operator:				* See Notes						
01. Wind Indicator (Flag/Sock/etc.) Visible & Functional						-	-	-	-	-
02. Cattle Guard(s)						-	-	-	-	-
03. Cattle Guard Object Markers						-	-	-	-	-
04. Well Sign						-	-	-	-	-
05. Area of Operations (E, H, J, W, U)						-	-	-	-	-
06. Fire Stipulations (specify NNC in Notes)						-	-	-	-	-
07. Trash Contained						-	-	-	-	-
08. Scoria/gravel Inadequate on Area Of Operations						-	-	-	-	-
09. Outdoor Light(s) Not Left On						-	-	-	-	-
10. Weeds and/or Vegetation on Area of Operations						-	-	-	-	-
11. Main Pumping Unit						-	-	-	-	-
12. Well Head						-	-	-	-	-
13. Muffler(s)						-	-	-	-	-
14. Cage(s)						-	-	-	-	-
15. Chemical Storage and/or Barrels						-	-	-	-	-
16. Tank Battery						-	-	-	-	-
17. Stairs & Walkways						-	-	-	-	-
18. Load Line(s)						-	-	-	-	-
19. Catch Basin(s)						-	-	-	-	-
20. Vent Line(s)						-	-	-	-	-
21. Heater Treater and/or Separator						-	-	-	-	-
22. Propane Tank(s)						-	-	-	-	-
23. Heater Treater and/or Separator Walkways						-	-	-	-	-
24. Sign(s) Other (hazard, safety, anchor markers)						-	-	-	-	-
25. Flare Pit						-	-	-	-	-
26. Flare Pit Igniter						-	-	-	-	-
27. Shack(s) and/or Building(s)						-	-	-	-	-
28. Cathodic Protection						-	-	-	-	-
29. Line Heater(s)						-	-	-	-	-
30. Pump(s) (recycle, etc.)						-	-	-	-	-
31. Pad Drainage						-	-	-	-	-
32. Pad Erosion (List N,NE,E,SE,S,SW,W,NW)						-	-	-	-	-
33. Reserve Pit						-	-	-	-	-
34. Flowline(s) and/or Pipeline(s)						-	-	-	-	-
35. Riser(s)						-	-	-	-	-
36. Fence						-	-	-	-	-
37. Gate(s)						-	-	-	-	-
38. Electric Panel and/or Pole						-	-	-	-	-
39. Bone Yard (storage if permitted)						-	-	-	-	-
40. Access Road: B= Blading/Ruts, C= Culvert, D= Drainage, G= Cattle Guard, S= Surfacing, T= Turnouts, V= VegGrass, X= Signing, Z= Weeds						-	-	-	-	-
41. Appearance (Rating 1, 2, 3, 4, 5)						-	-	-	-	-
1. Special Use Facilities						-	-	-	-	-
Date				7/16/2019		-	-	-	-	-
FS Inspector Name						-	-	-	-	-
Company Rep										
Date Rep Signed										

* SEE NOTES ON BACKSIDE OF THIS SHEET

WRITE INSPECTION NOTES HERE

2018	-
-	
Notes By:	
-	

2017	-
-	
Notes By:	
-	

2016	-
-	
Notes By:	
-	

2015	-
-	
Notes By:	
-	

Field notes: Number of characters: 0

7/16/2019	
Inspect By:	

INSERT PHOTOS ON NEXT PAGE

INSERT PHOTOS HERE

*Size Photo to a
3 inch height
with the "Lock
Aspect" ratio
checked*

Notes:

Notes:

Notes:

5 YEAR FINAL RECLAMATION SITE INSPECTION FORM

USDA Forest Service			Dakota Prairie Grasslands			F18-2800-2019 v1	
Operator:		Well #		Ownership			
Legal		QQ	Sec	Twlp	Rng	API #	Status
Reclamation Plan Date:		Seed Date:		P&A Date:		Road #	
Compliance Codes							
O = OK		I = Inadequate/Not To Spec		M = Monitoring		NA = Not Applicable	
NC = Non-Compliance		* Indicates "Describe situation in notes on backside"					
Inspection Items		Year or Current Date:		2018	2017	2016	2015
Operator:		* See Notes					
1. Erosion Stability							
A. Access Route Condition				-	-	-	-
B. Pad Condition				-	-	-	-
C. Reserve Pit Area Condition				-	-	-	-
D. Gully Rill / Sheet Erosion / Wind Scouring				-	-	-	-
E. Holes Forming				-	-	-	-
F. Bare Spots				-	-	-	-
2. Revegetation & Plant Vigor							
A. Access Route % Cover (Ocular estimate of cover)				-	-	-	-
B. Pad Area % Cover (Ocular estimate of cover)				-	-	-	-
C. Plant Vigor (Healthy Appearance)				-	-	-	-
D. Representative of Seed Mixture				-	-	-	-
E. Accumulation of Litter				-	-	-	-
F. Noxious Weeds (Describe in Notes)				-	-	-	-
G. Invasive Plants (Describe in Notes)				-	-	-	-
3. Fence Condition							
A. Gate(s) Closed				-	-	-	-
B. Built to Standard				-	-	-	-
C. Loose/Broken/Sagging Wires				-	-	-	-
D. Signs of Cattle Within Fenced Area				-	-	-	-
4. Reclamation Status/Timeframes							
A. All Facilities Removed (Includes S.U.)				-	-	-	-
B. Activity Lagging Behind (Describe in notes)				-	-	-	-
C. Beyond 5 Year Average Release Time				-	-	-	-
5. Follow-up Actions							
A. Additional Actions Required (Describe in notes)				-	-	-	-
B. Follow-up Action(s) As Specified				-	-	-	-
C. Request Range Survey				-	-	-	-
D. Notify Operator To Remove Fence				-	-	-	-
E. Notify Operator of FS Acceptance				-	-	-	-
F. Notify BLM of FS Acceptance				-	-	-	-
Date				-	-	-	-
FS Inspector Name				-	-	-	-

NOTE: Time Frames for Releasing Reclamation: Generally most sites can be released within five to seven (5-7) years of seeding. However, this is dependent upon adequate moisture; achieving vegetative cover that is representative of the seed mixture and 70% of the surrounding area; and achieving a minimum of three consecutive growing season without disturbance and/or damage. It is important to maintain all fences and gates to keep livestock out of the reclaimed area.

* SEE NOTES ON BACKSIDE OF THIS SHEET

WRITE INSPECTION NOTES HERE

2015	-
-	
Notes By:	
-	

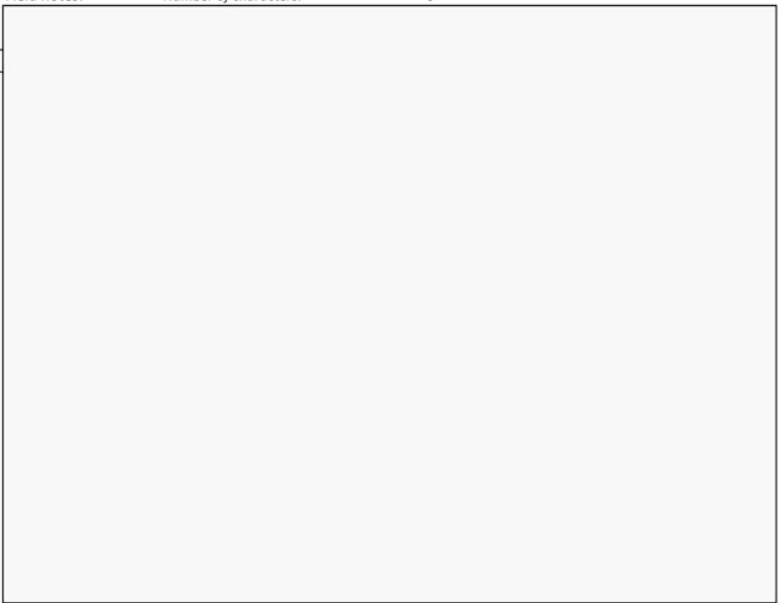
2016	-
-	
Notes By:	
-	

2017	-
-	
Notes By:	
-	

2018	-
-	
Notes By:	
-	

Field notes: Number of characters: 0

1/0/1900
Inspect By:



INSERT PHOTOS ON NEXT PAGE

INSERT PHOTOS HERE	
<i>Size Photo to a 3 inch height with the "Lock Aspect" ratio checked</i>	
Notes:	<input type="text"/>
Notes:	<input type="text"/>
Notes:	<input type="text"/>

Source: Forest Service LMNG Medora Ranger District office in Dickinson, North Dakota

References

- Airborne Drones (2019) Drones in oil and gas industry – (6 areas of application). <https://www.airboredrones.co/oil-and-gas-industry/>. Accessed 27 Jan 2021
- Al Amir N, Al Marar MS (2018) Eye in the sky: how the rise of drones will transform the oil and gas industry. Paper presented at the Abu Dhabi International Petroleum Exhibition & Conference, Abu Dhabi, UAE, November 2018. Paper Number: SPE-193211-MS. <https://doi.org/10.2118/193211-MS>
- Baynard CW, Mjachina K, Richardson RD, Schupp RW, Lambert JD, Chibilyev AA (2017) Energy development in Colorado's Pawnee National Grasslands: mapping and measuring the disturbance footprint of renewables and non-renewables. *Environ Manag* 59:995–1016. <https://doi.org/10.1007/s00267-017-0846-z>
- Bernath-Plaisted JS, Koper N (2016) Physical footprint of oil and gas infrastructure, not anthropogenic noise, reduces nesting success of some grassland songbirds. *Biol Conserv* 204. <https://doi.org/10.1016/j.biocon.2016.11.002>
- Botlink (2021) The 3 main categories of drones and their advantages and disadvantages. <https://botlink.com/blog/the-3-main-categories-of-drones-and-their-advantages-and-disadvantages>. Accessed 24 Oct 2021
- Casana J, Kantner J, Wiewel A, Cothren J (2014) Archaeological aerial thermography: a case study at the Chaco-era Blue J community, New Mexico. *J Archaeol Sci* 45:207–219. <https://doi.org/10.1016/j.jas.2014.02.015>
- Cho J, Lim G, Biobaku T, Kim S, Parsaei H (2015) Safety and security management with unmanned aerial vehicle (UAV) in oil and gas industry. *Proc Manuf* 3:1343–1349. <https://doi.org/10.1016/j.promfg.2015.07.290>
- Colorado Oil and Gas Conservation Commission (n.d.) Practice and procedure 2 CRR 404-1. <https://www.sos.state.co.us/CCR/GenerateRulePdf.do?ruleVersionId=6140&fileName=2%20CCR%20404-1>. Accessed 12 Feb 2021
- CSUR (Canadian Society for Unconventional Resources) (n.d.) Understanding well construction and surface footprint. http://www.atlanticaenergy.org/pdfs/natural_gas/Environment/Understanding_Well_Construction_CSUR.pdf. Accessed 21 Feb 2021
- Curran MF, Cox SE, Robinson TJ, Robertson KJ, Sherman ZA, Adams TA, Strom CF, Stahl PD (2019) Spatially balanced sampling and ground-level imagery for vegetation monitoring on reclaimed well pads. *Restor Ecol* 27(5):974–980. <https://doi.org/10.1111/rec.12956>
- Curran M, Hodza P, Cox SE, Lanning SG, Robertson BL, Robinson TJ, Stahl PD (2020) Ground-level unmanned aerial system imagery coupled with spatially balanced sampling and route optimization to monitor rangeland vegetation. *J Vis Exp* 160:e61052. <https://doi.org/10.3791/61052>
- Dabir L, Samiappan S, Nobrega RAA, Aanstoos JA, Younan NH, Moorhead RJ (2015) Fusion of synthetic aperture radar and hyperspectral imagery to detect impacts of oil spill in Gulf of Mexico. *IEEE International Symposium on Geoscience and Remote Sensing (IGARSS)*. <https://ieeexplore.ieee.org/stamp/stamp.jsp?tp=&arnumber=7326165>
- Dekker J (2021) Evaluation on datasets: personal communication. Minerals Area Manager, USFS Forest Service, Little Missouri National Grasslands, North Dakota
- Di Stéfano S, Karl JW, Bailey DW, Hale S (2020) Evaluation of the automated reference toolset as a method to select reference plots for oil and gas reclamation on Colorado Plateau rangelands. *J Environ Manag* 265:110578. <https://doi.org/10.1016/j.jenvman.2020.110578>
- Digital Aerolus (2021) Drones in the oil and gas industry. <https://digitalaerolus.com/drones-in-the-oil-and-gas-industry/>. Accessed 27 Jan 2021
- DJI (2021) Phantom 4 Pro V2.0 Specs. <https://www.dji.com/phantom-4-pro-v2/specs>. Accessed 26 Feb 2021
- Doujaaji B, Al-Tawfiq JA (2010) Hydrogen sulfide exposure in adult male. *Ann Saudi Med* 30(1): 76–80

- DroneDeploy (2020a) Optimizing today's asset inspections, session 293296. DroneDeploy Annual Conference. <https://ddc.dronedeploy.com/agenda/session/293296>
- DroneDeploy (2020b) Why and how to use drones in construction and infrastructure, session 347745. DroneDeploy Annual Conference. <https://ddc.dronedeploy.com/agenda/session/347745>
- DroneDeploy (2021a) DroneDeploy for Oil & Gas. Manage operations at scale with digital replicas of sites and assets. <https://www.dronedeploy.com/solutions/oil-and-gas/>. Accessed 27 July 2021
- DroneDeploy (2021b) Visible atmospheric resistant index (VARI). <https://support.dronedeploy.com/docs/understanding-ndvi-1#visible-atmospherically-resistant-index-vari>. Accessed 23 Feb 2021
- DroneDeploy (2021c) DroneDeploy for Esri. The drone data solution for GIS professionals. <https://www.dronedeploy.com/product/esri-integration-lp/>. Accessed 27 July 2021
- Dukowitz Z (2018) Interview with ecologist and FAA certified remote pilot Dr. Richard Alward. UAV Coach. <https://uavcoach.com/drones-ecology/>. Accessed 21 Feb 2021
- EIA (Energy Information Administration) (2020) North Dakota state profile and energy estimates, profile analysis. <https://www.eia.gov/state/analysis.php?sid=ND>. Accessed 15 Feb 2021
- Emran BJ, Tannant DD, Najjaran H (2017) Low-altitude aerial methane concentration mapping. *Remote Sens* 9(8):823. <https://doi.org/10.3390/rs9080823>
- ESRI (2021) Introduction to Ortho mapping. <https://pro.arcgis.com/en/pro-app/latest/help/data/imagery/introduction-to-ortho-mapping.htm>. Accessed 24 Oct 2021
- FIFA (Fédération Internationale de Football Association) (2015/2016) Laws of the Game. <https://img.fifa.com/image/upload/datz0pms85gbnqy4j3k.pdf>. Accessed 29 June 2021
- Gómez C, Green DR (2017) Small unmanned airborne systems to support oil and gas pipeline monitoring and mapping. *Arab J Geosci* 10:202. <https://doi.org/10.1007/s12517-017-2989-x>
- Green AW, Aldridge CL, O'Donnell MS (2017) Investigating impacts of oil and gas development on greater sage-grouse. *J Wildl Manag* 81(1):46–57. <https://doi.org/10.1002/jwmg.21179>
- Hausamann D, Zirnig W, Schreier G, Strobl P (2005) Monitoring of gas pipelines – a civil UAV application. *Aircr Eng Aerosp Technol Int J* 77(5):352–360. <https://doi.org/10.1108/00022660510617077>
- IFlight (2021) Nazgul Evoque F5. <https://shop.iflight-rc.com/Nazgul-Evoque-F5-with-Caddx-Polar-Vista-Digital-HD-System-pro1628>. Accessed 24 Oct 2021
- Jakes AF, DeCesaera NJ, Jones PF, Gates CC, Story SJ, Olimb SK, Kunkel KE, Hebblewhit M (2020) Multi-scale habitat assessment of pronghorn migration routes. *PLoS One* 15(12): e0241042. <https://doi.org/10.1371/journal.pone.0241042>
- JPL (Jet Propulsion Lab). What is UAVSAR? (2014) <https://uavsar.jpl.nasa.gov/education/what-is-uavsar.html>. Accessed 28 July 2021
- Kheraj S (2020) A history of oil spills on long-distance pipelines in Canada. *Can Hist Rev* 101(2): 161–191. <https://doi.org/10.3138/chr.2019-0005>
- Kridsada L, Chatchai L, Manop C, Thana S (2016) Sustainability through the use of unmanned aerial vehicle for aerial plant inspection. Paper presented at the Offshore Technology Conference Asia, Kuala Lumpur, Malaysia, March 2016. Paper Number: OTC-26576-MS. <https://doi.org/10.4043/26576-MS>
- Liu P, Li X, Qu JJ, Wang W, Zhao C, Pichel W (2011) Oil spill detection with fully polarimetric UAVSAR data. *Mar Pollut Bull* 62(12):2611–2618. <https://doi.org/10.1016/j.marpolbul.2011.09.036>
- Londe DW, Fuhlendor SD, Elmore D, Davis CA (2019) Landscape heterogeneity influences the response of grassland birds to energy development. *Wildl Biol* 1(11):1–11. <https://doi.org/10.2981/wlb.00523>
- Lubchenco J, McNutt MK, Dreyfus G, Murawski SA, Kennedy DM, Anastas PT, Chu S, Hunter T (2012) Science in support of the Deepwater horizon response. *Proc Natl Acad Sci* 109(50): 20212–20221
- Lustenberger P, Schumacher F, Spada M, Burgherr P, Stojadinovic B (2019) Assessing the performance of the European natural gas network for selected supply disruption scenarios using open-source information. *Energies* 12(24):4685. <https://doi.org/10.3390/en12244685>

- Marcellus Shale Coalition (2012) Recommended practices: site planning, development and restoration. MSC RP 2012-1 April 26, 2012. https://marcelluscoalition.org/wp-content/uploads/2013/03/RP_Site_Planning.pdf. Accessed 12 Feb 2021
- Marinho CA, de Souza C, Motomura T, da Silva AG (2012) In-service flares inspection by unmanned aerial vehicles (UAVs). 18th World Conference on Nondestructive Testing, 16–20 April 2012, Durban, South Africa. https://www.ndt.net/article/wcndt2012/papers/655_wcndtfinal00656.pdf. Accessed 20 Feb 2021
- McCormick S (2012) After the cap: risk assessment, citizen science and disaster recovery. *Ecol Soc* 17(4):31. <https://doi.org/10.5751/ES-05263-170431>
- McKim C (2020) UW student looks to transform reclamation monitoring. Wyoming Public Media. <https://www.wyomingpublicmedia.org/post/uw-student-looks-transform-reclamation-monitoring#stream/0>. Accessed 25 Feb 2021
- Mehrotra N, Srinivasan (2019) Analysing drone and satellite imagery using vegetation indices. Technology for Wildlife. <https://www.techforwildlife.com/blog/2019/1/22/analysing-drone-and-satellite-imagery-using-vegetation-indices>. Accessed 23 Feb 2021
- Minnick TJ, Alward RD (2015) Plant-soil feedbacks and the partial recovery of soil spatial patterns on abandoned well pads in a sagebrush shrubland. *Ecol Appl* 25(1):3–10. <https://doi.org/10.1890/13-1698.1>
- Minnick TJ, Alward R, Langton AM, Koenemann G, Johnston DB (2018) 9: Using a drone and multispectral camera to obtain accurate and complete information on reclamation success: well pad and habitat modification studies in western Colorado. Ecological Society of America Annual Meeting. New Orleans Ernest N. Morial Convention Center-339. <https://eco.confex.com/eco/2018/meetingapp.cgi/Paper/73783>. Accessed 21 Feb 2021
- Murray J (2020) Seven major oil and gas firms using drones in their operations. NS Energy. <https://www.nsenergybusiness.com/news/oil-and-gas-drones/>. Accessed 7 Feb 2021
- Nasen LC, Noble BF, Johnstone JF (2011) Environmental effects assessment of oil and gas lease sites in a grassland ecosystem. *J Environ Manag* 92(1):195–204. <https://doi.org/10.1016/j.jenvman.2010.09.004>
- National Park Service (2020) Geologic formations: how badlands buttes came to be. Badlands National Park. <https://www.nps.gov/articles/000/badl-geologic-formations.htm>. Accessed 27 Feb 2021
- NDDMR (North Dakota Department of Natural Resources) (2019) Oil and Gas: ArcIMS viewer. <https://www.dmr.nd.gov/OaGIMS/viewer.htm>. Accessed 4 Feb 2019
- Nelson JR, Grubestic TH (2018) Oil spill modeling: computational tools, analytical frameworks, and emerging technologies. *Prog Phys Geogr Earth Environ*. <https://doi.org/10.1177/2F0309133318804977>
- North Dakota Geological Survey (1997) Overview of the petroleum geology of the North Dakota Williston Basin. <https://www.dmr.nd.gov/ndgs/resources/>. Accessed 14 Feb 2021
- Olive A (2018) Oil development in the grasslands: Saskatchewan’s Bakken formation and species at risk protection. *Cogent Environ Sci* 4(1):1443666. <https://doi.org/10.1080/23311843.2018.1443666>
- Polinova M, Wittenberg L, Kutiel H, Brook A (2019) Reconstructing pre-fire vegetation condition in the wildland urban interface (WUI) using artificial neural network. *J Environ Manag* 238: 224–234. <https://doi.org/10.1016/j.jenvman.2019.02.091>
- Resolve (2021) Stage 3: exploratory drilling. <https://www.resolve.ngo/site-communityhealthguidebook/stage-3-exploratory-drilling.htm#>. Accessed 12 Feb 2021
- Seaman J (2017) H2S gas—what you need to know about hydrogen sulfide. Blacklinesafety. <https://www.blacklinesafety.com/blog/h2s-gas-need-know>. Accessed 15 Jan 2021
- Thompson SJ, Johnson DH, Niemuth ND, Ribic CA (2015) Avoidance of unconventional oil wells and roads exacerbates habitat loss for grassland birds in the North American great plains. *Biol Conserv* 192:82–90. <https://doi.org/10.1016/j.biocon.2015.08.040>

- University of Wyoming (2020) UW student's well pad reclamation research draws international attention. <https://www.uwyo.edu/uw/news/2020/05/uw-students-well-pad-reclamation-research-draws-international-attention.html>. Accessed 24 Oct 2021
- US DOT PHMSA (Department of Transportation Pipeline and Hazardous Materials Safety Administration) (2018) General Pipeline FAQs. <https://www.phmsa.dot.gov/faqs/general-pipeline-faqs>. Accessed 24 Oct 2021
- USDA (2019a) NAIP coverage 2000–2018. https://www.fsa.usda.gov/Assets/USDA-FSA-Public/usdafiles/APFO/status-maps/pdfs/NAIP_Coverage_2018.pdf. Accessed 26 Feb 2021
- USDA (2019b) FSGeodata Clearinghouse, download national datasets. <https://data.fs.usda.gov/geodata/edw/datasets.php>
- USDA (2021) NAIP imagery. <https://www.fsa.usda.gov/programs-and-services/aerial-photography/imagery-programs/naip-imagery/>. Accessed 26 Feb 2021
- USDA Forest Service (2021a) Oil & gas permitting & production. <https://www.fs.usda.gov/detail/dpg/landmanagement/resourcemanagement/?cid=fseprd496742>. Accessed 19 Feb 2021
- USDA Forest Service (2021b) Dakota Prairie Grasslands. Little Missouri National Grassland. <https://www.fs.usda.gov/recarea/dpg/recarea/?recid=79469>. Accessed 27 Feb 2021
- USDA Forest Service (2021c) Dakota Prairie Grasslands. Land & Resource Management. <https://www.fs.usda.gov/land/dpg/landmanagement>. Accessed 27 Feb 2021
- USDA Forest Service Dakota Prairie Grasslands (2019a) Compliance Inspection, Dakota Prairie Grasslands, F18-2800-2019v1. Document provided by US Forest Service, Dakota Prairie Grasslands Medora Ranger District
- USDA Forest Service Dakota Prairie Grasslands (2019b) 5 year final reclamation site inspection form Dakota Prairie Grasslands: F18-2800-2019 v1. Document provided by US Forest Service, Dakota Prairie Grasslands Medora Ranger District
- Viswambharan V (2018) Visible atmospherically resistant index (VARI) Analytic. <https://www.arcgis.com/home/item.html?id=13f98de823604c3baed7476ad0bf9281>. Accessed 23 Feb 2021
- Webb D (2019) Agency uses drones to monitor gas patches. The Daily Sentinel. https://www.gjsentinel.com/news/western_colorado/agency-uses-drones-to-monitor-gas-patches/article_239b15d6-0e57-11e9-b6c0-10604b9f6eda.html. Accessed 21 Feb 2021
- Weidner K (2017) Natural gas exploration: a landowner's guide to leasing in Pennsylvania. PennState Extension. <https://extension.psu.edu/natural-gas-exploration-a-landowners-guide-to-leasing-in-pennsylvania>. Accessed 12 Feb 2021
- Zhang J, Virk S, Porter W, Kenworthy K, Sullivan D, Schwartz B (2019) Applications of unmanned aerial vehicle based imagery in turfgrass field trials. *Frontiers in Plant Sci* 10(279). <https://doi.org/10.3389/fpls.2019.00279>
- Zhe M, Zhang X (2021) Time-lag effects of NDVI responses to climate change in the Yamzhog Yumco Basin, South Tibet. *Ecol Indic* 124:107431. <https://doi.org/10.1016/j.ecolind.2021.107431>

Chapter 8

Application of UAS to Detect Infrequent and Local Large-Scale Surficial Displacements: Critical Examples from the Fields of Landslide and Erosion Research



M. J. Stumvoll, M. Konzett, E. M. Schmaltz, and T. Glade

Abstract Both complex, slow-moving landslides and soil erosion depict the challenge that small process rates and changes in surface height can occur—yet over a larger area and, respectively or on different parts of an affected area or mass. While changes in the order of only millimetres per observation period are common for soil erosion, changes in surface height in the order of a few centimetres per observation period or year are observable for complex, slow-moving landslides. Structure-from-motion on aerial photography (SfM), unmanned aerial system (UAS)-based LiDAR (unmanned aerial vehicle laser scanning (ULS)) and terrestrial laser scanning (TLS) were applied within these two different fields of research to assess the user-friendly applicability of change detection in multi-temporal 3D surface models. Results are showcased by examples from landslide and erosion research in Austria. The study sites are used for livestock farming, hay production and cropland farming, respectively.

Examples demonstrate the applicability of SfM and ULS to be facing a variety of challenges. SfM and ULS registration errors prohibit or limit the evaluation of erosion processes using only variable ground control points (GCPs). The same can be asserted for the SfM-based digital terrain models (DTMs) of difference (DoDs) with respect to slow sliding processes. Vegetation cover has the highest impact with respect to data noise in data acquisition, SfM calculation and – pursuing data post-processing – on further data registration. Vegetation filtering is crucial, yet a time-

Authors M. J. Stumvoll and M. Konzett have equally contributed to this chapter

M. J. Stumvoll (✉) · T. Glade

ENGAGE – Geomorphological Systems and Risk Research, Faculty of Earth Sciences, Geography and Astronomy, University of Vienna, Vienna, Austria
e-mail: margherita.stumvoll@univie.ac.at

M. Konzett · E. M. Schmaltz

Federal Agency for Water Management, Institute for Land and Water Management Research, Petzenkirchen, Austria

consuming step, and limited in the case of SfM-based models. Fixed GCPs seem to be mandatory for registration of consecutive time steps. Yet, they can hardly be realized in natural systems with anthropogenic use. UAS-based SfM – and with constraints also ULS – are often described as the solution to investigate natural processes with “low-costs”. However, the “matter of expense” is not limited to the UAS hardware. High definition and expensive D-GNSS devices are mandatory for optimal GCP measurement. Post-processing is time- and resource-consuming. Accuracy evaluation of intermediate and final results requires expert’s knowledge. UAS-based SfM and ULS is no easy-to-use and straightforward technique, especially when it comes to the investigation of detailed, large-scale processes such as soil erosion and slow-moving landslides.

Keywords sUAS · Landslides · Surface erosion · LiDAR · ULS · TLS · Structure from motion

8.1 Application of UAS in Landslide and Erosion Research

The application of unmanned aerial systems (UAS) has strongly increased in earth science and geomorphology, mainly due to improvements of portable global positioning systems (GPS) and inertial measurement units (IMUs) as well as an increased affordability of UAS (Hackney and Clayton 2015). As airborne devices, UAS platforms provide the opportunity to hold manifold sensors, such as optical sensors (compact RGB- or thermal image cameras) or light detection and ranging (LiDAR) devices, which tremendously extends the spectrum of applicable methods and fields of research for UAS applications.

Structure-from-motion (SfM) photogrammetry used on the basis of aerial photographs from UAS rapidly developed for geosciences objectives in recent years (James and Robson 2012; Eltner et al. 2016; Smith et al. 2016; Aber et al. 2019b). They are frequently used for geomorphometric analyses (Pike et al. 2009; Mancini et al. 2013), geomorphic process monitoring (Marzoff and Poesen 2009; Oleire-Oltmanns et al. 2012) and the quantification of process rates (Immerzeel et al. 2014; Lucieer et al. 2014; Smith and Vericat 2015). Application of UAS-based techniques can therefore cover a variety of scales from plot (0.1 m) to basin (~100 m to up to ~1000 m) (Nex and Remondino 2014; Giordan et al. 2018). Here, the focus lies on the detailed, large-scale (small) processes of soil erosion and slow-moving landslides, thereby requiring high-resolution on basin scale.

While the application of SfM is relatively widespread in erosion studies (Eltner et al. 2014; Smith and Vericat 2015; Hänsel et al. 2016; Eltner et al. 2018; Candido et al. 2020; Meinen and Robinson 2020), the application of UAS-based LiDAR (unmanned aerial vehicle laser scanning (ULS)) has mostly been used in the monitoring of forests (Wieser et al. 2017; Liang et al. 2019; Prata et al. 2020) and landslide research (Pfeiffer et al. 2019; Zieher et al. 2019). In recent years, the

utilization of ULS in change detection studies focusing on alpine grasslands (Mayr et al. 2019), riverbeds (Backes et al. 2020) or coastal sand dunes (Sofonia et al. 2019) has increased. One of the key advantages of laser scanning compared to SfM is that some laser pulses are able to penetrate through sparse vegetation. This allows for measuring both vegetation (height) and bare soil (Carrivick et al. 2016), additionally facilitating an improved vegetation filtering. This is a crucial advantage in erosion studies if the study site is vegetated. However, the absence of ULS as a method for large-scale change detection is most likely based on point cloud accuracies, which tend to be lower or of the same magnitude compared to SfM but are coupled to higher acquisition costs.

In landslide research, a similar range of applications and related challenges can be observed. From a range of techniques for surface investigation of landslides, terrestrial laser scanning (Jaboyedoff et al. 2012; Abellan et al. 2016; Telling et al. 2017 and references therein) and UAS-based SfM have increasingly been applied in the last decade (for a concise review see Giordan et al. 2018). However, a variety of challenges arise in evaluating short- and long-term process behaviour of complex, slow-moving landslides (van Asch et al. 2007). With regard to landslide monitoring, change detection (changes in volume and direction over time) utilizing high-resolution, multi-temporal TLS- or UAS-based digital terrain data is only one of many fields of application (Niethammer et al. 2009; Niethammer et al. 2012; Lucieer et al. 2014; Turner et al. 2015; Eker et al. 2017; Peppia et al. 2017; Cignetti et al. 2019 to name only a few). The combination or rather comparison of both TLS- and UAS-based techniques is focus of an increasing number of studies in landslide research, concentrating, for example, on costs, applicability and accuracy (Rothmund et al. 2013; Hsieh et al. 2016; Casagli et al. 2017; Cook 2017; Zang et al. 2019). Non-linear behaviour as well as slow and small process rates of only a few centimetres or less per year (very slow to extremely slow, refer to Cruden and Varnes (1996)) impede the applicability of these techniques. High accuracies of change detection in a range of only a few centimetres per time step are hard to detect without extremely good conditions of data acquisition (non to sparse vegetation) and extremely precise post-processing regarding the co-registration of multiple time steps. Prokop and Panholzer (2009) found a limit of ± 0.05 m of change detection per observation period utilizing multi-temporal TLS data on sparsely vegetated slopes. Similar results were found by Kasperski et al. (2010) with ± 0.30 m. Cook (2017) found a value of ± 0.30 m in one study comparing UAS to TLS data, an error value of up to ± 0.10 – 0.15 m in another where only using UAS-based SfM (Cook and Dietze 2019). Only few studies investigate slow landslide surface displacements (cm/a or less) with UAV-based SfM on densely grass-covered slopes or compare the applicability of SfM and TLS-based approaches for such processes.

Although the application of UAS-platforms with SfM photogrammetry has been described as a low-cost alternative to other remote sensing techniques such as TLS, aerial photogrammetry and LiDAR (ALS) (Giordan et al. 2015; Cook 2017), several limitations concerning the accuracy of results and applicability in different environments have been identified (Rothmund et al. 2017; Onnen et al. 2020). In addition to the accuracy in spatial referencing routines, UAS-based SfM photogrammetry

methods are prone to errors when it comes to the multi-temporal compilation of highly resolved digital terrain models (DTMs) for a quantitative surface change detection in DTMs of Difference (DoDs). Those errors can emerge from a decreased accuracy of the orthophotos for example by flight routines that are inappropriate for the purpose, unfavourable environmental conditions (dense vegetation cover, sunlight conditions, etc.) or too low sensor resolutions resulting in a bad image quality. Several recent studies focus on reducing these limitations or on finding smart workarounds (Cook and Dietze 2019; Ludwig et al. 2020).

This chapter presents and critically discusses the applicability of UAS-based SfM and LiDAR (ULS and TLS) for detailed, large-scale (small) processes covering areas up to basin scale that are typical for soil erosion and slow-moving landslide processes. Examples for both processes are described in detail, covering general information on the processes, information on the respective study sites, data acquisition and post-processing and results. Results are discussed critically for both processes, especially with respect to the limitations.

8.2 Slow-Moving Landslides

8.2.1 *General Information*

Landslides are a natural phenomenon, shaping the earth's relief (Glade et al. 2005; Crozier 2010). From the different landslide types and processes (Varnes 1978; Cruden and Varnes 1996; Hungr et al. 2014), slow to very or extremely slow processes can depict a variety of velocities of 13 m/month to less than 16 mm/year (Cruden and Varnes 1996). Additionally, respective processes do behave non-linearly. Process activity can vary significantly over time, depending on the systems state, therefore complicating a clear distinction of process velocity within a short period of observation (Cruden and Varnes 1996; van Asch et al. 2007). The term "slow-moving" landslide can be sometimes misleading, both regarding the process type and rate; for a concise review on slow-moving landslides, the reader is referred to Lacroix et al. (2020). Slow processes can further turn into faster processes, for example from sliding into flowing. Cruden and Varnes (1996) define this sequence of movement as complex. According to this definition, the term slow-moving and complex landslide is applied here to describe a retrogressive earth slide – earth flow system, which has shown different phases of activity in the last 10 years on different parts of the landslide mass. Major activation occurred in 2011 (subsidence via sliding by 2 m in 2 weeks), reactivation in 2013 (formation of earth flow with 20 m/h) and processes have slowed down significantly since then to only a few centimetres to decimetres per year on the parts affected by sliding – as far as known. The detection of small changes in surface height induced by slow process velocities is of major interest to further improve our understanding of past, recent and future complex landslide dynamics.

8.3 Study Area: Hofermühle Landslide

8.3.1 Description of Site

The site to be used as example on the application of UAS-based SfM for the investigation of slow-moving landslide processes is located in the district of Waidhofen a.d. Ybbs, Lower Austria, Austria (Fig. 8.1a). The type, style and conditions being present for this particular process and study site are presumably exemplary for similar sites in the region, considering both preconditioning (geology, climate) and variable conditioning (land use, anthropogenic influences).

The site is located in the Flysch Zone (Penninic units), a geologically predestined zone wedged between Helvetic and Austroalpine units, which is known to be extremely prone to landslide processes in Austria (Schwenk 1992; Petschko et al. 2014; Tilch 2014; Stumvoll et al. 2019; Steger et al. 2020). Within the 0.15 km² hydrological catchment of the Hofermühle torrent, landslide processes can be defined as complex, being constituted by shallow earth sliding in the middle and gently inclined part of the catchment nearby the torrent, accumulation of material and resulting earth flowing down the steepening torrent path (Fig. 8.1b). While intense precipitation events are assumed to be the main trigger of flowing processes, both precipitation and snow melt are assumed to trigger sliding processes (Schweigl and Hervás 2009). Areas affected by recent sliding are grass covered, the respective

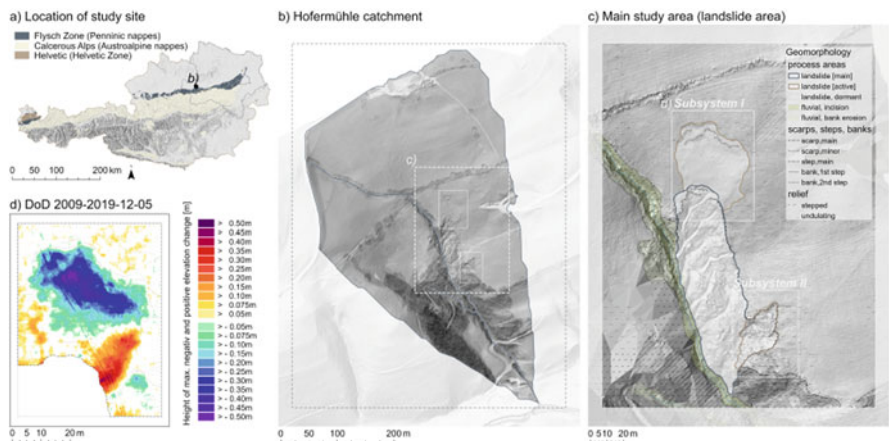


Fig. 8.1 Location of study area. (a) Location of the study site in the SW of Lower Austria, Austria; geological map after Weber (1997). (b) Hydrological catchment of the Hofermühle torrent. (c) Main study area, including Subsystems I and II. (d) Changes in surface elevation between 2009 and 2019 for Subsystem I based on ALS and TLS data (Stumvoll et al. 2021). Mesh-based change of surface elevation is displayed as maximum (positive or negative) height difference [m], excluding values between -0.05 and $+0.05$ m (noise). Relief shadings in (a + b) are based on an Austrian 10 m DEM (BMDW 2015) and a 1 m ALS DEM (NOEL GV 2009), respectively. Relief shading in (b + c) is based on a 0.05 m TLS DEM (2019-12-05), showing also a simplified morphological mapping (Stumvoll et al. 2021). Orthophoto in (b) from NOEL GV (2011)

pasture being used for hay production and mowed three to four times a year (Fig. 8.1c). Areas of older processes and more pronouncedly affected prohibit agricultural use and are covered by shrubbery (Fig. 8.1c process area: landslide [main]). The torrents path, being closely connected to the landslide, is accompanied by high trees, coniferous on the orographic right, deciduous on the left.

The area is monitored since 2015 with a variety of both surface and subsurface techniques (Stumvoll et al. 2021, 2022), including TLS and UAS. Vegetation is the main factor of uncertainty, regarding surface data acquisition and respective data post-processing and interpretation. Recent studies showed the main landslide area, known to be active since 2011 latest, is expanding (Stumvoll et al. 2021). Two related areas can be identified, both of which show individual landslide characteristics as well as a clear connection to the main landslide, which thereby is further retrograding upslope (Subsystems I and II) (Fig. 8.1c). Current findings by Stumvoll et al. (2021) indicate the sliding processes to be slowing down since most recent main activations in 2011 and 2013. Yet, respective processes are known to behave non-linearly. For the respective study, high-resolution raster (0.05 m) and mesh-based DEMs were generated via multi-temporal TLS data, starting in 2015. DoDs were generated on mesh-based DEMs. Assuming a range of ± 0.05 m for vegetation- and registration-induced errors as ‘no change’ still allowed for the detection of large-scale changes in the area of a few centimetres to decimetres. The respective magnitudes or dimension of change are common when it comes to investigate such slow-moving processes on such temporal resolution (e.g. Prokop and Panholzer 2009). Between 2009 (additional ALS data) and 2019, the area underneath the main scarp in Subsystem I (rotational slide) showed a max. change in surface elevation of approx. ± 0.50 m, most of which appeared between 2009 and 2015 (major landslide activation 2011 and 2013) (Fig. 8.1d). In the following years, changes of ± 0.15 – 0.20 m were detected between 2016 and 2018. No major changes were detected after 2018, except small and locally confined displacements of up to ± 0.05 m (Stumvoll et al. 2021).

8.3.1.1 Description of Research Aims

Within 5 years of intensive monitoring (2015–2020), changes in height and alterations of formations of the landslide surface and its surrounding have been of greatest interest; respective monitoring is planned to be extended to at least 10 years. To investigate process style, rates and related tendencies, multi-temporal high-resolution digital elevation data with precise (relative) position accuracy is required, especially on this scale of landslide process rates (\sim cm to dm/a). The area has subsequently been captured via aerial photography utilizing UASs starting in 2017. The data has been post-processed utilizing basic SfM workflows and acquired additionally to TLS data (starting 2015) to pursue the following questions: (a) What are the methodological advantages and disadvantages of a UAS-based approach compared to TLS with respect to both data acquisition and post-processing? (b) What kind of initial resolution and position accuracy can be achieved

with UAS-based SfM DEMs compared to TLS-based DEMs? (c) Is it possible to visualize real surface change with UAS-based data, GCPs and basic SfM calculations without in-depth post-processing of resulting point clouds and in-depth evaluation of the absolute and relative accuracy? d) Is UAV-based SfM a less cost- and time-consuming alternative to TLS for this setting? What are the implications of respective results?

8.3.2 *Flight Routines and Post-processing*

The four UAS flights used for this study were conducted between June 2017 and December 2020. For information on type of vehicle, camera parameters, flight parameters and results on mean ground sampling distance (GSD), DEM resolution and GCP position accuracy, please refer to Table 8.1. Flights were conducted manually for the first two campaigns (KR615 Hexacopter, Fig. 8.2a).

An implemented flight path planner was used for the second two flights to improve picture overlap, coverage and flight altitude with respect to flight time and battery capacity (Fig. 8.2b, c). Flight paths were chosen in a way that the entire main study area (Figs. 8.1c and 8.3a) was covered and especially areas with a high potential to be threatened by slope failures (e.g. upslope scarp areas, Subsystems I; Fig. 8.3b-e) are repeatedly covered by the photographs in two directions (70% side, 80% front picture overlap).

Flight altitude could not be adapted to the slope due to trees; relative altitude therefore increases downslope. Multiple ground control points (GCPs, Fig. 8.2d) were distributed in the observation area around the landslide and measured with a high-definition GNSS (Leica Viva CS15/GS15; APOS real-time position correction via SIM card; ~3 mm, horizontal and ~5 mm vertical accuracy; EPSG: 32633). Even though additional flights were conducted between the four listed in Table 8.1, only these were selected because (a) they had GCPs and (b) TLS data of similar or same acquisition times were available.

UAS data was post-processed in Agisoft Metashape Professional utilizing a basic and simple SfM workflow. Geotags (EXIF data) of raw RGB imagery were removed initially, as they were only available for epochs 3 and 4, and photos aligned (high precision). Ground control points (GCPs) were imported as markers and linked to images. Camera alignment was optimized and dense point clouds generated (high precision, mild filtering). DEMs and Orthomosaics were computed based on dense point clouds (Fig. 8.3) and exported as tiffs. Further post-processing was performed in ESRI ArcGIS Pro and is raster based (2.5D). The authors are aware of the fact that true 3D point-to-point distances (e.g. M3C2) are closer to reality (Lague et al. 2013). However, the aim of this study is to compare and evaluate the relative accuracy of DoDs based on both TLS and UAS, not the absolute. Initial mean ground sampling distance of the UAS data ranged from 1.31 to 2.92 cm/pix; calculated raster resolution of UAS-based DEMs ranged from ~0.02 m and ~0.07 m; DEMs were all resampled (cubic) to 0.10 m raster grid size to improve comparability.

Table 8.1 Information on UAS flight conditions, hardware, SfM results and TLS data epochs used for the investigation of the Hofermühle landslide

Date of UAS campaign	Epoch 1 2017-06-13	Epoch 2 2018-06-14	Epoch 3 2019-05-25	Epoch 4 2020-12-07
Field conditions	Minor, high grass height	Minor, high grass height	Good, fresh cut grass	Good, low grass height
UAS type/model	KR615 Hexacopter	KR615 Hexacopter	DJI Matrice 200	DJI Mavic Pro
Camera model	Sony DSC-RX100M3	Sony DSC-RX100M3	DJI XT2	Hasselblad L1D-20c
Geotag EXIF	No	No	Yes	Yes
Camera resolution	5472 × 3648	5472 × 3648	4000 × 3000	5472 × 3648
Focal length	8.8 mm	8.8 mm	8 mm	10.26 mm
Number of images	415	587	266	474
Flying altitude [mean]	60.2 m	81.2 m	122 m	55.8 m
Coverage area	0.0545 km ²	0.109 km ²	0.16 km ²	0.0608 km ²
Height range of covered area [m]	~643 to 562	~658 to 518	~655 to 510	~648 to 543
Ground resolution survey data [mean GSD]	1.4 cm/pix	1.91 cm/pix	2.84 cm/pix	1.19 cm/pix
Ground resolution DEM	2.79 cm/pix	3.82 cm/pix	5.67 cm/pix	2.38 cm/pix
Point density [mean]	1280 points/m ²	684 points/m ²	311 points/m ²	1770 points/m ²
Tie points	28,136	398,078	184,587	191,223
GCP count	6	12	10	21
GCP X error [m]	0.0215	0.0050	0.0024	0.0104
GCP Y error [m]	0.0345	0.0040	0.0033	0.0138
GCP Z error [m]	0.0531	0.0011	0.0006	0.0109
GCP total error [m]	0.0668	0.0065	0.0041	0.0204
Date of TLS campaign	2016-09-15	2018-06-06	2019-05-25	2020-11-18
Field conditions	Good, low grass height, 1 scan position only	Minor, high grass height, 1 scan position only	Good, fresh cut grass, 1 scan position only	Good, low grass height, 2 scan positions

(UAS pilots: 2017-06-13 Sabine Kraushaar, 2018-06-14 and 2019-05-25 Elmar Schmaltz, 2020-12-07 Robert Kanta)

TLS-based DEMs from similar or same times of acquisition were used for DoD comparison and validation (accuracy assessment). A mean point distance of 0.055 m (0.004° angular resolution; 800 m distance to main study area; for hardware specifications refer to Riegl LMS (2020), for detailed information on data analysis refer



Fig. 8.2 (a–c) UAV hardware used for flight campaigns at the study site and (d) exemplary ground control point. Main landslide area in the background of the first and second photograph (area with shrubbery). (©Photographs: see graphics)



Fig. 8.3 UAS-based orthomosaics of the Hofermühle landslide. (a) Overview of area covered by UAS flights (main study area, see Fig. 8.1c) by the example of epoch 4 (2020-11-18). (b–e) Detail for Subsystem I given for 4 consecutive epochs. (UAS pilots: 2017-06-13 Sabine Kraushaar, 2018-06-14 and 2019-05-25 Elmar Schmalz, 2020-12-07 Robert Kanta)

to Stumvoll et al. (2021)) enabled the generation of DEMs with 0.05 m raster resolution. Intensive data post-processing ensured both absolute (MSA onto ALS data) and relative accuracy of consecutive time steps. The TLS-based point clouds were filtered with respect to vegetation using Riegl RiSCAN Pro standard vegetation filter. This showed acceptable result in most cases, as TLS can penetrate vegetation

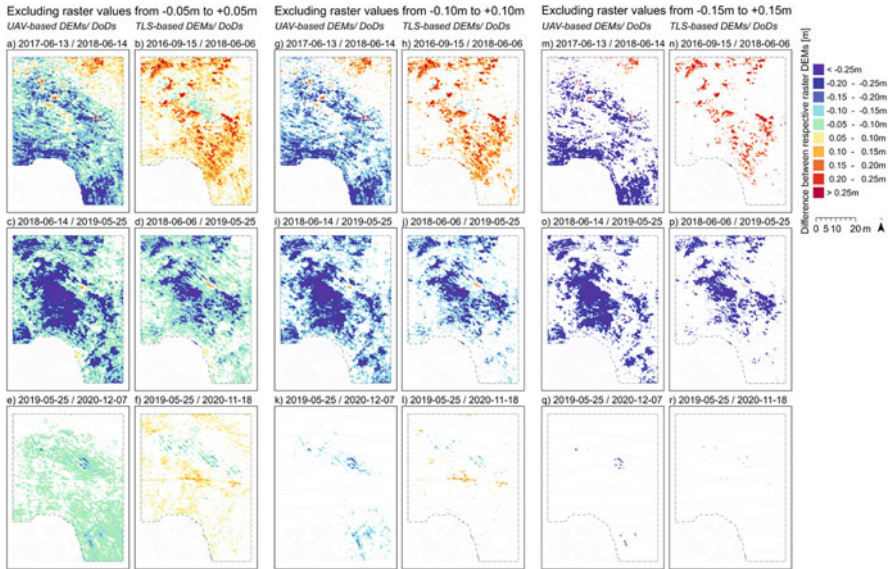


Fig. 8.4 UAS- and TLS-based DoDs for Subsystem I of the Hofermühle landslide (for location, see Fig. 8.1c, d). Change of surface elevation is displayed as raster height difference [m] for UAS-based DEMs (left columns) and TLS-based DEMs (right columns) of 0.10 m raster grid size, excluding values between -0.05 and $+0.05$ m (a–f), between -0.10 and $+0.10$ m (g–l) and between -0.15 and $+0.15$ m (m–r). (UAS pilots: 2017-06-13 Sabine Kraushaar, 2018-06-14 and 2019-05-25 Elmar Schmalz, 2020-12-07 Robert Kanta)

and give information on the real surface. For comparison with UAS data, TLS DEMs were resampled to 0.10 m.

For four-time steps (epochs), DoDs were calculated utilizing 3D Analyst Tool Raster Minus in ArcGIS Pro. Different error values of “no change” were applied to illustrate the importance of high accuracies; values of change in raster-based surface height were excluded for all values ± 0.05 m (Fig. 8.4a–f), ± 0.10 m (Fig. 8.4g–l) and ± 0.15 m (Fig. 8.4m–r) for both the UAS- (Fig. 8.4 left column of respective error value) and TLS-based DoDs (Fig. 8.4 right column of respective error value), respectively, and results are shown for one of the main active areas (Subsystem I) (refer to Figs. 8.1d and 8.3b–e). For data description and interpretation, it should be stated that changes in surface height of more than $+0.05$ m and less than -0.05 m could be proven to represent real change (both surface and non-surface) for the TLS-based DoDs (Stumvoll et al. 2021).

8.3.3 Results

For the UAS-based DoD, epochs 1 to 2 (2017-06-13 to 2018-06-14, Fig. 8.4a, g, m) show an overall negative change in surface height, in some places < -0.25 m. In

contrast, the TLS-based DoD for epochs 1 to 2 (2016-09-15 to 2018-06-06, Fig. 8.4b, h, n) depict an overall positive change. Even though epoch 1 differs, with the UAS epochs covering 9 months less, the trend should be the same – but is not. TLS-based DoDs can be assumed correct; while the 2016 data had good data acquisition conditions, the 2018 data depicts high grass heights, which could by some part be removed via vegetation filtering. The grass height changes are reflected in parts by the positive values of changes in surface height.

A higher error value of “no change” therefore should be applied; yet, considering a threshold of more than ± 0.05 m, both real negative in the upper and real positive changes in the lower part of Subsystem I would not be detectable (Fig. 8.4b – for comparison refer to Fig. 8.1d). The UAS-based DoDs are not able to depict the real surface change or even the trend of surface change for these two epochs, most probably due to poor position accuracy of the 2017-06-13 data (Table 8.1, 0.067 m total GCP RMSE, 0.053 m GCP RMSE for z), even though mean ground sampling distance (GSD) was low (0.014 m/pix). However, GSD can be assumed to vary intensively, as flight altitude changed due to the inclination of the slope.

A different case is perceptible for epochs 2 to 3 (2018-06-06, respectively, –06-14 and 2019-05-25). Both UAS- (Fig. 8.4c, i, o) and TLS-based DoDs (Fig. 8.4d, j, p) depict a negative change in surface height. Part of this negative change can be assumed alteration in grass height; 2018 data had high grass conditions, and 2019 data had low and fresh cut. Assuming changes of ± 0.15 m to represent real surface change (Fig. 8.4o+p) rather than grass height change still shows the results to be overestimated for the UAS-based DoD – even though GCP-based z RMSE was ~ 0.001 m for both UAS-based DEMs (Table 8.1). For the 2018 TLS data, parts of the respective grass vegetation could be removed via filtering; this might explain some of the UAS-based overestimation.

Data acquisition conditions were good regarding epoch 4 for both the UAS (2020-12-07) and the TLS campaign (2020-11-18), but not as good as for epoch 3 (freshly cut grass). Again, DoDs show differing results: the UAS-based rather negative (Fig. 8.4e), the TLS-based rather positive changes (Fig. 8.4f) for an error value of ± 0.05 m. The positive change for TLS-based DoDs is due to grass – the line-like feature in the middle of Subsystem I represents the newly sowed path of a trench dug end of 2018. The grass is different from the surrounding natural pasture, obviously depicting growth even towards the end of the vegetation period (November). Negative changes can be detected in the same or similar locations as were visible for the other DoDs, representing the area right underneath the newly developing head scarp (refer to Fig. 8.1d). These areas of negative changes in surface height correspond with the UAS-based DoDs (Fig. 8.4e, k, q), yet they overestimate the negative changes. Position accuracy of the respective UAS-based DEMs (GCP total RMSE 0.004 and 0.02 m, respectively) still seemed to be acceptable to indicate almost “no change” for an error value of ± 0.15 m (Fig. 8.4q) – similar to the TLS-based DoD (Fig. 8.4r) – even though GSD of epoch 3 (0.0284 m/pix) was lowest of all epochs.

While results for the first DoD, covering epochs 1 to 2, differ completely, results for the second (2–3) and third (3–4) show at least the same tendency. Yet, SfM-based

DoDs overestimate negative surface change for both, even though they were acquired at almost the same date as TLS data. GCPs were the only measure of position accuracy for the SfM-based DEMs. While GCPs are needed to improve geometry, also in the context of absolute metric distances, they can be a source of error when comparatively analysing different epochs (Cook and Dietze 2019 and references therein). The co-alignment of consecutive epochs without GCPs, resulting in a precise relative but no absolute position accuracy, could be an approach. The four UAS epochs were additionally processed following Cook and Dietze (2019) for comparison of respective results. Errors in height were in the range of 0.50 to more than 1.00 m, probably due to the fact that there are no non-vegetated and stable areas that can be used for appropriate tie point generation – a limitation, which has been mentioned by the authors (Cook and Dietze 2019). Results are therefore not presented here.

8.3.4 Discussion

Both UAS- and TLS-based surface investigation approaches have methodological advantages and disadvantages with respect to both data acquisition and post-processing. The study site is easily accessible by car, GNSS reception and APOS real-time correction typically show high quality. TLS data acquisition can be done by one person and takes approx. 1–2 h (two scan positions, ~30 min per scan plus change of location). UAS data acquisition normally takes 2–3 persons; GCPs layout and measurement takes approx. 1 h, the flight 30 min. With TLS, the entire watershed can easily be captured (see Fig. 8.1b), while UAS data coverage – also with respect to battery capacity, resolution and data volume – is confined to the main study area (see Fig. 8.1c). Precision with respect to real ground data is highly dependent on the vegetation cover. Trees alongside the torrent and in the lower part of the catchment cause data shadowing underneath (UAS) and in an uphill perspective (TLS). Grass cover and height are the most important limiting factors for the main areas of interest. This holds true for both techniques. Time of data acquisition should therefore be selected carefully and focus on times of low or no grass cover (November–February), which was improved in the last years – yet also depends on snow cover (possible from December to March), the farmer (mowing) and the availability of hardware and staff. The TLS is able to partly penetrate grass cover and capture real surface data, even from 1000 m distance (opposite valley side). Higher grass cover can be filtered from the TLS point clouds, as information on real surface data is also available. This does not hold true for the UAS-based SfM data, making it nearly impossible to distinguish real surface data via post-processing.

TLS data post-processing includes data registration, filtering and DEM/DoD calculation. Correct absolute and relative data registration of consecutive time steps is time-consuming and requires high computing capacity. The same holds true for vegetation filtering. TLS-based 3D point clouds covering the entire watershed typically have approx. 25 Mio points and ~ 500 MB after vegetation filtering.

Before filtering, the same point clouds can have up to 120 Mio points or more and ~ 3.5 GB data size. Yet, after establishing one project with correctly registered epochs, the addition of a new epoch is not that complicated. UAS post-processing includes photo quality examination, SfM computation with photo alignment, GCP marker localisation, dense cloud and DEM calculation. GCPs were used as only measure of position accuracy; further registration via ICP-based MSA (Besl and McKay 1992) was not performed for the UAS-based point clouds. Stable areas of “no change” are necessary for MSA registration. This can be assumed for areas further away from the main study area, which are covered with TLS. UAS coverage is smaller, and areas close to the main landslide cannot be assumed stable. Additionally, the grass cover of the study area shows a high diversity both over the year and over the area of investigation. Vegetation filtering is nearly impossible due to low or no ground points in areas of vegetation cover, therefore further impeding a co-registration of different epochs based on “surface” information, as it can be done for the TLS data.

Regarding surface resolution of point clouds and DEMs, respectively, one major difference between UAS-based SfM and TLS lies in the routine of data acquisition, apart from differences inherent to the technique. TLS (LiDAR)-based point clouds are absolute metric data, the initial measurements depict real distances and the absolute position of these distances in space (Heritage and Large 2009). UAS-based SfM calculates points. Camera positions and orientations as well as 3D features of known distance need to be known exactly in classical photogrammetry. In SfM, feature locations are automatically extracted in multiple pictures using a so-called iterative bundle adjustment and camera position and orientation can be calculated. In creating a sparse cloud with these extracted feature locations, the algorithms then use all available pixels to calculate dense point clouds (Westoby et al. 2012; Aber et al. 2019a).

The impact of various sources of uncertainty is influencing the calculation of point positions – the absolute, metric accuracy of a respective point cloud is hard to evaluate (Eltner et al. 2016 i.a.). TLS data is acquired using the same point distance of 0.004° and the same scan positions each time. A mean resolution of ~0.05 m can be achieved for the main study area. UAS data was acquired with differing hardware (vehicles and cameras), flight altitudes, picture overlap, flight paths and GCP count and position – and therefore differing resolution of SfM-based surface models, impeding the comparability of resulting models. Mean GSD of SfM data ranged from 1.31 to 2.92 cm/pix; calculated raster resolution of DEMs ranged from ~0.02 m and ~ 0.07 m – and is therefore in a similar order as the TLS data. Yet, the point density is a mean value for the entire area covered; there is no stable value. It could be argued that in the years which have already past and are still to come to maintain the long-time monitoring of this particular slow-moving landslide, the likelihood of changing devices is high – especially when considering the rapid development which has happened in the area of UAS-based SfM research. It seems therefore definitely necessary to develop a routine or protocol of UAS-based SfM considering technological advancements and changes in platforms as proposed by Eltner et al.

(2016) to be able to accurately process and analyse multi-temporal data from one study site taken under different conditions.

UAS data can be a powerful, flexible and especially low-cost tool to generate accurate and reliable DEMs and resultant products to be applied in landslide research – as demonstrated, for example, by Lucieer et al. (2014), Giordan et al. (2015), Turner et al. (2015), Clapuyt et al. (2016), Cook (2017) and Giordan et al. (2018). In reference to the “matter of expense”, low-cost UAS data is even considered a necessary tool to improve future landslide research, especially with respect to long-term monitoring projects (Lacroix et al. 2020). This might of course be true in many cases, especially considering areas difficult to access (Clapuyt et al. 2017) or regarding the immediate need of data after a landslide event for hazard monitoring (Gomez and Purdie 2016). However, the requirements on initial study site conditions are high – in the sense of, for example, atmospheric conditions, vegetation cover, stable areas for fine registration (MSA) and high-precision GNSS devices for GCP measurements (Aber et al. 2010a; Gomez and Purdie 2016; Gomes Pessoa et al. 2021) – to obtain results which can be useful when investigating surface changes on such detailed scale as it is the case with slow-moving landslides.

In-depth knowledge regarding camera properties, software algorithms, impact of GCP number and spatial pattern, vegetation filtering *inter alia* are necessary to evaluate UAS- and SfM-based results (Aber et al. 2010b; Clapuyt et al. 2016; Eltner et al. 2016; Sanz-Ablanedo et al. 2018; Anders et al. 2019; Gomes Pessoa et al. 2021). Expertise on these terms is no small “matter of expense” and requires experts’ knowledge. In our case, we used different kinds of UASs, ranging from commercial DJI products to non-commercial and specialized drones – none of which, with the exception of the DJI Mavic Pro, was less expensive than 2000€, not including the cameras. An expensive Leica GNSS (~50.000€) with real-time position correction was used to measure GCPs – and still the measurements uncertainties especially in z-direction (vertical) are too high to generate accurate and reliable DEMs. Additionally, software prices of over 3000€ (Agisoft Metashape, Pix4D) are not that different from TLS post-processing software. Post-processing of data is time-consuming for both TLS- and UAS-based data, yet TLS data can be used for co-registration right away with no uncertainties about internal distortion or geometric inaccuracies; this is not the case for UAS-based SfM data. Internal precision of the UAS and SfM-based DEMs is associated with the SfM Algorithm, the external precision with the GCPs (position, setting), which is mostly done by calculating the RMSE of ground control points compared to check points (Clapuyt et al. 2016; Sanz-Ablanedo et al. 2018). Both were not evaluated quantitatively by calculating, for example, the RMSE of measured to real GCP location, because flight and camera settings as well as GCP locations show large variations for all four epochs and there are no fixed (true) GCPs (Sanz-Ablanedo et al. 2018). The only evaluation of the RMSE for all GCPs was calculated by Agisoft Metashape (see Table 8.1), and this can be an overestimation of the real accuracy (Sanz-Ablanedo et al. 2018). This needs to be improved in future studies to enhance comparability of UAS-based SfM results.

Additional post-processing, advanced vegetation filtering (Anders et al. 2019) and co-registration utilizing MSA could improve the relative position accuracy;

however, UAS data would still have the disadvantage that (a) it does not cover the entire watershed due to high data volume and respective intensive or rather unmanageable data post-processing for an increasing number of time steps (long-term monitoring). (b) There are vegetation-induced data gaps and uncertainties, which are partly also the case with TLS data. However, TLS is still able to penetrate parts of the vegetation and to obtain information on the real ground surface (Anders et al. 2019). (c) As mentioned in other studies, the reproducibility of consecutive UAS-based DEMs is hampered due to the fact that it is a passive remote sensing technique, therefore strongly influenced by illumination conditions (e.g. clouds, haze) (Clapuyt et al. 2016). Additionally, UAS hardware has experienced an incredible development in the last decade (Giordan et al. 2018); with respect to long-term monitoring projects, this too can impede comparability of consecutive UAS and SfM campaigns. (d) The evaluation of results and error assessment requires detailed experts' knowledge. Optimized GCP layouts differ in literature (Sanz-Ablanedo et al. 2018), the measurement is time-consuming and requires a high-definition D-GNSS as acquisition errors propagate throughout SfM processing and DEM generation. As these GCP measurements are still not sufficient with respect to the relative position accuracy of consecutive time steps, intensive post-processing with respect to data registration will be required. Even then, it is not sure whether position accuracy will be enough to detect real surface change at the respective site due to the order of process magnitude and other influences on data accuracy.

8.4 Soil Erosion

8.4.1 General Information

The wide spectrum of water-induced erosion types are defined by their size and area of impact. They range from splash erosion triggered by the impact of one individual rain drop to rill and gully erosion as a result of incision by concentrated water runoff. Even though the size of the process is part of its definition, the limits are vague. According to the Soil Science Society of America (2001), rill erosion is defined as the process forming small channels of only several centimetres depth, while gully erosion further deepens the rills leading to channels of a depth > 0.5 m.

In an agricultural setting, if crop rotation is performed, the soil is, *inter alia*, affected through linear erosion initiated in predefined rills. These predefined rills can be the result of the cultivation process, such as trenches between rows in potato farming or furrows by seed drilling.

During an erosive event, interrill eroded sediments are transported into rill channels by overland flow, where the concentrated runoff is faster and therefore increases the total sediment transport efficiency (Bruno et al. 2008). Thus, rill erosion is considered the primary sediment-producing process (Bruno et al. 2008; Stefano et al. 2013). Especially, in a setting where plants are cultivated in rows, the concentrated flow in the trenches forms rills and produces sediment. Detection of rill

erosion, as well as the monitoring of the rills, is consequently a crucial management tool in order to reduce soil loss.

On small scale study sites – for example, plots or small areas (~0.5 ha) – various studies have shown the potential and possibilities of SfM to detect small erosional features (Eltner et al. 2014; Smith and Vericat 2015; Hänsel et al. 2016; Eltner et al. 2018; Candido et al. 2020). Nevertheless, with upscaling of the study area size, the errors also increase and therefore reduce the reliability of identified erosion and deposition processes (Smith and Vericat 2015; Eltner et al. 2018; Meinen and Robinson 2020).

Unmanned laser scanning (ULS), on the other side, has to the authors' knowledge not been applied to measure or monitor small scale erosion processes. The main application has been in forestry (Wieser et al. 2017; Liang et al. 2019; Prata et al. 2020) and landslide monitoring (Pfeiffer et al. 2019; Zieher et al. 2019), while the utilization for surface change detection is rather new (Mayr et al. 2019; Sofonia et al. 2019; Backes et al. 2020).

The presented case studies were conducted on in-use agricultural fields. One of the fields was cultivated with corn, while not 2 potatoes, but 2 fields! potatoes were planted. Since for both crops crop rotation is crucial, each study observed only 1 year on each field. Therefore, the focus of the case studies and this work is put on the detection of the smallest large-scale features – annual rill and linear sheet erosion – ranging from a few millimetres to a few centimetres.

8.5 Study Area: Böheimkirchen – Example for Linear Erosion

8.5.1 Description of Site

The first study site is located in Böheimkirchen, Austria (Fig. 8.5a). It is an agricultural field of approximately 2 ha on which corn is cultivated along the contour (Fig. 8.5b+c). The straight field has a mean slope of 9.3°. The selected field is located in a transitional zone between two soil types: Planosol in the lower-lying southern and western parts and Gleyic Cambisol in the north and north-eastern, upper parts of the field. Texture classes of the top horizon are silty loam and loamy sand, corresponding to grain size distributions of 10-62-28% and 38-49-13% (sand-silt-clay), respectively. This data is based on the Austrian Soil Survey (ÖBK); soil samples were not taken during the 2020 study.

8.5.1.1 Description of Research Aims

The aim of the study is to be able to predict, without explicitly modelling surface runoff, whether it can be expected to flow along the tillage direction (WNW-ESO in this case) or in the direction of the topographical slope (SSW in this case). By

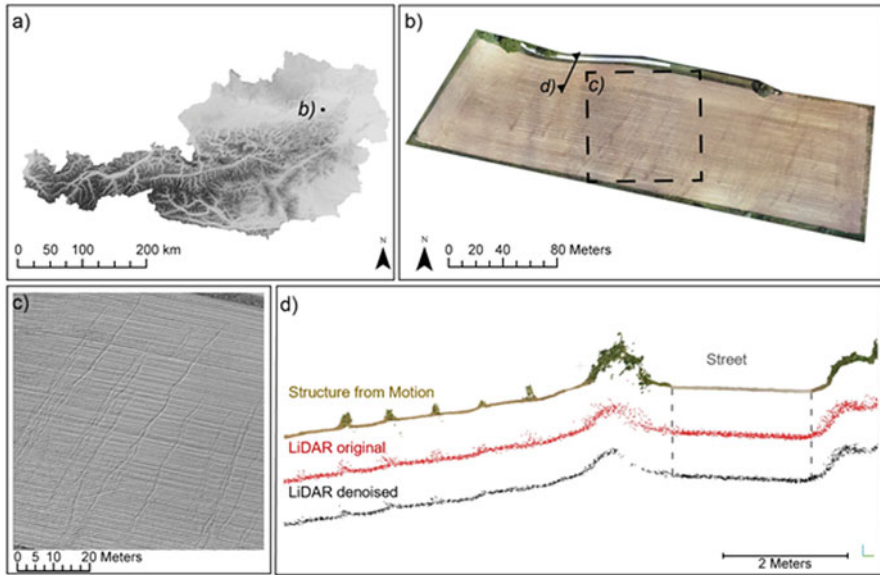


Fig. 8.5 Location of the Böhheimkirchen study site and areas/profile of examination. **(a)** Location of the study site in Austria close to the Alpine foreland. **(b)** Orthomosaic of the agricultural field. **(c)** Zoom in for rill examination. **(d)** Profile along slope of the point clouds generated with SfM and LiDAR. Denoised LiDAR cloud was cleaned applying SOR- and Noise Filter in CloudCompare. SfM cloud is displayed in RGB colours, while original and denoised LiDAR clouds are shown in red and black, respectively. Relief shading of **(a)** is based on an ALS-derived Austrian 10 m DEM (BMDW 2015), and **(b)** and **(c)** on the DEM, with a cellsize of 9 mm, generated with SfM of the survey (2020-06-03)

default, the latter is expected to be true – mainly due to the fact that the tillage direction or orientated roughness is not directly represented at DEM resolutions of >0.1 m cellsize (Nunes et al. 2018). Efforts have been made in this direction for example by Takken et al. (2001), who developed an algorithm based on several parameters (slope, angle between topographic and tillage direction, oriented roughness) to decide for each cell, which of the two possible directions (tillage or topographic) is more likely and then combine the resulting flow directions (correcting the conflicting flow directions created in the process). Other sources on the topic are for example Ludwig et al. (1995) or Souchere et al. (1998).

The actual effort of the study is twofold: (1) apply the algorithm of Takken et al. (2001) and find out if it is able to predict the surface runoff regime (flow in tillage or topographic direction) recorded by the UAS mission, i.e. which is visible in the orthophoto and represented by the DEM elevation. (2) use the high-resolution DEM from the UAS mission directly in order to create an alternative approach that is better able to reproduce the runoff pattern that is evident in the data. Approach number 2 is only expected to yield results when a large range of different field conditions, geometries and topographies are investigated.

8.5.2 *Flight Routines and Post-processing*

The UAS flight took place after a 20 mm/day precipitation event in June 2020 – the precipitation data is only available in a daily format, yet since erosion was triggered, it can be assumed that the precipitation fell in a shorter period than in a day. A DJI Matrice 600 octocopter mounted with a Sony Alpha 6000 camera and a Riegl MiniVUX-1UAV laser scanner was used for image and LiDAR data acquisition (cf. Fig. 8.6). Flying altitude was set to 25–45 m above ground resulting in a ground sampling distance (GSD) of 0.61–1.11 cm/pixel. Side and frontal overlap of images were set to 80% and 75%, respectively, leading to a total amount of 623 images.

Using Agisoft Metashape and RiProcess for each data acquisition method a point cloud and digital surface model were generated. Point densities have mean values of 16,000 points/m² for SfM and 1000 points/m² for LiDAR point clouds. While a root mean square error of 0.023 m was observed for the ground control points with SfM, no registration errors were determined for the LiDAR cloud. The study is still ongoing with no results published yet. Nevertheless, the high-resolution point clouds and DEMs are in use to qualitatively analyse the observed rills (Fig. 8.5c) and will be used here to present noise challenges of ULS point clouds (Fig. 8.5d).



Fig. 8.6 DJI Matrice 600 with (a) the mounted LiDAR Riegl MiniVux-1UAV laser scanner and (b) the Sony Alpha 6000 optical camera

8.5.3 Results

Comparison of two derived point clouds shows a high noise in the LiDAR data, whereas SfM generated a more precise cloud. This is especially visible in the street section of the profile (Fig. 8.5d), where mean differences of the z extent account for 0.0026 m in the SfM cloud and 0.0495 m in the raw LiDAR cloud. Through the application of Statistical Outlier Removal Filter (SOR) and Noise Filter, which are integrated within CloudCompare, this noise could be reduced to 0.0159 m. Filtering of the point cloud reduced point density to 640 points/m², which should still be sufficient for topographic change detection (Resop et al. 2019). Through multiple iterations of filtering, the precision of ULS point clouds gets reduced continuously but at the cost of losing points, which requires individual evaluation for each survey. These precision drawbacks of ULS data can be problematic in further processing and analysis and therefore need consideration whether the method is applicable for the investigated process.

8.5.4 Study Area Herzogbirbaum and Hollabrunn – Example for Change Detection

8.5.4.1 Description of Sites

Two agricultural fields in the Austrian Weinviertel were chosen for the investigation (Fig. 8.7a). The first site is in Herzogbirbaum, while the second one is situated – about 15 km distant – in Hollabrunn.

The area of interest of the Herzogbirbaum field has a mean slope of 4° and is approximately 290 m long, and 50 m wide, leading to an area of 1.4 ha (Fig. 8.7b). The soil the site is located on is a Chernozem, with a silty loam soil texture, consisting of 27% clay, 67% silt, and 6% sand.

The site of Hollabrunn is approximately 2 ha of size and has a mean slope of 4.5°, whereas the upper and lower parts have a lower slope than the middle section. The soil the site is situated on is as well twofold: The upper and lower parts are classified as Chernozem disrupted in the middle section by a band of *Kulturrohboden* (degraded chernozemic soil due to agricultural use). The chernozemic soil's texture is classified as loam, with 20% clay, 47% silt, and 33% sand, while the *Kulturrohboden* has a higher silt proportion – 17-52-31% clay, silt, and sand, respectively – and therefore is classified as silty loam. Additionally, the middle section is characterized by a high proportion of coarse fluvial rocks.

On both sites, the cultivated potatoes were planted before the first flight. Cultivation was done using the same machinery and along the topographical slope.

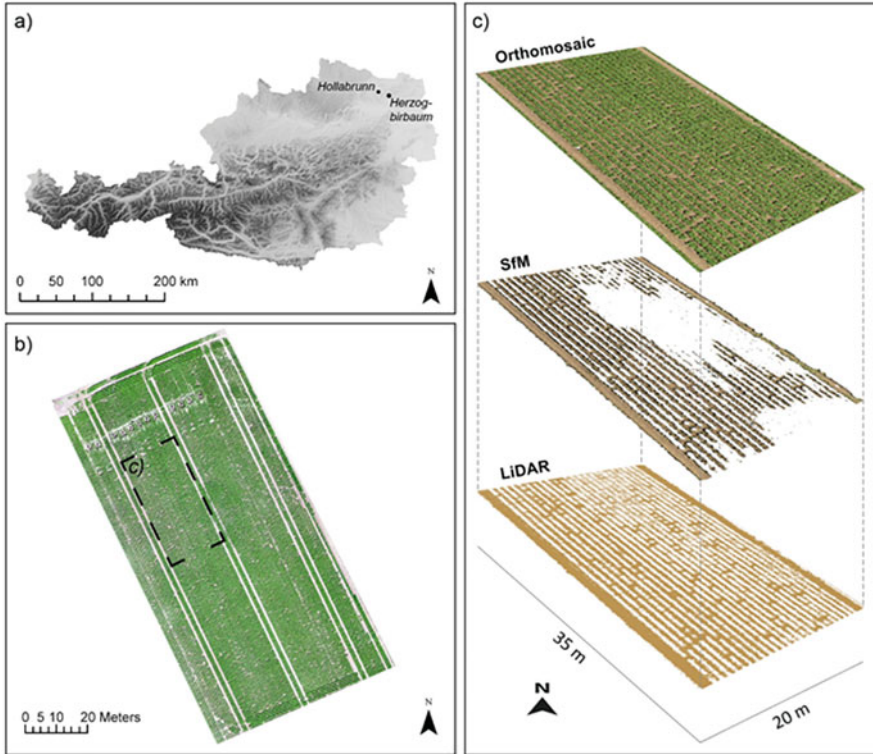


Fig. 8.7 Location of the two change detection study sites and close-ups of the Herzogbirbaum study site. (a) Position of Hollabrunn and Herzogbirbaum in the north-eastern of Austria. (b) Orthomosaic of the Herzogbirbaum study area on 2020-06-10 showing a vegetation cover of 74%. (c) Orthomosaic and vegetation filtered point clouds of a more detailed scenery. Relief shading of (a) is based on an ALS-derived Austrian 10 m DEM (BMDW 2015)

8.5.4.2 Description of Research Aims

The aim of this study is to investigate the soil erosion reduction in potato farming through different measurements. Conventionally potatoes are planted in rows, resulting in the area between the rows as the optimal location for surface runoff. The three counter measurements – greening, dyking, and greened dykes between the rows – are contrasted with the conventional method by using the UAS data to assess which method resulted in the lowest soil loss.

8.5.5 Flight Routines and Post-processing

Five UAS flights per study site were conducted between April and September of 2020 for image acquisition, whereas on the latter three flights, additionally LiDAR

data was taken. For each of the sites, the first two flights of the season were performed using a DJI Matrice 200 quadcopter with a nadir-faced Zenmuse XT2 camera – whereas only optical photographs were used. The latter three surveys were operated using a DJI Matrice 600 hexacopter with a mounted Riegl MiniVUX-1 UAV laser scanner and a Sony Alpha 6000 camera (refer to Fig. 8.6). Flying altitude for all surveys was set to 25 m above ground resulting in a ground sampling distance of 0.99 and 0.62 cm/pixel for the Zenmuse XT2 and Sony Alpha 600, respectively. Frontal overlap of the images was set between 80% and 85% and side overlap to 75–80%.

Processing was done with Agisoft Metashape for observed photographs and RiProcess for LiDAR data. Root mean square error (RMSE) of ground control points used in SfM procedure varied between 0.012 m and 0.032 m. Level of detection was calculated using the standard deviation of the RMSE for each flight, resulting in a level of detection (LoD) range of 0.038 m and 0.071 m. The vegetation classifier of Agisoft Metashape was applied on all clouds with mixed results depending on the vegetation cover. Mean point densities of the raw LiDAR point clouds varied between 1700 and 2500 points/m². On the dataset of June, where vegetation filtering was necessary and still possible, the TerrainFilter module of OPALS was applied. The resulting point clouds had a mean point density of 350–400 points/m². This is on the lower end to be suitable for surface change detection (Resop et al. 2019), but it includes areas where because of the dense vegetation no ground points at all could be observed, for example, top of rows. Since the areas between the rows are way more important – in which a high point density can be observed – the actual point density in the areas of interest should be higher than 350–400 points/m².

8.5.6 Results

Small scale volume changes calculations – for example, rill erosion – with these datasets have shown to be difficult for various reasons: (a) Vegetation cover has shown to be a crucial limiting factor in the study. While vegetation cover for the first two flights was rather low – ranging between 0% and 9% – it increased severely after the second flight reaching up to 74% in June (third survey) and even 97% in July (fourth survey) in Herzogbirbaum. In Hollabrunn, vegetation cover was generally lower than in Herzogbirbaum, with coverage reaching 50% in June and 73% in July. Before the fifth flight in September, haulm destruction was performed on the plants, leading to dried-out potato plants covering the soil. While vegetation can easily be filtered for the second flight, later flights have proven to be difficult. Vegetation filters applied on point clouds generated with SfM struggle to deliver consistent vegetation-free point clouds with datasets where the observed vegetation cover is higher than 50%. Using LiDAR, a tolerable vegetation-free point cloud can be generated with vegetation covering about 75% of the soil. In the case of the June Herzogbirbaum survey (Fig. 8.7c), this leads to a sparse vegetation free point cloud

with a large area in the northeast of the area of interest where no ground points could be classified when filtering the SfM cloud. On the contrary, the filtered LiDAR cloud still has enough ground points – even though they are sparser in the area where no ground points could be observed with SfM – to feature the soil surface. (b) Since the farmer actively uses the field, it was not possible to install fixed checkpoints on the field, which were either high enough to surpass vegetation but not hinder (spraying) machines or impede the farmer’s work. As a compromise, soil anchors were placed on the ridges of the potato dams, in which GCPs were put before each survey. This setup worked fine until the third survey, from which again vegetation was so dense that the GCPs could not be placed in the soil anchors. (c) It was also observed that using three-dimensional control points in a LiDAR study is necessary. Planar control points – like those usually used in an SfM study – do not result in a high enough point density on the control point surface and result in a higher error. (d) As a result of the aforementioned difficulties, a satisfying point cloud registration could not be achieved. Since the field per se is in constant change – soil subsidence, vegetation growing – fixed checkpoints or at least checkpoints at the same location in each survey, showed to be crucial.

8.5.7 Discussion

To measure large-scale erosion processes with remote sensing techniques, various criteria must be fulfilled. Foremost, the LoD must be smaller than the actual process extent. In most large-scale erosion investigations with UAV-generated point clouds, this will be the most limiting factor. But also, vegetation – and consequently filtering of vegetation – as well as, mainly in the case of ULS, cloud density play crucial roles. In this regard, both techniques used in this work come with their virtues and drawbacks. While SfM struggles to filter vegetation covering more than 50% of the ground, the point density and precision of a SfM point cloud are superior to a point cloud generated with ULS. Regarding change detection, each point cloud used in this work, even though flight routes were planned with high overlaps, low flying altitude, and a cross-pattern, has a high RMSE, and therefore, the LoD of two clouds were too high to assess large-scale erosion quantitatively.

Referring to SfM, Eltner et al. (2018) and Candido et al. (2020) have proven that it is possible to generate point clouds with an optimized setup, of which the RMSE is within a few millimetres. Investigating small areas – from plot scale to small fields reaching up to 20×70 m – and working with fixed targets are both measures to increase data reliability (Eltner et al. 2018). Additionally, their areas of interest were kept free of vegetation which further reduces uncertainties within the data since significant vegetation makes SfM unsuitable as a method (Candido et al. 2020). Within the framework of this study, these optimizations were not able to be made. The field size was given in the case of Böheimkirchen. In the case of Herzogbirbaum and Hollabrunn, the extent of the experimental setup determined the width and length of the area of interest. Since all fields were in active use and cultivated,

vegetation growth was unavoidable, resulting in inadequate (Eltner et al. 2018; Candido et al. 2020) datasets after June for Herzogbirbaum and July for Hollabrunn. Fixed targets were not installed since they would have needed to surpass vegetation and be lower than spraying machinery.

The studies of Eltner et al. (2018) and Candido et al. (2020) further highlighted and supported previous investigations that once you measure surface changes in a sub-centimetre range, soil erosion and deposition is not the only process altering the soil topography – swelling and shrinking (Eltner et al. 2018; Kaiser et al. 2018; Candido et al. 2020), consolidation and surface crusting (Eltner et al. 2016; Eltner et al. 2018; Candido et al. 2020), raindrop impact and soil compaction (Hänsel et al. 2016; Candido et al. 2020), or disturbance by animals cause changes on the soil surface (Candido et al. 2020). Additionally, they advise performing SfM investigations on large-scale (Candido et al. 2020) to medium-sized (Eltner et al. 2018) plots or fields since, with increasing plot size, data reliability decreased (Smith and Vericat 2015; Eltner et al. 2018; Meinen and Robinson 2020).

As mentioned before, the quality of ULS point clouds is less vulnerable to vegetation but more limited by its point density. Two factors influencing point density aside from the flight routine are vegetation and precision of the point cloud since in order to filter vegetation and deviating points, point density will decrease. However, the lower limit of a suitable point density is strongly connected to the extent of the investigated process. For example, a point density of 300–400 points/m² might be sufficient to investigate a large landslide, while the investigation of small erosion features most likely needs a point density higher than 2000 points/m². With this in mind, ULS has shown its potential to monitor erosion or mass movement processes of a larger scale and magnitude than presented in this work in various landscapes (Mayr et al. 2019; Sofonia et al. 2019; Backes et al. 2020). To discuss the RMSE of ULS point clouds, values found in literature will be used since the registration error of those was not determined in this work. The reported registration errors vary between 0.05 ± 0.31 m (Sofonia et al. 2019) and 0.46 m (Backes et al. 2020). Babbel et al. (2019) and Mayr et al. (2020) reported higher errors in densely vegetated areas than on bare earth regions or buildings. How these uncertainties influence the quality of a vegetation-filtered point cloud has not been established, as far as we know. Mayr et al. (2020), who initially reported a registration error of 0.19 m, was able to reduce this error with a target-based registration to 0.041 m. Corresponding to SfM, fixed reference targets for point cloud registration, in general, showed to be crucial to reduce registration errors (Cramer et al. 2018; Haala et al. 2020; Mayr et al. 2020). Nevertheless, the reported vertical accuracies of 0.03 m (Cramer et al. 2018) and 0.09 m (Babbel et al. 2019) or the 3D mean absolute error of 0.041 m by Mayr et al. (2019) are still too high to monitor large-scale erosion. Therefore, Mayr et al. (2020) concluded that a ULS investigation is suitable if the surface changes are greater than 0.2 m. Using a hybrid georeferencing method (Mandlbürger et al. 2017; Gliira et al. 2019) with both imagery and LiDAR data, Haala et al. (2020) reduced the elevation accuracy to 0.8 cm. An error below 1 cm should be sufficient to assess the impact of a large-scale erosion event quantitatively. Therefore, the hybrid georeferencing method seems to enhance not only the

registration errors of ULS data but also the applicability of point clouds generated with UAVs.

Both methods – SfM and ULS – are limited by registration errors to reliably make statements on large-scale erosion processes. While precise ground control point measurements are needed for the georeferencing of a cloud, registering two different point clouds requires fixed targets in a survey. Depending on the setting, vegetation filtering can be crucial to monitor surface changes. We found that vegetation filtering with LiDAR is possible even at a high level of coverage (75%), whereas SfM seems to be limited to a coverage of about 50% because of a lack of ground observations. Moreover, recent studies have pointed out that SfM and LiDAR are not competing techniques but rather enhance the results if combined (Haala et al. 2020).

8.6 Conclusion

UAS-based SfM and LiDAR (ULS) were applied within two different fields of research (landslide and erosion research) to assess the user-friendly applicability of DEM-based change detection and the informative value of respective DoD calculations for the detailed investigation of large-scale (small) processes. Both complex, slow-moving landslides and soil erosion depict the challenge of small process rates and changes in surface height. These occur not only locally but also over larger areas and, respectively, on different parts of an affected area. While changes in the order of only millimetres per observation period are common for soil erosion (annual rill- and linear sheet erosion), changes in surface height in the order of a few centimetres per observation period or year are observable for parts of a complex, slow-moving landslide (e.g. rotational, retrogressive sliding). The investigation of both processes faces similar challenges when it comes to high-resolution change detection, despite the differences in their inherent nature. Challenges recognized for both examples in this study include, but are not limited to:

- UAS application has become significantly more user-friendly in the last years. Vehicle size, battery capacity, flight path planners and internal GNSS receivers – to mention a few sticking points – have improved. Flight parameters (altitude, picture overlap, point distance, etc.) have to be chosen with care with respect to the required resolution of respective surface models, data size used for post-processing and battery capacity.
- Flight altitudes of only a few meters are commonly used in plot-scale soil erosion research to generate high resolutions, especially with respect to SfM. This would not be feasible for the agricultural fields (rill erosion) investigated here. The flight altitudes for the soil erosion sites of 25–45 m should also be used when investigating the landslide processes, where altitudes of 60–120 m were applied. However, only one small landslide part was investigated there; the entire watershed is of interest to explore the process in its entirety. Again, the lower altitudes are more desirable but not feasible – vegetation cover (trees) prohibit low flight

altitudes and data size would increase drastically over time, complicating data processing. Both fields of research therefore face the same problem of generating data, which is detailed enough but can capture the entire area of interest.

- Fixed GCPs are necessary to obtain accurate registration over consecutive time steps. However, this is not always feasible. For example, areas affected by sliding at the Hofermühle are used for hay production; areas affected by soil erosion are in-use agricultural fields. The possibilities to install fixed GCPs are limited or impossible, especially as there are none or few areas of “no change” (streets, houses) in close vicinity of the respective study areas. While such areas would be available further away, they are not covered by the UAS flights as this would drastically increase the number of photographs and data post-processing efforts. In addition, the further away they are, the less accurate is their impact on the overall point cloud calculation. However, GCPs are needed to (a) improve the geometry of SfM-based models, (b) to enable the absolute referencing of surface models to, for example, compare with other georeferenced data and (c) to enable vertical and horizontal positioning and co-registering of consecutive models. The fact that there are no stable or distinct features or areas in close vicinity to the respective study sites requires the use of alternating GCP layout; their measurement accuracy is one important source of uncertainty for these kinds of detailed scenarios.
- Data post-processing includes the generation of surface models utilizing SfM algorithms for aerial RGB pictures. Point clouds are calculated with this method, whereas with ULS – and TLS, which has been used for data comparison – points are measured (absolute distances). LiDAR, too, inherits certain measurement uncertainties but is a direct, metric measurement of distances. Data inaccuracies related to distance calculations with SfM are more complicated to determine. Point cloud calculations with insufficient data (overlap, flight height differences, GCPs) can lead to internal distortions and incorrect geometries, which do not occur with LiDAR. The evaluation of respective clouds is difficult. Additionally, the influence of dense vegetation cover (grass, potato plants) can prohibit ground point detection for SfM, while LiDAR can still partly penetrate vegetation. Without ground points, a model of the bare earth cannot be calculated – it rather seems likely that in the case of densely grass-covered areas (landslide), the grass itself represents the surface after SfM calculation. Without real surface information, small changes in surface height cannot be calculated, respectively quantified.
- Data registration of consecutive time steps is the most important step in post-processing – and one most problematic. As mentioned, variable GCPs showed to be not accurate enough in both fields of research and were not sufficient for accurate vertical positioning of consecutive models. The installation of fixed GCPs is practically impossible. Therefore, co-registration with, for example, MSA may improve relative positioning of multiple time steps. However, this is again somewhat limited. Planar surfaces, areas of no change and clearly distinguishable true ground point information are needed for all time steps for this adjustment to deliver accurate results. The highest factor of uncertainty in this

context is again vegetation. The filtering of vegetation prior to MSA is possible for LiDAR-derived surface models, both in soil erosion and landslide research; SfM-derived models hamper the separation of real surface data. Choosing a reasonable time of data acquisition could improve this impact, for example, seasons of sparse vegetation cover and leaf density (winter). However, this may not align with time-sensitive research aims. Soil erosion in agricultural fields is of interest especially during the growing season. Respective landslide areas can be snow covered in winter. Additionally, apart from snow melt, precipitation is of high importance regarding triggering of events, not only for erosion. Precipitation values are highest in summer, where vegetation cover is highest, too. And last, the co-registration utilizing MSA is CPU-intensive. Considering the quantity of data which needs to be processed over time (long-term monitoring), this might become an issue when working with such high-resolution data.

UAS-based SfM and LiDAR are powerful tools when it comes to the investigation of natural processes, but their applicability is facing a variety of challenges when it comes to detailed, large-scale processes such as soil erosion and slow-moving landslides (sliding). Inaccuracies in SfM and ULS registration limit the evaluation of erosion processes using only variable GCPs. The same can be asserted for the SfM-based DoDs with respect to slow sliding processes. Vegetation cover has the highest impact with respect to data noise in data acquisition, SfM calculation and – pursuing data post-processing – further data registration. Vegetation filtering is crucial, yet a time-consuming step, and limited in the case of SfM-based models. Fixed GCPs seem to be mandatory for registration of consecutive time steps; however, they can hardly be realized in natural systems with anthropogenic use. UAS-based SfM – and with constraints also ULS – are often described as the solution to investigate natural processes with “low-costs”. Yet, the “matter of expense” is not limited to the UAS hardware. High-definition and expensive D-GNSS devices are mandatory for optimal GCP measurement. Post-processing is time- and resource-consuming. Accuracy evaluation of intermediate and final results requires expert’s knowledge.

References

- Abellan A, Derron M-H, Jaboyedoff M (2016) “Use of 3D point clouds in Geohazards” special issue: current challenges and future trends. *Remote Sens* 8:130
- Aber JS, Marzolf I, Ries JB (2010a) Chapter 4: Lighting and atmospheric conditions. In: Aber JS, Marzolf I, Ries JB (eds) *Small-format aerial photography*. Elsevier, Amsterdam, pp 41–56
- Aber JS, Marzolf I, Ries JB (2010b) Chapter 11: Image processing and analysis. In: Aber JS, Marzolf I, Ries JB (eds) *Small-format aerial photography*. Elsevier, Amsterdam, pp 159–181
- Aber JS, Marzolf I, Ries JB, Aber SEW (2019a) Chapter 3: Principles of photogrammetry. In: Aber JS, Marzolf I, Ries JB, Aber SEW (eds) *Small-format aerial photography and UAS imagery*, 2nd edn. Academic, pp 19–38
- Aber JS, Marzolf I, Ries JB, Aber SEW (2019b) *Small-format aerial photography and UAS imagery*, 2nd edn. Elsevier Academic Press

- Anders N, Valente J, Masselink R, Keesstra S (2019) Comparing filtering techniques for removing vegetation from UAV-based photogrammetric point clouds. *Drones* 3:61
- Babbel BJ, Olsen MJ, Che E, Leshchinsky BA, Simpson C, Dafni J (2019) Evaluation of Uncrewed aircraft systems' Lidar data quality. *ISPRS Int J Geo Inf* 8:532
- Backes D, Smigaj M, Schimka M, Zahs V, Grznárová A, Scaioni M (2020) River morphology monitoring of a small-scale alpine riverbed using drone photogrammetry and LiDAR. *Int Arch Photogramm Remote Sens Spatial Inf Sci XLIII-B2-2020:1017–1024*. <https://doi.org/10.5194/isprs-archives-XLIII-B2-2020-1017-2020>
- Besl PJ, McKay ND (1992) A method for registration of 3-D shapes. *IEEE Trans Pattern Anal Mach Intell* 14:239–256. <https://doi.org/10.1109/34.121791>
- BMDW (2015) Digital elevation model (DEM) based on airborne laserscan data of the austrian federal states; raster resolution 10m. ed. g. a. Bundesministerium für Digitalisierung und Wirtschaftsstandort (BMDW). Austria: data.gv.at (Open Data Österreich)
- Bruno C, Stefano CD, Ferro V (2008) Field investigation on rilling in the experimental Sparacia area, South Italy. *Earth Surf Process Landf* 33:263–279
- Candido BM, Quinton JN, James MR, Silva MLN, de Teotônio CS, de Lima W, Beniaich A, Eltner A (2020) High-resolution monitoring of diffuse (sheet or interrill) erosion using structure-from-motion. *Geoderma* 375:114477
- Carrivick JL, Smith MW, Quincey DJ (2016) *Structure motion geosciences*. Wiley
- Casagli N, Frodella W, Morelli S, Tofani V, Ciampalini A, Intrieri E, Raspini F, Rossi G, Tanteri L, Lu P (2017) Spaceborne, UAV and ground-based remote sensing techniques for landslide mapping, monitoring and early warning. *Geoenvironmental Disasters* 4:9. <https://doi.org/10.1186/s40677-017-0073-1>
- Cignetti M, Godone D, Wrzesniak A, Giordan D (2019) Structure from motion multisource application for landslide characterization and monitoring: the Champlas du col case study, Sestriere, North-Western Italy. *Sensors (Basel, Switzerland)* 19:2364. <https://doi.org/10.3390/s19102364>
- Clapuyt F, Vanacker V, Van Oost K (2016) Reproducibility of UAV-based earth topography reconstructions based on structure-from-motion algorithms. *Geomorphology* 260:4–15. <https://doi.org/10.1016/j.geomorph.2015.05.011>
- Clapuyt F, Vanacker V, Schlunegger F, Van Oost K (2017) Unravelling earth flow dynamics with 3-D time series derived from UAV-SfM models. *Earth Surf Dyn* 5:791–806. <https://doi.org/10.5194/esurf-5-791-2017>
- Cook KL (2017) An evaluation of the effectiveness of low-cost UAVs and structure from motion for geomorphic change detection. *Geomorphology* 278:195–208. <https://doi.org/10.1016/j.geomorph.2016.11.009>
- Cook KL, Dietze M (2019) Short communication: a simple workflow for robust low-cost UAV-derived change detection without ground control points. *Earth Surf Dyn* 7:1009–1017. <https://doi.org/10.5194/esurf-7-1009-2019>
- Cramer M, Haala N, Laupheimer D, Mandlbürger G, Havel P (2018) Ultra-high precision UAV-based LIDAR and dense image matching. *ISPRS – Int Arch Photogramm Remote Sens Spat Inf Sci XLII-1:115–120*
- Crozier MJ (2010) Landslide geomorphology: an argument for recognition, with examples from New Zealand. *Geomorphology* 120:3–15. <https://doi.org/10.1016/j.geomorph.2009.09.010>
- Cruden DM, Varnes DJ (1996) Landslide types and processes. In: Turner AK, Schuster RL (eds) *Landslides: investigation and mitigation*. National Academy Press, Washington, DC, pp 36–75
- Eker R, Aydın A, Hübl J (2017) Unmanned aerial vehicle (UAV)-based monitoring of a landslide: Gallenzerkogel landslide (Ybbs-Lower Austria) case study. *Environ Monit Assess* 190:28. <https://doi.org/10.1007/s10661-017-6402-8>
- Eltner A, Baumgart P, Maas H-G, Faust D (2014) Multi-temporal UAV data for automatic measurement of rill and interrill erosion on loess soil. *Earth Surf Process Landf* 40:741–755

- Eltner A, Kaiser A, Castillo C, Rock G, Neugirg F, Abellán A (2016) Image-based surface reconstruction in geomorphometry – merits, limits and developments. *Earth Surf Dyn* 4:359–389. <https://doi.org/10.5194/esurf-4-359-2016>
- Eltner A, Maas H-G, Faust D (2018) Soil micro-topography change detection at hillslopes in fragile Mediterranean landscapes. *Geoderma* 313:217–232
- Giordan D, Manconi A, Tannant DD, Allasia P (2015) UAV: Low-cost remote sensing for high-resolution investigation of landslides. In: 2015 IEEE international geoscience and remote sensing symposium (IGARSS), pp 5344–5347
- Giordan D, Hayakawa Y, Nex F, Remondino F, Tarolli P (2018) Review article: the use of remotely piloted aircraft systems (RPASs) for natural hazards monitoring and management. *Nat Hazards Earth Syst Sci* 18:1079–1096. <https://doi.org/10.5194/nhess-18-1079-2018>
- Glade T, Anderson MG, Crozier MJ (2005) *Landslide hazard and risk*. Wiley, Chichester
- Glira P, Pfeifer N, Mandlbürger G (2019) Hybrid orientation of airborne lidar point clouds and aerial images. *ISPRS Ann Photogramm Remote Sens Spat Inf Sci IV-2/W5:567–574*
- Gomes Pessoa G, Caceres Carrilho A, Takahashi Miyoshi G, Amorim A, Galo M (2021) Assessment of UAV-based digital surface model and the effects of quantity and distribution of ground control points. *Int J Remote Sens* 42:65–83. <https://doi.org/10.1080/01431161.2020.1800122>
- Gomez C, Purdie H (2016) UAV- based photogrammetry and Geocomputing for hazards and disaster risk monitoring – a review. *Geoenvironmental Disasters* 3:23. <https://doi.org/10.1186/s40677-016-0060-y>
- Haala N, Kölle M, Cramer M, Laupheimer D, Mandlbürger G, Glira P (2020) Hybrid georeferencing, enhancement and classification of ultra-high resolution UAV lidar and image point clouds for monitoring applications. *ISPRS Ann Photogramm Remote Sens Spat Inf Sci V-2-2020:727–734*
- Hackney C, Clayton A (2015) 2.1.7. Unmanned aerial vehicles (UAVs) and their application in geomorphic mapping. In: Clarke L, Nield JM (eds) *Geomorphological techniques* (Online Edition). GB: British Society for Geomorphology, London
- Hänsel P, Schindewolf M, Eltner A, Kaiser A, Schmidt J (2016) Feasibility of high-resolution soil erosion measurements by means of rainfall simulations and SfM photogrammetry. *Hydrology* 3: 38
- Heritage GL, Large ARG (2009) Principles of 3D laser scanning. In: *Laser scanning for the environmental sciences*. Wiley-Blackwell, Hoboken, pp 21–34
- Hsieh Y-C, Chan Y-C, Hu J-C (2016) Digital elevation model differencing and error estimation from multiple sources: a case study from the Meiyuan Shan landslide in Taiwan. *Remote Sens* 8: 199
- Hungr O, Leroueil S, Picarelli L (2014) The Varnes classification of landslide types, an update. *Landslides* 11:167–194. <https://doi.org/10.1007/s10346-013-0436-y>
- Immerzeel WW, Kraaijenbrink PDA, Shea JM, Shrestha AB, Pellicciotti F, Bierkens MFP, de Jong SM (2014) High-resolution monitoring of Himalayan glacier dynamics using unmanned aerial vehicles. *Remote Sens Environ* 150:93–103. <https://doi.org/10.1016/j.rse.2014.04.025>
- Jaboyedoff M, Oppikofer T, Abellán A, Derron M-H, Loye A, Metzger R, Pedrazzini A (2012) Use of LIDAR in landslide investigations: a review. *Nat Hazards* 61:5–28. <https://doi.org/10.1007/s11069-010-9634-2>
- James MR, Robson S (2012) Straightforward reconstruction of 3D surfaces and topography with a camera: accuracy and geoscience application. *J Geophys Res Earth Surf* 117:F03017. <https://doi.org/10.1029/2011JF002289>
- Kaiser A, Erhardt A, Eltner A (2018) Addressing uncertainties in interpreting soil surface changes by multitemporal high-resolution topography data across scales. *Land Degrad Dev* 29:2264–2277
- Kasperski J, Delacourt C, Allemand P, Potherat P, Jaud M, Varrel E (2010) Application of a Terrestrial Laser Scanner (TLS) to the Study of the Séchilienne Landslide (Isère, France). *Remote Sens* 2:2785–2802

- Lacroix P, Handwerger AL, Bièvre G (2020) Life and death of slow-moving landslides. *Nat Rev Earth Environ* 1:404–419. <https://doi.org/10.1038/s43017-020-0072-8>
- Lague D, Brodu N, Leroux J (2013) Accurate 3D comparison of complex topography with terrestrial laser scanner: application to the Rangitikei canyon (N-Z). *ISPRS J Photogramm Remote Sens* 82:10–26. <https://doi.org/10.1016/j.isprsjprs.2013.04.009>
- Liang X, Wang Y, Pyörälä J, Lehtomäki M, Yu X, Kaartinen H, Kukko A, Honkavaara E, Issaoui AEI, Nevalainen O, Vaaja M, Virtanen J-P, Katoh M, Deng S (2019) Forest in situ observations using unmanned aerial vehicle as an alternative of terrestrial measurements. *For Ecosyst* 6:3–16
- Lucieer A, de Jong SM, Turner D (2014) Mapping landslide displacements using Structure from Motion (SfM) and image correlation of multi-temporal UAV photography. *Prog Phys Geogr Earth Environ* 38:97–116. <https://doi.org/10.1177/0309133313515293>
- Ludwig B, Boiffin J, Chadluf J, Auzet A-V (1995) Hydrological structure and erosion damage caused by concentrated flow in cultivated catchments. *Catena* 25:227–252. [https://doi.org/10.1016/0341-8162\(95\)00012-H](https://doi.org/10.1016/0341-8162(95)00012-H)
- Ludwig M, Runge CM, Friess N, Koch TL, Richter S, Seyfried S, Wraase L, Lobo A, Sebastià M-T, Reudenbach C, Nauss T (2020) Quality assessment of photogrammetric methods—a workflow for reproducible UAS Orthomosaics. *Remote Sens* 12:3831
- Mancini F, Dubbini M, Gattelli M, Stecchi F, Fabbri S, Gabbianelli G (2013) Using unmanned aerial vehicles (UAV) for high-resolution reconstruction of topography: the structure from motion approach on coastal environments. *Remote Sens* 5:6880–6898
- Mandlbürger G, Wenzel K, Spitzer A, Haala N, Glira P, Pfeifer N (2017) *Improved topographic models via concurrent airborne Lidar and dense image matching*. *ISPRS Ann Photogramm Remote Sens Spat Inf Sci IV-2/W4:259–266*
- Marzolf I, Poesen J (2009) The potential of 3D gully monitoring with GIS using high-resolution aerial photography and a digital photogrammetry system. *Geomorphology* 111:48–60. <https://doi.org/10.1016/j.geomorph.2008.05.047>
- Mayr A, Bremer M, Rutzinger M, Geitner C (2019) Unmanned aerial vehicle laser scanning for erosion monitoring in alpine grassland. *ISPRS Ann Photogramm Remote Sens Spat Inf Sci IV-2/W5:405–412*
- Mayr A, Bremer M, Rutzinger M (2020) 3D point errors and change detection accuracy of unmanned aerial vehicle laser scanning data. *ISPRS Ann Photogramm Remote Sens Spat Inf Sci V-2-2020:765–772*
- Meinen BU, Robinson DT (2020) Mapping erosion and deposition in an agricultural landscape: optimization of UAV image acquisition schemes for SfM-MVS. *Remote Sens Environ* 239: 111666
- Nex F, Remondino F (2014) UAV for 3D mapping applications: a review. *Appl Geomat* 6:1–15. <https://doi.org/10.1007/s12518-013-0120-x>
- Niethammer U, Rothmund S, Joswig M, Malet JP, Bogaard T (2009) UAV-based remote sensing of the slow-moving landslide super-Sauze. In: Malet J-P, Remaitre A, Boogard T (eds) *Proceedings of the international conference on landslide processes: from geomorphologic mapping to dynamic modelling*. CERG Editions, Strasbourg, pp 69–74
- Niethammer U, James MR, Rothmund S, Travelletti J, Joswig M (2012) UAV-based remote sensing of the super-Sauze landslide: evaluation and results. *Eng Geol* 128:2–11. <https://doi.org/10.1016/j.enggeo.2011.03.012>
- NOEL GV (2009) Digital elevation model (DEM) based on airborne laserscan data; raster resolution 1m. ed. Department for Hydrology and Geoinformation. Federal State Government of Lower Austria. St. Pölten, Lower Austria
- NOEL GV (2011) Digital orthophoto (2011-04-09). ed. Department for Hydrology and Geoinformation. Federal State Government of Lower Austria. St. Pölten, Lower Austria
- Nunes JP, Wainwright J, Bielders CL, Darboux F, Fiener P, Finger D, Turnbull L (2018) Better models are more effectively connected models. *Earth Surf Process Landf* 43:1355–1360. <https://doi.org/10.1002/esp.4323>

- Oleire-Oltmanns S, Marzolf I, Peter KD, Ries JB (2012) Unmanned Aerial Vehicle (UAV) for monitoring soil erosion in Morocco. *Remote Sens* 4:3390–3416
- Onnen N, Eltner A, Heckrath G, Van Oost K (2020) Monitoring soil surface roughness under growing winter wheat with low-altitude UAV sensing: potential and limitations. *Earth Surf Process Landf* 45:3747–3759. <https://doi.org/10.1002/esp.4998>
- Peppas MV, Mills JP, Moore P, Miller PE, Chambers JE (2017) Brief communication: landslide motion from cross correlation of UAV-derived morphological attributes. *Nat Hazards Earth Syst Sci* 17:2143–2150. <https://doi.org/10.5194/nhess-17-2143-2017>
- Petschko H, Brenning A, Bell R, Goetz J, Glade T (2014) Assessing the quality of landslide susceptibility maps – case study Lower Austria. *Nat Hazards Earth Syst Sci* 14:95–118. <https://doi.org/10.5194/nhess-14-95-2014>
- Pfeiffer J, Zieher T, Rutzinger M, Bremer M, Wichmann V (2019) Comparison and time series analysis of landslide displacement mapped by airborne, terrestrial and unmanned aerial vehicle based platforms. *ISPRS Ann Photogramm Remote Sens Spat Inf Sci IV-2/W5:421–428*
- Pike RJ, Evans IS, Hengl T (2009) Chapter 1: Geomorphometry: a brief guide. In: Hengl T, Reuter HI (eds) *Developments in soil science*. Elsevier, pp 3–30
- Prata GA, Broadbent EN, de Almeida DRA, Peter JS, Drake J, Medley P, Corte APD, Vogel J, Sharma A, Silva CA, Zambrano AMA, Valbuena R, Wilkinson B (2020) Single-pass UAV-borne GatorEye LiDAR sampling as a rapid assessment method for surveying Forest structure. *Remote Sens* 12:4111
- Prokop A, Panholzer H (2009) Assessing the capability of terrestrial laser scanning for monitoring slow moving landslides. *Nat Hazards Earth Syst Sci (NHSS)* 9:1921–1928. <https://doi.org/10.5194/nhess-9-1921-2009>
- Resop JP, Lehmann L, Hession WC (2019) Drone laser scanning for modeling Riverscape topography and vegetation: comparison with traditional aerial Lidar. *Drones* 3:35
- Riegl LMS (2020) Datasheet RIEGL VZ-6000. Austria, Horn: Riegl Laser Measurement Systems GmbH. http://www.riegl.com/uploads/tx_pxpriegl/downloads/RIEGL_VZ-6000_Datasheet_2020-09-14.pdf. Last accessed 2021-06-09
- Rothmund S, Niethammer U, Malet J-P, Joswig M (2013) Landslide surface monitoring based on UAV-and ground-based images and terrestrial laser scanning: accuracy analysis and morphological interpretation. *First Break* 31:81–87
- Rothmund S, Vouillamoz N, Joswig M (2017) Mapping slow-moving alpine landslides by UAV – opportunities and limitations. *Lead Edge* 36:571–579. <https://doi.org/10.1190/tle36070571.1>
- Sanz-Ablanedo E, Chandler JH, Rodríguez-Pérez JR, Ordóñez C (2018) Accuracy of unmanned aerial vehicle (UAV) and SfM photogrammetry survey as a function of the number and location of ground control points used. *Remote Sens* 10:1606
- Schweigl J, Hervás J (2009) Landslide mapping in Austria. In: EUR – scientific and technical research reports, 61. Office for Official Publications of the European Communities European Commission OPOCE, Luxembourg
- Schwenk H (1992) Massenbewegungen in Niederösterreich 1953–1990. *Jahrb Geol Bundesanst* 135:597–660
- Smith MW, Vericat D (2015) From experimental plots to experimental landscapes: topography, erosion and deposition in sub-humid badlands from structure-from-motion photogrammetry. *Earth Surf Process Landf* 40:1656–1671
- Smith MW, Carrivick JL, Quincey DJ (2016) Structure from motion photogrammetry in physical geography. *Prog Phys Geogr Earth Environ* 40:247–275. <https://doi.org/10.1177/0309133315615805>
- Sofonia J, Phinn S, Roelfsema C, Kendoul F (2019) Observing geomorphological change on an evolving coastal sand dune using SLAM-based UAV LiDAR. *Remote Sens Earth Syst Sci* 2: 273–291
- Soil Science Society of America (2001) Glossary of soil science terms. <https://www.soils.org/publications/soils-glossary/>. Last accessed 2021-03-01

- Souchere V, King D, Daroussin J, Papy F, Capillon A (1998) Effects of tillage on runoff directions: consequences on runoff contributing area within agricultural catchments. *J Hydrol* 206:256–267. [https://doi.org/10.1016/S0022-1694\(98\)00103-6](https://doi.org/10.1016/S0022-1694(98)00103-6)
- Stefano CD, Ferro V, Pampalona V, Sanzone F (2013) Field investigation of rill and ephemeral gully erosion in the Sparacia experimental area, South Italy. *Catena* 101:226–234
- Steger S, Schmaltz E, Seijmonsbergen AC, Glade T (2020) The Walgau – a landscape shaped by landslides. In: Embleton-Hamann C (ed) *Landscapes and landforms of Austria, world geomorphological landscapes*. Springer
- Stumvoll MJ, Canli E, Engels A, Thiebes B, Groiss B, Glade T, Schweigl J, Bertagnoli M (2019) The “Salcher” landslide observatory—experimental long-term monitoring in the Flysch Zone of Lower Austria. *Bull Eng Geol Environ* 79:1831–1848. <https://doi.org/10.1007/s10064-019-01632-w>
- Stumvoll MJ, Schmaltz EM, Glade T (2021) Dynamic characterization of a slow-moving landslide system – assessing the challenges of small process scales utilizing multi-temporal TLS data. *Geomorphology* 389:107803. <https://doi.org/10.1016/j.geomorph.2021.107803>
- Stumvoll MJ, Schmaltz EM, Kanta R, Roth H, Grall B, Luhn J, Flores-Orozco A, Glade T (2022) 4D subsurface landslide dynamics – investigating landslide behavior using high resolution hydrological and geotechnical information. *Catena* 214:106203. <https://doi.org/10.1016/j.catena.2022.106203>
- Takken I, Jetten V, Govers G, Nachtergaele J, Steegen A (2001) The effect of tillage-induced roughness on runoff and erosion patterns. *Geomorphology* 37:1–14
- Telling J, Lyda A, Hartzell P, Glennie C (2017) Review of Earth science research using terrestrial laser scanning. *Earth Sci Rev* 169:35–68. <https://doi.org/10.1016/j.earscirev.2017.04.007>
- Tilch N (2014) Identifizierung gravitativer Massenbewegungen mittels multitemporaler Luftbildauswertung in Vorarlberg und angrenzender Gebiete. *Jahrbuch der Kaiserlich-Königlichen Geologischen Bundesanstalt* 154:21–39
- Turner D, Lucieer A, De Jong SM (2015) Time series analysis of landslide dynamics using an Unmanned Aerial Vehicle (UAV). *Remote Sens* 7:1736–1757
- van Asch TWJ, Van Beek LPH, Bogaard TA (2007) Problems in predicting the mobility of slow-moving landslides. *Eng Geol* 91:46–55. <https://doi.org/10.1016/j.enggeo.2006.12.012>
- Varnes DJ (1978) Slope movement. Types and processes. In: Schuster RL, Krizek RJ (eds) *Landslides: analysis and control*. Transportation Research Board, National Academy Press, Washington, DC, pp 11–33
- Weber L (1997) Flächendeckende Beschreibung der Geologie von Österreich 1:500.000 im Vektorformat. Exzerpt (Basiskarte Geologie) aus der Metallogenetischen Karte von Österreich 1:500.000. Geologische Bundesanstalt, Wien, Österreich.
- Westoby MJ, Brasington J, Glasser NF, Hambrey MJ, Reynolds JM (2012) ‘Structure-from-motion’ photogrammetry: a low-cost, effective tool for geoscience applications. *Geomorphology* 179:300–314. <https://doi.org/10.1016/j.geomorph.2012.08.021>
- Wieser M, Mandlbürger G, Hollaus M, Otepka J, Glira P, Pfeifer N (2017) A case study of UAS borne laser scanning for measurement of tree stem diameter. *Remote Sens* 9:1154
- Zang Y, Yang B, Li J, Guan H (2019) An accurate TLS and UAV image point clouds registration method for deformation detection of chaotic hillside areas. *Remote Sens* 11:647
- Zieher T, Bremer M, Rutzinger M, Pfeiffer J, Fritzmann P, Wichmann V (2019) Assessment of landslide-induced displacement and deformation of above-ground objects using uav-borne and airborne laser scanning data. *ISPRS Ann Photogramm Remote Sens Spat Inf Sci IV-2/W5:461–467*. <https://doi.org/10.5194/isprs-annals-IV-2-W5-461-2019>

Chapter 9

Polar and Cryospheric Remote Sensing Using sUAS



Clare B. Gaffey, Anshuman Bhardwaj, Karen E. Frey, and Lyndon Estes

Abstract Monitoring efforts for remote high-latitude and high-altitude glacierized regions heavily rely on remote sensing. Rapid ongoing changes in polar and cryospheric environments owing to contemporary climate change have attracted more attention towards these regions than ever before. Satellite remote sensing has its own limitations related to low sun angles in high latitudes, high acquisition costs for high-resolution images, and persistent cloud cover over ice-dominated land and ocean surfaces. As such, over the past several years, small unoccupied aerial systems (sUAS) have become a viable data collection tool to address the challenges related to spaceborne or expensive airborne remote sensing for monitoring the cryosphere and polar regions. This chapter discusses sUAS adaptations for collecting data on snow, glaciers, permafrost, polar biology, the ocean, and atmosphere; the challenges of conducting sUAS operations in polar latitudes; and the advantages and disadvantages of the technology. It also provides resources that can be used to guide future efforts in applying sUAS to polar and cryospheric research.

Keywords sUAS · UAV · Polar · Glaciology · Cryosphere · Remote sensing

9.1 Introduction

Polar regions present some of the planet's harshest conditions for environmental data collection. Persistent freezing temperatures, dangerous terrain such as sea ice or glacial crevasses, passing polar bears, and aircraft icing all complicate work in the Arctic. Further, conducting research with appropriate logistical support is expensive in remote regions. Frequent cloud cover and limited or no sunlight for months of the

C. B. Gaffey (✉) · K. E. Frey · L. Estes
Graduate School of Geography, Clark University, Worcester, MA, USA
e-mail: cgauffey@clarku.edu

A. Bhardwaj
School of Geosciences, Meston Building, King's College, University of Aberdeen, Aberdeen,
UK

year confound observations from satellite-based optical sensors. Unoccupied aerial systems (UAS) have increasingly been used as a tool to overcome some of these challenges to analyze various aspects of cryosphere and high latitude processes. Ocean, atmosphere, biology, and ice studies have benefited from the increasing accessibility of UAS technology. This chapter explores numerous applications that have been successfully pursued, the advantages and disadvantages of the technology, potential future uses in this realm, and helpful resources to prepare and empower prospective cold-region UAS researchers.

9.1.1 UAS and Its Components

The parameters of what constitutes a small UAS (sUAS) or larger categories have been developed by states and organizations to best fit their individual context. For Antarctic operations, these categories have been defined as “small” for UAS weighing less than 2 kg, “medium” for those between 2 and 25 kg, and “large” for systems greater than 25 kg (CONMAP 2016). Organizations for Arctic operations have cited sUAS as any system weighing less than 5 kg (Storvold et al. 2015). Still, countries in these regions are free to develop their own definitions depending on their needs. For example, Iceland distinguishes size categories of UAS based on the environments they are flown in (urban versus rural) and also based on purpose (commercial or leisure). In the US, the Federal Aviation Administration (FAA) regulates operations of sUAS, defined as any drone weighing under 25 kg. Similarly but differing in categorization, the US National Aeronautics and Space Administration (NASA) has classified two categories of sUAS. Category I are considered models or sUAS that are less than or equal to 25 kg, and category II sUAS are between 25 and 150 kg (UNOLS2019). The cryosphere and polar applications discussed in this chapter fit the description of NASA’s Category I of sUAS and of the FAA’s standard sUAS.

There are three major types of sUAS with some nuance between them. These categories are (i) multirotors, which are suitable for covering shorter distances and have hovering capability, (ii) fixed-wings, which can fly farther and for longer periods of time; and (iii) hybrid models of the two that incorporate the benefits of each. Hybrids, though expected to become more popular, are currently costlier and rarer in environmental monitoring studies compared to multirotors and fixed-wing aircraft. The main components of a sUAS are the aerial platform and the ground control station. The aerial platform includes the airframe, sensor payload, navigation, and power system. The ground control station controls the movement of the aerial platform and requires a communication system to relay information between the station and platform (Giordan et al. 2020).

Off-the-shelf platforms that are ready to fly upon purchase have been successfully used for several polar and cryosphere studies (e.g., Rohner et al. 2019; Rossini et al. 2018). While convenient, ready-to-fly systems have some limitations that can impair the collection of the high quality data that is required for scientific research. Icing

and the voltage drop of batteries provide additional risks in cold conditions. Lithium polymer (LiPo) batteries are sensitive to cold-weather drainage, yet LiPo batteries are widely used for sUAS owing to their lower weight, high capacity, and discharge rates (Reagan 2020). Increased payload (weight) of sUAS contributes to battery drain in cold conditions. Lithium-ion polymer batteries can provide better performance at low temperatures than LiPo batteries (Grepow 2020). However, users' choice of battery for off-the-shelf sUAS is limited by the manufacturer. Still, cold temperatures reduce the performance of both LiPo and lithium-ion battery types, and steps to minimize exposure to low temperatures preflight are through the use of hand warmers, insulation, and flight practices such as pre-survey hovering to maintain battery health (Carter 2019).

Additional challenges in flying can occur in situations when pilot commands need to override the preinstalled flight software, such as removing legal altitude safeguards when monitoring mountain glaciers. Flying in mountainous terrain also increases the risk of the sUAS losing its Global Navigation Satellite System (GNSS) connectivity which increases collision risk. In cases where mountains or other structures limit visibility and degrade communication between the GNSS constellation and the sUAS, autonomous flight is risky and most commercial platforms prohibit takeoff (Stoven-Dubois et al. 2018). This risk can be reduced when GNSS is disabled in place of manually flying in attitude mode. Another common internal command is the "return to home" feature that is installed as a fail-safe in prebuilt systems, though it may be executed in unwanted situations and prevent pilot commands from overriding it. An example situation may be when taking off from the deck of a ship which has drifted from its initial "home" position. If the sUAS battery reserves run low or it loses connection with the controller during flight, the sUAS will likely automatically travel to and attempt to land at its initial position from takeoff. However, that initial location may be open water due to the drift of the ship (Raoult et al. 2020). Nevertheless, for many research applications, off-the-shelf sUAS have demonstrated their suitability. Da-Jiang Innovations (DJI) (<https://www.dji.com/>) is the most popular, ready-to-fly brand for multirotor systems in recent polar and cryosphere studies (Gaffey and Bhardwaj 2020). Chandler et al. (2020) quantified landscape changes of an Icelandic glacier snout, covering an 0.5 km² area using a DJI Phantom 3 quadcopter. Alonzo et al. (2020) used a DJI Phantom 4 to create dense point clouds to estimate shrub biomass for 85 × 85 m plots, flying at 55 m above ground level to achieve a ground sample distance of ~1.5 cm. Still, other studies encountered challenges with using the off-the-shelf system. For example, Alfredsen et al. (2018) found that the default DJI Phantom 3 camera was limited by poor lighting conditions when used for mapping river ice. In another study, Van der Sluijs et al. (2018) used a DJI Inspire 1 Pro to map permafrost thaw features but found that their chosen preinstalled Zenmuse X5 camera had a relatively slow-rolling shutter that produced motion distortions that had to be corrected post-flight. The ease of off-the-shelf sUAS is enticing, but research into systems, familiarity with environmental conditions of the study site, and taking advantage of test flights are all encouraged to build confidence in the fit of a particular sUAS for any application. For scientific inquiry, users may choose to

build their own sUAS by assembling the various parts needed for flight, navigation, communication, and sensing, which provides investigators with customization capability of its specifications and allows pilots to have more control over how a sUAS may behave. The former benefit is useful when thinking about various payloads, sampling capabilities, and other factors that are the center of a study design. The benefit of granting pilots greater control is that it is helpful when it is unclear how built-in software will behave in certain conditions, or if the pilot is able to override internal commands.

9.1.2 Brief History of sUAS for Polar and Cryospheric Applications

In 1997, the Arctic Research Consortium of the United States (ARCUS) prepared a report titled “Logistics Recommendations for an Improved U.S. Arctic Research Capability” that included a recommendation to employ remotely piloted aircraft to increase efficiency and comprehensiveness of data acquisition (ARCUS 1997). The first Arctic UAS flight for academic purposes was flown in April 1999 in Utqiagvik (formerly Barrow), Alaska, with funding support from the US Department of Energy’s Atmospheric Radiation Measurement Program (ARM) (Curry et al. 2004). The aircraft flown was a fixed-wing Aerosonde (www.aerosonde.com) that was meant to obtain meteorological observations. Before long, two of these aircraft were lost due to airframe icing and one was lost to carburetor icing. Following the losses to the extreme arctic environment, efforts funded by the National Science Foundation Office of Polar Programs adapted Aerosonde to the cold climate and supported the development of miniaturized instruments to be efficiently carried by the sUAS. These initial instruments supported data collection to measure radiative fluxes, cloud and precipitation characteristics, and capture sea ice imagery. Updated versions of the Aerosonde with varying payloads were tested and flown from the Alaskan site over a five-year period (2000–2005) (Crowe et al. 2012; Curry et al. 2004). Since the development of the Aerosonde and the increased capacity for sUAS technology in general, the inclusion of sUAS platforms for polar studies has grown. A previous review (Bhardwaj et al. 2016a) identified one of the first sUAS applications in glaciology (Hodson et al. 2007), which used sUAS-collected imagery in Svalbard to resolve spatial gradients in the ratio of supraglacial cryoconite (i.e., windblown dust and microbes that create small depressions on glacier surfaces). This type of application is only possible with centimeter-resolution imagery that freely accessible satellite imagery cannot provide. Beyond 2007, the number of published studies in polar and cold regions that utilized sUAS for environmental monitoring continued to grow, and we explore additional applications in Sect. 9.2 below.

9.1.3 General Research Design Using UAS

Several steps are involved when conducting an analysis using sUAS (Fig. 9.1). Though the environmental applications vary widely, there are some common steps that are true for all flights. Pre-planning is an essential first step that involves researching the legality of performing flights within a region of interest. Many countries require sUAS operators to obtain state-issued licenses in order to legally fly for commercial or academic purposes. Other steps may include registering sUAS components and/or acquiring permits and permissions, especially if flying near airports or other restricted areas. Beyond purchasing a sUAS, learning to fly, and

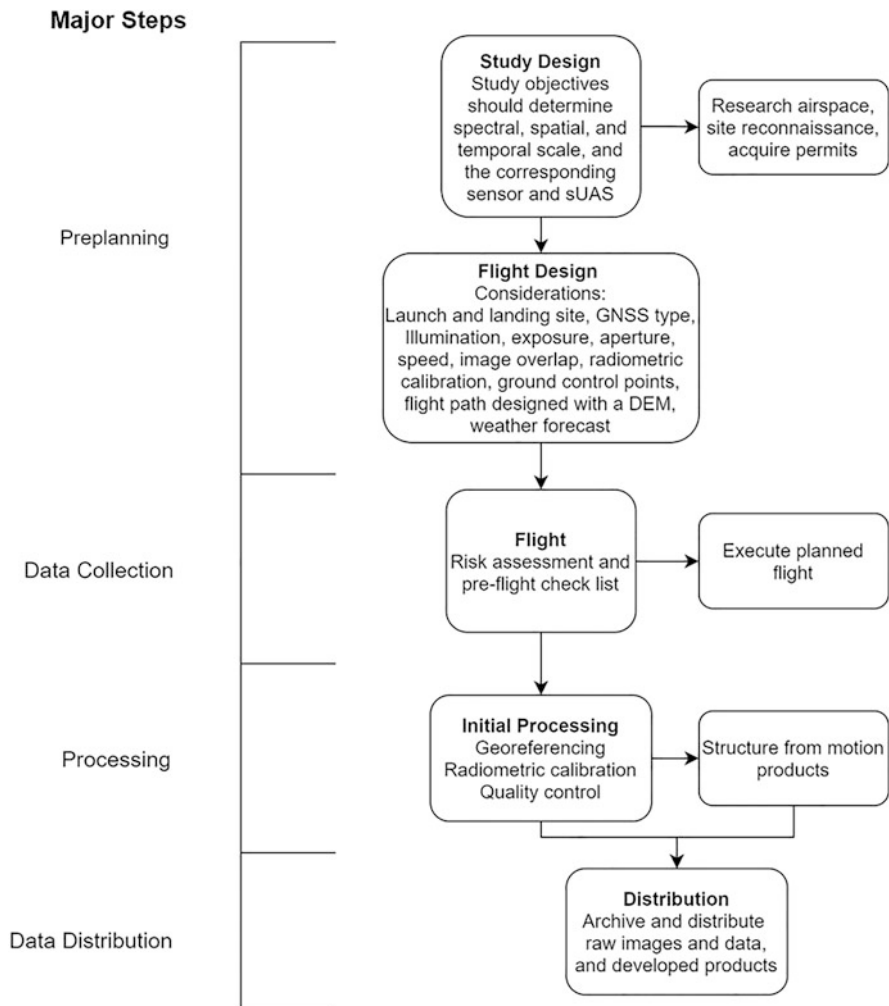


Fig. 9.1 Example workflow for a research project involving sUAS

securing permissions, plans have to be made that suit both the study design and ensure safe operations for people and the greater environment. Considerations of how to retrieve equipment will need to be addressed prior to flights as crashes, lost signals, wind gusts, and technical failure are all possible and likely scenarios. Performing extensive site reconnaissance in advance of flights is recommended to identify obstructions and alter flight altitude or survey path if needed (Duffy et al. 2018). Inspection of the study area surroundings is also recommended when drafting a retrieval plan for equipment should the mission fail. Reconnaissance should be done well in advance using high resolution imagery, which is available with freely available tools such as Google Earth (<https://earth.google.com/web/>) as well as in person to identify potential obstacles at various scales. Conditions in the Arctic are often cold, wet, and windy, which can lead to icing. Ice fog can create low visibility situations, and insects or other wildlife may become distractions to the pilot during operations. The Arctic region also introduces technical challenges, such as limited GNSS coverage and extreme magnetic declination that has the potential to confound automatic flight controls. In general, high latitudes are less well served by GNSS compared to equatorial regions (Sheridan 2020). Determination of which type of region-specific GNSS (e.g., GPS, GLONASS, BEIDOU, GALILEO) to use should be done during mission planning. Typically, the quality of GNSS positioning is dependent on having at least four satellites with wide spacing between them. Specific guidance on how to select GNSS type based on location and how to calculate the geometric dilution of precision, an index to indicate the quality of spacing between satellites, is offered in Sheridan (2020). Installing redundant GNSS devices on sUAS and other steps can be taken to better safeguard operations. There are several options for collecting GNSS data, including on-board real-time kinematic (RTK) and post-processed kinematic (PPK) technologies, which would require a base station in the vicinity of the flight. The inclusion of a base station is especially important for repeated flights if end products will be compared with additional flights or other means of geospatial data. For more details on the unique challenges polar regions impose on sUAS operations and suggestions for how to mitigate them, please refer to Gaffey and Bhardwaj (2020).

Following the initial study design that includes considerations of both what data would best suit the research objective and what is feasible given the environment (both natural and political), the flight design should be meticulously planned. While flight-day conditions will likely cause deviations from Plan A, a well-planned mission will be able to adapt and recover. Examples of evidence of good planning involve having spare parts handy as well as the tools required to install them or make repairs. Test flights in locations that mimic the intended field site are highly recommended. These can greatly help investigators tune the sensor and flight parameters needed to provide high-quality data. Testing sensor response to surface brightness (e.g., fresh snow or varying illuminations with vegetation or structure shadows) at the expected altitude, orientation, shutter, and traveling speed are among some examples of flight variables that the study design will ultimately need to consider. Calculations that incorporate desired image overlap, size of study area, and vertical terrain variations can be done with mission planning software ahead of

time to maximize the usability of the resulting data. Decisions on the roles of pilots and observers, where the sUAS will take off and land, the survey design, and the length of time the sUAS is deployed will need to be made ahead of time. Another important part of preflight planning is to have the best available short-to-medium range weather forecast (up to 10 days in advance) prior to the planned field visit. This helps to avoid most windy or rainy/snowy periods within the day to ensure stable and consistent imaging.

Once the flights are completed, it is important to immediately check the data for its completeness and quality. Several backups of this data on different storage devices should be made to mitigate any hardware failure. After the data have undergone standard quality control and georeferencing (find more specifics on this in Eltner et al. (2016) and Assmann et al. (2019)), structure from motion photogrammetry (SfM) products can be created. SfM software reconstructs three-dimensional geometries from images. Many applications involve an RGB camera flown on a sUAS to create 3-D point clouds and meshes that then can be developed into digital surface models (DSMs) as well as orthomosaics (2-D reconstructions of the entire study area stitched together based on tie point matching individual images). From these products, scientists are able to apply further quantitative methods of inquiry to examine a wide range of natural processes.

9.2 Applications

9.2.1 Overview of Topics

The studies discussed below are a sampling of the many applications that have been executed successfully. This chapter focuses on polar research and includes examples of sUAS-based studies of the cryosphere conducted in non-polar regions, such as mid-latitude montane glaciers. sUAS have been applied to studies of aerosols and black carbon, oceanic and sea ice processes, glacier dynamics, and the ecosystem resilience of flora and fauna. Categories of applications that are discussed here fall within snow research, glaciology, ecology, permafrost, ocean, and atmosphere.

9.2.2 Snow Research

The most widespread application of sUAS in cryospheric research has been for estimating snow depth. Snow depth measurements are traditionally done using manual measurements with probes, but this can be troublesome over large areas or complex terrain, while requiring interpolation to provide continuous estimates within a region of interest. Remotely-sensed measurements are better suited to detecting nuance over continuous surfaces. In most cases, this has been done by differencing snow-free and snow-covered DSMs, using a baseline snow-free DSM

generated from either sUAS (most common and most recommended method for maintaining DSM consistency), LiDAR, or satellite image sources. Recently, some researchers have flown radar sensors to directly measure depth (e.g., Jenssen et al. 2020). With the advent of lightweight drone-mounted radar sensors, real-time snow depth monitoring with high accuracy is expected to become more common in the coming years (e.g., Jenssen and Jacobsen 2020; Tan et al. 2017).

Snow cover can be particularly troublesome to measure with optical sensors. Freshly fallen snow forms homogenous surfaces that provide few of the textural differences that SfM software needs for generating tie points (Mali and Kuiry 2018). Depending on the sun and sensor angles, glare from the bright reflectance of snow and ice can also saturate image pixels (Bühler et al. 2016). This effect can also distort heterogenous surface cover that may include dark shadows, vegetation, or bare ground which contrasts with patches of snow cover, causing artifacts to emerge owing to varying sensor exposure needs (Lamsters et al. 2019). Additionally, vegetation has been found to further hinder snow depth estimates as short vegetation, such as tall grasses or shrubs compressed by snow, can result in an underestimation of snow depth when using a snow-free digital surface model baseline that includes vegetation. In fact, this type of canopy can become compressed to the point where it can produce “negative” snow depths on difference maps (Nolan et al. 2015). Other changes in surface topography beneath the snow cover can also contribute to this type of error including frost heave (Nolan et al. 2015), permafrost creep (Goetz et al. 2019), or erosion (Avanzi et al. 2018). To overcome some of these challenges, Cimoli et al. (2017) suggested applying image content enhancement by increasing the contrast between the pixels without reducing the dynamic range and radial lens distortion correction, which improves the image geometry for SfM processing. Further, maintaining a fine ground sampling resolution that sufficiently distinguishes the intersection of snow and vegetation can help alleviate errors (Fernandes et al. 2018). Measuring ground control points in the same locations in the snow-on and snow-off DSMs supports accurate georeferencing when using the differencing technique (Goetz and Brenning 2019). Though more expensive, sUAS flown LiDAR also increases the accuracy of snow depth estimates, particularly in vegetated areas (Harder et al. 2020).

9.2.3 *Glaciology*

Glaciology has been one of the most popular subjects for sUAS investigation within polar and cryospheric studies (Gaffey and Bhardwaj 2020). Repeated sUAS surveys to create SfM orthomosaics and DSMs have been helpful tools for analyzing glacier dynamics and surface changes. Postprocessing of these products has been used to monitor plume dynamics (Jouvet et al. 2018), flow velocity (Jones et al. 2018), and calving events (Ryan et al. 2015), as well as to inspect hazards (Fugazza et al. 2018), calculate melt and ablation (Bash et al. 2018), and more. An example of the SfM products and the glacial process information that can be extracted is in Fig. 9.2. Here,

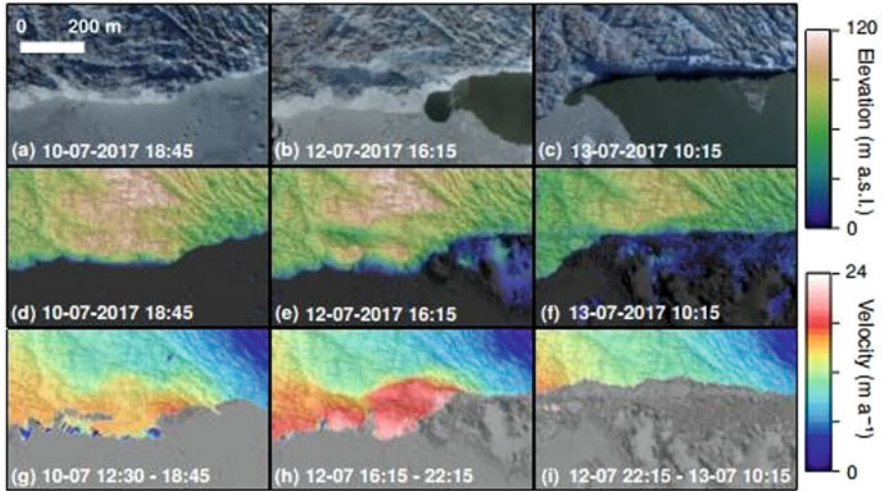


Fig. 9.2 Example of orthophotos (a–c), DSMs (d–f), and velocity fields (e–i) showing the lead-up to and aftermath of a calving event that occurred on Greenland’s Store Glacier in July 2017. (Reproduced with permission from Chudley et al. (2019a) under CC 4.0 (<https://creativecommons.org/licenses/by/4.0/legalcode>))

orthophotos and DSMs collected on flights on different days are used to determine changes in velocity fields of a glacier terminus. A detailed description of the processing steps between data collection and glacier surface tracking can be found in Benoit et al. (2019).

Many studies used processes similar to this one to determine flow and calving rates of glaciers worldwide. A notable study that included this type of workflow was done by Jouvét et al. (2018), who took advantage of the temporal resolutions UAS provided to fly over the terminus of Greenland’s Bowdoin Glacier every 12 h (with two exceptions) between July 7 and July 18, 2016, totaling 22 flights. This provided high spatial and temporal resolution velocity fields capable of detecting changes in surface ice flow rates, as well as daily snapshots depicting the stages of the calving front and breakup of the ice mélange (i.e., a mixture of sea ice, icebergs, and snow that is discharged from the marine-terminating glacier).

Other observations centered on glacier hydrology used sUAS imagery to monitor drainage of ice-dammed marginal lakes, supraglacial lakes, and streams (e.g., St. Germain and Moonman 2019). Among additional in situ geophysical tools, Chudley et al. (2019b) used bathymetric maps created from depth-corrected sUAS-derived DSMs to investigate drainage events of supraglacial lakes on the Greenland Ice Sheet (Fig. 9.3). They were able to observe process differences in supraglacial lakes on fast-flowing and slow-flowing sectors of the ice sheet. This work adds to increased understanding of ice sheet hydrology, which is essential for predictions of global sea level rise.



Fig. 9.3 Tom Chudley and Poul Christoffersen of the Scott Polar Research Institute launch a Skywalker X8 on the Greenland ice sheet to map ice dynamics. (The image also appears in Chudley et al. (2019a) and is reproduced with permission under CC 4.0. (<https://creativecommons.org/licenses/by/4.0/legalcode>))

Studies focused on calculating mass balance and detecting the melt of glaciers have been conducted globally. Outside of the polar regions, examples of such studies have taken place in China and the greater Himalayan region (Brun et al. 2016; Che et al. 2020), Switzerland and the extended Alps (Rossini et al. 2018), Canada (Bash and Moorman 2020), and tropical glaciers such as those in the Peruvian Andes (Wigmore and Mark 2017). Detection and quantification of features on glaciers and ice sheets have also received substantial attention, such as ice cliffs (Kraaijenbrink et al. 2016), cryoconite holes (Cook et al. 2020), crevasses (Florinsky and Bliakharskii 2019), and debris cover (Vincent et al. 2016). While most of these studies used RGB cameras, a few adapted additional sensors. For example, Kraaijenbrink et al. (2018) flew a thermal infrared sensor over a section of Lirung Glacier in the central Himalaya of Nepal to identify ground objects, validate radiometric values with a hand-held infrared sensor, and ultimately estimate debris thickness on the glacier. However, difficulties arose as the thermal imager increased energy consumption, which decreased the potential sUAS flight time. Additionally, the glacial surface temperature conditions rapidly changed, impeding the feasibility of performing multiple flights. Still, the spatial variability of glacier surface temperatures was not replicated with Landsat 8 thermal imagery, nor would the satellite be able to provide revisit times suitable for diurnal studies. Therefore, sUAS thermal data collection was concluded to be more appropriate for estimating the thickness of small- to moderate-scale debris.

9.2.4 Other Polar Applications

9.2.4.1 Flora and Fauna

Unlike longer-term processes such as those centered on glacier movement that should be monitored over several years or multiple seasons, studying the phenology of Arctic vegetation requires repeated data collection over the summer season. The short and rapidly progressing growing season at high latitudes further constrains studies that rely on satellite imagery that are limited by low sun angles and persistent cloud cover. For these reasons, sUAS are becoming a prevalent tool for monitoring tundra vegetation (Beamish et al. 2020). Multirotors flown at low altitudes are a popular method for monitoring different aspects of Arctic and Antarctic vegetation. Riihimäki et al. (2019) used a DJI Phantom 4 quadcopter flown at 30 m above ground level (AGL) to estimate the fractional cover of tundra vegetation. The study classified the proportional presence of vegetation and used models of fractional vegetation cover to upscale the measurements to satellite imagery, allowing a much larger area to be characterized than that which could be captured by sUAS flights. Such upscaled analysis can be useful for evaluating the extent of phenomena such as greening that is caused by Arctic “shrubification” (e.g., Sturm et al. 2001).

Several shrub cover, vegetation height, and land cover classification applications have been published. Fraser et al. (2016) used sUAS SfM to build a model of vegetation heights and classified eleven types of tundra vegetation in their 2-hectare study site near Tuktoyaktuk, Northwest Territories, Canada. In Alberta, Lovitt et al. (2017) used a multirotor flown at 110 m AGL to evaluate the role of vegetation in shaping the surface complexity of peatland areas. In a 0.4 km² peatland site in Finland, Räsänen and Virtanen (2019) used sUAS optical imagery with machine learning techniques to create detailed maps of vegetation and ground cover classes. Compared to similar land cover maps created from high-resolution satellite imagery (two maps produced from WorldView-2 (2 m resolution) and PlanetScope (3.7 m resolution)), the highest classification accuracy was achieved by the sUAS imagery.

Antarctic cyanobacterial mats have been a focus of study by several investigators (e.g., Lucieer et al. 2014; Malenovsky et al. 2017). Turner et al. (2014) flew visible, multispectral, and thermal infrared cameras to resolve components of moss ecosystems. Sotille et al. (2020) calculated the normalized difference vegetation index from sUAS and satellite imagery to broadly identify lichens, mosses, and algae in ice-free areas of Hope Bay on the Antarctic Peninsula. Bollard-Breen et al. (2015) used a custom-built fixed-wing sUAS to identify cyanobacterial mats, estimate their extent, and discriminate between mat types. They were also able to detect human disturbances on the mat in the form of footprints. Unfortunately, the mats are fragile and take years to recover after a shoe-print impact, so the authors encouraged the use of sUAS technology for future examinations of the mats when possible.

Animal population surveys and behavior studies conducted with sUAS have also been performed. Some studies used sUAS as a tool to determine thresholds of noise and/or the proximity to which the animal of interest becomes disturbed by sUAS presence (e.g., Mustafa et al. 2018; Rümmler et al. 2018). Through this exercise, Weimerskirch et al. (2018) determined that for a sample of eleven seabird species in the Crozet Islands of the South Indian Ocean, a DJI Phantom 3 flown above 50 m relative to the animals provided negligible impacts. Imagery collected by sUAS has aided studies in identifying mass and body conditions of pinnipeds (Goebel et al. 2015; Krause et al. 2017) and estimating populations of seabirds and pinnipeds including distinguishing demographics such as pups versus adults (Lee et al. 2019; Korczak-Abshire et al. 2019; Zmarz et al. 2018). In a comparison of three aerial platforms for monitoring populations of marine species that visit the water surface often (i.e., whales, seals, and porpoises), sUAS were considered more logistically sensible than kites or blimps and were ultimately the recommended platform for aerial surveys of marine animals (Verfuss et al. 2019). For survey purposes, sUAS are a non-invasive tool that can save humans the effort of negotiating potentially dangerous terrain, while minimizing human-wildlife interaction.

9.2.4.2 Permafrost

Permafrost is perennially frozen soil that exists at high latitudes and in alpine environments. Monitoring permafrost is currently of great interest largely because of the threats it poses when thawing. In many areas, warming temperatures borne of climate change have been thawing previously permanent frozen soil (Park et al. 2016). Human infrastructure built upon thawing permafrost destabilizes and creates costly and hazardous damage. More indirectly, immense amounts of organic material that were previously locked away in the frozen soil are able to decompose as the permafrost thaws, adding more greenhouse gases (both CO₂ and CH₄) to the atmosphere and further accelerating climate change (Park et al. 2016). Moreover, a direct health impact of thawing permafrost can be in the form of exposure to previously hibernating ancient microbes (Graham et al. 2012).

The formation and degradation of permafrost over time can create identifiable landforms that provide indications of the morphology and stability of frozen ground. Features of permafrost landscapes such as pingoes (Hodson et al. 2019), ice wedge polygons (Kartoziiia 2019; Zhang et al. 2020), and thermokarst lakes and ponds (Freitas et al. 2019) have been the target of sUAS optical imaging. Such surface manifestations of permafrost are often too small to be identified or monitored using freely available medium resolution satellite imagery. One interesting effort by Van der Sluijs et al. (2018) used both fixed-wing and multirotors UAS to carry five optical and one thermal sensor to identify thaw slump features. Additionally, they collected high-resolution soil stratification images along a headwall, which would have been a dangerous task to sample otherwise. By comparing a previously available LiDAR survey as a baseline with repeated sUAS surveys, they were able to quantify the annual volume of displaced material owing to thaw processes. The

thermal imagery described terrain characteristics and processes of slump development.

Furrows, ridges in rock glaciers, and other patterned ground indicative of permafrost can be difficult to distinguish on images that are coarser than a few meters in resolution. Lousada et al. (2018) flew a sUAS to map ice-wedge polygon networks and found that these systems could only be analyzed adequately with 20 cm/pixel imagery or finer, precluding the use of free satellite imagery. Van der Sluijs et al. (2018) also noted that permafrost dynamics such as injection ice and terrain uplift were difficult to detect prior to the general use of sUAS. Therefore, high spatial resolutions obtained by sUAS have benefitted monitoring capabilities of these types of features.

9.2.4.3 Ocean and Atmosphere

The measurement of atmospheric characteristics using sUAS is unique from the applications discussed previously that largely used optical sensors to detect ground objects. sUAS are well suited to collecting basic physical atmospheric measurements of temperature, humidity, and pressure, but they have also been fitted for more intricate tasks such as collecting air samples. While there are not many available studies or datasets of UAS-collected atmospheric properties in the polar regions, there have been notable works of this kind above sea ice. The developers of the Aerosonde, the U.S. Department of Energy Atmospheric Radiation Measurement (DOE ARM), established a facility at Oliktok Point, Alaska, just 260 km from their initial station in Utqiagvik. There, ARM has been involved in the development, support, and operations of UAS, with the goal of routine Arctic sampling. At this facility, de Boer et al. (2018) collected measurements of the thermodynamic state, turbulence, radiation, aerosol properties, cloud microphysics, turbulent fluxes, and albedo over sea ice to provide a detailed characterization of the lower atmosphere with UAS and tethered balloons. In the Weddell Sea of Antarctica, Jonassen et al. (2015) used multirotors and fixed-wing UAS to collect stratified air samples and physical properties for atmospheric boundary layer profiling above sea ice. In the Arctic, the Alaska Center for UAS Integration (ACUASI, <https://acuasi.alaska.edu/>) at the University of Alaska, Fairbanks, has been using a ~115 kg fixed-wing UAS to measure meteorological variables and sea ice extent, thickness, ridging, melt ponds, and other characteristics. The international MOSAiC expedition (Multidisciplinary Drifting Observatory for the Study of Arctic Climate) of 2019–2020, a year-long cruise in the Central Arctic Ocean, also included sUAS in their arsenal for data collection. Researchers from the University of Colorado, Boulder (Fig. 9.4), used a fixed-wing sUAS to collect information on the atmospheric boundary layer and surface albedo over sea ice. With the increasing amount of experience that started with some of the early adapters mentioned here, sUAS are expected to grow as a persistent tool for unraveling ocean-atmosphere interactions.



Fig. 9.4 John Cassano and Gina Jozef of the University of Colorado, Boulder, prepare to launch a DataHawk2 fixed-wing UAS above Arctic Ocean sea ice during the MOSAiC expedition. The DataHawk2 is equipped to measure sea ice surface and atmospheric infrared radiation, high frequency (turbulent) wind velocity and temperature, pressure, and relative humidity. Additional recorded measurements of airspeed, ground speed, and altitude provide high-frequency 3-D wind speed and direction estimates. (Photograph taken by Delphin Ruché)

9.3 Discussion

9.3.1 *Advantages and Disadvantages of the Technology*

sUAS can be described as an emerging technology whose adaptation has largely come from decentralized, ground-up efforts within many corners of environmental monitoring. As such, investigators have independently adjusted parameters around study designs and data collection. This tendency has resulted in a wide diversity of processing procedures, which highlights the need identified by Manfreda et al. (2018) to harmonize and standardize the approaches used for acquiring and preprocessing sUAS-collected data. Manfreda et al. (2018) called on researchers to define a clear and referenced workflow that includes the planning and acquisition of data, the generation of SfM products, and best practices to assess the accuracy and precision of SfM products by means of comparative experiments to assess the reliability of different procedures to identify the most appropriate methodology for environmental monitoring. Though consistency resulting from harmonization may be preferable for the quality of UAS-based monitoring and the reproducibility of methods, it is worth mentioning that it may also undermine observational flexibility, which is an important feature of sUAS investigations. Such flexibility is required for

Table 9.1 Summary of advantages and disadvantages of sUAS as a tool for polar and cryospheric studies

Advantages	Disadvantages
Lower cost than manned vehicle operations. High-resolution data collection. On-demand. Temporally flexible, revisit time can be shaped to study design. Wide variety of miniaturization of sensors. Under-cloud flights collect data at times when satellites cannot. Ability to access potentially hazardous areas. Freedom of customization to fit needs. Limits disturbance to fragile landscapes (e.g., microbial mats).	Limited payload. Cold conditions can cause battery drain and icing, spatially constraining study area survey. Increased responsibility of safety on the researcher. Communication of flight activity with airspace and relevant authorities. Knowledge of UAS design and maintenance required. Extra parts will always be needed. Potential legality issues and extra permitting.

extreme polar environments, where improvisation may be needed during field campaigns. Nevertheless, despite the need for operational flexibility, greater harmonization would undoubtedly benefit sUAS operations in the cryosphere. This need for harmonization extends from details around preflight planning all the way to postprocessing and extraction of information. Best practices covering mission and flight planning, sensor configuration, calibration, and correction are examples of some of the gaps that currently exist (e.g., Manfreda et al. 2018). Despite this, efforts are being made towards defining best practices for individual tasks such as building the most robust ground control point network, and comparing SfM software and the user-chosen parameters within to produce accurate products (e.g., Hendrickx et al. 2019; Sanz-ablanedo et al. 2018; Tahar 2013; Tonkin and Midgley 2016). Additionally, studies are being produced that offer standardized workflows based on the target of study. With the aim of promoting comparable and reproducible sUAS imagery for multispectral imaging vegetation, Assmann et al. (2019) proposed a workflow for sUAS data collection and processing based on personal experience in the Yukon Territory, Canada, synthesized with protocols suggested by the High Latitude Drone Ecology Network (<https://arcticdrones.org/>). Organizations and working groups tailored to specific fields have made strides to publish advice and create common standards, some of which are discussed in Sect. 9.3.3.

A summary of the advantages and disadvantages of the use of sUAS in polar and cryospheric applications is in Table 9.1. Though the advantages are universal for many environmental applications, the unique challenges of working in harsh, cold-climate areas add disadvantages to the list. Having spare parts and the tools to assemble them is always recommended, but in remote environments, the level of required planning increases. Still, sUAS provide capabilities that benefit certain situations. For example, the usage of sUAS for surveys eliminates the risk of trampling vegetation in fragile high-latitude ecosystems. Additionally, sUAS

surveys reduce the risk to human life when accessing remote areas such as islands for animal surveys (Zmarz et al. 2018) or investigating hard-to-reach potential hazards such as those associated with glaciers in areas heavily trafficked by tourists (Fugazza et al. 2018).

Several studies successfully acquired high-resolution imagery in difficult-to-access areas. An example of this was capturing the evolution of ice morphology in the Antarctic by Li et al. (2020), who repeatedly flew a sUAS to monitor the formation of ice dolines. The sUAS flights were performed with both LiDAR and a camera to model the ice morphology and the authors found that the camera SfM was most cost-effective, while the LiDAR was superior in resolving fine features. However, unlike camera-based SfM that can be insensitive to crevasse features, LiDAR is not sensitive to illumination differences and is capable of resolving snow morphology, including crevasse topography and texturally homogeneous fresh snow (Li et al. 2020). Other studies of ice morphological features found that UAS-based optical cameras were a useful tool for monitoring surface-level changes (e.g., geometry, orientation, patterns), but reconstruction of crevasse depth is complicated by low illumination and inefficient relational sensor orientation (Chudley et al. 2019a; Ryan et al. 2015). Although the cost of LiDAR sensors has been decreasing and the miniaturization of sensors has allowed the platforms to be more effectively used as payloads for sUAS, the price of sensors is still too high to be considered for many researchers. For more information on LiDAR technologies best suited for sUAS, please see Bhardwaj et al. (2016b).

High-altitude missions in areas such as mountain glaciers and ice sheet environments introduce additional challenges of lower air density and cold temperatures that decrease sUAS battery life drastically. Flying at high altitudes requires additional consideration of the type and specifications of the sUAS to be used. Companies such as SkymineUAV (<https://www.skymineuav.com/>), which primarily caters to the high-altitude mining industries, sell specialized software and hardware and offer training that can be applied to data gathering in alpine environments. In the case of building a custom sUAS, Paredes et al. (2017) provided several suggestions for both multirotor and fixed-wing sUAS designs to best perform in these types of environments. While fixed-wing systems are better suited for high-altitude flying because most of the vehicle's frame is utilized in generating lift, multirotors can successfully offer extended flight times and carry heavier payloads in these environments when utilizing larger propellers (in diameter and/or length) coupled with high-voltage batteries.

9.3.2 Potential Uses for sUAS in the Future

The applications explained above offer a representative yet relatively small pool of examples across the cryosphere and polar sciences. There is still much to be learned, synthesized, and improved upon for standardized methods of using sUAS for data collection. Beyond this, there are areas of scientific research where sUAS has the

potential to be a useful tool but has been underutilized or even unattempted. Some suggestions for future applications of sUAS in the polar regions are listed in Table 9.2. However, several innovative planetary research applications are also emerging. For example, polar and several other cold-arid, high-altitude environments are considered the best Mars analogues on Earth, and recent studies have used sUAS to effectively characterize Mars analogue features in high-latitude and high-altitude cryospheric settings (Bhardwaj et al. 2019; Sam et al. 2020a, b). Considering that NASA has sent the first sUAS to Mars with the agency's Mars 2020 rover mission, more such analogue studies employing sUAS in polar environments are bound to provide immense scope for comparable planetary geomorphological research.

A limitation of sUAS data collection is the spatial constraint on the area that can be surveyed compared to larger aircraft. However, the choice between sUAS platforms can be tailored to fit research design needs. For example, fixed-wing sUAS are less dependent on battery power in relation to flight time and distance covered than multirotor platforms. Large-scale data coverage of sUAS is less available compared to traditional remote sensing systems. To expand the footprint of sUAS-collected data, we recommend using sUAS as a scaling tool to connect to satellite data via models. This approach has been used in some studies outlined in this chapter, such as in modeling fractional cover of tundra vegetation (Riihimäki et al. 2019), yet much potential remains. Upscaling sUAS with satellite or airborne imagery could additionally be applied to many of the suggested future applications in Table 9.2.

9.3.3 Resources for Updated Legalities in Polar Regions and Helpful Organizations

sUAS platforms offer increased autonomy for researchers who would otherwise hire manned aircraft for data collection. However, the use of sUAS places greater responsibility on the researcher to ensure a safe and legal operation. Though a sUAS flight may be technically possible in an area of interest, jurisdiction over airspace and rules on the operation of sUAS may preclude operations. Acquiring permits, when necessary, can take several months, so planning well in advance of a flight is encouraged particularly in difficult-to-access areas, such as the polar regions. The Arctic Monitoring and Assessment Programme (AMAP) Unmanned Aircraft Systems Expert Group (UASEG) has compiled an aircraft systems operator's handbook that includes many considerations for safety and useful information on Arctic airspace authorities (Storvold et al. 2015). We recommend consulting this handbook prior to flight planning in high latitude areas. In fact, AMAP has undertaken considerable efforts to open airspace in the Arctic for research sUAS endeavors. In 2008, the UASEG was formed from a meeting of the eight Arctic nations (Canada, Finland, Greenland/Faroe Islands/Denmark, Iceland, Norway, Russia, Sweden, and

Table 9.2 Possible UAS capabilities in key Arctic research topics

Topics			
Lower atmosphere	Oceanic and sea ice processes	Glacier monitoring	Ecosystem dynamics
Aerosols and black carbon	Sea ice properties	Glacier mass balance	Terrestrial
Optical particle counters for measuring aerosol concentration and size distribution. Filter samplers for aerosol composition. Cloud condensation nuclei. Spectrometers for measuring aerosol and surface spectral radiative properties.	Precision GNSS and laser altimeter for measuring sea ice thickness (free-board) and roughness. Ground-penetrating radar for measuring snow on ice. Camera for characterizing sea ice types, concentrations and melt pond fractions. Spectrometers for sea ice spectral albedo measurements.	Laser altimeter or laser scanner for mapping surface elevation and thereby glacier mass and year to year total glacier mass changes. Ground-penetrating radar (GPR) for facies characterization, englacial and subglacial drainage, and changes in accumulation and melt.	Hyperspectral imagers with very high resolution for vegetation mapping and monitoring of vegetation health. Multispectral for land cover classifications to scale up with satellite imagery. LiDAR or optical point clouds to monitor vegetation height and biomass. Hyperspectral/multispectral/GPR- based monitoring of permafrost degradation. Terrestrial habitat monitoring using high-resolution RGB and thermal cameras.
Clouds	Ocean properties	Glacier dynamics	Marine
Cloud particle imager for measuring cloud particle size and shape distribution in water, mixed phase and ice clouds. Radiometers for measuring cloud radiative properties.	IR thermometer for measuring sea surface temperature. Synthetic aperture radar for measuring surface winds and waves.	Camera (visual or infrared), for estimating calving rates and dynamic mass loss rates compared to mass loss by melting. Synthetic aperture radar/optical feature tracking for estimating glacier flow velocities.	Cameras (visual or infrared) for marine bird or mammal surveys. Hyperspectral mapping of shallow-water benthic habitats.
Surface energy fluxes	Ocean color	Glacier hazards	
Turbulent flux probes and radiometers for measuring ocean-ice-atmosphere energy	Imaging spectrometer for measuring ocean color to determine nutrient and chlorophyll	Bathymetric LiDAR for glacial lake volume estimation. Thermal and RGB cameras for glacial lake outlet and	

(continued)

Table 9.2 (continued)

exchange and characterizing the effects of leads and melt ponds.	concentrations. Monitoring harmful algal blooms.	dam monitoring. LiDAR/RGB/thermal sensors for studying ice avalanches, landslides, and other mass movements.	
Meteorology	Energy transport	Glacial/periglacial geomorphology	
Air temperature, humidity, wind, and pressure. Dropsondes for profile measurements through the atmospheric boundary layer.	Infrared probe for measuring sea surface temperature. Synthetic aperture radar for measuring ocean currents (along with track interferometry).	RGB cameras for mapping and reconstructing past glacial events in a valley. GPR for finding status of buried ice in periglacial environments.	
Biogeochemistry		Glacier albedo	
CH ₄ , CO ₂ and N ₂ O sensors for in situ concentrations and flux estimates.		Multispectral sensors for monitoring glacier albedo changes owing to black carbon deposition.	

Adapted with permission from AMAP’s *Enabling Science use of UAS for Arctic Environmental Monitoring*, Ch. 7, Crowe et al. (2012) and Gaffey and Bhardwaj (2020). Reproduced under CC 4.0 (<https://creativecommons.org/licenses/by/4.0/legalcode>) with additional applications inserted

United States) where they and observer countries unanimously agreed that UAS represented a key tool for understanding climate change in the Arctic and its global impact (Crowe et al. 2012). UASEG hosted meetings with civil aviation authorities to work towards increasing access in the Arctic for scientists to use these technologies. Still, regulations vary among countries and rules are still being developed, updated, and changed. Owing to this, scientists still need to research specific restrictions for Arctic locations though the hope remains that eventually a harmonized regulatory environment will develop in the future (Table 9.3).

Similar to AMAP, organizations have created handbooks and guidelines for safe operations in the Antarctic as well. The Council of Managers of National Antarctic Programs (COMNAP) UAS working group has created guidelines for UAS missions in Antarctica with contributions from the Scientific Committee on Antarctic Research (SCAR) and encouragement from the Antarctic Treaty Consultative Meetings (ATCM) and Committee for Environmental Protection (CEP) (US ATCM 2014). The purpose of this operator’s handbook was to identify and manage risks and offer strategies to mitigate those risks, which is particularly important in unique and protected environments such as Antarctica. Recommendations covered include record keeping of flights and accident incident reporting, identification of all major components of the UAS, and routine sharing of operational and certification information in support of facilitating best practices (CONMAP 2016).

Lastly, an operator’s guide with helpful advice for marine-based missions comes from the University-National Oceanographic Laboratory System

Table 9.3 Summary of networks and resources helpful for planning sUAS missions in polar regions

Name	Description	URL Link
Arctic Monitoring & Assessment Programme (AMAP)	A working group of the Arctic Council that has created UAS operator handbooks specific to the Arctic.	Amap.no
Council of Managers of National Antarctic Programs (COMNAP)	Similar to AMAP, but created handbooks focused on Antarctic operations.	Comnap.aq
University-National Oceanographic Laboratory System (UNOLS)	Their scientific Committee for Oceanographic Aircraft has produced an operator's handbook for marine-based flights.	Unols.org
International Society for Atmospheric Research using Remotely piloted Aircraft	A professional organization to support knowledge exchange for atmospheric and environmental research with UAS.	Isarra.org
International Conference on Unmanned Aerial Systems (ICUAS) Association	A nonprofit organization to promote overall UAS usage and hosts annual conferences.	Icuas.com Uasconferences.com
UAVCoach	An online community with UAS pilot training and other resources.	Uavcoach.com
High Latitude Drone Ecology Network (HILDEN)	A network of high-latitude ecologists that share protocols and experience with using UAS.	Arcticdrones.org
DIY Drones	An online community to support effective purchasing, building, and usage of UAS.	DIYdrones.com

(UNOLS) Scientific Committee for Oceanographic Aircraft Research (SCOAR) (UNOLS2019). While this report is tailored to US flight operations, particularly in its detailed discussions of legality and obligations stemming from the Federal Aviation Administration (FAA), features are included that would benefit ship-based plans irrespective of national jurisdiction. Included are helpful guidance such as decision-making flow charts for pre-cruise planning, communication plans for Antarctic operations, and other preflight, shipboard, and post-cruise considerations. Duffy et al. (2018) provide accounts of first-hand experience and advice for managing sUAS operations from a moving ship. As an additional resource, they credit much of what they have learned to DIYdrones.com, an online community that includes blogs, discussions, and specialized groups to support sUAS endeavors everywhere.

9.4 Conclusions

Environmental monitoring and scientific inquiry into the cryosphere and polar regions, though varied in scope, have benefited from the increased application of sUAS technology. sUAS adds flexibility to investigations of the biosphere,

atmosphere, cryosphere, remote sensing, and the intersections between them that might have required temporal, radiometric, or spatial resolution needs that were not previously met by available satellite or manned aircraft imagery. While examples of snow depth, glaciology, ecology, and atmospheric data collection were covered here, there is still much untapped potential, including the applications suggested in Table 9.2. Future studies adopting a multi-sensor approach for monitoring polar and cryospheric subjects can reveal more holistic details. If the last decade was more about the development of UAS technology in general, the next decade should be dedicated to making this tool easily customizable as per project needs. Most importantly, considering the high costs of field investigations in extreme environments and the accelerating rate of climate change, researchers and institutions across the globe should move towards forming mutual data sharing policies, including protocols for uniform data compilation, archiving, and dissemination protocols.

References

- Alfredsen K, Haas C, Tuhtan JA, Zinke P (2018) Brief communication: mapping river ice using drones and structure from motion. *Cryosphere* 12(2):627–633. <https://doi.org/10.5194/tc-12-627-2018>
- Alonzo M, Dial RJ, Schulz BK, Andersen HE, Lewis-Clark E, Cook BD, Morton DC (2020) Mapping tall shrub biomass in Alaska at landscape scale using structure-from-motion photogrammetry and lidar. *Remote Sens Environ* 245(April):111841. <https://doi.org/10.1016/j.rse.2020.111841>
- Assmann JJ, Kerby JT, Cunliffe AM, Myers-Smith IH (2019) Vegetation monitoring using multispectral sensors – best practices and lessons learned from high latitudes. *J Unmanned Veh Syst* 7(1):54–75. <https://doi.org/10.1139/juvs-2018-0018>
- Avanzi F, Bianchi A, Cina A, De Michele C, Maschio P, Pagliari D, Passoni D, Pinto L, Piras M, Rossi L (2018) Centimetric accuracy in snow depth using unmanned aerial system photogrammetry and a multistation. *Remote Sens* 10(5):1–17. <https://doi.org/10.3390/rs10050765>
- Bash EA, Moorman BJ (2020) Surface melt and the importance of water flow – an analysis based on high-resolution unmanned aerial vehicle (UAV) data for an Arctic glacier. *Cryosphere* 14:549–563. <https://doi.org/10.5194/tc-14-549-2020>
- Bash EA, Moorman BJ, Gunther A (2018) Detecting short-term surface melt on an Arctic glacier using UAV surveys. *Remote Sens* 10:1547. <https://doi.org/10.3390/rs10101547>
- Beamish A, Reynolds MK, Epstein H, Frost GV, Macander MJ, Bergstedt H, Bartsch A, Kruse S, Miles V, Tanis CM, Heim B (2020) Recent trends and remaining challenges for optical remote sensing of Arctic tundra vegetation: a review and outlook. *Remote Sens Environ* 246 (March):111872. <https://doi.org/10.1016/j.rse.2020.111872>
- Benoit L, Gourdon A, Vallat R, Irrazaval I, Gravey M, Lehmann B, Prasicek G, Gräff D, Herman F, Mariethoz G (2019) A high-resolution image time series of the Gorner Glacier – Swiss Alps – derived from repeated unmanned aerial vehicle surveys. *Earth Syst Sci Data* 11(2): 579–588. <https://doi.org/10.5194/essd-11-579-2019>
- Bhardwaj A, Sam L, Akanksha, Martín-Torres FJ, Kumar R (2016a) UAVs as remote sensing platform in glaciology: present applications and future prospects. *Remote Sens Environ* 175: 196–204. <https://doi.org/10.1016/j.rse.2015.12.029>
- Bhardwaj A, Sam L, Bhardwaj A, Martín-Torres FJ (2016b) LiDAR remote sensing of the cryosphere: present applications and future prospects. *Remote Sens Environ* 177:125–143. <https://doi.org/10.1016/j.rse.2016.02.031>

- Bhardwaj A, Sam L, Martín-Torres FJ, Zorzano M-P, Ramírez Luque JA (2019) UAV imaging of a Martian brine analogue environment in a fluvio-aeolian setting. *Remote Sens* 11:2104
- Bollard-Breen B, Brooks JD, Jones MRL, Robertson J, Betschart S, Kung O, Cary SC, Lee CK, Pointing SB (2015) Application of an unmanned aerial vehicle in spatial mapping of terrestrial biology and human disturbance in the McMurdo Dry Valleys, East Antarctica. *Polar Biol* 38(4): 573–578. <https://doi.org/10.1007/s00300-014-1586-7>
- Brun F, Buri P, Miles ES, Wagnon P, Steiner J, Berthier E, Ragetli S, Kraaijenbrink P, Immerzeel WW, Pellicciotti F (2016) Quantifying volume loss from ice cliffs on debris-covered glaciers using high-resolution terrestrial and aerial photogrammetry. *J Glaciol* 62(234):684–695. <https://doi.org/10.1017/jog.2016.54>
- Bühler Y, Adams MS, Bosch R, Stoffel A (2016) Mapping snow depth in alpine terrain with unmanned aerial systems (UASs): potential and limitations. *Cryosphere* 10(3):1075–1088. <https://doi.org/10.5194/tc-10-1075-2016>
- Carter J (2019) 8 tips for flying in cold weather. *The Drone Girl*, November 17. <https://www.thedronegirl.com/2018/01/02/drone-cold-weather-tips/>
- Chandler BMP, Evans DJA, Chandler SJP, Ewertowski MW, Lovell H, Roberts DH, Schaefer M, Tomczyk AM (2020) The glacial landsystem of Fjallsjökull, Iceland: spatial and temporal evolution of process-form regimes at an active temperate glacier. *Geomorphology* 361: 107192. <https://doi.org/10.1016/j.geomorph.2020.107192>
- Che Y, Wang S, Yi S, Wei Y, Cai Y (2020) Summer mass balance and surface velocity derived by unmanned aerial vehicle on debris-covered region of baishui river glacier no. 1, yulong snow mountain. *Remote Sens* 12(20):1–15. <https://doi.org/10.3390/rs12203280>
- Chudley TR, Christoffersen P, Doyle SH, Abellan A, Snooke N (2019a) High- accuracy UAV photogrammetry of ice sheet dynamics with no ground control. *Cryosphere* 13:955–968. <https://doi.org/10.5194/tc-13-955-2019>
- Chudley TR, Christoffersen P, Doyle SH, Bougamont M, Schoonman CM, Hubbard B, James MR (2019b) Supraglacial lake drainage at a fast-flowing Greenlandic outlet glacier. *Proc Natl Acad Sci U S A* 116(51):25468–25477. <https://doi.org/10.1073/pnas.1913685116>
- Cimoli E, Marcer M, Vandecrux B, Bøggild CE, Williams G, Simonsen SB (2017) Application of low-cost UASs and digital photogrammetry for high-resolution snow depth mapping in the Arctic. *Remote Sens* 9:1144. <https://doi.org/10.3390/rs9111144>
- Cook JM, Tedstone AJ, Williamson C, Mccutcheon J, Hodson AJ, Dayal A, Skiles M, Hofer S, Bryant R, McAree O, Mcgonigle A (2020) Glacier algae accelerate melt rates on the South-Western Greenland Ice Sheet. *Cryosphere* 14:309–330. <https://doi.org/10.5194/tc-14-309-2020>
- Council of Managers of National Antarctic Programs (CONMAP) (2016) Antarctic Unmanned Aerial Systems (UAS) operator's handbook (ATCM XXXIX No. 31)
- Crowe W, Davis KD, la Cour-Harbo A, Vihma T, Lesenkov S, Eppi R, Weatherhead EC, Liu P, Raustein M, Abrahamsson M, Johansen KS (2012) Enabling science use of unmanned aircraft systems for Arctic environmental monitoring, vol 6, Oslo. Retrieved from <http://www.amap.no/documents/download/938>
- Curry JA, Maslanik J, Holland G, Pinto J (2004) Applications of Aerosondes in the Arctic. *Bull Am Meteorol Soc* 85(12):1855–1861. <https://doi.org/10.1175/BAMS-85-12-1855>
- de Boer G, Ivey M, Schmid B, Lawrence D, Dexheimer D, Mei F, Hubbe J, Bendure A, Hardesty J, Shupe MD, McComiskey A (2018) A bird's-eye view: development of an operational ARM unmanned aerial capability for atmospheric research in Arctic Alaska. *Bull Am Meteorol Soc* 99(6):1197–1212. <https://doi.org/10.1175/BAMS-D-17-0156.1>
- Duffy JP, Cunliffe AM, Debell L, Sandbrook C, Wich SA, Shutler JD, Myers-Smith IH, Varela MR, Anderson K (2018) Location, location, location: considerations when using lightweight drones in challenging environments. *Remote Sens Ecol Conserv* 4(1):7–19. <https://doi.org/10.1002/rse2.58>
- Eltner A, Kaiser A, Castillo C, Rock G, Neuring F, Abellán A (2016) Image-based surface reconstruction in geomorphometry—merits, limits and developments. *Earth Surf Dyn* 4(2): 359–389. <https://doi.org/10.5194/esurf-4-359-2016>

- Fernandes R, Prevost C, Canisius F, Leblanc SG, Maloley M, Oakes S, Holman K, Knudby A (2018) Monitoring snow depth change across a range of landscapes with ephemeral snowpacks using structure from motion applied to lightweight unmanned aerial vehicle videos. *Cryosphere* 12:3535–3550. <https://doi.org/10.5194/tc-12-3535-2018>
- Florinsky IV, Bliakharskii DP (2019) Detection of crevasses by geomorphometric treatment of data from unmanned aerial surveys. *Remote Sens Lett* 10(4):323–332. <https://doi.org/10.1080/2150704X.2018.1552809>
- Fraser RH, Olthof I, Lantz TC, Schmitt C (2016) UAV photogrammetry for mapping vegetation in the low-Arctic. *Arctic Sci* 2(3):79–102. <https://doi.org/10.1139/as-2016-0008>
- Freitas P, Vieira G, Canário J, Folhas D, Vincent WF (2019) Identification of a threshold minimum area for reflectance retrieval from thermokarst lakes and ponds using full-pixel data from Sentinel-2. *Remote Sens* 11(6). <https://doi.org/10.3390/rs11060657>
- Fugazza D, Scaioni M, Corti M, D'Agata C, Azzoni RS, Cernuschi M, Smiraglia C, Dialaiuti GA (2018) Combination of UAV and terrestrial photogrammetry to assess rapid glacier evolution and conditions of glacier hazards. *Nat Hazards Earth Syst Sci* 18:1055–1071. <https://doi.org/10.5194/nhess-18-1055-2018>
- Gaffey C, Bhardwaj A (2020) Applications of unmanned aerial vehicles in cryosphere: latest advances and prospects. *Remote Sens* 12(6):948. <https://doi.org/10.3390/rs12060948>
- Giordan D, Adams MS, Aicardi I, Alicandro M, Allasia P, Baldo M et al (2020) The use of unmanned aerial vehicles (UAVs) for engineering geology applications. *Bull Eng Geol Environ* 79(7):3437–3481. <https://doi.org/10.1007/s10064-020-01766-2>
- Goebel ME, Perryman WL, Hinke JT, Krause DJ, Hann NA, Gardner S, LeRoi DJ (2015) A small unmanned aerial system for estimating abundance and size of Antarctic predators. *Polar Biol* 38(5):619–630. <https://doi.org/10.1007/s00300-014-1625-4>
- Goetz J, Brenning A (2019) Quantifying uncertainties in snow depth mapping from structure from motion photogrammetry in an alpine area. *Water Resour Res* 55(9):7772–7783. <https://doi.org/10.1029/2019WR025251>
- Goetz J, Fieguth P, Kasiri K, Bodin X, Marcer M, Brenning A (2019) Accounting for permafrost creep in high-resolution snow depth mapping by modelling sub-snow ground deformation. *Remote Sens Environ* 231:111275. <https://doi.org/10.1016/j.rse.2019.111275>
- Graham DE, Wallenstein MD, Vishnivetskaya TA, Waldrop MP, Phelps TJ, Pfiffner SM, Onstott TC, Whyte LG, Rivkina EM, Gilichinsky DA, Elias DA (2012) Microbes in thawing permafrost: the unknown variable in the climate change equation. *ISME J* 6(4):709–712. <https://doi.org/10.1038/ismej.2011.163>
- Grepow (2020) What is the best lithium battery for cold weather? Grepow Blog, August 5. <https://www.grepow.com/blog/the-best-lithium-battery-for-cold-weather/>
- Harder P, Pomeroy JW, Helgason WD, Helgason WD (2020) Improving sub-canopy snow depth mapping with unmanned aerial vehicles: Lidar versus structure-from-motion techniques. *Cryosphere* 14(6):1919–1935. <https://doi.org/10.5194/tc-14-1919-2020>
- Hendrickx H, Vivero S, De Cock L, De Wit B, De Maeyer P, Lambiel C, Delaloye R, Nyssen J, Frankl A (2019) The reproducibility of SfM algorithms to produce detailed Digital Surface Models: the example of PhotoScan applied to a high-alpine rock glacier. *Remote Sens Lett* 10(1):11–20. <https://doi.org/10.1080/2150704X.2018.1519641>
- Hodson A, Anesio AM, Ng F, Watson R, Quirk J, Irvine-Fynn T, Dye A, Clark C, McCloy P, Kohler J, Sattler B (2007) A glacier respire: quantifying the distribution and respiration CO₂ flux of cryoconite across an entire arctic supraglacial ecosystem. *J Geophys Res Biogeosci* 112(4):1–9. <https://doi.org/10.1029/2007JG000452>
- Hodson AJ, Nowak A, Redeker KR, Holmlund ES, Christiansen HH, Turchyn AV (2019) Seasonal dynamics of methane and carbon dioxide evasion from an open system pingo: Lagoon pingo, svalbard. *Front Earth Sci* 7(February):1–12. <https://doi.org/10.3389/feart.2019.00030>
- Jenssen ROR, Jacobsen S (2020) Drone-mounted UWB snow radar: technical improvements and field results. *J Electromagn Waves Appl* 34(14):1930–1954. <https://doi.org/10.1080/09205071.2020.1799871>

- Jenssen ROR, Eckerstorfer M, Jacobsen S (2020) Drone-mounted ultrawideband radar for retrieval of snowpack properties. *IEEE Trans Instrum Meas* 69(1):221–230. <https://doi.org/10.1109/TIM.2019.2893043>
- Jonassen MO, Tisler P, Altsta B, Scholtz A, Vihma T, Lampert A, König-Langlo G, Lüpkes C (2015) Application of remotely piloted aircraft systems in observing the atmospheric boundary layer over Antarctic sea ice in winter. *Polar Res* 34:25651. <https://doi.org/10.3402/polar.v34.25651>
- Jones C, Ryan J, Holt T, Hubbard A (2018) Structural glaciology of Isunguata Sermia, West Greenland. *J Maps* 14(2):517–527. <https://doi.org/10.1080/17445647.2018.1507952>
- Jouvet G, Weidmann Y, Kneib M, Detert M, Seguinot J, Sakakibara D, Sugiyama S (2018) Short-lived ice speed-up and plume water flow captured by a VTOL UAV give insights into subglacial hydrological system of Bowdoin Glacier. *Remote Sens Environ* 217:389–399. <https://doi.org/10.1016/j.rse.2018.08.027>
- Kartozia A (2019) Assessment of the ice wedge polygon current state by means of UAV imagery analysis (Samoylov Island, the Lena Delta). *Remote Sens* 11(13). <https://doi.org/10.3390/rs11131627>
- Korczak-Abshire M, Zmarz A, Rodzewicz M, Kycko M, Karsznia I, Chwedorzewska KJ (2019) Study of fauna population changes on Penguin Island and Turret Point Oasis (King George Island, Antarctica) using an unmanned aerial vehicle. *Polar Biol* 42(1):217–224. <https://doi.org/10.1007/s00300-018-2379-1>
- Kraaijenbrink PDA, Shea JM, Pellicciotti F, Jong SMD, Immerzeel WW (2016) Object-based analysis of unmanned aerial vehicle imagery to map and characterise surface features on a debris-covered glacier. *Remote Sens Environ* 186:581–595. <https://doi.org/10.1016/j.rse.2016.09.013>
- Kraaijenbrink PDA, Shea JM, Litt M, Steiner JF, Treichler D, Koch I, Immerzeel WW (2018) Mapping surface temperatures on a debris-covered glacier with an unmanned aerial vehicle. *Front Earth Sci* 6(May):64. <https://doi.org/10.3389/feart.2018.00064>
- Krause DJ, Hinke JT, Perryman WL, Goebel ME, LeRoi DJ (2017) An accurate and adaptable photogrammetric approach for estimating the mass and body condition of pinnipeds using an unmanned aerial system. *PLoS One* 12(11):1–21. <https://doi.org/10.1371/journal.pone.0187465>
- Lamsters K, Karušs J, Krievāns M, Ješkins J (2019) Application of unmanned aerial vehicles for glacier research in the Arctic and Antarctic. In: *Proceedings of the 12th international scientific and practical conference*, vol 1, pp 131–135. [https://doi.org/Print ISSN 1691-5402](https://doi.org/Print%20ISSN%201691-5402). Online ISSN 2256-070X
- Lee WY, Park M, Hyun CU (2019) Detection of two Arctic birds in Greenland and an endangered bird in Korea using RGB and thermal cameras with an unmanned aerial vehicle (UAV). *PLoS One* 14(9):1–17. <https://doi.org/10.1371/journal.pone.0222088>
- Li T, Zhang B, Xiao W, Cheng X, Li Z, Zhao J (2020) UAV-based photogrammetry and LiDAR for the characterization of ice morphology evolution. *IEEE J Sel Top Appl Earth Obs Remote Sens* 13:4188–4199. <https://doi.org/10.1109/JSTARS.2020.3010069>
- Lousada M, Pina P, Vieira G, Bandeira L, Mora C (2018) Evaluation of the use of very high resolution aerial imagery for accurate ice-wedge polygon mapping (Adventdalen, Svalbard). *Sci Total Environ* 615:1574–1583. <https://doi.org/10.1016/j.scitotenv.2017.09.153>
- Lovitt J, Rahman MM, McDermid GJ (2017) Assessing the value of UAV photogrammetry for characterizing terrain in complex peatlands. *Remote Sens* 9(7):715. <https://doi.org/10.3390/rs9070715>
- Lucieer A, Turner D, King DH, Robinson SA (2014) Using an Unmanned Aerial Vehicle (UAV) to capture micro-topography of Antarctic moss beds using an Unmanned Aerial Vehicle (UAV) to capture micro-topography. *Int J Appl Earth Obs Geoinf* 27:53–62. <https://doi.org/10.1016/j.jag.2013.05.011>
- Malenovský Z, Lucieer A, King DH, Turnbull JD, Robinson SA (2017) Unmanned aircraft system advances health mapping of fragile polar vegetation. *Methods Ecol Evol* 8(12):1842–1857. <https://doi.org/10.1111/2041-210X.12833>

- Mali VK, Kuiry SN (2018) Assessing the accuracy of high-resolution topographic data generated using freely available packages based on SfM-MVS approach. *Measurement* 124:338–350. <https://doi.org/10.1016/j.measurement.2018.04.043>
- Manfreda S, McCabe MF, Miller PE, Lucas R, Madrigal VP, Mallinis G, Ben Dor E, Helman D, Estes L, Ciralo G, Müllerová J (2018) On the use of unmanned aerial systems for environmental monitoring. *Remote Sens* 10(4). <https://doi.org/10.3390/rs10040641>
- Mustafa O, Barbosa A, Krause DJ, Peter H-U, Vieira G, Rummeler M-C (2018) State of knowledge: Antarctic wildlife response to unmanned aerial systems. *Polar Biol* 41(11):2387–2398. <https://doi.org/10.1007/s00300-018-2363-9>
- Nolan M, Larsen C, Sturm M (2015) Mapping snow depth from manned aircraft on landscape scales at centimeter resolution using structure-from-motion photogrammetry. *Cryosphere* 9(4): 1445–1463. <https://doi.org/10.5194/tc-9-1445-2015>
- Paredes JA, Saito C, Abarca M, Cuellar F (2017) Study of effects of high-altitude environments on multicopter and fixed-wing UAVs' energy consumption and flight time. In: *IEEE international conference on automation science and engineering, 2017–August*, pp 1645–1650. <https://doi.org/10.1109/COASE.2017.8256340>
- Park H, Kim Y, Kimball JS (2016) Widespread permafrost vulnerability and soil active layer increases over the high northern latitudes inferred from satellite remote sensing and process model assessments. *Remote Sens Environ* 175:349–358. <https://doi.org/10.1016/j.rse.2015.12.046>
- Raoult V, Colefax AP, Allan BM, Cagnazzi D, Castelblanco-Martínez N, Ierodiaconou D, Johnston DW, Landeo-Yauri S, Lyons M, Pirota V, Schofield G, Butcher PA (2020) Operational protocols for the use of drones in marine animal research. In: *Drones*. (vol 4, Issue 64, pp 1–35. MDPI AG. <https://doi.org/10.3390/drones4040064>
- Räsänen A, Virtanen T (2019) Data and resolution requirements in mapping vegetation in spatially heterogeneous landscapes. *Remote Sens Environ* 230(May):111207. <https://doi.org/10.1016/j.rse.2019.05.026>
- Reagan J (2020) LiPo batteries: a drone user's guide. *Dronegenuity*. <https://www.dronegenuity.com/lipo-drone-batteries-users-guide/>
- Riihimäki H, Luoto M, Heiskanen J (2019) Estimating fractional cover of tundra vegetation at multiple scales using unmanned aerial systems and optical satellite data. *Remote Sens Environ* 224(January):119–132. <https://doi.org/10.1016/j.rse.2019.01.030>
- Rohner C, Small D, Beutel J, Henke D, Lüthi MP, Vieli A (2019) Multisensor validation of tidewater glacier flow fields derived from synthetic aperture radar (SAR) intensity tracking. *Cryosphere* 13:2953–2975. <https://doi.org/10.5194/tc-13-2953-2019>
- Rossini M, Di Mauro B, Garzonio R, Baccolo G, Cavallini G, Mattavelli M, De Amicis M, Colombo R (2018) Rapid melting dynamics of an alpine glacier with repeated UAV photogrammetry. *Geomorphology* 304:159–172. <https://doi.org/10.1016/j.geomorph.2017.12.039>
- Rummeler MC, Mustafa O, Maercker J, Peter HU, Esefeld J (2018) Sensitivity of Adélie and Gentoo penguins to various flight activities of a micro UAV. *Polar Biol* 41:2481–2493. <https://doi.org/10.1007/s00300-018-2385-3>
- Ryan JC, Hubbard AL, Box JE, Todd J, Christoffersen P, Carr JR, Holt TO, Snooke N (2015) UAV photogrammetry and structure from motion to assess calving dynamics at Store Glacier, a large outlet draining the Greenland ice sheet. *Cryosphere* 9(1):1–11. <https://doi.org/10.5194/tc-9-1-2015>
- Sam L, Bhardwaj A, Singh S, Martin-Torres FJ (2020a) UAV imaging of small caves in Icelandic lava field as possible Mars analogues. In: *Proceedings of the 3rd international planetary caves conference, San Antonio, TX, USA*
- Sam L, Bhardwaj A, Singh S, Martin-Torres FJ, Zorzano MP, Ramírez Luque JA (2020b) Small lava caves as possible exploratory targets on Mars: analogies drawn from UAV imaging of an Icelandic lava field. *Remote Sens* 12:1970
- Sanz-ablanedo E, Chandler JH, Rodríguez-Pérez JR, Ordóñez C (2018) Accuracy of Unmanned Aerial Vehicle (UAV) and SfM photogrammetry survey as a function of the number and

- location of ground control points used. *Remote Sens* 10:1606. <https://doi.org/10.3390/rs10101606>
- Sheridan I (2020) Drones and global navigation satellite systems: current evidence from polar scientists. *R Soc Open Sci* 7(3). <https://doi.org/10.1098/rsos.191494>
- Sotille ME, Bremer UF, Vieira G, Velho LF, Petsch C, Simões JC (2020) Evaluation of UAV and satellite-derived NDVI to map maritime Antarctic vegetation. *Appl Geogr* 125(September). <https://doi.org/10.1016/j.apgeog.2020.102322>
- St Germain SL, Moorman BJ (2019) Long-term observations of supraglacial streams on an arctic glacier. *J Glaciol* 65(254):900–911. <https://doi.org/10.1017/jog.2019.60>
- Storvold R, Sweatle C, Ruel P, Wuennenberg M, Tarr K, Raustein M, Hillesøy T, Lundgren T, Sumich M (2015) Arctic science RPAS operator's handbook. Retrieved from <https://oaarchive.arctic-council.org/handle/11374/719>
- Stoven-Dubois A, Jospin L, Cucci DA (2018) Cooperative navigation for an UAV tandem in GNSS denied environments. In: Proceedings of the 31st international technical meeting of the Satellite Division of The Institute of Navigation. <https://doi.org/10.33012/2018.15949>
- Sturm M, Racine C, Tape K (2001) Increasing shrub abundance in the Arctic. *Nature* 411:546. Retrieved from. <https://doi.org/10.1038/35079180>
- Tahar KN (2013) An evaluation on different number of ground control points in unmanned aerial vehicle photogrammetric block. In: International archives of the photogrammetry, remote sensing and spatial information sciences, ISPRS 8th 3DGeoInfo conference & WG II/2 workshop, Istanbul, Turkey, vol XL-2/W2, pp 27–29
- Tan A, Eccleston K, Platt I, Woodhead I, Rack W, McCulloch J (2017) The design of a UAV mounted snow depth radar: results of measurements on Antarctic Sea ice. In: 2017 IEEE conference on Antenna Measurements & Applications (CAMA), pp 316–319. <https://doi.org/10.1109/CAMA.2017.8273437>
- The Arctic Research Consortium of the U.S. (ARCUS) (1997) Logistics recommendations for an improved U.S. Arctic Research Capability. Fairbanks
- Tonkin TN, Midgley NG (2016) Ground-control networks for image based surface reconstruction: an investigation of optimum survey designs using UAV derived imagery and structure-from-motion photogrammetry. *Remote Sens* 8(9):16–19. <https://doi.org/10.3390/rs8090786>
- Turner D, Lucieer A, Malenovsky Z, King DH, Robinson SA (2014) Spatial co-registration of ultra-high resolution visible, multispectral and thermal images acquired with a micro-UAV over antarctic moss beds. *Remote Sens* 6(5):4003–2024. <https://doi.org/10.3390/rs6054003>
- University-National Oceanographic Laboratory System (UNOLS) (2019) Unmanned Aerial Systems (UAS) operations from the U.S. Academic Research Fleet: operator's handbook
- US ATCM (2014) Considerations for the use of unmanned aircraft systems (UAS) for research, monitoring, and observation in Antarctica (ATCM XXXVII); Antarctic Treaty Consultative Meeting: Brasilia, Brazil
- Van der Sluijs J, Kokelj SV, Fraser RH, Tunnicliffe J, Lacelle D (2018) Permafrost terrain dynamics and infrastructure impacts revealed by UAV photogrammetry and thermal imaging. *Remote Sens* 10:1734. <https://doi.org/10.3390/rs10111734>
- Verfuss UK, Aniceto AS, Harris DV, Gillespie D, Fielding S, Jiménez G, Johnston P, Sinclair RR, Sivertsen A, Solbø SA, Storvold R (2019) A review of unmanned vehicles for the detection and monitoring of marine fauna. *Mar Pollut Bull* 140(February 2018):17–29. <https://doi.org/10.1016/j.marpolbul.2019.01.009>
- Vincent C, Wagnon P, Shea JM, Immerzeel WW, Kraaijenbrink P, Shrestha DJM, Immerzeel WW, Kraaijenbrink P, Shrestha D, Soruco A, Arnaud Y, Brun F, Berthier E, Sherpa SF (2016) Reduced melt on debris-covered glaciers: investigations from Changri Nup Glacier, Nepal. *Cryosphere* 10:1845–1858. <https://doi.org/10.5194/tc-10-1845-2016>

- Weimerskirch H, Pudor A, Schull Q (2018) Flights of drones over sub-Antarctic seabirds show species- and status-specific behavioural and physiological responses. *Polar Biol* 41:259–266. <https://doi.org/10.1007/s00300-017-2187-z>
- Wigmore O, Mark B (2017) Monitoring tropical debris covered glacier dynamics from high resolution unmanned aerial vehicle photogrammetry, Cordillera Blanca, Peru. *Cryosphere* 11: 2463–2480. <https://doi.org/10.5194/tc-11-2463-2017>
- Zhang W, Liljedahl AK, Kanevskiy M, Epstein HE, Jones BM, Jorgenson MT, Kent K (2020) Transferability of the deep learning mask R-CNN model for automated mapping of ice-wedge polygons in high-resolution satellite and UAV images. *Remote Sens* 12(7). <https://doi.org/10.3390/rs12071085>
- Zmarz A, Rodzewicz M, Dąbski M, Karsznia I, Korczak-Abshire M, Chwedorzewska KJ (2018) Application of UAV BVLOS remote sensing data for multi-faceted analysis of Antarctic ecosystem. *Remote Sens Environ* 217:375–388. <https://doi.org/10.1016/j.rse.2018.08.031>

Chapter 10

Coastal Dune Eco-geomorphology: sUAS Applications and Opportunities



Alex Smith, Brianna Lunardi, Elizabeth George, Jacob Lehner,
and Chris Houser

Abstract Coastal dune systems are dynamic in response to regional environmental controls and form complex networks of stable and active surfaces operating over multiple scales. As these systems adapt to climate change, it is critical to increase the spatiotemporal monitoring record to provide further insight on the eco-geomorphological processes and feedbacks affecting coastal dune evolution through time. Since the 2010s, small unoccupied aircraft systems (sUAS) have been increasingly used for monitoring topographic change and classifying vegetation in coastal dune environments. Concurrently, advances in survey methodologies have limited the error and uncertainty of measuring multitemporal change. Further opportunities remain for applying sUAS and the large datasets they produce to address knowledge gaps and test conceptual models of coastal dune eco-geomorphology. The aim of this chapter is to briefly introduce some of the fundamental concepts on the biotic and abiotic processes at work in coastal dune systems, review sUAS studies that have monitored coastal dune eco-geomorphology, present findings and considerations from ongoing coastal monitoring studies conducted by the authors, and discuss further opportunities to apply sUAS in coastal dune research. Specifically, this chapter focuses on (1) vegetation zonation and distribution in coastal dunes; (2) aeolian processes, dune building, and the role of vegetation; (3) coastal dune disturbances, recovery, and vegetation feedbacks; and (4) topographic change, error, and uncertainty.

Keywords Coastal dunes · Eco-geomorphology · sUAS · Topographic change · Vegetation zonation · Aeolian

A. Smith (✉) · B. Lunardi · E. George · J. Lehner · C. Houser
School of the Environment, University of Windsor, Windsor, ON, Canada
e-mail: absmith9@uwindsor.ca

10.1 Introduction

Coastal dune systems are comprised of complex ‘mosaics’ of stable and active sand surfaces that evolve in response to aeolian and hydrological processes operating over a range of scales (Carter et al. 1990a; Hesp 2002; Houser et al. 2017). Often in sandy coastal environments, backshore vegetation affects sedimentation processes and has a fundamental role in the initiation and stabilization of foredunes (Hesp 2002) and in foredune recovery following storm events (Houser et al. 2015, 2018). Foredunes provide protection for inland habitats from abiotic processes including sand burial, salt spray and flooding during periods of high-water levels and wave run-up. Continual monitoring of coastal dune eco-geomorphology is critical to improving our understanding of the processes and feedbacks controlling these systems. Additionally, increasing the spatiotemporal record of observations can be used to investigate how these systems are adapting to climate change (e.g., sea level rise and change in storm frequency and/or magnitude) and increased anthropogenic impacts. Small unoccupied aircraft systems (sUAS) offer an efficient and low-cost method to simultaneously collect vegetation and topographic data that can be used to monitor environmental changes over time. As a result, the number of studies using sUAS to monitor coastal dune dynamics is likely to increase rapidly over the coming years. To best utilize this technology and the large datasets it produces, it is important not only to improve surveying methodologies and to limit uncertainty but also to address knowledge gaps through innovative applications and by promoting further collaboration between ecologists and geomorphologists (Houser et al. 2021).

The purpose of this chapter is to provide a brief background on some of the biotic and abiotic processes operating within coastal dune systems, review sUAS studies that have been used to monitor these systems, present additional findings and considerations from coastal monitoring studies conducted by the authors, and discuss knowledge gaps and further opportunities to apply sUAS for coastal dune research. Furthermore, this chapter will focus primarily on studies that have used structure from motion (SfM) photogrammetry to produce RGB orthomosaics, multispectral vegetation indices, and digital surface models (DSM) or ‘bare earth’ digital terrain models (DTM). A technical review of sUAS data collection and SfM processing is beyond the scope of this work but can be found in a number of papers (e.g., Westoby et al. 2012; Mancini et al. 2013). Therefore, the remainder of this chapter will introduce fundamental coastal dune system concepts and discuss sUAS applications to monitor (1) vegetation zonation and distribution in coastal dunes; (2) aeolian processes, dune building, and the role of vegetation; (3) coastal dune disturbances, recovery, and vegetation feedbacks; and (4) topographic change, error, and uncertainty.

10.2 Vegetation Zonation and Distribution in Coastal Dunes

In oceanic and lacustrine environments, the zonation of coastal vegetation is controlled by cross-shore gradients of environmental processes such as tides, waves, and wind that essentially filter plant communities based on their unique tolerance levels (Maun 2009). While a range of biotic (e.g., herbivory; Gedge and Maun 1994) and abiotic (e.g., sand abrasion; Rozema et al. 1985) stressors can affect the germination and survival of propagules, seedlings, and plants, zonation in coastal dune systems is thought to be primarily controlled by species tolerance to sand burial (Maun 1998) and salt spray (Du and Hesp 2020). In the most exposed backshore environments, species growing on the beach and foredune have developed unique adaptations to tolerate or avoid adverse environmental conditions (Hesp 1991). Aeolian processes or wind-blown sand (see Sect. 10.3.1) can cause the episodic burial of plants depending on the synchronization of sediment supply and transport competency (e.g., Houser 2009). Harmful effects of burial include a decrease in light required for photosynthesis, reduction in oxygen due to increased pore moisture content or soil compaction, and exposure to soil pathogens (Armstrong 1980; Maun and Riach 1981; Baldwin and Maun 1983). Alternatively, sediment burial can cause an increased 'vigour', defined by Maun (1998) as, '*an improvement in growth characters (physiological, ecological) of an individual plant and (or) increase in density, cover, and biomass per unit area*'. The tolerance, or limit at which plants can survive and emerge from burial, depends on the species type, propagation from either seeds or rhizomes, inter- and intra-species variability in seed mass, depth and duration of burial, and life cycle stage (Maun 1998, 2009). For instance, buried seedlings of *Ammophila breviligulata* may fail to emerge at depths greater than 6 cm, whereas mature plants can emerge from a single burial event of up to 100 cm (Maun and Lapierre 1984, 1986). Most backshore vegetation species can tolerate a certain range of burial, beyond which it will be lethal.

Salt spray develops when breaking waves produce bubbles that burst and eject salt particles into the overlying airflow (Boyce 1954; Du and Hesp 2020). The production of salt spray increases with higher energy nearshore conditions, concomitant with an increase in wave height, surfzone width, and number of breaking waves (Hesp 1988). Landward of the swash zone, soil salinity is controlled by the rate of salt spray deposition and precipitation that redistributes salt through soil leaching or by washing off salt accumulated on vegetation (Boyce 1954; Maun 2009; Du and Hesp 2020). During onshore winds, the rate of salt spray deposition generally increases with wind velocity (Boyce 1954; Randall 1970; McDonald et al. 1982) and decreases with distance from the shoreline (Barbour 1978). Topographic controls can also affect salt spray deposition, with exposed stoss slopes of foredunes and secondary dune ridges experiencing higher depositional rates than sheltered lee slopes and interdune areas (Randall 1970). The accumulation of salt on plants can be influenced by the size, shape, and orientation of leaves, with small, thin, and horizontal leaves more efficient at trapping salt than large, wide, and vertical leaves

(Boyce 1954; Barbour 1978; Maun 2009; Du and Hesp 2020). Salt spray and soil salinity can inhibit seed germination, cause tissue necrosis, reduce resource allocation for plant reproduction, and can lead to a decrease in plant biomass (Boyce 1954; Seneca 1969; Barbour 1970; Cheplick and Demetri 1999). Plants may increase salt tolerance or limit exposure by increasing leaf thickness through hypertrophy, shedding old leaves, epicuticular wax, low profile growth patterns, and extrusion of salt from roots (Boyce 1954; Randall 1970; Clayton 1972; Ahmad and Wainwright 1976; Hesp 1991; Maun 2009).

Plant exposure to sand burial and salt spray generally decreases in a landward direction; however, cross-shore variability in environmental processes can alter the characteristic zonation in coastal dunes. For example, Dech and Maun (2005) found distinct gradients of grass, shrub, and tree communities on the lee slope of a blowout eroding a relic secondary foredune ridge at Pinery Provincial Park, Canada. The presence or absence of species was controlled by rates of sand burial, consisting primarily of grass species more typical of the backshore with high growth rates, rhizome production and clonal propagation (e.g., *Calamovilfa longifolia*) and trees capable of forming adventitious roots (e.g., *Juniperus virginiana*) in areas with high sedimentation rates. Alongshore, variable exposure to abiotic processes can affect the distribution of vegetation in coastal dune environments. For example, Silva et al. (2008) found that changes in vegetation density and species type occurred from south to north at Moçambique Beach, Brazil. Over several kilometers, shoreline curvature exposed the northern section of the study site to increased wave and wind energy that generally led to a decrease in vegetation cover, unless species with a high tolerance to sand burial and salt spray were present (e.g., *Scaevola plumieri* and *Spartina ciliata*). Therefore, varying gradients of cross-shore vegetation zonation and alongshore distributions can occur due to non-uniform environmental controls.

10.2.1 Monitoring Vegetation Patterns and Dynamics with sUAS

Monitoring of cross- and alongshore vegetation patterns can reveal both local and regional process controls and eco-geomorphological feedbacks within coastal dune systems. In this regard, sUAS provides an effective tool to delineate complex vegetation and sedimentation patterns across the beach and dune. To demonstrate this, we present data collected by the authors at Cavendish, Brackley, and Stanhope Beaches, within Prince Edward Island National Park (PEINP; Fig. 10.1). sUAS surveys were conducted during July 2019, coinciding with the peak growing season for *Ammophila breviligulata*, which represented the primary species growing on the upper beach and foredune. The position and density of backshore vegetation were measured from RGB orthomosaics that were used to create a 1 cm² binary raster from a supervised image classification in ArcGIS consisting of bare sand (0) and vegetation (1). Average vegetation density was then measured using a 1 m² moving

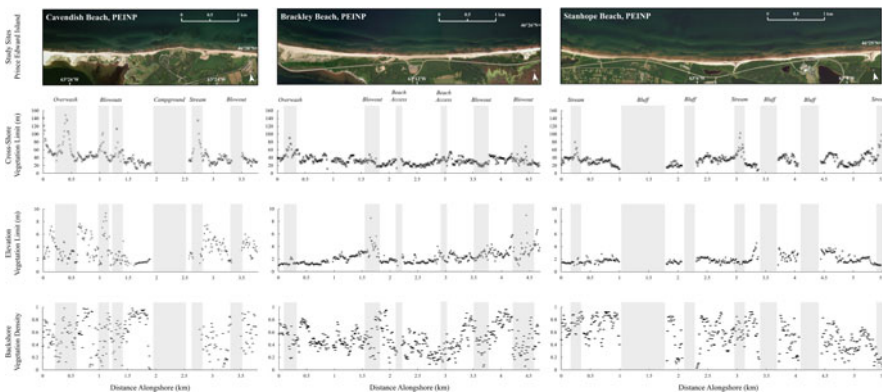


Fig. 10.1 The cross-shore and elevation vegetation limit and average density plotted alongshore for three study sites within Prince Edward Island National Park (PEINP), including Cavendish, Brackley, and Stanhope Beaches. Vegetation limits represent the seaward most position where vegetation density was ≥ 0.05 . Average vegetation density was measured between the vegetation limit and the crest of the foredune. Areas in grey represent historical disturbances from either blowouts or overwash, bluffs where no foredune was present, stream outlets, and beach access points or campgrounds where flights were restricted due to the increased number of people

window to produce a resampled 1 m^2 vegetation density raster, ranging from entirely bare sand (0) to fully vegetated (1). Except for areas with major disturbances (e.g., overwash fans and blowouts), the lee slope of the foredune was highly vegetated and displayed limited alongshore variability across all three sites (Fig. 10.1). As a result, we focus on the cross-shore and elevational vegetation limits and the average vegetation density measured between the seaward limit and the foredune crest. The vegetation limit was taken as the seaward most position where density values were ≥ 0.05 to provide a lower limit of detection and estimate of increased backshore sedimentation rates (e.g., Keijsers et al. 2015). Cross-shore measurements were automated and taken every 1 m alongshore and maintained an orientation perpendicular to the shoreline and foredune ridge across the entirety of the study area.

The regional environmental setting is micro-tidal with an average tidal range of 0.7 m and a spring tide elevation of ~ 1.1 m (Forbes et al. 2004). During the fall and winter months, the north coast of PEI is exposed to strong storm events that can generate significant wave heights of up to 7 m and peak wave periods up to 11 s (Parkes et al. 2006; Manson et al. 2016). Longer-term sea level rise of 3.2 mm y^{-1} , an average of 0.5 m y^{-1} of shoreline transgression, frequent fall and winter storm events, and reduction in winter sea ice cover often results in a cyclical scarp and recovery foredune state and landward retreat of the system (Forbes et al. 2004; Ollerhead et al. 2013; Smith et al. 2020a). Vegetation patterns at all three sites reveal a distinct limit in the cross-shore extent (~ 10 m) and elevation (~ 1 m) at which vegetation can establish near or above the spring tide level. Despite this consistency, intra-site variability in the vegetation limits is evident alongshore. This appears to be driven by historical disturbances in areas where the foredune has been breached and sediment deposited landward through overwash fans or in areas of the foredune that

are being eroded by blowouts (Fig. 10.1). In these locations, and similarly in areas adjacent to outlet streamchannels, the cross-shore vegetation extent typically increases in distance (i.e., moves further landward). Among these features, an increase in the elevation limit only appears to be affected by the presence of blowouts that maintain a bare sand surface as sediment is transported from the beach and foredune further inland. Patterns of vegetation density vary more widely alongshore between the vegetation limit and dune crest and may indicate various stages of foredune scarping and recovery across the study area. Although these data represent a limited ‘snapshot’ view of the vegetation patterns during our survey, it is apparent that sUAS can be used to effectively monitor the alongshore variability of vegetation limits and density in response to regional environmental controls and historical disturbances.

sUASimagery can also be used to differentiate between vegetation species and zonal communities in coastal dune environments. For example, De Giglio et al. (2019) used a multispectral camera that captured images in the red, green, and near-infrared (NIR) bands and used to map the zonation of five simplified cross-shore vegetation communities located along 350 m of coastline within the Po Delta Regional Park, Italy. Through photo-interpretation and in situ global positioning system (GPS) surveys, ground control points were recorded in each class and used for classification and validation of four supervised approaches. These included pixel-based (i.e., based on a pixel’s spectral signature) maximum likelihood (ML) and support vector machine (SVM) and object-based (i.e., based on a segmented group of pixel’s spectral, geometric, and other contextual information) nearest neighbor (NN) and SVM algorithms. In this study, the object-based SVM provided the best overall accuracy (82%). Alternatively, the pixel-based SVM produced a lower accuracy (76%) but may be better suited for identifying smaller-scale features such as individual plant canopies or footpaths intersecting the dunes.

Suo et al. (2019) used multispectralimagery and vegetation indices to map the distribution of plant species within the Brittas-Buckroneyn dune complex, Ireland. The sUAS used in this study was equipped with a three-band RGB camera and four multispectral cameras capturing green, red, red edge, and NIR bands. Additionally, the multispectral bands were used to calculate multiple vegetation indices including the normalized differential vegetation index (NDVI), found by:

$$\text{NDVI} = \frac{\text{NIR} - R}{\text{NIR} + R} \quad (10.1)$$

NDVI is commonly used to monitor the vitality of coastal dune vegetation and ranges between -1 and 1 , often with values >0 representing vegetation. Control points were classified from an orthomosaic, consisting of seven coastal dune species in addition to beach, sand, stream, road, and built area, and were used to train and validate ML classifications from varying combinations of multispectral bands and vegetation indices. Suo et al. (2019) found an overall accuracy of 69% and 60% using only the three-band RGB and four-band multispectral sensors, respectively. When additional spectral bands and indices were included, classification accuracy

generally increased with the best results found from utilizing eight bands that included RGB, multispectral, and NDVI with an overall accuracy of 78%. It should be noted that coarser satellite-derived vegetation indices such as NDVI can be effective for mapping regional to global-scale vegetation coverage in coastal dunes systems (e.g., Jackson et al. 2019), whereas higher-resolutions UAS imagery can be used to improve the precision of smaller-scale classifications through the identification of individual plant species.

Laporte-Fauret et al. (2020a) used a multi-method approach that utilized a sUAS-derived orthomosaic in combination with hyperspectral imagery obtained from aerial and ground-based measurements. These data were used to classify mobile dune and grey dune sand surfaces, seven vegetation species, sparse vegetation, and grey dune vegetation, distributed along 18 km of the Aquitaine coastline, France. Control points were identified from the orthomosaic and compared to the corresponding pixel-scale spectra from the aerial and field-based hyperspectral imagery to produce an end-member spectral library consisting of 550 spectra from 50 samples for each of the 11 landcover classes. Following the initial division of sand and vegetation classes using an NDVI threshold (i.e., bare sand ≤ 0.061 and vegetation ≥ 0.061), a random forest (RF) classification obtained 100% accuracy for mobile and grey dune sand surfaces. For the vegetation classes, the overall accuracy of the RF classification was improved from 82% to 92% by merging *Otanthus maritimus*, which often grows in isolated patches, with the sparse vegetation class. Hyperspectral sensors are increasingly being integrated with sUAS (e.g., Adão et al. 2017) and have the potential to improve classifications of isolated or interspersed vegetation species across spatially extensive coastal dune systems.

Beyond mapping vegetation limits and species distributions, sUAS can also be used to monitor vegetation dynamics through time. Nolet et al. (2018) conducted seven sUAS surveys over a 1-year period to determine the optimal response of *Ammophila arenaria* to observed burial rates at the Zandmotor, the Netherlands. The response of vegetation, identified across the study area using a k-means classification, was determined by the change in density measured from a 40 cm² raster grid and for NDVI values recorded from each 5 cm² pixel. Topographic changes, measured at both resolutions (i.e., 5 and 40 cm²), were found by removing all pixels classified as vegetation, interpolating the surface to create a continuous topographic raster, and differencing the elevation between two subsequent time series. Nolet et al. (2018) proposed a Gaussian response curve (GRC; Eq.) for *A. arenaria* (f) along a sand burial gradient (x), found by:

$$f(x) = ae^{-\frac{1}{2}(x-b)^2/c^2} \quad (10.2)$$

where a is the response (i.e., change in density or NDVI), b is the position of x at the maximum value for a , and c is the tolerance of the response to x or the standard deviation for the GCR. The GCR was then fitted to their data set using quantile regression to parameterize growth rates in response to burial gradients, finding that the optimal burial rates or b for *A. arenaria* were ~ 31 cm per growing season (i.e.,

April–August) for both the NDVI and density response metrics. Additionally, by extrapolating the regression curves, the maximum tolerance to sand burial at the 95th quantile ($\approx b + 2c$) was estimated at 96 and 78 cm for NDVI and density, respectively. While these observations may not be readily transferable beyond the unique environmental setting and study period, this work highlights the potential for sUAS studies to improve our understanding of vegetation response rates to sand burial (e.g., Maun 1998) and to better parameterize eco-geomorphological models aimed at capturing the positive feedback between vegetation and dune building processes (e.g., Baas and Nield 2010).

10.3 Aeolian Processes, Dune Building, and the Role of Vegetation

10.3.1 Aeolian Processes and Foredune Development

The transport and deposition of wind-blown sand are responsible for producing a range of bedforms and landforms in coastal environments, ranging from aeolian ripples to transgressive dunefields. Aeolian processes across the beach and foredune are complex and often difficult to predict due to non-uniform patterns of sediment supply, erodibility, and erosivity. As winds transition from the marine to terrestrial environment, topographic features such as berms can alter the boundary layer wind profile, and surface moisture due to tide and swash can limit the upwind sediment supply and transport across the foreshore and into the backshore (Short and Hesp 1982; Bauer et al. 1990; Bauer 1991; Sherman and Bauer 1993). The rate of sediment transport across the backshore can be further limited by the fetch length, depending on the flow velocity, dry beach width, and obliquity of the incident wind angle (Davidson-Arnott and Law 1996; Bauer and Davidson-Arnott 2003; Delgado-Fernandez 2010). At the beach-dune boundary, the extension of the foredune into the boundary layer can cause the development of an adverse pressure gradient that results in an area of flow stagnation and localized reduction in transport competency near the dune toe (Walker and Nickling 2003; Hesp et al. 2005; Hesp and Smyth 2019). Streamline compression and acceleration of airflow typically occurs up the stoss slope and, in the absence of surface roughness features such as vegetation, the potential for sediment transport increases approaching the dune crest, before flow detachment and deceleration, sediment fallout, and secondary airflow patterns develop in the lee (Walker and Nickling 2002; Walker and Hesp 2013; Walker 2020).

Vegetation can further modify aeolian processes in the backshore by increasing the aerodynamic roughness length (z_o) relative to the sand surface (e.g., Olson 1958), causing a reduction in near-surface wind velocity and limiting further grain entrainment, thereby decreasing sediment transport potential and increasing the rate of deposition. The efficiency at which vegetation traps sediment is affected by the

density and height of vegetation and wind velocity (Bressolier and Thomas 1977). For example, Kuriyama et al. (2005) found that during low to moderate wind conditions, a 95% reduction in sediment flux occurred when vegetation density reached 28%. Arens (1996) found an exponential decrease in sediment transport downwind of the leading edge of dense vegetation, but only during low magnitude velocities. When winds exceeded 10 m s^{-1} , sediment was transported and deposited across the stoss slope of the dune through ‘jettation’ or topographically accelerated flow capable of transporting grains through short-term suspension. At higher wind speeds, vegetation bends and becomes more streamlined, resulting in a reduction in z_o (Hesp 1983). Hesp et al. (2013) found a distinct ‘speed-up’ of flow up occurring within a vegetation canopy during high wind velocities, in contrast to an earlier study that recorded a ‘slow-down’ of flow within the canopy during lower velocities (Hesp et al. 2005), inferring that more grains could be transported through suspension, saltation across streamlined vegetation, and through increased turbulence transfer to the bed during high-magnitude wind events.

If deposition rates are within a species tolerance range, plants colonizing the backshore can respond with an increased ‘vigour’ by growing vertically and increasing tiller density (Maun 1998). This promotes further deposition and can lead to the formation of ephemeral dunes if colonized by annual species or incipient dunes if colonized by perennials (Hesp 1981). This represents a positive feedback between deposition and vegetation growth that is the primary mechanism for the initiation of foredunes. For example, Hesp (1984) observed the processes responsible for the formation of incipient foredunes in Southeastern Australia. Continuous backshore colonies of *Spinifex sericeus* seedlings were observed to have the highest growth rates in areas of maximum backshore deposition and, as a result, promoted further deposition, leading to the formation of an incipient foredune. Incipient dunes may intercept the sediment supply to the established foredune, allowing for the seaward landform to grow in volume. Over time, the incipient foredune may become established depending on further morphological development and vegetation colonization. The precise definition of foredunes, morphological description, and their classification largely come from the work of Hesp (1981, 1983, 1984, 1989, 2002). According to these studies, incipient foredunes are the seaward most dune deposits within discrete or continuous zones of pioneer plant, seedling, or rhizome-stolon growth. Established foredunes are typically continuous shore parallel ridges that form behind the upper beach surface and have been colonized by woody, matted, or tufted vegetation species.

The morphology of foredunes is also affected by the density of vegetation. If density is low, the approaching airflow is less perturbed by a relatively small increase in z_o , and sediment transport is able occur more evenly across the stoss slope (Hesp 1983; Keijsers et al. 2015). As a result, foredunes in areas of low-density vegetation are typically shorter, with rounded crests and elongated stoss slopes (Hesp 1989; Ruggiero et al. 2018). In contrast, high-density vegetation increases z_o and is more efficient at trapping saltating grains at the upwind edge of vegetation growth (Hesp et al. 2005; Keijsers et al. 2015). This results in the formation of taller foredunes, with peaked crests and narrower stoss slopes (Hesp 1989, 2002; Arens et al. 2001;

Ruggiero et al. 2018). This latter effect is often more desirous for coastal managers due to the protection that taller dunes provide from overtopping and flooding during storm surge events (Seabloom et al. 1994), which in some areas has led to the introduction of species such as *Ammophila arenaria* and *Ammophila breviligulata* that grow at higher densities than native dune grasses (e.g., Ruggiero et al. 2018).

10.3.2 Monitoring Coastal Dune Eco-geomorphology with sUAS

Coastal dune initiation and evolution can be effectively monitored with sUAS and used to identify important spatiotemporal controls on dune building processes. For example, van Puijenbroek et al. (2017) used sUAS surveys to test the influence of vegetation cover, species type (i.e., *Ammophila arenaria*, *Elytrigia juncea*, or both in combination), initial nebkha dune size, and position relative to the foredune on subsequent changes in nebkha dune volume occurring over the summer and winter seasons at Texel Island, the Netherlands. During the summer, nebkha dunes located seaward of the foredune grew in volume at faster rates, and the volume change of all dunes was positively correlated with initial dune volume and vegetation cover. Over the winter, higher growth rates were observed for the landward nebkha dunes, and a loss of ~8% of all dunes occurred during this period. The volume change for the landward nebkha dunes was positively correlated to initial dune volume, whereas the volume change of the seaward dunes was affected by a species type with increased volume observed for dunes covered by *A. arenaria*. The influence of vegetation and morphology on nebkha dune volume change was found to be dependent on seasonality and position relative to the foredune that influences exposure to storm events and sediment supply.

sUAS can be used to map sediment supply and transport limiting conditions that contribute to dune building. For example, bare sand surfaces provide an initial source of sediment that can be mobilized by the wind and can be accurately classified from high-resolution sUAS imagery (Fig. 10.2). In the absence of cohesive forces including surface moisture and salt and algal crusts (Sherman and Hotta 1990), the erodibility of sand is highly influenced by the grain diameter. Bae et al. (2019) used a sUAS to capture three-band RGB images at varying heights to conduct a textural analysis aimed at measuring the characteristic grain size for six classes of beach sediments, ranging from very fine sand (0.063–0.125 mm) to very fine gravel (2–44 mm). This study found that the delineation of six classes could be made with lower altitude flights at 3 and 5 m with a total accuracy of 91% and 80%, respectively. Fairley et al. (2018) monitored grain sizes up to 0.4 mm and surface moisture up to 60% in intertidal estuaries in Southwest England and Wales, using a sUAS equipped with multispectral sensors including green, red, red edge, and NIR bands. The spectral reflectance values had a positive correlation with grain size and a negative correlation with surface moisture, both significant at the 95% confidence

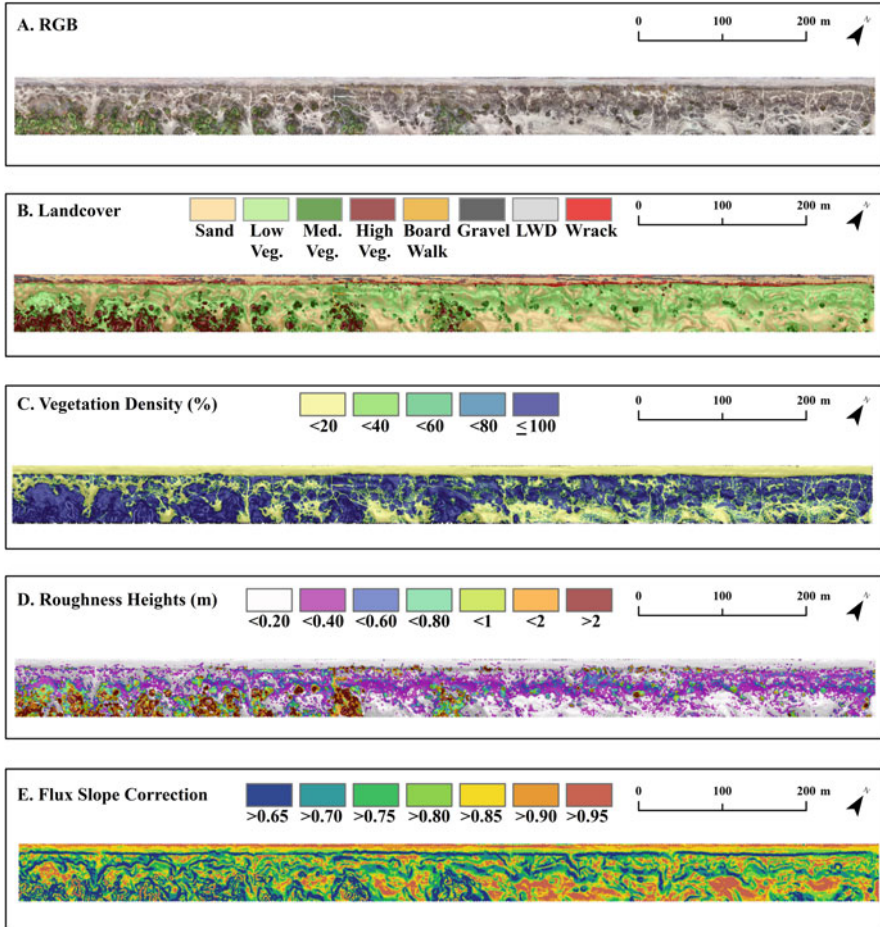


Fig. 10.2 Surface roughness features and potential slope-modified sediment flux were identified and mapped at Pinery Provincial Park, using an RGB ortho-mosaic (a), landcover classification (b), vegetation density (c), height of the roughness features (d), and flux slope correction (e)

level or higher. Given that cross- and alongshore transport gradients can be highly affected by grain size variability (e.g., Hallin et al. 2019) and surface moisture in the intertidal zone (e.g., Delgado-Fernandez et al. 2012), monitoring sediment supply and erodibility with sUAS may improve upon predictions of non-uniform aeolian processes across the beach and dune.

The height and distribution of surface roughness features (e.g., vegetation) and topographic slope can also affect sediment transport and can be measured using sUAS. Here, we present data collected by the authors at Pinery Provincial Park (PPP), Canada. Using a sUAS equipped with a three-band RGB camera, an orthomosaic with a 10 cm² pixel resolution was produced along a 1 km section of a scarped and eroding foredune system on Lake Huron (Fig. 10.2a). A maximum

likelihood (ML) classification of eight simplified landcover classes including bare sand, low vegetation (e.g., *Ammophila breviligulata*), medium vegetation (e.g., *Juniperus communis*), high vegetation (e.g., *Juniperus virginiana*), boardwalk, gravel, wrack, and large woody debris (LWD; Fig. 10.2b). Classification accuracy was assessed using a confusion matrix and reported as the overall accuracy percentage ($A\%$) and the kappa coefficient (k) which provides a normalized value of the agreement between classified and ground control points, ranging from no agreement (0) to perfect agreement (1).

Similar to the methodology described in Sect. 10.2.1, the orthomosaic was used to classify the 10 cm^2 pixels into a binary raster with bare sand (0) and vegetation (1). The average vegetation density from all three classes (i.e., low, medium, and high) was then measured using a 50 cm^2 moving window to produce a resampled 50 cm^2 vegetation density raster, ranging from entirely bare sand (0) to fully vegetated (1) (Fig. 10.2c). The height of surface roughness features (R_h) (i.e., vegetation, boardwalk, wrack, and LWD; Fig. 10.2d) was estimated by the minimum and maximum point elevation from a structure from motion (SfM) point cloud within a 50 cm^2 area, interpolating those values into a raster, and differencing the elevations. A similar approach using LiDAR data has been found to be a good predictor of sediment mobility (Pelletier et al. 2009) and aerodynamic roughness length (z_o) (Brown and Hugenholz 2012). This latter study also found that predictions of z_o could be improved by measuring the variability in canopy heights (R_c ; Eq. 10.3) in areas of uniform vegetation, taken by:

$$R_c = \frac{1}{N} \sum \left[\frac{\sigma_{h_{ij}}}{h_{ij}} \right] \overline{R}_h \quad (10.3)$$

where N is the number of samples, σ_h is the standard deviation of canopy elevation values and h is the average canopy elevation within an $i \times j$ kernel window, and \overline{R}_h is the average roughness height of a given vegetation class. Lastly, a low pass filtered digital terrain model (DTM) (see Sect. 10.5.2) was converted into a slope raster to determine the slope correction coefficient (G) (Eq. 10.4; Fig. 10.2e; Bagnold 1973).

$$G = \frac{\tan \alpha}{\cos \theta (\tan \alpha + \tan \theta)} \quad (10.4)$$

Here, α is the angle of repose for dry sand taken as $\sim 34^\circ$. Mapping G across the surface can be used to predict slope dependent sediment flux rates and has been previously coupled with computational fluid dynamics (CFD) models to simulate transport potential over dune and interdune topography (Smith et al. 2017a, b).

The foredune ridge and swale and beach face were separated during classification due to the presence of recently deposited vegetation mixed in with the wrack, thereby reducing the model accuracy. Following separation and reclassification, 500 control points were used for validation for both surfaces with a $A\%$ of 93% and 94% and k of 0.90 and 0.91 for the foredune ridge and swale and beach face,

respectively. It should be noted that no attempt to delineate individual species was made due to limited field identifications and that the simplified vegetation classes likely contributed to the high accuracy of our classification. The beach is composed of gravel ridges backed by fine grain sand supplied by the eroding foredune. LWD and wrack litter the beach and have been deposited near the scarp base by waves and have average heights of 0.17 and 0.14 m (Table 10.1). The eroding foredune is highly vegetated with densities ranging between 0.5 and 1, with bare sand surfaces primarily found in the swale in the NE section of the survey, along deer and human foot paths, and on the deflation basins and lateral walls of blowouts. Average heights for low vegetation (0.42 m) and medium vegetation (1.09 m) correspond well to field observations of *A. breviligulata* (~0.55 m) and *J. communis* (~0.96 m) taken during our survey. Variability in canopy height among the vegetation classes indicates non-uniform plant morphology that could further influence surface roughness and sediment transport patterns across the study area.

Changes in slope may also limit sediment transport in both cross- and alongshore directions. The beach is relatively flat with a slope correction coefficient or G of ~0.90 before falling to ~0.65 at the scarp base that has formed continuously alongshore. This localized reduction in flux potential may aide in the deposition of sediment at the scarp base and could lead to ramp building and foredune recovery when the lake level drops and sediment supply to the beach increases. Behind the foredune, the lowest values for G are recorded near the rim of blowouts, and the highest values occur in the relatively flat swale between the foredune and secondary dune and deflationary areas within blowouts and landward of the secondary dune ridge. It should be noted that coarse sand and gravel and a limited fetch length across the beach and primary and secondary airflow patterns across the dune ridges will also affect the potential for sediment transport. However, improved predictions of complex transport patterns may be possible by integrating sUAS surveys with in situ field measurements (e.g., anemometry, sediment traps, moisture probes, etc.). While this requires further study, there are a number of research opportunities to couple field-based data with high-spatiotemporal resolutions UAS surveys to monitor and predict aeolian transport gradients in coastal environments.

Table 10.1 The area (km²), percent cover (% Total), surface roughness feature heights (R_h), and canopy height variability (R_c), reported for eight simplified landcover classes including sand, gravel, large woody debris (LWD), wrack, low vegetation, medium vegetation, high vegetation, and boardwalk

	Sand	Gravel	LWD	Wrack	Low veg.	Med. veg.	High veg.	Boardwalk
Area (km ²)	26.43	3.27	0.46	2.19	26.36	5.41	5.53	0.49
% Total	38	5	1	3	38	8	8	1
R_h (m)	–	–	0.17	0.14	0.42	1.09	1.84	0.78
R_c (m)	–	–	–	–	0.09	–	0.94	–

10.4 Coastal Dune Disturbances, Recovery, and Vegetation Feedbacks

10.4.1 Storm Impacts and Foredune Recovery

Storm events can cause foreduneerosion depending on the elevation of wave run-up, relative to the dune toe and crest, ranging from collisions to inundation (Edelman 1969; Sallenger Jr 2000). During collision events that can lead to foredune scarping (Fig. 10.3), vegetation may provide protection through swash attenuation. Feagin et al. (2019) conducted a flume study to test the ability of above- and below-ground biomass to limit erosion of a model embryo dune in response to swash incursions. In this study, four species were tested including *Spartina patens*, *Panicum amarum*, *Sesuvium portulacastrum*, and *Ipomoea pes-caprae*. The presence of vegetation was found to limit erosion in all cases compared to the unvegetated model control. Above-ground biomass was found to be significantly correlated with a reduction in dune erosion, whereas the root system or below-ground biomass may initially enhance erosion due to uprooting; however, excavated roots may then offer protection from subsequent swash incursions. This study suggests that backshore areas covered by grasses or graminoids (e.g., *S. patens*) may be at a higher risk than areas covered by non-graminoids (e.g., *S. portulacastrum*) due to higher below versus above-ground biomass, respectively. Despite this, Feagin et al. (2019) indicate that graminoid species are more effective at modifying aeolian processes leading to enhanced dune building which can offer additional protection during storm events due to an increase in elevation. Other recent flume studies have found plant architecture (Maximiliano-Cordova et al. 2019) and below-ground biomass, in particular

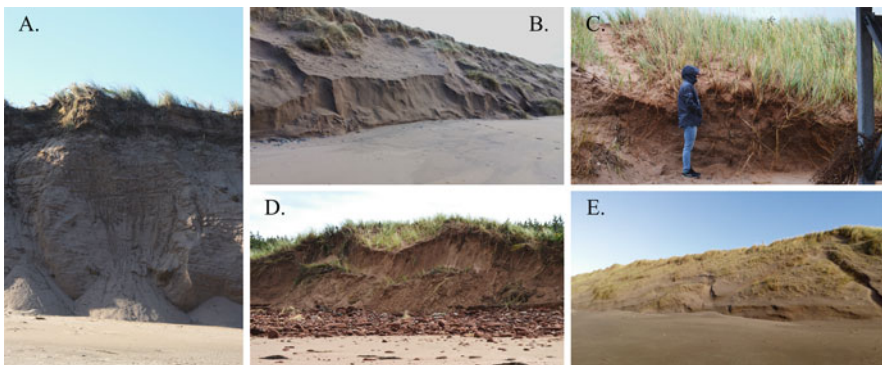


Fig. 10.3 Examples of post-storm foredune cliffing and scarping at Prince Edward Island National Park (PEINP), Canada (a, c, d), and County Kerry, Ireland (b, e). Dune cliffs and scarps can maintain near-vertical slopes following storm events due to cohesive forces including increased surface moisture and rhizome and root networks (c). Additional slope failure may occur through grain avalanche chutes (a), slides (d), and slumping (e)

buried shoots (De Battisti et al. 2019), can limit swash-induced erosion of backshore dunes.

The density of vegetation has also been found to control the form and extent of foredune slope failure and post-storm recovery processes. Based on observations from Magilligan Strand, Northern Ireland, a conceptual model relating scarp processes to vegetation density was proposed by Carter and Stone (1989). According to this study, non-vegetated slopes experience extensive and spatially continuous slope failure through avalanching in rapid response to wave incursions, basal wetting, and undercutting. Sparsely vegetated slopes experience a greater depth of basal undercutting that can result in multiple tabular slides along ‘pseudoshear’ planes near the base of the vegetation root system which can offer temporary protection to the foredune during subsequent wave incursions. Lastly, highly vegetated slopes are more resistant to basal undercutting and typically maintain a vertical scarp during storm events, with slumping and shallow rotational slides occurring following the event. Post-storm, dune scarps begin to dry and experience a reduction in cohesion, leading to additional slope failures or the formation of small avalanche chutes as the slope readjusts to the angle of repose (Carter et al. 1990b).

Following storm and scarping events, aeolian processes at the beach-dune boundary can be modified by scarp morphology and incident wind angle. For example, an adverse pressure gradient and reduction in upwind velocities can become more prominent with an increase in slope angle and scarp height; however, as winds approach at a more oblique angle, the reduction in wind speed is less pronounced (Hesp and Smyth 2019). Flow separation at the scarp base can lead to the formation of coherent turbulent flow structures which may aid in the development of echo dunes (Tsoar 1983; Carter et al. 1990b; Piscioneri et al. 2019; Hesp and Smyth 2019). As sediment accumulates at the scarp base, dune ramps allow sediment to bypass the scarp face and to be transported across the stoss slope (Christiansen and Davidson-Arnott 2004). Ultimately dune ramps may be ephemeral unless they are colonized by vegetation which can occur following scarping events through the establishment of new roots from slump block vegetation, tidal reworking of fragmented root ‘balls’, propagation of seeds, and expansion of rhizomes (Carter and Stone 1989; Carter et al. 1990b). Dune erosion and recovery represents a negative feedback that returns the landform to its initial pre-storm state, but only if there is adequate time to allow for dune building and increased vegetation coverage prior to subsequent events (Houser et al. 2015).

10.4.1.1 Monitoring Storm Impacts and Foredune Recovery with sUAS

The rapidity at which sUAS can be deployed to survey extensive sections of the coastline is ideal for monitoring initial storm impacts, prior to reworking of near-shore and subaerial sediment and subsequent slope adjustments of scarped foredunes. For example, Turner et al. (2016) surveyed Narrabeen-Collaroy Beach, Australia, following a high magnitude storm event with significant wave heights of 8.1 m and maximum wave heights up to 14.9 m. This study reported an average of

20 m³/m of erosion from the subaerial beach system along their ~1 km study area. Smith et al. (2020a) monitored the impacts of a post-tropical storm at Brackley Beach, Prince Edward Island National Park (PEINP), with peak significant wave heights of between 7 and 8 m and a 1.2 m storm surge (DalCoast 2019). The post-storm survey covered a ~6 km section of the beach-dune system, although uncertainties arising from variability in tide level, wave run-up, and vegetation (see Sect. 10.5) limited the extent at which volumetric changes could be accurately measured, between the upper swash limit and dune scarp. A total of 11,232 m³ ± 2659 m³ of erosion was observed at the 95% confidence level across the beach and dune. These patterns were not uniform, with a high variability in dune scarping or cliffing and deposition or erosion on the upper beach occurring alongshore.

Guillot et al. (2018) monitored the partial recovery of foredunes using sUAS at Truc Vert beach, France, following a highly active 2013/2014 North Atlantic storm season that led to extensive coastal erosion in Western Europe (e.g., Masselink et al. 2016). Alongshore variability in foredune erosion was associated with the presence of megacusps that are dependent on the pre-storm nearshore bar morphology and spacing (e.g., Castle et al. 2017). Three years following the event, the system recovered by 40 m³/m or ~60% of its pre-storm volume. Similarly, Laporte-Fauret et al. (2020b) monitored the recovery of the foredune system at Truc Vert, following the 2013/2014 storm season. After the initial storm season, the average landward retreat of the dune toe was 9.3 m along the ~4 km study area. By 2018, the dune toe advanced seaward by 7.9 on average, followed by further erosion during the 2018/2019 season, indicating the sensitivity of foredune recovery to subsequent storm events or seasons. George et al. (2021) monitored the recovery of a beach-dune system 2 months following a major storm event at Brackley Beach, PEINP. Following the storm event, the beach showed limited initial recovery at ~50% of the pre-storm volume, however, a consistent ramp of 1.9 m³/m formed along the dune scarp that may aid in foredune recovery by facilitating sediment transport across the stoss slope.

With increasing accessibility to sUAS and improvement to the instrumentation integrated with these systems, further research opportunities exist to monitor storm impacts and recovery. For example, Doughty and Cavanaugh (2019) found that sUAS-derived NDVI imagery was significantly correlated with field measurements of above-ground biomass in coastal marsh ecosystems and allowed for a calibrated model to predict the dried weight of vegetation across their entire study area. A similar approach could be applied to coastal dune systems to monitor the effectiveness of above-ground biomass on attenuating wave run-up and mitigating foredune erosion during collision events, beyond controlled flume experiments (e.g., Feagin et al. 2019). Pre- and post-storm classifications of vegetation species and density, and corresponding patterns of topographic change, could reveal additional controls on the form and extent of foredune scarping and capture negative feedbacks resulting in dune recovery (Carter and Stone 1989; Carter et al. 1990b). Lastly, the integration of advanced survey sensors such as LiDAR topo-bathy could allow for improved monitoring of storm impacts and recovery by capturing the

morphological controls and sediment transport pathways between the nearshore, beach, and dune at scales not previously possible.

10.4.2 Dune Blowouts

Coastal dune morphology, sediment transport gradients, and ecosystems can become rapidly modified by the initiation and expansion of dune blowouts (Fig. 10.4a). Blowouts are shallow saucer, deep bowl (Fig. 10.4b), or elongated trough (Fig. 10.4c) features that erode pre-existing dune or machair environments (Carter et al. 1990b). These features are typically initiated in areas of localized erosion and

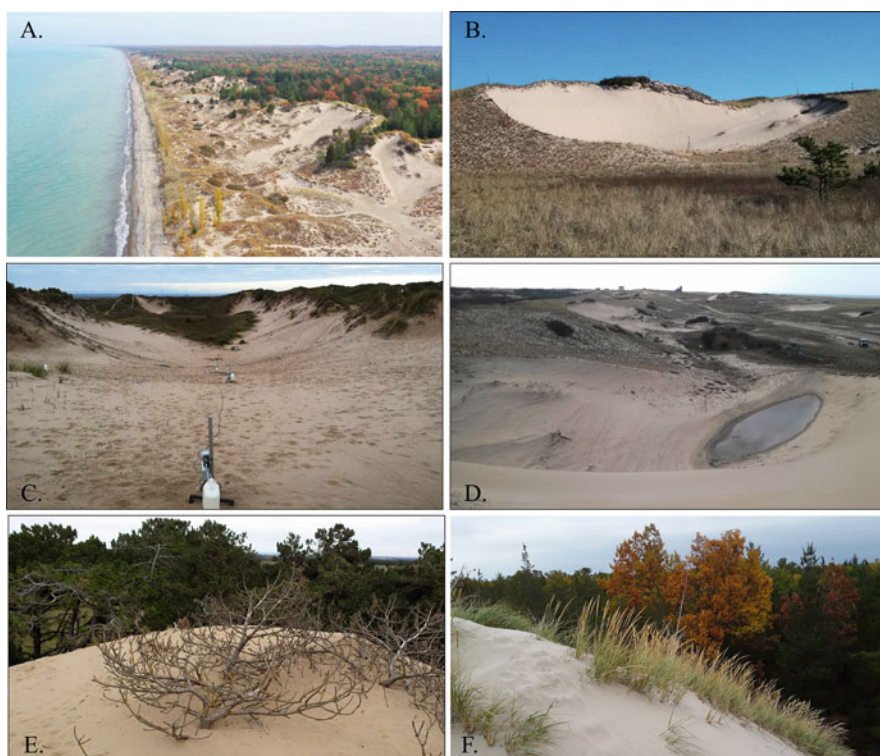


Fig. 10.4 Examples of blowouts and depositional lobes at Pinery Provincial Park, Canada (a, f) Cape Cod National Seashore, USA (b, c) and on the Sefton Coast, England (c, e). Blowouts can erode pre-existing dune deposits (a) and develop into shallow saucer, deep bowl (b), or elongated trough (c) shapes. Lateral and downward deflation of blowouts are limited by the ability to accelerate airflow, rates of sediment transport, and the proximity to the water table (d) or other non-erodible surface layer. Sediment is transported through the primary axis and deposited downwind of the crest in depositional lobes that increase the rates of burial that can stress or kill vegetation (e) unless species have a high tolerance (f)

vegetation disturbances and can be caused by a range of biotic and abiotic processes (Hesp 2002). Although less often depicted in the literature, undisturbed (i.e., not caused by erosion or vegetation die off) blowout initiation has been described in areas of low deposition between mobile dune ridges and from initial gaps in the incipient foredune that persist as the landform develops (Hesp 1984; Carter and Wilson 1988; Gares and Nordstrom 1988; Carter et al. 1990b). Regardless of initiation history, blowout expansion and maintenance are controlled primarily by aeolian processes.

Blowout expansion typically occurs in the direction of the prominent wind regime but may also be aligned to high magnitude events occurring from diverging angles (e.g., Hesp and Walker 2012). The orientation of the initial disturbance may also control the expansion direction due to significant topographic steering of oblique airflow into blowouts (Hesp and Hyde 1996; Hesp and Pringle 2001). Winds entering blowouts may undergo further steering and acceleration through the blowout axis and can produce jet flows that increase the rate of sediment transport (Carter et al. 1990b; Hesp and Hyde 1996). Blowout expansion occurs through rapid deflation that may be limited by the underlying water table (Fig. 10.4d) or other non-erodible surface layer, and lateral erosion through basal undercutting, slumping, and grainfall avalanching (Carter et al. 1990b). As the blowout expands, sediment supplied from deflation or lateral erosion is transported through the axis and over the blowout crest (Delgado-Fernandez et al. 2018). Downwind of the crest, flow separation, and reduction in wind velocity promote sediment fall out and the formation of depositional lobes (Smith et al. 2017c). High burial rates across the depositional lobe may stress or kill vegetation species with a low tolerance to burial (Fig. 10.4e) and may be colonized by high tolerance species (Fig. 10.4f) that are more typical of backshore environments (Dech and Maun 2005; Hesp and Martínez 2007).

10.4.2.1 Monitoring Blowouts with sUAS

To the authors' knowledge, there has yet to be a sUAS study focusing specifically on blowout evolution in coastal environments; however, Ruessink et al. (2018) monitored the development of foredune 'notches' or human excavated features that mimic trough blowout morphology and dynamical function. This study was conducted at National Park Zuid-Kennemerland, the Netherlands, where notches have been created to promote increased sediment transport landward of the foredune in an attempt to improve biodiversity and connectivity between ecosystems. This study used multiple aerial LiDAR and sUAS surveys to monitor the topographic and volume changes that have occurred within a 3-year period following initial notch excavation. Over time, the notches expanded laterally, causing slope avalanching and slumping unless upheld vertically by the roots of *Ammophila arenaria*. The landward transfer of sediment was observed at a rate of $\sim 22,750 \text{ m}^3/\text{yr.}$, leading to high levels of accretion beyond the lateral walls and across the depositional lobe of up to 8 m, infilling of the dune slack backing the foredune, decreased density of *A. arenaria*, and burial of shrubs (i.e., *Salix sepens*). This study highlights the

extensive eco-geomorphological impacts dune notches or blowouts can have on coastal dune systems.

Further opportunities exist not only to monitor the rates of volume transfer, vegetation burial and emergence, and longer-term ecosystem responses associated with blowout development but also to advance our understanding of the processes responsible for their evolution. For example, Carter et al. (1990b) described ‘stacked’ blowouts as being a common feature in Ireland that develop on the downwind ridge of other blowouts near the area separating sediment deposition and secondary flow reattachment. Similarly, small-scale ‘ridge saucers’ have been found to form on blowout ridges at Cape Cod National Seashore, USA (Abhar et al. 2015; Smith et al. 2017c). As these features expand through downcutting and lateral erosion, the ridge separating the two blowouts can collapse, causing cannibalization, rapid deflation, and asymmetric expansion that ultimately alters sediment transport pathways through the blowout and across the depositional lobe (Smith et al. 2017c); however, the processes responsible for initiation, location in which they form, and longer-term significance of blowout evolution require further study. Additionally, sUAS studies could be designed to examine blowout closure and vegetation feedbacks by testing and refining conceptual models of blowout evolution. For instance, Gares and Nordstrom (1995) proposed a model of cyclical blowout development, including (1) Initial wind excavated foredune notches (year 1), (2) Rapid deflation and formation of a depositional lobe (years 2–5), (3) Lateral expansion and progressive reduction in flow acceleration and sediment flux (years 5–10), and (4) Backshore deposition near the blowout throat, slumping of the lateral walls, revegetation, and closure (years 10–20). sUAS surveys are ideal to continuously monitor rapid topographic and vegetation changes often associated with blowouts and may be used to provide new insight on blowout initiation, expansion, and closure.

10.5 Topographic Change, Error, and Uncertainty

sUAS are increasingly used to monitor multi-temporal topographic and volumetric changes occurring in coastal dune systems resulting from seasonal or annual change (Brunier et al. 2016; Casella et al. 2016; Scarelli et al. 2017; Taddia et al. 2017, 2019; van Puijenbroek et al. 2017; Grottoli et al. 2019; Ruessink et al. 2018; Laporte-Fauret et al. 2019; Pagán et al. 2019; Hilgendorf et al. 2020; Rotnicka et al. 2020; Zanutta et al. 2020), storm impacts (Drummond et al. 2015; Turner et al. 2016; Casella et al. 2020; Smith et al. 2020a) and recovery (Guillot et al. 2018; Laporte-Fauret et al. 2020b; George et al. 2021), and the impact of urbanization (García-Romero et al. 2019a, b). A major challenge in coastal monitoring is the handling of error and uncertainty that can affect the quality of structure from motion (SfM) photogrammetry processing, generation of ‘bare earth’ DTMs, and measurements of topographic or volumetric change. Survey error is quantifiable and is commonly measured by georeferencing the point cloud to ground control points by taking the root mean square error ($\text{RMSE}_{(x,y,z)}$; Eq. 10.5) from the residuals (e) among all

ground control points (i) for the x , y , and z coordinates, and combining the error terms using the root sum of squares to produce a universal georeferencing error (RMSE_{GR} ; Eq. 10.6), given by:

$$\text{RMSE}_{(x,y,z)} = \sqrt{\frac{\sum_{i=1}^n e_i^2}{n}} \quad (10.5)$$

$$\text{RMSE}_{\text{GR}} = \sqrt{\text{RMS}_x^2 + \text{RMS}_y^2 + \text{RMS}_z^2} \quad (10.6)$$

Uncertainty is less tangible and can vary within and between surveys depending on the presence or alteration of surficial features, environmental conditions, and topographic representation (Fisher and Tate 2006). SfM studies in coastal environments are often able to obtain centimeter-scale georeferencing accuracy; however, significant sources of uncertainty can arise from wave run-up, slope, texture, and illumination of the surface and the density, distribution, height, and tonal variability of vegetation (e.g., Mancini et al. 2013; Gonçalves and Henriques 2015; Brunier et al. 2016; Turner et al. 2016; Scarelli et al. 2017; Guisado-Pintado et al. 2019; Smith et al. 2020a). Through time, uncertainty can limit the confidence of reported topographic (Δz ; Eq. 10.7) or volumetric (Δv ; Eq. 10.8) change measurements, found by:

$$\Delta z = z_{t_2} - z_{t_1} \quad (10.7)$$

$$\Delta v = xy\Delta z \quad (10.8)$$

where z_{t_1} and z_{t_2} are the surface elevations in the first and second-time series and x and y are the length and width of the raster cell, respectively. A range of uncertainty associated with these measurements can be reported by the propagated error (PE; Eq. 10.9), taken as:

$$\text{PE} = \sqrt{\sigma_{t_1}^2 + \sigma_{t_2}^2} \quad (10.9)$$

where σ_{t_1} and σ_{t_2} are the combined error terms for the first and second time series, respectively. Note that error sources most often represent RMSE_{GR} , but may also include interpolation and vegetation error terms (see Sect. 10.5.2). The uncertainty of topographic change can be reported as $\Delta z \pm \text{PE}$ and the volumetric change uncertainty as $\Delta v \pm xy\text{PE}$. To limit the uncertainty of reported change, a two-tailed t-test (Wheaton et al. 2010) can be used to determine the t-score (t ; Eq. 10.10), by:

$$t = \frac{\Delta z}{PE} \tag{10.10}$$

A threshold can then be applied to limit uncertainty between data series by removing values that fall below an acceptable confidence level (CL). For example, Smith et al. (2020a) removed values falling below a 95% CL (i.e., $|t| > \sim 1.96$), lowering the percent uncertainty (%U; Eq. 10.11) from reported post-storm volume change from 42% to 23%.

$$\%U = \frac{U_{\Delta v}}{\Delta v} 100 \tag{10.11}$$

Reporting uncertainty or applying CL-based thresholds is important to improve the confidence that measurements represent actual change, rather than propagated error between datasets.

Alternatively, Wernette et al. (2020) used a non-uniform probabilistic measure of uncertainty based on the area of overlap between two error distributions, ranging from 0 (low confidence) to 1 (high confidence). Wernette et al. (2020) integrated $RMSE_{GR}$ with DTM interpolation error, measured through ordinary kriging, for each time series. The intersection of two error distributions (c ; Eq. 10.12), assuming normal distribution, is found by:

$$c = \begin{cases} \frac{z_{t_2}\sigma_{t_1}^2 - \sigma_{t_2} \left(z_{t_1}\sigma_{t_2} + \sigma_{t_1} \sqrt{(z_{t_1} - z_{t_2})^2 + 2(\sigma_{t_1}^2 - \sigma_{t_2}^2) \log\left(\frac{\sigma_{t_1}}{\sigma_{t_2}}\right)} \right)}{\sigma_{t_1}^2 - \sigma_{t_2}^2} & \text{for } z_{t_2} > z_{t_1} \\ \frac{z_{t_1}\sigma_{t_2}^2 - \sigma_{t_1} \left(z_{t_2}\sigma_{t_1} + \sigma_{t_2} \sqrt{(z_{t_2} - z_{t_1})^2 + 2(\sigma_{t_2}^2 - \sigma_{t_1}^2) \log\left(\frac{\sigma_{t_2}}{\sigma_{t_1}}\right)} \right)}{\sigma_{t_2}^2 - \sigma_{t_1}^2} & \text{else} \end{cases} \tag{10.12}$$

The probability of change (P ; Eq. 10.13) is then found by subtracting the area of overlap between error distributions from one.

$$P = 1 - \left| \frac{1}{2} \operatorname{erf}\left(\frac{c - z_{t_1}}{\sqrt{2}\sigma_{t_1}}\right) + \frac{1}{2} \operatorname{erf}\left(\frac{c - z_{t_2}}{\sqrt{2}\sigma_{t_2}}\right) \right| \tag{10.13}$$

Here, erf (Eq. 10.14) is the error function with the form:

$$\operatorname{erf}(x) = \frac{2}{\sqrt{\pi}} \int_0^x e^{-t^2} dt \tag{10.14}$$

This approach allows for spatially dependent sources of error to be mapped for each pixel across the study area and included in evaluations of uncertainty, which can arise due to georeferencing and interpolation errors. Furthermore, Wernette et al. (2020) suggested this approach could be adapted to integrate additional error terms such as vegetation (see Sect. 10.5.2).

10.5.1 Vegetation Filtering, Correction, or Removal

Vegetation is one of the most significant sources of uncertainty in monitoring coastal dune morpho-dynamics with sUAS and usually results in the overestimation of the sand surface, requiring additional post-processing methods to achieve a representative ‘bare earth’ DTM. Taddia et al. (2017, 2019) used a point cloud filtering approach to remove areas covered by *Ammophila arenaria* and *Echinophora spinosa* by taking the lowest elevation value within a 5 m² window and, relative to the lowest point, retaining all other points that did not exceed a maximum threshold of 0.15 m and 15°. Where terrain points were removed in areas of high slopes, field-measured GPS points were integrated to supplement the point density prior to DTM interpolation. Comparisons between DTM and GPS profiles showed good agreement with an average elevation difference of 1.2 cm. Similarly, Guisado-Pintado et al. (2019) compared the minimum point cloud elevation within 2 m² quadrats to points sampled in the field with a GPS, and across distinct beach-dune zones with varying vegetation and topographic characteristics. The average difference between the GPS reference and minimum SfM point cloud elevation was ~0.44 m, with higher divergence recorded in areas with increased vegetation density and topographic slope. Rotnicka et al. (2020) generated a 20 cm² DTM during initial SfM processing in order to remove micro-scale surface features, before using a 60 cm² moving window to smooth the surface with a low pass filter. This study determined that annual sediment budgets could be accurately measured in areas of marram grass (*A. arenaria*) with less than 20% density, whereas the increasing uncertainty associated with higher vegetation densities was proportional to yearly changes occurring over the 4-year study period.

Alternatively, an elevation correction or offset has been used to lower the DSM surface in areas of vegetation. Bastos et al. (2018) used a maximum likelihood (ML) classification to map low profile vegetation species (i.e., *Lotus criticus* and *Vulpia alopecurus*) and taller herbaceous and woody species (i.e., *A. arenaria* and *Artemisia campestris*), corresponding to average field measured heights of 0.24 and 0.44 m, respectively. The DSM was then corrected using two approaches, including (1) removal of areas classified as vegetation from the DSM, integrating GPS points taken from the field and interpolating the remaining values, and (2) subtracting the average height of the low and high vegetation from the DSM across the corresponding classifications. Bastos et al. (2018) found that using an uncorrected DSM overestimated the foredune volume by up to 10% and applying the second method improved the accuracy of surface elevations relative to GPS points, although

the first method provided a better representation of the dune slope. Meng et al. (2017) used a similar approach by mapping vegetation patterns with a support vector machine (SVM) algorithm and subtracting field measurements of two dominant species including low profile *Panicum vaginatum* with an average height of 0.37 m and taller *Spartina alterniflora* with an average height of 1.63 m from a classified DSM. They found that the initial uncorrected DTM overestimated the surface by ~80% of the vegetation height for both low and tall vegetation classes, and applying the correction improved the accuracy relative to GPS control points made within each class. By applying the surface offset, the mean absolute error (MAE) and root RMSE were reduced for all vegetation classifications by between 32% and 50%.

Vegetation has also been ‘masked’ or removed from topographic change measurements due to the increased uncertainty of the underlying terrain. Removing vegetated areas from DSMs can be an effective method, particularly when GPS ground control points and in situ vegetation height measurements are lacking. For example, Smith et al. (2020a) limited post-storm change measurements to a narrow section between the upper beach and foredune scarp because of the uncertainty associated with the swash zone and the vegetated foredune. Landward of the scarp, the presence of high-density *Ammophila breviligulata* led to the overestimation of the foredune elevations across the upper stoss and lee slopes, and they were removed from further analysis. Cumulatively, these studies have identified vegetation as a major challenge to producing accurate DTMs and sediment budgets from sUAS data. The approach used to filter, correct for, or mask vegetation requires a trade-off between additional field measurements and data processing for the former two approaches or limits the spatiotemporal extent that topographic changes can be observed for the latter. Regardless of which approach is used, reporting or systematically reducing uncertainty is critical to improving the confidence in monitoring topographic changes in coastal dune systems.

10.5.2 Monitoring Coastal Dune Morpho-Dynamics with sUAS

Using Pinery Provincial Park (PPP) as an example, we demonstrate how errors associated with DTM interpolation and vegetation can be integrated into a spatially dependent uncertainty analysis when monitoring coastal dune systems through time. Two sUAS surveys were conducted by the authors in July 2019 and again in October 2020. PPP is highly influenced by fluctuations in lake levels which increased by over 1 m between 2017 and 2020 (Fig. 10.5a). Along the study area, the sandy beach has been replaced by one or two gravel ridges during this period of lake level rise (Fig. 10.5b). A steep and continuous 1–2 m scarp with a slope up to 90° is maintained by a rhizome and root matrix (Fig. 10.6c). Fine grain sand has accumulated on the upper beach, supplied by the eroding foredune through grain

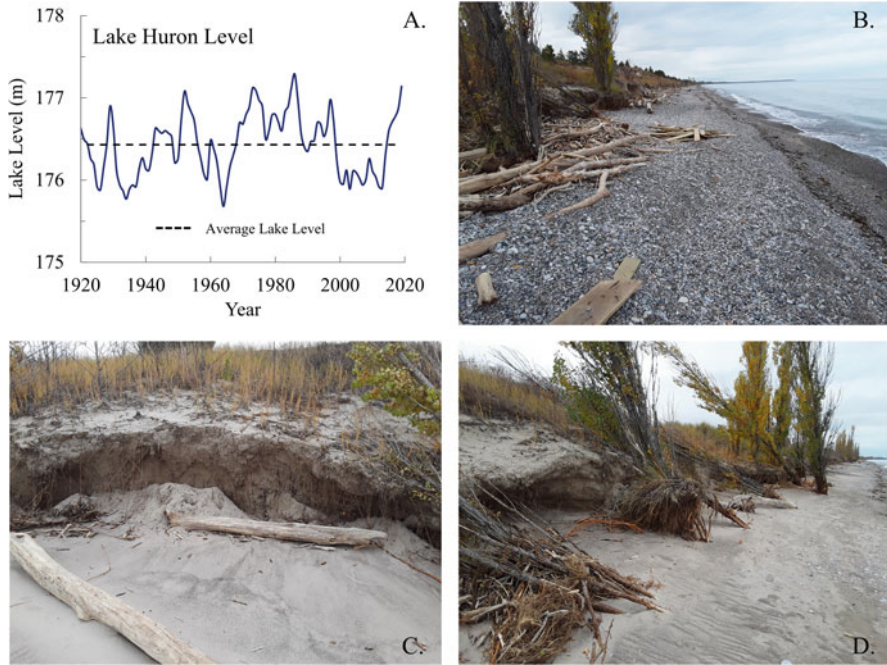


Fig. 10.5 Lake Huron water level fluctuations occurring over the past 100 years (a; Fisheries and Oceans Canada). The beach-dune system at Pinery Provincial Park, Canada, is highly sensitive to changes in lake levels which are currently ~ 1 m above the longer-period average, leading to the formation of gravel ridges on the beach (b) with sand limited to the upper beach where sediment eroded from the dune scarp is trapped by wrack and large woody debris (c). Later successional species (e.g., *Populus balsamifera*) are now located directly on the foredune and beach increasing their exposure to abiotic processes (d)

avalanching and slumping, and is trapped by large woody debris (LWD) (Fig. 10.5c). This section of the foredune is densely vegetated by *Ammophila breviligulata*, but woody vegetation (e.g., *Populus balsamifera*) was also observed on the foredune and beach (Fig. 10.5d) indicating that later successional species are being increasingly exposed to abiotic processes as the existing dune deposits are eroded.

Two overlapping survey flight lines or grids during time 1 (t_1) and three grids during time 2 (t_2) were flown at an altitude of 55 m, with 80% frontal and 70% side overlap between flight lines, and an average point (p) density of ~ 1800 p m² for both surveys. Images were processed using the SfM software Pix4D following the basic quality control measures described in (Smith et al. 2020a). A total of 4 GCPs in t_1 and 15 GCPs in t_2 were used for the point cloud georeferencing with RMSR_{GR} of 0.006 and 0.012 m, respectively (Table 10.2). It should be noted that due to GPS error during the initial survey, GCPs were limited to permanent marker posts on the foredune and were surveyed during the second survey period. As a result, we constrain volumetric measurements to the beach, foredune, and swale given the

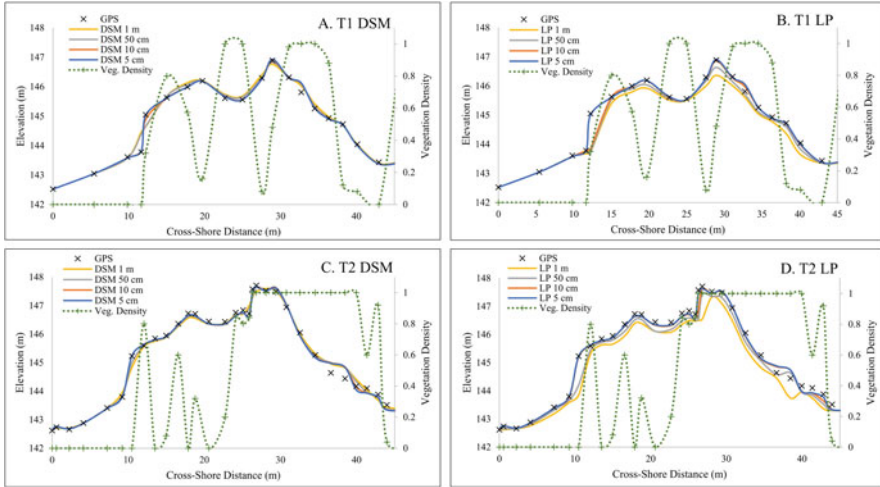


Fig. 10.6 GPS control points were measured across transect 1 (T1) and transect 2 (T2) and were compared to the structure from motion (SfM) point cloud using two methods to determine the best strategy to maintain the characteristic dune slope and provide the most accurate elevation values in areas of low vegetation. The average of all points (DSM) and lowest point (LP) were found within varying search radii of 0.05, 0.1, 0.5, and 1 m. Vegetation density is also shown on the secondary y-axis to indicate areas where surface elevations may be influenced by increased plant cover

Table 10.2 Error, uncertainty, and probability of change occurring between time series one (t_1) and two (t_2). Total error (σ) for each time series includes terms for point cloud georeferencing (RMSEGR), vegetation (RMSEVeg), and interpolation (SDEInt). Total volumetric change (Δv) and Δv at the 95% and 99% confidence levels (CL) were measured. Total uncertainty ($U\Delta v$) and the percent uncertainty ($\%U$) decreases with an increase in CL threshold, improving the confidence of change reported.

Error	RMSE _{GR} (m)	RMSE _{Veg} (m)	SDE _{Int} (m)	σ (m)
t_1	0.006	0.11	0.01–1.37	0.01–1.45
t_2	0.015	0.11	0.02–2.32	0.03–2.32
Probability	Change	Δv (m ³)	$U_{\Delta v}$ (m ³)	$\%U$
Total change	Accretion	16706.87	± 3618.64	22
	Erosion	-3981.35	± 1521.71	38
95% CL	Accretion	16425.05	± 3093.14	19
	Erosion	-3675.09	± 1084.60	30
99% CL	Accretion	15645.40	± 2447.28	16
	Erosion	-3150.72	± 635.78	20

absence of additional landward GCPs. A limited number of GCPs for t_1 , all located at a similar elevation, may have contributed to a lower georeferencing error relative to t_2 when GCPs were more distributed across the surface and sampled a larger range of elevations. Future studies should investigate GCP sampling on the accuracy of SFM processing and contribution to non-uniform error terms; however, this is beyond the scope of this current work.

To measure the error associated with vegetation, two GPS transects recorded during t_2 were used to sample ground points across the foredune with varying densities of low vegetation. GPS points were then compared to the SfM-derived point cloud within varying search radii of 0.05, 0.1, 0.5, and 1 m. A radius of 0.05 m was chosen as the minimum search distance, maintaining a sample size of at least 2 points due to non-uniform point distribution. In general, point density decreased in areas of high topographic slope (e.g., foredune scarp) and at the edges of dense vegetation. Two different methods were then applied for comparison, including the following: (1) All points within each search radius were averaged (i.e., DSM), and (2) only the lowest point within each search radius was retained (i.e., LP). Profiles for each method, search radii, and transect can be seen in Fig. 10.6. The DSM method maintains the characteristic slope of the foredune profile except for the near-vertical scarp in T1 for the 0.5 and 1 m search radii (Fig. 10.6a) but overestimates the surface in areas of dense vegetation. Beyond the 0.05 m search radius, the LP approach significantly alters the shape of the dune profile by underpredicting elevation values on high sloping surfaces associated with the dune scarps and peaked crests in T1 and T2 (Fig. 10.6b, d). Despite this deformation at larger scales, the 0.05 LP method was found to have the lowest root mean square error within vegetation (RMSE_{veg}) of 0.11 m, followed by 0.13 for the DSM method taken at the same scale among the 34 GPS control points measured within low vegetation. Topographic slope and vegetation density were uncorrelated with RMSE_{veg} ; therefore, we apply a universal RMSE_{veg} to areas of low vegetation identified from the maximum likelihood (ML) classification described in Sect. 10.3.2.

Following the application of the LP filter, a 10 cm^2 raster was interpolated using ordinary kriging. The standard deviational error per pixel (SDE_{Int} ; Eq. 10.15) was taken as the error associated with DTM interpolation, by:

$$\text{SDE}_{\text{Int}} = \sqrt{\frac{\sum_{i=1}^n (z_i - \bar{z})^2}{n - 1}} \quad (10.15)$$

where z_i represents elevation values within the search neighborhood range (i) and \bar{z} is the average elevation. SDE_{Int} was used in this analysis because it provides a conservative level of error that is slightly higher than other metrics including variance or standard error. Lastly, combining RMSE_{GR} , RMSE_{veg} , and SDE_{Int} from the root sum of squares, a spatially dependent error raster is produced for each time series (i.e., σ_{t_1} and σ_{t_2} ; Fig. 10.7). Given the lack of field measurements for medium and high vegetation, areas classified from these groups were ‘masked’ or removed from our topographic surfaces (i.e., z_{t_1} and z_{t_2}) due to the high level of

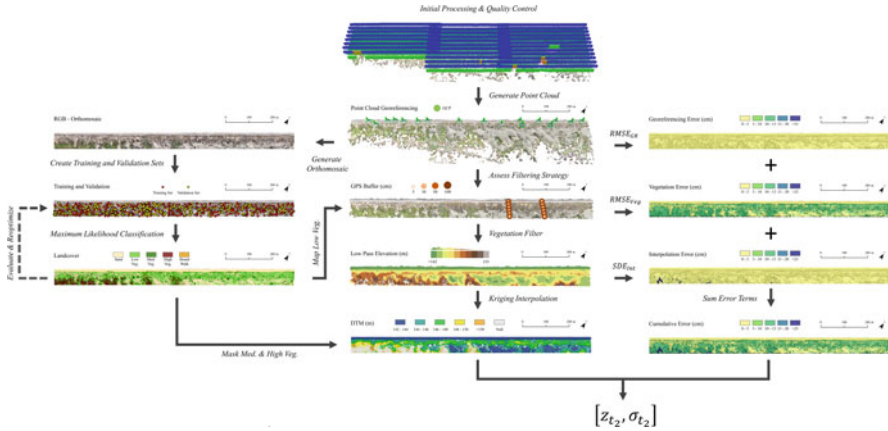


Fig. 10.7 Flow chart indicating the methods used to produce a digital terrain model (z_{t_2}) and spatially dependent error raster (σ_{t_2}) for the second time series. Following initial SfM processing, a dense point cloud (i.e., $\sim 1800 \text{ p m}^2$) was georeferenced by ground control points (GCPs) with a root mean square error (RMSE_{GR}) of 0.015 m. An orthomosaic was then produced and used to identify areas of low, medium, and high vegetation using a maximum likelihood classification. In areas of low vegetation, field sampled GPS points were compared to the point cloud within varying search radii of 0.05, 0.10, 0.50, and 1 m using all points (i.e., DSM) and the lowest point (i.e., LP) within each radius. The lowest root-mean-square error (RMSE_{Veg}) of 0.11 m was found using the 0.05 m LP method and was applied to pixels classified as low vegetation. Next, the point cloud was filtered and interpolated using ordinary kriging with a standard deviational error (SDE_{Int}) ranging between 0.03 and 2.32 mapped for each pixel. Lastly, areas classified as medium and high vegetation were ‘masked’ or removed from z_{t_2} and all error terms were combined by taking the root sum of squares to produce σ_{t_2} .

uncertainty associated with these values. The probability of change can then be found by using Eq. 10.13, with a graphical summary of the methodology used for our analysis provided in Fig. 10.7.

There is a high probability of change (P) occurring across the majority of the study area (Fig. 10.8a), representing topographic changes over a 15-month period at PPP. A slight decrease in P occurs primarily where minimal topographic changes were recorded in areas with increased SDE_{Int} due to localized reduction in point density (e.g., across high sloping terrain and near the edges of dense vegetation) and/or increased RMSE_{Veg} within areas classified as low vegetation. Topographic change at the 99% CL (Fig. 10.8b), shows a distinct area of 1–2 m of erosion alongshore where the dune scarp has retreated landward by up to 5 m. Much of the NE half of the survey falls below the CL threshold due to the increased spatial coverage of low vegetation and low magnitude topographic change. Across the SW half, high rates of deposition occur across the beach and swale and within the blowout basins that have formed through breaks in the foredune. Given the time between surveys, it is unclear precisely what processes were responsible for these changes; however, a highly erosive and discontinuous foredune that is further eroded by blowouts may have aided in the landward transport of sediment during this period

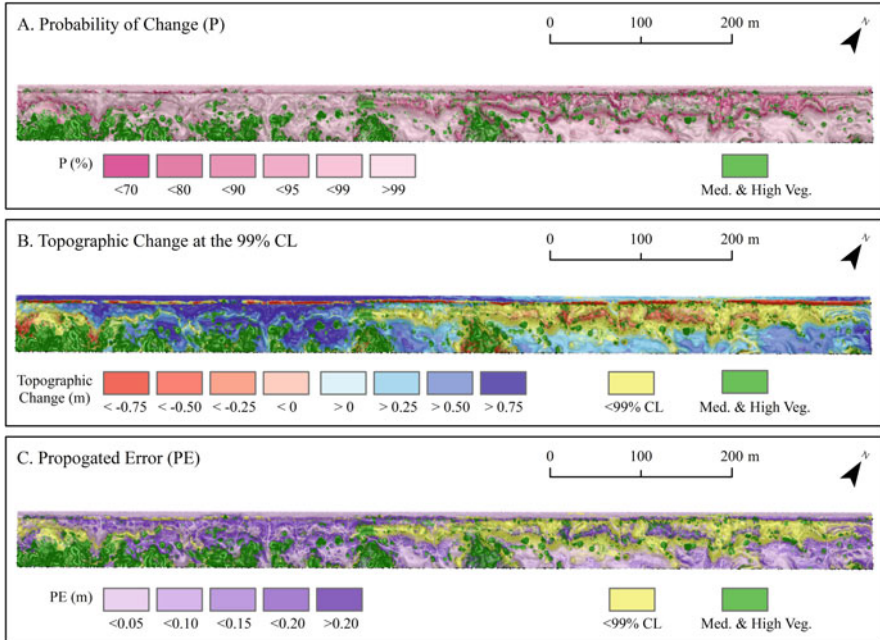


Fig. 10.8 The probability (P) of topographic changes recorded at Pinery Provincial Park, Canada, between July 2019 and October 2020 (a). Topographic changes were masked in areas outside of the 99% confidence level (CL) and in locations with medium and high vegetation that were removed due to the increased uncertainty of the underlying terrain (b). Propagated error (PE) indicates areas with increased cumulative error between surveys and error terms with the highest values located in areas with low vegetation and increased point spacing, corresponding to an increase in $RMSE_{Veg}$ and SDE_{Int} , respectively (c)

of rapid lake level rise. The propagated error (PE; Fig. 10.8c) indicates the combined error terms for each metric and time series, with increased PE most visible in areas classified as low vegetation. The proportion of PE relative to topographic change is also used to measure the percent uncertainty ($\%U$) for the sediment budgets and is provided in Table 10.2.

By combining error terms for georeferencing, vegetation, and DTM interpolation, we have identified spatially dependent patterns of uncertainty associated with topographic and volumetric changes occurring at PPP. Applying a CL threshold can limit the $\%U$ of sediment budgets by removing lower magnitude change measurements that are within the range of uncertainty (Table 10.2). While the use of a CL threshold depends on the user's objective, it is important to report the uncertainty of change (e.g., $U_{\Delta v}$ or $\%U$) to improve the confidence in topographic and volumetric change measurements through time. The results presented in this section provide a basic guideline for combining non-uniform error terms, measuring uncertainty, and determining the probability of change. Additional opportunities remain to measure errors associated with GCP distribution, topographic slope, and

vegetation. For instance, a non-linear low-pass filter may improve upon the production of ‘bare earth’ DTMs by increasing the search radius with decreasing topographic slope; however, additional research is required to determine the optimal vegetation filtering strategies to monitor coastal dune morpho-dynamics with sUAS.

10.6 Discussion and Conclusion

Advances in aerial and orbital sensors have significantly improved our capability to monitor coastal systems from a local to global scale, including aerial photography since the 1920s, satellite imagery since the 1970s, and LiDAR surveys since the 2000s (Anders and Byrnes 1991; Stockdon et al. 2002; Gens 2010). Since the 2010s, sUAS and structure from motion (SfM) photogrammetry have provided an efficient and low-cost alternative to monitoring coastal systems, and the number of studies utilizing this technology is likely to grow rapidly in the coming years. The influx of high-resolution eco-geomorphological data will provide new insight on how coastal dune systems evolve in response to environmental drivers operating over multiple spatial and temporal scales (e.g., Sherman and Bauer 1993; Houser and Ellis 2013). Classifying backshore vegetation (De Giglio et al. 2019; Suo et al. 2019; Laporte-Fauret et al. 2020a) and landforms (Sturdivant et al. 2017) can be improved by using high-quality sUAS imagery and may lead to the development of more consistent process-based definitions when monitoring changes through time (Smith et al. 2020b). Over longer time periods (i.e., decadal to centennial scale), an improved observational record will likewise improve our understanding of how coastal dune systems respond to climate change.

According to the IPCC Special Report Ocean and Cryosphere (2019), it is likely that the global mean sea level will rise between 0.29–0.59 and 0.61–1.10 m by 2100 under a low (RCP 2.6) and high (RCP 8.5) green house gas emission scenario, respectively. While the effect on coastal systems will vary due to site specific environmental controls, geological framework, and anthropogenic impacts (e.g., Cooper and Pilkey 2004), widespread shoreline transgression has been observed over the last few decades on a global scale (Luijendijk et al. 2018) and historic rates could accelerate with SLR. Fore dunes may be able to migrate landward and upward to keep pace with rising sea level as described by the Robin-Davidson-Arnott (RD-A) model (Davidson-Arnott 2005; Davidson-Arnott and Bauer 2021), but this may also require minimal human intervention and sufficient landward accommodation space to allow for transgression of the system (Ollerhead and Davidson-Arnott 2022). Similarly, a reduction in suitable environments for vegetation may occur due to ‘coastal squeeze’ or limit coastal ecosystems’ ability to migrate landward in response to SLR due to the presence of shore parallel structures (e.g., Pontee 2013). As a result, a loss of later successional species and areal coverage of backshore vegetation could occur with medium to high SLR projections (Feagin et al. 2005).

Regional environmental and anthropogenic drivers will further influence localized coastal dune eco-geomorphology including, but not limited to, isostasy (Ollerhead and Davidson-Arnott 2022), changes in storminess (Masselink et al. 2016), reduction in winter sea ice (Forbes et al. 2004), increased number of growing days (i.e., temperatures $>5^{\circ}\text{C}$) and vegetation coverage (Jackson and Cooper 2011), beach recreation (Houser et al. 2013), urbanization (Smith et al. 2017b), and desired coastal management outcomes that promote dune stabilization (Seabloom and Wiedemann 1994) or destabilization (Delgado-Fernandez et al. 2019). Given the range of site-dependent controls that are likely to influence the evolution of coastal dune systems over the coming decades, it is critical to examine how these systems are evolving and to reveal important sources of similarity and disparity between systems that will lead to improved management practices and climate adaptation strategies. sUAS can be used to address these challenges because of the increased accessibility, relative ease of operation, and efficiency of sUAS to collect topographic and ecological data over several kilometers of shoreline and will allow for research to be conducted broadly by scientists, coastal managers, and citizen science initiatives from around the world.

This chapter has reviewed some of the current applications and challenges of applying sUAS to monitor coastal dune eco-geomorphology, including (1) vegetation zonation and distribution in coastal dunes; (2) Aeolian processes, dune building, and the role of vegetation; (3) Coastal dune disturbances, recovery, and vegetation feedbacks; and (4) topographic change, error, and uncertainty. It should be noted that the review of sUAS studies is not exhaustive, and several additional publications will likely be available prior to this chapter. We have also discussed some of the opportunities in which high spatiotemporal resolutions UAS data can be used to monitor topographic and vegetation change, fill-in knowledge gaps, test conceptual models, and provide an improved record of the response of coastal dune systems to climate change. With sUAS increasingly being used to monitor coastal environments, the ability to capture feedbacks between sedimentation and vegetation processes offers a broad range of opportunities for ecologists, geomorphologists, and coastal managers to research coastal dune systems. To fully realize the potential for sUAS applications, further sharing through open source data repositories and collaboration between disciplines is needed to address knowledge gaps, develop innovative research methodologies, and advance our understanding of coastal dune eco-geomorphology.

Acknowledgments The authors would like to thank Prince Edward Island National Park and Parks Canada and Pinery Provincial Park and Ontario Parks for permitting research. We also thank two anonymous reviewers for their constructive feedback that has helped improve this work. Funding was provided by the Natural Sciences and Engineering Research Council (NSERC) of Canada.

References

- Abhar KC, Walker IJ, Hesp PA, Gares PA (2015) Spatial-temporal evolution of aeolian blowout dunes at Cape Cod. *Geomorphology* 236:148–162
- Adão T, Hruška J, Pádua L, Bessa J, Peres E, Morais R, Sousa JJ (2017) Hyperspectral imaging: a review on UAV-based sensors, data processing and applications for agriculture and forestry. *Remote Sens* 9(11):1110
- Ahmad I, Wainwright SI (1976) Ecotype differences in leaf surface properties of *Agrostisstolonifera* from salt marsh, spray zone and inland habitats. *New Phytol* 76(2):361–366
- Anders FJ, Byrnes MR (1991) Accuracy of shoreline change rates as determined from maps and aerial photographs. *Shore Beach* 59(1):17–26
- Arens SM (1996) Patterns of sand transport on vegetated foredunes. *Geomorphology* 17(4):339–350
- Arens SM, Baas ACW, Van Boxel JH, Kalkman C (2001) Influence of reed stem density on foredune development. *Earth Surf Process Landf* 26(11):1161–1176
- Armstrong W (1980) Aeration in higher plants. In: *Advances in botanical research*, vol 7. Academic Press, London, pp 225–332
- Baas AC, Nield JM (2010) Ecogeomorphic state variables and phase-space construction for quantifying the evolution of vegetated aeolian landscapes. *Earth Surf Processes Landf J Br Geomorphol Res Group* 35(6):717–731
- Bae S, Yu J, Wang L, Jeong Y, Kim J, Yang DY (2019) Experimental analysis of sand grain size mapping using UAV remote sensing. *Remote Sens Lett* 10(9):893–902
- Bagnold RA (1973) The nature of saltation and of ‘bed-load’ transport in water. *Proc R Soc Lond Math Phys Sci* 332(1591):473–504
- Baldwin KA, Maun MA (1983) Microenvironment of Lake Huron sand dunes. *Can J Bot* 61(1):241–255
- Barbour MG (1970) Seedling ecology of *Cakile maritima* along the California coast. *Bull Torrey Bot Club*, pp 280–289
- Barbour MG (1978) Salt spray as a microenvironmental factor in the distribution of beach plants at Point Reyes, California. *Oecologia* 32(2):213–224
- Bastos AP, Lira CP, Calvão J, Catalão J, Andrade C, Pereira AJ, Taborda R, Rato D, Pinho P, Correia O (2018) UAV derived information applied to the study of slow-changing morphology in dune systems. *J Coast Res* 85:226–230
- Bauer BO (1991) Aeolian decoupling of beach sediments. *Ann Assoc Am Geogr* 81(2):290–303
- Bauer BO, Davidson-Arnott RG (2003) A general framework for modeling sediment supply to coastal dunes including wind angle, beach geometry, and fetch effects. *Geomorphology* 49(1–2):89–108
- Bauer BO, Sherman DJ, Nordstrom KT, Gares PA (1990) Aeolian transport measurement and prediction across a beach and dune at Castroville, California. In: *Coastal dunes. Form and process*, Wiley, Chichester, pp 39–55
- Boyce SG (1954) The salt spray community. *Ecol Monogr* 24(1):29–67
- Bressolier C, Thomas YF (1977) Studies on wind and plant interactions on French Atlantic coastal dunes. *J Sediment Res* 47(1):331–338
- Brown OW, Hugenholtz CH (2012) Estimating aerodynamic roughness (z_0) in mixed grassland prairie with airborne LiDAR. *Can J Remote Sens* 37(4):422–428
- Brunier G, Fleury J, Anthony EJ, Gardel A, Dussouillez P (2016) Close-range airborne Structure-from-Motion Photogrammetry for high-resolution beach morphometric surveys: examples from an embayed rotating beach. *Geomorphology* 261:76–88
- Carter RWG, Stone GW (1989) Mechanisms associated with the erosion of sand dune cliffs, Magilligan, Northern Ireland. *Earth Surf Process Landf* 14(1):1–10
- Carter B, Wilson P (1988) Geomorphological, sedimentological and pedological influences on coastal dune development in Ireland. *J Coast Res, Special Issue*:27–31

- Carter RWG, Nordstrom KF, Psuty NP (1990a) The study of coastal dunes. In: Coastal dunes: form and process. Wiley, Chichester, pp 1–14
- Carter RWG, Hesp PA, Nordstrom KF (1990b) Erosional landforms in coastal dunes. In: Coastal dunes. Form and process. Wiley, Chichester, pp 217–250
- Casella E, Rovere A, Pedroncini A, Stark CP, Casella M, Ferrari M, Firpo M (2016) Drones as tools for monitoring beach topography changes in the Ligurian Sea (NW Mediterranean). *Geo-Mar Lett* 36(2):151–163
- Casella E, Drechsel J, Winter C, Benninghoff M, Rovere A (2020) Accuracy of sand beach topography surveying by drones and photogrammetry. *Geo-Mar Lett* 40(2):255–268
- Castelle B, Bujan S, Ferreira S, Dodet G (2017) Fore-dune morphological changes and beach recovery from the extreme 2013/2014 winter at a high-energy sandy coast. *Mar Geol* 385:41–55
- Cheplick GP, Demetri H (1999) Impact of saltwater spray and sand deposition on the coastal annual *Triplasis purpurea* (Poaceae). *Am J Bot* 86(5):703–710
- Christiansen MB, Davidson-Arnott R (2004) Rates of landward sand transport over the fore-dune at Skallingen, Denmark and the role of dune ramps. *Geografisk Tidsskrift-Dan J Geogr* 104(1): 31–43
- Clayton JL (1972) Salt spray and mineral cycling in two California coastal ecosystems. *Ecology* 53(1):74–81
- Cooper JAG, Pilkey OH (2004) Sea-level rise and shoreline retreat: time to abandon the Bruun Rule. *Glob Planet Chang* 43(3–4):157–171
- DalCoast (2019) Department of Oceanography (D of O) Dalhousie Ocean Forecast System – DalCoast HFX. Dalhousie University, Halifax. <http://extrememarine.ocean.dal.ca/dalcoast/web/home.php>
- Davidson-Arnott RG (2005) Conceptual model of the effects of sea level rise on sandy coasts. *J Coast Res* 21(6 (216)):1166–1172
- Davidson-Arnott RG, Bauer BO (2021) Controls on the geomorphic response of beach-dune systems to water level rise. *J Great Lakes Res* 47(6):1594–1612
- Davidson-Arnott RG, Law MN (1996) Measurement and prediction of long-term sediment supply to coastal foredunes. *J Coast Res* 12:654–663
- De Battisti D, Fowler MS, Jenkins SR, Skov MW, Rossi M, Bouma TJ, Neyland PJ, Griffin JN (2019) Intraspecific root trait variability along environmental gradients affects salt marsh resistance to lateral erosion. *Front Ecol Evol* 7:150
- De Giglio M, Greggio N, Goffo F, Merloni N, Dubbini M, Barbarella M (2019) Comparison of pixel-and object-based classification methods of unmanned aerial vehicle data applied to coastal dune vegetation communities: casal borsetti case study. *Remote Sens* 11(12):1416
- Dech JP, Maun MA (2005) Zonation of vegetation along a burial gradient on the leeward slopes of Lake Huron sand dunes. *Can J Bot* 83(2):227–236
- Delgado-Fernandez I (2010) A review of the application of the fetch effect to modelling sand supply to coastal foredunes. *Aeolian Res* 2(2–3):61–70
- Delgado-Fernandez I, Davidson-Arnott R, Bauer BO, Walker IJ, Ollerhead J, Rhew H (2012) Assessing aeolian beach-surface dynamics using a remote sensing approach. *Earth Surf Process Landf* 37(15):1651–1660
- Delgado-Fernandez I, Smyth TA, Jackson DW, Smith AB, Davidson-Arnott RG (2018) Event-scale dynamics of a parabolic dune and its relevance for mesoscale evolution. *J Geophys Res Earth* 123(11):3084–3100
- Delgado-Fernandez I, Davidson-Arnott RG, Hesp PA (2019) Is ‘re-mobilisation’ nature restoration or nature destruction? A commentary. *J Coast Conserv* 23(6):1093–1103
- Doughty CL, Cavanaugh KC (2019) Mapping coastal wetland biomass from high resolution unmanned aerial vehicle (UAV) imagery. *Remote Sens* 11(5):540
- Drummond CD, Harley MD, Turner IL, Matheen ANA, Glamore WC (2015) UAV applications to coastal engineering. In: Australasian coasts & ports conference 2015: 22nd Australasian coastal and ocean engineering conference and the 15th Australasian port and harbour conference. Engineers Australia and IPENZ, p 267

- Du J, Hesp PA (2020) Salt spray distribution and its impact on vegetation zonation on coastal dunes: a review. *Estuar Coasts* 43(8):1885–1907
- Edelman T (1969) Dune erosion during storm conditions. *Coast Eng* 1968:719–722
- Fairley I, Mendzil A, Togneri M, Reeve DE (2018) The use of unmanned aerial systems to map intertidal sediment. *Remote Sens* 10(12):1918
- Feagin RA, Sherman DJ, Grant WE (2005) Coastal erosion, global sea-level rise, and the loss of sand dune plant habitats. *Front Ecol Environ* 3(7):359–364
- Feagin RA, Furman M, Salgado K, Martinez ML, Innocenti RA, Eubanks K, Figlus J, Huff TP, Sigren J, Silva R (2019) The role of beach and sand dune vegetation in mediating wave run up erosion. *Estuar Coast Shelf Sci* 219:97–106
- Fisher PF, Tate NJ (2006) Causes and consequences of error in digital elevation models. *Prog Phys Geogr* 30(4):467–489
- Forbes DL, Parkes GS, Manson GK, Ketch LA (2004) Storms and shoreline retreat in the southern Gulf of St. Lawrence. *Mar Geol* 210:169–204. <https://doi.org/10.1016/j.margeo.2004.05.009>
- García-Romero L, Delgado-Fernández I, Hesp PA, Hernández-Calvento L, Hernández-Cordero AI, Viera-Pérez M (2019a) Biogeomorphological processes in an arid transgressive dunefield as indicators of human impact by urbanization. *Sci Total Environ* 650:73–86
- García-Romero L, Delgado-Fernández I, Hesp PA, Hernández-Calvento L, Viera-Pérez M, Hernández-Cordero AI, Cabrera-Gámez J, Domínguez-Brito AC (2019b) Airflow dynamics, vegetation and aeolian erosive processes in a shadow zone leeward of a resort in an arid transgressive dune system. *Aeolian Res* 38:48–59
- Gares PA, Nordstrom KF (1988) Creation of dune depressions by foredune accretion. *Geogr Rev* 78:194–204
- Gares PA, Nordstrom KF (1995) A cyclic model of foredune blowout evolution for a leeward coast: Island Beach, New Jersey. *Ann Assoc Am Geogr* 85(1):1–20
- Gedge KE, Maun MA (1994) Compensatory response of two dune annuals to simulated browsing and fruit predation. *J Veg Sci* 5(1):99–108
- Gens R (2010) Remote sensing of coastlines: detection, extraction and monitoring. *Int J Remote Sens* 31(7):1819–1836
- George E, Lunardi B, Smith A, Lehner J, Wernette P, Houser C (2021) Storm impact and recovery of a beach-dune system in Prince Edward Island. *Geomorphology* 384:107721
- Gonçalves JA, Henriques R (2015) UAV photogrammetry for topographic monitoring of coastal areas. *ISPRS J Photogramm Remote Sens* 104:101–111
- Grottoli E, Ciavola P, Duo E, Ninfo A (2019) UAV application for monitoring the annual geomorphic evolution of a coastal dune in Punta Marina (Italy). In: Chirici G, Gianinetto M (eds) *Earth observation advancements in a changing world, AIT series trends in earth observation*, vol 1. Associazione Italiana di Telerilevamento (AIT), Firenze, p 103
- Guillot B, Castelle B, Marieu V, Bujan S, Rosebery D (2018) UAV monitoring of 3-year Foredune Partial Recovery from a Severe Winter: Truc Vert Beach, SW France. *J Coast Res* 85(10085): 276–280
- Guisado-Pintado E, Jackson DW, Rogers D (2019) 3D mapping efficacy of a drone and terrestrial laser scanner over a temperate beach-dune zone. *Geomorphology* 328:157–172
- Hallin C, Almström B, Larson M, Hanson H (2019) Longshore transport variability of beach face grain size: implications for dune evolution. *J Coast Res* 35(4):751–764
- Hesp PA (1981) The formation of shadow dunes. *J Sediment Res* 51(1):101–112
- Hesp P (1983) Morphodynamics of incipient foredunes in New South Wales, Australia. In: *Developments in sedimentology*, vol 38. Elsevier, Amsterdam, pp 325–342
- Hesp PA (1984) Foredune formation in Southeast Australia. In: *Coastal geomorphology in Australia*. Academic Press, Sydney, pp 69–97
- Hesp P (1988) Surfzone, beach, and foredune interactions on the Australian South East Coast. *J Coast Res* 3:15–25
- Hesp PA (1989) A review of biological and geomorphological processes involved in the initiation and development of incipient foredunes. *Proc R Soc Edinb B Biol Sci* 96:181–201

- Hesp PA (1991) Ecological processes and plant adaptations on coastal dunes. *J Arid Environ* 21(2): 165–191
- Hesp P (2002) Foredunes and blowouts: initiation, geomorphology and dynamics. *Geomorphology* 48(1–3):245–268
- Hesp PA, Hyde R (1996) Flow dynamics and geomorphology of a trough blowout. *Sedimentology* 43(3):505–525
- Hesp PA, Martínez ML (2007) Disturbance processes and dynamics in coastal dunes. In: *Plant disturbance ecology: the process and the response*. Elsevier/AP, Amsterdam/Boston, pp 215–247
- Hesp PA, Pringle A (2001) Wind flow and topographic steering within a trough blowout. *J Coast Res* 34:597–601
- Hesp PA, Smyth TA (2019) CFD flow dynamics over model scarps and slopes. *Phys Geogr* 42(1): 1–24
- Hesp PA, Walker IJ (2012) Three-dimensional aeolian dynamics within a bowl blowout during offshore winds: Greenwich Dunes, Prince Edward Island, Canada. *Aeolian Res* 3(4):389–399
- Hesp PA, Davidson-Arnott R, Walker IJ, Ollerhead J (2005) Flow dynamics over a foredune at Prince Edward Island, Canada. *Geomorphology* 65(1–2):71–84
- Hesp PA, Walker IJ, Chapman C, Davidson-Arnott R, Bauer BO (2013) Aeolian dynamics over a coastal foredune, Prince Edward Island, Canada. *Earth Surf Process Landf* 38(13):1566–1575
- Hilgendorf Z, Marvin MC, Turner CM, Walker IJ (2020) Assessing geomorphic change in restored coastal dune ecosystems using a multi-platform aerial approach
- Houser C (2009) Synchronization of transport and supply in beach-dune interaction. *Prog Phys Geogr* 33(6):733–746
- Houser C, Ellis J (2013) Beach and dune interaction
- Houser C, Labude B, Haider L, Weymer B (2013) Impacts of driving on the beach: case studies from Assateague Island and Padre Island National Seashores. *Ocean Coast Manag* 71:33–45
- Houser C, Wernette P, Rentschlar E, Jones H, Hammond B, Trimble S (2015) Post-storm beach and dune recovery: implications for barrier island resilience. *Geomorphology* 234:54–63
- Houser C, Bishop M, Wernette P (2017) Multi-scale topographic anisotropy patterns on a Barrier Island. *Geomorphology* 297:153–158
- Houser C, Wernette P, Weymer BA (2018) Scale-dependent behavior of the foredune: implications for barrier island response to storms and sea-level rise. *Geomorphology* 303:362–374
- Houser C, Smith A, George E, Lehner J, Lunardi B (2021) Loose and limited concepts: using co-author network analysis to identify potential gaps in our understanding of coastal barriers. *J Coast Res* (Accepted)
- Jackson DWT, Cooper JAG (2011) Coastal dune fields in Ireland: rapid regional response to climatic change. *J Coast Res nSPEC*(64):293–297
- Jackson DW, Costas S, González-Villanueva R, Cooper A (2019) A global ‘greening’ of coastal dunes: an integrated consequence of climate change? *Glob Planet Chang* 182:103026
- Keijsers JGS, De Groot AV, Riksen MJPM (2015) Vegetation and sedimentation on coastal foredunes. *Geomorphology* 228:723–734
- Kuriyama Y, Mochizuki N, Nakashima T (2005) Influence of vegetation on aeolian sand transport rate from a backshore to a foredune at Hasaki, Japan. *Sedimentology* 52(5):1123–1132
- Laporte-Fauret Q, Marieu V, Castelle B, Michalet R, Bujan S, Rosebery D (2019) Low-cost UAV for high-resolution and large-scale coastal dune change monitoring using photogrammetry. *J Mar Sci Eng* 7(3):63
- Laporte-Fauret Q, Lubac B, Castelle B, Michalet R, Marieu V, Bombrun L, Launeau P, Giraud M, Normandin C, Rosebery D (2020a) Classification of Atlantic coastal sand dune vegetation using in situ, uav, and airborne hyperspectral data. *Remote Sens* 12(14):2222
- Laporte-Fauret Q, Castelle B, Marieu V, Bujan S, Michalet R, Rosebery D (2020b) Coastal dune morphology evolution combining Lidar and UAV surveys, Truc Vert beach 2011–2019. *J Coast Res* 95(sp1):163–167

- Luijendijk A, Hagenaars G, Ranasinghe R, Baart F, Donchyts G, Aarninkhof S (2018) The state of the world's beaches. *Sci Rep* 8(1):1–11
- Mancini F, Dubbini M, Gattelli M, Stecchi F, Fabbri S, Gabbianelli G (2013) Using unmanned aerial vehicles (UAV) for high-resolution reconstruction of topography: the structure from motion approach on coastal environments. *Remote Sens* 5(12):6880–6898
- Manson GK, Davidson-arnott RGD, Ollerhead J, Manson GK, Davidson-arnott RGD, Ollerhead J (2016) Attenuation of Wave Energy by Nearshore Sea Ice: Prince Edward Island, Canada. Stable URL: <https://www.jstor.org/stable/43752188> Prince Edward Island, Canada Attenuation of Wave Energy by Nearshore Sea 32, 253–263
- Masselink G, Castelle B, Scott T, Dodet G, Suarez S, Jackson D, Floc'h F (2016) Extreme wave activity during 2013/2014 winter and morphological impacts along the Atlantic coast of Europe. *Geophys Res Lett* 43(5):2135–2143
- Maun MA (1998) Adaptations of plants to burial in coastal sand dunes. *Can J Bot* 76(5):713–738
- Maun MA (2009) *The biology of coastal sand dunes*. Oxford University Press, Oxford
- Maun MA, Lapierre J (1984) The effects of burial by sand on *Ammophila breviligulata*. *J Ecol* 72: 827–839
- Maun MA, Lapierre J (1986) Effects of burial by sand on seed germination and seedling emergence of four dune species. *Am J Bot* 73(3):450–455
- Maun MA, Riach S (1981) Morphology of caryopses, seedlings and seedling emergence of the grass *Calamovilfa longifolia* from various depths in sand. *Oecologia* 49(1):137–142
- Maximiliano-Cordova C, Salgado K, Martínez ML, Mendoza E, Silva R, Guevara R, Feagin RA (2019) Does the functional richness of plants reduce wave erosion on embryonic coastal dunes? *Estuar Coasts* 42(7):1730–1741
- McDonald RL, Unni CK, Duce RA (1982) Estimation of atmospheric sea salt dry deposition: wind speed and particle size dependence. *J Geophys Res Oceans* 87(C2):1246–1250
- Meng X, Shang N, Zhang X, Li C, Zhao K, Qiu X, Weeks E (2017) Photogrammetric UAV mapping of terrain under dense coastal vegetation: an object-oriented classification ensemble algorithm for classification and terrain correction. *Remote Sens* 9(11):1187
- Nolet C, van Puijenbroek M, Suomalainen J, Limpens J, Riksen M (2018) UAV-imaging to model growth response of marram grass to sand burial: implications for coastal dune development. *Aeolian Res* 31:50–61
- Ollerhead J, Davidson-Arnott R (2022) Evolution and management of Atlantic Canadian coastal dunes over the next century. *Phys Geogr* 43(1):98–121
- Ollerhead J, Davidson-Arnott R, Walker IJ, Mathew S (2013) Annual to decadal morphodynamics of the foredune system at Greenwich Dunes, Prince Edward Island, Canada. *Earth Surf Process Landf* 38(3):284–298
- Olson JS (1958) Lake Michigan dune development I. Wind-velocity profiles. *J Geol* 66(3):254–263
- Pagán JL, Bañón L, López I, Bañón C, Aragonés L (2019) Monitoring the dune-beach system of Guardamar del Segura (Spain) using UAV, SfM and GIS techniques. *Sci Total Environ* 687: 1034–1045
- Parkes GS, Manson GK, Chagnon R, Ketch LA (2006) Storm-surge, wind, wave, and ice climatology. In: *Impacts of sea level rise and climate change on the coastal zone of Southeastern New Brunswick*. Environment Canada, Ottawa, pp 95–239
- Pelletier JD, Mitsova H, Harmon RS, Overton M (2009) The effects of interdune vegetation changes on eolian dune field evolution: a numerical-modeling case study at Jockey's Ridge, North Carolina, USA. *Earth Surf Process Landf* 34(9):1245–1254
- Piscioneri N, Smyth TA, Hesp PA (2019) Flow dynamics over a foredune scarp. *Earth Surf Process Landf* 44(5):1064–1076
- Pontee N (2013) Defining coastal squeeze: a discussion. *Ocean Coast Manag* 84:204–207
- Randall RE (1970) Salt measurement on the coast of Barbados, West Indies. *Oikos* 21:65–70
- Rotnicka, J., Dłużewski, M., Dąbski, M., Rodzewicz, M., Włodarski, W. and Zmarz, A., 2020. Accuracy of the UAV-based DEM of Beach–Foredune topography in relation to selected morphometric variables, land cover, and multitemporal sediment budget. *Estuar Coasts*, v43 n8: 1939–1955

- Rozema J, Bijwaard P, Prast G, Broekman R (1985) Ecophysiological adaptations of coastal halophytes from foredunes and salt marshes. *Vegetatio* 62(1–3):499–521
- Ruessink BG, Arens SM, Kuipers M, Donker JJA (2018) Coastal dune dynamics in response to excavated foredune notches. *Aeolian Res* 31:3–17
- Ruggiero P, Hacker S, Seabloom E, Zarnetske P (2018) The role of vegetation in determining dune morphology, exposure to sea-level rise, and storm-induced coastal hazards: a US Pacific Northwest perspective. In: *Barrier dynamics and response to changing climate*. Springer, Cham, pp 337–361
- Sallenger AH Jr (2000) Storm impact scale for barrier islands. *J Coast Res* 16(Part 3):890–895
- Scarelli FM, Sistilli F, Fabbri S, Cantelli L, Barboza EG, Gabbianelli G (2017) Seasonal dune and beach monitoring using photogrammetry from UAV surveys to apply in the ICZM on the Ravenna coast (Emilia-Romagna, Italy). *Remote Sens Appl Soc Environ* 7:27–39
- Seabloom EW, Wiedemann AM (1994) Distribution and effects of *Ammophila breviligulata* Fern. (American beachgrass) on the foredunes of the Washington coast. *J Coast Res*, pp 178–188
- Seneca ED (1969) Germination response to temperature and salinity of four dune grasses from the Outer Banks of North Carolina. *Ecology* 50:45–53
- Sherman DJ, Bauer BO (1993) Dynamics of beach-dune systems. *Prog Phys Geogr* 17(4):413–447
- Sherman DJ, Hotta S (1990) Aeolian sediment transport: theory and measurement. In: *Coastal dunes: form and process*, vol 17. Wiley, Chichester, p 37
- Short AD, Hesp PA (1982) Wave, beach and dune interactions in southeastern Australia. *Mar Geol* 48(3–4):259–284
- Silva GMD, Hesp P, Peixoto J, Dillenburg SR (2008) Fore-dune vegetation patterns and alongshore environmental gradients: Moçambique beach, Santa Catarina Island, Brazil. *Earth Surf Process Landf J Br Geomorphol Res Group* 33(10):1557–1573
- Smith AB, Jackson DW, Cooper JAG (2017a) Three-dimensional airflow and sediment transport patterns over barchan dunes. *Geomorphology* 278:28–42
- Smith AB, Jackson DW, Cooper JAG, Hernández-Calvento L (2017b) Quantifying the role of urbanization on airflow perturbations and dunefield evolution. *Earth's Future* 5(5):520–539
- Smith A, Gares PA, Wasklewicz T, Hesp PA, Walker IJ (2017c) Three years of morphologic changes at a bowl blowout, Cape Cod, USA. *Geomorphology* 295:452–466
- Smith A, Lunardi B, George E, Houser C (2020a) Monitoring storm impacts on Sandy coastlines with UAVs. In: *Spatial variability in environmental science-patterns, processes, and analyses*. IntechOpen, London
- Smith A, Houser C, Lehner J, George E, Lunardi B (2020b) Crowd-sourced identification of the beach-dune interface. *Geomorphology* 367:107321
- Stockdon HF, Sallenger AH Jr, List JH, Holman RA (2002) Estimation of shoreline position and change using airborne topographic lidar data. *J Coast Res* 18(3):502–513
- Sturdivant EJ, Lentz EE, Thieler ER, Farris AS, Weber KM, Remsen DP, Miner S, Henderson RE (2017) UAS-SfM for coastal research: geomorphic feature extraction and land cover classification from high-resolution elevation and optical imagery. *Remote Sens* 9(10):1020
- Suo C, McGovern E, Gilmer A (2019) Coastal dune vegetation mapping using a multispectral sensor mounted on an UAS. *Remote Sens* 11(15):1814
- Taddia Y, Corbau C, Zambello E, Russo V, Simeoni U, Russo P, Pellegrinelli A (2017) UAVs to assess the evolution of embryo dunes. *Int Arch Photogramm Remote Sens Spat Inf Sci* 42:363
- Taddia Y, Corbau C, Zambello E, Pellegrinelli A (2019) UAVs for structure-from-motion coastal monitoring: a case study to assess the evolution of embryo dunes over a two-year time frame in the Po River Delta, Italy. *Sensors* 19(7):1717
- Tsoar H (1983) Wind tunnel modeling of echo and climbing dunes. In: *Developments in sedimentology*, vol 38. Elsevier, Amsterdam, pp 247–259
- Turner IL, Harley MD, Drummond CD (2016) UAVs for coastal surveying. *Coast Eng* 114:19–24
- van Puijenbroek ME, Nolet C, De Groot AV, Suomalainen JM, Riksen MJ, Berendse F, Limpens J (2017) Exploring the contributions of vegetation and dune size to early dune development using unmanned aerial vehicle (UAV) imaging. *Biogeosciences* 14(23):5533

- Walker IJ (2020) Aeolian (windblown) sand transport over beaches. In: *Sandy Beach morphodynamics*, Elsevier, Amsterdam, pp 213–253
- Walker I, Hesp PA (2013) Fundamentals of aeolian sediment transport: airflow over dunes. In: *Treatise on geomorphology*. Elsevier Inc., Amsterdam, pp 109–133
- Walker IJ, Nickling WG (2002) Dynamics of secondary airflow and sediment transport over and in the lee of transverse dunes. *Prog Phys Geogr* 26(1):47–75
- Walker IJ, Nickling WG (2003) Simulation and measurement of surface shear stress over isolated and closely spaced transverse dunes in a wind tunnel. *Earth Surf Process Landf J Br Geomorphol Res Group* 28(10):1111–1124
- Wernette P, Lehner J, Houser C (2020) What is ‘real’? Identifying erosion and deposition in context of spatially variable uncertainty. *Geomorphology* 355:107083
- Westoby MJ, Brasington J, Glasser NF, Hambrey MJ, Reynolds JM (2012) ‘Structure-from-Motion’ photogrammetry: a low-cost, effective tool for geoscience applications. *Geomorphology* 179:300–314
- Wheaton JM, Brasington J, Darby SE, Sear DA (2010) Accounting for uncertainty in DEMs from repeat topographic surveys: improved sediment budgets. *Earth Surf Process Landf J Br Geomorphol Res Group* 35(2):136–156
- Zanutta A, Lambertini A, Vittuari L (2020) UAV photogrammetry and ground surveys as a mapping tool for quickly monitoring shoreline and beach changes. *J Mar Sci Eng* 8(1):52

Chapter 11

Using Small Unoccupied Aircraft Systems (sUAS) for Characterizing Rivers and Streams in Forested Environments



David A. Reid, Marwan A. Hassan, Carina Helm, and Steve Bird

Abstract Small unoccupied aerial systems (sUAS) are rapidly becoming a required component of a field geomorphologist's toolbox. In a fluvial context, work to date with sUAS has largely focused on rivers of intermediate size and with clear sight lines, with few studies completed in small channels with closed, heavily forested canopies. While the capabilities, advantages and drawbacks of sUAS-based data collection approaches in larger channels are relatively well known, less information is available to characterize their performance in smaller, more vegetated fluvial systems. Recent advances in the capability of consumer-grade sUAS have allowed researchers to push the boundaries of geomorphic data collection in these more challenging environments. Using a combination of recent literature and the author's first-hand experience, this chapter describes approaches, opportunities and challenges related to the application of sUAS-based methods in rivers and streams within forested landscapes or other environments with confined flying conditions and limited sight lines.

Keywords sUAS · Fluvial geomorphology · Forested watershed · Small rivers · River ecology · Grain size · Riparian vegetation

11.1 Introduction

Small unoccupied aerial systems (sUAS) have become an essential tool for researching and characterizing fluvial environments (Tamminga et al. 2015; Woodget et al. 2017; Hamshaw et al. 2019; Piégay et al. 2020). While

D. A. Reid (✉) · M. A. Hassan
Department of Geography, University of British Columbia, Vancouver, B.C., Canada
e-mail: david.reid@geog.ubc.ca

C. Helm
Hatfield Consultants, North Vancouver, B.C., Canada

S. Bird
Fluvial Systems Research Inc, Surrey, BC, Canada

photogrammetric principles have been applied to imagery for geomorphic purposes for over half a century (e.g. El Ashrey and Wanless 1967), the collection of imagery from sUAS platforms is comparatively recent, with early applications beginning in the mid-2000s (Tamminga et al. 2015). From their early use in river systems for topographic mapping (Lejot et al. 2007), sUAS have become standard equipment for data collection pertinent to bathymetry (Tamminga et al. 2015) and hydrometrics (Tauro et al. 2016), geomorphic change detection (Cook 2017), vegetation coverage (Watanabe and Kawahara 2016), evaluation of aquatic habitat (Roncoroni and Lane 2019) and mapping of in-stream wood in fluvial environments (Sanhueza et al. 2019).

Numerous studies have highlighted the various capabilities and limitations of sUAS use in large and intermediate river systems (Tamminga et al. 2015), and in small systems with relatively unobstructed sightlines (Woodget and Austrums 2017). In most cases, the survey precision achievable with sUAS is comparable to that from other methods. When flights are supplemented with accurate ground control points (GCPs), uncertainty can be less than 10 cm (Watanabe and Kawahara 2016), even in clear-water submerged areas (Woodget and Austrums 2017). Survey coverage is more difficult to assess, but is typically limited by the presence of vegetation obscuring the channel (Meinen and Robinson 2020) and deep or opaque streamflow rendering submerged areas of the channel bed difficult to resolve (Dietrich 2017; Carrivick and Smith 2019).

While sUAS have become standard data collection instruments in river systems with few flight or sight line obstructions, small rivers and streams bordered by or overlain by forest canopies have, to date, remained challenging to survey with sUAS-based methods. Channels of this type possess characteristics rendering them distinct from larger and more open systems which are relevant for undertaking sUAS surveys. Several example images of channels overlain by dense forest canopies are shown in Fig. 11.1. For this chapter, we define channels as likely to be influenced by canopy coverage and riparian vegetation if they are narrower than the average height of the surrounding forest. This definition follows others focusing on the influence of in-stream wood on channel morphology (Hassan et al. 2005; Reid and Hassan 2020). While the specific nature of canopy coverage will vary with different tree species, channels with forested riparian areas where tree height is similar to or exceeds channel width will be largely obstructed from overhead view and are typically difficult to characterize with aerial imagery from above the canopy. Beneath the canopy, additional vegetation may be present, especially along channel banks. Bank vegetation may protrude into the channel but in some cases overhangs the channel margin, providing an opportunity to capture imagery of bed areas beneath. In this regard, several aspects of the methodology presented in this chapter are relevant to larger channels with forested banks.

Small channels in forested regions are of high ecological value and often possess complex morphologies (Montgomery et al. 2003), and channel form can be affected by the presence of in-stream wood originating from the riparian zone and hillslopes (Hassan et al. 2019). While these channels compose a great deal of river network length (Wohl 2017), they are challenging to study due to complex terrain and

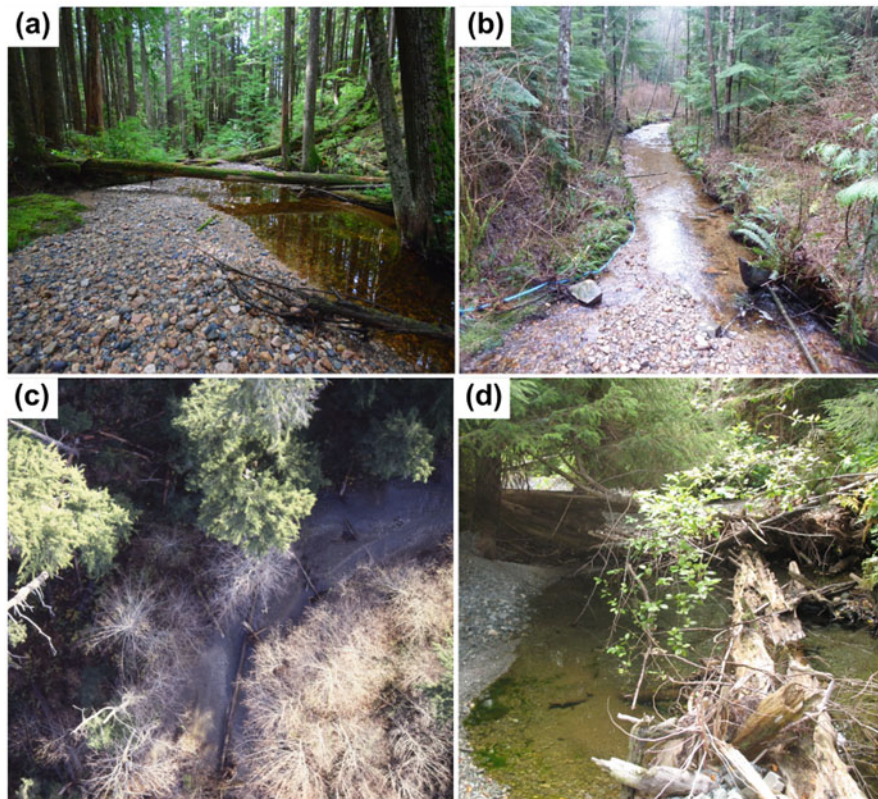


Fig. 11.1 Example images highlighting aspects of forested streams with closed canopies. **(a)** example channel (Wilson Creek, B.C., width = 10 m), with closed canopy but relatively little understory. Surveys in this channel will produce good results; **(b)** while this channel is small (width = 3 m, East Creek, B.C.) and has relatively complete canopy coverage, a good survey result should be attainable as sightlines are clear; **(c)** example overhead view of a channel (Carnation Creek, B.C., width = 15–20 m) where a sub-canopy survey would provide substantial improvements in coverage; **(d)** channel section (Carnation Creek, B.C.) where sub-canopy flights are not feasible given dense low-elevation vegetation inhibiting flights. (All images are taken by the authors)

riparian and canopy vegetation, rendering traditional remote-sensing approaches difficult to apply. While other methods have been investigated to capture imagery below forest canopies in small channels (e.g. Bird et al. 2010), characterizing streamchannels sub-canopy has traditionally been considered impractical using sUAS approaches. While sUAS-based mapping of forested channels has lagged behind the remote sensing technologies applied in larger rivers, recent improvements in equipment and methodology provide an opportunity for widespread application in smaller streams in forested environments.

Relying upon a combination of recent literature and the author's experience in applying sUAS in geomorphic data collection, this chapter aims to describe

approaches for collecting image-based geomorphic and ecological information from consumer-grade sUAS in rivers and streams bordered by, and often overlain with, forest canopies. This chapter will first review the techniques for data collection in these settings, followed by an overview of data processing approaches to obtain the best quality product from the survey. An evaluation of sUAS methods against traditional survey approaches will be conducted, and then an example of how these surveys have been applied will be presented.

11.2 Data Collection Strategies

In many aspects, the approach for undertaking a detailed sUAS survey in channels with closed canopies is similar to approaches taken in larger systems. The key distinction, however, arises in the flight strategy, where low-flying heights are required to clear overhead obstacles and oblique imagery is necessary to capture channel areas partly obscured by bank vegetation. Given broad similarities, the general approach to channel surveys with sUAS will be described here only briefly, with detail dedicated to the methods required for sub-canopy flights. A detailed description of general sUAS survey approaches in river environments can be found in Tamminga et al. (2015). We will focus our methodology on the use of consumer-grade sUAS, which are relatively inexpensive and widely used.

11.2.1 Ground Control Point (GCP) Placement

As with many sUAS-based surveys where precision in the order of centimetres is required, the placement of surveyed ground control points (GCPs) is necessary. These points allow for accurate georectification of imagery, which is otherwise limited by the on-board GPS provided with the sUAS. The recommended density of points varies by study, from a minimum of 5 points within a section (Harwin et al. 2015) to upwards of 20 points (Sanz-Ablanedo et al. 2018). Beyond 20 points per section, improvements in accuracy are possible, but at a diminishing rate, and the accuracy of the GCP becomes relatively more important (Agüera-Vega et al. 2016). Expressed in terms of GCPs per 100 images, a recommended density of 2 GCPs per image is suggested by Sanz-Ablanedo et al. (2018). In addition to the placement of GCPs, checkpoints are commonly included in surveys in order to evaluate the accuracy of the rectified imagery. In our study, checkpoints are identical to GCPs but are not used for rectification of imagery; rather, they are used as an independent measure of rectification error. While few studies report a recommended checkpoint density (but see Sanz-Ablanedo et al. 2018), we recommend, at a minimum,

including an equal number of checkpoints to GCPs. As with GCPs, checkpoints should be distributed evenly over the study area, and if possible, some should be placed in submerged bed areas in order to evaluate post-correction submerged bed survey accuracy.

The placement of GCPs in small, forested streams will involve consideration of sightlines for both the flight and the GCP marker survey. GCPs should be placed over the full survey area, but with consideration of vegetation that might render points invisible from the air. In some cases, low-density vegetation may allow GCPs or checkpoints to be partly visible in imagery, but the resulting image quality may be insufficient to retain for inclusion in subsequent analysis, rendering the GCP unusable.

Several methods exist for surveying the location of GCPs and checkpoints. If some existing survey benchmarks are available, then use of a total station may be a practical option to obtain sub-centimetre accuracy. Even if benchmarks are not available, a survey transect with a total station will still allow all image bundles to be correctly referenced to one another, if not in absolute space. The primary downside of a total-station survey approach is the need for multiple people to undertake the work, equipment cost and the comparatively longer survey time required (Harwin et al. 2015). Additionally, vegetation can lead to short sightlines, further slowing the survey process if large areas are to be covered. Another option is to use a differential GPS (DGPS) system, a solution where no existing survey benchmarks are needed to obtain absolute positioning with sub-10 cm accuracy. Advantages of this approach are that fewer personnel are required to collect the data and that points can be marked more rapidly and over a larger area, with fewer line-of-sight problems than with the total station approach. The main drawbacks of the DGPS approach are the potential for lower or variable accuracy in comparison to the total station when GPS signal acquisition is difficult, high equipment cost and accuracy that can vary depending on the particular survey location and conditions.

11.2.2 Camera Calibration and Settings

If a consumer-grade sUAS is to be employed and carefully surveyed GCPs are available, then self-calibration within photogrammetric software is usually possible. However, if higher-quality cameras are to be used or if GCPs are absent, then pre-calibration of sUAS cameras may provide an improvement in results. A description of calibration approaches is given by Harwin et al. (2015). Given the low flight elevation, commonly mixed lighting conditions and images of water surfaces, a polarizing filter can help reduce the presence of glare on the water surface in images. Best results are often obtained in cloudy and calm weather when lighting contrast is reduced.

11.2.3 Flight Paths and Image Acquisition

The primary distinction between sUAS survey strategies in larger or open channels and strategies for sub-canopy flights lies in the approach to image acquisition. In open environments or at higher elevations, flights with imagery collected at the nadir (i.e. from directly overhead) often produce good results, but may miss overhanging or very steep regions (Carrivick and Smith 2019). Given the need to fly at low elevations below canopies and also the difficulty of capturing channel margins obscured by vegetation, the inclusion of oblique and convergent imagery can substantially improve results. In this context, ‘oblique imagery’ refers to images captured with a camera angle other than 90°, while ‘convergent’ refers to frames capturing the same channel region but from different approach directions. This approach, which has been adopted in several studies (Wackrow and Chandler 2011; James and Robson 2014; Harwin et al. 2015), helps capture better imagery in places where a region of interest is obscured from above, but with a clear view from the side. Recent work (Helm et al. 2020) indicates that a camera angle of 20–30° from vertical provided good results, and combining oblique and nadir imagery poses no obstacle during structure-from-motion analysis. An example of a data collection scheme with nadir, oblique and convergent imagery using flight paths parallel to the channel centreline is shown in Fig. 11.2.

Other key considerations for a sub-canopy survey are flying height, flight speed and image collection frequency. Flying height will be limited by the particular characteristics of the canopy overlying the channel; however, flying as high as possible within the constraints placed by the canopy will allow for coverage with a minimum of images. As flight elevation decreases, image collection frequency will need to increase or sUAS ground speed to decrease in order to maintain sufficient coverage and focus. At elevations below 5 m above ground level (AGL), low flight speeds ($< 1 \text{ ms}^{-1}$) and high image collection frequency (2–3-second interval) will be necessary. Depending on the nature of the riparian vegetation, lower flying heights and increasingly oblique imagery may be required in order to capture particularly challenging areas.

An example comparison of a channel area surveyed with (a) only nadir and (b) nadir and oblique imagery is shown in Fig. 11.3. More than 30% of bank areas are omitted when only nadir imagery is used, and substantial improvements in bank coverage are apparent when oblique imagery is included as well.

11.2.4 Bathymetry and Grain Size Calibration and Additional Survey Data

Depending on the application of the survey results, reference surface sediment texture data and water depth may be desirable to collect. This information will be needed to generate grain size maps and to obtain topography of submerged areas.

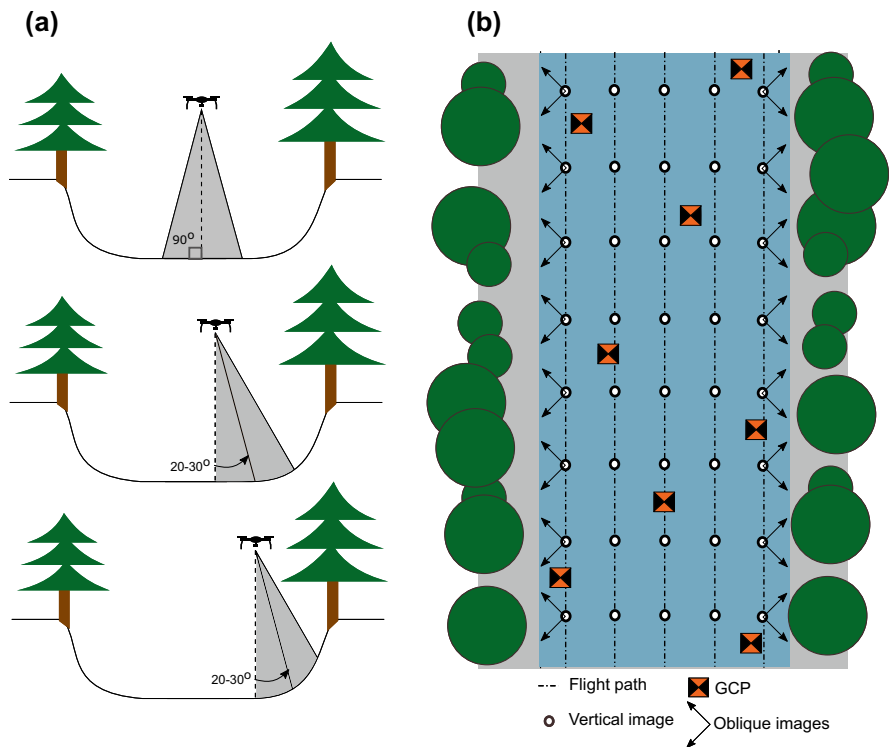


Fig. 11.2 (a) Example channel cross-sections contrasting oblique and nadir imagery across flight paths. To characterize the channel banks and near-bank bed areas, the camera can be tilted 20–30° from vertical. (b) plan view of the flight path of the sUAS with the parallel flight lines shown as dashed lines. Additional passes may be needed if channel width increases, but flying height is restricted by overhead obstacles, such as trees, indicated here as green circles. Flying heights are typically the same for all passes. (Figure is modified from Helm et al. 2020)

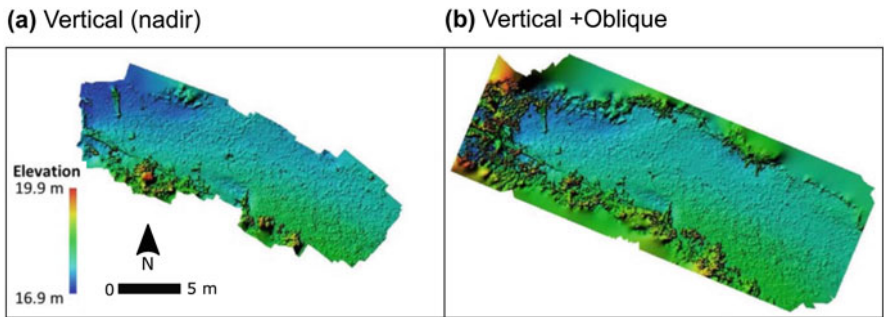


Fig. 11.3 Difference in the proportion of bed that can be covered between only a vertical image photoset (a) and after the incorporation of oblique and convergent imagery (b) along a section of Carnation Creek, B.C. The DEM with both vertical and oblique imagery (panel b) has improved coverage of channel bank and near-bank areas

Supplementary point measurements of submerged areas are helpful for assessing the outcome of bathymetry correction methods, which are discussed in Sect. 11.3.2. Similarly, field measurements of grain size data are helpful when assessing the performance of grain size detection methods from sUAS imagery. Typically, bed areas would be delineated within which a sediment sample would be collected via pebble count and then compared to grain size statistics derived from imagery. It is also possible to use on-screen methods to obtain grain size statistics (Tamminga et al. 2015).

When riparian vegetation is particularly dense or low-lying, obtaining surface elevation from sUAS imagery can be difficult. For hydrodynamic modeling applications or other circumstances when detailed data on riparian topography is needed, supplemental surveys with a total station, automatic level or GPS may be necessary. Similarly, if streamflow is opaque and therefore submerged topography remains obscured, additional survey measurements are often needed to capture submerged bed topography.

11.2.5 Other Considerations

When undertaking a sUAS survey in a small stream with a closed canopy and dense riparian vegetation, several additional factors related to data acquisition are worthy of consideration. First, depending on the specific characteristics of the sUAS, prop-wash can disturb the water surface, rendering submerged bed areas difficult to resolve.

In situations where very low-flying heights are required, oblique imagery may help reduce this issue by capturing bed areas not directly below the aircraft.

Given the constrained space within which the sUAS is being operated, it is usually not feasible to operate the instrument using pre-programmed flight paths. In most cases, it is necessary to manually fly the sUAS, and the pilot will typically need to be within a relatively short distance of the instrument in order to maintain visual contact. While many newer sUAS have good obstacle avoidance systems and are stable in flight, older models and larger sUAS could be difficult to pilot given space constraints. Similarly, fixed-wing units are unlikely to perform well in these settings.

In forested regions with deciduous vegetation, undertaking surveys in the winter or early spring may improve outcomes as more bed areas may be visible when leaves are absent. However, falling leaves can obscure much of the sediment on the bed surface during autumn, leading to difficulties in estimating sediment texture, and very low temperatures can reduce sUAS battery life and limit performance. Similarly, in regions with seasonally fluctuating water levels, timing surveys to correspond with the driest season will minimize challenges related to bathymetric correction.

11.3 Data Processing

There are several photogrammetric software packages available for processing imagery collected with a sUAS (e.g. Pix4D, Agisoft Metashape, OpenDroneMap and MicMac). These software packages can be used to produce dense point clouds, orthophotos and digital elevation models which can be used for further geomorphological investigation. The process for generating these outputs is similar along densely vegetated channels to other environments. Therefore, this section focuses on how dense point clouds can be processed to characterize the topography, bathymetry and grain size of small forested channels. A summary of data collection, processing and analysis considerations is also shown in Fig. 11.4.

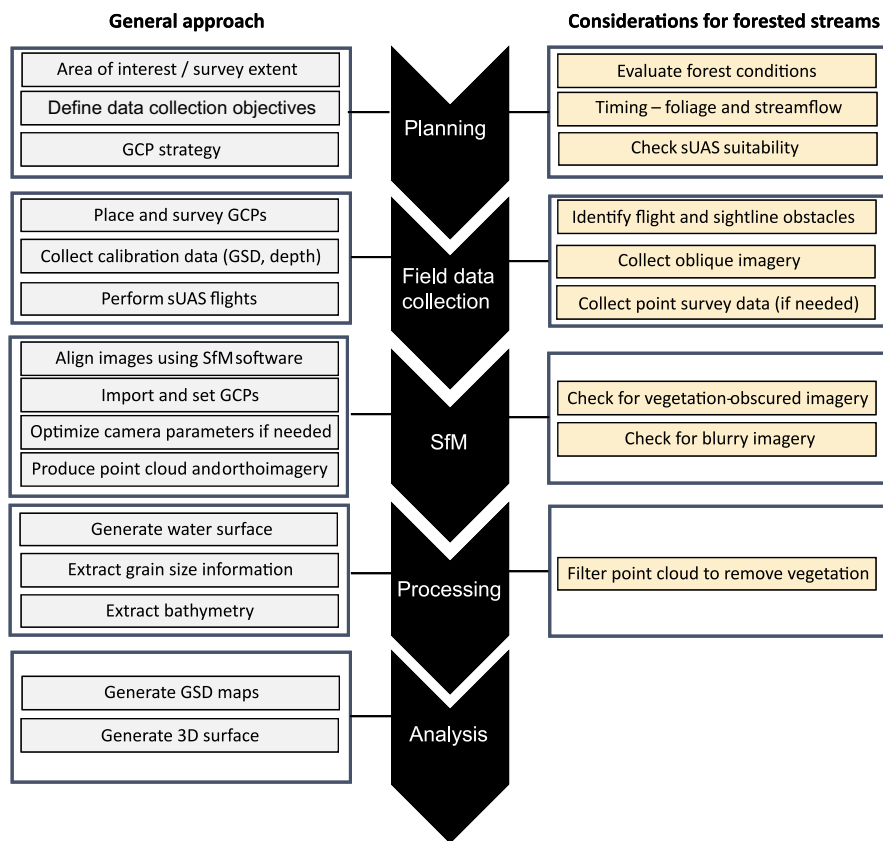


Fig. 11.4 Workflow diagram for collecting, processing and analysing sUAS imagery in forested channels with closed canopies and dense riparian vegetation. The left side of the chart indicates steps applicable for all surveys, while task considerations specific to forested streams are shown on the right

11.3.1 General Approach

Vegetation captured in imagery during sUAS surveys in closed-canopy channels can pose difficulties during image processing, and risk becomes incorporated into point clouds as noise. Before a high-quality DEM can be generated, unwanted image elements must be removed from the point cloud. This removal can often be achieved within the photogrammetry software or through a number of functions available in other cloud processing software packages. Here we will describe a noise-reduction approach using CloudCompare, a popular and open-source program which contains a suite of tools for processing and analysing point clouds. The key function of interest is the Cloth Simulation Filter (Zhang et al. 2016), an algorithm which separates ground and non-ground points by inverting the point cloud and then ‘draping’ a simulated surface over the inverted terrain. Points exceeding a user-defined threshold, such as a maximum distance from the mean surface, may then be classified as non-ground points. The user can select the terrain class that most closely describes their study area (e.g. flat or sloped) and then modify advanced parameters to best reflect their study site. Helm et al. (2020) found that a cloth resolution of 0.1 m and maximum distance from the cloud of between 0.5 and 1.0 m was adequate for filtering non-ground points, but experimentation is recommended to determine parameters most suited to a given dataset.

11.3.2 Extraction of Bathymetry

Due to the refractive effect of overlying water (Dietrich 2017), a difficulty encountered with DEM generation from sUAS imagery lies in extracting accurate estimates of bed elevations in submerged areas. Several approaches have been proposed for extracting corrected bathymetry and submerged bed elevations, and these can broadly be divided into two categories: spectral depth techniques where a relationship between the colour intensity of a pixel and its water depth is determined (e.g. Legleiter 2012) and through-water techniques, where a system of equations is used to correct for the effect of refraction (e.g. Javernick et al. 2014; Dietrich 2017). Spectral techniques can be more suited to streams with partially opaque streamflow, which contributes to a greater intensity and variety in the colour of submerged pixels with changes in depth (Tomsett and Leyland 2019). In contrast, through-water techniques are better suited to clear streamflow that permits direct observation of the submerged channel bed.

The through-water technique as described by Dietrich (2017) has shown promising results for small streams with low-flying heights (Helm et al. 2020). This approach corrects for the effect of refraction, which causes an overestimated apparent elevation of submerged bed areas. To apply this technique, the water surface needs to be delineated. This can be achieved by surveying water edge points in the field, or by using software such as CloudCompare to manually pick points along the margin of the wetted channel identified from the dense point cloud, which are then

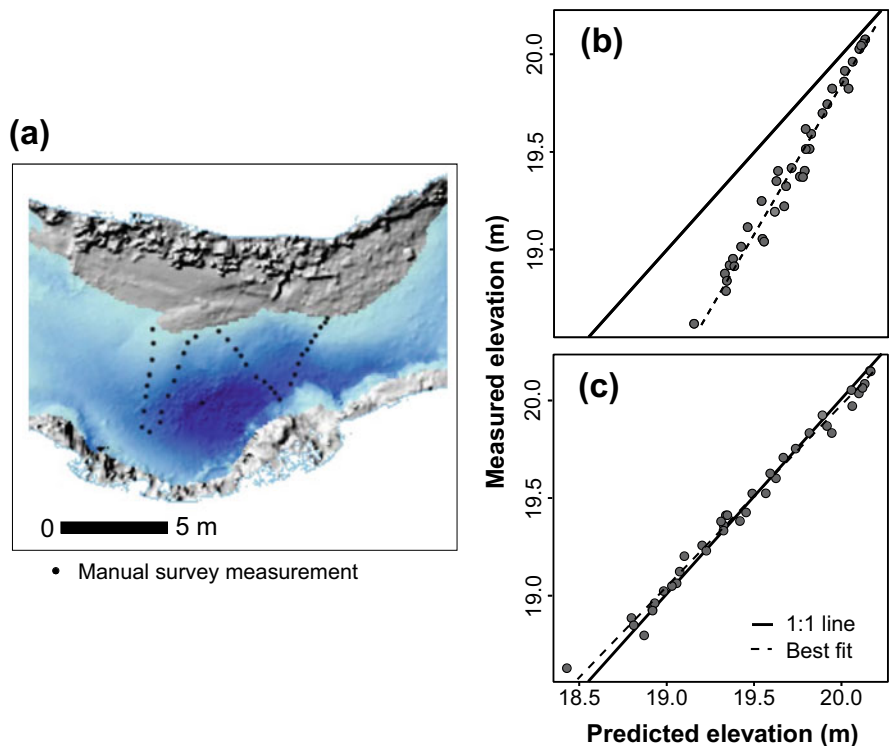


Fig. 11.5 An example of applied bathymetric corrections on bed topography along a section of Carnation Creek, B.C. (a) measurement points used to perform bathymetric calibration; (b) relationship between uncalibrated sUAS-based submerged bed area elevation and manually surveyed elevation; (c) relationship between corrected sUAS-based elevation in submerged bed areas and manually surveyed elevations

interpolated. By determining the distance from the generated water surface mesh to the estimated bed elevations in the point cloud below, the corrected water depth for a location can be calculated as a function of the multiple viewing angles used to observe each point, as shown by Dietrich (2017). An example of a generated water surface and bathymetry correction evaluated against field measurements is shown in Fig. 11.5. Depending on water depth, the correction effect can be substantial.

11.3.3 Extraction of Grain Size Information

Information on sediment texture of exposed channel bed areas is often desirable to extract from the sUAS imagery as texture characteristics can help inform patterns in channel form and process (e.g. Montgomery and Buffington 1997). In small, forested streams, texture often varies over short distances as a function of wood

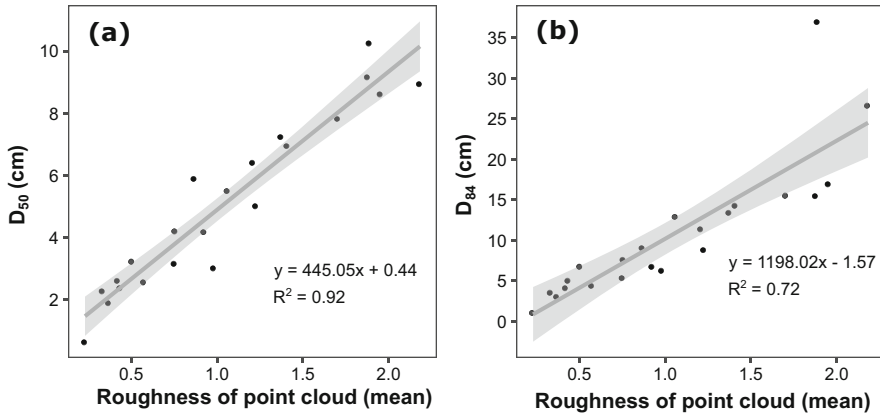


Fig. 11.6 Example relationships between (a) the median (D_{50}) and (b) 84th percentile (D_{84}) surface sediment calibre and the average roughness value of training sites as determined from sUAS-derived bed surfaces collected in Carnation Creek, B.C.

obstructions and meso-scale topographic variation (Montgomery et al. 2003). The techniques required for extracting grain size from sUASimagery predominantly involve either deriving a relationship between (1) image texture or roughness of the point cloud and (2) grain size parameters of sample sites (e.g. Carbonneau et al. 2012; Tamminga et al. 2015; Woodget and Austrums 2017; Helm et al. 2020). Both techniques require that calibration sites be set up in the field for constructing the relationship. The individual sites should be homogeneous in texture and established to capture the variability in grain size encountered across the channel. Grain size distributions at these calibration sites can be determined using an array of techniques, such as the Wolman grid method (Wolman 1954) or photo-sieving methods (Carbonneau et al. 2004). The sites must be geolocated so that their position in the point-cloud or orthophoto can be determined. Once a regression relationship is determined between a grain size metric for the field sites (e.g. their D_{50} or D_{84} , see Fig. 11.6), and roughness or image texture, a moving window analysis can be conducted to predict grain size across the channel (e.g. Woodget and Austrums 2017; Helm et al. 2020). These techniques present a semi-automated method of determining grain size over a large area. However, the use of machine-learning algorithms for grain size determination is becoming more common and is likely to further improve the efficiency of extracting grain size estimates from sUASimagery (Müller and Hassan 2019).

11.4 Comparison to Alternative Survey Methods

Prior to widespread use of sUAS technology, a number of surveying alternatives were available to capture channel attributes in small, forested streams. These include a variety of GPS-based, linear-survey and imagery-based methods. In this section,

we will discuss advantages and disadvantages of sUAS in comparison to commonly applied alternative data collection approaches.

A comparative summary of common survey methods is shown in Table 11.1 and a visual example in Fig. 11.7, ranging from low cost (survey level, handheld GPS) to

Table 11.1 Comparison of survey methods in small, forested streams

Method	Points/day ^a	Points/m ²	Relative cost	Uncertainty (m), xy (z) ^b	Coverage
Survey level	10 ² -10 ³	<0.5	Low	0.003 (0.003) ^c	Moderate
Laser Rangefinder	10 ² -10 ³	0.5-1	Low	0.2 (0.4) ^c	Moderate
Total station	10 ² -10 ³ +	0.5-1	High	0.003 (0.003) ^c	High
DGPS	10 ² -10 ³ +	0.5-1	High	0.01 (0.02)	High
Base GPS	10 ¹ -10 ² +	0.5-1	Low	5 (10)	Moderate
Pole-mounted camera -GCP	10 ³ -10 ⁴	10-100	Intermediate	0.1 (0.1)	Low
sUAS -no GCP	10 ⁴ -10 ⁵ +	>1000	Intermediate	5 (5)	Moderate
sUAS - GCP	10 ⁴ -10 ⁵ +	>1000	High	0.1 (0.1)	Moderate

^aAssuming a 1000 m² example survey area

^bInstrument uncertainty – true uncertainty will also depend on GCP accuracy

^cAssuming measurement captured at distance of 100 m

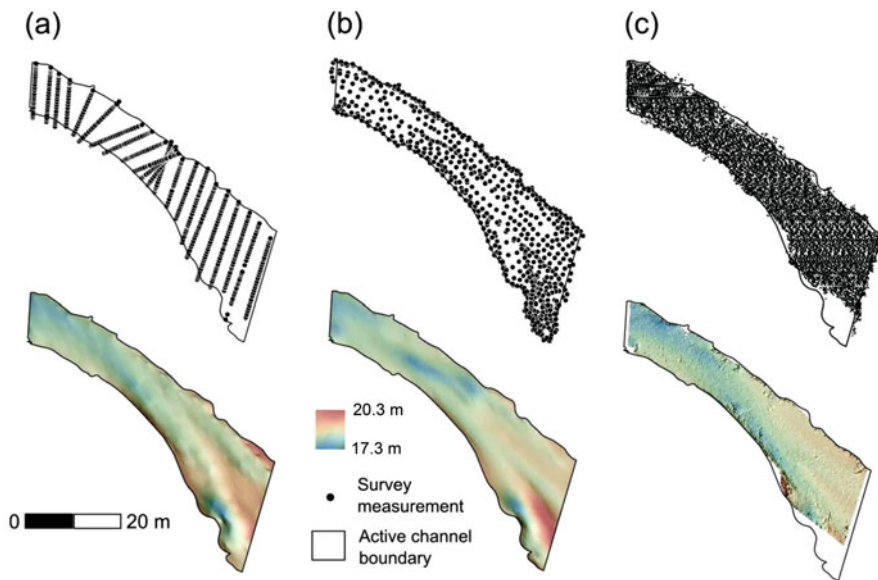


Fig. 11.7 Comparison of survey outcomes for (a) automatic level cross-section survey, (b) total station survey and (c) sUAS survey. Top panels illustrate survey point data, while bottom panels show interpolated surfaces. Note that for (c), data points have been sub-sampled by a factor of 1000 for illustration purposes, and areas with no points indicate regions where data collection was not possible due to dense vegetation or other sightline obstructions

high cost (differential GPS). Relative to traditional survey methods, sUAS are capable of capturing a much greater number of measurement points over space and time. However, for precise surveys, GCPs are required, which add time and cost to the survey. For this reason, the sUAS-GCP combination becomes expensive relative to some options. This cost can be mitigated, however, if permanent GCPs can be installed in locations where repeat surveys are desired. For sub-canopy data collection, sUAS surveys without GCPs are mainly useful for qualitative evaluations of channel areas; detailed comparisons or measurements are difficult without accurate georeferencing given the small field of view afforded by low-elevation flights. Recent work demonstrating the potential for sUAS-derived change detection without control points (Cook and Dietze 2019) may prove useful in sub-canopy environments if a sufficiently large field of view can be obtained.

In addition to cost, survey point density and measurement uncertainty, achievable survey coverage is an important consideration. While all methods outlined in Table 11.1 are limited by sight line obstructions, total station and DGPS methods are capable of capturing data in regions somewhat obscured by vegetation, as stadia rod positioning and elevation can be changed with a total station survey, and DGPS rover positioning is tolerant of mild line-of-sight obstructions. In contrast, sUAS imagery is not capable of capturing surface elevation values when dense vegetation is present within a few meters of the ground, or when streamflow is opaque and the channel bed is obscured. This is mainly a limitation when capturing stream bank topography, which is necessary for undertaking hydrodynamic modeling or for assessing changes in channel topography in detail. Stream banks may be densely vegetated, and photogrammetric software is unable to resolve small exposed ground areas. For these features, more flexible ground-based methods remain superior for capturing topography.

11.5 Present Limitations of Sub-canopy sUAS Flights

Sub-canopy sUAS surveys provide a flexible, low cost, and relatively rapid method of capturing detailed information on forested channels which are often challenging to survey with alternative methods. However, in order for them to serve as a complete replacement for existing methods, several limitations need to be overcome. First, low-elevation vegetation, such as shrubs or small trees, still obscures ground areas during sub-canopy flights, particularly along channel margins. Oblique imagery is helpful here, but only if vegetation is sufficiently elevated above the ground surface. Presently, additional survey instrumentation is needed to capture these obscured regions in detail. Similarly, other features of small, forested streams, such as large logjams or overhanging logs, may obscure channel areas. However, it is often difficult to survey bed areas under logjams using any method, and traditional survey approaches may not offer a substantial advantage.

An ongoing challenge with low-elevation flights over water is that prop-wash from the sUAS can disturb the water surface, rendering submerged areas difficult to

resolve during image analysis. This is especially noticeable with larger consumer-grade sUASs (such as the DJI Phantom series), and the use of lighter sUAS should help reduce downdraft.

As with all imagery-based data collection approaches, submerged bed areas remain difficult to characterize if water is deep or opaque. While capturing submerged bed 359 topography with consumer-grade sUAS is likely to pose a challenge in the near term, new Lidar-based sUAS data collection methods may present a solution even in 361 systems with partially opaque streamflow (Mandlbürger et al. 2020).

11.6 Example of Application

11.6.1 Channel Survey of Carnation Creek, B.C.

This section describes an example application of sub-canopy sUAS flights, where a detailed stream channel survey was undertaken along a 3 km section of densely forested channel. The purpose of this study was to develop and test a method to map and characterize channel unit morphology over large areas using sUAS imagery. For this chapter, however, the focus of the example is on the data collection and resulting survey products.

This work was undertaken along a portion of Carnation Creek, a forested stream located on coastal Vancouver Island, B.C. (Fig. 11.8). The channel mainstem is approximately 8 km long and has a drainage area of 11.2 km² (Tschaplinski and Pike 2017; Reid et al. 2019). The focus of research is along the lowermost 3 km of the channel, which possesses a gradient of 0.5–1% and is dominated by a pool-riffle channel morphology. The average bankfull channel width (w_b) is close to 15 m. The channel is located within the Coastal Western Hemlock Biogeoclimatic Zone, common along coastal British Columbia (Hartman et al. 1982). The environment is typical of the Pacific Northwest: precipitation rates are high and dominated by rain (between 2900 and 5000 mm/year), the majority of which falls during the autumn and winter months (Tschaplinski and Pike 2017). Visual estimates suggest that over 50% of the channel is hidden below a forest canopy composed of both coniferous and deciduous tree species, and a dense understory of ferns and shrubs is also present. The height of the riparian canopy is variable, ranging between 15 and 40 m.

11.6.1.1 Survey Approach

During the survey, 3.0 km of channel was flown with a sUAS beneath the forest canopy in July 2018, with coverage beginning near the river mouth (Fig. 11.8). An additional section was surveyed approximately 5.6 km upstream, corresponding to an existing survey site.

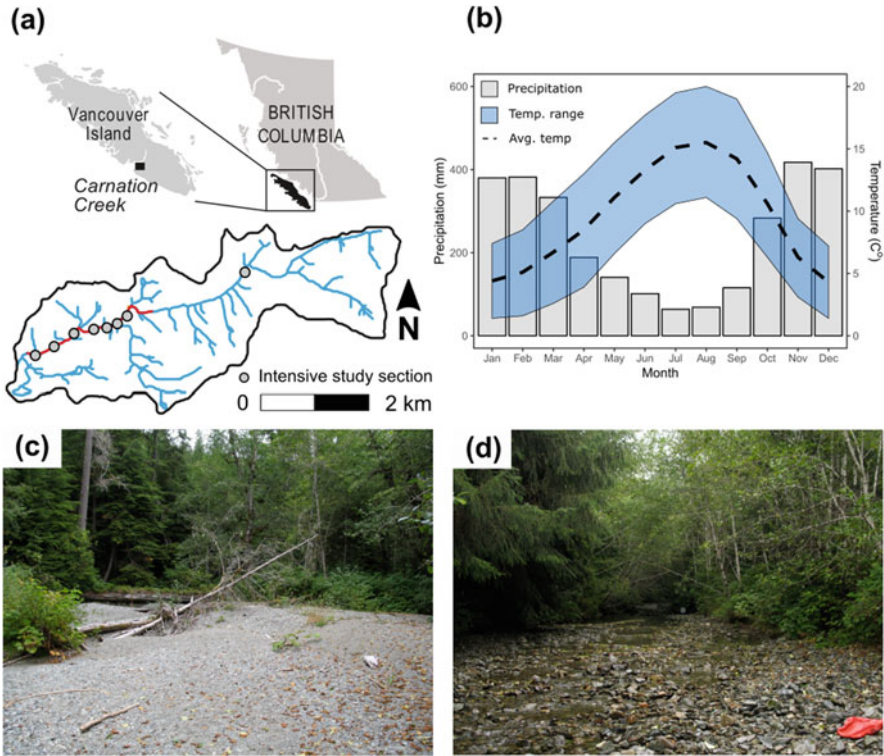


Fig. 11.8 (a) Location of the Carnation Creek study watershed. Red line indicates extent of sUAS survey, while grey circles indicate locations of intensive study segments, ascending from SA2 downstream to SA9 upstream; (b) temperature and precipitation summary for the Carnation Creek watershed; (c) example image highlighting a relatively open channel section with minimal canopy cover; (d) example image of a channel section with a relatively dense and low elevation canopy

The sUAS survey involved low-level flights (5–15 m above ground level) conducted in tandem with placement of ground control points (GCPs) surveyed in with a total station. The flights were undertaken with a DJI Phantom 4 Advanced sUAS, a consumer-grade sUAS with a camera with a focal length of 8.8 mm (24 mm in 35 mm format equivalent) and a field of view of 84°. The sUAS also possessed multi-directional obstacle avoidance and vision systems. During flight, it was necessary to disable obstacle avoidance in order to pass within smaller-than-allowable distances of trees and other vegetation. Each sUAS battery provided 25 min of flight time, and to maximize efficiency during fieldwork, a portable generator was used to charge batteries on-site.

Images were acquired at 2-second intervals while moving at approximately 1 m/s horizontal velocity. The 3.0 km of channel was divided into roughly 80 segments, covered by 300–1000 photos each. Each segment was first flown using flight lines parallel to the channel direction, with imagery collected at 90° relative to the bed

plane. Segments were then flown again with oblique and convergent imagery (as in Fig. 11.2) to improve coverage near bank areas.

At least ten GCPs were placed in each of the 80 channel segments with additional checkpoints positioned to assess the accuracy of corrected survey outputs. All GCPs and checkpoints were surveyed with a Leica TPS 1100 total station, and surveyed points were tied into benchmarks previously established along the channel. GCP precision was typically 2 cm in the XY-plane and 1 cm in the Z-plane. Following suggested approaches in recent literature (Harwin et al. 2015; Agüera-Vega et al. 2016; Sanz-Ablanedo et al. 2018), the majority of the GCPs were distributed on dry exposed bars along the periphery of the channel, with a smaller number situated towards the centre. Checkpoints were distributed as evenly as possible across all channel areas, including submerged areas. When two workers were on site, both would survey in GCPs, and then one would undertake the flight. If three people were available, two would survey GCPs, and one would fly the sUAS at the same time.

In order to characterize bed sediment texture, sampling areas were demarcated with fluorescent orange markers to enable identification in post-processed imagery. Once these regions had been demarcated, the sUAS was flown at the usual elevation and also hovered 2 m above the site to provide imagery suitable for photo-sieving analysis, i.e. extraction of grain size information from images (Tamminga et al. 2015).

11.6.1.2 Data Processing

Channel elevation, bathymetry and grain size data were extracted from the sUAS imagery. Using Agisoft (now called Metashape) PhotoScan Professional to generate georeferenced dense point clouds, digital elevation models of the channel were produced. As described in Sect. 11.3, the Cloth Simulation Filter (Zhang et al. 2016) function of CloudCompare was employed to remove the influence of vegetation during the DEM construction process. A cloth resolution of 0.1 m and maximum ground sample distance of between 0.5 and 1.0 m were found to adequately filter the bed points.

To adjust elevation in submerged channel areas, the refraction-correction approach described by Dietrich (2017) was used. Streamflow was less than $0.1 \text{ m}^3\text{s}^{-1}$ and clear during the survey, enabling an unobstructed view of the channel bed. Removal of overhanging vegetation using the Cloth Simulation Filter in CloudCompare and subsampling the DEMs to a spacing of 0.02 m using the minimum elevations in the point cloud helped ensure that the refraction correction was based on channel bed points and not on overhanging vegetation points that may have been incorporated in the point cloud.

To generate predictive maps of bed surface sediment texture, a relationship between the roughness of the point cloud for 22 training sites and their median grain size (D_{50}) was established using the approach described by Woodget and Austrums (2017) as determined through photo-sieving analysis. Using an in-house photo-sieving program based in MATLAB, the grain size distribution of each

training site was determined and then related to the corresponding point cloud roughness. A moving window analysis was then used to estimate grain size across the exposed bed to generate continuous maps of D_{50} .

11.6.1.3 Results and Discussion

To assess survey accuracy, channel-averaged vertical survey error was estimated by calculating the root-mean-square-error (RMSE) and the mean error (ME) of differences between the elevations of the total station-surveyed checkpoints and those estimated from the DEMs. Vertical errors for dry bar areas were found to be 0.093 m and 0.025 m for the RMSE and ME, respectively ($n = 1203$), while slightly greater error values were obtained for the submerged bed points (RMSE = 0.11 m, ME = 0.025 m, $n = 521$). While these errors are larger than those obtained from a total station, they are within the typical range of grain sizes found on the channel bed and are likely sufficient to enable year-to-year comparisons. Factors such as shadows from the riparian vegetation and reflections from the canopy may have influenced the success of the refraction correction (Dietrich 2017), leading to slightly higher errors in submerged areas.

The sUAS survey performance was also evaluated through a comparison of known channel boundaries previously surveyed in Carnation Creek. A detailed description of these channel sections can be found in Reid et al. (2019), with example comparison maps shown for four sites in Fig. 11.9 and summarized for all sites in Table 11.2. These channel sections range in complexity from simple, relatively open single-thread reaches (Fig. 11.9a, b) to sections with dense vegetation, log jams and narrow side channels (Fig. 11.9c, d). When including side channels (such as in Fig. 11.9c), which were generally difficult to access with the sUAS, survey coverage slightly exceeded 80%. When narrow side channels are excluded, coverage increases to 87%. When examining individual study sections that contained side channels, coverage ranged from a low of 54% to a high of 89% and exceeded 94% when side channels were absent (Table 11.2). Generally, narrow (width < 3 m) side channels could not be effectively surveyed unless they were free of low elevation (height < 3 m) vegetation, but oblique imagery was advantageous in situations where a clear flight path was present alongside an obscured channel area. Similarly, bank top elevations were difficult to capture in most locations due to understory vegetation obscuring the ground surface. The inclusion of bathymetric calibration greatly increased the area over which bed topography could be estimated, as 20–40% of bed area in most sites was submerged.

To illustrate the detailed and spatially continuous data collection capacity of the sUAS along Carnation Creek, D_{50} , hydraulic radius (R_h , calculated as cross-sectional channel area divided by wetted perimeter length) and channel slope are shown along the full survey extent in Fig. 11.10. Small-scale spatial variability is apparent for all variables, with fluctuations in D_{50} , R_h , and gradient reflecting different unit morphologies found along the channel. D_{50} (Fig. 11.10a) gradually increases in an upstream direction, followed by a rapid increase beyond 3 km.

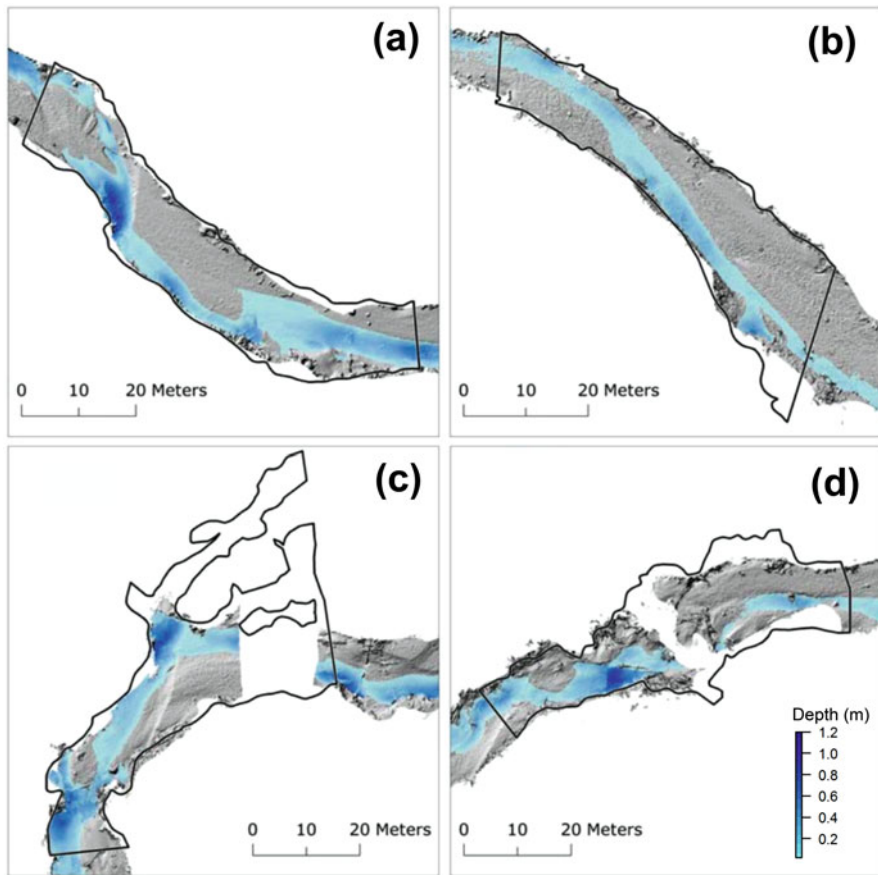


Fig. 11.9 Example comparison maps between sUAS-derived surfaces and total-station-based perimeters of active channel areas for two Carnation Creek study sections illustrating good sUAS coverage (a and b) and two with relatively poor coverage (c and d) resulting from dense low-elevation vegetation and other flight obstructions close to the channel

Hydraulic radius (Fig. 11.10b) decreases gradually in an upstream direction, with the lowest values found in the vicinity of the coarsest sediment. Further insight can be gained in channel pattern by examining slope (Fig. 11.10c), which fluctuates between 0.5% and 1.5% until beyond 3 km when it increases to more than 3%, again reflecting a change in morphology. A key benefit of the detailed mapping potential of sUAS imagery is shown in Fig. 11.11. In forested channels, sediment texture often varies over short distances as a result of wood obstructions (Montgomery et al. 2003) rendering traditional sediment sampling and widespread channel characterization efforts difficult. While coverage gaps are still present with sUAS data collection, the ability to capture detailed spatial variation provides a significant advantage over alternative survey approaches. Overall, the results of the Carnation Creek sUAS survey demonstrate many of the strengths and weaknesses of

Table 11.2 sUAS survey coverage comparison in Carnation Creek

Study section	Length (m)	Width (m)	TS points/m ^{2a}	sUAS coverage % (all) ^b	sUAS coverage % (main channel) ^c
SA-2	82	13.8	0.51	90	90
SA-3	68	19.6	0.72	83	83
SA-4	62	21.2	0.69	54	74
SA-5	75	13.7	0.61	81	84
SA-6	70	14.9	0.70	91	91
SA-7	51	19.6	0.63	67	79
SA-8	58	16.9	0.40	94	94
SA-9	148	11	1.04	89	99
Average			0.69	81	87

^aBased on 2015 total station feature-based survey

^bIncludes comparison to total-station surveyed side channels

^cExcludes comparison to total-station surveyed side channels

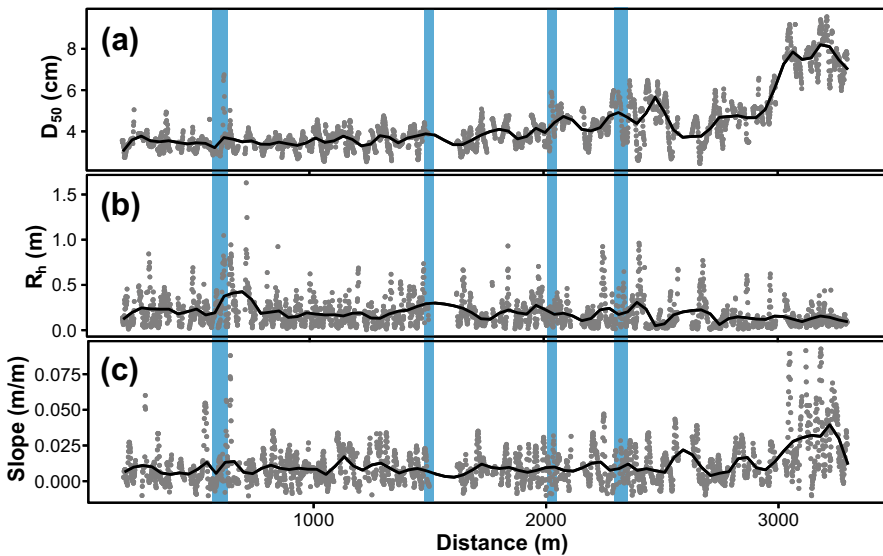


Fig. 11.10 Cross-section averaged series of (a) median grain size (D_{50}), (b) hydraulic radius (R_h) and (c) water surface slope derived from sUASimagery. Grey points illustrate each cross-section average, while the black line represents a smoothed fit to the data. Blue bands correspond to comparative study-sections, outlined in Fig. 11.9

the approach applied in a small, forested stream. This work highlights the potential for detailed data collection over a large area and several ongoing challenges which, if resolved, would provide a 10–20% improvement in survey coverage. The key strength of the sUAS approach is that data on many variables can be collected concurrently, including topography, bathymetry and grain size. Collectively, the

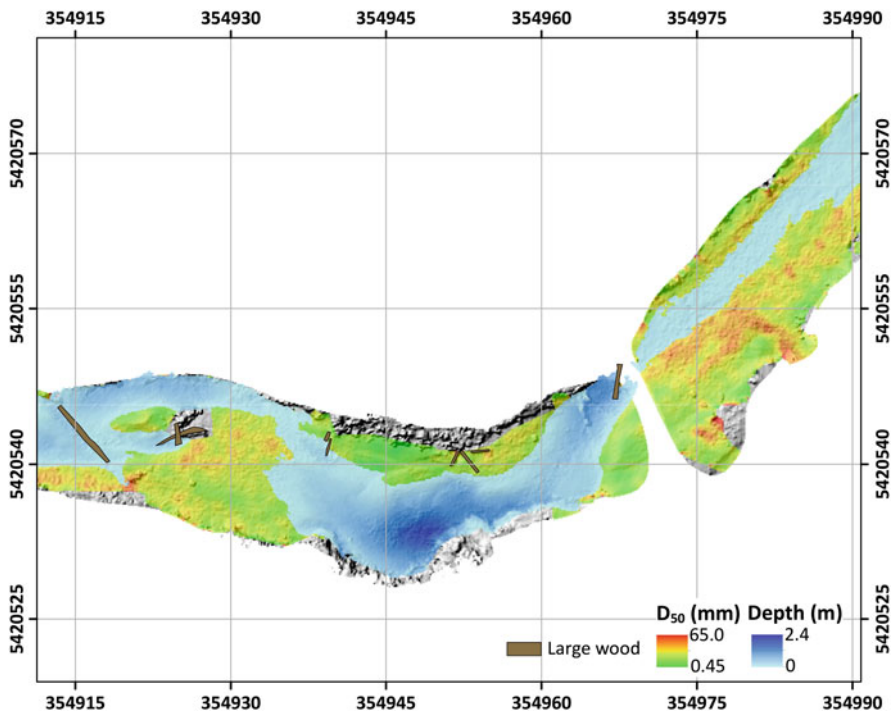


Fig. 11.11 Example channel section displaying median grain size (D_{50}) predicted from channel bed roughness

ability to acquire detailed concurrent data on many variables presents a powerful advantage in sUAS systems.

Currently, the need to mark GCPs adds either substantial time or personnel requirements to surveys when large areas are to be flown at low elevation. When three people were available to assist with data collection, the rate of survey progress was quite rapid, and if permanent GCPs were installed, repeat surveys would require only one person and would be much faster than traditional survey alternatives. It is also worth noting that time saved in the field with the Carnation Creek sUAS survey was countered by an increase in data processing time and computing requirements relative to traditional survey data. However, distributed computing and improved SfM software are helping to reduce this requirement.

While this chapter section focused mainly on data collection and processing, further analysis with the data collected here can be found in Helm et al. (2020). Many researchers have similarly capitalized on the sUAS data collection advantages in larger or less view-obstructed systems to provide a comprehensive understanding of river processes or change over time (Tamminga et al. 2015; Piégay et al. 2020), and the future of sUAS as standard data collection instruments along forested channels appears promising.

11.7 Future Opportunities

Several promising advances in sUAS appear likely to improve survey outcomes in small streams. A current limitation of sUAS work beneath forest canopies or in confined environments is that automated flights are not practical, as small branches and vegetation pose a hazard to flight but are difficult for many sUAS to detect and avoid.

If pre-programmed flight paths can be followed, then the pilot may be able to assist with other tasks related to data collection and improve survey efficiency. Second, built-in RTK systems are now available on consumer-grade sUAS, with listed vertical and horizontal survey precision specifications of less than 10 cm. While this type of accuracy may be difficult to achieve in forested channels located in valley bottoms with limited sky view, the potential of eliminating the need for ground control points renders this new sUAS technology appealing. New methods are also becoming available to detect characteristics of in-stream wood (Sanhueza et al. 2019), water velocity and bed roughness (Bandini et al. 2020) and water quality, including temperature (Koparan et al. 2020). This can provide additional information and a more holistic view of habitat conditions which are particularly relevant if hydrodynamic modeling is to be undertaken.

11.8 Concluding Remarks

Forested streams with closed canopies have presented a challenge for researchers and managers aiming to characterize key aspects of river topography and aquatic habitat. This chapter has aimed to describe the role that sUAS survey approaches can play in advancing research and improving data collection in small streams located in forested areas, with application to other areas where confined flying environments are a challenge for conducting sUAS surveys.

By applying several techniques described in this chapter, such as oblique image capture and careful structure-from-motion post-processing, the use of sUAS in small, closed-canopy streams to capture river topography, bathymetry and grain size information is possible and can provide results comparable to or better than many traditional survey methods. While several limitations remain in the application of sUASs for stream survey applications, advances in sUAS capability will help reduce the ongoing dependency on other survey instrumentation needed to conduct full channel surveys.

Acknowledgements The authors wish to thank Conor McDowell for providing data and helpful feedback on aspects of data processing, while Steve Voller and Andrew Westerhof helped with field logistics at Carnation Creek. We are grateful to two reviewers for their suggestions, which improved the chapter.

References

- Agüera-Vega F, Carvajal-Ramirez F, Martínez-Carricondo P (2016) Accuracy of digital surface models and orthophotos derived from unmanned aerial vehicle photogrammetry. *J Surv Eng* 143(2):4016,025. [https://doi.org/10.1061/\(asce\)su.1943-5428.0000206](https://doi.org/10.1061/(asce)su.1943-5428.0000206)
- Bandini F, Lüthi B, Peña-Haro S, Borst C, Liu J, Karagkiolidou S, Hu X, Lemaire GG, Bjerg PL, Bauer-Gottwein P (2020) A drone-borne method to jointly estimate discharge and Manning's roughness of natural streams. *Water Resour Res* 57. <https://doi.org/10.1029/2020WR028266>
- Bird S, Hogan D, Schwab J (2010) Photogrammetric monitoring of small streams under a riparian forest canopy. *Earth Surf Process Landf* 35(8):952–970. <https://doi.org/10.1002/esp.2001>
- Carbonneau PE, Lane SN, Bergeron NE (2004) Catchment-scale mapping of surface grain size in gravel bed rivers using airborne digital imagery. *Water Resour Res* 40(7):1–11. <https://doi.org/10.1029/2003WR002759>
- Carbonneau P, Fonstad MA, Marcus WA, Dugdale SJ (2012) Making riverscapes real. *Geomorphology* 137(1):74–86. <https://doi.org/10.1016/j.geomorph.2010.09.030>
- Carrivick JL, Smith MW (2019) Fluvial and aquatic applications of Structure from Motion photogrammetry and unmanned aerial vehicle/drone technology. *Wiley Interdiscip Rev Water* 6(1):e1328. <https://doi.org/10.1002/wat2.1328>
- Cook K (2017) An evaluation of the effectiveness of low-cost UAVs and structure from motion for geomorphic change detection. *Geomorphology* 278:195–208
- Cook KL, Dietze M (2019) Short Communication: a simple workflow for robust low-cost UAV-derived change detection without ground control points. *Earth Surf Dyn* 7(4):1009–1017. <https://doi.org/10.5194/esurf-7-1009-2019>
- Dietrich JT (2017) Bathymetric structure-from-motion: extracting shallow stream bathymetry from multi-view stereo photogrammetry. *Earth Surf Process Landf* 42(2):355–364. <https://doi.org/10.1002/esp.4060>
- El Ashrey M, Wanless H (1967) Shoreline features from their changes. *Photogramm Eng* 33:184–189
- Hamshaw SD, Engel T, Rizzo DM, O'Neil-Dunne J, Dewoolkar MM (2019) Application of unmanned aircraft system (UAS) for monitoring bank erosion along river corridors. *Geomat Nat Haz Risk* 10(1):1285–1305. <https://doi.org/10.1080/19475705.2019.1571533>
- Hartman GF, Andersen BC, Scrivener JC (1982) Seaward movement of coho salmon (*Oncorhynchus kisutch*) fry in Carnation Creek, an unstable coastal stream in British Columbia. *Can J Fish Aquat Sci* 39(4):588–597. <https://doi.org/10.1139/f82-083>
- Harwin S, Lucieer A, Osborn J (2015) The impact of the calibration method on the accuracy of point clouds derived using unmanned aerial vehicle multi-view stereopsis. *Remote Sens* 7(9):11,933–11,953. <https://doi.org/10.3390/rs70911933>
- Hassan MA, Church M, Lisle TE, Brardinoni F, Benda L, Grant GE (2005) Sediment transport and channel morphology of small, forested streams. *J Am Water Resour Assoc* 97331:853–876
- Hassan M, Bird S, Reid D, Ferrer-Boix C, Hogan D, Brardinoni F, Chartrand S (2019) Variable hillslope-channel coupling and channel characteristics of forested mountain streams in glaciated landscapes. *Earth Surf Process Landf* 44:736–751. <https://doi.org/10.1002/esp.4527>
- Helm C, Hassan MA, Reid D (2020) Characterization of morphological units in a small, forested stream using close-range remotely piloted aircraft imagery. *Earth Surf Dyn* 8(4):913–929. <https://doi.org/10.5194/esurf-8-913-2020>
- James MR, Robson S (2014) Mitigating systematic error in topographic models derived from UAV and ground-based image networks. *Earth Surf Process Landf* 39(10):1413–1420. <https://doi.org/10.1002/esp.3609>
- Javernick L, Brasington J, Caruso B (2014) Modeling the topography of shallow braided rivers using Structure-from-Motion photogrammetry. *Geomorphology* 213:166–182. <https://doi.org/10.1016/j.geomorph.2014.01.006>
- Koparan C, Koc AB, Sawyer C, Privette C (2020) Temperature profiling of waterbodies with a uav-integrated sensor subsystem. *Drones* 4(3):1–10. <https://doi.org/10.3390/drones4030035>

- Legleiter CJ (2012) Remote measurement of river morphology via fusion of LiDAR topography and spectrally based bathymetry. *Earth Surf Process Landf* 37(5):499–518. <https://doi.org/10.1002/esp.2262>
- Lejot J, Delacourt C, Piegay H, Fournier T, Tremelo M-L, Allemand P (2007) Very high spatial resolution imagery for channel bathymetry and topography from an unmanned mapping controlled platform. *Earth Surf Process Landf* 34(March):1705–1725. <https://doi.org/10.1002/esp>
- Mandlburger G, Pfennigbauer M, Schwarz R, Flöry S, Nussbaumer L (2020) Concept and performance evaluation of a Novel UAV-Borne Topo-Bathymetric LiDAR sensor. *Remote Sens* 12(6). <https://doi.org/10.3390/rs12060986>
- Meinen BU, Robinson DT (2020) Streambank topography: an accuracy assessment of UAV-based and traditional 3D reconstructions. *Int J Remote Sens* 41(1):1–18. <https://doi.org/10.1080/01431161.2019.1597294>
- Montgomery DR, Buffington JM (1997) Channel-reach morphology in mountain drainage basins. *Bull Geol Soc Am* 109(5):596–611. [https://doi.org/10.1130/0016-7606\(1997\)109<0596:CRMIMD>2.3.CO](https://doi.org/10.1130/0016-7606(1997)109<0596:CRMIMD>2.3.CO)
- Montgomery D, Collins B, Buffington JM, Abbe TB (2003) Geomorphic effects of wood in rivers. *Am Fish Soc Symp* 37:1–28
- Müller T, Hassan M (2019) Identifying surface grain size distributions from images using computer vision and machine learning methods, in AGU Fall. Meet Abst 2019:EP54C-13
- Piégay H, Arnaud F, Belletti B, Bertrand M, Bizzi S, Carbonneau P, Dufour S, Liébault F, Ruiz-Villanueva V, Slater L (2020) Remotely sensed rivers in the Anthropocene: state of the art and prospects. *Earth Surf Process Landf* 45(1):157–188. <https://doi.org/10.1002/esp.4787>
- Reid DA, Hassan MA (2020) Response of in-stream wood to riparian timber harvesting: field observations and long-term projections. *Water Resour Res* 56(8):1–17. <https://doi.org/10.1029/2020WR027077>
- Reid DA, Hassan M, Bird S, Hogan D (2019) Spatial and temporal patterns of sediment storage over 45 years in Carnation Creek, B.C., a previously glaciated mountain catchment. *Earth Surf Process Landf* 44:1584–1601. <https://doi.org/10.1002/esp.4595>
- Roncoroni M, Lane S (2019) A framework for using small Unmanned Aircraft Systems (sUASs) and SfM photogrammetry to detect salmonid redds. *Eco Inform* 53(100):976
- Sanhueza D, Picco L, Ruiz-Villanueva V, Iroumé A, Ulloa H, Barrien-tos G (2019) Quantification of fluvial wood using UAVs and structure from motion. *Geomorphology* 345(106):837. <https://doi.org/10.1016/j.geomorph.2019.106837>
- Sanz-Ablanedo E, Chandler JH, Rodríguez-Pérez JR, Ordóñez C (2018) Accuracy of Unmanned Aerial Vehicle (UAV) and SfM photogrammetry survey as a function of the number and location of ground control points used. *Remote Sens* 10(10):1606. <https://doi.org/10.3390/rs10101606>
- Tamminga A, Hugenholtz C, Eaton B, Lapointe M (2015) Hyperspatial remote sensing of channel reach morphology and hydraulic fish habitat using an Unmanned Aerial Vehicle (UAV): a first assessment in the context of river research and management. *River Res Appl* 31:379–391
- Tauro F, Petroselli A, Arcangeletti E (2016) Assessment of drone-based surface flow observations. *Hydrol Process* 30(7):1114–1130. <https://doi.org/10.1002/hyp.10698>
- Tomsett C, Leyland J (2019) Remote sensing of river corridors: a review of current trends and future directions. *River Res Appl* 35(7):779–803. <https://doi.org/10.1002/rra.3479>
- Tschaplinski PJ, Pike RG (2017) Carnation Creek watershed experiment—long-term responses of coho salmon populations to historic forest practices. *Ecology* 98(2). <https://doi.org/10.1002/eco.1812>
- Wackrow R, Chandler JH (2011) Minimising systematic error surfaces in digital elevation models using oblique convergent imagery. *Photogramm Rec* 26(133):16–31. <https://doi.org/10.1111/j.1477-9730.2011.00623.x>
- Watanabe Y, Kawahara Y (2016) UAV photogrammetry for monitoring changes in river topography and vegetation. *Procedia Eng* 154:317–325. <https://doi.org/10.1016/j.proeng.2016.07.482>

- Wohl E (2017) The significance of small streams. *Front Earth Sci* 11(3):447–456. <https://doi.org/10.1007/s11707-017-0647-y>
- Wolman MG (1954) A method of sampling coarse river-bed material. *Trans Am Geophys Union* 35(6):951. <https://doi.org/10.1029/TR035i006p00951>
- Woodget AS, Austrums R (2017) Subaerial gravel size measurement using topographic data derived from a UAV-SfM approach. *Earth Surf Process Landf* 42(9):1434–1443. <https://doi.org/10.1002/esp.4139>
- Woodget AS, Austrums R, Maddock IP, Habit E (2017) Drones and digital photogrammetry: from classifications to continuums for monitoring river habitat and hydromorphology. *Wiley Interdiscip Rev Water* 4(4):e1222. <https://doi.org/10.1002/wat2.1222>
- Zhang W, Qi J, Wan P, Wang H, Xie D, Wang X, Yan G (2016) An easy-to-use airborne LiDAR data filtering method based on cloth simulation. *Remote Sens* 8(6):1–22. <https://doi.org/10.3390/rs8060501>

Index

A

Above ground level (AGL), 18, 27, 134, 237, 245, 306, 316
Aeolian, 264, 265, 270–277, 280, 292
Aerial surveillance, 160
Aerosondes, 238, 247
Agisoft Metashape, 46, 76, 99, 134, 138, 139, 209, 216, 220, 223, 309
Alaska Center for UAS Integration, 247
Albedo, 26, 247, 252, 253
Alignment, 127, 130, 132, 138–141, 149, 150, 209, 215
Altitude, 2, 4, 75, 76, 86, 88, 98, 125–127, 134, 141, 146, 160, 163, 168, 209, 213, 215, 220, 223, 224, 226, 237, 240, 248, 250, 272, 286
Antarctic, 236, 245, 250, 253, 254
Antarctic Treaty Consultative Meetings (ATCM), 253
ArcGIS, 102, 163, 166, 187, 191, 209, 212, 266
Archaeology, 73, 75, 89
Arctic, 235, 236, 238, 240, 245, 247, 248, 251–254
Arctic Monitoring and Assessment Programme (AMAP), 251, 253, 254
Arctic Research Consortium of the United States (ARCUS), 238
Atmosphere, 236, 241, 246, 247, 252, 254
Austria, 207, 218, 219, 222
Autonomous flight software, 124
Autonomous underwater vehicle (AUV), 9
Autopilot, 125, 134

B

Bathymetry, 10, 302, 306–311, 317, 320, 322

C

Camera angle, 22, 98, 124–128, 134, 144, 146, 152, 153, 306
Change detection, 28, 31, 124, 205, 206, 218, 221–224, 226, 302, 314
Channel, 72, 74, 79, 81, 84, 130, 132, 135, 152, 153, 217, 268, 302–304, 306, 307, 309–312, 314–322
Channel morphology, 132, 302, 315
Channel survey, 304, 315
Check points, 128, 216, 305, 317
Citizen science, 6, 7, 42, 46–49, 53–67, 292
Civil engineering, 75
Climate change, 8, 72, 74, 88, 89, 177, 246, 255, 264, 291, 292
Climatology, 2, 32, 48, 67, 73, 75
CloudCompare, 101, 102, 112, 219, 221, 310
Coastal, 7, 8, 45, 46, 64–66, 72–75, 81–83, 85–89, 97, 159, 160, 181, 205, 264–266, 268–270, 272, 275–282, 284, 285, 291, 292, 315
Coastal erosion, 7, 66, 72, 74, 77, 88, 89, 278
Coastal geography, 65
Coastal wetlands, 7, 75, 77, 78, 85, 86, 88, 89
Committee for Environmental Protection (CEP), 253
Council of Managers of National Antarctic Programs (COMNAP), 253, 254

Course angle, 128, 134, 135
 Cryosphere, 8, 236, 237, 241, 249, 250, 254, 291
 Cultural resource management, 89
 Cultural resources, 73, 74, 89, 90

D

Da-Jiang Innovations (DJI), 9, 18, 22, 76, 88, 134, 163, 167–169, 181, 216, 220, 223, 237, 245, 246, 315, 316
 Delta, 72, 83, 85, 268
 Deltaic plain, 72, 73, 89
 DEM of Difference (DoD), 206, 208–210, 212–214, 226, 228
 Dense cloud, 141, 151, 215
 Deposition, 83–85, 88, 218, 225, 253, 265, 270, 271, 275, 278, 280, 281, 289
 Digital elevation models (DEM), 7, 66, 75, 87, 103, 114–116, 119, 120, 127, 128, 207, 209, 214, 215, 217, 219, 222, 226, 307, 309, 310, 317
 Digital surface model (DSM), 7, 30, 32, 33, 100, 101, 104, 124, 129, 141, 151–153, 220, 241, 242, 264, 284, 285, 287–289
 DIY Drones, 254
 Doming, 128, 152, 153
 Drone swarms, 9, 67
 Dune blowouts, 279
 Dune building, 264, 270, 272, 276, 277, 292
 Dune disturbances, 264, 292
 Dune recovery, 278
 Dune scarps, 277, 278, 286, 288, 289

E

Earthen mounds, 75, 77–79, 82, 86, 87, 175
 Eco-geomorphology, 264, 292
 Education, 88
 Embryo dunes, 276
 Environmental sciences, 36, 95
 Environmental surface inspections, 162
 Erosion, 8, 31, 65, 66, 72, 75–79, 81, 83–85, 89, 158, 171, 173, 190, 204, 205, 217, 218, 220, 223–226, 228, 242, 276–281, 287, 289
 Error reduction, 140

F

Federal Aviation Administration (FAA), 6, 15, 17, 18, 42, 48, 65, 75, 126, 167, 181, 236, 254
 Fixed-wing, 5, 18, 160, 236, 238, 247, 248, 250, 251, 308
 Flight control software, 127, 128, 134

Flight path, 7, 19, 82, 88, 125, 128, 134, 152, 153, 167, 168, 209, 215, 226, 306–308, 318, 322
 Flight plan, 7, 21, 22, 76, 125–128, 134
 Floodplain, 130, 132, 153
 Foredune, 264–268, 270–278, 280, 281, 284–286, 288, 289, 291

G

Geoarchaeology, 74, 88
 Geographic information systems (GIS), 2, 42, 43, 61, 67, 166, 187, 191, 192
 Geography, 2–10, 42–67, 76, 181, 192
 Geology, 43, 75, 207
 Geomorphology, 2, 66, 73–76, 253
 Glaciology, 238, 241–244, 255
 GlobalMapper, 99, 101, 104–112, 114, 116–119
 Global navigation satellite system (GNSS), 3, 5, 125, 129, 137–139, 141, 146, 214, 226, 237, 240, 252
 Global shutter, 134
 Gradual selection, 138, 140, 141, 151
 Grain size, 2, 218, 272, 273, 306, 308, 309, 312, 317, 318, 320–322
 Grasslands, 7, 96, 102, 107, 109, 117, 118, 127, 157–192, 205
 Ground control point (GCP), 24, 125, 128, 129, 136, 137, 168, 209, 211, 213, 215–217, 224, 226, 227, 249, 288, 290, 304–305, 313, 317
 Ground control station, 14, 125, 236
 Ground sampling distance (GSD), 45, 98, 100, 101, 104, 126, 127, 134, 141, 146, 209, 213, 215, 220, 223
 Ground truth calibration, 119, 120
 Gulf of Mexico, 74, 79, 84, 159, 160

H

High latitude drone ecology network, 249, 254
 Human geography, 42
 Hybrid, 225, 236
 Hydroacoustic, 10
 Hyperspectral, 2, 5, 9, 43, 46, 160, 252, 269

I

Image acquisition, 44, 124, 125, 127, 128, 130, 132, 134–136, 146, 153, 222, 306
 Image overlap, 7, 124, 125, 127, 128, 130, 134, 141, 148, 151, 153, 240
 Imagery, 2–5, 7, 9, 10, 14, 17–19, 22, 24, 26, 29–31, 43–46, 48, 58–61, 63–67, 75,

- 87–89, 124–130, 132, 134–146,
149–153, 158–160, 163, 164, 166–170,
172, 177, 181, 186, 187, 189–192, 209,
225, 238, 240, 243–247, 249–252, 255,
268, 269, 272, 278, 291, 302–312,
314–317, 319, 320
- Inertial measurement units (IMUs), 4, 204
- Infrared, 18, 43, 160, 175, 244, 248, 252, 253
- International Conference on Unmanned Aerial
Systems (ICUAS), 254
- International Society for Atmospheric Research
using Remotely piloted Aircraft, 254
- L**
- Land cover, 2, 7, 29–31, 33, 44, 56, 60–62, 103,
245, 252
- Land features, 95–120
- Landsat, 3, 29, 30, 44, 45, 163, 244
- Landslides, 8, 9, 66, 204–212, 215, 216, 218,
225–228, 253
- Land use, 42, 207
- Large-scale, 2, 4, 42, 46, 74, 76, 96, 159,
204–206, 208, 218, 224–226, 228, 251
- Levees, 72, 79, 84
- Level of detection (LoD), 223
- Light Detection and Ranging (LiDAR), 2, 4, 5,
8, 9, 18, 26, 31, 33, 43, 46, 63, 67, 88,
95, 99, 103, 114–116, 119, 120,
204–206, 215, 219–228, 242, 246, 250,
252, 253, 274, 278, 280, 291
- Louisiana, 7, 72–76, 78, 81, 83, 85, 88, 192
- Low altitude, 7, 10, 16, 89, 245
- M**
- Mass movement, 9, 225, 253
- Mean absolute error (MAE), 139, 140,
142–146, 149, 151, 152, 225, 285
- Mission design, 7, 124–153
- Mission planning, 18, 19, 57, 124, 125, 127,
128, 134, 141, 240
- Mississippi River, 72, 74, 84, 85, 89
- Mississippi River Delta (MRD), 72, 74, 75
- Missouri, 7, 96, 97, 125, 130, 132, 158, 163,
165, 190, 192
- Monitoring, 5, 7, 14, 21, 34, 36, 42, 44–47, 49,
57, 59, 64–66, 74, 75, 85, 86, 88, 89,
161, 181, 190, 204, 205, 208, 215–218,
228, 236–238, 242, 245–248, 250,
252–255, 264, 266–270, 272–275,
277–281, 284–291
- Multidisciplinary drifting Observatory for the
Study of Arctic Climate (MOSAIC),
247, 248
- Multirotors, 44, 62, 63, 128, 158, 236, 246, 247,
250, 251
- Multispectral, 3, 16–18, 22, 23, 26, 28–30, 34,
43–46, 63, 64, 75, 87, 88, 245, 249, 252,
253, 268, 269, 272
- N**
- National Science Foundation Office of Polar
Programs, 238
- Native American, 7, 72–75, 82, 84, 88, 89
- Natural hazard, 2, 5, 124, 160
- Negative feedback, 277, 278
- North Dakota, 158, 162, 163, 165, 166, 190,
192, 198
- O**
- Oblique, 22, 30, 78, 82, 85, 87, 128, 134,
143–146, 152, 168, 169, 179, 187, 277,
280, 306, 307, 317, 322
- Oblique imagery, 128, 134, 143, 145, 150, 152,
153, 304, 306–308, 314, 318
- Oceans, 236, 241, 246–248, 252, 253, 286,
291
- Oil and gas (O&G), 7, 8, 84, 158–161, 163,
166, 187–192
- OpenDroneMap (ODM), 99, 101, 309
- Open-source, 7, 46, 99, 101, 104, 119, 292,
310
- Orthogonal, 134, 146, 152
- Orthomosaic, 7, 22, 26, 27, 63, 76, 80, 86, 96,
97, 99–102, 104, 168, 169, 172–175,
179, 181, 183, 184, 186, 187, 209, 211,
219, 222, 241, 242, 264, 266, 268, 269,
273, 274, 289
- P**
- Panchromatic, 3
- Parrot ANAFI, 97
- Permafrost, 8, 237, 241, 242, 246–247, 252
- Photogrammetry, 2, 63, 99, 123–153, 160, 169,
172, 175, 178, 191, 192, 204, 205, 215,
241, 264, 281, 291, 310
- Physical geography, 6, 73, 75
- Pix4D, 46, 98–101, 104–112, 114, 117–119,
216, 286, 309
- Pixel matching errors, 140

- Point cloud, 7, 26, 29–31, 33, 75, 76, 86, 87, 96, 97, 99–102, 104–120, 127, 129, 136, 138, 140, 141, 146, 150, 152, 205, 209, 211, 214, 215, 219–227, 237, 241, 252, 274, 281, 284, 286–289, 309–312, 317, 318
- Point cloud (vegetation) filtering, 211, 213, 222, 225, 284
- Point cloud registration, 101, 102, 224, 225
- Point density, 104, 106, 107, 110–112, 114, 117–119, 141, 152, 215, 220, 221, 223–225, 284, 288, 289, 314
- Polar, 8, 235–238, 240–242, 244, 247, 249–251, 254, 255
- Pole aerial photography (PAP), 7, 180, 186, 187, 192
- Policy, 6, 8–10, 14–36, 42, 255
- Positive feedback, 270, 271
- Post-processed kinematic (PPK), 3, 5, 24, 240
- Projection accuracy, 140
- Q**
- Quality assessment, 48
- R**
- Radar, 160, 242, 252, 253
- Real-time kinematic (RTK), 3, 5, 24, 86, 240, 322
- Reconnaissance, 7, 16, 61, 73, 75, 76, 85, 89, 240
- Remote pilot certification, 6
- Remote sensing, 10, 42, 45–46, 64, 65, 67, 73, 159, 160, 189, 205, 217, 224, 251, 255, 303
- Reprojection error, 140
- Resolution, 2–4, 7, 8, 10, 14, 16, 24, 27–31, 43–48, 59–61, 67, 75, 86, 87, 95, 96, 98, 100, 101, 104, 105, 118, 126, 134, 141, 142, 146, 153, 163, 164, 179–181, 188, 206, 208–211, 214, 215, 219, 226, 240, 242, 243, 245–247, 252, 255, 269, 272, 273, 275, 291, 292, 310, 317
- Restricted flight, 4, 15, 16, 20, 307
- Riparian, 8, 132, 153, 302, 306, 308, 309, 315, 318
- Root mean square error (RMSE), 101, 102, 105, 106, 117, 126, 139, 140, 142–146, 149, 151, 152, 213, 216, 220, 223–225, 281, 285, 288, 289, 318
- S**
- Salt spray, 264–266
- Satellite, 2–4, 14, 19, 29, 30, 43–46, 67, 87, 163, 238, 240, 242, 244–247, 249, 251, 252, 255, 291
- Scientific Committee for Oceanographic Aircraft Research (SCOAR), 254
- Scientific Committee on Antarctic Research (SCAR), 253
- Sea ice, 235, 238, 241, 243, 247, 248, 252, 267, 292
- Sea level rise, 243, 264, 267
- Shadows, 4, 22, 35, 130, 140, 146, 151, 179, 184, 240, 242, 318
- Shell midden, 75, 79, 82, 83, 86, 87, 89
- Shoreline, 65, 74–77, 79, 81–85, 265–267, 291, 292
- Shortwave infrared (SWIR), 3
- Slow-moving, 79, 136, 204–208, 215, 216, 226, 228
- Small unoccupied aerial systems (sUAS), 2–10, 14, 15, 17, 18, 20, 24–27, 29, 31, 33, 35, 36, 49, 72–90, 95, 96, 98, 120, 124–153, 192, 235–255, 264–292, 301–322
- Small unoccupied aerial vehicles (sUAVs), 158–160, 163, 186, 187, 189, 191, 192
- Snow, 207, 214, 228, 240–243, 250, 252, 255
- Soil erosion, 8, 204, 206, 222, 225–228
- Sparse cloud, 140, 141, 215
- Storm impacts, 277, 278, 281
- Storm surge, 74, 78, 79, 81, 83, 84, 86, 88, 89, 272, 278
- Streams, 130–132, 140, 152, 153, 243, 267, 268, 302–305, 308–315, 320, 322
- Structure from motion (SfM), 14, 32, 95, 241, 264, 274, 281, 287, 288, 291
- Sub-canopy, 303, 304, 306, 314, 315
- Subsidence, 7, 72, 74–76, 79, 83, 84, 86, 88, 89, 206, 224
- T**
- Terrain, 3, 35, 86, 88, 95, 100, 124, 125, 127, 128, 130, 132, 148, 150, 151, 153, 161, 163, 168, 169, 172, 205, 235, 237, 240, 241, 246, 247, 264, 274, 284, 285, 289, 290, 302, 310
- Terrestrial laser scanning (TLS), 3, 96, 205–217, 227

- Texture, 128–130, 151, 218, 221, 282, 306, 308, 311, 312, 317, 319
- Thermal infrared (TIR), 3, 244, 245
- 360° video, 169, 184, 187
- Topographic change, 221, 269, 278, 282, 285, 289, 290
- Topographic change error, 264, 281–292
- Topographic change uncertainty, 264, 281–292
- Traditional cultural properties (TCPs), 73, 75, 89
- Tree canopies, 130, 134, 136, 140, 144, 151
- Trees, 27, 30, 32, 59–61, 78, 82, 86, 96, 102, 106–108, 117–119, 130, 132, 137, 140, 144, 168, 208, 209, 214, 226, 266, 302, 307, 314–316
- U**
- UAVCoach, 254
- Underwater, 9
- University-National Oceanographic Laboratory System (UNOLS), 236, 253, 254
- Unmanned aerial systems, 124
- Unmanned aerial vehicle laser scanning (ULS), 204–206, 218, 220, 221, 224–228
- Unmanned Aircraft Systems Expert Group (UASEG), 251, 253
- Unoccupied aerial systems (UAS), 4, 9, 14–19, 22–25, 29–31, 33–35, 42–45, 48, 49, 61, 67, 76, 120, 204–223, 226–228, 236–241, 244, 247–249, 252–255
- Unpiloted aerial vehicles/unpiloted aerial systems (UAV/UAS), 4, 9, 14–18, 22–25, 29, 30, 33–35, 42, 43, 45, 48, 49, 61, 66, 67, 76, 160, 191, 204–224, 226, 236–239, 244, 247–250, 252–255
- US Department of Energy’s Atmospheric Radiation Measurement Program (DOE ARM), 238, 247
- US Forest Service (USFS), 7, 161
- US National Aeronautics and Space Administration (NASA), 30, 45, 160, 236, 251
- V**
- Vegetation, 7, 8, 10, 16, 18, 22, 28–31, 44, 59, 75, 77, 78, 82, 85–89, 95, 100, 117, 125, 129, 130, 140, 141, 144, 158–162, 169, 171–173, 175–177, 179, 181, 183, 186–191, 205, 206, 208, 211, 213–217, 222–228, 240, 242, 245, 249, 251, 252, 264–282, 284–292, 302–306, 308–310, 313, 314, 316–319, 322
- Vegetation burial, 281
- Vegetation density, 266–268, 271, 273, 274, 277, 284, 287, 288
- Vegetation filtering, 120, 205, 213–216, 223, 226, 228, 284–285, 291
- Vegetation zonation, 266
- Vertical take-off and landing (VTOL), 5, 18, 19
- W**
- Water depth, 306, 310, 311
- Wax Lake Deltas, 83–85
- WebODM, 99
- Well pads, 170, 171
- Wetlands, 74, 77–79, 82, 84, 86, 89, 97, 160
- Woody debris, 132, 152, 153, 274, 275, 286
- Workflow, 6, 14–36, 46, 99, 100, 134, 138, 140, 141, 160, 208, 209, 239, 243, 248, 249, 309